transactions of the ASME

journal of heat transfer

Published Quarterly by
The American Society of
Mechanical Engineers
Volume 98 • Series C • Number 4
NOVEMBER 1976

EDITORIAL STAFF
Editor, **J. J. JAKLITSCH, JR.**
Production Editor,
MARINA EVDOCHENKO
Editorial Prod. Asst., **BARBARA SIGNORELLI**

HEAT TRANSFER DIVISION
Chairman, **R. W. GRAHAM**
Secretary, **A. S. RATHBUN**
Senior Technical Editor, **E. M. SPARROW**
Technical Editor, **W. AUNG**
Technical Editor, **B. T. CHAO**
Technical Editor, **D. K. EDWARDS**
Technical Editor, **R. EICHHORN**
Technical Editor, **P. GRIFFITH**
Technical Editor, **J. S. LEE**
Technical Editor, **R. SIEGEL**

POLICY BOARD, COMMUNICATIONS
Chairman and Vice-President
S. P. KEZIOS

Members-at-Large
R. E. ABBOTT
I. BERMAN
R. C. DEAN, JR.
J. W. HOLL

Policy Board Representatives
Basic Engineering, **J. E. FOWLER**
General Engineering, **S. P. ROGACKI**
Industry, **J. E. ORTLOFF**
Power, **A. F. DUZY**
Research, **G. P. COOPER**
Codes and Stds., **P. M. BRISTER**
Nom. Com. Rep.,
A. R. CATHERON

Business Staff
345 E. 47th St.
New York, N. Y. 10017
212/752-6800
Mng. Dir., Com., **C. O. SANDERSON**

OFFICERS OF THE ASME
President, **E. C. MILLER**
Exec. Dir. & Sec'y, **ROGERS B. FINCH**
Treasurer, **J. D. PAULUS**

EDITED and PUBLISHED *quarterly at the* offices of The American Society of Mechanical Engineers, United Engineering Center, 345 E. 47th St., New York, N. Y. 10017. Cable address, "Mechaneer," New York, Second-class postage paid at New York, N. Y., and at additional mailing offices.

CHANGES OF ADDRESS must be received at Society headquarters seven weeks before they are to be effective. Please send old label and new address.

PRICES: To members, $25.00, annually; to nonmembers, $50.00. Single copies, $15.00 each. Add $1.50 for postage to countries outside the United States and Canada.

STATEMENT from By-Laws. The Society shall not be responsible for statements or opinions advanced in papers or . . . printed in its publications (B 13, Par. 4).

COPYRIGHT © 1976 by the American Society of Mechanical Engineers. Reprints from this publication may be made on conditions that full credit be given the TRANSACTIONS OF THE ASME, SERIES C—JOURNAL OF HEAT TRANSFER, and the author and date of publication stated.

INDEXED by the Engineering Index, Inc.

TECHNICAL NOTES

(Contents continued on page 563)

Downloaded 04 Feb 2011 to 194.85.80.107. Redistribution subject to ASME license or copyright; see http://www.asme.org/terms/Terms_Use.cfm

CONTENTS (CONTINUED)

DISCUSSION

ERRATUM

R. R. Gilpin
Assoc. Professor.

B. K. Wong
Graduate Student.

Department of Mechanical Engineering,
University of Alberta,
Edmonton, Alberta, Canada

"Heat-Valve" Effects in the Ground Thermal Regime

A one-dimensional model of a freezing and thawing ground with a seasonally varying surface cover was analyzed. Analytical and numerical techniques were used primarily to study the factors that produce differences between the yearly means of the air and ground temperatures. It was shown that the variation of the surface cover characteristics in phase with the annual air temperature wave can generate the heat-valve effect which is responsible for raising the average ground temperature above the average air temperature. This temperature difference was, however, very sensitive to changes to the surface cover properties indicating how disturbances to the surface cover could cause melting of a permafrost soil.

Introduction

The construction of pipelines in permafrost regions has recently increased interest in the prediction of the thermal regime in the ground. Accurate predictions are particularly important for permafrost soils with high ice contents since thawing of such a soil results in a drastic reduction in its bearing strength. Gold and Lachenbruch [1][1] have recently reviewed the state of knowledge concerning the ground thermal regime and some of the phenomena that are observed.

One interesting observation that relates to the prediction of ground temperatures is that the mean ground temperatures tend to be consistently 3-4°C warmer than mean air temperatures at any location [1-3]. Here mean temperatures are defined as the temperatures averaged over a year, that is the yearly means. Since considerable variations in the mean ground temperature have been observed to exist from one place to another in an area of the same mean air temperature [1, 4], the air temperature must not be the only controlling parameter. The variability of the ground temperature is also illustrated by the fact that the zone of discontinuous permafrost, that is the region in which ground temperatures can be either above or below 0°C, exists over a range of mean air temperatures from −1.0 to −9.5°C. The difference between the mean air and the mean ground temperatures and its variability with location has been attributed to a number of factors including the seasonal variation of the thermal resistance of the surface cover, phase change in the ground and the radiative fluxes incident on the surface [1, 5, 6]. The sensitivity of the ground temperature to changes in the surface cover has been graphically illustrated by the fact that in some areas construction activity which disturbed the cover has caused thawing of a previously permafrost soil [7]. The effect of the surface cover is often described as being that of a heat-valve. In the winter the thermal insulation at the ground surface is provided by a layer of snow 20–80-cm thick while in the summer the only thermal insulation on the ground is provided by several centimeters of vegetation cover. Since the winter snow cover is a much better thermal insulator than the summer vegetation a heat-valve effect is produced at the ground surface. That is, in the winter when heat is leaving the ground the valve closes and in the summer when heat is flowing to the ground the valve opens.

To quantify this effect a simple model of the ground and its surface cover will be analyzed. This model will be used to illustrate the role of a seasonally varying surface cover coupled with phase change in the ground in determining the mean ground temperature and the amplitude of temperature variation at the ground surface.

The Model

Fig. 1 shows the model that will be studied. The model is one-dimensional and includes two layers. The surface layer is introduced to approximate the effects of a snow cover in winter and a vegetation cover in summer. It is assumed that it has negligible heat capacity and a seasonally dependent thermal resistance. The net energy flux at its upper boundary is approximated by a convective type boundary condition as proposed by Scott [6] and Wheeler [8]. This approximation assumes that the energy flux equations applicable at the surface can be linearized such that the net energy flow between the environment and the surface, q_a, can be written as

$$q_a = h_0(T_s - T_{ea})$$

where h_0 is an overall energy transfer coefficient including the contributions due to radiation, convection of sensible heat and mass

---

[1] Numbers in brackets designate References at end of paper.

Contributed by the Heat Transfer Division for publication in the JOURNAL OF HEAT TRANSFER. Manuscript received by the Heat Transfer Division June 21, 1976.

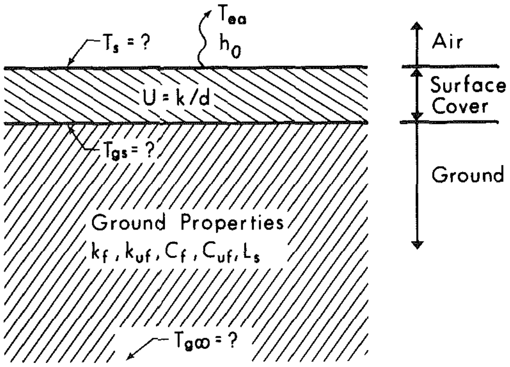

Fig. 1 The model of the ground and its surface cover used in the analysis

transfer, and T_{ea} is an equivalent air temperature which accounts for radiative fluxes received by the surface. In the terminology of building heat transfer this equivalent air temperature would be the more familiar Sol-Air Temperature (S.A.T.). It would be estimated in the same way using the net radiative flux, R_{net}, received by the ground. That is

$$T_{ea} = T_a + R_{\text{net}}/h_0$$

In this paper it will be assumed that the equivalent air temperature is a known function of time during the year and ground temperatures will be related to it.

The resistance of the surface cover layer can be combined with the heat transfer coefficient at its upper surface to give an overall heat transfer factor, U, for the transport of heat from the ground to the atmosphere. The heat flux to the ground is therefore given by

$$q_g = U(T_{gs} - T_{ea})$$

where $U^{-1} = d/k + 1/h_0$. The temperature T_{gs} is the temperature at the ground surface, that is, at the interface between the ground and the vegetation cover. In practice for some highly organic soils this interface may not be easy to define, however, for the purposes of this model it is the interface between the regions where the effect of heat capacity is negligible (the surface cover) and where it is not negligible (the ground). The heat transfer coefficient between a surface and the atmosphere, h_0, is typically of the order of 25 W/m^2/°C. The thermal conductivity of dry moss is approximately 0.06 W/m-°C. Therefore with even 2 cm of moss $k/d \ll h_0$ and the overall U-factor is essentially the U-factor of the surface cover. The overall U-factor will therefore be referred to as the surface cover U-factor in this paper. The equivalent air temperature and the U-factor will both be approximated by harmonic functions with periods of one year but not necessarily in phase with one another. The boundary condition applicable at the surface of the ground is, therefore,

$$-k\frac{\partial T}{\partial x} = (\overline{U} + \Delta U \sin \omega(t + \phi_U)) \times$$
$$(\overline{T}_{ea} + \Delta T_{ea} \sin \omega(t + \phi_T) - T); \quad x = 0 \tag{1}$$

In the ground, freezing of the soil moisture will be assumed to occur at a discrete temperature, T_f. Properties will also change discontinuously across this temperature. The equations of heat conduction and energy conservation then give an expression for the time rate of change of enthalpy

$$\frac{\partial h}{\partial t} = k\frac{\partial^2 T}{\partial x^2}; \quad k = k_{uf}; \quad T > T_f$$
$$k = k_f; \quad T < T_f \tag{2}$$

The enthalpy, h, can be related to temperature by the nonlinear expression

$$h = \rho C_f(T - T_f); \quad T < T_f$$
$$h = \rho C_{uf}(T - T_f) + \rho L_s; \quad T > T_f \tag{3}$$

where the enthalpy is defined as zero for the soil in its frozen state at $T = T_f$.

The boundary condition applied deep in the ground is that the geothermal gradient is negligibly small. That is

$$\frac{\partial T}{\partial x} = 0; \quad x \to \infty$$

The condition that was applied on the time coordinate throughout this problem is that the dependent variables must be periodic with a period of one year.

In the nondimensional variables defined in the Nomenclature equations (1), (2) and (3) become

$$\frac{\partial \psi}{\partial \tau} = R_k \frac{\partial^2 \theta}{\partial \zeta^2} \tag{4}$$

$$\psi = (\theta - \theta^*); \quad \theta < \theta^*$$

Nomenclature

d = depth of surface cover
h = enthalpy of ground
h_0 = overall heat transfer coefficient
k = thermal conductivity
ℓ = characteristic depth = $(2\pi k_f/(\omega\rho C_f))^{1/2}$
m_s = soil moisture content percent dry weight
n = spacial index in difference equations
p = transformed time variable
q_a = heat flux from air to surface
q_g = heat flux from surface into ground
t = time
t_c = time in one year
z = parameter p on the complex plane
B_g = surface cover parameter = $\ell\overline{U}/(k_f R_k)$
C = heat capacity of the ground
H = characteristic enthalpy = $\rho C_f \Delta T_{ea}$
L_s = latent heat of fusion of soil
R_k = ratio of conductivities
= k_{uf}/k_f, $T > T_f$
= 1, $T < T_f$
Sf = Stefan number for ground = $C_f\Delta T_{ea}/L_s$
T = temperature
$T_{\max}$ = maximum ground surface temperature
$T_{\min}$ = minimum ground surface temperature
U = U-factor of surface cover = k/d
ϵ = amplitude parameter = $\Delta U/\overline{U}$
ζ = nondimensional depth in ground = x/ℓ
ν = time index in difference equations
ρ = soil density
τ = nondimensional time = $\omega(t + \phi_T)/2\pi$
ϕ = phase angle between temperature and U-factor = $\omega/2\pi\ (\phi_U - \phi_T)$
ϕ_T = phase angle of temperature variation
ϕ_U = phase angle of U-factor variation
ψ = nondimensional enthalpy = h/H
ω = frequence of temperature wave = $2\pi/t_c$
Δ = prefix to indicate amplitude of a variable
θ = nondimensional temperature = $(T - \overline{T}_{ea})/\Delta T_{ea}$
θ^* = freezing temperature = $(T_f - \overline{T}_{ea})/\Delta T_{ea}$

Subscripts

a = actual air temperature
ea = equivalent air temperature
f = freezing or frozen state
uf = unfrozen state
s = surface between air and surface cover
gs = interface between surface cover and ground
$g\infty$ = ground below active layer
0, 1, 2, etc. = order of approximation
$\overline{A}$ = used to indicate average of a parameter, A
$\tilde{A}$ = Laplace transform of a parameter, A

$$\psi = R_c(\theta - \theta^*) + 1/\mathrm{Sf}; \quad \theta > \theta^* \tag{5}$$

with the boundary conditions

$$-\frac{\partial \theta}{\partial \zeta} = (B_g/R_k)(1 + \epsilon \sin 2\pi(\tau + \phi))(\sin 2\pi\tau - \theta); \quad \zeta = 0 \tag{6}$$

and

$$\frac{\partial \theta}{\partial \zeta} = 0; \quad \zeta = \infty$$

In these equations the parameter B_g represents the ratio of the thermal conductance of the surface cover to an effective thermal conductance of the ground. It is therefore equivalent to a Biot number for the surface cover. When this parameter is large the effect of the surface cover will be negligible. In that case the temperature at the ground surface will closely follow the equivalent air temperature. Alternatively when B_g is small the surface cover is a very good insulator and the amplitude of the temperature wave at the ground surface would be much smaller than the amplitude of variation in the equivalent air temperature. The parameters ϵ and ϕ represent, respectively, the amplitude and the phase of the variation in the insulating value of the surface cover. Parameters Sf, R_k, and R_c are determined by the properties of the soil and in particular the soil moisture content. The Stefan number, Sf, which represents the relative importance of the sensible and latent heats of the soil is equivalent to the "fusion parameter" used in some depth of thaw calculations [9]. The final parameter, θ^*, is the "climate" parameter in this problem. That is, if the average environmental temperature that the ground sees, $\overline{T}_{ea}$, is greater than the freezing temperature, T_f, then θ^* is negative. Alternatively, positive values of θ^* indicate a colder climate where the average temperature is less than freezing. θ^* has been normalized by the amplitude of the harmonic temperature wave, ΔT_{ea}, so that a value of $\theta^* = 1$ corresponds to a climate in which the peak summer temperature, $\overline{T}_{ea} + \Delta T_{ea}$, is just equal to the freezing temperature. Geographically this condition is approached in the Arctic Islands where the mean July temperature is only 4°C. In the opposite limit values of $\theta^* < -1$ correspond to climates where freezing does not occur even in midwinter.

In this problem the heat-valve effect of the surface cover is contained in the product of U-factor of the surface cover and the temperature difference across it in equation (6). A second heat-valve effect occurs in the active layer of the ground (that is the layer of ground that undergoes phase change during the seasonal cycle of temperatures). This effect, which is the result of the fact that the conductivities of the frozen and unfrozen soil are different, produces a difference between the mean temperature at the ground surface and mean temperature below the active layer. This temperature difference which was examined in detail in reference [10] is not generally very large. Therefore, in this paper only the mean ground surface temperature will be calculated with the assumption that the mean ground temperature below the active layer will be close to this value.

The basic effects of the seasonally varying surface cover can be demonstrated for the problem of periodic heat flow to a semi-infinite medium without phase change. This problem lends itself to an analytic solution when the amplitude, ϵ, of the variation in surface cover properties is small. The results obtained from this calculation will also be used as a check for a finite difference calculation which will include phase change and a large amplitude of surface cover variation.

The equations for the case of no phase change in the ground can be obtained by considering a soil with no moisture content. In that case the properties of the frozen and unfrozen soil are the same and the latent heat of fusion is zero giving $R_k = 1$, $R_c = 1$ and $1/\mathrm{Sf} = 0$. Using these values in equations (4)–(6) and substituting equation (5) in equation (4) give the appropriate equations for this problem.

$$\frac{\partial \theta}{\partial \tau} = \frac{\partial^2 \theta}{\partial \zeta^2} \tag{7}$$

$$-\frac{\partial \theta}{\partial \zeta} = B_g(1 + \epsilon \sin 2\pi(\tau + \phi)(\sin 2\pi\tau - \theta); \quad \zeta = 0 \tag{8}$$

and

$$\frac{\partial \theta}{\partial \zeta} = 0; \quad \zeta = \infty$$

There are now only three parameters involved—B_g, ϵ and ϕ. The parameter ϵ in equation (8) is physically limited to the range 0–1. Therefore, the expansion of the solution for θ in terms of a series in ϵ, thus

$$\theta = \theta_0 + \epsilon\theta_1 + \epsilon^2\theta_2 \ldots \tag{9}$$

might be expected to give a good estimate of θ for most values of ϵ. Substituting equation (9) in equations (7) and (8) and selecting terms of equal order gives the appropriate equations for θ_0, θ_1, etc. The equations to be solved for θ_0 are

$$\frac{\partial \theta_0}{\partial \tau} = \frac{\partial^2 \theta_0}{\partial \zeta^2}$$

$$-\frac{1}{B_g}\frac{\partial \theta_0}{\partial \zeta} = \sin 2\pi\tau - \theta_0; \quad \zeta = 0$$

and

$$\frac{\partial \theta_0}{\partial \zeta} = 0; \quad \zeta = \infty$$

The solution for θ_0 which is the solution for a constant property surface cover will follow that used by Lachenbruck [11] for periodic heat flow in a stratified medium. Taking the Laplace transform of these equations and solving for the transformed temperature variable θ_0 gives,

$$\tilde{\theta}_0 = \frac{2\pi B_g}{(p^2 + (2\pi)^2)(B_g + \sqrt{p})} e^{-\sqrt{p}\zeta} \tag{10}$$

Since the only part of the solution of interest is that it represents the steady periodic state the initial condition used is not important. For the transform in equation (10) $\theta(\zeta) = 0$ at $t = 0$ was assumed. The residuals of equation (10) at $p = \pm 2\pi i$ are responsible for the desired periodic components of the solution. Solving for these residuals gives

$$\theta_0 = \{A \sin 2\pi(\tau - \zeta/\sqrt{4\pi}) - B \cos 2\pi(\tau - \zeta/\sqrt{4\pi})\} e^{-\sqrt{\pi}\zeta} \tag{11}$$

where

$$A = \frac{B_g(B_g + \sqrt{\pi})}{((B_g + \sqrt{\pi})^2 + \pi)}$$

$$B = \frac{B_g\sqrt{\pi}}{((B_g + \sqrt{\pi})^2 + \pi)}$$

The amplitude of θ_0 at the ground surface, $\zeta = 0$, is equal to

$$\Delta\theta_{gs} = \sqrt{A^2 + B^2} = B_g((B_g + \sqrt{\pi})^2 + \pi)^{-1/2} \tag{12}$$

which is the same as that obtained by Lachenbruck [11] in the limit when the top strata is assumed to have negligible heat capacity.

The equations to be solved for θ_1 are

$$\frac{\partial \theta_1}{\partial \tau} = \frac{\partial^2 \theta_1}{\partial \zeta^2} \tag{13}$$

$$-\frac{1}{B_g}\frac{\partial \theta_1}{\partial \zeta} = -\theta_1 + \sin 2\pi(\tau + \phi)\sin 2\pi\tau - \theta_0 \sin 2\pi(\tau + \phi);$$

$$\zeta = 0 \tag{14}$$

$$\frac{\partial \theta_1}{\partial \zeta} = 0, \quad \zeta = \infty \tag{15}$$

Using the solution for θ_0 at $\zeta = 0$ in equation (11) and taking the Laplace transform of these equations gives the transformed temperature variable, $\tilde{\theta}_1$.

$$\begin{aligned}\tilde{\theta}_1 = \{&(\cos 2\pi\phi(1 - A) + B \sin 2\pi\phi)\, 8\pi^2/p \\ &+ (\sin 2\pi\phi(1 - A) + B \cos 2\pi\phi)\, 2\pi \\ &+ \sin 2\pi\phi\, Bp\}\, e^{\sqrt{p}\zeta}\, ((4\pi)^2 + p^2)^{-1} B_g(B_g + \sqrt{p})^{-1}\end{aligned} \tag{16}$$

The function $\tilde{\theta}_1(x, z)$ on the complex plane, z, has poles at $z = \pm 4\pi i$

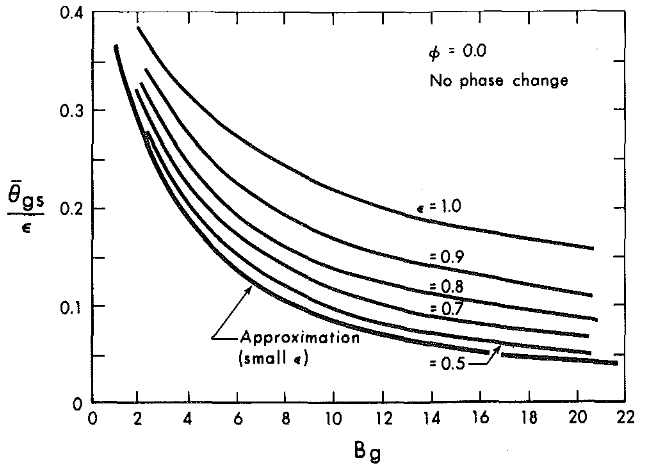

Fig. 2 The effects on the mean temperature difference produced by the insulating value of the surface cover and the amplitude of its seasonal variation

and a branch point at $z = 0$. Its inversion to the real t plane can be performed by integration around a semicircular contour with a branch cut along the negative real axis (see Lauchenbruch [11]). Using such a contour it can be shown that

$$\theta_1(x, t) = \sum \text{Res}(\pm 4\pi i) + I_1 + I_2$$

where

$$I_1 = \frac{1}{2\pi i} \int_0^{\infty} e^{-tr} [\bar{\theta}_1(x, re^{-i\pi}) - \bar{\theta}(x, re^{i\pi})] dr$$

and

$$I_2 = \frac{1}{2\pi i} \lim_{\rho \to 0} \int_{c_\rho} e^{tz} \bar{\theta}_1(x, z) dz \tag{17}$$

The residuals at $\pm 4\pi i$ give a component of the harmonic ground temperature variation which has a frequence of twice the annual ground temperature wave. This harmonic when combined with the fundamental harmonic in equation (11) produces an asymmetry of the temperature wave about its mean value. It does not however change the mean value since the average of these harmonics over a yearly cycle is zero.

Evaluating I_1 for $t \to \infty$ shows that this term decays exponentially with time for large times. It, therefore, represents transient temperatures that result from the arbitrary choice of the initial ground temperature distribution and is of no interest in this calculation. I_2 is the integral from $-\pi$ to $+\pi$ around a small circle, c_ρ, of radius ρ encompassing the origin. Inserting the expression for $\bar{\theta}_1$ into this integral and taking its limit $\rho \to 0$ inside the integral the value of I_2 can be evaluated.

$$I_2 = [(1 - A) \cos 2\pi\phi + B \sin 2\pi\phi]/2$$

Referring to equation (9) the average value of θ to first order in ϵ can now be calculated. The average of θ_0 in equation (11) is zero and the only term to contribute to $\bar{\theta}_1$ is the constant value I_2. Substituting the expressions for A and B into I_2 gives

$$\bar{\theta} = \frac{\epsilon}{2} \left[\frac{(B_g\sqrt{\pi} + 2\pi) \cos 2\pi\phi + B_g\sqrt{\pi} \sin 2\pi\phi}{(B_g + \sqrt{\pi})^2 + \pi} \right] \tag{18}$$

It will also be noted that the average ground temperature is not a function of depth in the ground. This is the expected result when no phase change occurs in the ground. The average ground surface temperature $\overline{T}_{gs}$ can therefore be calculated directly from equation (18) knowing that

$$(\overline{T}_{gs} - \overline{T}_{ea})/\Delta T_{ea} = \bar{\theta}_{gs} = \bar{\theta}$$

To study the effects of phase change and of large amplitude variations in surface cover equations (4)–(6) were solved numerically. The model that results from using these equations is called the enthalpy model, the rationale of which has been discussed by Shamsundar and Sparrow [12]. The important feature of this model is that the enthalpy rather than the position of the fusion front is used as the dependent variable that determines where phase change is occurring.

For the numerical calculations the top 8 m of the ground was divided into forty equally spaced depth intervals. This depth was chosen so that the calculated temperature fluctuation at the bottom node was insignificant.

A straight forward Euler scheme was used for time stepping the solution ahead. Equation (4) in different form becomes

$$\psi_n{}^{\nu+1} = \psi_n{}^{\nu} + \left[R_k \frac{\Delta\theta}{\Delta\zeta}\bigg|_- + R_k \frac{\Delta\theta}{\Delta\zeta}\bigg|_+ \right] \frac{\Delta\tau}{\Delta\zeta} \tag{19}$$

where ν is the time index and n is the spacial index. In the interior of the nodal grid $\Delta\theta/\Delta\zeta|_- = (\theta_{n-1}{}^{\nu} - \theta_n{}^{\nu})/\Delta\zeta$, $\Delta\theta/\Delta\zeta|_+ = (\theta_{n+1}{}^{\nu} - \theta_n{}^{\nu})/\Delta\zeta$, and R_k, which is the temperature dependent conductivity ratio, is chosen on the basis of the average value of θ in the appropriate node interval. For the node at the ground surface $R_k\ \Delta\theta/\Delta\zeta|_-$ must be replaced by the value of $R_k\ \partial\theta/\partial\zeta$ calculated from the boundary condition in equation (6). Similarly, $\Delta\theta/\Delta\zeta|_+$ is set equal to zero for the bottom node of the grid.

For known values of ψ and θ at a time index ν a new set of values of ψ at time $\nu + 1$ can thus be calculated from equation (19) and its boundary conditions. Since θ is a unique function of ψ (the reverse is not true) equation (5) can then be used to calculate values of θ at time $\nu + 1$. This completes one iteration and gives all the starting values required for the next. To start the calculation an arbitrary initial thermal state of the ground must be chosen. Usually, a uniform temperature equal to the mean equivalent air temperature, that is $\theta = 0$, was used. The solution was then stepped ahead through enough yearly cycles so that the ground temperatures reached a steady periodic state. Time steps of the order of 2×10^{-4} years were required to maintain stability of the solution.

For most conditions the ground temperatures were periodic within 0.5°C after five cycles. For some cases where the ground temperature was near 0°C much longer times were required, 15–20 cycles, before the effects of the initial conditions disappeared. For each numerical calculation the main outputs that were of interest were the average temperature of the node at the ground surface as well as its maximum and minimum temperatures during the last yearly cycle in the calculation.

Results

The phase angle ϕ in equation (18), as defined in the notation, is the difference in parts of a year between the phase of the U-factor variation and that of the equivalent air temperature variation. Therefore for $\phi = 0$ the minimum winter temperature coincides with the minimum surface heat conductance. This would be the normal situation since the snow cover in winter normally has a much lower heat conductance than the summer vegetation. If, however, the snow cover was being removed or compacted by some means it is possible that the opposite situation may occur. In this case $\phi = 0.5$. For most of the following results $\phi = 0$ will be used although with a simple change of sign the results equally well apply to the case of $\phi = 0.5$.

Fig. 2 summarizes the effects of surface cover variations on the mean ground temperature in the absence of phase change. In the figure $\bar{\theta}_{gs}/\epsilon$ represents the mean temperature difference between the ground surface and the air normalized by the amplitude of the equivalent air temperature wave, ΔT_{ea}, and the amplitude of the surface cover variation, ϵ. Equation (17) suggests that this parameter should be a unique function of B_g for small ϵ and $\phi = 0$. The curve marked "approximation" in Fig. 2 is the result calculated from equation (17). To compare this analytic result with the results of the finite difference calculations the computer simulations were run at about 100 different combinations of B_g and ϵ in the ranges $0 < \epsilon < 1$ and $1 < B_g < 20$. The numerically calculated mean ground temperatures were normalized as in Fig. 2 and curves fitted to the results. A check of the accuracy of the numerical scheme used in the computer simulation was provided by the fact that the numerically calculated results were within 10 percent of the first order analytic results for ϵ less than 0.5. The numerically obtained curves for ϵ in the range 0.5–1.0 are shown in Fig. 2 along with the approximation for small ϵ.

The physical magnitude of the mean temperature difference can now be estimated from Fig. 2 for some typical field conditions. The typical surface cover for the zone of discontinuous permafrost was considered to consist of an average of 6 cm of dry moss in summer and an average of 40 cm of settled snow in the winter [4, 13]. Using these estimated surface cover depths and the thermal conductivities given at the bottom of Table 2 the corresponding mean U-factors during the summer and winter seasons can be calculated. The procedure discussed in reference [10] for obtaining the best fit sine wave for this variation in U-factor then gives $\overline{U} = 0.6$ and $\epsilon = 0.65$ for the case considered. The soil properties considered typical [2] were those for a fine grained soil with a moisture content of 30 percent of dry weight (Table 1).

Table 1 Soil properties for a fine grained soil dry density 1200 kg/m^3 and moisture content of 30 percent of dry weight [9]

$k_f = 1.7$ Watts/m-°C
$k_{uf} = 1.1$ Watts/m-°C
$\rho C_f = 1.6 \times 10^6$ Joules/m^3-°C
$\rho C_{uf} = 2.4 \times 10^6$ Joules/m^3-°C
$\rho L_s = 120 \times 10^6$ Joules/m^3

The results in Fig. 2 do not account for the effects of phase change or the changes in soil properties that result. Therefore to estimate the mean ground temperature from this figure the averages of the frozen and unfrozen properties were used. With these surface cover and soil properties, the value of B_g was calculated as 2.05. These values in Fig. 2 give $(\overline{T}_{gs} - \overline{T}_{ea})/\Delta T_{ea} = 0.19$. For a northern climate $\Delta T_{ea} = 22$°C is typical. It follows then that for these conditions the average ground surface temperature will be about 4.2°C warmer than the mean equivalent air temperature.

In Fig. 3 the effects of the parameters B_g and ϵ on the maximum and minimum temperatures at the ground surface are shown. In this figure the "approximate" curves are the temperature limits obtained from equation (12). These curves, which represent the amplitude of the temperature wave at the ground surface when no seasonal variation in the surface cover occurs, are the same as those obtained by Lachenbauch [11]. As was the case for the mean temperature calculations, the numerically calculated results agreed with the approximate curves for values of ϵ less than 0.5. The dashed curves in Fig. 3 for values of ϵ greater than 0.5 were again obtained by fitting curves to the numerically calculated results. They show that a large amplitude variation in surface cover produces an additional decrease in the amplitude of the surface temperature wave over and above that calculated by Lachenbauch for the equivalent constant property surface cover. An asymmetry in the ground surface variation about its average value is also apparent in Fig. 3.

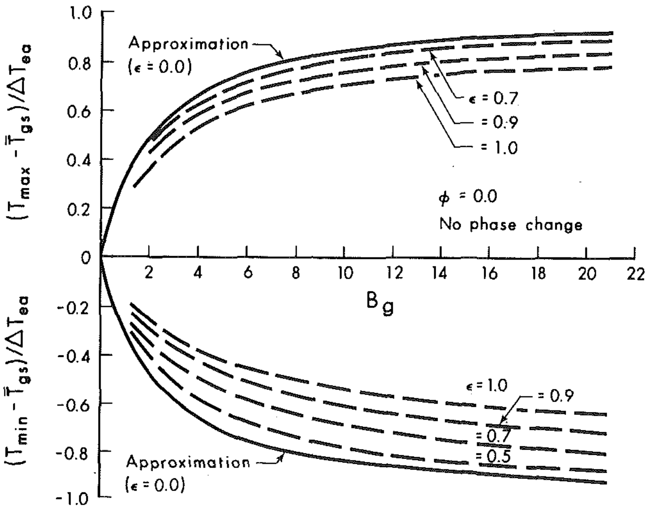

Fig. 3 The effects on the amplitude of the ground surface temperature wave produced by variations in the surface cover

The influence of phase change on these results will be illustrated using the typical field conditions described previously. In Fig. 4 the maximum, mean, and minimum temperatures experienced at the ground surface are shown for these conditions. The dashed lines are the results predicted for the typical field conditions when phase change was not considered. The solid curves were obtained from numerical calculations including the effects of phase change. The first observation to be made is that phase change produces a nonlinear relationship between the mean ground surface temperature and the equivalent air temperature and the maximum effect of the phase change occurs when the mean ground temperature is near the freezing point. When the effects of phase change were neglected the mean ground surface temperature was found to be 4.2°C warmer than the equivalent air temperature (dashed line). With phase change the mean ground temperature is raised an additional 2.2°C when the ground is near 0°C. As a result the average ground temperature is above freezing; that is there is no permafrost, for this particular combination of surface cover and soil properties unless the equivalent air temperature is less than −6.4°C.

The other major effect of phase change is to decrease the amplitude of the temperature wave at the ground surface. This effect is generated by the fact that the minimum ground temperature tends to stay near the freezing point for mean ground temperatures above freezing and the maximum ground temperature stays near freezing for mean temperatures below freezing. This behavior occurs even without a variation of surface cover properties, however with the surface cover variation an asymmetry in the effect occurs. That is, for the type of surface cover variations considered the minimum ground temperature is increased more than the maximum ground temperature is decreased. This is of course consistent with the fact that the mean temperature increases due to these surface cover variations. One interesting effect of phase change is that the minimum ground temperature for a permafrost soil will be much colder than the minimum ground temperature for a nonpermafrost soil even though their mean temperatures may only be a few degrees different. This effect appears in Fig. 4 as a very sharp drop in minimum ground temperatures at an equivalent air temperature of about −7°C.

The results in Fig. 4 were for one particular set of surface cover conditions. To illustrate the sensitivity of the mean ground temperature to changes in the surface cover Table 2 gives the calculated ground temperatures for various surface covers at three values of the

Table 2 Calculated ground temperatures

Case No.	Mean Summer Surface Cover	Mean Winter Surface Cover	Mean Ground Surface Temperature $\overline{T}_{ea}$=-3.0	$\overline{T}_{ea}$=-7.2	$\overline{T}_{ea}$=-10.5
1	6 cm Dry moss	40 cm Settled Snow	2.6	-1.0	-5.4
2	Same as No. 1	80 cm Settled Snow	5.9	2.3	0.3
3	Same as No. 1	20 cm Settled Snow	-0.2	-4.9	-8.6
4	3 cm Dry moss	Same as No. 1	4.4	1.8	-0.3
5	Same as No. 4	10 cm Packed Snow	-3.9	-8.0	-11.1

k(Dry Moss) = 0.06 Watts/m-°C (Ref. 9); k(Settled Snow) = 0.12 Watts/m-°C (Ref. 14); k(Packed Snow) = 0.30 Watts/m-°C (Ref. 14)

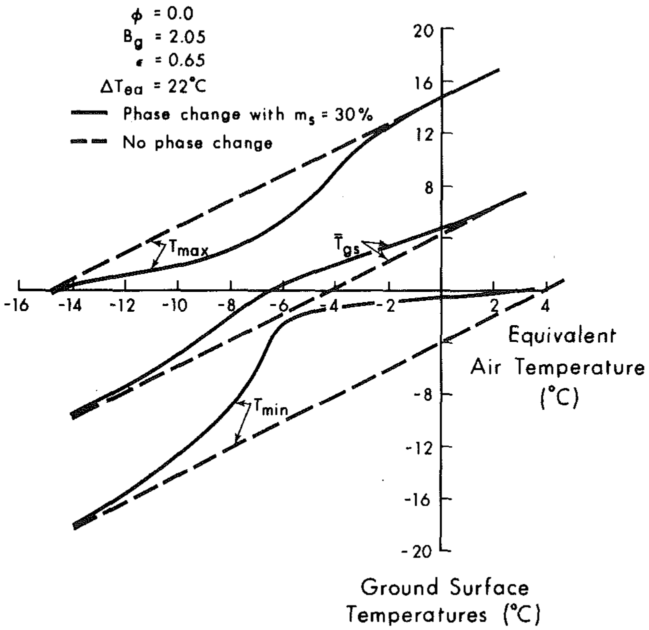

Fig. 4 The relationship between the ground surface temperatures and the equivalent air temperature for a typical surface cover

mean equivalent air temperature (−3.0, −7.2, and −10.5°C). These values are estimated to correspond, respectively, to the southern fringe, the middle and the northern limit of the discontinuous permafrost zone. Case 1 uses the "typical" surface cover conditions used in Fig. 4. In Cases 2–4 the effects of factor of two changes in the summer and winter U-factors are shown. These estimates were chosen to represent the possible range of surface cover properties that may be encountered for naturally occurring surfaces. It will be noted that at all three locations permafrost may or may not exist depending on the properties of the surface cover. This is consistent with the fact that the zone of discontinuous permafrost extends over an air temperature range of about 8.5°C. A comparison of the differences between the calculated ground temperatures in Case 1 and those in Cases 2–4 shows that a factor of two change in the surface cover properties can produce changes of from 1.8 to 5.7°C in the mean ground temperature. It is therefore apparent that the sensitivity of the ground temperature to surface cover changes is dependent on the equivalent air temperature and the type of change involved. However, it may be reasonable to use the average sensitivity of 3.5°C for a factor of two change in surface cover as an approximate guide for estimation purposes. A comparison of Case 1 and Case 4 at an equivalent air temperature of −7.2°C shows how a disturbance that reduces the thickness of the vegetation cover in summer could result in the melting of a permafrost soil. The ground temperature which was −1.0°C in Case 1 was raised above freezing (1.8°C) in Case 4 just by decreasing the summer vegetation cover from 6 to 3 cm. It has been suggested that in areas where summer vegetation is likely to be disturbed by construction activity, compaction of the winter snow cover would be a good method of insuring that a permafrost soil stayed frozen. Case 5 indicated that this measure could be very effective in lowering the mean ground temperature and thus maintaining the ground in a permafrost state.

Conclusions

In the ground thermal regime, differences between the mean air temperature and mean ground temperature can be produced by a number of phenomena. Seasonal variations in ground surface cover is one of the main factors. The difference in mean temperatures is the result of the fact that variations in the thermal characteristics of the surface cover occur in phase with variations in the temperature gradients across the surface cover thus producing a heat-valve effect. It was found that the effect of phase change occurring in the ground was to amplify the heat-valve effect when the mean ground temperature was near the freezing point. This produced a nonlinear relationship between the mean ground temperature and the mean equivalent air temperature.

It was also demonstrated that changes by a factor of two in the thermal characteristics of the summer or winter surface cover could produce changes in the mean ground temperature of 3.5°C on the average. The exact amount of the change depended on the location and type of change involved. This means that disturbances to the surface cover which produce such changes in its thermal characteristics could cause melting of a permafrost soil if its original temperature was within abut 3.5°C of the freezing point. Also, since the ground temperature is very sensitive to the characteristics of the ground surface cover, the accurate prediction of ground temperatures would require very good data on the properties of the surface cover layer and their seasonal variations.

Prediction of ground temperatures would also require a knowledge of the relationship between the equivalent and the actual air temperatures. In the model studied the equivalent air temperature was assumed to be known and the ground temperature was calculated relative to it. To complete this model investigations are continuing into methods of calculating the equivalent air temperature from the balance of energy fluxes at the air-surface cover interface.

Acknowledgments

This work was funded by the National Research Council of Canada.

References

1 Gold, L. W., and Lachenbruck, A. H., "Thermal Conditions in Permafrost: The North American Contribution to the Second International Conference," National Academy of Science Publication, Yakutsk, Siberia, 1973.

2 Brown, R. J. E., *Permafrost in Canada*, University of Toronto Press, Toronto, 1970, p. 10.

3 McCormick, G., "Northern Canada: Surface Temperatures," *The Northern Engineer*, Vol. 4, No. 1, 1972, pp. 19–20.

4 Judge, A. S., "The Thermal Regime of the MacKenzie Valley: Observations of the Natural State," Task Force on Northern Oil Development, Report No. 73-38, Information Canada Cat. No. R72-11973, Ottawa, Canada, 1973.

5 Gilpin, R. R., and Wong, B. K., "A Study of Some Factors that Influence Ground Temperature," *Proceedings of the Fourth Canadian Congress of Applied Mechanics*, Montreal, 1973, pp. 771–772.

6 Scott, R. F., "Predicted Depth of Freeze or Thaw by Climatological Analysis of Cumulative Heat Flow," U.S. Army Cold Regions Research and Engineering Laboratory Technical Report 195, 1969.

7 Bliss, L. C., and Wein, R. W., "Changes to the Active Layer Caused by Surface Disturbance," *Proceedings, Conference on Permafrost Active Layer*, Technical Memo 103, National Research Council of Canada, Ottawa, 1971, pp. 37–47.

8 Wheeler, J. A., "Simulation of Heat Transfer From a Warm Pipe Buried in Permafrost," presented at the 24th National Meeting of AIChE, New Orleans, Mar. 1973.

9 Sanger, F. J., "Degree-Days and Heat Conduction in Soils," *Proceedings, International Permafrost Conference*, Lafayette, Ind., National Academy of Sciences, National Research Council Publ. No. 1287, 1963, pp. 253–262.

10 Gilpin, R. R., and Wong, B. K., "The Ground Temperature Regime and Its Relationship to Soil Properties and Ground Surface Cover," ASME Paper No. 75-WA/HT-98, 1975.

11 Lachenbruck, A. H., "Periodic Heat Flow in a Stratified Medium With Application to Permafrost Problems," *Experimental and Theoretical Geophysics*, Geological Survey Bulletin 1083-A, Washington, D. C., 1959.

12 Shamsundar, N., and Sparrow, E. M., "Analysis of Multidimensional Conduction Phase Change Via the Enthalpy Model," JOURNAL OF HEAT TRANSFER, TRANS. ASME, Series C, Vol. 97, 1975, pp. 333–340.

13 Potter, J. G., "Snow Cover," Department of Transport, Meteorological Branch, Toronto, 1965.

14 Mellor, M., "Review of the Properties of Snow and Ice," U.S. Corps of Engineers, SIPRE Report No. 4, Hanover, N. H., 1951.

G. Comini[1]
Professor.

S. Del Giudice[1]
Asst. Professor.

Istituto di Fisica Tecnica,
Facoltà di Ingegneria dell' Università di Padova,
Padova, Italy

Thermal Aspects of Cryosurgery

Tissue reactions to cryosurgical procedures depend on temperature variations and on rates of temperature variations induced by freezing probes. In this paper thermal responses of biological systems undergoing freezing are obtained through the application of the finite element method to the solution of the nonlinear bio-equation. This model allows realistic predictions of isotherm fields and of rates of freezing in practically any cryosurgical procedure.

Introduction

Certain well known phenomena, concerning the destructive effects of freezing on living tissues, account for the broad applicability of modern cryogenic surgery in virtually all of the surgical specialities [1].[2]

The employment of heat sinks at low temperatures as surgical tools is relatively safe since there is little or no body reaction to localized freezing. Shape, rate of growth, and ultimate size of the "cryolesion" in different biological tissues can be determined and reproduced by controlling known or easily measurable parameters such as temperature, shape, dimensions, and time of application of the cryoprobe. Even biological variabilities, such as heat capacity, thermal conductivity, metabolic heat generation, and blood perfusion rate can, at least in principle, be evaluated and accounted for in planning cryosurgical instrumentation and specific surgical procedures.

However, despite its variety of very promising applications, cryosurgery, as presently practiced, is highly empiric. Extensive bibliographic surveys of papers describing the various cryosurgical procedures show that control of the cryolesion is mostly an art that is gained from experience [2].

Actually, analytical and numerical heat-transfer models have been developed to aid the surgeon in predicting the rate of growth and ultimate steady-state size of the frozen region [3–8]. However, analytical solutions have only been obtained for a few one-dimensional cases while digital computer programs, based on the finite difference method, have been successfully used only with reference to relatively simple two-dimensional configurations.

In this paper we describe applications of the finite element method representative of analyses that can be performed to investigate the thermal response of complex biological systems undergoing cryosurgery. Since complicated geometries, different materials, temperature dependent thermophysical properties, and time-dependent boundary conditions can be accounted for in our codes, the results obtained should be of a certain interest even if, as yet, our model has not been verified experimentally "in vivo."

Formulations of the finite element method for nonlinear heat conduction problems involving phase change have been reported in [9, 10]. The program used for the present research, however, includes, as a new feature, the term concerning the heat exchange between blood and tissue.

Basis of Freezing Injury [11–15]

At slow rates of cooling, tissues tend to freeze extracellularly. Slow cooling rates encourage also the growth of a few crystals to very large size. When these develop in the extracellular spaces, migration of water out of the cells occurs because of pressure gradients induced, probably, by the combined influence of concentration differences and capillarity. The ultimate end of such a process is dehydration of the cells and the development of external ice crystals which can be many times the size of individual cells.

As the rate of cooling is increased, the migration of water out of the cells may become inadequate to support the rapid growth of extracellular crystals. As a consequence, intracellular ice formation occurs, probably from growth of external ice through minute water-filled pores in the cell membrane.

There is much experimental evidence that cells can be damaged during freezing by mechanical and/or biochemical causes.

It is difficult to prove any mechanical injury resulting from the presence of extracellular ice crystals in soft animal tissues. Probably the best evidence against the universality of a mechanical basis of extracellular freezing injury is found in the frostbite literature. Many investigators have demonstrated tissue freezing and yet, with appropriate remedial action, have avoided tissue loss.

Quite a different situation instead is found with respect to intracellular ice formation, which is almost invariably lethal to cells. However, it is fair to say that, while the proposition that intracellular freezing can be mechanically injurious is entirely acceptable in view of the complex internal structure of nucleated cells, there is no conclusive evidence to support the mechanical nature of the intracellular ice-formation injury.

---

[1] Also: Laboratorio per la Tecnica del Freddo del C.N.R., corso Stati Uniti, Padova, Italy.

[2] Numbers in brackets designate References at end of paper.

Contributed by the Heat Transfer Division for publication in the JOURNAL OF HEAT TRANSFER. Manuscript received by the Heat Transfer Division May 19, 1976.

Rapid freezing can also cause macroscopic mechanical damage to relatively large specimens, due to the freezing and hardening of the outer surface prior to freezing and expansion of the interior. The large stresses resulting from this differential expansion might explain why cells are more likely to be destroyed by freezing "in vivo" than "in vitro" conditions.

Other than the physical development of ice crystals and the histological distortion they produce, the only other known immediate direct result of freezing is dehydration. As water is removed from the cells to form ice during extracellular freezing, there occurs a gradual concentration of cell solutes, an event that leads to damaging biochemical reactions which often prove lethal.

While the nature of the reactions, or combination of reactions, producing cell injury is not well known, there is much evidence that damaging biochemical processes proceed with a time-temperature relationship. Injury increases with increasing time and is greater with lower rates of cooling, since slower cooling means a longer time of exposure at the most dangerous temperatures between the initial freezing point and the eutectic point. At temperatures below the eutectic point the rate of all chemical reactions drops markedly since no liquid water is present. At very low temperatures the rate of nearly all biologically significant reactions becomes vanishingly slow. All liquid water will either have frozen or set into a rigid glass, so that prolonged permanence at temperatures below −130 to −160°C, does not produce measurable chemical alterations.

Macroscopic Aspects of Freezing in Living Tissues

In most biological substances water is the major component. Thus, when these materials are cooled below 0°C, ice formation occurs, starting at a temperature T_i, usually in the vicinity of −1°C, which depends on the molar concentration of the soluble cell components. As the temperature is progressively reduced, more and more water is turned into ice and the latent heat of ice formation adds to the sensible heat involved in cooling both ice and the unfrozen solution. This leads to large variations in heat capacity with respect to temperature, while thermal conductivity also changes considerably, mainly because the thermal conductivity coefficient of ice is almost four times greater than that of water. For most biological materials the largest part of the freezing process takes place in a temperature interval between −1 and −8°C, while the largest variations of heat capacity occur between −1 and −3°C. Only at temperatures ranging from −20 to −40°C and below is there no more measurable change with temperature in the amount of ice present, and the remaining water, if any, can be considered as nonfreezable [16]. However, for practical purposes, a lower limit T_f to the phase change interval can be defined on the basis of a ratio of ice to total water content of, say, 90 percent. This choice, in addition to providing an easily applicable criterion, allows one to approximate heat capacity and thermal conductivity curves below T_f by means of constant values. In [17, 18] it has been shown that a triangle and a straight line can be used to interpolate heat capacity and thermal conductivity of biological materials in the phase-change zone (see Fig. 1). Different shapes for the interpolating curves have also been tested but improvements obtained, if any, do not justify additional complications [17].

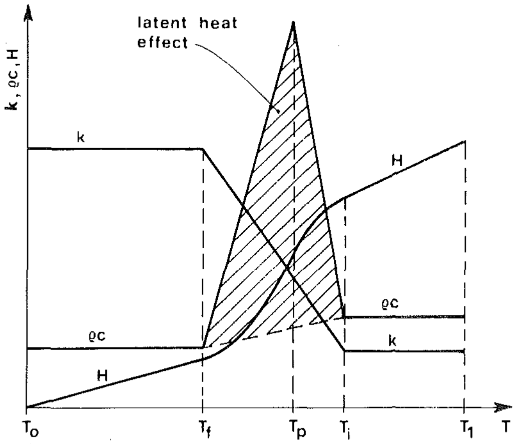

Fig. 1 Estimation of heat capacity and thermal conductivity in phase change problems

For homogeneous biological materials, values of heat capacity and thermal conductivity above and below freezing, and values of the latent heat effect can be estimated very simply from the knowledge of the total mass fraction of water [18].

In living animal tissues, the effects of metabolism and of blood flow must not be overlooked [19].

Rates of metabolic heat generation Q_m and of blood flow $\dot{m}_b$ are both functions of temperature. For convenience, linear variations of these quantities can be assumed, starting, for example, from zero values at $T_{ib} = -0.5$°C, the initial freezing point of plasma [20] (see Fig. 2).

Average values of Q_m and $\dot{m}_b$ for several tissues are reported in literature [3–5, 21–23].

In cryosurgical applications the systemic arterial temperature is always greater than the local tissue temperature and, as such, the warm blood heats the tissue and interferes very effectively with the spread of the cold field.

The heat exchange between blood and tissue is given by the expression:

$$h_{ar}a_{ar}(T_{ar} - T) + h_{ve}a_{ve}(T_{ve} - T) + \dot{m}_b c_b(T_{ar} - T)$$

where T_{ar}, T_{ve} are, respectively, local temperatures of arterial and venous blood; h_{ar}, h_{ve} are overall heat transfer coefficients between arterial and venous blood and the tissue, and a_{ar}, a_{ve} are areas of heat transfer per unit volume of tissue [19, 22].

Heat transfer takes place from the arteries into the tissue space and from the tissue space to the veins. Besides, blood is perfusing capil-

Nomenclature

a_{ar}, a_{ve} = average heat transfer area per unit volume (m^{-1})
c = specific heat capacity (J/kg·K)
h = overall heat transfer coefficient (W/m^2·K)
H = enthalpy per unit volume (J/m^3)
k = thermal conductivity (W/m·K)
ℓ_x, ℓ_y; ℓ_r, ℓ_z = direction cosines of the outward normal to the boundary surface
$\dot{m}_b$ = blood flow rate per unit volume (kg/m^3·s)
q = heat flux density (W/m^2)
Q_m = rate of metabolic heat generation (W/m^3)
r, z = cylindrical coordinates (m)
s = distance in the direction of the temperature gradient (m)
t = time (s)
T = temperature (°C)
x, y = Cartesian coordinates (m)
α = convective heat transfer coefficient (W/m^2·K)
Γ = boundary surface (m^2)
ρ = density (kg/m^3)
Ω = domain of definition (m^3)

Subscripts

a = air
ar = arterial
b = blood
f = final
i = initial
m = metabolic
P = peak
t = at the time instant t
ve = venous
w = surface
0, 1, 2 = reference

Superscripts

e = element

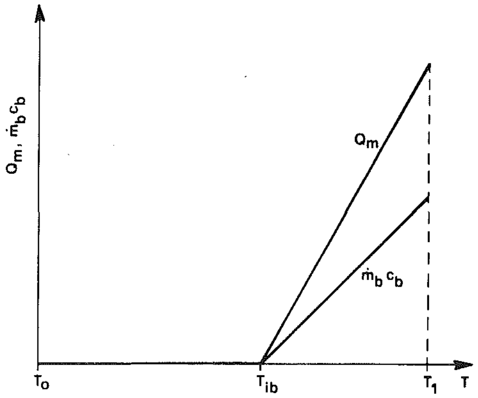

Fig. 2 Estimation of metabolic heat generation and blood perfusion rate in living tissues

laries at a local flow rate per unit volume $\dot{m}_b$. The blood enters the capillaries at the local arterial temperature T_{ar} but, because of the large surface-to-volume ratio and the relatively long residence time of blood in the capillaries, it equilibrates with the tissue temperature T before being collected in the venous system.

Generally, the terms $h_{ar}a_{ar}(T_{ar} - T)$ and $h_{ve}a_{ve}(T_{ve} - T)$ are not known, due to the complexity of the geometrical and physiological parameters involved. Volumetric average blood perfusion rates $\dot{m}_b$, instead, are better known for various organs and tissues. Consequently, heat exchange between blood and tissue is usually calculated from the expression

$$\dot{m}_b c_b (T_b - T)$$

and, in order to obtain analytical or numerical solutions, the average blood temperature T_b is assumed to equal the systemic arterial temperature T_{ar} [3–5, 19, 23].

When studying temperature distributions in tissues which are perfused primarily by capillary vessels the foregoing approximation yields satisfactory results [23].

Formulation of the Problem

The problem considered in this paper is governed, in a two-dimensional region Ω, by the nonlinear parabolic equation

$$\rho c \frac{\partial T}{\partial t} = \frac{\partial}{\partial x}\left(k_x \frac{\partial T}{\partial x}\right) + \frac{\partial}{\partial y}\left(k_y \frac{\partial T}{\partial y}\right) + Q_m + \dot{m}_b c_b (T_b - T) \quad (1)$$

subjected to boundary conditions

$$T = T_w \quad (2)$$

on part of the boundary Γ_1 and

$$\left(k_x \frac{\partial T}{\partial x} \ell_x + k_y \frac{\partial T}{\partial y} \ell_y\right) + q + \alpha (T - T_a) = 0 \quad (3)$$

on part of the boundary Γ_2.

In cylindrical coordinates, condition (2) does not change, while equation (1) and condition (3) can be expressed, respectively, as

$$r\rho c \frac{\partial T}{\partial t} = \frac{\partial}{\partial r}\left(rk_r \frac{\partial T}{\partial r}\right) + \frac{\partial}{\partial z}\left(rk_z \frac{\partial T}{\partial z}\right) + rQ_m + r\dot{m}_b c_b (T_b - T) \quad (1a)$$

and

$$\left(rk_r \frac{\partial T}{\partial r} \ell_r + rk_z \frac{\partial T}{\partial z} \ell_z\right) + rq + r\alpha (T - T_a) = 0 \quad (3a)$$

Therefore, by replacing k, ρc, Q_m, $\dot{m}_b c_b$, q, and α with rk, $r\rho c$, rQ_m, $r\dot{m}_b c_b$, rq, and $r\alpha$, solutions to problems (1)–(3) and (1a), (2), (3a) can be obtained using the same program.

Equations (1)–(3) and (1a) and (3a) refer to unsteady thermal fields in biological systems where ρc is the heat capacity, k is the thermal conductivity, Q_m is the rate of metabolic heat generation, and the quantity $\dot{m}_b c_b (T_b - T)$ represents the heat exchange between blood and tissue. The terms ℓ_x, ℓ_y and ℓ_r, ℓ_z are the direction cosines of the outward normal to the boundary surface, while q represents the imposed heat flux per unit area and α is the convective heat-transfer coefficient.

The spacewise discretization of equation (1), subjected to boundary conditions (2) and (3), can be accomplished using Galerkin's method as shown in [9, 24].

Let the unknown function T be approximated, throughout the solution domain at any time t, by the relationship

$$T = \sum_{j=1}^{n} N_j(x, y) T_j(t) = \mathbf{NT} \quad (4)$$

where N_j are the usual shape functions defined piecewise element by element, T_j or $\mathbf{T}$ being the nodal parameters. The simultaneous equations, allowing the solution for n values of T_j, are obtained typically, for point j, by equating to zero the integral, over the domain Ω, of the product of the weighting function N_j by the residual resulting from substitution into equation (1) of equation (4). After making use of Green's theorem, in order to avoid second derivatives in the integrals imposing unnecessary continuity conditions between elements, the n equations can be written down in matrix form as

$$\mathbf{KT} + \mathbf{C\dot{T}} + \mathbf{F} = 0 \quad (5)$$

Typical matrix elements are

$$K_{j\ell} = \sum \int_{\Omega^e} \left[\left(k_x \frac{\partial N_j}{\partial x}\frac{\partial N_\ell}{\partial x} + k_y \frac{\partial N_j}{\partial y}\frac{\partial N_\ell}{\partial y}\right) + \dot{m}_b c_b N_j N_\ell\right] d\Omega + \sum \int_{\Gamma_2{}^e} \alpha N_j N_\ell d\Gamma \quad (6)$$

$$C_{j\ell} = \sum \int_{\Omega^e} \rho c N_j N_\ell d\Omega \quad (7)$$

$$F_j = \sum \int_{\Omega^e} N_j (Q_m + \dot{m}_b c_b T_b)\, d\Omega + \sum \int_{\Gamma_2{}^e} N_j (q - \alpha T_a)\, d\Gamma \quad (8)$$

where (j, $\ell = 1, n$).

In the foregoing the summations are taken over the contributions of each element, Ω^e is the element region and $\Gamma_2{}^e$ refers only to elements with external boundaries on which condition (3) is specified.

It must be noted that the set of equations (5) is highly nonlinear since thermophysical properties k, ρc, Q_m, and $\dot{m}_b$ are strongly dependent on T.

Special Features of the Numerical Model

The set of ordinary differential equations (5), which defines the discretized problem (5), can be solved using the three level scheme described in [9].

If it is assumed that the temperature varies linearly in the small time interval between $t - \Delta t$ and $t + \Delta t$, equation (5) can be approximated as

$$\mathbf{K}_t(\mathbf{T}_{t+\Delta t} + \mathbf{T}_t + \mathbf{T}_{t-\Delta t})/3 + \mathbf{C}_t(\mathbf{T}_{t+\Delta t} - \mathbf{T}_{t-\Delta t})/(2\Delta t) + \mathbf{F}_t = 0. \quad (9)$$

This, after some algebra, results in the following recurrence formula for final integration:

$$\mathbf{T}_{t+\Delta t} = -[\mathbf{K}_t + 3\mathbf{C}_t/(2\Delta t)]^{-1}[\mathbf{K}_t\mathbf{T}_t + \mathbf{K}_t\mathbf{T}_{t-\Delta t} + 3\mathbf{C}_t\mathbf{T}_{t-\Delta t}/(2\Delta t) + 3\mathbf{F}_t] \quad (10)$$

in which iterations are avoided since only central values of matrices $\mathbf{K}$ and $\mathbf{C}$ occur. The scheme is apparently not self-starting, but as we shall always refer to known stationary conditions, two starting values can be easily assumed.

Algorithm (10) has been found to be unconditionally stable [9]. Oscillations arising from sudden variations in boundary conditions can be kept under control, for example by adopting the automatic time step adjustment feature described in [9]. Undulations arising from the "numerical noise" inherent in the approximations made can be greatly reduced if, at each time step after the first one, instead of letting simply

$$\mathbf{T}_{t-\Delta t} = \mathbf{T}_t \tag{11}$$

vector $\mathbf{T}_{t-\Delta t}$ is redefined as

$$\mathbf{T}_{t-\Delta t} = (\mathbf{T}_{t+\Delta t} + \mathbf{T}_t + \mathbf{T}_{t-\Delta t})/3 \tag{12}$$

before starting again the calculations indicated in formula (10) [25].

The program for implementing algorithm (10) follows the usual pattern [26]. However, matrices **K** and **C** are now time dependent, through the variations of coefficients with temperature, and a completely new solution has to be obtained at each stage.

The evaluation of temperature-dependent quantities in integrals (6) and (7) requires special care, particularly if a rather coarse mesh is employed and spatial variation of the quantities is abrupt. Numerical integration has obviously to be adopted here and therefore ρc, k, Q_m, and $\dot{m}_b$ must be estimated at integrating points in Ω^e.

In the program, a new variable H (enthalpy), is defined as an integral of the heat capacity versus temperature curve (see Fig. 1):

$$H = \int_{T_0}^{T} \rho c dT \tag{13}$$

since, in the phase change zone, enthalpy is a much smoother function of temperature than heat capacity. Thus, it is reasonable to interpolate enthalpy rather than heat capacity directly, writing the relationship:

$$H = \sum_{j=1}^{n} N_j(x, y) H_j(t) = \mathbf{NH} \tag{14}$$

where again N_j are the shape functions and H_j are the enthalpy values at nodal points.

By definition we have:

$$\rho c = dH/dT \tag{15}$$

Therefore, evaluation of the foregoing derivative with reference to the oriented direction **s** of the temperature gradient yields

$$\rho c = \frac{\partial H}{\partial s} \Big/ \frac{\partial T}{\partial s} = \left(\frac{\partial H}{\partial x}\ell_{sx} + \frac{\partial H}{\partial y}\ell_{sy}\right) \Big/ \frac{\partial T}{\partial s} \tag{16}$$

where ℓ_{sx}, ℓ_{sy} are the direction cosines of **s**.

Since we have

$$\ell_{sx} = \frac{\partial T}{\partial x} \Big/ \frac{\partial T}{\partial s}; \quad \ell_{sy} = \frac{\partial T}{\partial y} \Big/ \frac{\partial T}{\partial s} \tag{17}$$

and

$$\frac{\partial T}{\partial s} = \left[\left(\frac{\partial T}{\partial x}\right)^2 + \left(\frac{\partial T}{\partial y}\right)^2\right]^{1/2} \tag{18}$$

from equation (15) it follows that

$$\langle \rho c \rangle = \left(\frac{\partial H}{\partial x}\frac{\partial T}{\partial x} + \frac{\partial H}{\partial y}\frac{\partial T}{\partial y}\right) \Big/ \left[\left(\frac{\partial T}{\partial x}\right)^2 + \left(\frac{\partial T}{\partial y}\right)^2\right] \tag{19}$$

This averaging process always gives representative values of heat capacity and preserves a correct heat balance by avoiding the possibility of missing peak values of the quantity ρc. Obviously, in zones at constant temperature ($\partial T/\partial s \cong 0$), recourse is made to direct evaluation of heat capacity.

Similar techniques are used in the program also for the best determination of thermal conductivity values.

Sample Problems

In this paper parabolic isoparametric elements [24] have been used instead of the triangular elements utilized in [9].

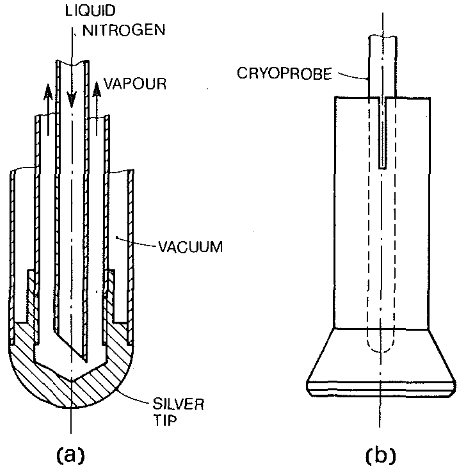

Fig. 3 Typical cryosurgery probe tips: (*a*) the active portion is hemispherical in shape; (*b*) the active portion is disk-shaped

In order to check the program, comparisons have been made with existing analytical solutions, first with reference to solidification of infinite slabs and corner regions, and then for the case of steady heat conduction in finned surfaces and in bodies with uniformly distributed internal heat generation. Finite elements and analytical solutions correlated to within 1 percent or better in all the test problems run [27].

Analytical and finite difference determinations of thermal profiles for cryosurgical probes by Cooper, et al. [3–5] were also considered.

Comparisons were made for transient temperature fields emanating from a spherical probe since solutions of this problem, in addition to being of great practical importance, have been obtained by Cooper using both analytical and numerical methods.

Spherical symmetry was accounted for in the finite element model. Despite the rather coarse—4 elements, 23 point—mesh utilized, comparisons with Cooper's solutions show good agreement [27]. Slight discrepancies are more than justified, in the authors' opinion, by differences in the representation of physical parameters. Different estimates of thermophysical properties might also have occurred since not all the values of the parameters used in the calculations are reported by Cooper.

It has thus been found once again that the use of isoparametric elements greatly reduces the amount of geometrical data necessary to define the problems without affecting the accuracy reached.

In the following examples we illustrate some applications of the new program which are of considerable significance to cryosurgery.

Temperature Fields Produced by a Hemispherical Probe. A typical probe for use in neurosurgical applications presents an "active" portion which is hemispherical in shape. As it is shown in Fig. 3(*a*), liquid nitrogen flows from a pressurized supply through the inner tube and reaches the hemispherical tip where it is vaporized by the heat received from the surroundings. The annulus formed by the inner tube and its neighbor allows the vapor to escape to the room. The outermost annulus is evacuated with the aid of a vacuum pump, thus providing thermal insulation along the stem [28]. The insulation should prevent the probe stem from acting as a lesion-generating surface during the cryosurgical procedure. However, the shape of the frozen regions produced by this type of probes seems to indicate the presence of sensible axial heat conduction [28]. The cryoprobes used in the aforementioned investigation [28] were prototypes of unusually large size, immersed in a 1.5 percent gelatin—98.5 percent water medium. Thus, in order to obtain a more realistic estimation of the influence of axial heat conduction we decided to simulate the application of a standard hemispherical cryoprobe to brain tissue.

The mesh used is represented in Fig. 4: 14 parabolic elements and

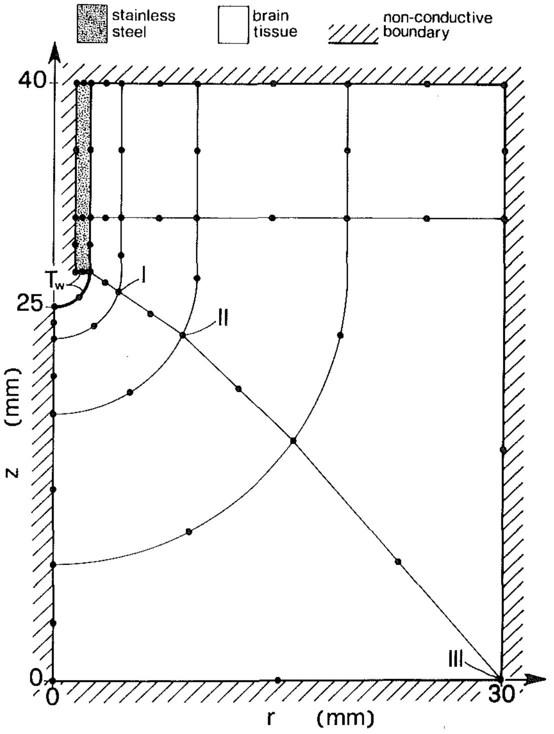

Fig. 4 Axial section illustrating the finite element mesh used for studying thermal fields produced by a hemispherical probe with the "active" area mantained at $T_w = -196°C$

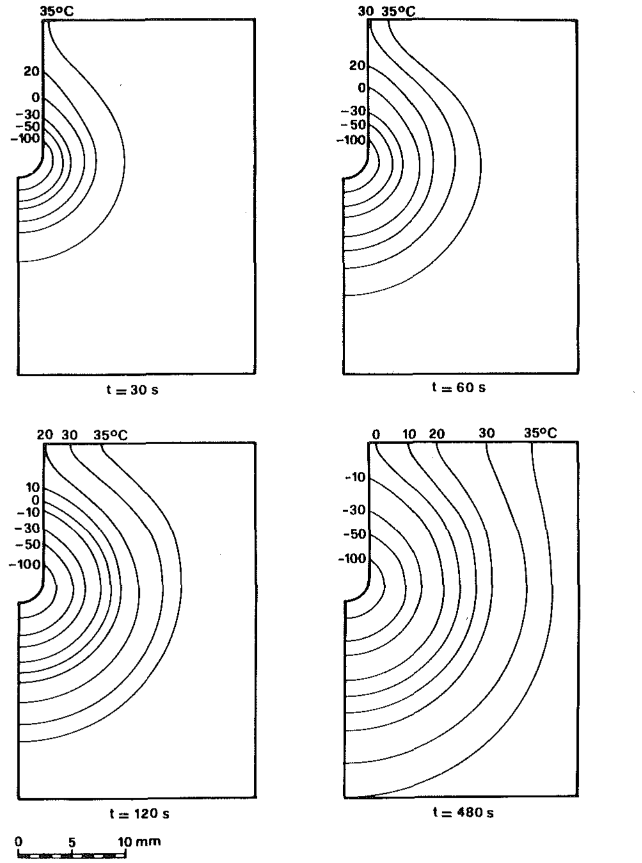

Fig. 5 Isotherm fields produced by a hemispherical probe in brain tissue

59 nodal points are utilized and the existing axial symmetry is taken into account. A hemispherical probe with a radius of 2.38 mm and an external tube in stainless steel 0.1 mm thick was selected. (In the drawing the stem thickness has been exaggerated to allow representation.)

Thermophysical properties of stainless steel have been assumed as follows:

$$k = 16.4\ \mathrm{W/m \cdot K}, \quad \rho c = 3.6\ \mathrm{MJ/m^3 \cdot K}, \quad Q_m = \dot{m}_b = 0$$

Thermophysical properties of brain tissue, perfused with blood at a systemic arterial temperature of 37°C, have been estimated as indicated in a previous section and are reported in Table 1.

Initial temperatures were taken to be stationary and equal to 37.8°C throughout the domain. The time response of the probe during cool-down was considered instantaneous.

Computing time was of the order of 80 s for 200 time steps on a CDC 7600 machine.

The isotherm fields during freezing are shown in Fig. 5 with refer-

Table 1 Thermophysical properties of living tissues considered in the calculations

Heat capacity ρc (MJ/m³·K)

	T_O (°C)	T_f (°C)		T_p (°C)	T_i (°C)	T_1 (°C)
	−200	−8	−7	−3	−1	50
brain	1.93	1.93	= = =	79.3	3.60	3.60
angioma	2.01	= = =	2.01	103.	3.89	3.89
healthy tissue	1.80	1.80	= = =	64.7	3.16	3.16

Thermal conductivity k (W/m·K)

	T_O (°C)	T_f (°C)		T_i (°C)	T_1 (°C)
	−200	−8	−7	−1	50
brain	2.00	2.00	= = =	0.52	0.52
angioma	2.22	= = =	2.22	0.56	0.56
healthy tissue	1.68	1.68	= = =	0.48	0.48

Metabolic heat generation and blood perfusion rate

	brain		angioma		healthy tissue	
	Q_m (kW/m³)	$c_b\dot{m}_b$ (kW/m³·K)	Q_m (kW/m³)	$c_b\dot{m}_b$ (kW/m³·K)	Q_m (kW/m³)	$c_b\dot{m}_b$ (kW/m³·K)
$T_O = -200°C$	0	0	0	0	0	0
$T_{ib} = -0.5°C$	0	0	0	0	0	0
$T_1 = 50°C$	33.8	40.3	33.8	48.5	33.8	24.2

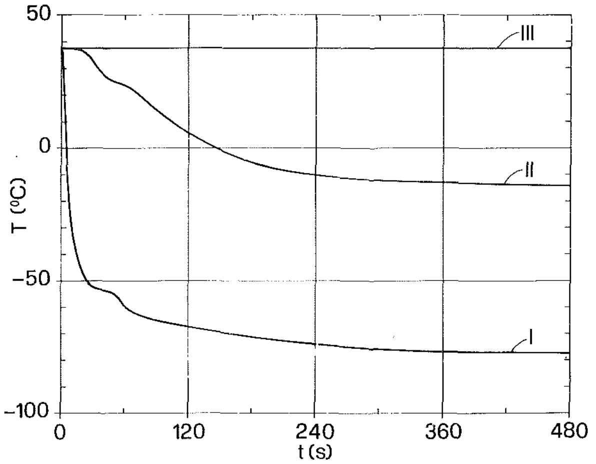

Fig. 6 Time-temperature curves for representative points I, II, III in Fig. 4

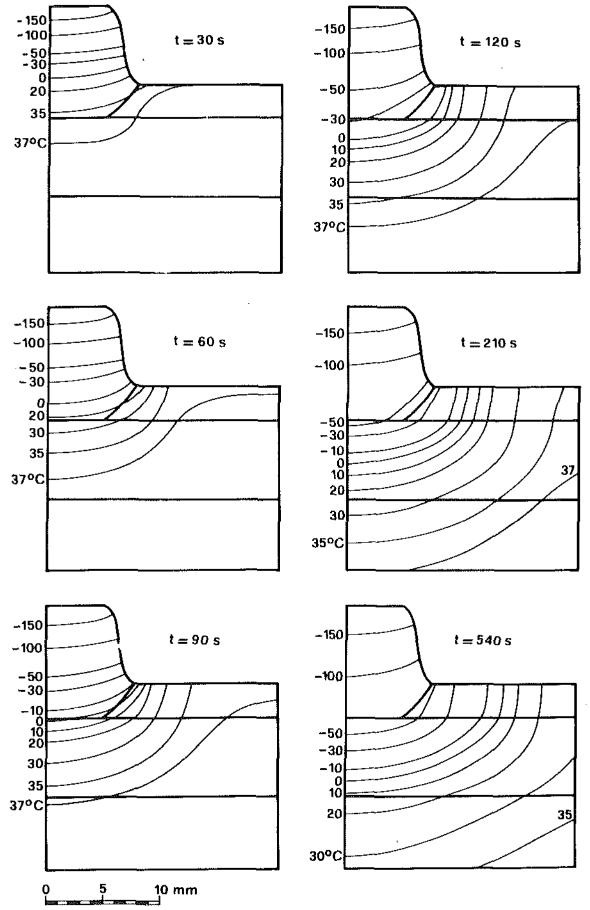

Fig. 8 Isotherm fields produced by a disk-shaped probe in the treatment of a large angioma in an infant

ence to several values of time for a surface temperature of −196°C in correspondence with the "active" area of the probe and nonconductive faraway boundaries. A thermal resistance between probe and tissue might have been easily taken into account by the program. However, as a first approximation, its effects were neglected since no reliable experimental information on them was available to the authors.

From the shape of the isotherm fields, the presence of sensible heat conduction in the axial direction along the probe stem can be inferred.

Time-temperature curves concerning representative points of the domain, such as, for example, points I, II, III in Fig. 4 are of great interest for the surgeon. Curves of this type, which can be drawn from the computer output for any point in the domain, are shown in Fig. 6.

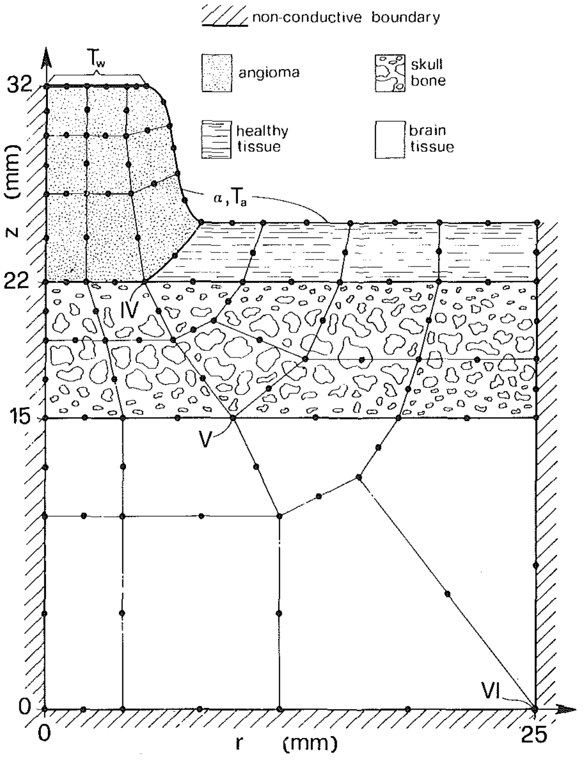

Fig. 7 Axial section illustrating the finite element mesh used for studying thermal fields produced by a disk-shaped probe with the active area mantained at T_w = −196°C. Convective boundary conditions with α = 12 W/m²k, T_a = 22°C are assumed at the exposed surface. Internal boundaries are taken as nonconductive

In this example, cooling rates in the freezing zone are of the order of 3 K/s for point I and 0.1 K/s for point II. Steady state or, better, no significant temperature variation takes place after, approximately, 300 s.

Temperature Fields Produced by a Disk-Shaped Probe. A disk-shaped probe can be obtained from a standard hemispherical probe by fitting a removable tip adapter as shown in Fig. 3(*b*). Disk-shaped probes are normally used on the surface of the body and are pressed against the tissue with force, so as to assure good thermal contact over the active freezing area.

An application of this cryosurgical procedure can be the treatment of large angiomas in infants. In the present example we investigate the development of thermal fields during the removal of an angioma located in an area of the head close to the brain.

The mesh used is represented in Fig. 7: 31 parabolic elements and 118 nodal points are utilized and the existing axial symmetry is taken into account.

Thermophysical properties of the skull bone have been assumed as follows:

$$k = 0.38\ \mathrm{W/m \cdot K}, \quad \rho c = 1.88\ \mathrm{MJ/m^3 \cdot K}, \quad Q_m = \dot{m}_b = 0$$

Estimated thermophysical properties of brain, angioma, and healthy tissue surrounding the angioma are reported in Table 1.

A systemic arterial temperature of 37°C was assumed for all the tissues. Initial temperatures were taken to be stationary and equal to 37.5°C throughout the domain. The time response of the probe *during cool-down was considered instantaneous.*

Neglecting thermal resistance effects, boundary conditions were

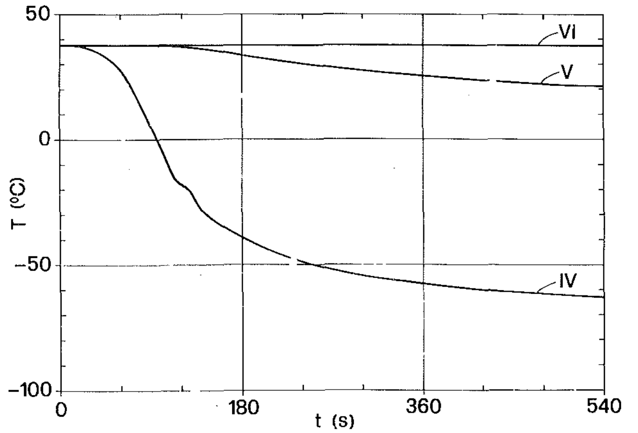

Fig. 9 Time-temperature curves for representative points IV, V, VI in Fig. 7

defined once again by a known surface temperature of −196°C in correspondence with the freezing area of the probe. A constant air temperature T_a = 22°C and a convective heat transfer coefficient α = 12 W/m^2·K at the exposed external surface were assumed. Faraway internal boundaries were considered nonconductive.

Computing time was of the order of 80 s for 100 time steps on a CDC 7600 machine.

Isotherm fields at different values of time are illustrated in Fig. 8, while time-temperature curves for the representative points IV, V, VI shown in Fig. 7, are reported in Fig. 9.

Conclusions

The finite element method formulated for nonlinear heat conduction coupled with distributed convection allows the solution of a great number of freezing problems in living tissues.

The procedure used in this paper can be very valuable in the analysis of thermal response of biological systems subjected to cryosurgical procedures.

Acknowledgments

The cooperation of Prof. F. Mazzoleni, M.D., and of the staff at the Institute of Plastic Surgery of the University of Padua, directed by Prof. G. Dogo, M.D., is gratefully acknowledged.

References

1 Cooper, I. S., "Cryogenic Surgery: Introduction," *Cryogenics in Surgery*, von Leden, H., and Cohan, W. G., eds., Medical Examination Publishing Co., New York, 1971, pp. 13–14.

2 Union Carbide Corporation, *Bibliography of Cryogenic Procedures in Surgery*, 87-0039, F-2878-A, Linde Division, New York, N. Y.

3 Cooper, T. E., and Trezek, G. J., "Analytical Prediction of the Temperature Field Emanating from a Cryogenic Surgical Cannula," *Cryobiology*, Vol. 7, 1970, pp. 79–93.

4 Cooper, T. E., and Trezek, G. J., "Rate of Lesion Growth Around Spherical and Cylindrical Cryoprobes," *Cryobiology*, Vol. 7, 1971, pp. 183–190.

5 Cooper, T. E., and Trezek, G. J., "Mathematical Predictions of Cryogenic Lesion," *Cryogenics in Surgery*, von Leden, H., and Cohan, W. G., eds., Medical Examination Publishing Co., New York, 1971, pp. 128–149.

6 Cravalho, E. G., "An Analytical Prediction of the Spatial Extent of Necrosis in Cryosurgery," *Cryobiology*, Vol. 8, 1971, p. 396.

7 Warren, R. P., Bingham, P. E., and Carpenter, J. D., "Heat Flow in Living Tissue During Cryosurgery," ASME Paper, 74-WA/BIO-6, 1974.

8 Hrycak, P., Levy, M. J., and Wilchins, S. J., "Cryosurgery of Lesions Through Contact Freezing and Estimates of Penetration Time," *1975 Advances in Bioengineering*, Bell, A. C., and Nerem, R. M., eds., ASME, New York, 1975, p. 36.

9 Comini, G., et al., "Finite Element Solution of Nonlinear Heat Conduction Problems With Special Reference to Phase Change," *International Journal Num. Meth. Engineering*, Vol. 8, 1974, pp. 613–624.

10 Del Giudice, S., Lewis, R. W., and Comini, G., "Finite Element Simulation of Freezing Processes in Soils," 1976, to appear.

11 Meryman, H. T., "Review of Biological Freezing," *Cryobiology*, Meryman, H. T., ed., Academic Press, London, 1971, pp. 1–114.

12 Mazur, P., "Physical and Chemical Basis of Injury in Single-Celled Micro-Organisms Subjected to Freezing and Thawing," *Cryobiology*, Meryman, H. T., ed., Academic Press, London, 1971, pp. 213–315.

13 Love, R. M., "The Freezing of Animal Tissue," *Cryobiology*, Meryman, H. T., ed., Academic Press, London, 1971, pp. 317–405.

14 Farrant, J., "Cryobiology: the Basis for Cryosurgery," *Cryogenics in Surgery*, von Leden, H., and Cohan, W. G., eds., Medical Examination Publishing Co., New York, 1971, pp. 15–41.

15 Aguirre-Puente, J., Vignes, M., and Viaud, P., "Congélation des Milieux Dispersés," Rapport 72-3, Laboratoire d' Aérothermique du C.N.R.S., Meudon, France, 1972.

16 IIF/IIR, *Recommendations for the Processing and Handling of Frozen Foods*, Second ed., *Annexe au Bull. IIF*, Paris, 1972.

17 Bonacina, C., et al., "On the Estimation of Thermophysical Properties in Nonlinear Heat Conduction Problems," *International Journal of Heat Mass Transfer*, Vol. 17, 1974, pp. 861–867.

18 Comini, G., Bonacina, C., and Barina, S., "Thermal Properties of Foodstuffs," *Annexe 1974–3 au Bull. IIF*, pp. 163–172.

19 Ferro, V., and Filippi, M., "Current Trends in the Calculation of the Cooling Process in Biological Materials," *XIVth International Congress Refrigeration*, Paper C1.1, IIF/IIR, Moscow, 1975.

20 Wessling, F. C., and Blackshear, P. L., "The Thermal Properties of Human Blood during the Freezing Process," JOURNAL OF HEAT TRANSFER, TRANS. ASME, Series C, Vol. 95, 1973, pp. 246–249.

21 Eberhart, R. C., Jackson, M., and Trezek, G. J., "Application of a Heat-Transfer Model to Determine Regional Blood Flow Rate," JOURNAL OF HEAT TRANSFER, TRANS. ASME, Series C, Vol. 95, 1973, pp. 113–119.

22 Keller, H. K., and Seiler, L., Jr., "An Analysis of Peripheral Heat Transfer in Man," *Journal of Applied Physiology*, Vol. 30, 1971, pp. 779–786.

23 Shitzer, A., "Studies of Bio-Heat Transfer in Mammals," in *Topics in Transport Phenomena*, Gutfinger, C., ed., Wiley, New York, 1975, pp. 211–343.

24 Zienkiewicz, O. C., and Parekh, C. J., "Transient Field Problems: Two-Dimensional and Three-Dimensional Analysis by Isoparametric Finite Elements," *International Journal Num. Meth. Engineering*, Vol. 2, 1970, pp. 61–71.

25 Wood, W. L., and Lewis, R. W., "A Comparison of Time Marching Schemes for the Transient Heat Conduction Equation," *International Journal Num. Meth. Engineering*, Vol. 9, 1975, pp. 679–690.

26 Zienkiewicz, O. C., *The Finite Element Method in Engineering Science*, Second ed., McGraw-Hill, London, 1971.

27 Comini, G., and Del Giudice, S., 1976, unpublished results.

28 Cooper, T. E., and Petrovic, W. K., "An Experimental Investigation of the Temperature Field Produced by a Cryosurgical Cannula," JOURNAL OF HEAT TRANSFER, TRANS. ASME, Series C, Vol. 96, 1974, 415–420.

N. Shamsundar[1]
E. M. Sparrow

**Department of Mechanical Engineering,
University of Minnesota,
Minneapolis, Minn.**

Effect of Density Change on Multidimensional Conduction Phase Change

An analysis of transient multidimensional solidification in the presence of a growing shrinkage cavity has been performed. The enthalpy model, which had previously been applied only for cases with no density change, has been extended to accommodate substances which undergo a change of density upon phase change. The extended enthalpy model was implemented by an efficient, implicit finite difference scheme. A solidification model was adopted in which the shrinkage cavity is at the top of the container within which the phase change is taking place. Solutions were carried out for solidification of a liquid in a long, horizontal rectangular container with convectively cooled walls. Results are presented for the time variations of various heat transfer quantities and for the evolution of the shrinkage cavity and the solid-liquid interface, for parametric values of the Biot number, liquid-solid density ratio, and Stefan number. The influence of the density ratio and the Stefan number on the heat transfer results was most marked at times near the completion of solidification, whereas the Biot number had a major effect at all times.

Introduction

For most substances that participate in conduction-dominated solid-liquid phase change problems, the change of phase is accompanied by density change. The presence of the density change has far reaching consequences. For example, in castings, undesired cavities and dimensional nonuniformities are produced. In thermal storage applications, similar cavities occur which inhibit heat transfer. With regard to the freezing of lakes and rivers, the fact that ice is lighter than water plays a profound role in the development of aquatic life.

Notwithstanding its importance, density change has generally not been accounted for in conduction phase change analyses. In the few instances known to the authors where consideration was given to density change, the problems were such that cavities were not produced [1, 2].[2]

In the present paper, a method of analysis is described and applied for solving multidimensional transient solidification problems in which a cavity is formed owing to the shrinkage associated with the density change. The method is a generalization of that of [3], wherein the enthalpy model, coupled with an implicit finite difference scheme, was developed and employed to solve multidimensional phase change problems in the absence of density change. The present method, as well as that of [3], is capable of accommodating substances that have a discrete phase change temperature (pure substances and eutectics) as well as substances that change phase over a range of temperatures.

In the presentation that follows, the enthalpy method is first generalized to include density change. It is then shown that the integral representation which embodies the enthalpy method is equivalent to the several differential equations which would be needed to define the problem with a temperature-based model. Next, a physical model for transient solidification with shrinkage is adopted, and finite-difference discretization of the enthalpy integral representation is described with respect to a specific problem. In this problem, a liquid-filled closed container is subjected to convective cooling on its external surfaces. Numerical solutions were performed for substances which are characterized by density changes of 10 and 20 percent and for parametric values of the Stefan number and the Biot number. Results are presented for the time-dependent positions of the shrinkage cavity and of the solid-liquid interface. In addition, information is given for the local and surface-averaged heat transfer rates, the solid fraction, and the surface temperature distribution. These quantities are of interest as indicators of thermal performance as, for example, in phase change energy storage systems.

The literature on multidimensional conduction phase change (without density change) has been surveyed in [4], with an abbreviated version available in [3]. Another survey is given in [5].

---

[1] Present address: Department of Mechanical Engineering, University of Houston, Houston, Texas.

[2] Numbers in brackets designate References at end of paper.

Contributed by the Heat Transfer Division for publication in the JOURNAL OF HEAT TRANSFER. Manuscript received by the Heat Transfer Division December 29, 1976.

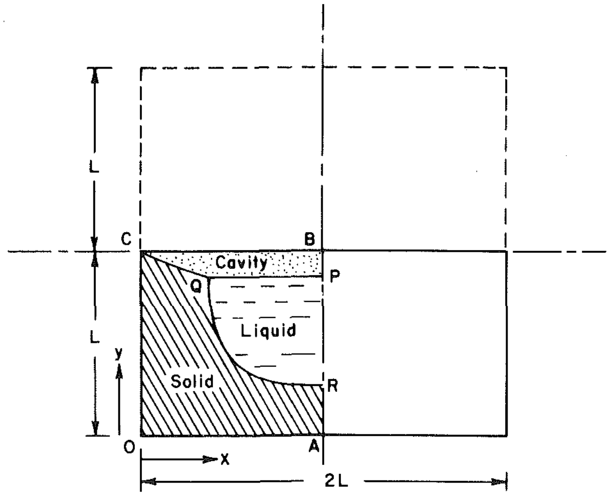

Fig. 1 Schematic diagram of the solidifying phase change material

Generalized Enthalpy Model

The rationale and the motivation for employing the enthalpy model instead of a temperature-based model are discussed in [3]. For its generalization to accommodate density change associated with phase change, the model has to include terms involving induced liquid motion (as well as other convective motions that may be present).

Consider an arbitrary control volume V with surface A. For small liquid velocities (negligible dissipation and compression work) and in the absence of distributed heat sources, the energy conservation equation may be written as

$$\frac{d}{dt}\int_V \rho i dV + \int_A \rho i v_n dA = \int_A k\frac{\partial T}{\partial n}dA \qquad (1)$$

where the symbols are defined in the Nomenclature. The second term on the left-hand side, which represents convective transport across the surface A, was not present in the model of [3] where density change was not considered. Equation (1) will be called the enthalpy equation. It is applicable whether or not there is an interfacial surface which lies in the volume V.

There is nothing in the enthalpy equation that reveals the presence or absence of phase change. It is in the enthalpy-temperature relationship that such information should be sought. Inasmuch as the i versus T relationship is needed even for a single-phase problem with variable properties, it is possible, in the enthalpy model, to consider phase change problems as just a particular class of nonlinear heat transfer problems with temperature dependent properties, and no special recognition of the position of the interface is necessary.

A simplified form of the enthalpy equation can be obtained for the case in which the liquid is at the saturation temperature throughout the transient period. To derive this form, the mass conservation equation

$$\frac{d}{dt}\int_V \rho dV + \int_A \rho v_n dA = 0 \qquad (2)$$

is multiplied by i_ℓ, the enthalpy of the saturated liquid, and then subtracted from equation (1). From this, there results

$$\frac{d}{dt}\int_V \rho(i - i_\ell)dV + \int_A \rho(i - i_\ell)v_n dA = \int_A k\frac{\partial T}{\partial n}dA \qquad (3)$$

Consider the second term on the left-hand side. For those parts of A that lie within the solid, $v_n = 0$ and the integral vanishes. For the parts of A that are in the liquid, the integral will vanish if the enthalpy i is equal to i_ℓ. Therefore, if the liquid is at the saturation temperature, the enthalpy equation reduces to

$$\frac{d}{dt}\int_V \rho(i - i_\ell)dV = \int_A k\frac{\partial T}{\partial n}dA \qquad (4)$$

It is noteworthy that equation (4) does not reflect the presence or absence of liquid motion. Therefore, equation (4) obviates the need for solving for the velocity field in the liquid.

If liquid superheat is encountered, bounds on the solution may be obtained by employing a method due to Nesselman [6]. In this method, two sets of calculations are made in both of which the liquid is assumed to be at its saturation temperature. In one of these, the latent heat is assigned its true value λ. In the other, a fictitious latent heat $\lambda' = \lambda + (i_{\text{sup}} - i_\ell)$ is used, where i_{sup} is the enthalpy of the superheated liquid. The use of λ' is equivalent to assuming that the liquid has no thermal resistance and that all its enthalpy of superheat is conveyed to the interface without attenuation. The actual solution lies between these two solutions.

The equivalence of the enthalpy equation to the set of differential equations of a temperature-based model will now be examined. When V is a single phase region within which $di = cdT$, it is readily demonstrated that the enthalpy equation reduces to

$$\rho c(\partial T/\partial t + \mathbf{v}\cdot \text{grad}T) = \text{div}(k\text{grad}T) \qquad (5)$$

For a solid, $\mathbf{v} = 0$ and the familiar heat conduction equation emerges.

When V contains both a solid and a liquid portion, there is an interfacial region within V. If the substance under consideration undergoes phase change over a range of temperatures, the interfacial region is characterized by large variations in physical properties, but as long as $di = cdT$, equation (5) applies therein.

On the other hand, if the substance has a discrete phase change temperature, the interface is a sharply defined surface. Across this surface, to be denoted by Σ, many physical quantities experience discrete jumps. In temperature-based models, special interfacial conservation conditions have to be written but, as outlined in the

Nomenclature

A = surface area
Bi = Biot number, hL/k_s
c = specific heat
E = sensible heat of solidified material, equation (25)
F = volume fraction of solidified material, equation (23)
Fo = Fourier number, $k_s t/\rho_s c_s L^2$
h = convective heat transfer coefficient
i = specific enthalpy
i_ℓ = i for liquid saturation state
i_s = i for solid saturation state
k = thermal conductivity
L = container dimension, Fig. 1
n = normal coordinate
Q = surface-integrated heat transfer rate
q = local heat transfer rate
S = grouping, SteΔ^2/δ_τ
Ste = Stefan number, $c_s(T_{sat} - T_\infty)/\lambda$
T = temperature
T_{sat} = saturation temperature
T_∞ = coolant temperature
t = time
V = volume
v_n = velocity normal to surface
x, y = coordinates
Δ = dimensionless spatial step size
δ_τ = dimensionless time step
θ = enthalpy variable, equation (9)
λ = latent heat of fusion
ρ = density
$\hat{\rho}$ = density ratio, ρ_ℓ/ρ_s
τ = dimensionless time, equation (12)
ϕ = temperature variable, equation (11)

Subscripts

h = horizontal surface
ℓ = liquid
s = solid
v = vertical surface

following and detailed in [4], these conditions are actually embedded in the integral equations representing conservation of energy and mass.

By using methods similar to those employed in [3], or by applying Kotchine's Theorem [7] to the enthalpy equation (1), the following interfacial energy balance is obtained

$$(\rho_s i_s - \rho_\ell i_\ell)v_\Sigma + \rho_\ell i_\ell v_\ell = (k\partial T/\partial n)_\ell - (k\partial T/\partial n)_s \qquad (6)$$

Here, v_Σ is the velocity of the interface and v_ℓ is the velocity of the liquid at the interface, and the subscripts s and ℓ represent values on the solid side of Σ and the liquid side of Σ, respectively.

In analogous fashion, the interfacial mass balance equation is obtained from (2) as

$$(\rho_s - \rho_\ell)v_\Sigma + \rho_\ell v_\ell = 0 \qquad (7)$$

and may be used to obtain from (6) the following simpler relation by eliminating v_ℓ

$$\rho_s \lambda v_\Sigma = (k\partial T/\partial n)_s - (k\partial T/\partial n)_\ell \qquad (8)$$

Here, $\lambda = i_\ell - i_s$ represents the latent heat of fusion. Equation (8) is the interfacial equation employed in the conventional model based on temperature.

Solidification Model and Problem Definition

When most substances solidify, they contract (water is a notable exception). The reduction in volume may result in many small cavities, or may be more or less concentrated in one location. Distributed cavities are undesirable for many reasons. In castings, they result in reduced strength and stress concentration. In thermal storage applications, they undermine thermal performance. Various means are available to control shrinkage cavities so that they are concentrated in one location, and it will be assumed that the shrinkage is so confined. Even with this, enough information is not available to predict where the concentrated cavity will occur, and plausible assumptions have to be made. The actual location of the cavity is governed by nonequilibrium effects, crystalline growth, surface tension effects, cooling rates, etc.

Two reasonable models present themselves. In the first, it is assumed that gravity plays no role and that the shrinkage cavity is located centrally with respect to the walls of the container. Thus, for example, for the square container investigated in [3], the cavity would be situated about the center of the square. In that case, no additional calculations beyond those of [3] would be necessary because the presence of the cavity would not affect the solidification process as long as there is a liquid zone between the solid and the cavity.

The other model pictures the cavity as occurring at the top part of the container. This model assumes that gravity is strong enough to enable small vapor bubbles formed within the liquid to overcome the viscous resistance and ascend to the top. This assumption may be reasonable if solidification is slow, as in thermal storage, and is the one adopted in this paper. After a thin crust of solid forms, the cavity acts as an effective barrier to heat loss, and no further solidification occurs at the top. Vapor bubbles are free to rise through the liquid pool and enter the cavity and cause it to grow.

This model is depicted in Fig. 1 for a long horizontal container of rectangular cross section ($2L \times L$) whose walls are represented by the solid lines. A substance that solidifies at a discrete temperature is present in the container. Initially, the container is full of saturated liquid. At some later time, all three phases are present, as shown in the figure. The cavity $BCQP$ contains vapor and, because only small temperature differences are allowed in thermal storage applications, may be considered to have no heat passing through it. The surface BC is, therefore, effectively adiabatic.

Also shown in the figure is the $2L \times 2L$ square cross-sectional container treated in [3] (dashed lines). For that container as well, BC is an adiabatic surface because it is a surface of symmetry. For both containers, AB is a surface of symmetry, and both are exposed to convective cooling on the faces $0A$ and $0C$. The coolant temperature T_∞ and the heat transfer coefficient h are assumed to be uniform and independent of time. On this basis, the portions $0ABC$ of the two containers shown in Fig. 1 have the same boundary conditions. This is the reason for choosing the dimensions of the present rectangular container.

The solid-liquid interface, QR, intersects the adiabatic surfaces CQ and PQ at the triple point Q at an angle determined by surface tension properties. In the absence of information about these properties for substances being considered for thermal energy storage, it will be assumed that QR is normal to PQ at Q. It is expected that this assumption will have only a local region of influence.

The preceding solidification model is one among various possibilities. When better models become available, they may be incorporated into the enthalpy model in an analogous fashion.

All properties (except enthalpy) are assumed independent of temperature.

Finite Difference Discretization

In order to obtain the finite difference representation of the enthalpy equation, the solution region $OABC$ is split into a number of small elements, nodes are placed at the centers of the elements, and the enthalpy equation is applied to each element. As in [3], a square grid with step size Δ is adopted. The elements are laid out so that there are nodes along all the boundaries. The nodes are numbered sequentially, using subscripts i and j. Before the difference equations are presented, a set of dimensionless variables will be introduced.

For a single-phase element, the dimensionless nodal enthalpy variable θ is defined by

$$\theta = (i - i_s)/\lambda \qquad (9)$$

For a two-phase element, i in equation (9) is replaced by $(i_s V_s + i_\ell V_\ell)/(V_s + V_\ell)$, which is a volume average of the specific enthalpies. With this, equation (9) becomes

$$\theta = V_\ell/(V_s + V_\ell) \qquad (10)$$

where V_s and V_ℓ are the volumes of solid and liquid in the element. For all the nodes, the dimensionless temperature variable ϕ is defined as

$$\phi = c_s(T - T_{\text{sat}})/\lambda \qquad (11)$$

The dimensionless spatial coordinates are X, Y, obtained by dividing the physical coordinates x, y by L. The dimensionless time variable τ is defined as

$$\tau = \text{Ste Fo} = (c_s(T_{\text{sat}} - T_\infty)/\lambda)(k_s t/\rho_s c_s L^2) = k_s(T_{\text{sat}} - T_\infty)t/\rho_s \lambda L^2 \qquad (12)$$

where Ste and Fo are the Stefan and Fourier numbers, respectively.

Next, these definitions are used to transform the modified enthalpy equation (4) which is applicable because the liquid, being initially at the saturation condition, remains so throughout the transient. In the finite difference formulation, equation (4) is satisfied only in an integral sense. For a single-phase element, $\int_v \rho(i - i_\ell)dV$ is replaced by $\rho V(i - i_\ell)$, where V is the volume of the element and ρ and i are nodal values. With this, and for ρV = constant (as it is for all solid elements), equations (9), (11), and (12) may be used to transform equation (4) into

$$\text{Ste}\,\frac{\partial\theta}{\partial\tau} = \frac{1}{(V/L^3)}\int_{A/L^2} \frac{\partial\phi}{\partial(n/L)}\,d(A/L^2) \qquad (13)$$

where A is the surface area of the element.

For a solid-liquid element, the temperature is assumed to be T_{sat} as long as both phases are present. In this case,

$$\int_V \rho(i - i_\ell)dV = \rho_s(i_s - i_\ell)V_s + \rho_\ell(i_\ell - i_\ell)V_\ell = -\rho_s\lambda V_s \qquad (14)$$

For all solid-liquid elements, $V_s + V_\ell = V$, so that the enthalpy

Table 1 Coefficients for equation (16)

Node location	i	j	$-a_0$	a_1	a_2	a_3	a_4	c
Corner O	0	0	$4(1 + \mathrm{Bi}\Delta)$	2	2	0	0	$4\mathrm{Bi}\Delta\mathrm{Ste}$
Surface OA	i	0	$2(2 + \mathrm{Bi}\Delta)$	1	2	1	0	$2\mathrm{Bi}\Delta\mathrm{Ste}$
Corner A	$1/\Delta$	0	$2(2 + \mathrm{Bi}\Delta)$	0	2	2	0	$2\mathrm{Bi}\Delta\mathrm{Ste}$
Surface OC	0	j	$2(2 + \mathrm{Bi}\Delta)$	2	1	0	1	$2\mathrm{Bi}\Delta\mathrm{Ste}$
Surface AB	$1/\Delta$	j	4	0	1	2	1	0
Interior	i	j	4	1	1	1	1	0

equation (4), together with equations (10)–(12) and (14), becomes

$$\mathrm{Ste}\frac{\partial\theta}{\partial\tau} = \frac{1}{(V_s + V_\ell)/L^3}\int_{A/L^2}\frac{\partial\phi}{\partial(n/L)}\,d(A/L^2) \qquad (15)$$

Since the liquid is at the saturation temperature, it is not necessary to write a conservation equation for it.

Equations (13) and (15) are the enthalpy equations for the elements. In order to obtain difference equations, the right-hand sides are replaced by appropriate difference expressions in terms of the values of the temperature variable ϕ at the node considered and at its neighbors. If the node lies on an external boundary, the integrals in equation (13) and (15) are split into their components over the external surface and the interior surface. For the first component, the convective boundary condition or the symmetry condition is used, as applicable. For the second, difference expressions are written.

Next, the derivatives with respect to τ are replaced by implicit differences. For the low Ste values encountered in thermal storage applications (below 0.1), explicit differences are unsuitable because of the stability restriction to which they are subject [4]. Furthermore, as discussed in [4], the implicit method is more efficient than the Crank-Nicolson scheme for the present problem.

For a compact presentation, a single prototype equation can be written that is applicable for all solid and solid-liquid elements.

$$S(\theta^k_{i,j} - \theta^{k-1}_{i,j}) = a_0\phi^k_{i,j} + a_1\phi^k_{i+1,j} + a_2\phi^k_{i,j+1} + a_3\phi^k_{i-1,j} + a_4\phi^k_{i,j-1} - c \qquad (16)$$

where a_0, a_1, a_2, a_3, a_4, and c are coefficients whose values for various node locations are given in Table 1. In addition, S stands for $\mathrm{Ste}\Delta^2/\delta\tau$, where $\delta\tau$ is the step size in time. The quantity Bi is the Biot number hL/k_s. Superscripts represent the time level, and subscripts represent the spatial position.

The solid-vapor elements adjacent to the cavity boundary CQ will now be considered. As previously discussed, the heat flux across CQ is taken to be zero. At those nodes located just below CQ, equation (16) is employed with coefficients taken from the bottom line of Table 1. This equation contains the ϕ value at a node located above CQ. This ϕ value is, of course, a fictitious one, and is chosen so as to satisfy the condition of zero heat flux across CQ. Many of the candidate schemes for obtaining this fictitious value are unsuitable because they do not satisfy sufficiency conditions for the convergence of the iterative method to be used for solving the difference equations. The following scheme, described by Shaw [8], is adequate for the purpose. The two situations in which a fictitious node can be found are shown in Fig. 2(a). The lines DL and EM are drawn normal to CQ and are prolonged until they respectively intersect the lines FG and GH that join the nearest nodes lying below CQ. The fact that CQ is adiabatic is expressed by setting $\phi_D = \phi_L$ and $\phi_E = \phi_M$, where ϕ_L and ϕ_M are obtained by linear interpolation.

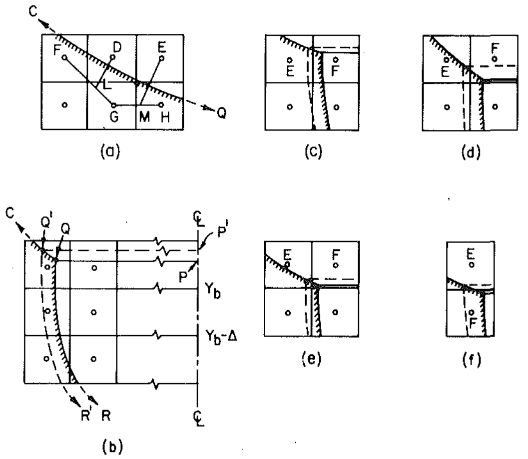

Fig. 2 Sketches related to the equations for the solid-vapor and three-phase elements

Finally, the three-phase element surrounding Q will be treated. The growth of the cavity is governed by the movement of Q with time. The three-phase element is unique in that not only its mass but also the sum $(V_s + V_\ell)$ is time-dependent, and it is not possible to use the enthalpy equation inasmuch as $(V_s + V_\ell)$ is not equal to V. There are two unknowns associated with the three-phase element. One is the liquid volume $(V_\ell + \delta V_\ell)$ at time $(\tau + \delta\tau)$, and the other is the vertical position of PQ (the free surface of the liquid) at that time. One relation needed for finding these unknowns is an overall mass balance for the entire container. To obtain a second condition, it is assumed that the solid-liquid interface QR (Fig. 2(b)) is, in the neighborhood of Q, a parabolic surface in addition to being normal to PQ.

For obtaining the desired equations, Fig. 2(b) is employed. In the sketch, the interfaces at two successive time levels τ^{k-1} and τ^k are shown, respectively as dashed and solid lines. Let V_{liq} be the time-dependent volume of liquid bounded by PQ, QR, and the horizontal surface $Y = Y_b$. In addition, let M_{inc} denote the sum of the increases in the masses of all the solid-liquid elements between times τ^{k-1} and τ^k. Then, as shown in [4], the equation representing overall mass conservation is as follows

$$M_{\text{inc}}/\rho_s L^2 + (1 - \rho_\ell/\rho_s)(V^{k-1}_{\text{liq}} - V^k_{\text{liq}})/L^2 - (1 - ½(X^k_* + X^{k-1}_*))(Y^{k-1}_* - Y^k_*) = 0 \qquad (17)$$

where X_* and Y_* are the coordinates of the triple point Q. Next, the volumes of liquid in the row of elements between $Y = Y_b$ and $Y = Y_b - \Delta$ are summed to get the quantity V_1 at time τ^k. Similarly, V_2 is found for the row of elements below this row at the same time. The quantity V_2 ceases to exist when the second row of elements below the three-phase element becomes fully solid. The finite difference calculations have to be stopped at this stage which, fortunately, does not occur until the solidification is 98 to 99 percent complete. For the small time interval remaining until solidification is complete, the void shape is calculated by a special procedure described in [4].

With η_* representing $(Y^k_* - Y_b)/\Delta$, it is shown in [4] that the following equations furnish the interconnection between V^k_{liq} and Y^k_*

$$V^k_{\text{liq}} = \eta_*(V_1 + (1 + 2\eta_*)(V_1 - V_2)/6) \qquad (18)$$

$$1 - X^k_* = V_1 + (V_1 - V_2)(1/(1 + \eta_*) + 3\eta_*)/6 \qquad (19)$$

Equations (17), (18), and (19) are to be solved along with the previously described difference equations (16).

In the preceding paragraphs, it was tacitly assumed that the same element is in the three-phase regime throughout the time interval $\delta\tau$. It is possible that the triple-point Q moves either to the right as in Figs. 2(c), 2(d), and 2(e) or downwards as in Fig. 2(f). All these situations are treated by assuming that during the small time interval $\delta\tau$, the change in the mass contained in the element E is negligible, and then applying the procedure for the three-phase element to F instead of to E. At E, which at τ^k contains no liquid, the appropriate single-phase finite difference equation is used. A more complete description is available in [4].

In addition to the algebraic equations listed so far, the following relations between θ and ϕ are required. These are obtained from the definitions (9)–(11).

Solid and solid-vapor: $\theta = \phi$, θ and $\phi \leq 0$

Solid-liquid, liquid-vapor,

$$\text{and three phase: } 0 < \theta < 1, \quad \phi = 0 \qquad (20)$$

Saturated liquid: $\theta = 1, \quad \phi = 0$

The initial condition for the problem is $\theta = 1$ at all the nodes.

Solution of the Algebraic Equations

In [3], the finite difference equations corresponding to each time step were solved by the nonlinear Gauss-Seidel iterative method. The reasons for employing an iterative method in preference to others were briefly touched upon in [3], and a comparison with other methods of solving algebraic equations is given in [4]. In this paper, we shall use a selectively applied overrelaxation method instead of the usual Gauss-Seidel method, following the ideas advanced by Meyer [9].

For concreteness, a nodal equation representative of Table 1 will be considered.

$$S\theta^k_{i,j} + 4\phi^k_{i,j} = S\theta^{k-1}_{i,j} + \phi^k_{i,j-1} + \phi^k_{i,j+1} + \phi^k_{i-1,j} + \phi^k_{i+1,j} \qquad (21)$$

The right-hand side of equation (21) is evaluated using the most recently computed ϕ values, as in the Gauss-Seidel method. Suppose first that the right-hand side is found to be positive. Since $\phi \leq 0$ according to equation (20), it follows that $\theta_{i,j}$ on the left-hand side of equation (21) is also positive. However, when θ is positive, ϕ is zero (equation (20)), so that the second term on the left-hand side of equation (21) is deleted. Thus, the new value of $\theta_{i,j}$ is obtained by dividing the right-hand side by S. If, on the other hand, the right-hand side is negative, then $\theta_{i,j} = \phi_{i,j}$, and the new θ value is computed by dividing by $(S + 4)$.

In the first case, where the new θ is greater than zero (two-phase element), it is used as input for the next iteration. In the other case, the new θ is negative (solid element), and the following overrelaxation formula is used to compute the next input

$$\theta^{k,p+1}_{\text{in}} = \theta^{k,p}_{\text{in}} + \omega(\theta^{k,p}_{\text{out}} - \theta^{k,p}_{\text{in}}) \qquad (22)$$

In this equation, $\theta^{k,p}_{\text{in}}$ is the input to equation (21) for the pth iteration, $\theta^{k,p}_{\text{out}}$ is the output of that equation, and $\omega > 1$ is the successive overrelaxation (SOR) parameter.

Except for this modification (SOR at solid nodes only), the iterative procedure is as described in [3]. The employment of this selective SOR scheme results in substantial improvement in the speed with which the iterations converge. As noted by Meyer [9], global overrelaxation, that is, applying equation (22) at all nodes, results in failure to converge. A heuristic explanation for this is given in [4].

For all equations besides those of Table 1, no overrelaxation is applied.

Computational Details. The equations and procedures described in the foregoing were incorporated into a computer program written in PASCAL-II for a CDC 6400 computer. A listing of the program is given in [4]. The program was designed for interactive operation, and could be stopped and restarted at any intermediate stage. The step size in time and the SOR parameter ω were varied during the runs for increased computational efficiency. All results were accumulated on permanent files for printing and further processing at a later time.

As in the work described in [3], many trial runs were made to determine the proper step sizes, spatial as well as in time, and the criterion used for terminating the iterations. Full details of the various runs and tests are given in [4].

In the beginning stages of solidification, the number of active nodes and unknowns is small, and the value of the SOR parameter ω does not greatly influence the convergence rate, which is already fast ($\omega = 1.5$ was used). At later times, ω was gradually increased to obtain nearly optimum convergence rates. The most effective ω values were near 1.7 for cases with Ste = 0.1 and 1.8 for cases with Ste = 0.01, regardless of the other parameters. The use of the selective SOR scheme improved the convergence rates greatly. As many as 1600 equations could be solved in 50–150 iterations.

For the present problem, the density ratio of the phases, $\hat{\rho} = \rho_\ell/\rho_s$, is an additional parameter besides the Stefan number Ste and the Biot number Bi. For the computations, values of 0.8 and 0.9 for $\hat{\rho}$ were selected, together with the values 0.1, 1, and 10 for Bi. Since the results given in [3] showed that the influence of Ste on all the results is small, the values chosen for Ste were 0.01 and 0.1, without the intermediate value of 0.05 dealt with in [3].

Evaluation of Final Results

The local surface heat fluxes q are obtained by employing the convective boundary condition $q = h(T_w - T_\infty)$ in conjunction with the local wall temperatures of the numerical solutions. Surface-integrated heat transfer rates for the horizontal and vertical surfaces, $0A$ and $0C$, respectively (Fig. 1), are also evaluated. These are denoted by Q_h and Q_v, and their sum by Q.

Two alternative ways of defining the solidified fraction are possible, one based on mass and the other on volume. If the mass basis is used, then the fraction ranges from zero to one, regardless of the value of $\hat{\rho}$. In order to underscore the fact that shrinkage is present, the volume basis is preferable. This definition is

$$F = (\text{volume of solid at time } t)/(\text{volume of container}) \qquad (23)$$

The range of the volume-based F is zero to $\hat{\rho}$. The computation of F from the θ distribution is similar to that in [3], with modifications at the three-phase element and the elements on the cavity boundary CQ. The summation for finding F extends over the solid elements, the two-phase elements (solid-vapor and solid-liquid), and the three-phase element.

The values of F, as well as being of interest in their own right, also serve as input to an indirect method of determining the surface-integrated heat flux Q. Such an indirect method was evolved because the grid fineness requirements for determining q and Q for Bi = 10 were found to be prohibitive. For the container as a whole, an instantaneous energy balance can be written as

$$\frac{d}{d\tau}(F - E) = 2\text{Bi}\,\frac{(Q/A)}{h(T_{\text{sat}} - T_\infty)} \qquad (24)$$

where A is the area of the container wall through which Q passes. The quantity E is a measure of the sensible energy of the solidified material

$$E = \int_{V_s} \rho_s(i - i_s)dV/\rho_s\lambda V \qquad (25)$$

in which V is the total volume of the container. The left-hand side of equation (24) is evaluated from a table of F and E versus τ by differentiation. The use of cubic splines was found to be an efficient and accurate means of performing the differentiation.

For computing interface positions, use is made of the θ values in the solid-liquid elements and the definition (10), which gives the corresponding values of V_s. Owing to the moderate grid size, some smoothing of the V_s values had to be performed before an interface surface was fitted. The algorithm for finding the interfaces is based on the employment of cubic splines, and is described in [4]. It should be emphasized that the interface locations are not needed during the finite difference computations and, therefore, may be found at a later time.

Results and Discussion

In the presentation that follows, the results of the present investigation will be supplemented by those of [3] which pertain to substances with negligible density change. The relationship between the two sets of results will be discussed at the end of this section.

Heat Flux Distributions and Locations of Interfaces. It is illuminating to study the local heat flux distributions and the interface locations together, since there is a close relation between the two. To conserve space, the local heat flux and interface results for $\hat{\rho} = 0.9$ are not presented here, but are available in [4]. The spatial distributions of the dimensionless heat flux $q/h(T_{\text{sat}} - T_\infty)$ on the cooled surfaces $0A$ and $0C$ (see Fig. 1) at various instants of time are shown in Figs. 3 and 4. Each of the figures pertains to a single value of Bi, and includes results for $\hat{\rho} = 0.8$ as well as results for $\hat{\rho} = 1$ from [3]. For reasons recounted earlier, local distributions are not available for Bi = 10.

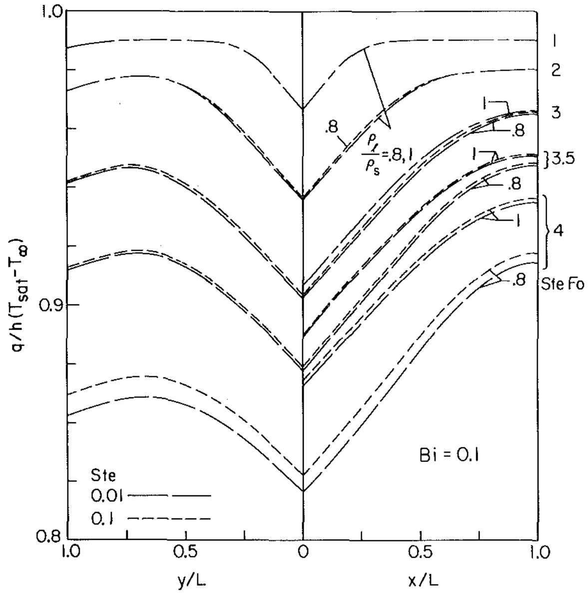

Fig. 3 Local surface heat flux distributions at various instants of time, Bi = 0.1, ρ_ℓ/ρ_s = 0.8 and 1.0

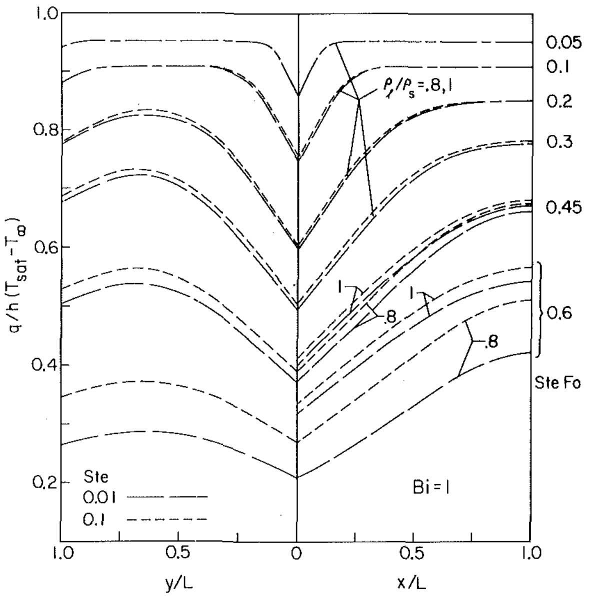

Fig. 4 Local surface heat flux distributions at various instants of time, Bi = 1, ρ_ℓ/ρ_s = 0.8 and 1.0

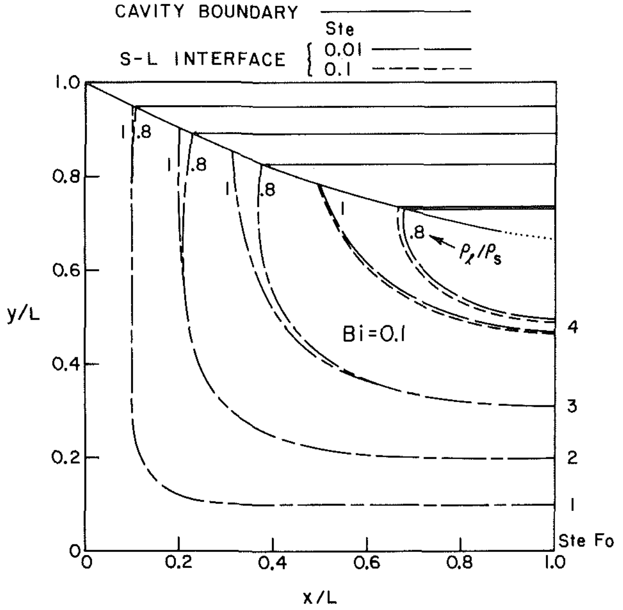

Fig. 5 Solid-liquid interfaces and shrinkage cavity shapes at various instants of time, Bi = 0.1, ρ_ℓ/ρ_s = 0.8 and 1.0

Each figure is subdivided into two parts. The left half contains the heat flux distributions for the vertical face $0C$, whereas the right half is for the flux distributions for the horizontal face $0A$. The corresponding abscissa variables are y/L and x/L, respectively. When $\hat{\rho} = 1$, the heat flux distributions for the two sides are identical, and to preserve clarity, no results corresponding to $\hat{\rho} = 1$ are plotted on the left-hand side.

The curves for Ste = 0.01 and 0.1 are represented by long and short dashes, respectively, as shown in the key at the bottom left of each figure. When the results for the two Ste overlap, a curve is drawn using dashes that are alternately long and short. The density ratios $\hat{\rho}$ to which the curves correspond are indicated by labels. Finally, the values of the time variable τ = SteFo for the successive curves are indicated next to the right-hand margins. The ordinate scales are markedly different for different Bi, thereby underscoring the important role of this parameter. The ordinate variable is also equivalent to $(T_w - T_\infty)/(T_{\text{sat}} - T_\infty)$.

Interface and cavity shapes are shown in Figs. 5 and 6. Each of these figures corresponds in sequence to those for the local heat flux (Figs. 3 and 4). The values of τ = SteFo at which the interfacial curves have been drawn are a subset of the τ values used for the local heat flux results. At any instant, the cross section contains three regions, namely, the solid, the unfrozen liquid, and the cavity arising from shrinkage. The solid-liquid interface is represented by long dashes for Ste = 0.01 and by short dashes for Ste = 0.1. The cavity boundaries (solid-vapor and liquid-vapor) are shown as full lines. As was pointed out earlier, the finite difference computations stop just short of the completion of solidification, and the cavity boundary which is shown as a dotted line is the result of a continuation computation.

As may be observed from Figs. 3–6, the manner in which the heat flux distributions and the interfaces vary with time is generally the same for all parameter values. Hence, it is adequate to discuss all the cases concurrently.

When the time elapsed since the onset of solidification is small, the heat flux is very nearly uniform all along the cooled surfaces, except near the corners O and C. Correspondingly, the solid-liquid interface is straight and parallel to the cooled surface, except near the corner O and, to a lesser extent, near C. In the corner region near O, there is heat loss from two adjacent surfaces, and the solid layer is thicker than elsewhere. The larger resistance of this thicker layer to heat flow by conduction accounts for the reduction in the heat flux in the vicinity of the corner. The reason for the slight reduction in heat flux near C is the nearness of the cavity. Except for this small effect near C, the flux distributions are nearly the same on the two cooled surfaces. Similarly, the solid-liquid interface is also close to being symmetric about the diagonal OB, except that its vertical leg is cut short at the cavity boundary. At these small values of time, the results show no noticeable influence of Ste nor of $\hat{\rho}$, for a given τ value. Consequently, results for values of $\hat{\rho}$ and Ste different from those considered can be obtained from the information presented in the figures.

As time increases, the one-dimensional regions gradually disappear, and the influences of the corners permeate the entire solid region. The lengths of the heat flow paths from the remaining pool of liquid (the energy source) to the vertical surface OC become longer than the paths to corresponding points on the horizontal surface OA. This is espe-

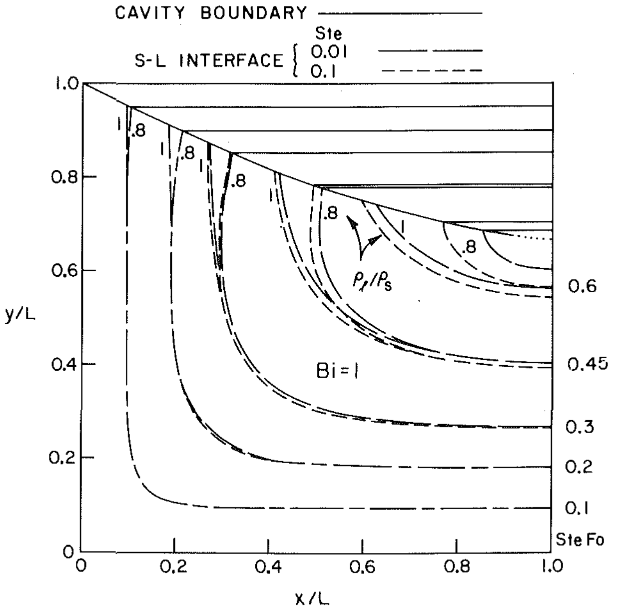

Fig. 6 Solid-liquid interfaces and shrinkage cavity shapes at various instants of time, Bi = 1, ρ_ℓ/ρ_s = 0.8 and 1.0

cially so for points near the corner C, because of their location in the triangular region adjacent to the cavity.

The net result of these changes is that the heat flux distributions and interface shapes become more and more asymmetric as time progresses. The fluxes on the vertical surface are observed to be smaller than the fluxes on the horizontal surface, the more so when the shrinkage is larger. When Bi = 1, as Fig. 4 shows, the heat flux curve for the vertical surface is appreciably lower than the corresponding curve for the horizontal surface at values of τ close to complete solidification. Also, at such τ values, it may be seen that the heat flux curves tend to separate with $\hat{p}$ and Ste. The probable reason for this separation is that, at a given τ, some cases are closer to the end of solidification than others (see Figs. 5 and 6), so that the thermal resistance of the solid layer is different from one case to another. In addition, the role of sensible energy becomes important.

From the figures depicting the interfaces and cavity, it can be observed that the final cavity shape for a given density ratio is practically independent of Bi, that is, of the rate of cooling. This is further supported by the cavity shape obtained for Bi = 10, which, however, is not shown among the results.

Surface-Integrated Heat Flux and Frozen Fractions. The variation with time of the surface-integrated heat transfer Q and the frozen fraction F is relevant for thermal storage applications. Figs. 7–9 show these results for Bi = 0.1, 1, and 10, respectively. In each of these figures, curves are given for all three $\hat{p}$ values (0.8, 0.9 and 1) and for Ste = 0.01 and 0.1. In addition to the overall heat transfer rate Q, results are also given for the heat transfers Q_h and Q_v through the horizontal and vertical walls of the container. The area A used in the dimensionless variables is that area through which the corresponding Q passes. The Q_h and Q_v results are unavailable for Bi = 10.

The Biot number has a marked effect on the thermal characteristics. A low Bi, 0.1, signifies that the convective resistance dominates the resistance to conduction in the solidified portion. Since the convective resistance is constant in time, the heat fluxes are also nearly constant, and the solidification rate, as shown by the slope of the F versus τ curve, is nearly constant (see Fig. 7). The heat fluxes decrease somewhat faster as the end of solidification is approached (F approaches $\hat{p}$). As this state is neared, the influence of Ste becomes noticeable but, during most of the time, there is no observable effect of Ste. The fluxes Q_h and Q_v from the individual surfaces are also equal to each other at small values of τ, but diverge at larger times.

When the Biot number is raised to 1 (Fig. 8), the heat flux Q as well as its components Q_h and Q_v decrease almost linearly with τ. In agreement with this, the solidification rate is faster in the beginning than at later times. In contrast to the Bi = 0.1 case, the influence of Ste manifests itself earlier and is also larger in magnitude, especially near the end of freezing.

Finally, when the Biot number is taken equal to 10 (Fig. 9), the time-dependent resistance of the solidified portion is much larger than the convective resistance. Consequently, the thermal characteristics show a strong dependence on time. The heat fluxes and freezing rates decrease very rapidly soon after solidification sets in. Over the bulk of the transient period, the heat flux averages to only a tenth of its initial value.

Effect of Density Change. Calculations which take account of density changes are more complicated and demanding than those in which the density change is neglected. A logical undertaking would, therefore, be to investigate how the simpler calculations for a model problem in which density change is neglected can be used to obtain approximate solutions to a problem with density change.

Let the model problem be identical to the actual problem (i.e., the problem with $\rho_\ell < \rho_s$) in all respects except one, which is that the

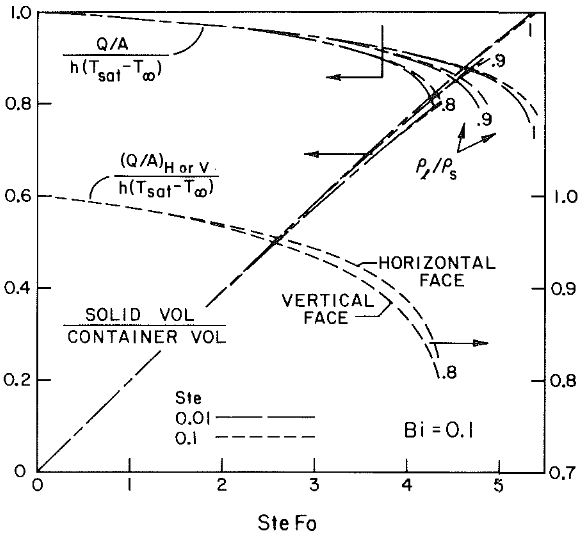

Fig. 7 Time variation of the surface-integrated heat transfer rate and of the frozen fraction, Bi = 0.1

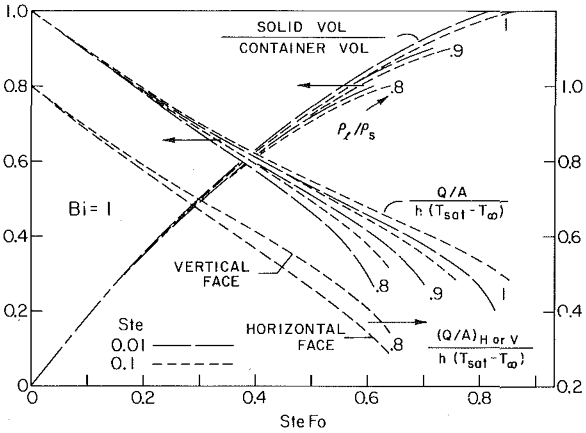

Fig. 8 Time variation of the surface-integrated heat transfer rate and of the frozen fraction, Bi = 1.0

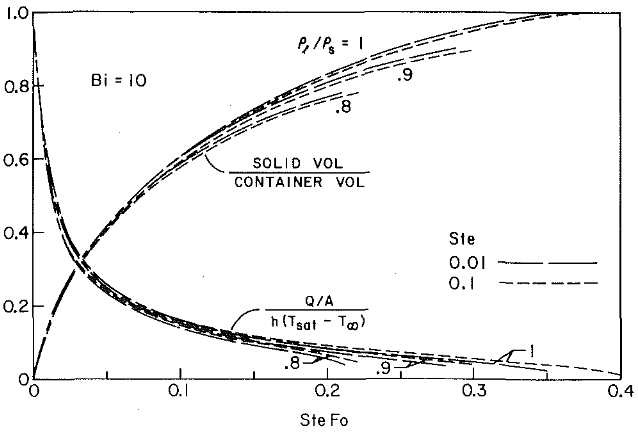

Fig. 9 **Time variation of the surface-integrated heat transfer rate and of the frozen fraction, Bi = 10**

densities of both phases of the model substance are equal to ρ_ℓ. Then, in both problems, the respective liquids are initially at T_{sat} and fill their containers as shown in Fig. 1. Furthermore, with respect to the common region *OABC*, the mass and the latent energy contained are also the same for the two problems. As a consequence of the aforementioned choice of density, the τ values corresponding to the same instant of time t are different in the two problems (see equation (12)). In particular, the τ for the actual problem is ρ_ℓ/ρ_s (<1) times τ of the model problem.

With these considerations in mind, a typical figure, for example, Fig. 8, may be considered. It can be verified by reading numbers from the curves that at large values of τ (where the curves for different values of $\hat{\rho}$ fan out), the dimensionless heat extraction rates read from the $\hat{\rho} = 1$ curve at a specific τ ($\equiv \tau'$) and from the $(\rho_\ell/\rho_s) < 1$ curve at $\tau = (\rho_\ell/\rho_s)\tau'$ are very nearly equal. This indicates that in this range of τ, the heat extraction rates at a given instant of time t are nearly equal for the model problem and for the actual one. At smaller values of τ, this conclusion is no longer valid but, since τ' and $(\rho_\ell/\rho_s)\tau'$ will not be very different if τ' is itself small, the deviations between the corresponding extraction rates may not be objectionably large.

Overall Energy Balance. A very useful and reliable check on the discretization procedure, the computer program, and the accuracy of the entire calculations is to make an overall energy balance. For doing this, equation (24) is integrated from $\tau = 0$ to τ to get

$$F - E = 2\text{Bi} \int_0^\tau \frac{Q}{hA(T_{\text{sat}} - T_\infty)} d\tau \qquad (26)$$

By employing F, E, and Q obtained as functions of τ from the finite difference calculations, the left and right sides of this equation may be evaluated independently. Comparison of the two values constitutes the accuracy test. Since the deviations between the two values increases monotonically with τ, it is sufficient to use for each case a τ value close to the end of solidification. The deviations were found to range from 0.5 to 2.1 percent, which is entirely satisfactory for engineering purposes.

Concluding Remarks

The enthalpy model was extended to accommodate conduction phase change accompanied by density change. The model was applied to the situation where the liquid is at its saturation temperature throughout the entire transient period, thereby obviating the need for determining the velocity field in the liquid. A procedure for estimating the effects of liquid superheat was also discussed. A solidification model was adopted in which the shrinkage cavity is at the top of the container within which the phase change is taking place. The enthalpy approach is also compatible with other possible solidification models. An efficient, implicit finite difference scheme was employed in the implementation of the enthalpy model.

Computations were performed for solidification of a liquid situated in a long, horizontal rectangular container with convectively cooled walls. Transient results were obtained for local and surface-integrated heat flux rates, surface temperatures, frozen fractions, and interface and cavity shapes, all for parametric values of the Stefan number, Biot number, and liquid-solid density ratio. At all times, the Biot number had a major effect on all the results except the final cavity shape. The influence of the Stefan number and density ratio was most marked at times near the completion of solidification. It was found that under certain circumstances, results for a model problem in which density change is neglected can be employed to approximate the results for an actual problem with density change.

Acknowledgment

This research was performed under the auspices of Grant No. GI-34871, initially sponsored by NSF (RANN) and subsequently by ERDA.

References

1 Heitz, W. L., and Westwater, J. W., "Extension of the Numerical Method for Melting and Freezing Problems," *International Journal of Heat and Mass Transfer*, Vol. 13, 1970, pp. 1371–1375.

2 Bilenas, J. A., and Jiji, L. M., "Numerical Solution of a Nonlinear Free Boundary Problem of Axisymmetric Fluid Flow in Tubes With Surface Solidification," Heat Transfer 1970, *Proceedings of the Fourth International Heat Transfer Conference*, Paris—Versailles, Vol. 1, Paper No. Cu. 2.1, 1970.

3 Shamsundar, N., and Sparrow, E. M., "Analysis of Multidimensional Conduction Phase Change via the Enthalpy Model," JOURNAL OF HEAT TRANSFER, TRANS. ASME, Series C, Vol. 97, 1975, pp. 333–340.

4 Shamsundar, N., "Multidimensional Conduction Phase Change With Density Change, and Application to Thermal Energy Storage," PhD thesis, Department of Mechanical Engineering, University of Minnesota, Minneapolis, Minn., 1976.

5 Duda, J. L., Malone, M. F., Notter, R. H., and Vrentas, J. S., "Analysis of Two-Dimensional Diffusion-Controlled Moving Boundary Problems," *International Journal of Heat and Mass Transfer*, Vol. 18, 1975, pp. 901–910.

6 Nesselmann, K., "Systematik der Gleichungen für Gefrieren und Schmelzen von Eisschichten nebst Anwendung auf Trommelgefrierapparate und Susswasserkühler," Kältetechnik, Vol. 1, 1949, pp. 169–172.

7 Truesdell, C., and Toupin, R., "The Classical Field Theories," in *Handbuch der Physik*, S. Flügge, ed., Vol. III/1, Springer Verlag, New York, N. Y., 1960, pp. 525–527.

8 Shaw, F. S., *An Introduction to Relaxation Methods*, Dover Publications, New York, N. Y., 1953, pp. 129–133.

9 Meyer, G. H., "Multidimensional Stefan Problems," *SIAM Journal on Numerical Analysis*, Vol. 10, 1973, pp. 522–538.

J. H. Wright
U. S. Energy Research and Development Administration,
Washington, D. C.

R. I. Loehrke
Department of Mechanical Engineering,
Colorado State University,
Fort Collins, Colo.

The Onset of Thermohaline Convection in a Linearly-Stratified Horizontal Layer

The convective stability of a horizontal layer of water with salt and heat addition from below was studied experimentally. The layer was bounded above and below by porous metal plates through which heat and salt could diffuse. A well-mixed region of warm, salty water below the lower plate and another of cooler, fresher water above the upper plate set the temperature and concentration difference for the intervening quiescent layer. With a fixed, constant concentration gradient established between the plates the temperature difference was slowly increased until convective motions were observed. The instability boundary for this system lies within the unstable region predicted by linear theory for a horizontal layer with constant gradients and stress-free boundaries and approaches the linear boundary at high Rayleigh numbers.

Introduction

Considerable analytical work has been directed at establishing the criteria for the onset of convection in a quiescent, horizontal, multicomponent fluid layer. Buoyancy effects have been considered from two points of view. The double-diffusive or thermohaline (when the diffusing quantities are heat and salt) stability problem focuses on externally imposed gradients of two diffusing species with no coupling between the diffusive processes. The Soret driven or thermal diffusion instability problem concentrates on the coupling effect, specifically the concentration gradient induced by an imposed temperature gradient. The Soret coefficient is generally quite small [1][1] so that in most situations where concentration differences are imposed across the fluid layer the uncoupled analysis should be adequate.

The particular problem examined in this paper is the stability of a quiescent horizontal layer of water with heat and salt (NaCl) diffusing upward due to externally applied temperature and concentration differences. In this situation the temperature gradient is destabilizing. Linear theory, reviewed in detail by Turner [2, 3] and Schechter, et al. [4], predicts the onset of convection in a fluid layer of depth L with constant temperature and concentration gradients as an oscillatory instability over a broad range of parameters. The important parameters in this problem are the thermal and concentration Rayleigh numbers

$$\mathrm{Ra}_t = \frac{g\beta_t L^4 dT/dz}{\nu D_t}$$

and

$$\mathrm{Ra}_c = \frac{g\beta_c L^4 dC/dz}{\nu D_c}$$

and the diffusivity ratios, the Lewis number Le = D_t/D_c and the Prandtl number Pr = ν/D_t where g is the acceleration of gravity, β_t is the coefficient of fractional density change due to a unit change in temperature T, β_c is the coefficient of fractional density change due to a unit change in concentration C, ν is the kinematic viscosity, and z is the vertical coordinate positive upward. For heat and salt addition from below both Ra_t and Ra_c are positive. An analytical solution has been obtained only for stress-free, perfectly conducting boundaries. For these conditions the instability boundary is given by:

$$\mathrm{Ra}_t{}^c = \mathrm{Ra}_t{}^{c0} + \mathrm{Ra}_c \tag{1}$$

for

---

[1] Numbers in brackets designate References at end of paper.

Contributed by the Heat Transfer Division of THE AMERICAN SOCIETY OF MECHANICAL ENGINEERS and presented at the National Heat Transfer Conference. Revised manuscript received by the Heat Transfer Division June 25, 1976. Paper No. 76-HT-29.

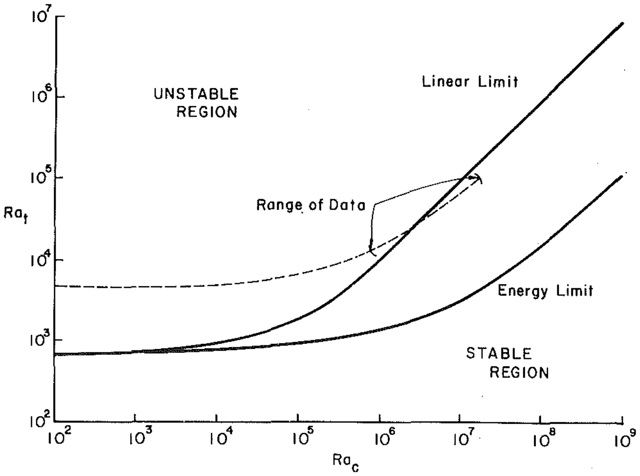

Fig. 1 Stability boundary according to linear theory (equation (2)), energy theory (equation (4)) and Shirtcliffe's empirical curve fit - - - (equation (6)) for Le = 95.4 and Pr = 6.27

$$\frac{Ra_c}{Ra_c{}^*} < 1$$

and

$$Ra_t{}^c = Ra_t{}^{c0}\frac{(Le+1)(1+LePr)}{PrLe^2} + \frac{Ra_c}{Le^2}\left(\frac{1+LePr}{1+Pr}\right) \qquad (2)$$

for

$$\frac{Ra_c}{Ra_c{}^*} > 1$$

where $Ra_t{}^c$ is the critical value of thermal Rayleigh number at a given Ra_c, $Ra_t{}^{c0}$ is the critical value in absence of concentration gradient and for this problem $Ra_t{}^{c0} = 27\pi^4/4 = 657$ and $Ra_c{}^* = Ra_t{}^{c0}(Pr + 1)/Pr(Le - 1)$. For $Ra_t > Ra_t{}^c$ small disturbances to the quiescent, constant gradient solution will grow and convective motions will ensure. In the domain of equation (1) growth is monotonic. Oscillatory instabilities are predicted for $Ra_c > Ra_c{}^*$ with the frequency of the neutral disturbances, equation (2), given by

$$\sigma_i{}^2 = \frac{D_t{}^2}{L^4}\frac{Pr}{3(Pr+1)}\frac{Ra_c}{Le} \qquad (3)$$

For salt and heat diffusing through water $Le \approx 100$ and $Ra_c{}^* \approx 8$. Thus, except for extremely thin layers or small concentration differences equation (2) will define the stability boundary. For large Ra_c equation (2) reduces to

$$Ra_t{}^c = \frac{Ra_c}{Le^2}\left(\frac{1+LePr}{1+Pr}\right)$$

or

$$Sy^c = Le\left(\frac{1+Pr}{1+LePr}\right) \approx \frac{1+Pr}{Pr} \text{ for } LePr \gg 1$$

The stability number, Sy, defined as

$$Sy = \frac{\beta_c \Delta C}{\beta_t \Delta T} = \frac{Ra_c}{Ra_t\, Le} = \frac{-(\partial\rho/\partial z)_c}{(\partial\rho/\partial z)_t}$$

is a measure of the competing effects of concentration and temperature on the density gradient through layer. Uniform layer density, $d\rho/dz = 0$, is equivalent to $Sy = 1$. Linear theory indicates that at high Ra_c convection will begin in a saltwater-heat system ($Pr \approx 6$) when the layer is just slightly more dense below than above.

Joseph [5] has studied the stability of a horizontal layer using energy methods. His nonlinear analysis focuses on the growth and decay of the energy of disturbances to the quiescent, diffusive state. He defines a system as "globally stable" if the disturbance energy tends to zero as time goes to infinity for all bounded initial disturbance energies. For the case where the fluid is destabilized by heating and stabilized by salt the global stability boundary is given by

$$Ra_t = Ra_t{}^{c0} + Ra_c$$

for

$$Ra_c < Ra_c{}^{**}$$

and

$$\sqrt{Ra_t} = \frac{\sqrt{Ra_t{}^{c0}\,(Le^2-1)}}{Le} + \frac{\sqrt{Ra_c}}{Le} \qquad (4)$$

for

$$Ra_c > Ra_c{}^{**}$$

where

$$Ra^{**} = \frac{Ra_t{}^{c0}}{Le^2-1}$$

The energy method predicts when the layer will be stable while the linear method discussed earlier is an instability theory which predicts when the layer will be unstable. A sketch of the energy (stability) limit and the linear (instability) limit for a fluid layer between free surfaces is shown in Fig. 1.

The two limits coincide when

$$Ra_c < \frac{Ra_t{}^{c0}}{Le^2-1}$$

but for larger values of Ra_c, the limits diverge, with the area between them being open to sublinear instabilities. For large Ra_c in a salt-heat system this area is indeed large, $1 \lesssim Sy < 100$.

Only one attempt has previously been made to experimentally determine the stability boundary in a double-diffusive system. Shirtcliffe [6] investigated the onset of convection in a stratified sugar-water system subject to transient heat addition from below. In his experiment sugar solutions were introduced into an open tank in a series of horizontal layers whose successive concentration increased downwards. After several hours, the layers diffused together to pro-

Nomenclature

C = concentration of salt per unit volume of solution
ΔC = concentration difference between boundaries
D_c = solute diffusivity
D_t = thermal diffusivity
g = acceleration of gravity
L = depth of layer
T = temperature
ΔT = temperature difference between boundaries
z = vertical coordinate positive upward
β_c = coefficient of fractional density change due to a unit change in concentration
β_t = coefficient of fractional density change due to a unit change in temperature
ν = kinematic viscosity
ρ = density
σ_i = frequency

Dimensionless Parameters

Le = Lewis number, D_t/D_c
Pr = Prandtl number, ν/D_t
Ra_c = concentration Rayleigh number, $g\beta_c L^4 dC/dz/\nu D_c$
Ra_t = thermal Rayleigh number, $g\beta_t L^4 dT/dz/\nu D_t$
$Ra_t{}^c$ = critical thermal Rayleigh number
$Ra_t{}^{c0}$ = critical thermal Rayleigh number in absence of solute gradient
Sy = Stability number, $\beta_c \Delta C/\beta_t \Delta T$

duce a smooth concentration profile with zero slope at the lower, solid boundary. The tank was then heated rapidly from below until instabilities were observed in the form of temperature oscillations recorded by thermocouples near the bottom of the tank. The instabilities occurred in a thin layer at the bottom of the tank. No measurements of the depth of this layer were possible until convective cells had appeared. Shirtcliffe estimated what this depth should be by maximizing a parameter which he expected to control the stability. This parameter, $\mathrm{Ra}_e(z)$, was defined as

$$\mathrm{Ra}_e(z) = \mathrm{Ra}_t(z) + \frac{\mathrm{Pr}}{\mathrm{Le}(\mathrm{Pr}+1)}\mathrm{Ra}_c(z) \qquad (5)$$

where Ra_t and Ra_c are defined in terms of the temperature and concentration at the lower boundary and those at z. The unsteady temperature profiles were calculated for a constant imposed heat flux diffusing through a semi-infinite medium. Concentration gradients were measured using a scanning schlieren device. Using these inferred and measured values he was able to calculate values for $\mathrm{Ra}_t{}^c$ and Ra_c. From his experiments he concluded that the stability boundary could be best represented by

$$\mathrm{Ra}_t{}^c\,[1 + 4 \times 10^{-6}\,\mathrm{Ra}_t{}^c - 10^{-11}\,(\mathrm{Ra}_t{}^c)^2] - 0.88\,\frac{\mathrm{Ra}_c}{\mathrm{Le}} = \mathrm{Ra}_e \qquad (6)$$

where $\mathrm{Ra}_e = 5000$. This equation is plotted in Fig. 1 with the range of his experiments noted.

While the experiments provided qualitative agreement with the values predicted by linear theory for constant gradients, several of the conditions used in the derivation of the linear theory were not satisfied. The surfaces of the tank in which the experiment was conducted were impermeable to the sugar, resulting in an inability to establish a steady flux of solute through the layer, which caused a nonlinear concentration profile in addition to the nonlinear temperature profile. Also, the convection occurred in a thin bottom layer of the solution where the boundary conditions might most properly be called rigid-free. However, the predictions from linear theory for rigid-free and other possible boundary conditions [7] fall well below the value $\mathrm{Ra}_t{}^{c0} \cong 5000$ which results from equation (6).

In an attempt to better approximate the idealizations of the theories the present experiment was designed in which the subject layer was bounded by porous plates through which both heat and salt could diffuse to provide constant gradients throughout the entire layer.

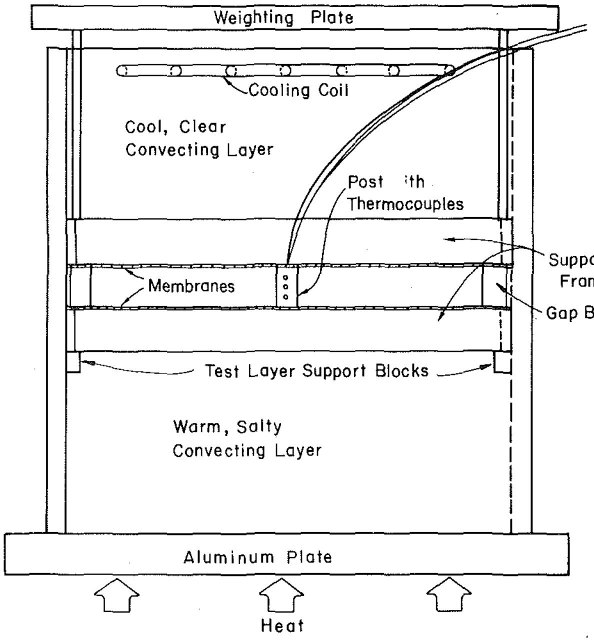

Fig. 2 Experimental apparatus

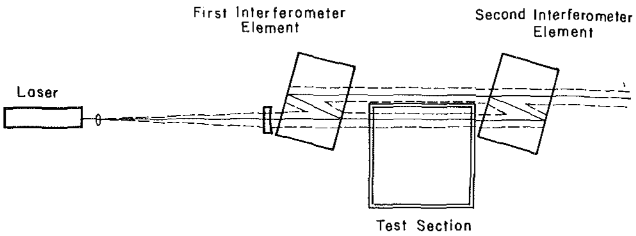

Fig. 3 Schematic of interferometer system viewed from above

Apparatus

The apparatus used in these experiments, shown schematically in Fig. 2, consists of a 15.2 cm square Plexiglas tank closed on the bottom by an aluminum plate and open on the top. Glued in each inside corner of the box are small Plexiglas support blocks placed so that their top surfaces are 5.7 cm from the bottom of the test section. Resting on these blocks is the plate assembly consisting of the support frames, porous plates and gap blocks. The square support frames, constructed of 0.32-cm wide Plexiglas strips 1.27 cm deep, nest snugly inside the tank. A porous stainless steel plate rests on top of the lower frame. A second porous plate is elevated above the first by small Plexiglas gap blocks positioned in the corners of the tank. A second frame inserted above the upper plate completes the plate assembly. The entire assembly is loaded in compression by the weight of a 1.4-kg plate which was transferred to the upper support frame corners through four vertical legs.

In operation heat from an electric resistance heater is added to the apparatus from below, convected through a lower, well-mixed salt-water layer up to the lower porous plate, conducted through the porous plates and intervening stratified fluid layer and removed by cooling water passing through a coil immersed in the upper well-mixed fresh water layer. The diffusion of salt through the system is slow enough to that provisions for addition and removal of this component over the course of an experiment are not necessary.

The porous plates used are diffusion-bonded wire mesh laminates approximately 0.15 cm thick (Dynapore No. 401460 and No. 401480 manufactured by Michigan Dynamics Corp., Garden City, Michigan). The particular plate or combination of plates used for a boundary surface was chosen by trial and error to provide the best compromise between the completing requirements of high permeability to salt flow and high resistance to momentum transfer between the convecting layers and the quiescent layer under study.

Temperature measurements in the test region were made using three equally spaced copper-constantan thermocouples. These thermocouples project 1.27 cm horizontally from a 0.64-cm vertical Plexiglas post which spans the gap between the porous plates (see Fig. 2). The concentration profile through the test region was deduced from the measured temperature profile and the fringe pattern produced by a calibrated laser interferometer.[2] One leg of the interferometer beam passed through the test region between the porous plates, its field covering the gap between the plates and extending roughly from 1.27 to 3.81 cm in from a side all as shown in Fig. 3. The thermocouple rake was located on one center line near the inner edge of the interferometer beam. Temperature and concentration effects on the index of refraction were calibrated independently so that by knowing the temperature profile and the fringe pattern the concen-

---

[2] Benchtop Interferometer, Optical Engineering Inc., Santa Rosa, Calif.

tration profile could be calculated. The effects of the slightly nonuniform Plexiglas test section walls were determined before each test run and subtracted from the fringe pattern measured during a test.

Three different plate spacings (0.58, 1.19, 2.54 cm) were used which, together with a range of initial concentration gradients, provided almost a four order of magnitude range in concentration Rayleigh number. The allowable range of concentration gradients was limited on the low end by the sensitivity of the interferometer and on the high end by excessive refractive bending of the laser beam traversing the test section.

To initiate a stability test, the tank was first filled with a degassed-salt water solution. Then the porous plate assembly was lowered into place, with care taken to avoid trapping any air below the plates, and the interferometer aligned. A picture of the interferometric pattern was taken under these uniform density conditions to obtain a record of the fringes introduced by the walls of the test section itself. The picture was taken by removing the lens from a 35-mm camera and allowing the interference image to fall directly on the film to make the exposure. After the reference fringe picture was taken, the salt solution above the top membrane was replaced with fresh, degassed water. During this final filling process, some mixing occurred through the top membrane into the test region which resulted in an initial stabilizing concentration gradient between the plates. The experiment was allowed to stand for several days after filling (usually two days for the 0.58-cm spacing, three to four days for the 1.19-cm spacing, and four to five days for the 2.54-cm spacing) while the concentration step diffused to a near linear profile. A low voltage was supplied to the heater during this period in order to maintain convective mixing of the bulk fluid layers above and below the central test region.

Once a uniform concentration gradient was established the heating rate was slowly increased to provide an increase in layer temperature difference without appreciably altering the constant temperature gradient. Records of temperature and fringe pattern pictures were taken at several times during the heating cycle before the onset of convection. The incremental step increases in the heating rate were made especially small as the expected critical point was neared so that the temperature and concentration gradients recorded just before motion was observed would be very close to the critical values. The critical point was defined by the appearance of oscillations in the thermocouple output. Visible distortion in the refractive index profile near the plate boundaries closely followed the onset of temperature oscillation. Further increase in the heating rate produced unsteady convective motions in the layer. The temperature and concentration gradients measured at the critical point were converted to thermal and concentration Rayleigh numbers using property data tabulated by the Office of Saline Water [6].

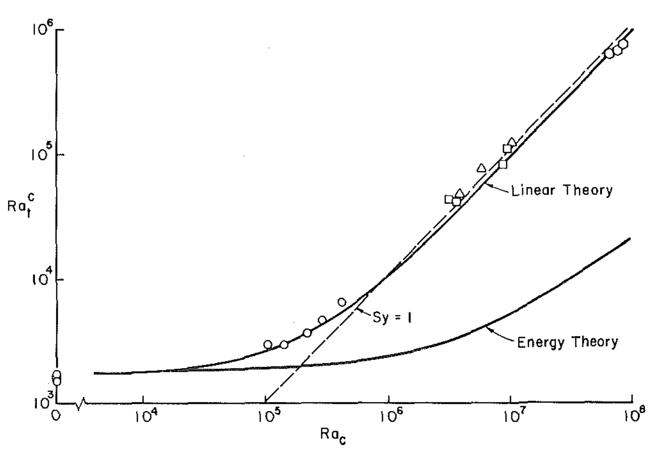

Fig. 4 Comparison of experimental results with theoretical stability boundaries for Le = 95.4 and Pr = 6.27. Solid lines are for linear theory (equation (2)) and energy theory (equation (4)) both using $Ra_t{}^{c0} = 1708$. The symbols are for experiments with ○: 0.58-cm gap, □: 1.19-cm gap, △: 1.19-cm gap with double bottom plate and ○: 2.54-cm gap.

Table 1 Conditions at the onset of convection

Test	Spacing L(cm)	ΔC (ppm)	ΔT (°C)	Ra_c	Ra_t^c
A-1	0.58	0	0.36	0	1504
A-2		0	0.41	0	1716
A-3		0	0.37	0	1575
A-4		110	0.69	1.08×10^5	2.99×10^3
A-5		150	0.69	1.47×10^5	2.99×10^3
A-6		230	0.83	2.25×10^5	3.59×10^3
A-7		310	1.09	3.03×10^5	4.69×10^3
A-8		440	1.53	4.31×10^5	6.58×10^3
B-1	1.19	395	1.22	3.30×10^6	4.43×10^4
B-2		450	1.18	3.76×10^6	4.31×10^4
B-3		1100	2.28	9.19×10^6	8.31×10^4
B-4		1200	3.04	1.00×10^7	1.11×10^5
BD-1		479	1.34	4.00×10^6	4.89×10^4
BD-2		740	2.16	6.18×10^6	7.87×10^4
BD-3		1300	3.51	1.09×10^7	1.27×10^5
C-1	2.54	865	1.82	6.95×10^7	6.45×10^5
C-2		1000	1.93	8.04×10^7	6.85×10^5
C-3		1109	2.12	8.91×10^7	7.51×10^5

One series of three tests was run without any concentration gradient to calibrate the apparatus. For these experiments the test section was filled with fresh water and the heating rate was slowly advanced until a distortion in the linear refractive index profile first appeared near the plate boundaries. Since temperature oscillations were neither expected nor observed under these conditions only changes in the mean temperature profile could be used as a criterion for stability.

Results

The values obtained for the critical thermal Rayleigh numbers at fixed concentration Rayleigh numbers for all of the runs are presented in Table 1 and plotted in Fig. 4. For the three runs made in absence of salt gradient, $Ra_c = 0$, the critical values obtained, $Ra_t{}^{c0} = 1504$, 1716, and 1575, agree more closely with those predicted for rigid boundaries than for free boundaries [7]. Also shown in Fig. 4 is the stability boundary according to energy theory for a layer with rigid boundaries. The data fall well within the region open to instability according to energy theory. For highly stratified layers (large Ra_c) the onset of convection was observed to occur under conditions of near uniform layer density, Sy = 1.

Although no calculations are reported in the literature for the linear problem with rigid boundaries the experimental data are well correlated by linear prediction for free boundaries and constant gradients, equation (2), when the value of $Ra_t{}^{c0} = 657$ is replaced by that appropriate for rigid boundaries, $Ra_t{}^{c0} = 1708$. The oscillatory nature of the instability is also in agreement with linear theory. Most of the data were collected with the layer bounded above and below by single porous plates. With this configuration the oscillation period was not constant. Also, the interferometric fringe patterns showed that the gradients in the layer following the onset of the oscillations were much sharper near the lower plate than near the upper indicating penetration into the layer of convecting currents from the mixed region below the lower plate. The changes of period and phase caused by these large disturbances precluded accurate determination of an oscillation frequency.

In order to eliminate this problem three tests at the 1.19-cm spacing were repeated with the single lower plate replaced by a composite of two porous plates with a thin layer of Pellon polyester felt sandwiched between. With this added resistance several clean cycles of the tem-

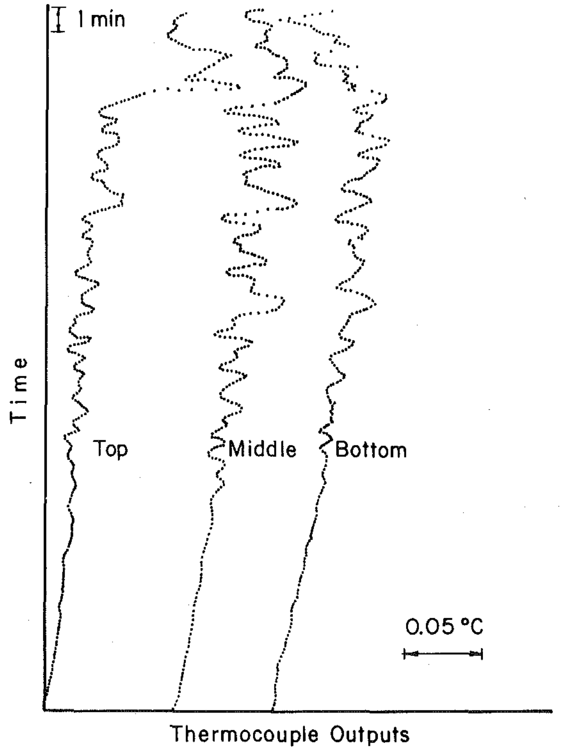

Fig. 5 Thermocouple records for test BD-2 at onset of convection

perature oscillation were obtained from which an oscillation period could be determined. A record of the three thermocouple outputs versus time at the onset of convection for one of these tests is shown in Fig. 5. The critical Rayleigh number for the layer was not altered by this lower boundary change (Fig. 4). The measured periods for these tests are compared with the predictions of linear theory for free boundaries, equation (3), in Table 2. Platten and Chavepeyer [8] have calculated that for Soret driven instabilities the boundary conditions do not influence the form of the period dependence on concentration difference but that the magnitudes are different for fixed and free boundaries.

Experimental Uncertainty

The uncertainty in the experimentally determined critical values of the stability parameters can be assessed from estimates of the possible errors in the terms which enter into the thermal and concentration Rayleigh numbers,

$$\mathrm{Ra}_t = \frac{g\beta_t L^4 dT/dZ}{\nu D_t}$$

and

$$\mathrm{Ra}_c \frac{g\beta_c L^4 dC/dZ}{\nu D_c}$$

Errors in the determination of the temperature gradient at the critical point arise from three sources; uncertainty in the thermocouple calibration, uncertainty in the thermocouple position and resolution of the point in time of the onset of convection. The amplified output of the calibrated copper-constantan thermocouples operated in a differential model was used to determine the temperature difference between thermocouple pairs in the layer. With this arrangement temperature differences could be determined to within ±0.005–±0.03°C depending on the magnitude of the difference. The uncertainty in the thermocouple spacing was about ±0.25 mm. The rate of change of temperature difference near the critical point was maintained at a low level by minimizing the incremental changes in heating rate. Considering all of the above factors the uncertainty in magnitude of the critical temperature gradient was about ±5 percent.

Table 2 Oscillation period at onset of convection—test series with double thickness lower plate

Test No.	Observed period (s)	Period calculated from equation (3) (s)
BD-1	94	61
BD-2	48	49
BD-3	30	37

Errors in the concentration gradient measurement arise from uncertainty in the fringe-concentration gradient calibration, uncertainty in the fringe-temperature gradient correction and uncertainty in the fringe count at the critical point. The sensitivity of the interferometer system to temperature and concentration gradients was determined by calibration. The concentration gradient during a test run could be determined at any time prior to the onset of convection from the fringe count by correcting for temperature effects using the measured temperature gradient. The overall uncertainty in the concentration gradient measurement considering the above sources for possible error was about ±15 percent. The change in concentration gradient over the course of a test run was negligible compared to the uncertainty in the measurement so an average of several measurements prior to convection was used to characterize the gradient at the onset of convection.

The uncertainty in the fluid property data used in the determination of the Rayleigh numbers was estimated to be about ±5 percent.

The source of the largest possible error in the Rayleigh numbers is the uncertainty in the layer thickness. Although the spacer blocks at the four corners of the plates set the gap at these locations to within ±0.13 mm the porous plates were not perfectly flat so the gap may have varied by as much as ±0.76 mm from the nominal value at other locations. This uncertainty could introduce errors of up to ±50 percent at the smallest layer thickness and ±10 percent at the largest layer thickness. However, since the length term appears in both Ra_c and Ra_t the effect would be to move the data points in Fig. 4 along a diagonal line parallel to the Sy = constant curves except for the three data points where $\mathrm{Ra}_c \equiv 0$.

Conclusions

The results of these experiments on a linearly-stratified horizontal fluid layer indicate that at high concentration Rayleigh numbers the onset of convection occurs under conditions of near zero density gradient. At low concentration gradients the observed instability boundary deviates from the neutral density curve and, within experimental error, approaches the theoretical value $\mathrm{Ra}_t = 1708$ in absence of concentration gradient. The conditions at the onset of convection in these controlled experiments fall well within the region open to instability according to energy theory and approach the boundary predicted by linear theory for stress-free boundaries at high Rayleigh numbers. The data are well correlated by the equation

$$\mathrm{Ra}_t{}^c = 1708\frac{(\mathrm{Le}+1)(1+\mathrm{LePr})}{\mathrm{PrLe}^2} + \frac{\mathrm{Ra}_c}{\mathrm{Le}^2}\left(\frac{1+\mathrm{LePr}}{1+\mathrm{Pr}}\right)$$

The oscillatory nature of the instability has been observed. Limited measurements of the oscillation period are in reasonable agreement with the predictions of linear theory.

Acknowledgment

This work was supported by the Office of Naval Research on project NR 083-250.

References

1 Hurle, D. T. J., and Jakeman, E., "Significance of the Soret Effect in the Rayleigh-Jeffrey's Problem," *Physics of Fluids*, Vol. 12, 1969, pp. 2704–2705.

2 Turner, J. S., *Buoyancy Effects in Fluids*, Cambridge University Press, 1973.

3 Turner, J. S., "Double-Diffusive Phenomena," *Annual Review of Fluid Mechanics*, Vol. 6, 1974, pp. 37–56.

4 Schechter, R. S., Velarde, M. G., and Platten, J. K., "The Two-Component Bénard Problem," *Adv. Chem. Phys.*, Vol. 26, 1974, pp. 265–301.

5 Joseph, D. D., "Global Stability of the Conduction-Diffusion Solution," *Arch. Rational Mech. Anal.*, Vol. 36, 1970, pp. 285–292.

6 Shirtcliffe, T. G. L., "An Experimental Investigation of Thermosolutal Convection at Marginal Stability," *J. Fluid Mech.*, Vol. 35, 1969, pp. 677–688.

7 Nield, D. A., "The Thermohaline Rayleigh-Jeffrey's Problem," *J. Fluid Mech.*, Vol. 29, 1967, pl. 545–558.

8 Platten, J. K., and Chavepeyer, G., "Oscillatory Motion in Benard Cell Due to the Soret Effect," *J. Fluid Mech.*, Vol. 60, 1973, pp. 305–320.

Axial Heat Conduction Effects on Thermal Instability of Horizontal Plane Poiseuille Flows Heated From Below

K. C. Cheng
R.-S. Wu

Department of Mechanical Engineering,
University of Alberta,
Edmonton, Alberta, Canada

A linear stability analysis is used to study the effect of axial heat conduction on the onset of instability for longitudinal and transverse vortex disturbances for plane Poiseuille flow in the thermal entrance region of a horizontal parallel-plate channel heated from below with a constant temperature difference between two plates. The basic flow solution for temperature (Graetz problem) incorporates axial heat conduction effects and the fluid temperature is taken to be uniform at the far upstream location $\bar{x} = -\infty$ *to allow for upstream heat penetration through the thermal entrance* $\bar{x} = 0$*. Numerical results for the critical Rayleigh numbers are obtained for an entrance temperature parameter* $\theta_0 = 1$ $(T_0 = T_2)$ *and Peclet numbers 1, 5, 10, 50. It is found that the transverse vortex disturbances are preferred over the longitudinal vortex disturbances for* $Pe \lesssim 1$ *and* $Pr \gtrsim 1$ *(low Re) in the developing regions upstream and downstream of the thermal entrance. For other conditions, the longitudinal rolls have priority of occurrence. The Prandtl number effect on the onset of the longitudinal vortices is clarified.*

1 Introduction

Thermal instability of a plane Poiseuille flow concerned with the onset of a secondary flow in the form of longitudinal vortex rolls in the thermal entrance region of horizontal parallel-plate channels heated from below was studied theoretically by Hwang and Cheng [1][1] considering the axial heat conduction term in the energy equation for the basic flow. Recent studies by Hennecke [2] and Hsu [3] on the Graetz problem with axial heat conduction effects show clearly that the usual thermal condition of a uniform entrance fluid temperature at $X = 0$ used in the classical Graetz problem is unrealistic for the low Peclet number flow regime ($Pe \lesssim 50$) because of upstream heat penetration through the thermal entrance at $X = 0$; and that the fluid temperature must be taken to be uniform far upstream at $X = -\infty$. In view of the predominance of axial heat conduction effects near the thermal entrance $X = 0$ for very low Peclet number flows, the instability analysis [1] based on a uniform entrance temperature at $X = 0$ for the basic flow solution must be regarded as an approximate one when Peclet number is very small.

A deductive analysis of the Graetz problem by Ostrach [4] clarifies the importance of the axial heat conduction term in the energy equation. However, for the very low Peclet number flow regime, the problem is of the elliptic type and the concept of the thermal boundary layer is not applicable. Consequently, the thermal boundary-layer thickness cannot be used as a characteristic length in normalizing the equation. An explicit criterion for the neglect of viscous dissipation is also clearly given in [4]. When the Reynolds number is very small, a question of the priority of the occurrence of transverse rolls [5–7] over longitudinal rolls arises. Recently, Kamotani and Ostrach [8] determined experimentally the critical Rayleigh numbers for thermally developing laminar channel flow and compared the experimental results with results from linear stability theory [1]. A difference as large as an order of magnitude between the two results is observed, but apparently this is somewhat similar to the discrepancy between the experimental [9] and theoretical [10–13] results for longitudinal vortex instability of natural convection flow on inclined surfaces. The difference can be attributed to infinitesimal disturbances in theory and measurable disturbances in experiment. In the laboratory, disturbances are never spatially distributed as in the theory, so measurements can never really be made at the neutral limit. Measuring instruments indicate the accumulated effect of a number of unstable disturbances, some of which are caused by the instrument itself and others which are already amplified and convected with the base flow [8].

---

[1] Numbers in brackets designate References at end of paper.

Contributed by the Heat Transfer Division for publication in the JOURNAL OF HEAT TRANSFER. Manuscript received by the Heat Transfer Division February 25, 1976.

The purpose of this investigation is to study the effects of axial heat conduction on thermal instability of a plane Poiseuille flow between two horizontal flat plates where the lower plate is maintained at a higher constant temperature T_1 ($X \geq 0$) than the upper plate at T_2 which is identical with the uniform entrance fluid temperature T_0 at the far upstream ($X = -\infty$). The mathematical formulation for the basic flow in the thermal entrance region of the parallel-plate channel heated from below is similar to that used by Hennecke [2] and Hsu [3] which is considered to be the most rigorous analysis of the Graetz problem. The onset of convective instability for both longitudinal and transverse vortex rolls in the low Peclet number flow regime is studied by using linear stability theory.

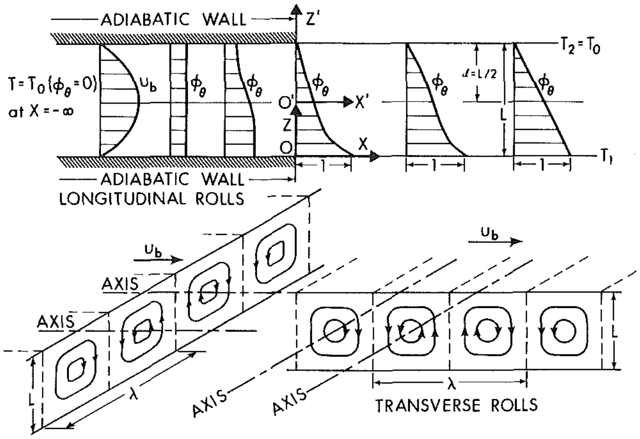

Fig. 1 Coordinate system and transverse and longitudinal vortex disturbances for plane Poiseuille flow

2 Temperature Solutions for Basic Flow

Neglecting viscous dissipation effects, the governing equations in dimensionless form for the thermal entrance region problem (see Fig. 1) with axial heat conduction are [3]

$$\frac{2}{3} u_b \frac{\partial \theta_b}{\partial x'} = \frac{\partial^2 \theta_b}{\partial z'^2} + \left(\frac{8}{3\mathrm{Pe}}\right)^2 \frac{\partial^2 \theta_b}{\partial x'^2} \qquad (1)$$

$$\theta_{b1}(-\infty, z') = \theta_0, \quad \partial\theta_{b1}(x', 1)/\partial z' = \partial\theta_{b1}(x', -1)/\partial z' = 0 \quad \text{for} \quad -\infty < x' \leq 0 \qquad (2)$$

$$\theta_{b2}(\infty, z') = \theta_f, \quad \theta_{b2}(x', 1) = 1, \quad \theta_{b2}(x', -1) = -1 \quad \text{for} \quad 0 \leq x' < \infty \qquad (3)$$

$$\theta_{b1}(0, z') = \theta_{b2}(0, z'), \quad \partial\theta_{b1}(0, z')/\partial x' = \partial\theta_{b2}(0, z')/\partial x' \quad \text{at} \quad x' = 0 \qquad (4)$$

where the dimensionless variables are defined in the Nomenclature and $u_b = (3/2)(1 - z'^2)$ for a plane Poiseuille flow.

Following the procedures outlined in [3, 14], the temperature solutions θ_{b1} and θ_{b2} in the adiabatic and heated regions, respectively, which satisfy the conditions at $x' = \pm\infty$ can be written as

$$\theta_{b1}(x', z') = \theta_0 + \sum_{n=1}^{\infty} B_n Y_n(z') \exp(\alpha_n{}^2 x') + \sum_{n=1}^{\infty} A_n F_n(z') \exp(\epsilon_n{}^2 x'), \quad -\infty < x' \leq 0 \qquad (5)$$

$$\theta_{b2}(x', z') = z' + \sum_{n=1}^{\infty} C_n R_n(z') \exp(-\beta_n{}^2 x') + \sum_{n=1}^{\infty} D_n Z_n(z') \exp(-\gamma_n{}^2 x'), \quad 0 \leq x' < \infty \qquad (6)$$

where α_n, ϵ_n and Y_n, F_n are the even and odd eigenvalues and eigenfunctions, respectively, for the adiabatic region. Similarly, β_n, γ_n and R_n, Z_n are the even and odd eigenvalues and eigenfunctions, respectively, for the heated region. The details of the solution method and the computed eigenvalues and eigenfunctions as well as the series expansion coefficients for the case $\theta_0 = 1$ are given elsewhere [15, 16]. A fourth-order Runge-Kutta method [17] using 200 equal steps is employed to obtain the eigenvalues and eigenfunctions from the numerical solution of the characteristic equations and their boundary conditions. The series coefficients are calculated by matching both the temperatures and the axial temperature gradients at $x = 0$ after constructing orthonormal functions from the nonorthogonal eigenfunctions [3]. In this study, the infinite series are truncated at $n = 12$ and 8 for Pe = 1, 5 and Pe = 10, 50, ∞, respectively. For the instability problem, it is more convenient to shift the coordinate origin to the lower plate as shown in Fig. 1. The basic temperature profile now becomes $\phi_\theta = (1 - \theta_b/2)$.

3 Perturbation Equations

The derivation of the perturbation equations is based on the method of small disturbances (a linearization about the basic flow) using the Boussinesq approximation. Introducing the sum of the basic flow and the disturbance flow as $U = U_b(Z) + U'$, $V = V'$, $W = W'$, $T = T_b + \theta'$ and $P = P_b + P'$, subtracting out the basic flow equations from the conservation equations for mass, momentum, and energy,

Nomenclature

A_n, B_n, C_n, D_n = coefficients of infinite series in equations (5) and (6)
a_1, a_2, a = wave numbers in x and y directions and $(a_1{}^2 + a_2{}^2)^{1/2}$
c = amplification or damping factor, $c = 0$ at onset of instability
$D = d/dz$
Gr = Grashof number, $g\beta(\Delta T)L^3/\nu^2$
g = gravitational acceleration
$i = (-1)^{1/2}$
L, ℓ = height of channel and $L/2$
P, P_b = fluid pressure ($P_b + P'$) and basic flow pressure
Pe = Peclet number, $4U_m\ell/\alpha$ = RePr
Pr = Prandtl number, ν/α
p = dimensionless perturbation pressure, $P'/(\rho\nu^2/L^2)$
Ra = Rayleigh number, PrGr
Re = Reynolds number, $4U_m\ell/\nu$
T, T_b, T_m, T_0 = fluid temperature $(T_b + \theta')$, basic flow temperature, $(T_1 + T_2)/2$ and uniform upstream temperature
T_1, T_2 = constant lower and upper plate temperatures
U_b, U_m, u_b = axial and mean velocities and (U_b/U_m) of basic flow
U', V', W' = disturbance velocity components
u, v, w = dimensionless perturbation velocity components $(U', V', W')/(\nu/L)$
X, Y, Z = cartesian coordinates with origin at lower plate
X', Z' = coordinates with origin at center of channel
$x, y, z = (X, Y, Z)/L$
$x', z' = (X'/(3/8)\ell\mathrm{Pe}, Z'/\ell)$
$\bar{x}, \bar{z}$ = transformed coordinates, $(x/(3\mathrm{Pe}/16), z)$
Y_n, R_n, F_n, Z_n = eigenfunctions
α = thermal diffusivity
$\alpha_n, \beta_n, \epsilon_n, \gamma_n$ = eigenvalues
β = coefficient of thermal expansion
θ = dimensionless disturbance temperature, $\theta'/\Delta T$
θ_b, θ_0 = dimensionless temperature and uniform entrance temperature, $(T_b - T_m)/(T_2 - T_m)$ and $(T_0 - T_m)/(T_2 - T_m)$
ν = kinematic viscosity
ρ = density
ϕ_u, ϕ_θ = dimensionless basic velocity and temperature profiles, $(1/2)u_b = 3(z - z^2)$, $(1 - \theta_b)/2$
$\Delta T = (T_1 - T_2)$

Superscripts and Subscripts

$'$ = perturbation quantity
$+$ = amplitude of disturbance quantity
$*$ = transformed perturbation variable or critical value
b = basic flow quantity in unperturbed state
1, 2 = upstream and downstream regions

one obtains the following disturbance equations after neglecting nonlinear terms:

$$\frac{\partial U'}{\partial X}+\frac{\partial V'}{\partial Y}+\frac{\partial W'}{\partial Z}=0 \tag{7}$$

$$U_b\frac{\partial U'}{\partial X}+W'\frac{\partial U_b}{\partial Z}=-\frac{1}{\rho}\frac{\partial P'}{\partial X}+\nu\nabla^2 U' \tag{8}$$

$$U_b\frac{\partial V'}{\partial X}=-\frac{1}{\rho}\frac{\partial P'}{\partial Y}+\nu\nabla^2 V' \tag{9}$$

$$U_b\frac{\partial W'}{\partial X}=-\frac{1}{\rho}\frac{\partial P'}{\partial Z}+\nu\nabla^2 W'+g\beta\theta' \tag{10}$$

$$U_b\frac{\partial \theta'}{\partial X}+U'\frac{\partial T_b}{\partial X}+W'\frac{\partial T_b}{\partial Z}=\alpha\nabla^2\theta' \tag{11}$$

where $\nabla^2=\partial^2/\partial X^2+\partial^2/\partial Y^2+\partial^2/\partial Z^2$ and the disturbances are taken to be independent of time [1, 8, 10].

After introducing the dimensionless variables, $(x, y, z)=(X, Y, Z)/L$, $(u, v, w)=(U', V', W')/(\nu/L)$, $p=P'/(\rho\nu^2/L^2)$, $\theta=\theta'/(\Delta T)$ and the parameter $\mathrm{Gr}=g\beta(\Delta T)L^3/\nu^2$, the disturbance equations become

$$\frac{\partial u}{\partial x}+\frac{\partial v}{\partial y}+\frac{\partial w}{\partial z}=0 \tag{12}$$

$$\mathrm{Re}\phi_u\frac{\partial u}{\partial x}+\mathrm{Re}\frac{d\phi_u}{dz}w=-\frac{\partial p}{\partial x}+\nabla^2 u \tag{13}$$

$$\mathrm{Re}\phi_u\frac{\partial v}{\partial x}=-\frac{\partial p}{\partial y}+\nabla^2 v \tag{14}$$

$$\mathrm{Re}\phi_u\frac{\partial w}{\partial x}=-\frac{\partial p}{\partial z}+\nabla^2 w+\mathrm{Gr}\theta \tag{15}$$

$$\mathrm{Re}\phi_u\frac{\partial \theta}{\partial x}+u\frac{\partial \phi_\theta}{\partial x}+w\frac{\partial \phi_\theta}{\partial z}=\frac{1}{\mathrm{Pr}}\nabla^2\theta \tag{16}$$

where $\phi_u=3z(1-z)$, $\phi_\theta=(T_b-T_2)/\Delta T=(1-\theta_b)/2$ and the operator is understood to be $\nabla^2=\partial^2/\partial x^2+\partial^2/\partial y^2+\partial^2/\partial z^2$. The dependent variables u, v, and p can be eliminated from the continuity and three momentum equations and one obtains a single equation as

$$\mathrm{Re}\phi_u\frac{\partial}{\partial x}(\nabla^2 w)-\mathrm{Re}\frac{d^2\phi_u}{dz^2}\frac{\partial w}{\partial x}=\nabla^2\nabla^2 w+\mathrm{Gr}\nabla_1{}^2\theta$$

where

$$\nabla_1{}^2=\partial^2/\partial x^2+\partial^2/\partial y^2 \quad \text{and} \quad \nabla^2=\nabla_1{}^2+\partial^2/\partial z^2 \tag{17}$$

A separable solution for w and θ may be sought in the following form [1]:

$$f(x, y, z)=f^+(z)\exp[cx+i(a_1x+a_2y)] \tag{18}$$

where c is the amplification factor and the wave numbers a_1 and a_2 are real. Confining attention to neutral stability, one has $c=0$. After substituting equation (18) for the disturbances w and θ, respectively, into equations (17) and (16), one obtains

$$\begin{aligned}(D^2-a^2)^2w^+-ia_1\mathrm{Re}\phi_u(D^2-a^2)w^+&\\ +ia_1\mathrm{Re}(d^2\phi_u/dz^2)w^+&=\mathrm{Gr}a^2\theta^+\end{aligned} \tag{19}$$

$$(D^2-a^2)\theta^+-ia_1\mathrm{Pe}\phi_u\theta^+=\mathrm{Pr}[u^+\partial\phi_\theta/\partial x+w^+\partial\phi_\theta/\partial z] \tag{20}$$

where $a^2=a_1{}^2+a_2{}^2$ and $D=d/dz$. The two foregoing disturbance equations involve three unknowns and u remains to be specified. The following two cases [6] are of interest in this study:

1 For longitudinal rolls ($a_1=0$), and the x-momentum equation (13) gives

$$(D^2-a^2)u^+=\mathrm{Re}(d\phi_u/dz)w^+ \tag{21}$$

It is noted that at neutral stability the x-dependence for the disturbance quantities can be neglected and one has $\partial p/\partial x=0$.

2 For transverse rolls ($a_2=0$), the continuity equation (12) gives [6]

$$u^+=iDw^+/a_2 \tag{22}$$

At this point, it is more convenient to introduce the transformations, $x=(3\mathrm{Pe}/16)\bar{x}$, $z=\bar{z}$, $u^+=\mathrm{Re}u^*$, $w^+=w^*$, $\theta^+=\mathrm{Pr}\theta^*$, $u^+=\mathrm{Re}\,u^*$, $\mathrm{Ra}=\mathrm{GrPr}$ and one obtains:

1 Longitudinal rolls

$$(D^2-a_2{}^2)^2w^*=\mathrm{Ra}a_2{}^2\theta^* \tag{23}$$

$$(D^2-a_2{}^2)u^*=(d\phi_u/d\bar{z})w^* \tag{24}$$

$$(D^2-a_2{}^2)\theta^*=(16/3\mathrm{Pr})u^*\partial\phi_\theta/\partial\bar{x}+w^*\partial\phi_\theta/\partial\bar{z} \tag{25}$$

2 Transverse rolls

$$\begin{aligned}(D^2-a_1{}^2)^2w^*-ia_1\mathrm{Re}\phi_u(D^2-a_1{}^2)w^*&\\ +ia_1\mathrm{Re}(d^2\phi_u/d\bar{z}^2)w^*&=\mathrm{Ra}a_1{}^2\theta^*\end{aligned} \tag{26}$$

$$u^*=(i/a_1\mathrm{Re})Dw^* \tag{27}$$

$$(D^2-a_1{}^2)\theta^*-ia_1\mathrm{Pe}\phi_u\theta^*=(16/3\mathrm{Pr})u^*\partial\phi_\theta/\partial\bar{x}+w^*\partial\phi_\theta/\partial\bar{z} \tag{28}$$

The boundary conditions at the rigid and highly conductive walls applicable to the two foregoing types of disturbances are

$$w^*=Dw^*=u^*=\theta^*=0 \quad \text{at} \quad \bar{z}=0 \text{ and } 1 \tag{29}$$

In this study, the oblique modes ($a_1\neq 0, a_2\neq 0$) are not considered [6] since the two foregoing modes are observed experimentally. For transverse rolls, the disturbance u^* may be eliminated by substituting equation (27) into equation (28) and only the real part of the disturbance equations is considered to have physical significance. It is seen that equation (26) is the Orr-Sommerfeld type equation and is coupled with the energy equation (28).

4 Method of Solution

Considering the expressions for the basic temperature profiles θ_{b1} and θ_{b2}, it is obvious that an analytical solution of the present characteristic value problem is not practical. An iterative technique using the higher order finite-difference scheme [18] is used for the simultaneous solution of the coupled disturbance equations [1]. The details of the numerical solution method are described in [16].

5 Results and Discussion

The critical Rayleigh numbers at the onset of secondary motion are of primary interest in this study. The graphical results are presented in Figs. 2–7 and the numerical results are listed in [16] for the case $\theta_0=1$. One notes that for heating from below, one obtains $\theta_0>-1$ but only the case $\theta_0=1$ ($T_0=T_2$) is considered in this study. The effects of Prandtl number on the onset of longitudinal vortex rolls in both the upstream and downstream regions are shown in Figs. 2–4 for Pe = 1, 10 and 50, respectively.

For $\theta_0=1$ and Pe = 1, the instability results for Pr = 0.7, 1, 10, 100, and ∞ are practically identical and the critical Rayleigh number de-

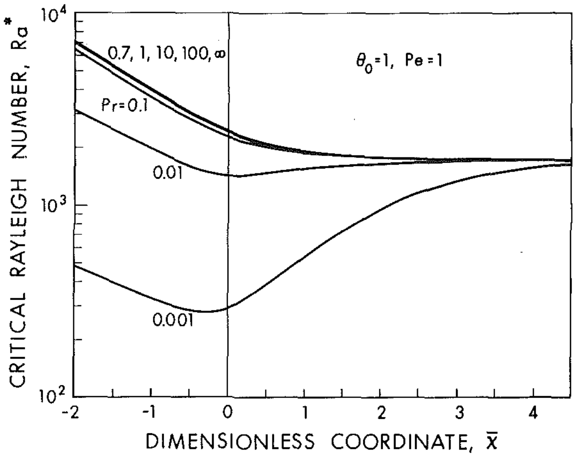

Fig. 2 Prandtl number effect on critical Rayleigh number versus $\bar{x}$ for $\theta_0=1$ and Pe = 1

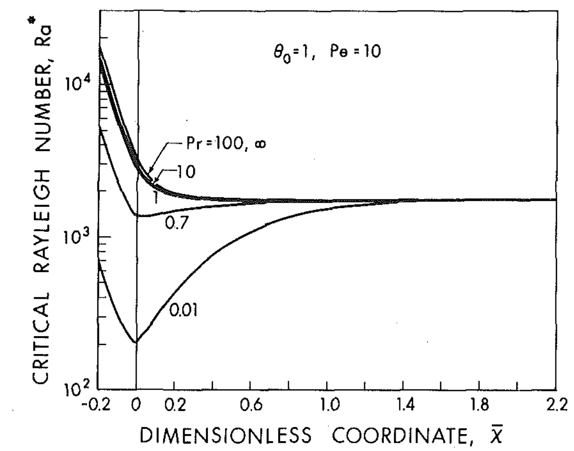

Fig. 3 Prandtl number effect on Ra* versus $\bar{x}$ for $\theta_0 = 1$ and Pe = 10

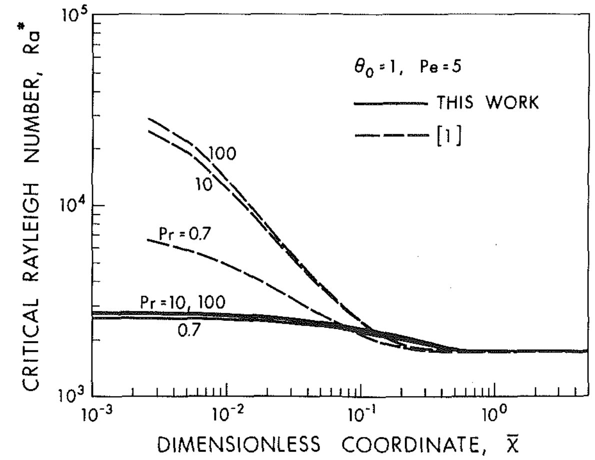

Fig. 5 Comparison of instability results between present work and [1] for $\theta_0 = 1$ and Pe = 1

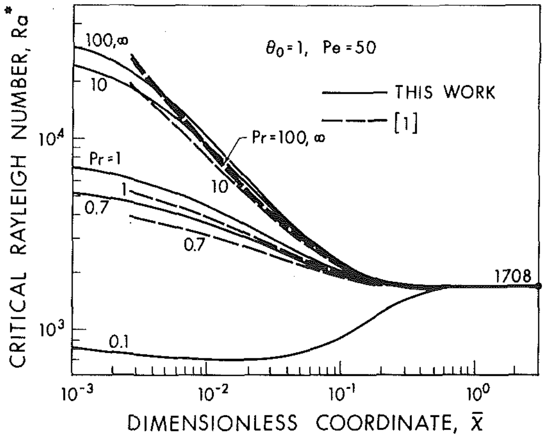

Fig. 4 Comparison of instability results between present work and [1] for $\theta_0 = 1$ and Pe = 50

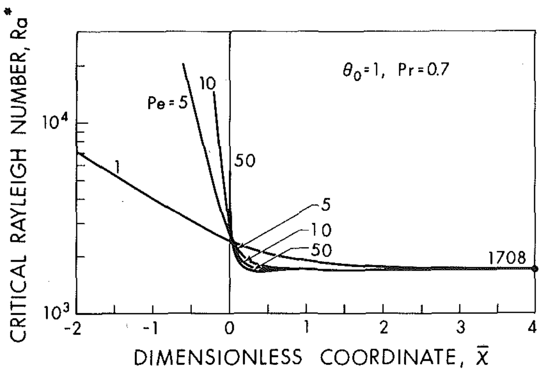

Fig. 6 Peclet number effect on Ra* versus $\bar{x}$ for $\theta_0 = 1$ and Pr = 0.7

creases monotonically from the asymptotic value of Ra* = ∞ at $\bar{x} \approx -6$ to Ra* = 1708 at $\bar{x} = 3.0$ for a linear basic temperature profile. The independence of the critical Rayleigh number Ra* on Prandtl number for Pr $\gtrsim 0.7$ in the case of Pe = 1 can be explained from the perturbation equation (25). It is found that when Pe = 1, the relative magnitude of the ratio $R = (\partial\phi_\theta/\partial\bar{x})/(\partial\phi_\theta/\partial\bar{z})$ is less than 10^{-3} and consequently the forcing term $(16/3\mathrm{Pr})(\partial\phi_\theta/\partial\bar{x})u^*$ on the right-hand side of equation (18) can be neglected in comparison with the term $(\partial\phi_\theta/\partial\bar{z})w^*$ for the range Pr = 0.7 ~ ∞. Thus, the coupled effect of the vertical basic temperature gradient $\partial\phi_\theta/\partial\bar{z}$ and the vertical velocity disturbance w^* dominates. On the other hand, when Pe = 5 and 10, the ratio R is found to be less than 10^{-2} and 10^{-1}, respectively. It is thus seen that the instability result is independent of Prandtl number when Pr ≥ 10 for Pe = 5 and Pr ≥ 100 for Pe = 10. The foregoing argument assumes that the axial and vertical basic temperature gradients, $\partial\phi_\theta/\partial x$ and $\partial\phi_\theta/\partial z$ are of the same order of magnitude which is verified by the numerical results [15, 16]. From the foregoing discussion, it is also clear that the role of Prandtl number becomes increasingly important as the Prandtl number decreases for a given Peclet number. When Pr is small, the term $(16/3\mathrm{Pr})u^*\partial\phi_\theta/\partial\bar{x}$ also destabilizes the flow. As is seen from Figs. 2–3, a local minimum for Ra* exists when the Prandtl number is small. This means that when the Prandtl number is small, the region near the thermal entrance $\bar{x} = 0$ is more unstable than the fully developed region. The practical implications are believed to be important for liquid metals. Noting that the basic temperature profile ϕ_θ is a function of Peclet number only, one sees that the effect of Prandtl number appears through the disturbance equation (25) only.

The instability results for Pe = 50 are shown in Fig. 4 where the unpublished results related to the earlier analysis [1] based on the assumption that the fluid temperature is uniform at the thermal entrance $\bar{x} = 0$ are also plotted for comparison. One should note that the simplified model [1] predicts Ra* = ∞ at $\bar{x} = 0$ whereas the present model predicts a finite value for Ra* at $\bar{x} = 0$. At Pe = 50, the concept of a thermal boundary layer is applicable [15, 16] and the lower Ra* at a given $\bar{x}$ from [1] for a given Pr can be attributed to the larger unstable thermal boundary layer thickness caused by the somewhat artificial absence of the upstream heat penetration through $\bar{x} = 0$. The effect of the axial heat conduction is seen to decrease the thermal boundary layer thickness and the axial temperature gradient $\partial\phi_\theta/\partial\bar{x}$. One should note that at Pe = 50, the lower limit for Pr exists because of the critical Reynolds number Re = 14,170. At Pr = 0.1, the entrance region is seen to be more unstable than the fully developed region.

In order to examine critically the effect of upstream heat conduction on the critical Ra*, the instability results for Pr = 0.7, 10, 100 and Pe = 5 are compared in Fig. 5 with the unpublished results of the earlier study [1] which neglected the upstream heat penetration through $\bar{x} = 0$. At Pe = 5, the earlier model is apparently inadequate to predict Ra*. It is noted that the trend of the Prandtl number effect on Ra* between the present and earlier analyses for Pe = 50 (see Fig. 4) and Pe = 5 is just opposite. This is caused by the fact that at Pe = 50, the problem is basically parabolic and the concept of a thermal boundary layer is applicable whereas at Pe = 5, the problem is elliptic and the heat from the lower plate already penetrates to the upper plate at $\bar{x} = 0$. It is then clear that the larger unstable fluid layer near $\bar{x} = 0$ from the present physical model leads to the considerably lower Ra*.

The effect of Peclet number on Ra* for Pr = 0.7 (air) is shown in Fig. 6. The Peclet number effect on Ra* in the upstream region is seen to be opposite to that in the downstream region. The lower Ra* for Pe = 1 in the adiabatic region is due to the larger unstable fluid layer caused by the axial heat conduction. The developing temperature profiles shown in [15, 16] clearly confirm the foregoing statement. The instability results for Pr = 10 (water) are also shown in Fig. 7. The thermal entrance length for Pe = 1 is longer than those of Pe = 5, 10, 50 and correspondingly the asymptotic value Ra* = 1708 for a fully developed basic flow with a linear temperature profile is approached at a farther downstream location.

The case of transverse rolls is of special interest in this study and the numerical results for Pe = 1 and Pr = 1, 100 are listed in [16]. The graphical results are presented in Fig. 8 where the instability results for the case of longitudinal vortex rolls are also plotted for comparison. It is seen that the onset of the transverse rolls has priority over that of the longitudinal rolls in the upstream region as well as part of the downstream region ($x \lesssim 1.2$). Note that the case of Pr = 100 is more unstable than that of Pr = 1 for transverse rolls but the opposite is true for longitudinal rolls. It is also found that for Pe = 1, Pr $\lesssim$ 0.1 the transverse rolls have no priority over the longitudinal rolls. Similarly, the numerical results reveal that Ra* for transverse rolls is higher than that for longitudinal rolls at $\bar{x} = 0$ for Pe $\geq$ 5. It is thus concluded that the onset of the transverse rolls has priority over that of the longitudinal rolls only when Pe $\lesssim$ 1 and Pr $\gtrsim$ 1 (or small Re) and it occurs in the upstream and downstream regions near the thermal entrance $\bar{x} = 0$. For fully developed region, the longitudinal rolls appear to have priority but the difference in Ra* is so small that the transverse rolls may occur under certain conditions.

For a given Pe, as Pr → ∞ one obtains Re → 0. The perturbation equations for transverse rolls in the fully developed region then become:

$$(D^2 - a_1^2)^2 w^* = a_1^2 \mathrm{Ra} \theta^* \tag{30}$$

$$(D^2 - a_1^2)^2 \theta^* - i a_1 \mathrm{Pe} \phi_u \theta^* = w^* \partial \phi_\theta / \partial \bar{z} \tag{31}$$

where $\partial \phi_\theta / \partial \bar{z} = -1$. The calculation for Pe = 1 gives Ra* = 1717.06 and $a_1^* = 3.117$. The fact that Ra* is larger than the value of 1708 for longitudinal rolls suggests that the term involving Pe in equation (31) may have a stabilizing effect.

The physical reasons for the priority of the "transverse-vortex disturbances" over the "longitudinal vortex disturbances" under the conditions stated earlier are not immediately clear from the study of the disturbance equations and a consideration of the energy exchange between the main flow and the perturbation. However, it appears that when Re is large the transverse rolls tend to be washed out. In addition, one notes that the developing basic temperature profiles show a negative axial temperature gradient near upper plate ($\bar{z} \approx 0.6 \sim 1.0$) for $x \gtrsim -0.1$ at Pe = 1 [15]. At Pe = 5, the region of negative axial temperature gradient is rather small and negligible [15]. It appears that the horizontal density gradients also play some role for the onset of transverse rolls.

The streamline pattern of the transverse-roll type disturbances in a longitudinal cross section is of particular interest. The secondary flow field configuration at the onset of instability is shown in Fig. 9 for the fully developed condition with Pe = 1, Pr = 100, Ra* = 1717.07, $a_1^* = 3.117$. The stream function is defined by $u = -\partial\psi/\partial\bar{z}$ and $w = \partial\psi/\partial\bar{x}$. From the normal modes of disturbances, one has $w = w^+(\bar{z}) e^{ia_1\bar{x}}$ and $\psi = \psi^+(\bar{z})e^{ia_1\bar{x}}$. Noting that $w^+ = w^*$, one obtains $\psi = (w^*/ia_1)e^{ia_1\bar{x}}$ where only the real part is considered to have physical meaning. The contour lines are based on $|\psi_{max}| = 1$ and the dimensionless wavelength $\lambda = 2\pi/a_1 = 2.0156$. The streamline pattern is quite similar to that of the longitudinal rolls and the eyes of the vortices are seen to be located at the center of the channel.

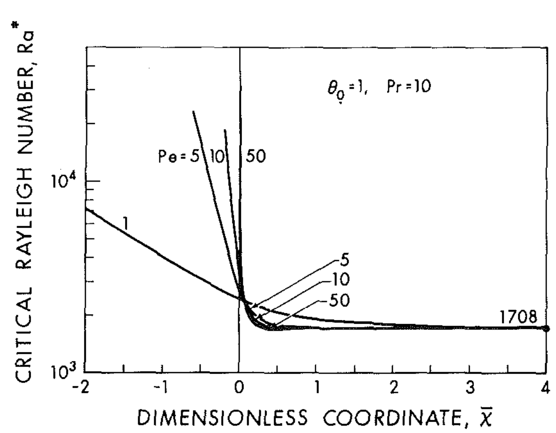

Fig. 7 Peclet number effect on Ra* versus x for $\theta_0 = 1$ and Pr = 10

6 Concluding Remarks

1 The effects of axial heat conduction on the thermal instability of horizontal plane Poiseuille flow heated from below are studied for both longitudinal and transverse vortex disturbances. It is found that the transverse rolls with axes normal to the main flow are the preferred mode of disturbances for the very low Peclet number regime (say Pe $\lesssim$ 1) with Pr $\gtrsim$ 1 (or low Re) in the developing regions upstream and downstream of the thermal entrance. For other conditions, longitudinal rolls with axes parallel to the basic velocity are the preferred mode of disturbance. The observed Peclet number effect on the disturbance modes is consistent with experimental results for combined free and forced convection in porous media [21, 22].

2 For a given entrance temperature parameter θ_0 and Peclet number, the instability mechanism relating to the Prandtl number effect on the onset of longitudinal vortex rolls in the thermal entrance region is clarified by studying the relative order of magnitude of the forcing terms involving axial and transverse basic temperature gradients in the energy disturbance equation (25).

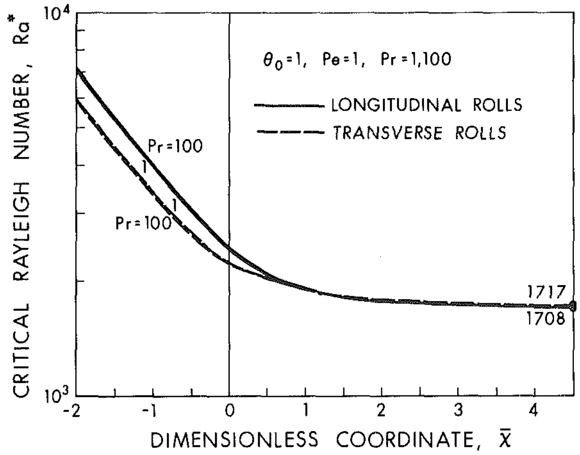

Fig. 8 Instability results for longitudinal and transverse vortex rolls at θ_0 = 1, Pe = 1, and Pr = 1, 100

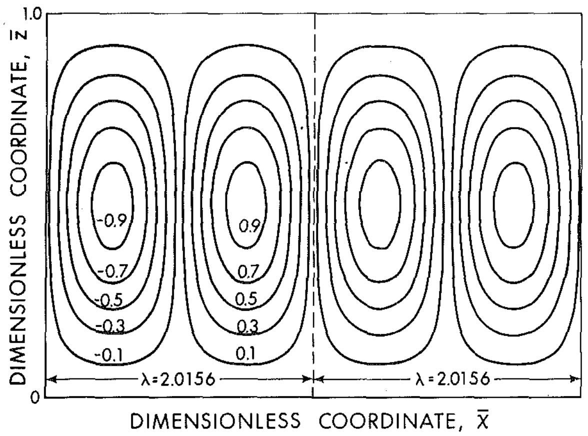

Fig. 9 Streamline pattern of transverse vortex disturbance for fully developed flow at θ_0 = 1, Pe = 1, Pr = 100, Ra* = 1717, and a^* = 3.117

3 For the low Peclet number regime (say $\mathrm{Pe} < 50$), the assumption of uniform entrance fluid temperature at the thermal entrance $\bar{x} = 0$ for the basic temperature solution is not valid because of upstream heat penetration through $\bar{x} = 0$ into the upstream adiabatic region. At $\mathrm{Pe} = 5$ and $\theta_0 = 1$, the predictions of critical Rayleigh number for longitudinal vortex rolls show considerable discrepancy between the two models with and without upstream heat penetration. The discrepancy increases with the decrease of Peclet number.

4 The present instability results can be used in predicting the onset of free convection effect on laminar heat transfer in wide horizontal rectangular channels [8]. For $\mathrm{Ra} > \mathrm{Ra}^*$, one has a finite amplitude thermal convection problem and the classical Graetz formulation for the thermal entrance region problem in a parallel-plate channel is not applicable. It should also be noted that the existence of stationary longitudinal vortex rolls is confirmed by experiment [8]. However, the case of transverse vortex rolls remains to be confirmed by experiment.

5 The numerical experiments using 20 eigenvalues are also carried out to confirm the accuracy of the present numerical results. For $\bar{x} \geq 0.1$, the accuracy of Ra^* is within 1 percent for $\mathrm{Pe} = 1, 5, 10, 50$ and at $\bar{x} = 0^+$, the error of Ra^* is about 1 percent for $\mathrm{Pe} = 1, 5$ and 2 percent for $\mathrm{Pe} = 10$. The convergence of the numerical solution is thus confirmed.

6 Physically, as a low velocity main flow is imposed on Benard cells "transverse-vortex disturbances" appear first. With a further increase of the steady main flow velocity, "longitudinal vortex disturbances" appear. The effect of superposed steady flow on unstable fluid layers described in [5, 23] is consistent with the present theoretical results.

7 Viscous dissipation effects are neglected within the scope of present work but should be studied in the future. Apparently, thermal radiation effects and other thermal boundary conditions such as convective boundary conditions are also of practical interest.

Acknowledgment

This work was supported by the National Research Council of Canada through grant NRC A1655 and a postgraduate scholarship to R. S. Wu.

References

1 Hwang, G. J., and Cheng, K. C., "Convective Instability in the Thermal Entrance Region of a Horizontal Parallel-Plate Channel Heated From Below," JOURNAL OF HEAT TRANSFER, TRANS ASME, Series C, Vol. 95, 1973, pp. 72–77.

2 Hennecke, D. K., "Heat Transfer by Hagen-Poiseuille Flow in the Thermal Development Region With Axial Conduction," *Wärme-und Stoffübertragung*, Vol. 1, 1968, pp. 177–184.

3 Hsu, C. J., "An Exact Analysis of Low Peclet Number Thermal Entry Region Heat Transfer in Transversely Nonuniform Velocity Fields," *AIChE Journal*, Vol. 17, 1971, pp. 732–740.

4 Ostrach, S., "Role of Analysis in the Solution of Complex Physical Problems," *Proceedings of the Third International Heat Transfer Conference, AIChE*, Vol. 6, 1966, pp. 31–43.

5 Ostrach, S., "Laminar Flows With Body Forces," *Theory of Laminar Flows*, F. K. Moore, ed., Princeton University Press, Princeton, N. J., 1964, pp. 624–627.

6 Hart, J. E., "Stability of the Flow in a Differentially Heated Inclined Box," *Journal of Fluid Mechanics*, Vol. 47, 1971, pp. 547–576.

7 Weber, J. E., "On Thermal Convection Between Non-Uniformly Heated Planes," *International Journal of Heat and Mass Transfer*, Vol. 16, 1973, pp. 961–970.

8 Kamotani, Y., and Ostrach, S., "Effect of Thermal Instability on Thermally Developing Laminar Channel Flow," JOURNAL OF HEAT TRANSFER, TRANS. ASME, Series C, Vol. 98, 1976, pp. 62–66.

9 Lloyd, J. E., and Sparrow, E. M., "On the Instability of Natural Convection Flow on Inclined Plate," *Journal of Fluid Mechanics*, Vol. 42, 1970, pp. 465–470.

10 Haaland, S. E., and Sparrow, E. M., "Vortex Instability of Natural Convection Flow on Inclined Surfaces," *International Journal of Heat and Mass Transfer*, Vol. 16, 1973, pp. 2355–2367.

11 Hwang, G. J., and Cheng, K. C., "Thermal Instability of Laminar Natural Convection Flow on Inclined Isothermal Plates," *Canadian Journal of Chemical Engineering*, Vol. 51, 1973, pp. 659–666.

12 Lee, J. B., and Lock, G. S. H., "Instability in Boundary-Layer Free Convection Along an Inclined Plate," *Transactions Canadian Society for Mechanical Engineering*, Vol. 1, 1972, pp. 197–203.

13 Kahawita, R. A., and Meroney, R. N., "The Vortex Mode of Instability in Natural Convection Flow Along Inclined Plates," *International Journal of Heat and Mass Transfer*, Vol. 17, 1974, pp. 541–548.

14 Hatton, A. P., and Turton, J. S., "Heat Transfer in the Thermal Entry Length With Laminar Flow Between Parallel Walls at Unequal Temperatures," *International Journal of Heat and Mass Transfer*, Vol. 5, 1962, pp. 673–679.

15 Wu, R. S., and Cheng, K. C., "Low Peclet Number Heat Transfer in the Thermal Entrance Region of Parallel-Plate Channels With Unequal Wall Temperatures," *Canadian Journal of Chemical Engineering*, to be published.

16 Wu, R. S., PhD thesis, Department of Mechanical Engineering, University of Alberta, Edmonton, Alberta, Canada, 1976.

17 Collatz, L., *The Numerical Treatment of Differential Equations*, 3rd ed., Springer-Verlag, Berlin, 1960, p. 69.

18 Thomas, L. H., "The Stability of Plane Poiseuille Flow," *Physical Review*, Vol. 91, 1953, pp. 780–783.

19 Forsythe, G. E., and Wasow, W. R., *Finite-Difference Methods for Partial Differential Equations*, Wiley, New York, Sec. 24.8, 1960.

20 Fröberg, C. E., *Introduction to Numerical Analysis*, Second ed., Addison-Wesley, Reading, Mass., 1969, p. 117.

21 Combarnous, M. A., and Bia, P., "Combined Free and Forced Convection in Porous Media," *Society of Petroleum Engineers Journal*, Vol. 11, 1971, pp. 399–405.

22 Combarnous, M. A., and Bories, S. A., "Hydrothermal Convection in Saturated Porous Media," *Advances in Hydroscience*, Vol. 10, V. T. Chow, ed., Academic Press, 1975, pp. 231–307.

23 Chandra, K., "Instability of Fluids Heated From Below," *Proceedings, Royal Society*, London, Series A, Vol. 164, 1938, pp. 231–242.

P. H. Oosthuizen

Professor,
Department of Mechanical Engineering,
Queen's University,
Kingston, Ontario, Canada

Numerical Study of Some Three-Dimensional Laminar Free Convective Flows

Three-dimensional buoyancy-induced flows over plates and cylinders have been considered. The three-dimensional flow results either from the fact that the body is inclined to the horizontal or from the fact that there is a longitudinal acceleration component. Both the cases where this acceleration component is constant and the case where it varies linearly with the distance along the body have been considered. The study is based on the use of the constant-property boundary-layer equations. These equations have been rewritten in terms of dimensionless variables, and thus the resulting equations do not explicitly depend on the nature of mechanism causing the three-dimensional flow. These equations have been solved numerically using finite-difference methods, with heat-transfer distributions for various representative situations being deduced.

Introduction

The present study is concerned with three-dimensional buoyancy-induced flows over plates and cylinders that lie in a vertical plane. The three-dimensional flow considered results either from the fact that the body is inclined with respect to the direction of the gravitational acceleration or from the fact that there exists a longitudinal acceleration component f, as indicated in Fig. 1. This acceleration component would normally be the result of bulk rotation of the fluid and the body. Of course, in such a case, f will vary linearly with the coordinate z as shown in Fig. 1. However, if the distance of the body from the axis of rotation is large compared to the length of the body, f can be treated as constant.

The solution procedure adopted can be applied to a cylinder of relatively arbitrary cross-sectional shape, as indicated in Fig. 1. However, results will be discussed only for flow over a circular cylinder and a flat plate. For these two types of bodies the solutions for the limiting cases of gravitational flow over horizontal bodies ($\phi = 0$ deg) and vertical bodies ($\phi = 90$ deg) are known (e.g., see references [1, 2][1]), and the solutions for these two values of ϕ are the same in the case of a flat plate. Several studies of two-dimensional flow in the case where the gravitational acceleration component is negligible compared to the longitudinal acceleration component are also available [3, 4]. No comprehensive studies of three-dimensional free convective flows of the type being considered here appear to be available. However, approximate solutions for a variety of such flows have been presented [5].

Governing Equations

The present study is based on adoption of the boundary-layer assumptions and the assumption that curvature effects are negligible. Because of this the governing equations can be written in terms of the coordinate system shown in Fig. 1. Therefore, assuming steady laminar flow and constant fluid properties, the governing equations are

$$\frac{\partial u}{\partial x} + \frac{\partial v}{\partial y} + \frac{\partial w}{\partial z} = 0 \tag{1}$$

$$u\frac{\partial u}{\partial x} + v\frac{\partial u}{\partial y} + w\frac{\partial u}{\partial z} = \nu\frac{\partial^2 u}{\partial y^2} + \beta|(T - T_\infty)(g\cos\phi - f\sin\phi)|\sin\theta \tag{2}$$

$$u\frac{\partial w}{\partial x} + v\frac{\partial w}{\partial y} + w\frac{\partial w}{\partial z} = \nu\frac{\partial^2 w}{\partial y^2} + \beta(T - T_\infty)(g\sin\phi + f\cos\phi) \tag{3}$$

$$u\frac{\partial T}{\partial x} + v\frac{\partial T}{\partial y} + w\frac{\partial T}{\partial z} = \frac{\nu}{\Pr}\frac{\partial^2 T}{\partial y^2} \tag{4}$$

It should be noted that the body shape affects the solution only through the term $\sin\theta$. It should further be noted that the direction of the x-coordinate is by assumption in the direction of flow. There-

---

[1] Numbers in brackets designate References at end of paper.

Contributed by the Heat Transfer Division of THE AMERICAN SOCIETY OF MECHANICAL ENGINEERS, and presented at the National Heat Transfer Conference, St. Louis, Mo., August 9–11, 1976. Revised manuscript received by the Heat Transfer Division August 30, 1976. Paper No. 76-HT-34.

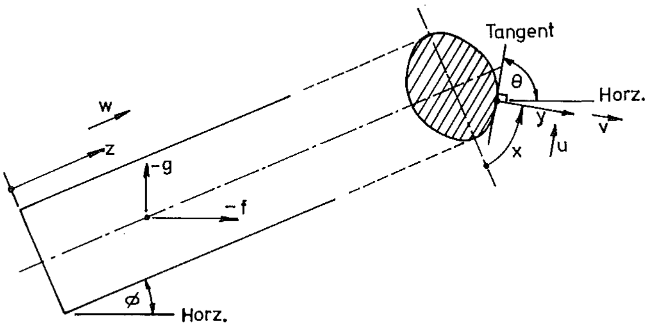

Fig. 1 Situation under consideration

fore if the longitudinal acceleration component $f \sin \phi$ is larger than the gravitational acceleration component $g \cos \phi$, the x direction will be opposite to that shown in Fig. 1. For this reason the modulus is included on the buoyancy term in the x-momentum equation.

The boundary conditions on equations (1)–(4) are assumed to be

$$z = 0;\ u = 0,\quad w = 0,\quad T = T_\infty \quad \text{for all } x \text{ and } y$$

$$y = 0;\ u = 0,\quad v = 0,\quad w = 0,\ T = T_w \quad \text{for all } x \text{ and } z$$

$$y \text{ large: } u \rightarrow 0,\quad w \rightarrow 0,\quad T \rightarrow T_\infty \quad \text{for all } x \text{ and } z \qquad (5)$$

T_w is the wall temperature, which here is assumed to be uniform. However, the solution procedure adopted may easily be extended to deal with uniform surface heat flux.

In addition, boundary conditions at $x = 0$ are required. For a cylinder these are

$$x = 0:\quad u = 0, \frac{\partial w}{\partial x} = 0,\quad \frac{\partial T}{\partial x} = 0 \quad \text{for all } z \text{ and } y \qquad (6)$$

while for a plate they are

$$x = 0;\quad u = 0, w = 0,\quad T = T_\infty \quad \text{for all } z \text{ and } y \qquad (7)$$

Dimensionless Equations for Constant *f*. The case where the longitudinal acceleration component f can be assumed constant will first be considered. If D is some convenient representative dimension of the body, the following Grashof number is introduced

$$G_D = \left|\frac{\beta(T_w - T_\infty)(g\cos\phi - f\sin\phi)\, D^3}{\nu^2}\right| \qquad (8)$$

and the following dimensionless variables are then defined:

$$\overline{u} = \left(\frac{uD}{\nu}\right)\frac{1}{G_D^{0.5}};\quad \overline{v} = \left(\frac{vD}{\nu}\right)\frac{1}{G_D^{0.25}} \qquad (9)$$

$$\overline{w} = \left(\frac{wD}{\nu}\right)\frac{1}{G_D^{0.5}}\left|\frac{g\cos\phi - f\sin\phi}{g\sin\phi + f\cos\phi}\right|;\quad \overline{T} = \left(\frac{T - T_\infty}{T_w - T_\infty}\right)$$

$$\overline{x} = \frac{x}{D};\quad \overline{y} = \left(\frac{y}{D}\right) G_D^{0.25} \qquad (9)$$

$$\overline{z} = \left(\frac{z}{D}\right)\left|\frac{g\cos\phi - f\sin\phi}{g\sin\phi + f\cos\phi}\right|$$

In terms of these variables, the governing equations introduced in the previous section become

$$\frac{\partial\overline{u}}{\partial\overline{x}} + \frac{\partial\overline{v}}{\partial\overline{y}} + \frac{\partial\overline{w}}{\partial\overline{z}} = 0 \qquad (10)$$

$$\overline{u}\frac{\partial\overline{u}}{\partial\overline{x}} + \overline{v}\frac{\partial\overline{u}}{\partial\overline{y}} + \overline{w}\frac{\partial\overline{u}}{\partial\overline{z}} = \frac{\partial^2\overline{u}}{\partial\overline{y}^2} + \overline{T}\sin\theta \qquad (11)$$

$$\overline{u}\frac{\partial\overline{w}}{\partial\overline{x}} + \overline{v}\frac{\partial\overline{w}}{\partial\overline{y}} + \overline{w}\frac{\partial\overline{w}}{\partial\overline{z}} = \frac{\partial^2\overline{w}}{\partial\overline{y}^2} + \overline{T} \qquad (12)$$

$$\overline{u}\frac{\partial\overline{T}}{\partial\overline{x}} + \overline{v}\frac{\partial\overline{T}}{\partial\overline{y}} + \overline{w}\frac{\partial\overline{T}}{\partial\overline{z}} = \frac{1}{\Pr}\frac{\partial^2\overline{T}}{\partial\overline{y}^2} \qquad (13)$$

The boundary conditions in terms of these variables are basically the same as given in equations (5)–(7). Thus the above set of equations show that $\overline{u}$, $\overline{v}$, $\overline{w}$, and $\overline{T}$ are functions of only $\overline{x}$, $\overline{y}$, and $\overline{z}$ for a given body shape and a given Prandtl number, with the values of f/g and ϕ not explicitly entering the solution.

The heat-transfer rate at the surface is given by applying Fourier's equation, which gives

$$q_w = -k\left.\frac{\partial T}{\partial y}\right|_{y=0} \qquad \text{i.e.,} \qquad \frac{N_D}{G_D^{0.25}} = -\left.\frac{\partial\overline{T}}{\partial\overline{y}}\right|_{\overline{y}=0} \qquad (14)$$

where N_D is the local Nusselt number based on D. This shows that $N_D/G_D^{0.25}$ is a function of only $\overline{x}$ and $\overline{z}$ for a given body shape and given Pr.

Flat-Plate Solution. As mentioned in the introduction, results will be considered here only for flow over a flat plate and a circular cylinder. For a flat plate, $\sin\theta$ is everywhere equal to 1, and the $\overline{x}$-momentum equation, i.e., equation (11), for this case becomes

$$\overline{u}\frac{\partial\overline{u}}{\partial\overline{x}} + \overline{v}\frac{\partial\overline{u}}{\partial\overline{y}} + \overline{w}\frac{\partial\overline{u}}{\partial\overline{z}} = \frac{\partial^2\overline{u}}{\partial\overline{y}^2} + \overline{T} \qquad (15)$$

Comparing this with equation (12) shows that in this case $\overline{u} = \overline{w}$, so that the flow direction relative to the $\overline{z}$ direction (i.e., to the leading edge of the plate), which is equal to $\tan^{-1}(u/w)$, will be given by using the definitions of $\overline{u}$ and $\overline{w}$ by

$$\arctan\left|\frac{g\sin\phi + f\cos\phi}{g\cos\phi - f\sin\phi}\right| \qquad (16)$$

at all points. The flow in this case is therefore essentially two-dimensional and is in the direction of the resultant acceleration vector. The heat-transfer rate for this case is therefore given by the well-known solution for two-dimensional flow over a vertical flat plate with a horizontal leading edge with $f = 0$, except that in the present case

Nomenclature

D = representative dimension of body
f = longitudinal acceleration component
f_0, f_i = coefficients in expressions for f, see equation (21)
g = gravitational acceleration component
G_D = Grashof number, see equations (8) and (22)
k = conductivity
N_D = Nusselt number based on D, i.e., $q_w D/k(T_w - T_\infty)$
ℓ = axial length of cylinder
$\overline{\ell} = \ell/(D\tan\phi)$
Pr = Prandtl number
q_w = local wall heat-transfer rate
T = temperature
T_w = wall temperature
T_∞ = ambient temperature
$\overline{T}$ = dimensionless temperature, see equation (9)
u, v, w = velocity components in x, y, and z directions, respectively
$\overline{u}, \overline{v}, \overline{w}$ = dimensionless velocity components, see equations (9) and (22)
x, y, z = coordinate system used, see Fig. 1
$\overline{x}$, $\overline{y}$, $\overline{z}$ = dimensionless coordinates, see equations (9) and (22)
β = coefficient of cubical expansion with temperature
ϕ = angle of inclination from horizontal
θ = surface angle
ν = kinematic viscosity

Subscripts

m = based on mean heat-transfer rate
H = value given by horizontal cylinder solution for given $\overline{\ell}$
V = value given by vertical plate solution for given $\overline{\ell}$

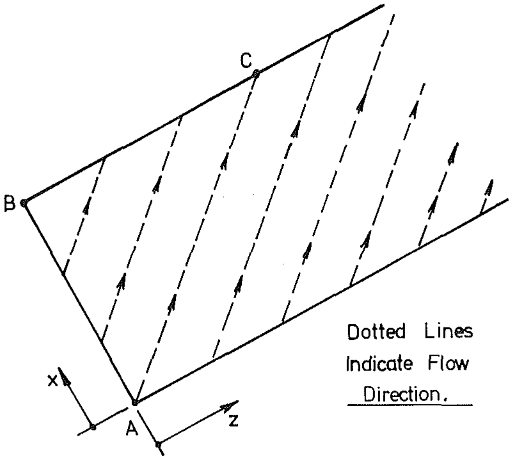

Fig. 2 Flow regions for flat plate with constant *f*

the distance from the leading edge in the direction given by equation (16) is used in place of the vertical distance. The above conclusions may, of course, be regarded as obvious, since the boundary-layer forms of the governing equations are being used. Their adequacy is essentially confirmed by visual studies of free convective flow over plates with nonhorizontal leading edges [6] showing that despite the leading-edge inclination the flow direction remains vertical.

For flow over a plate, therefore, the heat-transfer rate will be independent of $\bar{z}$ except for a region indicated by ABC in Fig. 2 near the "lower" edge of the plate (i.e., edge AB in Fig. 2) where this edge forms the "leading" edge for the flow. In region ABC the heat-transfer rate will vary in the $\bar{z}$-direction but not in the $\bar{x}$-direction. Because of the way in which $\bar{z}$ is defined, line AC is simply given by $\bar{z} = \bar{x}$. The two-dimensional flow solution, of course, still applies in this region provided the distance from the "lower" edge (i.e., edge AB) is used as the distance from the leading edge.

Stagnation-Point Solution. For flow over a circular cylinder, the heat-transfer rate in general will depend on both $\bar{x}$ and $\bar{z}$. However, in the vicinity of the leading edge, θ is near zero, and thus $\sin\theta \simeq \theta = 2\bar{x}$, with the reference length D being in this case, of course, taken as the cylinder diameter. In this case, if a new dimensionless velocity $u^* = \bar{u}/\bar{x}$ is defined, the solution becomes independent of $\bar{x}$, and the governing equations reduce to

$$u^* + \frac{\partial \bar{v}}{\partial \bar{y}} + \frac{\partial \bar{w}}{\partial \bar{z}} = 0 \tag{17}$$

$$u^{*2} + \bar{v}\frac{\partial u^*}{\partial \bar{y}} + \bar{w}\frac{\partial \bar{u}}{\partial \bar{z}} = \frac{\partial^2 u^*}{\partial \bar{y}^2} + 2\bar{T} \tag{18}$$

$$\bar{v}\frac{\partial \bar{w}}{\partial \bar{y}} + \bar{w}\frac{\partial \bar{w}}{\partial \bar{z}} = \frac{\partial^2 \bar{w}}{\partial \bar{y}^2} + \bar{T} \tag{19}$$

$$\bar{v}\frac{\partial \bar{T}}{\partial \bar{y}} + \bar{w}\frac{\partial \bar{T}}{\partial \bar{z}} = \frac{1}{\Pr}\frac{\partial^2 \bar{T}}{\partial \bar{y}^2} \tag{20}$$

In this case, then, the solution does not depend on $\bar{x}$, and the heat-transfer rate will therefore be such that, for a given Prandtl number, $\mathrm{N}_D/\mathrm{G}_D{}^{0.25}$ is a function of $\bar{z}$ above.

Dimensionless Equations for Variable *f*. Here, as discussed in the introduction, it is being assumed that the longitudinal acceleration component varies linearly with z, i.e., it is assumed that

$$f = f_0 + f_i\left(\frac{z}{D}\right) \tag{21}$$

with f_0 and f_i being constants.

The dimensionless variables used are basically the same as in the constant-f case except that here G_D, $\bar{w}$, and $\bar{z}$ are based on f_0, i.e., here

$$\mathrm{G}_D = \left|\frac{\beta(T_w - T_\infty)(g\cos\phi - f_0\sin\phi)\,D^3}{\nu^2}\right|$$

$$\bar{w} = \left(\frac{wD}{\nu}\right)\frac{1}{\mathrm{G}_D{}^{0.5}}\left|\frac{g\cos\phi - f_0\sin\phi}{g\sin\phi + f_0\cos\phi}\right| \tag{22}$$

$$\bar{z} = \left(\frac{z}{D}\right)\left|\frac{g\cos\phi - f_0\sin\phi}{g\sin\phi + f_0\cos\phi}\right|$$

The continuity equation (10) and the energy equation (13) are the same as in the constant-f case. However, the $\bar{x}$- and $\bar{z}$-momentum equations in the present case become

$$\bar{u}\frac{\partial \bar{u}}{\partial \bar{x}} + \bar{v}\frac{\partial \bar{u}}{\partial \bar{y}} + \bar{w}\frac{\partial \bar{u}}{\partial \bar{z}} = \frac{\partial^2 \bar{u}}{\partial \bar{y}^2} + T\sin\theta\left|1 - f_i\sin\phi\,\frac{(g\sin\phi + f_0\cos\phi)}{(g\cos\phi - f_0\sin\phi)^2}\,\bar{z}\right| \tag{23}$$

$$\bar{u}\frac{\partial \bar{w}}{\partial \bar{x}} + \bar{v}\frac{\partial \bar{w}}{\partial \bar{y}} + \bar{w}\frac{\partial \bar{w}}{\partial \bar{z}} = \frac{\partial^2 \bar{w}}{\partial \bar{y}^2} + \bar{T}\left|1 + \frac{f_i\cos\phi}{(g\cos\phi - f_0\sin\phi)}\,\bar{z}\right| \tag{24}$$

The boundary conditions are, of course, basically the same as in dimensional form.

For the variable-f case, results will be given only for a horizontal body, i.e., for $\phi = 0$. In this case, the dimensionless variables reduce to

$$\mathrm{G}_D = \left|\frac{\beta(T_w - T_\infty)gD^3}{\nu^2}\right|$$

$$\bar{w} = \left(\frac{wD}{\nu}\right)\frac{1}{\mathrm{G}_D{}^{0.5}}\left(\frac{g}{f_0}\right);\quad \bar{z} = \left(\frac{z}{D}\right)\left(\frac{g}{f_0}\right) \tag{25}$$

and the $\bar{x}$- and $\bar{z}$-momentum equations are

$$\bar{u}\frac{\partial \bar{u}}{\partial \bar{x}} + \bar{v}\frac{\partial \bar{u}}{\partial \bar{y}} + \bar{w}\frac{\partial \bar{u}}{\partial \bar{z}} = \frac{\partial^2 \bar{u}}{\partial \bar{y}^2} + \bar{T}\sin\theta \tag{26}$$

$$\bar{u}\frac{\partial \bar{w}}{\partial \bar{x}} + \bar{v}\frac{\partial \bar{w}}{\partial \bar{y}} + \bar{w}\frac{\partial \bar{w}}{\partial \bar{z}} = \frac{\partial^2 \bar{w}}{\partial \bar{y}^2} + \bar{T}\left(1 + \frac{f_i}{g}\bar{z}\right) \tag{27}$$

Solution Procedure

Solutions to the sets of equations outlined in the previous two sections have been obtained numerically. A set of grid planes normal to the $\bar{z}$ axis was introduced. On each of these planes a set of grid lines parallel to the $\bar{x}$ and $\bar{y}$ directions was then introduced. Finite-difference approximations written in terms of this grid system were then introduced into the governing set of partial differential equations, reducing them to a set of algebraic equations.

The first of the boundary conditions given in equation (6) gave the conditions at all points on the grid plane at $\bar{z} = 0$. Using these, the solution on the next grid plane was obtained, with this solution advancing in the $\bar{x}$-direction from $\bar{y}$ grid line to $\bar{y}$ grid line starting from the known conditions at the $\bar{y}$ grid line at $x = 0$ that are given in equations (6) and (7). Once the solution on the second grid plane had been obtained in this way, the solution was advanced, using the same procedure, to the next grid plane and so on. Basically the procedure used is the same as that used for two-dimensional flows [7]. It involves the use of three-point difference approximations for the $\bar{y}$-direction derivatives and two-point approximations for those in the $\bar{x}$- and $\bar{z}$-directions. An implicit difference scheme was used, with the $\bar{y}$-derivatives being expressed in terms of conditions on the $\bar{y}$ grid line to which the solution was advancing. The coefficients in the convective terms, such as $\bar{u}$ in the $\bar{u}(\partial\bar{u}/\partial\bar{x})$ term, were also evaluated on this grid line to which the solution was advancing. However, in order to work with a set of linear algebraic difference equations, these coefficients were dealt with iteratively. They were first approximated by the values on the line from which the solution was advancing, and the resultant set of equations was solved using the Thomas algorithm. This solution was then used to give the second approximation for the coefficient terms, and so on until convergence was achieved. In order to stabilize this iterative procedure, pseudo-time-derivative terms were introduced in the two momentum equations. The number of

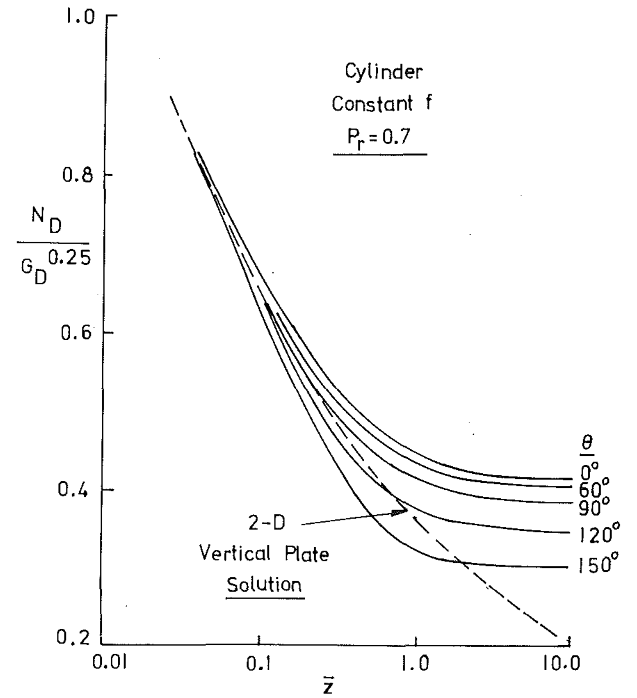

Fig. 3 Results for flow over cylinder with constant f for conditions indicated

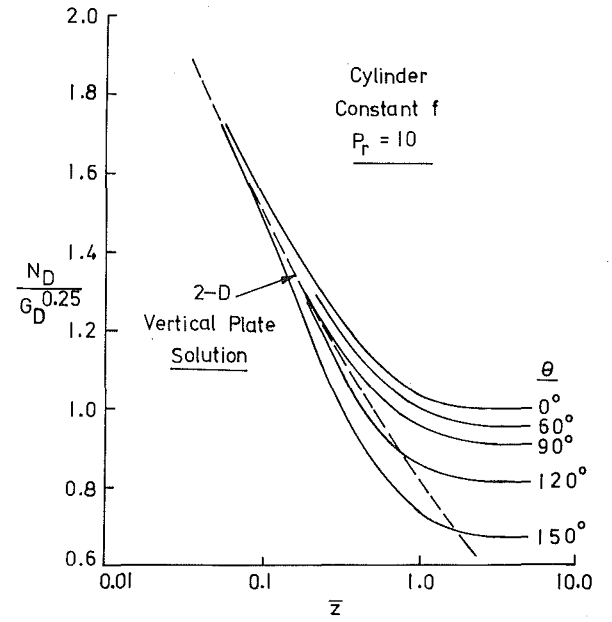

Fig. 4 Results for flow over cylinder with constant f for conditions indicated

iterations required to achieve convergence varied with coordinate position from a minimum of about three to a maximum of about ten. The basic procedure has previously been applied to a number of two-dimensional flow problems [7–9].

Variable grid spacing was used in all three coordinate directions. Calculations with various grid spacing and numbers of grid points were undertaken. However, because of the three-dimensional nature of the problem, it was not practical to explore in detail the effect of grid size and distribution on the solution. However, sufficient calculations were undertaken to indicate that the solutions given below are independent of grid spacing i.e., they are not unique to the spacing used. Typically, about 40 grid points were used in both the $\bar{y}$ and the $\bar{x}$ direction. Because of the form of the difference approximations used, the solution at any stage involved only conditions on two adjacent grid planes.

The above procedure gave the values of $\bar{u}$, $\bar{v}$, $\bar{w}$, and $\bar{T}$ at all grid points. Using this calculated distribution of $\bar{T}$, the distribution of the dimensionless heat-transfer rate could be derived.

Results

Consideration will first be given to results for the case where f is constant. As shown earlier, the flow over a plate in this case is two-dimensional. Results will therefore be given only for flow over a circular cylinder. In this case, as was shown earlier, the dimensionless heat-transfer rate is a function of $\bar{x}$ and $\bar{z}$ for a given Pr. The calculated variation for two values of Pr is shown in Figs. 3 and 4. In presenting the results in these diagrams, $\theta = \arcsin 2\bar{x}$, where D is the cylinder diameter, has been used instead of $\bar{x}$. It will be seen from the results for Pr = 0.7 in Fig. 3 that at small values of $\bar{z}$ the results for all θ tend to coincide, while for large $\bar{z}$ the results tend to be independent of $\bar{z}$. This is, of course, an obvious trend, since it will be seen from the form of the governing equations and the definition of $\bar{z}$ given in equation (9) that $\bar{z} = (z/D)$ (ratio of net x-acceleration component to net z-acceleration component). Hence at small $\bar{z}$ values, the z-acceleration dominates and the flow is effectively the same as that for two-dimensional flow in the z direction. If the x-acceleration component is entirely negligible, the well-known solution for two-dimensional flow over vertical surfaces gives

$$\frac{N_z}{G_z^{0.25}} = A(\mathrm{Pr}) \tag{28}$$

where A as indicated is a function of Prandtl number alone, N_z is the local Nusselt number based on z, and G_z is given by

$$G_z = \left| \frac{\beta(T_w - T_\infty)(g\cos\phi - f\sin\phi)\, z^3}{\nu^2} \right| \tag{29}$$

Rearranging equation (28), therefore, gives

$$\frac{N_D}{G_D^{0.25}} = \frac{A(\mathrm{Pr})}{\bar{z}^{0.25}} \tag{30}$$

The variation of $N_D/G_D^{0.25}$ with $\bar{z}$ given by this equation for the appropriate values of Pr is shown in Figs. 3 and 4, and it will be seen that the results for small $\bar{z}$ tend to the variation given by this equation.

Similarly, at large values of $\bar{z}$ the $\bar{x}$-acceleration component dominates, the flow is effectively two-dimensional and normal to the $\bar{z}$ axis, and $N_D/G_D^{0.25}$ for a given value of θ ceases to vary with $\bar{z}$. For Pr = 0.7 these results for large values of $\bar{z}$ are in agreement with the results of analytic studies of two-dimensional flow over horizontal cylinders [1].

Thus the results for constant f indicate that for a cylinder set at an arbitrary angle to the horizontal the heat-transfer rate near the bottom of the cylinder (i.e., for small z) will be effectively the same as if only the flow parallel to the z-axis existed, while for large z it will be effectively the same as if only the flow normal to the axis existed.

Turning next to the case where f varies with $\bar{z}$, results will be given only for Pr = 0.7 and for two values of f_i/g. The results for a cylinder are given in Figs. 5 and 6, and those for a plate are given in Figs. 7 and 8. In the case of a plate, results are given for $\bar{x}$ up to 1, with D here being taken as the "height" of the plate. The results for variable f show the same basic trends as those for the flow with constant f. Comparing these results with those for constant f shows that if the actual local f at any $\bar{z}$ is used in place of the constant value of f, the constant-f results give a fairly good description of the variable-f results.

The only experimental results that appear to be available for comparison with the present numerical results are the measurements of mean heat-transfer rates from essentially isothermal inclined cylinders that were obtained in an associated study that is described

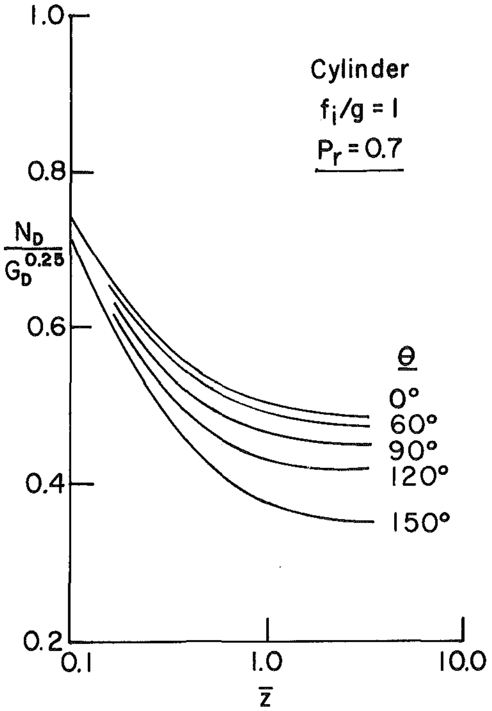

Fig. 5 Results for flow over cylinder with variable *f* for conditions indicated

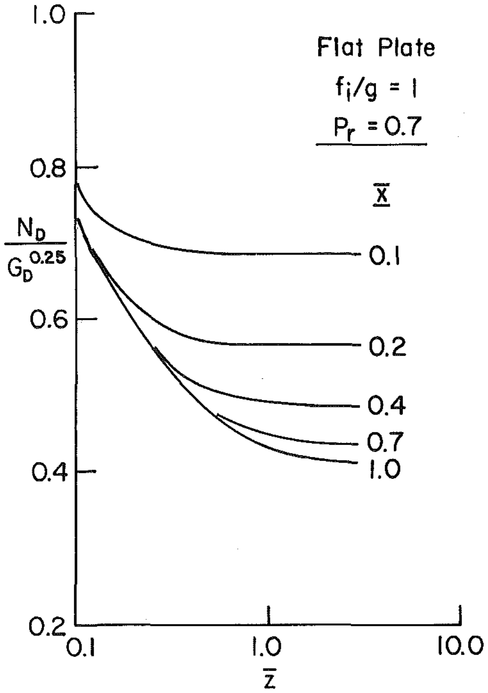

Fig. 7 Results for flow over flat plate with variable *f* for conditions indicated

elsewhere in this issue of the journal [10]. In that study the longitudinal acceleration component f was zero, and for that case G_D reduced to $[\beta g(T_w - T_\infty)D^3 \cos\phi]/\nu^2$ and $\bar{z}$ to $z/(D\tan\phi)$. In order to compare the numerical and experimental results it is necessary to derive the mean heat-transfer rate for a cylinder of given axial length from the local heat-transfer rate variations discussed above. This is obtained by noting that

$$\left.\frac{N_D}{G_D^{0.25}}\right|_m = \frac{1}{\bar{l}}\int_0^{\bar{l}}\left(\int_0^{\pi/2}\frac{N_D}{G_D^{0.25}}\,d\bar{x}\right)d\bar{z} \qquad (31)$$

where $\bar{l} = l/(D\tan\phi)$, with l being the axial length of the cylinder. Thus for a given Pr, by integrating the numerical derived variation

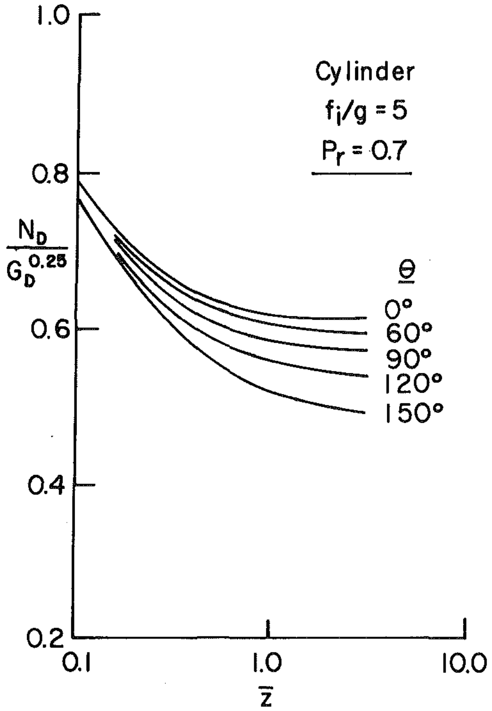

Fig. 6 Results for flow over cylinder with variable *f* for conditions indicated

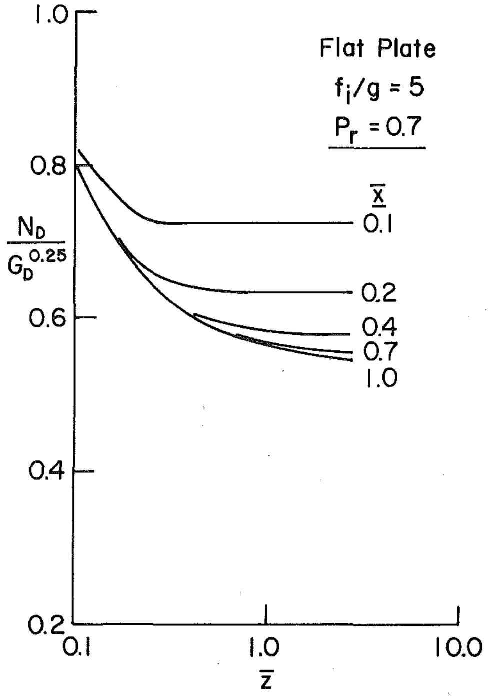

Fig. 8 Results for flow over flat plate with variable *f* for conditions indicated

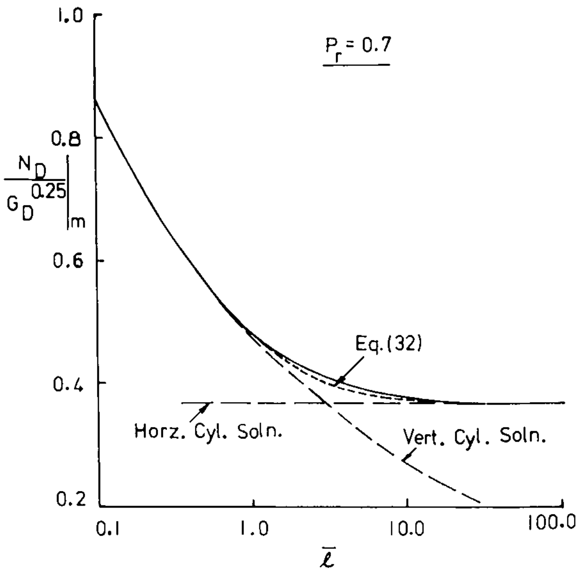

Fig. 9 Mean heat-transfer rate for cylinder with constant *f*

of $N_D/G_D^{0.25}$ with $\bar{x}$ and $\bar{z}$, the variation of $N_D/G_D^{0.25}|_m$ with $\bar{\ell}$ can be derived; the variation for the case of Pr = 0.7 is shown in Fig. 9. From this figure it will be seen that for small $\bar{\ell}$ the variation tends to that given by the vertical plate solution, which is given by equation (28) as $4A/3\bar{\ell}^{0.25}$. Similarly, for large values of $\bar{\ell}$ $N_D/G_D^{0.25}|_m$ becomes constant, i.e., the horizontal cylinder solution applies. From Fig. 9 it will be seen that the "vertical" plate solution applies for $\bar{\ell}$ less than about 1, and the "horizontal" cylinder solution applies for $\bar{\ell}$ greater than about 10. This conclusion is identical to that reached in the experimental study. Further, it has been found that the experimental results between these two limits can be fitted by the following equation:

$$(N_D/G_D^{0.25}|_m)^8 = (N_D/G_D^{0.25}|_{mV})^8 + (N_D/G_D^{0.25}|_{mH})^8 \quad (32)$$

The variation given by this equation is also shown in Fig. 9, with the horizontal and vertical solution values being those given by the numerical results indicated in the figure. In the experimental derivation of equation (32) the experimentally derived horizontal and vertical cylinder results were used, and these variations were roughly 10 percent higher than those derived numerically. It will be seen from Fig. 9 that equation (32), which was derived originally from the experimental results, describes the numerical results to well within the scatter of the experimental data. Therefore it is to be concluded that at least for the particular case of $f = 0$ the forms of the numerical and experimental results are in excellent agreement.

Conclusions

The governing equations for both constant and variable longitudinal acceleration have been written in terms of dimensionless variables that reduce them to a form that does not explicitly depend on the mechanism causing the three-dimensional flow. It is shown that for constant f the flow over a plate is two-dimensional, as is obvious from the form of the basic equations used. The numerical results obtained indicate that for small and large dimensionless z values the heat transfer is effectively given by two-dimensional flow solutions and that between these limiting situations the region of truly three-dimensional flow exists.

Acknowledgment

This work was supported by the National Research Council of Canada under contract number A5573.

References

1 Ede, A. J., "Advances in Free Convection," *Advances in Heat Transfer*, Vol. 4, Academic Press, New York, 1967, pp. 1–64.

2 Kreith, F., *Principles of Heat Transfer*, Second ed., International Textbook Co., 1965.

3 Kreith, F., "Convection Heat Transfer in Rotating Systems," *Advances in Heat Transfer*, Vol. 5, Academic Press, New York, 1968, pp. 129–251.

4 Lemlich, R., and Steinkamp, J. S., "Laminar Natural Convection to an Isothermal Flat Plate with Spatially Varying Acceleration," *AIChE Journal*, Vol. 10, No. 4, July 1964, pp. 445–447.

5 Stewart, W. E., "Asymptotic Calculation of Free Convection in Laminar Three-Dimensional Systems," *International Journal of Heat and Mass Transfer*, Vol. 14, No. 8, Aug. 1971, pp. 1013–1031.

6 Sparrow, E. M., and Husar, R. B., "Free Convection from a Plane Vertical Surface with a Non-Horizontal Leading Edge," *International Journal of Heat and Mass Transfer*, Vol. 12, No. 3, March 1969, pp. 365–369.

7 Wu, M. C. E., "Numerical and Experimental Studies of Some Problems Involving Axisymmetrical Laminar Free Convective Flows," MSc thesis, Queen's University, Kingston, Ont., Canada, 1971.

8 Oosthuizen, P. H., and Wu, M. C. E., "A Numerical Study of Laminar Free Convective Heat Transfer from Vertical Cones," *Trans. CSME*, Vol. 2, No. 1, 1973/74, pp. 9–14.

9 Oosthuizen, P. H., "A Numerical Study of Turbulent Free Convection from an Isothermal Vertical Plate," Report 1-70, Thermal and Fluid Sciences Group, Queen's University, Kingston, Ont., Canada, May 1970.

10 Oosthuizen, P. H., "Experimental Study of Free Convective Heat Transfer from Inclined Cylinders," JOURNAL OF HEAT TRANSFER, TRANS. ASME, Series C, Vol. 98, 1976.

R. M. Abdel-Wahed
E. M. Sparrow
S. V. Patankar

Department of Mechanical Engineering,
University of Minnesota,
Minneapolis, Minn.

Mixed Convection On a Vertical Plate With an Unheated Starting Length

The effect of an unheated starting length on combined forced and natural convection adjacent to a vertical plate has been investigated by solving the nonsimilar laminar boundary layer equations. The solutions were carried out numerically for prescribed values of the governing parameters which include the starting length Reynolds number Re_0, *a mixed convection parameter* $g\beta(\Delta T)\nu/U_\infty{}^3$, *and the Prandtl number (which was assigned a value of 0.7). The local heat transfer results show that the presence of the unheated starting length can significantly accentuate the effects of buoyancy relative to the case of no starting length. The degree of accentuation of the buoyancy effects is strongly influenced by the magnitude of* $g\beta(\Delta T)\nu/U_\infty{}^3$. *When this parameter is on the order of* 10^{-3}, *the natural convection contribution to the heat transfer coefficient is markedly increased owing to the starting length. On the other hand, when* $g\beta(\Delta T)\nu/U_\infty{}^3$ *is about* 10^{-5}, *the buoyancy contribution is essentially unaffected by the starting length. The shape of the velocity profile is also found to be highly responsive to the interaction between the buoyancy and the starting length. As a by-product of the research, the accuracy of a well-known integral momentum/energy solution for pure forced convection with a starting length was established. In addition, velocity profiles for mixed convection without a starting length were compared with those of experiment in order to appraise a proposed explanation for a disparity that had been previously identified in the literature.*

Introduction

It is well-established that buoyancy forces have only a modest effect on the heat transfer from the lower portion of a heated vertical plate situated in a forced convection upflow. This is because the forced convection freestream velocity persists very close to the plate surface (due to the small thickness of the boundary layer) and the natural convection velocities are small (owing to the short length of run along the plate). These characteristics correspond to the situation where both the hydrodynamic and thermal boundary layers originate at the leading edge of the plate. This case is the only one that has so far been investigated ([1-3][1] are representative of the recent literature).

It can be reasoned that the presence of an unheated hydrodynamic starting length should enhance the relative importance of the buoyancy forces by thickening the velocity boundary layer prior to the onset of heating and thereby reducing the velocities near the plate surface. The present investigation was undertaken to assess quantitatively the effect of an unheated starting length on the heat transfer characteristics of a buoyancy-affected forced convection flow on a heated vertical plate. The presence of a starting length activates two additional dimensionless parameters (in addition to the Prandtl number). One of these is the Reynolds number Re_0 that characterizes the starting length. The second is a group $g\beta(\Delta T)\nu/U_\infty{}^3$ which is an index of the relative strengths of the natural and the forced convection, but does not contain a length scale. It is, therefore, independent of the ratio $\mathrm{Gr}_x/\mathrm{Re}_x{}^2 \sim x$, which serves the dual function of a position variable and an index of natural to forced convection in the case where there is no unheated starting length.

The problem does not yield an analytical solution, so a numerical technique was employed. Results were obtained for starting length Reynolds numbers ranging from 1000 to 20,000, for $g\beta(\Delta T)\nu/U_\infty{}^3$ of 10^{-3}, 10^{-4}, and 10^{-5}, and for a Prandtl number of 0.7. For each of these cases, local heat transfer coefficients are presented for $\mathrm{Gr}_x/\mathrm{Re}_x{}^2$ between 0.01 to 10. Representative velocity profiles are also plotted to illustrate the buoyancy effects.

---

[1] Numbers in brackets designate References at end of paper.

Contributed by the Heat Transfer Division for publication in the JOURNAL OF HEAT TRANSFER. Manuscript received by the Heat Transfer Division June 16, 1976.

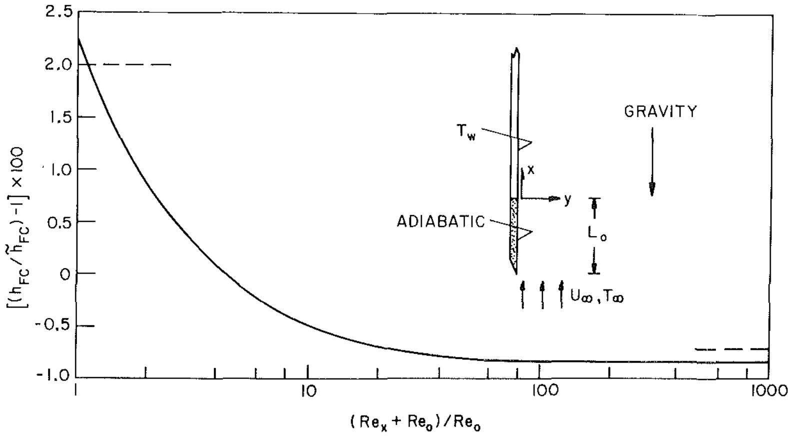

Fig. 1 Inset: schematic diagram of the physical problem; Graph: appraisal of the accuracy of $\tilde{h}_{fd}$ from the integral momentum/energy solution for pure forced convection

In addition to the just-described main focus of the paper, two related subjects were examined. The first is the case of pure forced convection heat transfer in the presence of an unheated starting length. In this case, we have assessed the accuracy of a well-known solution [4] based on the integrated momentum and energy equations. The second related subject is a comparison of computed velocity profiles for combined forces and natural convection without a starting length with those of experiment [1]. In [1], the lack of precise agreement in a limited comparison between the data and a numerical solution [5] was conjectured to be due to a restrictive velocity condition in the numerical procedure. A detailed examination of this matter undertaken here provides the opportunity of resolving the issue.

Analysis

A schematic diagram of the problem under consideration is shown in the inset of Fig. 1. As pictured there, a vertical plate is unheated over an initial length L_0. For surface locations above this initial length, the plate is at a uniform temperature T_w. The origin of coordinates was selected to coincide with the position at which heating begins. The freestream velocity and temperature are U_∞ and T_∞, respectively.

The governing equations are the incompressible boundary layer equations for x-momentum and energy, plus the continuity equation. The first of these includes the buoyancy force per unit mass $g\beta(T - T_\infty)$. The boundary conditions can be stated as

$$u = v = 0 \quad \text{at } y = 0, \quad u \rightarrow U_\infty \quad \text{as } y \rightarrow \infty \tag{1}$$

$$T = T_w \quad \text{at } y = 0, \quad T \rightarrow T_\infty \quad \text{as } y \rightarrow \infty \tag{2}$$

Equation (2) is relevant only for $x > 0$. Thermal boundary conditions need not be stated for $-L_0 < x < 0$ since $T = T_\infty$ throughout that region.

The solution of the problem was carried out numerically by the use of the Patankar-Spalding technique [6]. Special care was needed because of the great disparity in the thicknesses of the velocity and thermal boundary layers in the range of small x values. If grid points uniformly spaced across the velocity boundary layer were to be employed in a case where the thermal layer is much thinner than the velocity layer, too few points would fall within the thermal layer to provide an accurate solution. To deal with this situation, a nonuniform distribution was employed such that a greater density of points was concentrated near the plate surface. Extensive testing involving several candidate distributions was carried out in order to insure that high accuracy was obtained in the face of the steep temperature gradients near the wall. From these tests, it was concluded that the heat transfer results are accurate at least to one in the third significant figure, that is, to about 0.2 percent or better.

Nondimensionalization of the governing equations and boundary conditions revealed the presence of three independent parameters

$$\mathrm{Re}_0\,(\equiv U_\infty L_0/\nu), \quad g\beta(\Delta T)\nu/U_\infty{}^3, \quad \text{and Pr} \tag{3}$$

The dimensionless x coordinate selected for presentation of the results is $\mathrm{Gr}_x/\mathrm{Re}_x{}^2$

$$\mathrm{Gr}_x/Re_x{}^2 = (g\beta(\Delta T)x^3/\nu^2)/(U_\infty x/\nu)^2 \tag{4}$$

where it is emphasized once again that x is measured from the start of the heated section.

The local heat transfer results will be expressed by the local coefficient $h = q/(T_w - T_\infty)$. To obtain a presentation which clearly delineates the effects of buoyancy, the ratio h_{MC}/h_{FC} will be employed. In this ratio, h_{MC} is the local heat transfer coefficient for mixed convection (combined natural convection and forced convection) and h_{FC} is the local coefficient for pure forced convection. Both h_{MC} and h_{FC} correspond to the same unheated starting length and to the same

Nomenclature

Gr_x = Grashof number, $g\beta(\Delta T)x^3/\nu^2$
g = acceleration of gravity
h = local heat transfer coefficient, $q/(T_w - T_\infty)$
h_{MC} = local coefficient for mixed convection
h_{FC} = local coefficient for pure forced convection
$\tilde{h}_{FC}$ = forced convection coefficient from integral solution, equation (7)
k = thermal conductivity
L_0 = unheated hydrodynamic starting length
Pr = Prandtl number
q = local heat transfer per unit time and area
Re_0 = starting length Reynolds number, $U_\infty L_0/\nu$
Re_x = Reynolds number based on heated-section coordinate, $U_\infty x/\nu$
T = temperature
T_w = plate surface temperature
T_∞ = freestream temperature
U_∞ = freestream velocity
u = streamwise velocity component
v = transverse velocity component
x = streamwise coordinate along heated section, Fig. 1
y = transverse coordinate
β = thermal expansion coefficient
ΔT = temperature difference, $T_w - T_\infty$
ν = kinematic viscosity

streamwise location x. Therefore, the departure of h_{MC}/h_{FC} from unity is a direct measure of the augmentation of the forced convection heat transfer coefficient due to buoyancy.

The values of h_{FC} needed for the evaluation of the aforementioned ratio were also determined from numerical solutions. Since h_{FC} (actually Nu_{FC}) depends on the local Reynolds number Re_x for a fixed value of Re_0, it is necessary to interrelate Re_x and $\mathrm{Gr}_x/\mathrm{Re}_x{}^2$ so that both h_{MC} and h_{FC} correspond to the same x location. This interrelation is provided by

$$\mathrm{Re}_x = (\mathrm{Gr}_x/\mathrm{Re}_x{}^2)/(g\beta(\Delta T)\nu/U_\infty{}^3) \qquad (5)$$

Thus, for given coordinate and parameter values for the mixed convection solution, $\mathrm{Gr}_x/\mathrm{Re}_x{}^2$ and $g\beta(\Delta T)\nu/U_\infty{}^3$, respectively, the Re_x for the forced convection solution can be deduced from equation (5).

Results and Discussion

Heat Transfer Coefficients. The local heat transfer results are presented in Fig. 2. The figure is subdivided into three graphs, respectively, parameterized by values of $g\beta(\Delta T)\nu/U_\infty{}^3 = 10^{-5}$, 10^{-4}, and 10^{-3} (lower to upper). In each graph, the ratio h_{MC}/h_{FC} is plotted as a function of $\mathrm{Gr}_x/\mathrm{Re}_x{}^2$. Semilogarithmic coordinates are used in recognition of the fact that the range of h_{MC}/h_{FC} is much smaller than that of $\mathrm{Gr}_x/\mathrm{Re}_x{}^2$. The individual curves in each graph correspond to various unheated starting lengths characterized by Re_0 ranging from zero to 20,000. The curve for $\mathrm{Re}_0 = 0$ is the same in each graph, that is, it is independent of $g\beta(\Delta T)\nu/U_\infty{}^3$. Left- and right-hand ordinate scales are employed as indicated to avoid overlap among the graphs.

In addition to the computed curves for h_{MC}/h_{FC}, asymptotes for pure forced convection and pure natural convection are plotted in the graphs as dashed lines. The former is a horizontal line with an ordinate $h_{MC}/h_{FC} = 1$, whereas the latter is an upsloping curve whose equation is (for $\mathrm{Pr} = 0.7$)

$$h_{MC}/h_{FC} = 1.207\ (\mathrm{Gr}_x/\mathrm{Re}_x{}^2)^{1/4} \qquad (6)$$

Equation (6) was derived for the case of no starting length ($\mathrm{Re}_0 = 0$). It will also serve as the asymptote for the $\mathrm{Re}_0 > 0$ cases since, for large values of $\mathrm{Gr}_x/\mathrm{Re}_x{}^2$, the results become insensitive to the presence of a starting length.

The effect of the unheated starting length in enhancing the importance of buoyancy may be readily identified by comparing the curves for $\mathrm{Re}_0 > 0$ (finite starting length) with that for $\mathrm{Re}_0 = 0$ (no starting length). From such a comparison, it is seen that the buoyancy contribution to the heat transfer coefficient, as witnessed by the departure of h_{MC}/h_{FC} from unity, is markedly greater in the presence of a starting length when $g\beta(\Delta T)\nu/U_\infty{}^3 = 10^{-3}$. For example, at $\mathrm{Gr}_x/\mathrm{Re}_x{}^2 = 0.5$, the respective values of h_{MC}/h_{FC} are 1.24 and 1.84 for $\mathrm{Re}_0 = 0$ and $\mathrm{Re}_0 = 20{,}000$. Clearly, the starting length plays a role of first-order importance.

As $g\beta(\Delta T)\nu/U_\infty{}^3$ diminishes, so also does the effect of the starting length. At $g\beta(\Delta T)\nu/U_\infty{}^3 = 10^{-4}$, a comparison at $\mathrm{Gr}_x/\mathrm{Re}_x{}^2 = 0.5$, shows that the h_{MC}/h_{FC} values are 1.24 and 1.42 at $\mathrm{Re}_0 = 0$ and 20,000, respectively. Thus, although the effect of the starting length on the buoyancy contribution has diminished, it is by no means negligible. At a value of $g\beta(\Delta T)\nu/U_\infty{}^3 = 10^{-5}$, the buoyancy contribution to the heat transfer coefficient in the presence of a starting length is, percentagewise, about the same as that for the case of no starting length.

The effect of a starting length on the buoyancy contribution decreases both at small and at large $\mathrm{Gr}_x/\mathrm{Re}_x{}^2$. When $\mathrm{Gr}_x/\mathrm{Re}_x{}^2$ is small, the buoyancy contribution is also small, both in the presence and in the absence of a starting length. On the other hand, at large $\mathrm{Gr}_x/\mathrm{Re}_x{}^2$, natural convection is the dominant transfer mechanism. Since pure natural convection is not affected by a starting length, the modest influence of a starting length in a buoyancy-dominated flow is plausible.

For the case of $g\beta(\Delta T)\nu/U_\infty{}^3 = 10^{-3}$, the substantial effect of the starting length already in evidence at $\mathrm{Gr}_x/\mathrm{Re}_x{}^2 = 0.01$ would logically motivate solutions for lower values of $\mathrm{Gr}_x/\mathrm{Re}_x{}^2$. However, as demonstrated by equation (5), such solutions would correspond to values of $\mathrm{Re}_x < 10$ and, therefore, to $\mathrm{Re}_x\mathrm{Pr} < 7$. At such low values of $\mathrm{Re}_x\mathrm{Pr}$, the neglect of streamwise heat conduction cannot be justified by the customary order of magnitude arguments of boundary layer theory. Therefore, solutions were not performed for $\mathrm{Gr}_x/\mathrm{Re}_x{}^2$ below 0.01.

To employ the results presented in Fig. 2, it is necessary that values be available for the local heat transfer coefficient h_{FC} for pure forced convection in the presence of a starting length. As noted earlier, values of h_{FC} were determined from a numerical solution for each Re_0. Rather than plot this information directly, a more compact presentation will be made by employing the algebraic representation which describes the end result of an integral momentum and energy solution of the problem [4], that is

$$\tilde{h}_{FC}(x + L_0)/k$$
$$= 0.332\mathrm{Pr}^{1/3}(\mathrm{Re}_x + \mathrm{Re}_0)^{1/2} \Big/ \left[1 - \left(\frac{L_0}{x + L_0}\right)^{3/4}\right]^{1/3} \qquad (7)$$

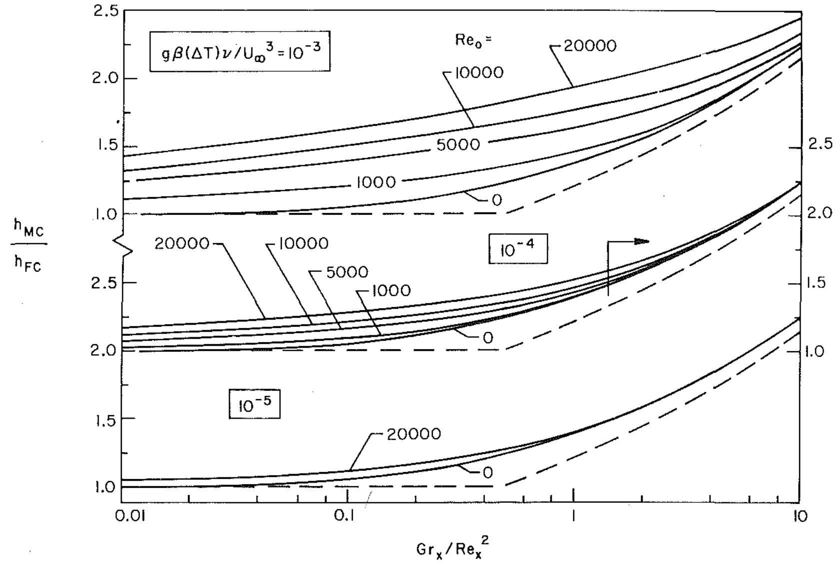

Fig. 2 **Local heat transfer coefficients for mixed convection in the presence of an unheated starting length**

Since equation (7) is based on an approximate analysis, $\tilde{h}_{FC}$ is subject to error. The errors were assessed by comparisons with the numerical solutions for h_{FC}, whose accuracy is about 0.2 percent (as mentioned earlier and to be confirmed shortly). For such a comparison, $[(h_{FC}/\tilde{h}_{FC}) - 1]$ is plotted as a function of $(\mathrm{Re}_x + \mathrm{Re}_0)/\mathrm{Re}_0$. Such a plot was found to be independent of Re_0 to within a tenth of a percent. It is presented in Fig. 1. Inspection of the figure shows that $\tilde{h}_{FC}$ is low by about 2 percent when $(\mathrm{Re}_x + \mathrm{Re}_0)/\mathrm{Re}_0 \approx 1$. With increasing values of this parameter, the error in $\tilde{h}_{FC}$ decreases and then changes sign, finally levelling off at a value $[(h_{FC}/\tilde{h}_{FC}) - 1] = -0.0085$.

The use of equation (7) in conjunction with Fig. 1 enables h_{FC} to be evaluated for subsequent application in Fig. 2. In light of the approximate nature of the analysis which led to equation (7), the relatively small errors in $\tilde{h}_{FC}$ are worthy of note.

Fig. 1 also contains horizontal lines which represent limiting values for small and large $(\mathrm{Re}_x + \mathrm{Re}_0)/\mathrm{Re}_0$. The limit as $(\mathrm{Re}_x + \mathrm{Re}_0)/\mathrm{Re}_0 \rightarrow 1$ is due to Spalding (7) and is based on a Leveque-type model. At large values of $(\mathrm{Re}_x + \mathrm{Re}_0)/\mathrm{Re}_0$, the limit is provided by the classical exact similarity solution for a plate without a starting length (e.g., [8]). The close agreement of the present results with these limits confirms the accuracy (about 0.2 percent) of our numerical solutions.

The heat transfer results can be viewed from another perspective in addition to that thus far discussed. Consider first the case of pure forced convection and let $h_{FC}/(h_{FC})_0$ denote the ratio of heat transfer coefficients with and without a starting length, where both h values correspond to the same distance x from the onset of heating. It is readily verified (e.g., from equation (7)) that $h_{FC}/(h_{FC})_0 \leq 1$. Next consider the ratio $h_{MC}/(h_{MC})_0$, where again the two h values are for the same x as well as for the same value of $g\beta(\Delta T)\nu/U_\infty{}^3$. By making use of Fig. 2, it can be shown that

$$1 > h_{MC}/(h_{MC})_0 > h_{FC}/(h_{FC})_0 \qquad (8)$$

Thus, the mixed convection results are less sensitive to the presence of an unheated starting length than are those for pure forced convection.

Velocity Profiles. The shapes of the velocity profiles are highly responsive to the interaction between the unheated starting length and the buoyancy. The hydrodynamic development which precedes the onset of heating causes the velocity boundary layer to be substantially thicker than the thermal boundary layer. As a consequence, the buoyancy force is confined to the inner portion of the velocity boundary layer. In contrast, in the absence of a starting length, the thicknesses of the two boundary layers are very nearly equal for $\mathrm{Pr} = 0.7$, so that the buoyancy force is active all across the velocity boundary layer.

Fig. 3 has been prepared to illustrate these characteristics. The figure is subdivided into two parts. A left-hand graph contains results for a starting length situation characterized by $\mathrm{Re}_0 = 10{,}000$ and $g\beta(\Delta T)\nu/U_\infty{}^3 = 10^{-3}$ and a right-hand graph which corresponds to no starting length ($\mathrm{Re}_0 = 0$). In each graph, u/U_∞ is plotted against $y\sqrt{U_\infty/\nu(x + L_0)}$, which is the forced convection similarity variable based on the distance $(x + L_0)$ measured from the start of hydrodynamic development. Such a coordinate cannot correlate all the results onto a single curve because of the effects of buoyancy and of the starting length, but its use tends to suppress large variations in boundary layer thickness and thereby avoids presentation difficulties. Since L_0 is finite for the left-hand graph and zero for the right-hand graph, a comparison of the abscissa scales of the two graphs does not yield a direct comparison of the boundary layer thicknesses for the two cases. However, the desired comparisons of the profile shapes can readily be made.

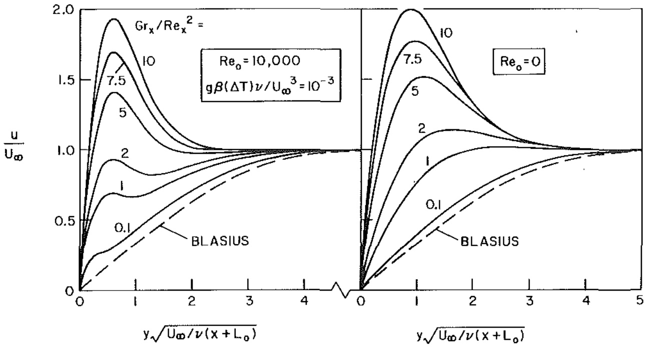

Fig. 3 Representative velocity profiles for mixed convection with and without an unheated starting length

In each graph, the successive curves are parameterized by increasing values of $\mathrm{Gr}_x/\mathrm{Re}_x{}^2$, corresponding to increasing downstream distances from the onset of heating. The Blasius velocity profile for pure forced convection is included for reference purposes (dashed line).

Inspection of Fig. 3 reveals marked differences in the shapes of the profiles with and without an unheated starting length. For small and intermediate values of $\mathrm{Gr}_x/\mathrm{Re}_x{}^2$, the profiles for the starting length case have a local maximum in the region near the plate surface, reflecting the fact that the buoyancy force is confined to that region. Even at large $\mathrm{Gr}_x/\mathrm{Re}_x{}^2$, the peaks in the profiles are relatively narrow. In contrast, the profiles for the no starting length case are fuller and the peaks are broader, indicating that bouyancy is active across the entire boundary layer. It may also be noted that the peaks are higher in the absence of a starting length. This is because the forced convection velocities on which the natural convection is superposed are larger for the no starting length case.

As a final matter with respect to the velocity profiles, attention will be turned to a comparison with the experimental data of Gryzagoridis [1] for combined forced and natural convection on a vertical plate without a starting length. In [1], velocity profile data are plotted for five values of $\mathrm{Gr}_x/\mathrm{Re}_x{}^2 = 0.46, 0.93, 2.73, 4.33$, and 8.74. A comparison was made with a computed velocity profile from [5] corresponding to $\mathrm{Gr}_x/\mathrm{Re}_x{}^2 = 2.35$. The level of agreement between the data for 2.73 and the computed profile for 2.35 was satisfactory, but not perfect. As an explanation for the absence of precise agreement, it was suggested that, whereas the buoyancy-induced flow actually starts ahead of the leading edge, the boundary layer solution method of [5] assumes that the condition $u = U_\infty$ prevails at the leading edge. We, however, anticipate that, for the case of combined forced and natural convection, this leading edge effect is likely to be small, especially at the larger values of $\mathrm{Gr}_x/\mathrm{Re}_x{}^2$. To confirm this expectation, we actually obtained *elliptic* solutions (by a method derived from [9]) for a calculation domain which included the region upstream of the leading edge and thus provided an account of the leading edge effect free from the boundary layer assumptions. The calculated velocity profiles matched almost perfectly with the profiles from the boundary layer solution. Further, our solutions agreed closely with those of [5]. Thus, the flow, if any, induced ahead of the leading edge does not seem an important factor. Moreover, the agreement between the present elliptic and boundary layer solutions as well as those of [5] suggests that the calculated velocity profiles are correct representations for the physical situation that was analyzed (nonstratified environment; uniform, vertical freestream velocity; constant property, nondissipative flow; isothermal plate).

The comparison of our numerical solutions with the experimental data of [1] is shown in Fig. 4. At the lowest value of $\mathrm{Gr}_x/\mathrm{Re}_x{}^2$ (= 0.46), the agreement between the computed and experimental results is excellent. However, at larger values of $\mathrm{Gr}_x/\mathrm{Re}_x{}^2$, the data consistently tend to fall below the computed curves. The extent of these deviations is moderate; for instance, at the peak of the curve for $\mathrm{Gr}_x/\mathrm{Re}_x{}^2 = 4.33$, the data lie about 8 percent below the curve.

We believe that the level of agreement evidenced in Fig. 4 is satisfactory, although the systematic deviation between analysis and experiment is a matter of some concern. The deviation might well be due to the fact that the experimental conditions do not coincide with the analytical model that was detailed in the paragraph just above the preceding one. In particular, experiments involving natural convection are known to be error prone owing to their susceptibility to extraneous influences from the surrounding environment.

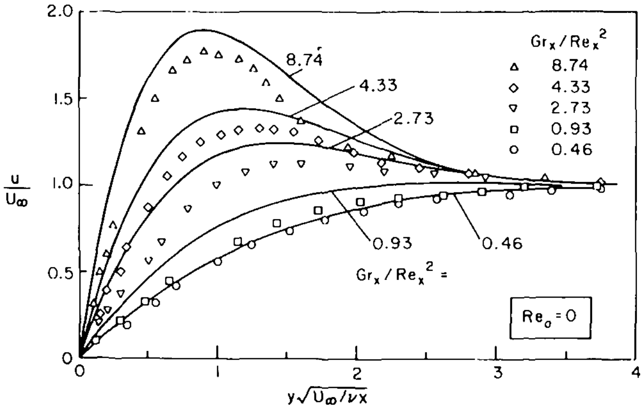

Fig. 4 Comparison of predicted and measured velocity profiles for mixed convection without an unheated starting length

Concluding Remarks

The local heat transfer results have shown that the effects of buoyancy on laminar forced convection adjacent to a heated vertical plate are accentuated by the presence of an unheated starting length. The degree of accentuation is governed by the parameter $g\beta(\Delta T)\nu/U_\infty^3$. When the parameter is on the order of 10^{-3}, the presence of a starting length markedly increases the importance of the natural convection contribution to the heat transfer coefficient. On the other hand, when $g\beta(\Delta T)\nu/U_\infty^3$ is on the order of 10^{-5}, the buoyancy contribution is essentially unaffected by the presence of a starting length.

The shapes of the velocity profiles are highly responsive to the interaction between the buoyancy and the starting length. In the presence of a starting length, the buoyancy induced peak in the velocity profile takes the form of a local maximum in the near-wall region when Gr_x/Re_x^2 is small. At intermediate and large values of Gr_x/Re_x^2, the velocity profiles are more skewed toward the wall than are their counterparts for the case of no starting length.

As a by-product of this investigation, we have established that the heat transfer results from a well known integral momentum/energy solution for pure forced convection with a starting length are accurate to better than two percent. In addition, the present velocity profile results for mixed convection without a starting length were compared with those of experiment in order to assess a proposed explanation for a previously noted disparity. Our findings corroborate an earlier numerical solution.

Acknowledgment

This research was performed under the auspices of NSF Grant ENG-7518141.

References

1 Gryzagoridis, J., "Combined Free and Forced Convection From an Isothermal Vertical Plate," *International Journal of Heat and Mass Transfer*, Vol. 18, 1975, pp. 911-916.

2 Chen, T. S., and Mucoglu, A., "Buoyancy Effects on Forced Convection Along a Vertical Cylinder," JOURNAL OF HEAT TRANSFER, TRANS. ASME, Series C, Vol. 97, 1975, pp. 198-203.

3 Oosthuizen, P. H., and Hart, A., "A Numerical Study of Laminar Combined Convective Flow Over Flat Plates," JOURNAL OF HEAT TRANSFER, TRANS. ASME, Series C, Vol. 95, 1973, pp. 60-63.

4 Eckert, E. R. G., and Drake, R. M., *Analysis of Heat and Mass Transfer*, McGraw-Hill, New York, 1972, pp. 315-319.

5 Oosthuizen, P. H., and Hart, R., "A Numerical Study of Laminar Combined Convective Flow Over Flat Plates," Report 4/71, Queen's University Thermal and Fluid Sciences Group, Aug. 1971.

6 Patankar, S. V., and Spalding, D. B., "Heat and Mass Transfer in Boundary Layers," Second ed., Intertext Books, London, 1970.

7 Spalding, D. B., "Contribution to the Theory of Heat Transfer Across a Turbulent Boundary Layer," *International Journal of Heat and Mass Transfer*, Vol. 7, 1964, pp. 743-761.

8 Evans, H. L., *Laminar Boundary-Layer Theory*, Addison-Wesley, Reading, Mass., 1970, p. 97.

9 Patankar, S. V., and Spalding, D. B., "A Calculation Procedure for Heat, Mass, and Momentum Transfer in Three-Dimensional Parabolic Flows," *International Journal of Heat and Mass Transfer*, Vol. 15, 1972, pp. 1787-1806.

K. C. Cheng
M. Takeuchi

Department of Mechanical Engineering,
University of Alberta,
Edmonton, Alberta, Canada

Transient Natural Convection of Water in a Horizontal Pipe With Constant Cooling Rate Through 4°C

A theoretical analysis is carried out to study the influence of an anomalous density-temperature relationship of water on the transient natural convection in horizontal cylinders with wall temperature decreasing at a uniform rate. Numercial solutions are obtained for three cases involving different cooling rates, pipe diameters, and initial uniform water temperatures for temperature conditions between 0 and 7°C. The transient flow and temperature fields, and local and overall heat transfer rates are presented to study the inversion of flow patterns caused by the maximum density at 4°C. The numerical results are compared with the experimental measurements and predictions of a quasi-steady boundary-layer model reported by Gilpin [2]*, and generally a good agreement is observed. Some implications on the subsequent freezing process are pointed out.*

1 Introduction

The satisfactory design and operation of a water distribution system in continuous or discontinuous permafrost regions requires an accurate prediction of water temperature in the system under various thermal boundary conditions. It is also necessary to estimate the amount of heat to be added to the water so that the water upon passing through the entire system and after remaining static during the maximum allowable time would not drop below a certain permissible minimum temperature [1].[1] For the computation of heat loss in a water system, one may consider the flow and nonflow situations. During the static period when water does not move through the pipes, the heat transfer between the water and the pipe wall takes place through the transient natural convection process. It is thus seen that the cooling of water in a horizontal pipe with, or without, main flow to the point at which the freezing process occurs is of considerable practical interest. The occurrence of the maximum density of water at 4°C introduces an additional interesting complexity in the study of the transient natural convection heat transfer. The anomalous behavior of water is also known to be the cause of some very striking and important natural phenomena such as limnetic waters.

Recently, Gilpin [2] carried out an experimental investigation on cooling of water in a horizontal cylinder with wall temperature decreasing at a constant rate through the maximum density point at 4°C and identified four flow regimes (transient, quasi-steady, inversion and quasi-steady states) before occurrence of the freezing process. Gilpin's approximate theoretical analysis [2] employed a quasi-steady boundary-layer model. In view of the experimental information provided by Gilpin's study and the approximate nature of the boundary-layer approximation, a numerical solution of the transient natural convection problem considered by Gilpin is apparently in order. The numerical solution to the governing Navier-Stokes and energy equations yields a complete time-dependent velocity and temperature fields thus enabling one to study the flow pattern, and local and overall heat transfer characteristics in detail up to reasonably high physical parameters ($10^5 \lesssim \mathrm{GrPr} \gtrsim 2 \times 10^6$). Specifically, the present investigation is concerned with the numerical simulation of the transient natural convection problem in horizontal pipes studied experimentally by Gilpin [2].

For recent literature on the effects of maximum density on free convection phenomenon, one may cite the works by Vanier and Tien [3, 4], Tien, Yen, and Dotson [5], Desai and Forbes [6], Watson [7], Forbes and Cooper [8], and Seki, Fukusako, and Nakaoka [9] for reference. Without the maximum density effects, the problem under consideration was studied experimentally by Deaver and Eckert [10] and numerically by Takeuchi and Cheng [11]. One notes that Quack's perturbation solution [12] is valid only for very low Rayleigh number regime which is not important practically.

2 Analysis

2.1 **The Temperature-Density Relationship.** With its maximum density at 3.94°C (usually approximated as 4°C), water

---

[1] Numbers in brackets designate References at end of paper.

Contributed by the Heat Transfer Division for publication in the JOURNAL OF HEAT TRANSFER. Manuscript received by the Heat Transfer Division June 14, 1976.

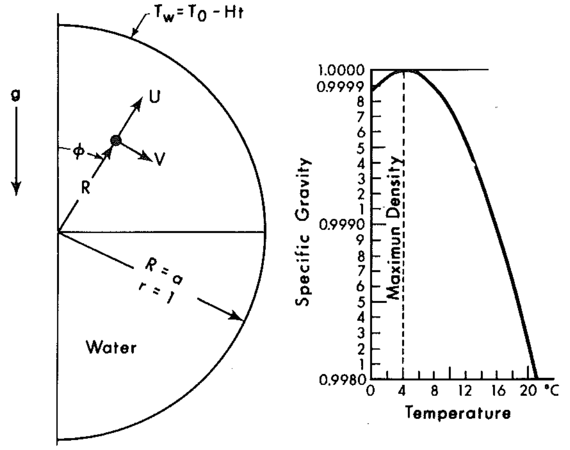

Fig. 1 Coordinate system and the dependence of the specific gravity of water on temperature

undergoes a normal thermal expansion from that temperature upward, and an inverse thermal expansion from that point downward (see Fig. 1). The density-temperature relationship for water can be approximated by the following equation for the temperature range 0 ~ 20°C [13].

$$1/\rho = (1/\rho_0)(1 + \beta_1 T + \beta_2 T^2 + \beta_3 T^3 + \beta_4 T^4) \qquad (1)$$

where $\rho_0 = 0.9998396$ (g/cm^3), $\beta_1 = -0.678964520 \times 10^{-4}$ (1/°C), $\beta_2 = 0.907294338 \times 10^{-5}$ (1/°C^2), $\beta_3 = -0.964568125 \times 10^{-7}$ (1/°C^3), and $\beta_4 = 0.873702983 \times 10^{-9}$ (1/°C^4). Fujii [13] notes that the foregoing expression agrees with the tabulated data of Landolt-Börnstein [14] with an error of less than one unit at the last digit.

2.2 **Formulation of the Problem.** Consideration is given to the two-dimensional transient convective motion generated by the buoyancy force on the water in a long horizontal circular cylinder (see Fig. 1) with wall temperature decreasing at a constant time rate as $T_w = T_0 - Ht$. Initially the water is assumed to be at a uniform temperature higher than 4°C and cooling continues until T_w = 0°C is reached. In this analysis, the Boussinesq approximation is made so that density variations only modify the body force term. Using the coordinate system shown in Fig. 1 and neglecting frictional heating, the dimensionless equations governing the problem with the maximum density effects can be shown to be:

$$\frac{\partial\xi}{\partial\tau} + u\frac{\partial\xi}{\partial r} + \frac{v}{r}\frac{\partial\xi}{\partial\phi} = \mathrm{Pr}\nabla^2\xi + \left(\frac{ga^3}{\nu^2}\right)\mathrm{Pr}^2\Delta T\left[\sin\phi\frac{\partial}{\partial r}(K_1\theta + K_2\theta^2 + K_3\theta^3 + K_4\theta^4) + \frac{\cos\phi}{r}\frac{\partial}{\partial\phi}(K_1\theta + K_2\theta^2 + K_3\theta^3 + K_4\theta^4)\right] \qquad (2)$$

$$\xi = \nabla^2\psi \qquad (3)$$

$$\frac{\partial\theta}{\partial\tau} + u\frac{\partial\theta}{\partial r} + \frac{v}{r}\frac{\partial\theta}{\partial\phi} = \nabla^2\theta + 1 \qquad (4)$$

where

$$K_1 = (\beta_1 + 2\beta_2 T_w + 3\beta_3 T_w^2 + 4\beta_4 T_w^3)/K$$
$$K_2 = (\beta_2 + 3\beta_3 T_w + 6\beta_4 T_w^2)\Delta T/K$$
$$K_3 = (\beta_3 + 4\beta_4 T_w)(\Delta T)^2/K$$
$$K_4 = \beta_4(\Delta T)^3/K$$
$$K = 1 + \beta_1 T_w + \beta_2 T_w^2 + \beta_3 T_w^3 + \beta_4 T_w^4 \qquad (5)$$

and

$$\tau = \kappa t/a^2,\ r = R/a,\ u = aU/\kappa,$$
$$v = aV/\kappa,\ \psi = \Psi/\kappa,\ \xi = a^2\Omega/\kappa,$$
$$\theta = (T - T_w)/\Delta T,\ \Delta T = a^2H/\kappa,\ U = \partial\Psi/R\partial\phi,$$
$$V = -\partial\Psi/\partial R,\ \Omega = -(1/R)[\partial(RV)/\partial R - \partial U/\partial\phi],$$
$$u = \partial\psi/r\partial\phi,\ v = -\partial\psi/\partial r,\ \nabla^2 = \partial^2/\partial r^2 + \partial/r\partial r + \partial^2/r^2\partial\phi^2 \qquad (6)$$

All other symbols are defined in the Nomenclature.

The initial and boundary conditions are

$$u = v = \psi = \xi = \theta = 0 \quad \text{at } \tau = 0$$
$$u = v = \psi = \partial\psi/\partial r = \theta = 0 \quad \text{at } r = 1 \text{ (wall)}$$
$$v = \partial u/\partial\phi = \psi = \xi = \partial\theta/\partial\phi = 0 \quad \text{along } \phi = 0, \pi \text{ (symmetry)} \qquad (7)$$

The characteristic temperature difference ΔT is defined using the constant wall cooling rate H and the physical parameter (ga^3/ν^2) represents the size of the cylinder. In view of the complex nature of the problem, a numerical solution appears to be the only practical approach for the present problem without employing the boundary-layer approximation. The peripherally average wall heat flux $\bar{q}$ at any time can be computed by considering the wall temperature gradient $(\partial\theta/\partial r)_{r=1}$ or the time rate of change of water temperature $(-\partial\theta/\partial\tau)$. The dimensionless average wall heat flux, $\bar{q}' = (\bar{q}a)/(\Delta Tk)$, is then obtained as

$$\bar{q}_1' = (1/\pi)\int_0^\pi (-\partial\theta/\partial r)_{r=1}d\phi,$$

$$\bar{q}_2' = (1/2) + (1/\pi)\int_0^\pi\int_0^1 (-\partial\theta/\partial\tau)rdrd\phi \qquad (8)$$

The time dependent Nusselt number is defined by

$$\mathrm{Nu} = (2a\bar{q}/k)/(T_b - T_w) = 2\bar{q}'/\theta_b,$$

$$\theta_b = (2/\pi)\int_0^\pi\int_0^1 \theta rdrd\phi \qquad (9)$$

3 Numerical Solution

In this study, the explicit DuFort-Frankel method is employed for the finite-difference solution of the parabolic-type equations (2) and

Nomenclature

a = inside radius of pipe
Gr = Grashof number, equation (12)
g = gravitational acceleration
H = constant wall cooling rate
$K, K_1, \ldots K_4$ = constants, equation (5)
k = thermal conductivity
Nu = Nusselt number, equation (9)
Pr = Prandtl number
$\bar{q}$ = average wall heat flux
q_ϕ = local wall heat flux
R = radial coordinate
r = dimensionless radial coordinate, R/a
T = temperature
T_b = mixed mean temperature
T_w = wall temperature
T_0 = uniform initial water temperature
t = time
U, V = velocities in R and ϕ directions
u, v = dimensionless velocities in R and ϕ directions, equation (6)
$[\beta]_m$ = effective mean thermal expansion coefficient, equation (11)
$\beta_1, \ldots \beta_4$ = constants, equation (1)
θ = dimensionless temperature, $(T - T_w)/\Delta T$
κ = thermal diffusivity
ν = kinematic viscosity
ξ = dimensionless vorticity, $a^2\Omega/\kappa$
ρ = density
τ = dimensionless time (Fourier number), $\kappa t/a^2$
ϕ = polar coordinate
Ψ = stream function
ψ = dimensionless stream function, Ψ/κ
Ω = vorticity
ΔT = characteristic temperature difference, a^2H/κ

Subscripts

b = mixed mean value
i, j = space subscripts of a grid point
w = value at wall

Table 1 Physical parameter, Δr and $\Delta \tau$

Case	T_0	ΔT	ga^3/ν^2	Pr	Δr r=0~0.4	 r=0.4~0.8	 r=0.8~1.0	$\Delta\tau$
I	7°C	15°C	1×10^7	10	1/15	1/20	1/30	5×10^{-4}
II	5	15	1×10^8	10	1/15	1/25	1/50	5×10^{-4}
III	6	60	2.5×10^8	10	r=0~0.6 1/20	r=0.6~0.8 1/30	r=0.8~1.0 1/60	1×10^{-4}

(4) and a line iterative method is used for the elliptic equation (3).

Some details on numerical solution procedures are given in [11]. Considering Gilpin's experimental data [2], numerical results are obtained for three cases (I, II, III) shown in Table 1 where the parametric values for ga^3/ν^2 correspond approximately to $2a$ = 2.54, 5.08, 7.62 cm (or $2a$ = 1, 2, 3 in.), respectively. The grid spacing used is uniform ($\Delta\phi = \pi/20$) in the ϕ-direction but in the r-direction three regions of different uniform mesh sizes are used with the grid lines more closely spaced near the wall than near the center (see Table 1). One notes that as the parameter (ga^3/ν^2) increases, a boundary-layer type flow appears and the velocity variation near the wall becomes large. During the initial period immediately after the start of cooling, the variation of the temperature field with time is large and a continually increasing smaller time step $\Delta\tau$ is required for an accurate solution. After the initial cooling period, the uniform time step shown in Table 1 is used to increase the computational efficiency. The singularity at the origin of the polar coordinates is avoided by using a finite-difference equation in Cartesian coordinates there.

The iteration for the stream function at any time step using a relaxation factor 1.5 is terminated when the following convergence criterion is satisfied.

$$\Sigma|(\psi_{i,j})^{n+1} - (\psi_{i,j})^n|/\Sigma|(\psi_{i,j})^{n+1}| < 0.5 \times 10^{-3} \qquad (10)$$

The number of iterations required decreases rapidly from 30 immediately after the start of the cooling to 2–4 for most other time steps. It is found that the number of iterations also reaches as high as 20 when the maximum density effect appears. The total time steps range from 900 to 1160 and the corresponding computing time is from 18 to 25 min on the IBM 360/67 depending on the initial temperature T_0 and the parametric value ga^3/ν^2. Two independent (alternative) means of calculating the average wall heat flux provide a means of checking the accuracy of the numerical solution. In evaluating $\overline{q}'$ from equation (8), five-point and three-point finite difference approximations are used for $(\partial\theta/\partial r)_{r=1}$ and $(\partial\theta/\partial\tau)$, respectively, and Simpson's rule is used for numerical integration. The agreement between $\overline{q}_1'$ and $\overline{q}_2'$ is found to be within 1 percent but a maximum difference of 2.5 percent is observed when the maximum density effect is significant.

4 Results and Discussion

4.1 Flow and Temperature Fields. The imposed time-dependent wall temperature T_w, center-line temperature T_c and mixed mean temperature $T_b = T_w + (2\Delta T/\pi)\int_0^\pi\int_0^1 \theta r dr d\phi$ for the three cases under consideration are shown in Fig. 2. The calculation is terminated when the wall temperature reaches the freezing temperature 0°C. For Case II, the time history of T_c and T_b exhibits a fluctuating phenomenon near the final stage and the numerical results are not presented. It is felt that a stable solution may be obtained by using a smaller time increment but the numerical solution obtained is sufficient to understand the maximum density effect. For Cases I and III, the value of the cooling parameter $C_T = 2aH^{4/5}(\nu/g\kappa^3)^{1/5} = 2\Delta T^{4/5}/(\mathrm{Pr}ga^3/\nu^2)^{1/5}$ for the temperature difference ($T_c - T_w$) proposed by Gilpin [2] becomes 0.438 and 0.698, respectively. Consequently, Cases I and III may be considered to correspond approximately to Cases C2($2a$ = 26 mm, C_T = 0.41) and B1($2a$ = 75 mm, C_T = 0.69) in Gilpin's experiment (see Fig. 8 of [2]).

The time-dependent temperature solution for T_c clearly exhibits the four flow regimes (transient, quasi-steady, inversion and quasi-steady states) identified by Gilpin before the onset of freezing process (see Fig. 4 of [2]). At quasi-steady state, the water temperature decreases approximately at the same time rate as the wall temperature and the inversion regime near 4°C is unique to water possessing maximum density. It should be pointed out that the definition of quasi-steady period in which flow patterns, velocities and the temperature difference between the water and the wall remain relatively constant follows that of [2]. One notes that Gilpin's theoretical model [2] is based on the existence of two quasi-steady states before and after the inversion. It is pointed out that the quasi-steady regime before the freezing has special implication for the ice formation problem. When the initial temperature T_0 is much higher than 4°C, one expects that the period of the initial quasi-steady regime may be quite long and a considerable computing time is required to reach the inversion regime. It is also expected that under a quasi-steady state the character of the governing equations (2) and (4) changes from parabolic-type to elliptic-type since the unsteady terms, $\partial\xi/\partial\tau$ and $\partial\theta/\partial\tau$, become negligible in comparison with other terms. As a result, a serious numerical difficulty may arise. Because of the reasons noted previously, the initial temperature close to 4°C is selected for numerical calculation in this study.

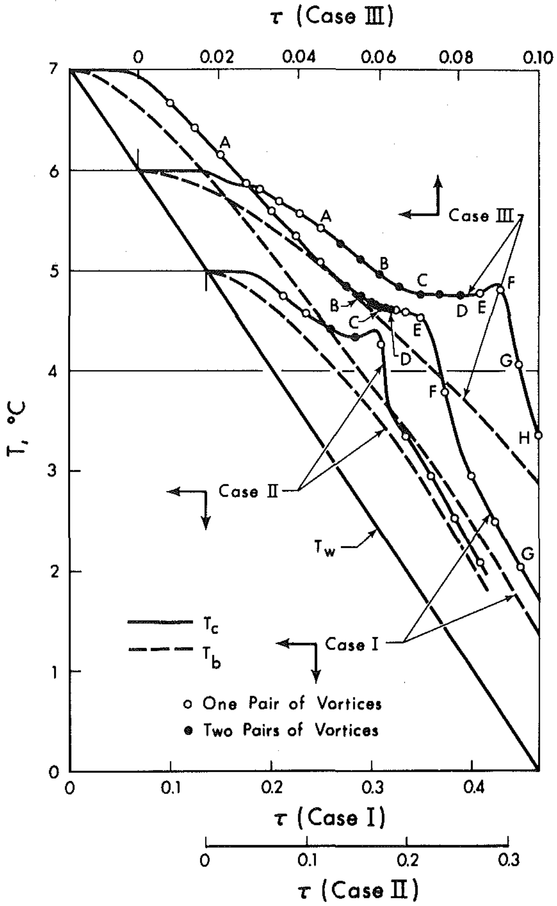

Fig. 2 Transient distributions of wall temperature T_w, center-line temperature T_c, and mixed mean temperature T_b

A quasi-steady state may be considered to be reached when the temperature variation with time at center, T_c, becomes approximately parallel to that at wall T_w. For Cases II (T_0 = 5°C) and III (T_0 = 6°C), the initial quasi-steady regime cannot be distinguished clearly since the initial temperature T_0 is quite close to 4°C. It is interesting to note that the variation of the mixed mean temperature T_b with time does not provide any information on the existence of the four flow regimes noted by Gilpin [2]. It is clear that the curves shown in Fig. 2 can be extrapolated to the supercooled region. In present investigation, the period τ = 0.1 ~ 0.25 preceding the inversion and the period between

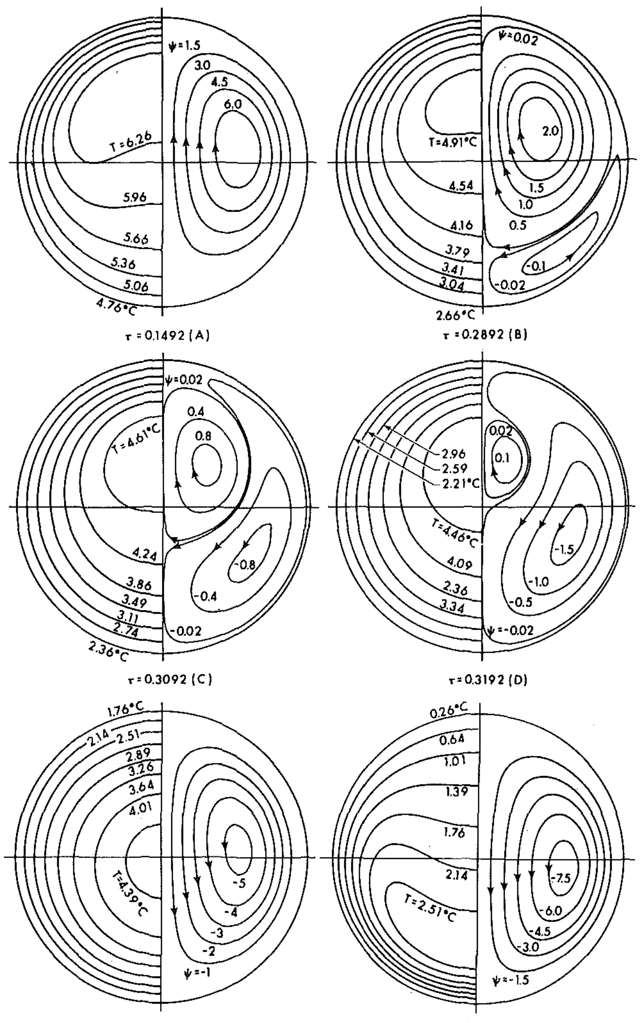

τ = 0.1492 (A) τ = 0.2892 (B)

τ = 0.3092 (C) τ = 0.3192 (D)

τ = 0.3492 (E) τ = 0.4492 (G)

Fig. 3 Transient streamline patterns and isotherms for Case I

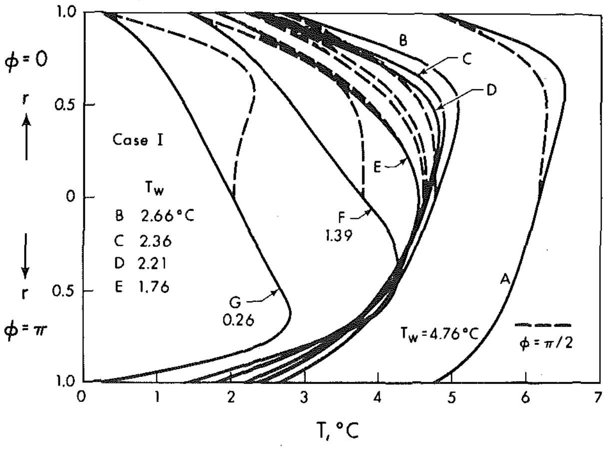

Fig. 5 Transient temperature profiles for Case I

τ = 0.4 and the onset of ice nucleation for Case I shown in Fig. 2 may be regarded to be quasi-steady states.

The streamline patterns and isotherms corresponding to the particular times noted by different symbols in Fig. 2 for Cases I and III are shown in Figs. 3 and 4, respectively. In Fig. 2, a circle on the center-line temperature curve indicates the regular flow pattern with a pair of counter-rotating vortices and a dot represents the flow pattern with two pairs of vortices. The dots and circles indicate the time steps with computer output for flow patterns and isotherms but only those identified by symbols are presented here. The temperature profiles along the horizontal and vertical axes corresponding to the flow and temperature fields for Case I shown in Fig. 3 are plotted in Fig. 5. One notes that the streamline patterns, isotherms and velocity profiles at τ = 0.1492(A) and 0.4492(G) for Case I (see Figs. 3 and 5) are quite similar. This observation confirms the existence of the two quasi-steady states before and after the inversion.

The parametric values for Case III (see Table 1) are higher and the temperature profiles along the vertical and horizontal axes (a), velocity profiles for u and v along the horizontal axis (b), and the dimensionless local wall heat flux distributions (c) for the particular

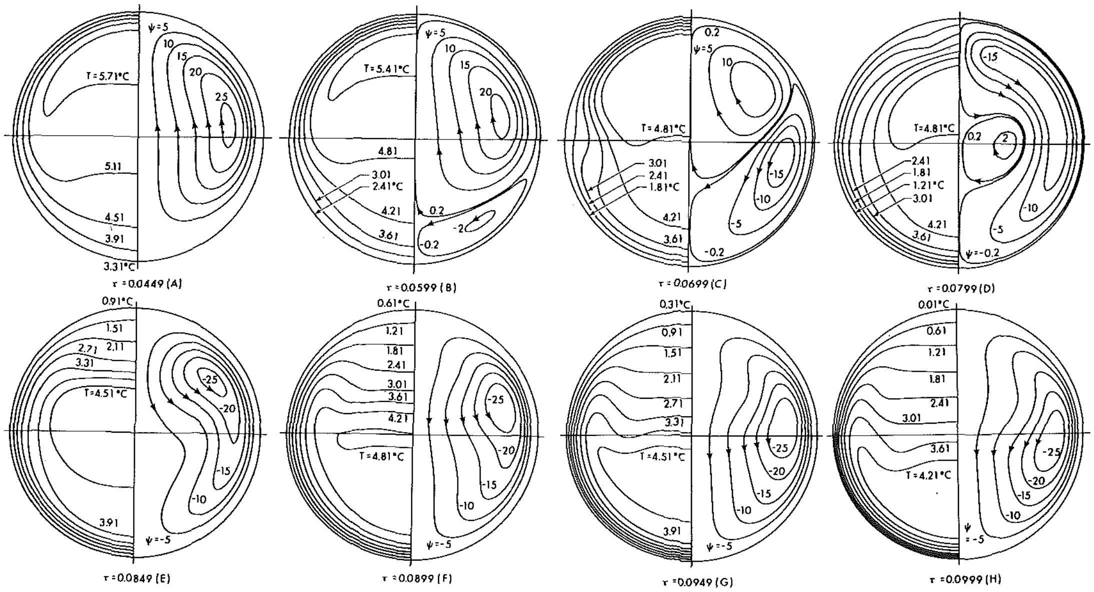

τ = 0.0449 (A) τ = 0.0599 (B) τ = 0.0699 (C) τ = 0.0799 (D)

τ = 0.0849 (E) τ = 0.0899 (F) τ = 0.0949 (G) τ = 0.0999 (H)

Fig. 4 Transient streamline patterns and isotherms for Case III

times noted in Figs. 2 and 4 are presented in Fig. 6 in order to study the maximum density effect during the inversion process. After passing through the transient regime (*A*), a boundary-layer type flow appears and one notes large downward velocity and temperature variations near the wall. In the core region, the water becomes stratified with a vertical temperature gradient. Near the top of the pipe, the warmer water in the core region is continually transported upward and the isotherms are closely spaced indicating larger local wall heat flux (see Fig. 6(*c*)). On the other hand, the cooler water near the wall is transported downward and the isotherms in the lower portion are sparsely spaced indicating poor wall heat-transfer. At $\tau = 0.0449$ (see Fig. 4(*A*)), the isotherm for 4°C already appears. It is thus seen that in a layer between the isotherm 4°C and the wall the buoyancy force changes sign and the lower portion is potentially unstable because of a top-heavy situation. With the growth of the unstable layer, an additional pair of vortices rotating opposite to the existing earlier one will eventually be set up near the bottom. The onset of instability occurs at $T_w \approx 3$°C. Thus, the inversion process begins.

The growth of the lower vortices and the decay of the upper vortices with time are clearly seen in Figs. 4 (*B*), 4(*C*), and 4(*D*). It is useful to note that the intensity of the vortex motion is indicated by the maximum absolute value of the stream function ψ. In the region near the wall where the two vortices meet, the cooler water near the wall will be carried directly into the core region and the isotherms become distorted and sparsely spaced (see Fig. 4(*C*) and curve *C* in Fig. 6(*c*)). Since the warmer core water is carried downward in the lower portion of the pipe, the heat transfer rate at the lower wall improves subsequently as shown in Fig. 6(*c*). At $\tau = 0.0799$ (Fig. 4(*D*)), the weak original vortices are seen to be completely engulfed by the strong vortices with a reversed circulation pattern. At $\tau = 0.0849$ Fig. 4(*E*), the original vortices disappear completely and the direction of the circulation is reversed. Thus, the inversion process ends. In Figs. 4(*F*), 4(*G*), 4(*H*), the core temperature is higher in the lower region and the stratification is opposite to the earlier one. It is interesting to note that at $\tau = 0.0999$, Fig. 4(*H*) a boundary-layer type flow with large upward velocity near the wall is formed and the situation is seen to be completely opposite to that of sketch Fig. 4(*A*). It is of interest to note that

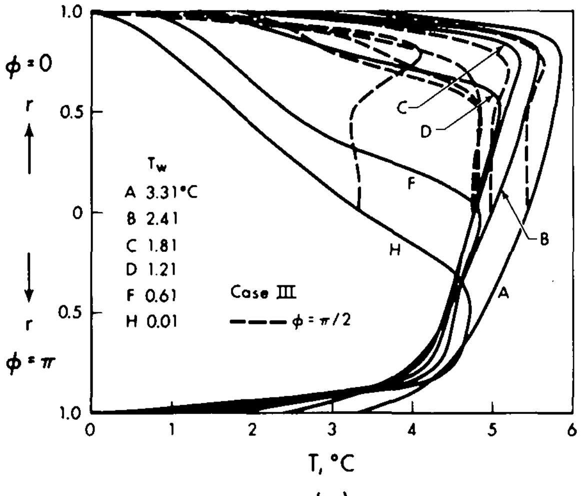

(a)

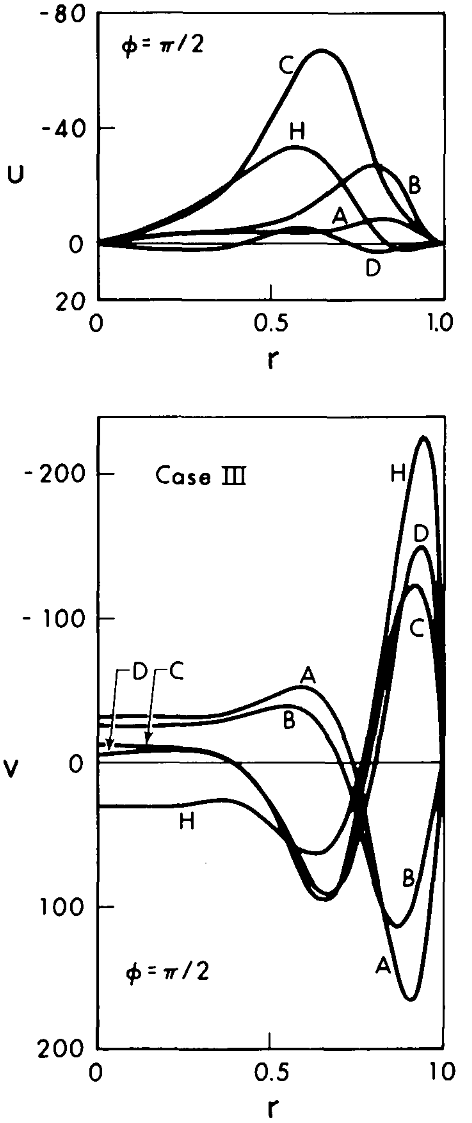

(b)

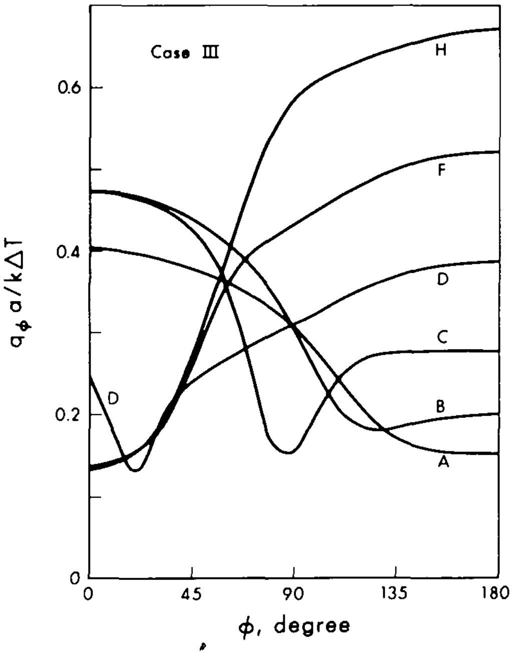

(c)

Fig. 6 Transient temperature (*a*) and velocity (*b*) profiles and dimensionless local wall heat flux distributions (*c*) for Case III

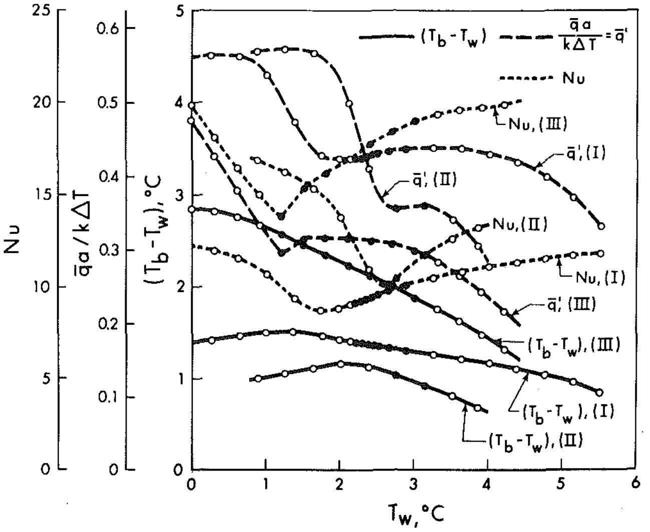

Fig. 7 Transient distributions for $(T_b - T_w)$, $\overline{q}a/k\Delta T = \overline{q}'$ and Nu

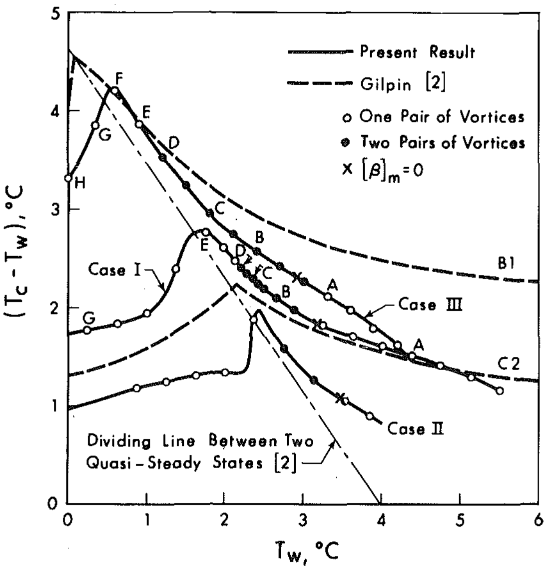

Fig. 8 Relationship between $(T_c - T_w)$ and T_w and comparison with Gilpin's results [2] during the inversion process

the vortex motions for the two quasi-steady states before and after the inversion process are opposite in direction but otherwise similar in character. In Fig. 6(*c*), the occurrence of the local minimum wall heat flux is caused by the maximum density effect.

For Case I shown in Fig. 3, the formation of the boundary-layer type flow is not apparent because of the smaller parametric values for ga^3/ν^2 and ΔT but the occurrence of the inversion process is quite similar. One notes that in sketch *E* of Fig. 3, the isotherms are nearly concentric and are similar to the pure conduction case. Furthermore, the flow pattern and isotherms shown in sketch (Fig. 3(*G*)) may be regarded to be the inverted ones of sketch (Fig. 3(*A*)) about the horizontal axis. This observation is also confirmed by the temperature profiles *A* and *G* shown in Fig. 5. In interpreting the graphical results, it is useful to recall that the symbols in each case refer to the same instants of time and the plottings may be contrasted to each other. Although the flow patterns during the inversion regime shown in Fig. 7 of [2] are not very distinct, one may conclude that the flow patterns from the present numerical solution agree with Gilpin's experimental observations [2].

4.2 **Heat Transfer Results.** The time-dependent temperature difference, $T_b - T_w$, the dimensionless average wall heat flux $\overline{q}a/k\Delta T$ and the Nusselt number for the three cases are shown in Fig. 7 where a circle denotes a flow pattern with one pair of vortices and a dot indicates that with two pairs of vortices. It is seen that a local minimum value exists for the Nusselt number (or $\overline{q}'$) and this coincides nearly with the complete decay (end of the inversion regime) of the original regular vortices near the center. Subsequently, the Nusselt number increases until the freezing process sets in. For Cases I and II, the local maximum exists for the temperature difference $(T_b - T_w)$ and it occurs after the disappearance of the original vortices.

Gilpin's presentation of the relationship between the temperature difference, $T_c - T_w$, and the wall temperature T_w (see Figs. 2 and 8 of [2]) provides a considerable physical insight into the inversion process. The results from this analysis are shown in Fig. 8 together with Gilpin's experimental results plotted for comparison. As noted earlier Gilpin's Cases C2 and B1 can be compared approximately with Cases I and III, respectively, in this study. The initial temperature in experiment [2] is higher ($T_0 > 10$°C) than that of the present study (near 4°C) but the agreement near the dividing line between the two results is good. In Fig. 8, the dash-dot line represents the dividing line between the two quasi-steady states obtained by Gilpin [2] from the quasi-steady model and boundary-layer approximation. The isotherms in Fig. 4 and the temperature profiles in Fig. 6 for Case III clearly show that the location of the instant maximum water temperature shifts from a point near the top to a point near the bottom along the vertical axis as the cooling process proceeds from the initial quasi-steady state to the final quasi-steady state. The local maximum for $(T_c - T_w)$ is apparently caused by the inversion of the thermal stratification in the core region during the inversion process. Numerical results from this study show that the local maximum occurs only after the complete decay of the original vortices.

Since the relationship between the density and water temperature is approximately symmetric with respect to the maximum density point at 4°C, the curve for $(T_c - T_w)$ versus T_w in the case of heating starting from the initial temperature near 0°C is expected to be the mirror image of that shown in Fig. 8 about the line through T_w = 4°C. Because of the anomalous thermal expansion of water at about 4°C, one may define the effective mean thermal expansion coefficient $[\beta]_m$ by the following relationship considering the average buoyancy force inside the pipe.

$$(2g/\pi)\int_0^\pi \int_0^1 [(\rho_w - \rho)/\rho] r dr d\phi = g[\beta]_m (T_b - T_w) \qquad (11)$$

where the buoyancy force is based on reference state at wall temperature. The condition for which $[\beta]_m$ is zero is denoted by a cross in Fig. 8. From Fig. 8, one may infer that the inversion process starts when $[\beta]_m$ becomes zero. The Rayleigh number can now be defined by the following equation.

$$\mathrm{GrPr} = 8(ga^3/\nu^2) \cdot |\,[\beta]_m| \cdot (T_b - T_w) \cdot \mathrm{Pr} \qquad (12)$$

The relationship between the Nusselt and Rayleigh numbers s shown in Fig. 9 for Cases I, II and III where the results from [11] for the quasi-steady state without the maximum density effects are also plotted for reference purpose. As noted earlier, the condition $[\beta]_m = 0$ represents the start of the inversion process and the Rayleigh number becomes zero at the threshold point. One may regard the regime with $[\beta]_m > 0$ as the initial period and that with $[\beta]_m < 0$ as the final period of the cooling process. For quasi-steady state the Nusselt number Nu = 8 for pure conduction is approached as GrPr → 0 [11]. However, for the present unsteady problem the state with $[\beta]_m = 0$ (GrPr = 0) is passed through instantaneously and the limiting Nusselt number Nu = 8 will not be approached. For the region with $[\beta]_m < 0$, one notes that a quasi-steady state [11] is approached from below after passing through the minimum Nusselt number point. This asymptotic behavior before the onset of ice nucleation as well as the approach toward the minimum Nusselt number clearly indicates the existence of two quasi-steady states.

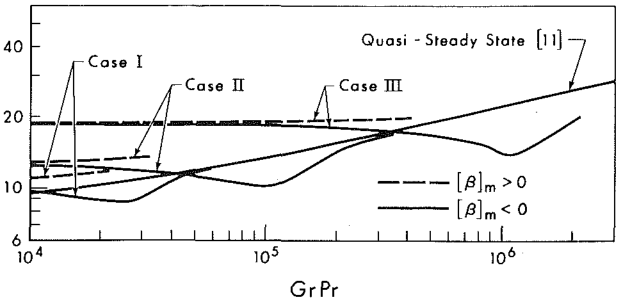

Fig. 9 Heat transfer dependence on Rayleigh number (GrPr) and quasi-steady results from [11]

5 Concluding Remarks

1 The transient natural convection problem in a long horizontal pipe with maximum density effect can be approached by a numerical method. It is expected that a numerical difficulty (stability or convergence) will arise for cases with large parametric values for ga^3/ν^2 and ΔT. The cases with higher parametric values were not attempted in this study because of higher computing cost caused by the necessity of using smaller Δr, $\Delta\phi$ and $\Delta\tau$. The numerical solution yields detailed streamline patterns and isotherms readily for flow visualization. The numerical method used can be extended to the transient natural convection problem with various other time-dependent thermal boundary conditions.

2 The present theoretical results generally confirm the experimental findings and the theoretical predictions based on the quasi-steady model and boundary-layer approximation reported by Gilpin [2]. The numerical results obtained in this study provide further insight into the inversion process which is unique to water possessing a maximum density at 4°C.

3 Based on the present theoretical results, it is clear that for the prediction on the rate of ice formation in a long horizontal cylinder with the initial liquid temperature higher than the freezing temperature, one must consider the natural convection effect. In this respect, the transient natural convection in a horizontal cylinder for the supercooling regime is also of considerable practical interest since in the experiments [2] supercooling of the water was observed at temperatures as low as −7°C before the ice nucleation occurs. The ice formation problem with free convection effect is an important technical problem which remains to be solved theoretically in the future.

4 In a theoretical and experimental study on the effect of liquid solidification in a tube upon laminar-flow heat transfer and pressure drop, Zerkle and Sunderland [15] pointed out the importance of free convection on their experimental results. It is very likely that the inversion process due to the maximum density effect may have some effect on their experimental results but this possibility has apparently not been pointed out in the literature.

Acknowledgement

This research was supported by the National Research Council of Canada through grant NRC A1655. The investigation was made possible through the encouragement of Professors T. Fujii and R. Echigo, Kyushu University, Japan. The authors wish to thank Dr. R. R. Gilpin for making reference [2] available to them at the manuscript stage and for his helpful discussions.

References

1 Muller, S. W., *Permafrost or Permanently Frozen Ground and Related Engineering Problems,* J. W. Edwards, Inc., Ann Arbor, Mich., 1947, pp. 144–149.

2 Gilpin, R. R., "Cooling of a Horizontal Cylinder of Water Through its Maximum Density Point at 4°C," *International Journal of Heat and Mass Transfer,* Vol. 18, 1975, pp. 1307–1315.

3 Vanier, C. R., and Tien, C., "Effect of Maximum Density and Melting on Natural Convection Heat Transfer From a Vertical Plate," *Chem. Eng. Prog. Symp. Ser.* No. 82, Vol. 64, 1968, pp. 240–254.

4 Vanier, C. R., and Tien, C., "Further Work on Free Convection in Water at 4°C," *Chem. Eng. Sci.,* Vol. 22, 1967, pp. 1747–1751.

5 Tien, C., Yen, Y. C., and Dotson, J. W., "Free Convective Heat Transfer in a Horizontal Layer of Liquid—The Effect of Density Inversion," *Heat Transfer—Tulsa* H. F. Rosson, ed., AIChE, Vol. 68, 1972, pp. 101–111.

6 Desai, V. S., and Forbes, R. E., "Free Convection in Water in the Vicinity of Maximum Density," *Environmental and Geophysical Heat Transfer,* HTD-Vol. 4, ASME, 1971, pp. 41–47.

7 Watson, A., "The Effect of the Inversion Temperature on the Convection of Water in an Enclosed Rectangular Cavity," *Quarterly Journal of Mechanics and Applied Mathematics,* Vol. 15, 1972, pp. 423–446.

8 Forbes, R. E., and Cooper, J. W., "Natural Convection in a Horizontal Layer of Water Cooled From Above to Near Freezing," JOURNAL OF HEAT TRANSFER, TRANS. ASME, Series C, Vol. 97, 1975, pp. 47–53.

9 Seki, N., Fukusako, S., and Nakaoka, M., "Experimental Study on Natural Convection Heat Transfer With Density Inversion of Water Between Two Horizontal Concentric Cylinders," JOURNAL OF HEAT TRANSFER, TRANS. ASME, Series C, Vol. 97, 1975, pp. 556–561.

10 Deaver, F. K., and Eckert, E. R. G., "An Interferometric Investigation of Convective Heat Transfer in a Horizontal Fluid Cylinder With Wall Temperature Increasing at a Uniform Rate," *Heat Transfer,* 1970, Vol. 4, Paper NC 1.1, Elsevier, Amsterdam.

11 Takeuchi, M., and Cheng, K. C., "Transient Natural Convection in Horizontal Cylinders With Constant Cooling Rate," to be published in *Wärme- und Stoffübertragung.*

12 Quack, H., "Natürliche Konvection innerhalb eines horizontalen Zylinders bei kleinen Grashof Zahlen," *Wärme- und Stoffübertragung,* Vol. 3, 1970, pp. 134–138.

13 Fujii, T., "Fundamentals of Free Convection Heat Transfer," (in Japanese), *Progress in Heat Transfer Engineering,* Vol. 3, Yokendo, Tokyo, 1974, p. 66.

14 "Landolt-Börnstein, Zahlenwerte und Funktionen," Band II, Teil 1, *Springer-Verlag,* 1971, pp. 36–37.

15 Zerkle, R. D., and Sunderland, J. E., "The Effect of Liquid Solidification in a Tube Upon Laminar-Flow Heat Transfer and Pressure Drop," JOURNAL OF HEAT TRANSFER, TRANS. ASME, Series C, Vol. 90, 1968, pp. 183–190.

N. Seki
Professor.

S. Fukusako
Assist. Professor.

T. Hirata
Graduate Student.

Department of Mechanical Engineering,
Hokkaido University,
Sapporo 060, Japan

Turbulent Fluctuations and Heat Transfer for Separated Flow Associated With a Double Step at Entrance to an Enlarged Flat Duct

An experimental study on heat-transfer in separated, reattached, and redevelopment regions behind a double step at entrance to a flat duct is presented. Measurements of turbulent fluctuation in a free shear layer are made by using a hot-wire anemometer. The experiments are carried out under a condition of uniform heat flux with the test fluid of air. Reynolds number ranges approximately from 4×10^3 to 2.5×10^5, and a step height ratio h/L is varied between 0.035 and 7.0. It is found that the heat-transfer rate in the separated region is closely connected with the behavior of transported heat to be represented by the product of velocity and temperature fluctuations in the free shear layer. An empirical equation is also proposed for the local Nusselt number in the separated and reattached regions.

Introduction

A study of heat-transfer characteristics of separated flow is of considerable importance in industrial practice. Although many investigations of separated flow have been reported, a complicated feature of the basic heat-transport mechanisms makes it difficult to grasp the characteristics of the flow clearly. Separation of flow occurs in various duct configurations, but most of the previous investigations have been performed mainly on ducts of circular and rectangular cross sections. For example, Ede, et al. [1][1] investigated the heat-transfer rate in a circular duct with abrupt convergence or divergence, whose diameter ratio was ½. Their experiments were carried out with a uniform heat flux, the test fluid being water. They reported that the heat-transfer rate in the region downstream was considerably affected in abrupt divergence rather than in abrupt convergence. Krall and Sparrow [2] measured the heat-transfer rate with water under a constant heat flux for a variety of diameter ratios of pipe and orifice. Their results show that the heat-transfer rate at the reattachment point is about $3 \sim 8$ times as large as that in the field of a fully developed flow in circular pipe. On the other hand, in case of a rectangular cross-sectional duct with a double backward-facing step, Abbott and Kline [3] demonstrated that two stalls quite different in length were formed on the opposed duct walls downstream of the double step. Filetti and Kays [4] experimented with air for such a configuration under a constant wall temperature; their results show that the heat-transfer rates at the two reattachment points for the long and short stalls were different. Recently, Seki, et al. [5] examined the heat-transfer rates of the long and short stalls in a wide range of step height ratio h/L, for a rectangular duct with air under a constant heat flux. They found that the heat-transfer rate at the reattachment point was well correlated with the distance between the reattachment point and the step.

The purpose of the present investigation is to examine the effect of heat transported by turbulence in the free shear layer on heat-transfer in the separated region and to propose an empirical equation for the local heat-transfer rate in the separated and reattached regions. Measurements are carried out with air under the condition of uniform heat flux in a rectangular duct having a double step at the entrance to the enlarged part. Reynolds number ranges approximately from 4×10^3 to 2.5×10^5. Namely, entrance velocity U and step height ratio h/L range from 4.4 m/s to 22 m/s and from 0.035 to 7.0, respectively.

Experimental Apparatus

Experiments were performed by using a Göttingen type of wind tunnel; the test section consists essentially of the contraction, steps,

---

[1] Numbers in brackets designate References at end of paper.

Contributed by the Heat Transfer Division for publication in the JOURNAL OF HEAT TRANSFER. Manuscript received by the Heat Transfer Division March 16, 1976.

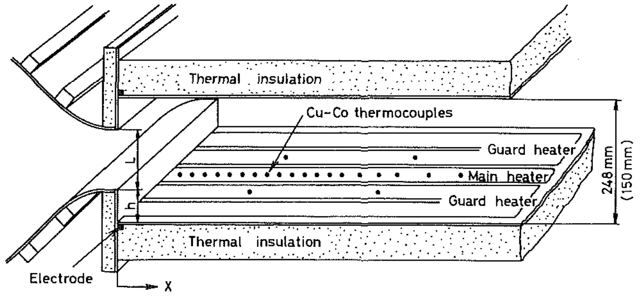

Fig. 1 Exploded view of test section

and heated plates. The data are obtained for two kinds of enlarged height (248 and 150 mm) of the wind tunnel, whose cross-sectional aspect ratios are 1.6 and 1.0, respectively. Stainless steel foils of a thickness of 50 μ are used as heaters; power is supplied by a-c electric current for heating the test section; the foils are fixed onto the walls of the test section by a binding agent. Heat loss to the surroundings is kept low by covering the test section with thermal insulating materials; the uncertainty of the data for the heat flux is estimated to be 3.2 percent of 2330 W/m^2 based on the measurement of the heat loss that leaks toward the rear side of the heating surface.

For the purpose of reducing the heat flow of the heater in a transverse direction, the heating section is divided into five segments as shown in Fig. 1; however, only the central one is used to measure wall temperatures. The heat flux from the walls is evaluated by the readings of both voltmeter and ammeter. Air, as a test fluid, is heated under the condition of uniform heat flux. The output of Cu-Co thermocouples, to measure the temperatures of the heated plates, were recorded with a self-balancing potentiometer.

The reattachment point, where heat-transfer rate shows a maximum value, is estimated from the temperature distribution of the wall. Two-dimensionality of flow in the reattached region is examined with thermocouples and confirmed by a flow visualization using an oil film method.

A Cu-Co thermocouple of 0.1 mm dia was put into the test section from a side wall to measure the temperature profiles of the flow field in order to prevent undesirable flow disturbances.

A Pitot-static probe was used, in all runs, to assure the uniformness of entrance velocity in the vertical direction with which Reynolds number was defined.

The fluctuations of $\sqrt{\overline{u'^2}}$, $-\overline{u'v'}$, and $\overline{v't'}$ are measured with a hot-wire anemometer by using a method reported by Shigetomi and Seki [6].

At a certain area of the separated flow region, the existence of instantaneous reverse flow originating from a large eddy motion of turbulence often makes it difficult to detect the fluctuation values precisely. However, such an area is carefully examined during the preliminary surveys of flow direction by a wool tuft method.

Seven cross sections in a flow direction are prepared for the measurement of turbulence fluctuation, temperature, and velocity distributions. These stations have a distance of 30, 85, 145, 205, 330, 470, and 660 mm from the step. All of the measurements are performed in a steady state.

Results and Discussion

Turbulence Behavior. Representative results for a short stall obtained by a hot-wire measurement at the aforementioned seven sections in the flow field are shown in Figs. 2 and 3, for a step height ratio of $h/L = 0.265$ and for an entrance velocity of $U = 12$ m/s (Re $= 1.25 \times 10^5$). Fig. 2 indicates the measured values of $\overline{u'^2}/U^2$ together with those of $-\overline{u'v'}/U^2$, where u' and v' are the components of fluctuating velocity parallel and normal to the mean streamlines, respectively. As a flow separated at the step edge forms a free shear layer, the turbulence generated in a mixing region passes through an exciting stage just after the step and then reaches a developed one in the separated region. After these stages, the turbulence decays gradually until the turbulence structure reaches a characteristic state of a fully developed duct flow.

In the studies of separated flow, many works related to velocity fluctuation in the free shear layer have been reported. Among them, Tani, et al. [7] reported the velocity fluctuations in a separated flow for a backward facing step, while Mueller and Robertson [8] measured the velocity fluctuations generated by a two-dimensional roughness element. The present results shown in Fig. 2 indicate the same trend as their publications. A tendency that the values of $\overline{u'^2}_{\max}$ and $-\overline{u'v'}_{\max}$ are approximately proportional to U^2 is also confirmed. However, in the present experiment regarding to an inner flow, the decay of turbulence in the redevelopment region occurs more rapidly than in their results owing to the deceleration of mean velocity caused by an abrupt change in area of the duct.

The convective heat-transfer rate at a wall may have some correlation to these velocity fluctuations. However, more directly speaking, it is evident that the most important factor contributing to the turbulent heat-transfer is the heat exchange rate, which is dependent on the fluctuation normal to the mean flow. Hence, it follows that the investigation for a value of $q_t = Cp\rho\overline{v't'}$ becomes an essential subject on such a problem.

Fig. 3 shows the typical results of $\overline{v't'}$ distributions at each section for an entrance velocity of $U = 12$ m/s and a wall heat flux of $q_w = 2330$ W/m^2, where $\overline{v't'}$ is made nondimensional by both U and the difference between wall temperature t_w and temperature on the center line of flow field t_c. It is seen that the position for maximum value of $\overline{v't'}$ approximately coincides with the mean dividing streamline just after the step, similarly as the distributions of velocity fluctuation does, but it deviates outward near the reattachment point thereafter, approaching the wall gradually. Sufficiently for downstream, the distribution of $\overline{v't'}$ is seen to approach that characteristic of fully developed flow in a duct.

The maximum values of the product of velocity and temperature fluctuations, $\overline{v't'}_{\max}$, seem to have a tendency to be minimal in the

Nomenclature

Cp = specific heat
f_R = function defined by equation (2)
h = step height
L = entrance height
Nu$_L$ = local Nusselt number, $\alpha L/\lambda$
q_t = heat transported by turbulence in the direction normal to mean flow, $Cp\rho\overline{v't'}$
q_w = heat flux from wall
Re = Reynolds number, UL/ν
t = temperature
T = nondimensional temperature, $(t_w - t_c)\lambda/q_wL$
u' = velocity fluctuation in the direction of mean flow
$\overline{u'v'}$ = average of the product of velocity fluctuations parallel and normal to mean flow
$\overline{v't'}$ = average of the product of velocity and temperature fluctuations normal to mean flow
U = entrance velocity
x = distance from a step
x_R = distance between reattachment point and step
x^* = nondimensional distance, x/x_R
α = local heat-transfer coefficient
λ = thermal conductivity
ν = kinematic viscosity
ρ = density

Subscript

max = maximum value

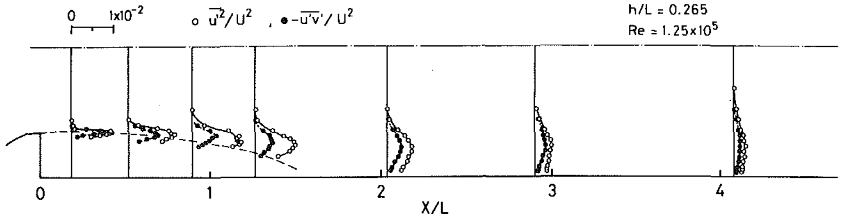

Fig. 2 Turbulence distribution downstream of the double step

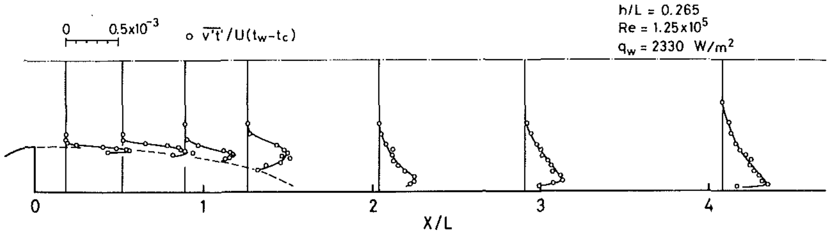

Fig. 3 $\overline{v't'}$ distribution downstream of the double step

reattached region, unlike the case of velocity fluctuations. A physical reason for these results could be understood from an inspection of measured results of T as shown in Fig. 4, where T is a nondimensional temperature. It is seen in the free shear layer that the temperature gradient just after the step is particularly steep but changes gradually to a gentle one as the reattachment is approached, as shown in Fig. 4. As the temperature difference between the fluid mass elements associated with a turbulent mixing motion to exchange heat is small under such a gentle gradient of temperature distribution, it seems that $\overline{v't'}_{\max}$ becomes smaller in the reattached region. In the separated region, as is observed from Fig. 4, the temperature gradient is steep in the vicinity of the wall, but a gentle gradient occurs farther from the wall, returning again to a steep gradient in the free shear layer. From this phenomenon it may be concluded that the variation of temperature gradient in the free shear layer has a relation with that of temperature distribution in the entire separated region. Consequently, provided that the heat transported by turbulence in the free shear layer has a close relation with the heat-transfer rate from the wall, the increase of the heat transported by turbulence in the free shear layer in a normal direction to the mean flow might result in an increase of the convective heat from the wall through the recirculating flow as a medium. Then, a dependency of heat-transfer from the wall on $\overline{v't'}_{\max}$ is successively discussed on behalf of the heat transported by turbulence in the free shear layer.

In Fig. 5, values of $\overline{v't'}_{\max}$ are plotted as a function of local heat-transfer coefficient at six sections, for a value of h/L = 0.265. The heat-transfer coefficient is defined as

$$\alpha = q_w/(t_w - t_c) \tag{1}$$

where q_w, t_w, and t_c are the heat flux from wall, wall temperature, and center-line fluid temperature, respectively.

A line with a slope of unity (+1) is also shown in Fig. 5 for reference. It is shown in the separated region ($x^* = 0.348$, 0.594, and 0.840) that the value of $\overline{v't'}_{\max}$ is approximately proportional to the heat-transfer coefficient in spite of a certain distance between the position of $\overline{v't'}_{\max}$ and the wall, where x^* is a nondimensional distance. That is, the heat convected by a recirculating flow reversed from the reattachment point is to be dissipated to the main stream by a velocity fluctuating motion normal to the mean flow. As a result, the relation that $\overline{v't'}_{\max}$ is approximately proportional to α is obtained.

On the other hand, in the redevelopment region ($x^* = 1.351$, 1.925, and 2.700), the measured results show a slope exceeding the value of unity (+1). These results seem to mean that the effect of the variation of $\overline{v't'}_{\max}$ on the heat-transfer rate from the wall is not larger than the case in the separated region. This may be due to a state that the position of $\overline{v't'}_{\max}$ is a little distance from the wall in the redevelopment region, as can be seen in Fig. 3, and therefore, the effect of heat exchange by a velocity fluctuation on the heat-transfer rate does not reach the wall so much as the case in the separated region.

From these considerations, it is found in the separated region that the heat-transfer coefficient is deeply connected with the heat transported by turbulence in the free shear layer. Namely, $\overline{v't'}_{\max}$ is proportional to α in the present experimental range.

Fig. 6 shows a plot of $\overline{v't'}_{\max}$ as a function of U under the same experimental conditions as described in Fig. 5 together with a solid line with a slope of two-thirds (+⅔). These results are interesting in comparison with those of velocity fluctuations. In the present experimental range the maximum values of $\overline{u'^2_{\max}}$ and $-\overline{u'v'}_{\max}$ at each section in the separated region are shown to have a proportional relation with U^2. However, the value of $\overline{v't'}_{\max}$ has a tendency to be approximately proportional to $U^{2/3}$ at each section in the separated region. Therefore, it might be suggested that the heat transported by turbulence in the free shear layer increases in proportion to $U^{2/3}$, and a relation of $\alpha \propto U^{2/3}$ is predictable in the separated region by taking the result shown in Fig. 5 into consideration.

On the other hand, the plotted results of $\overline{v't'}_{\max}$ versus U in the redevelopment region show a little larger slope than the value of two-thirds (+⅔). That is, the variation rate of $\overline{v't'}_{\max}$ against U increases gradually with increasing x^*. In the redevelopment region, it seems that the position of $\overline{v't'}_{\max}$ shifts slightly to the wall with increasing U for the lack of intermediation like a recirculating flow in the separated region. As a consequence, the increasing rate of $\overline{v't'}_{\max}$ against U has a larger value than the case in the separated region.

Nusselt Number. Recently, Seki, et al. [5] examined the relation between the Nusselt number at the reattachment point and x_R in a wide range of h/L with air. Fig. 7 shows the increase of x_R with increasing h/L, which indicates a good agreement with the result of Abbott and Kline [3]. It is already obtained in reference [5] that the Nusselt number at the reattachment point can be represented in terms of x_R as

$$\mathrm{Nu}_{L,\max}/\mathrm{Re}^{2/3} = 0.446 - 0.238 \left(\frac{x_R}{L}\right)^{0.161} \equiv f_R \tag{2}$$

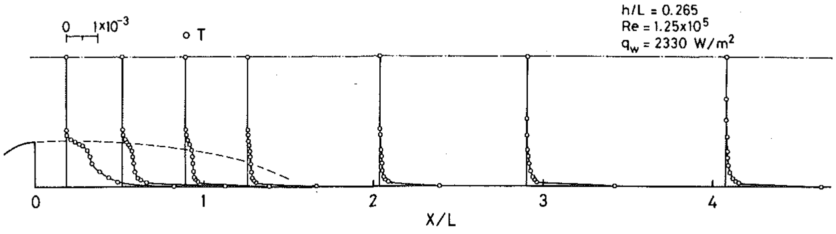

Fig. 4 Temperature distribution downstream of the double step

for all the stalls without any distinction of short and long ones, where subscript "max" means a value at the reattachment point and Nu_L is defined as

$$Nu_L = \alpha L/\lambda \tag{3}$$

in which λ is the thermal conductivity of air.

Since it can be seen in Figs. 5 and 6 that the local heat-transfer coefficient is proportional to $U^{2/3}$ in the separated region, the experimental data may be arranged under a relation such as $Nu_L \propto Re^{2/3}$. Obviously, the value of a function defined as $F(x^*) \equiv Nu_L/f_R Re^{2/3}$ becomes unity at a reattachment point. A close examination of $F(x^*) - x^*$ relation, obtainable by recasting the experimental results shown in Fig. 8, gives an empirical formula as $F(x^*) = 0.9 \exp[-1.7(x^* - 1)^2] + 0.1$. It must be noticed here that the empirical formula thus given must satisfy $F(x^*) = 1$ at $x^* = 1$. In Fig. 8, the abscissa indicates a value of x^*Re and the ordinate is $Nu_L/f_R F(x^*)$ multiplied by a function of x^* of the form of $x^{*2/3}[1.0 + (0.7x^{*0.133})^5]^{0.2}$. This function can be approximated to $x^{*2/3}$ in a separated region and to $x^{*0.8}$ in a fully developed region. This formula is determined to satisfy the relations as $Nu_L \propto Re^{2/3}$ in the separated and reattached regions and $Nu_L \propto Re^{0.8}$ in the fully developed region, with reference to the method of Churchill and Usagi [9].

Present experimental data for long and short stalls are indicated in Fig. 8. The range of the present experiments for a long stall was limited to $h/L < 1.5$ because of the streamwise length of the experimental apparatus. It can be seen that the Nusselt number in the separated and reattached regions is well correlated by the following empirical equation:

$$Nu_L = f_R\{0.9 \exp[-1.7(x^* - 1)^2] + 0.1\}Re^{2/3} \tag{4}$$

However, this equation should have the same range of application as for equation (2), that is,

$$4 \times 10^3 \leqq Re \leqq 8 \times 10^4 \tag{5}$$

$$0.2 \leqq x_R/L \leqq 16.0 \tag{6}$$

Further, just after the step, Abbott and Kline [3] reported the existence of a three-dimensional flow region; therefore, the experimental data in the range of $x^* < 0.2$ are eliminated from the results in Fig. 8. The proposed proportional relation between Nu_L and $Re^{2/3}$ in the present report is satisfied in the following range with an uncertainty of less than ±20 percent as is estimated in this figure:

$$0.2 \leqq x^* \leqq 1.3 \tag{7}$$

In the redevelopment region, Nu_L deviates from a relation proportional to $Re^{2/3}$, as can be seen from the measured results by Knight [10]. In addition, the Nusselt number in the fully developed region is reported by Kays and Leung [11], which is shown in Fig. 8 in a broken line. Their prediction indicated for reference, however, cannot strictly be compared with the authors' results due to the difference of the definition of Nusselt number. The experimental data deviate significantly from the present empirical equation (4) in the redevelopment region and may approach the broken line with a slope of +0.8 in the fully developed region. Furthermore, the representative results obtained by Krall and Sparrow [2] for an orifice in a circular tube with water, and those obtained by Filetti and Kays [4] for a rectangular cross-sectional duct with air, are also shown in Fig. 8. It is not always

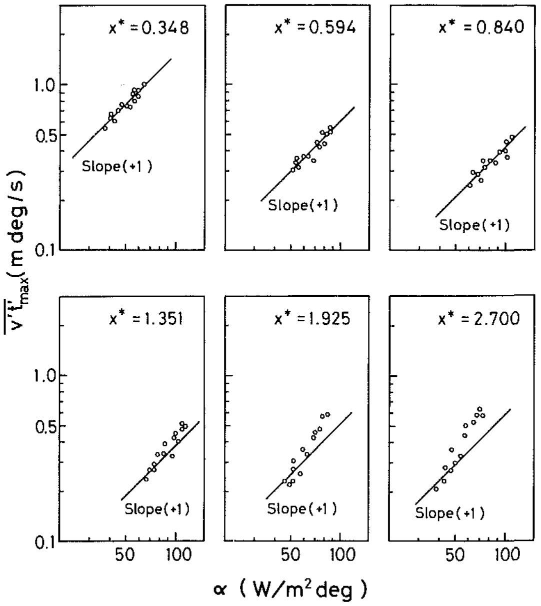

Fig. 5 Relation between $\overline{v't'}_{max}$ and local heat-transfer coefficient for $h/L = 0.265$

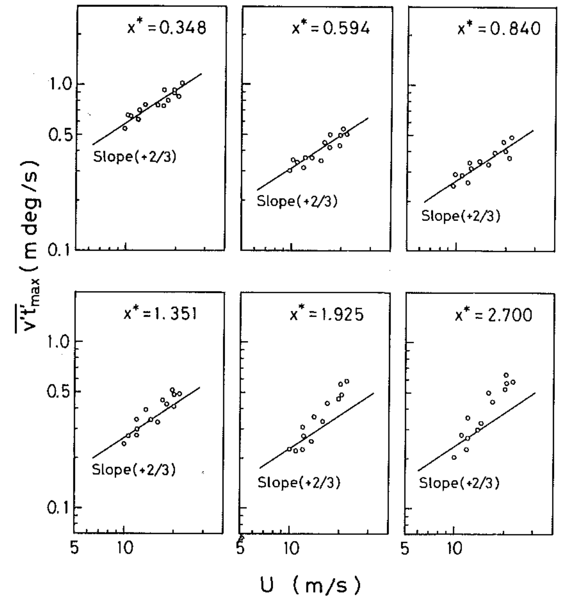

Fig. 6 Relation between $\overline{v't'}_{max}$ and entrance velocity for $h/L = 0.265$

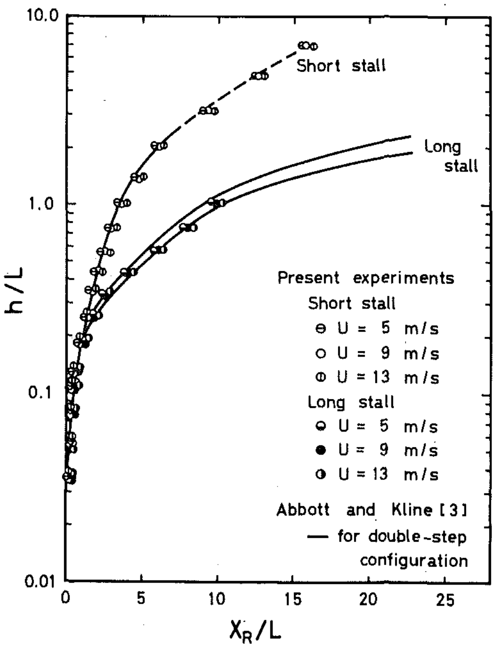

Fig. 7 Variation of x_R as a function of h/L

possible in a strict sense to compare their results with the present ones owing to the differences in experimental conditions. However, the trends could be compared with the authors' results by plotting their data so that they meet the present empirical equation (4) at the reattachment point. It should be noticed that their results have a similar feature to the present results. However, the data of Krall and Sparrow [2] indicate a little larger value in the separated region than the present ones and also show a different behavior in the redevelopment region. This difference might be caused by a difference in the behavior of $\overline{v't'}$ distribution for each cross-sectional shape of duct.

Summary and Conclusions

Measurements are provided for the heat-transfer rate in the separated, reattached, and redevelopment regions behind a double step at the entrance of a two-dimensional duct, under the condition of a uniform heat flux. Simultaneously, the fluctuation of $\overline{v't'}$ in the free shear layer is examined with a hot-wire anemometer. The test fluid is air and the range of Reynolds number is approximately 4×10^3 to 2.5×10^5. The following conclusions hold for the experimental range or measurements.

1 The behavior of heat-transfer rate in the separated region is correlated with the measurement of heat transported by turbulence in normal direction to a mean flow in the free shear layer.

2 The heat transported by turbulence in the free shear layer increases proportionally with the $\frac{2}{3}$ power of entrance velocity and with the heat-transfer rate in the separated region.

3 The local heat-transfer coefficient in the separated and reattached regions is represented by an empirical equation (4), of which the uncertainty is within ±20 percent and the applicable range is given by equations (5), (6), and (7).

Acknowledgment

The authors gratefully acknowledge Professor M. Arie, Hokkaido University, for his many suggestions to improve the manuscript.

The authors are grateful also to Mr. H. Kawabe for his contribution in the experimental measurements and Mr. K. Sawada for his assistance in installing the experimental apparatus.

References

1 Ede, A. J., Hislop, C. I., and Morris, R., "Effect on Local Heat Transfer Coefficient in a Pipe of an Abrupt Disturbance of the Fluid Flow: Abrupt Convergence and Divergence of Diameter Ratio 2/1," *IME Proceedings*, No. 38, 1956, pp. 1113–1130.

2 Krall, K. M., and Sparrow, E. M., "Turbulent Heat Transfer in the Separated, Reattached, and Redevelopment Regions of a Circular Tube," JOURNAL OF HEAT TRANSFER, TRANS. ASME, Series C, Vol. 88, 1966, pp. 131–136.

3 Abbott, D., and Kline, S., "Experimental Investigation of Subsonic Turbulent Flow Over Single and Double Backward Facing Steps," *Journal of Basic Engineering*, TRANS. ASME, Series D, Vol. 84, 1962, pp. 317–325.

4 Filetti, E. G., and Kays, W. M., "Heat Transfer in Separated, Reattached, and Redevelopment Regions Behind a Double Step at Entrance to a Flat Duct," JOURNAL OF HEAT TRANSFER, TRANS. ASME, Series C, Vol. 89, 1967, pp. 163–168.

5 Seki, N., Fukusako, S., and Hirata, T., "Effect of Stall Length on Heat Transfer in Reattached Region Behind a Double Step and Entrance to an Enlarged Flat Duct," *International Journal of Heat and Mass Transfer*, Vol. 19, 1976, pp. 700–702.

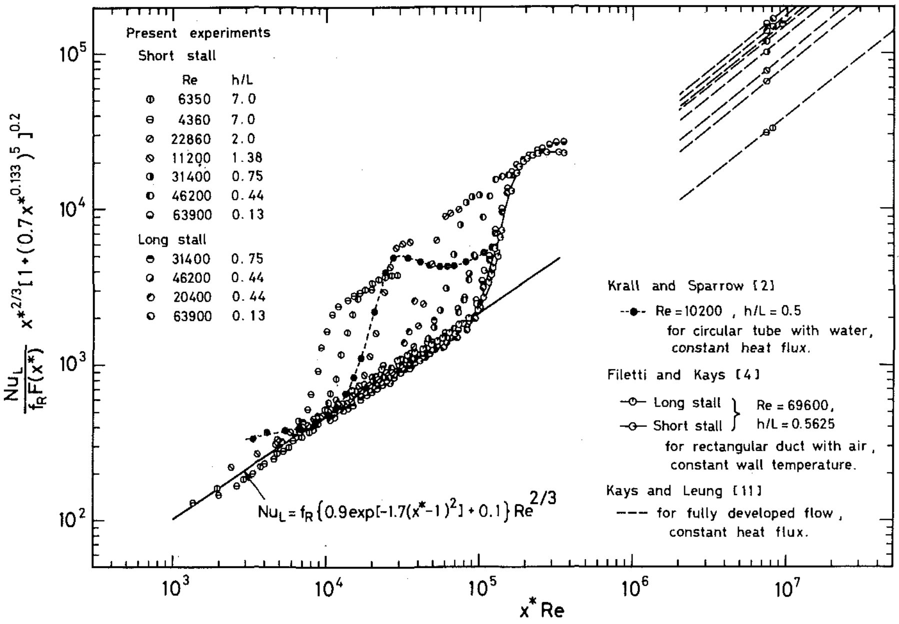

Fig. 8 Local heat-transfer results in the separated, reattached, and redevelopment regions

6 Shigetomi, F., and Seki, N., "The Behavior of the Temperature-Velocity Fluctuations and the Turbulent Prandtl Number in the Developing Thermal Turbulent Boundary Layer on a Flat Plate," *Bulletin of the JSME*, Vol. 17, 1974, pp. 351–358.

7 Tani, I., Iuchi, M., and Komoda, H., "Experimental Investigation of Flow Separation Associated with a Step or a Groove," Aeronautical Research Institute, University of Tokyo, Report No. 364, 1961, pp. 119–137.

8 Mueller, T. J., and Robertson, J. M., "A Study of the Mean Motion and Turbulence Downstream of a Roughness Element," *Developments in Theoretical and Applied Mechanics*, Plenum Press, Vol. 1, 1963, pp. 326–360.

9 Churchill, S. W., and Usagi, R., "A General Expression for the Correlation of Rates of Transfer and Other Phenomena," *AICHE Journal*, Vol. 18, 1972, pp. 1121–1128.

10 Knight, H. R., "Heat Transfer in Separated Flows," Imperial College, Mechanical Engineering Department, SF/TN/3, 1966.

11 Kays, W. M., and Leung, E. Y., "Heat Transfer in Annular Passages - Hydrodynamically Developed Turbulent Flow With Arbitrarily Prescribed Heat Flux," *International Journal of Heat and Mass Transfer*, Vol. 6, 1963, pp. 537–557.

A. F. Emery
F. B. Gessner

Department of Mechanical Engineering,
University of Washington,
Seattle, Wash.

The Numerical Prediction of Turbulent Flow and Heat Transfer in The Entrance Region of a Parallel Plate Duct

Velocity and temperature profiles were computed for turbulent flow, both in the entrance region and the fully developed state, in a duct with heated parallel plates. By starting the calculations at the duct inlet and using a finite difference technique and a three-dimensional mixing length originally defined for corner flows, it was possible to predict axial flow behavior and the nonasymptotic approach to fully developed flow with and without associated heat transfer.

Introduction

The ability to predict turbulent boundary layer growth in narrow angle diffusers and converging passages is of interest in several engineering applications. Many current prediction methods are of the integral type where the equations of motion are solved by integrating across the stream after auxiliary equations are introduced which include empirical information. Other solutions involve using transport equations for the Reynolds stresses, turbulent kinetic energy, and dissipation rate. Alternate methods are based on the numerical solution of the equations in differential form in which the only empiricism is associated with a description of the apparent viscosity of the turbulent fluid. Spalding and co-workers [1–2][1] have employed iterative numerical methods with a law-of-the-wall approach in computing many flows, including internal duct flows. Stephenson [3] followed Spalding's approach but employed transport equations for the turbulent kinetic energy and dissipation rate to treat the parallel duct problem, because it was felt that a mixing length model would not be adequate for predicting nonasymptotic flow development in the duct. In this paper we shall show that by appropriately defining the mixing length and beginning the computations from the duct inlet with no special starting procedures, it is possible to predict the nonasymptotic development of the duct flow. Pletcher [4, 5] utilized the duFort-Frankel method and a mixing length model for similar computations and presented a very good summary of the background and the present state-of-the-art. The testing of these approximate numerical techniques for two-dimensional duct flow is best done for parallel-sided, two-dimensional ducts to facilitate comparisons with previous theoretical work and with experimental data. Inasmuch as the accuracy of numerical methods for laminar flow is well-established, the questions about the applicability of these techniques to turbulent duct flow rests upon the ability to describe turbulent shear stress behavior and the complications introduced in the difference equations by the strong spatial effects due to turbulence.

The present state of knowledge of friction factor behavior for fully developed flow in rectangular ducts is relatively complete. Empirical correlations have been developed which apply over a wide range of operating conditions [6]. Some data on local flow conditions in the entrance region of rectangular ducts are available, and fairly extensive turbulence and mean flow data have been obtained for developing and fully developed flow conditions [7–9].

The most complete experiments for both friction factors and heat transfer in developing rectangular duct flows are reported by Sparrow, et al. [10, 11] for asymmetric heating and by Byrne, et al. [12] for symmetric heating. Byrne, et al. also give a momentum integral computer solution based upon the law-of-the-wall and report that there is no significant difference in results for isothermal and constant heat flux wall conditions. Their experiment involved heating one side only, and they inferred from the results for this condition, results which apply for both walls being heated.

The results reported herein apply for developing turbulent flow in a two-dimensional duct and were obtained as the first part of a study related to developing turbulent flow along a streamwise corner.

---

[1] Numbers in brackets designate References at end of paper.

Contributed by the Heat Transfer Division of THE AMERICAN SOCIETY OF MECHANICAL ENGINEERS and presented at the National Heat Transfer Conference St. Louis, Mo., August 9–11, 1976. Revised manuscript received by the Heat Transfer Division August 12, 1976. Paper No. 76-HT-36.

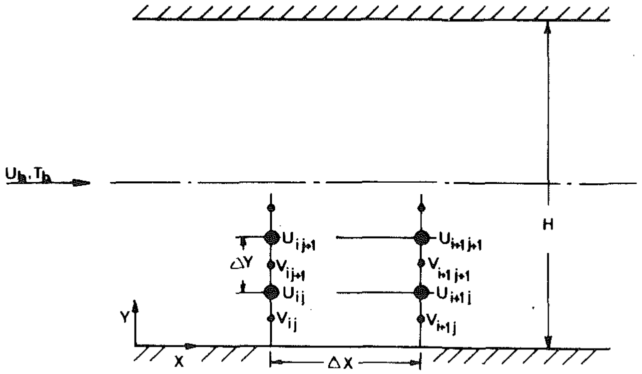

Fig. 1 **Schematic of the duct and the nodal grid pattern**

Numerical Approach

The field equations which represent the incompressible, two-dimensional flow between parallel walls are,

$$\frac{\partial u}{\partial x} + \frac{\partial v}{\partial y} = 0 \tag{1}$$

$$u\frac{\partial u}{\partial x} + v\frac{\partial u}{\partial y} = -\frac{1}{\rho}\frac{\partial \overline{p}}{\partial x} + \nu\left(\frac{\partial^2 u}{\partial y^2}\right) - \left(\frac{\partial \overline{u'v'}}{\partial y}\right) \tag{2}$$

$$u\frac{\partial T}{\partial x} + v\frac{\partial T}{\partial y} = \alpha\frac{\partial^2 T}{\partial y^2} - \frac{\partial \overline{v'T'}}{\partial y} \tag{3}$$

where v is found from the continuity equation, (1), and u and $\overline{p}$ are determined from equation (2) by using the technique of Patankar and Spalding [2]. We have further assumed that the axial velocity, u, is affected only by the spanwise-averaged axial pressure gradient. By introducing Prandtl's mixing length, we can express the turbulent shear stress as,

$$\overline{u'v'} = -\ell_p{}^2\frac{\partial u}{\partial y}\left|\frac{\partial u}{\partial y}\right|, \; \ell_p = \kappa\ell \tag{4}$$

where κ is an empirical constant which may or may not equal von Karman's constant (0.40 or 0.41) depending on the prescribed variation for ℓ. When three-dimensional duct flow is treated, then v and w must be calculated by using their respective momentum equations and permitting the pressure gradients $\partial p/\partial y$ and $\partial p/\partial z$ to vary with y and z as described in [2]. For this two-dimensional problem, we used the staggered grid shown in Fig. 1, where the axial and transverse velocities are defined at different positions in the mesh. This mesh, *as contrasted to the mathematical grid (where all the variables are* defined at the same nodal position), permits one to derive a finite difference approximation to the equations which ensures conservation of mass in the y-direction. Although some errors in mass conservation are normally not important, they were observed to cause significant errors when v was calculated using the y-momentum equation instead of equation (1). Laminar flow calculations showed that either equation (1) or the y-momentum equation were satisfactory when the staggered grid was used. The computations were begun at the duct inlet by assuming that the mixing length model applies for $x > 0$ and using only the conditions $u(0, y) = U_b$ and $u(x, 0) = 0$, $v(x, 0) = 0$ for $x \geq 0$. The transverse nodal spacing varied across the duct width, but was constant down the duct. The nodal spacing was much denser near the wall than at the midpoint to permit acceptable definition of the boundary layer thickness.

The appropriate difference equations are then,

$$\frac{u_{i+1j} - u_{ij}}{\Delta x} + \frac{v_{i+1j+1} - v_{i+1j}}{\Delta y} = 0 \tag{5}$$

$$u_{ij}\frac{u_{i+1j} - u_{ij}}{\Delta x} + v_{ij}\frac{u_{ij} - u_{ij-1}}{\Delta y} = -\frac{1}{\rho}\frac{\overline{p}_{i+1} - \overline{p}_i}{\Delta x} + \mu^*_{ij+1/2}\frac{u_{ij+1} - u_{ij}}{\Delta y^2} - \mu^*_{ij-1/2}\frac{u_{ij} - u_{ij-1}}{\Delta y^2} \tag{6}$$

where

$$\mu^*_{ij+1/2} = \mu + \mu_t = \mu + \rho\ell_p{}^2\left|\frac{u_{ij+1} - u_{ij}}{\Delta y}\right|$$

and T_{ij} satisfies a similar equation to that for u_{ij}.

Recasting equation (6) in the general form,

$$\alpha_j u_{i+1j} + \beta_j = \overline{p}_{i+1} \tag{7}$$

we may integrate to obtain

$$\dot{m} = \int \rho u_{i+1j} dy = \overline{p}_{i+1}\int \frac{\rho}{\alpha_j} dy - \int \frac{\beta_j}{\alpha_j}\rho dy \tag{8}$$

Since $\dot{m}$ is constant, $\overline{p}_{i+1}$ may be obtained from equation (8). Then by substitution into equation (6), the values of u_{i+ij} may be obtained, and from equation (5) the values of v_{i+ij}. Equation (6) uses the upwind differencing form for the transverse advection even though this is known to damp the high frequency oscillations of u. Its use was justified on the basis that: (a) the explicit differencing was used only to obtain a starting solution for the region $0 \leq x \leq 0.1\,H$; (b) the profiles thus obtained for flat plate simulation were in better agreement with known flat plate solutions; (c) these starting profiles provided a smoother transition to the duFort-Frankel scheme used further downstream; (d) the method has the correct advection characteristics (see reference [13]). After the starting solution was obtained, the difference equations were changed to the duFort-Frankel method which was first used by Pletcher [5] for developing flow in a pipe. All calculations for $x > 0.1\,H$ used the duFort-Frankel equation given as:

$$u_{ij}\frac{u_{i+1j} - u_{i-1j}}{2\Delta x} + \overline{v}_{ij}\frac{u_{ij+1} - u_{ij-1}}{2\Delta y}$$

Nomenclature

a = duct half-width
A^+ = empirical constant
C_f = fully developed skin friction coefficient ($\tau_w/1/2\rho U_b{}^2$)
C_{fx} = local skin friction coefficient ($\tau_{wx}/1/2\rho U_b{}^2$)
C_p = specific heat
H = duct width
ℓ = mixing length
ℓ_p, $\ell_{p,d}$ = Prandtl's mixing length, with damping
Q_w = wall heat flux per unit area
p, $\overline{p}$ = static pressure, spanwise averaged
Re_b = bulk Reynolds number ($U_b H/\nu$)
Re_x = local Reynolds number ($U_b x/\nu$)
St_x = local Stanton number ($Q_w/[\rho C_p U_b(T_w - T_b)]$)
T, T_b, T' = temperature, bulk temperature, fluctuating component
u, U_b, u' = axial velocity, bulk velocity, fluctuating component
U_0 = center-line velocity
u_τ = friction velocity
v, v' = transverse velocity, fluctuating component
x, y = rectangular coordinates ($x = -x_s$ at the duct inlet, $y = 0$ at the wall)
x_s = starting length
y^+ = normalized coordinate (yu_τ/ν)
μ, μ_t = dynamic viscosity, turbulent viscosity
ρ = density
δ = boundary layer thickness
δ^* = displacement thickness
τ_w = fully developed wall shear stress
τ_{wx} = local wall shear stress
ν = bulk kinematic viscosity
θ = momentum thickness
α = thermal diffusivity

$$= -\frac{1}{\rho}\frac{\overline{p}_{i+1} - \overline{p}_{i-1}}{2\Delta x} + \mu^*_{ij+1/2}\frac{u_{ij+1} - \overline{u}_{ij}}{\Delta y^2} - \mu^*_{ij-1/2}\frac{\overline{u}_{ij} - u_{ij-1}}{\Delta y^2} \tag{9}$$

where

$$\overline{v}_{ij} = \frac{v_{ij+1} + v_{ij}}{2}, \quad \overline{u}_{ij} = \frac{u_{i+1j} + u_{i-1j}}{2}$$

The stability criterion for a constant μ^* is found by the usual von Neumann Fourier [14] analysis to be,

$$v_{ij}\,\Delta x < u_{ij}\Delta y \tag{10}$$

For a variable μ^*, equation (2) can be rewritten as,

$$u\frac{\partial u}{\partial x} + \left(v - \frac{\partial \mu^*}{\partial t}\right)\frac{\partial u}{\partial y} = -\frac{1}{\rho}\frac{\partial \overline{p}}{\partial x} + \nu\frac{\partial^2 u}{\partial y^2}$$

and a conservative stability criterion is then easily seen to be,

$$\left(v_{ij} + \left|\frac{\partial \mu^*}{\partial y}\right|_{ij}\right)\Delta x < u_{ij}\,\Delta y \tag{11}$$

For the turbulent flows considered herein the term $|\partial\mu^*/\partial y|$ was found to be the dominant form.

A similar analysis shows that the duFort-Frankel method is never stable when upwind differencing is used. Equation (9) is then implemented in the same way as was equation (6) in forming the terms α_j and β_j and integrating to obtain $\overline{p}_{i+1}$.

Two further problems were encountered with the above differencing system. First, when the axial pressure gradient was large, the transverse spacing was not important, but for small pressure gradients, the axial flow velocities near the wall would eventually become zero because of an inadequate momentum transfer from the outer portion of the flow. The cure to this was simply to make Δy small enough. Furthermore, flat plate calculations showed that if the first transverse node was placed within the zone $y^+ < 5$ and the axial spacing was restricted to $\Delta x < 0.6\delta$, this problem did not occur. While larger values of Δy and Δx were permissible, poor flat plate results would result. Unlike Pletcher's pipe flow calculations, it was not possible to initiate the calculations without using an explicit starting calculation. Second, the turbulent computations always became unstable after a sufficient distance x. This was resolved by expressing μ_t as a weighted average of μ_t values computed at the closest and next closest pair of nodal points according to the following form,

$$\mu_{t_{ij+1/2}} = \frac{(\ell_p{}^2)_{ij+1/2}}{1+\gamma}\left\{\frac{u_{ij+1} - u_{ij}}{\Delta y} + \gamma\frac{u_{ij+2} - u_{ij-1}}{3\Delta y}\right\} \quad (0 \leq \gamma \leq 1)$$

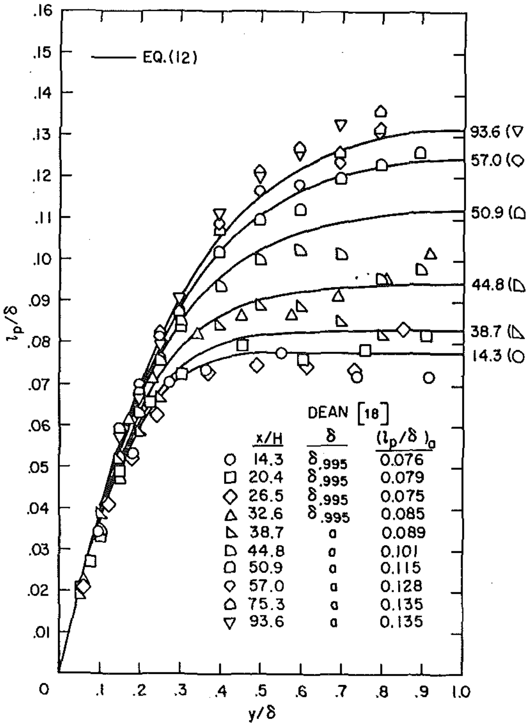

Fig. 2 Mixing length distribution in the entrance-region of a two-dimensional duct, $Re_b = 1.0 \times 10^5$

The best performance was obtained when $\gamma = 1$. This agrees with Pletcher's expression for the turbulent viscosity for a mathematical grid [5].

Mixing Length Model

In order to complete the system of equations an adequate mixing length model must be specified. Gessner and Emery [15, 16] have proposed a three-dimensional mixing length model for developing flow in rectangular ducts of arbitrary aspect ratio which reduces to the following limiting form for two-dimensional duct flow:

$$\ell_p{}^* = \frac{2\kappa}{F(y^*) + K(x^*)G(y^*)} \tag{12}$$

where

$$F(y^*) = 2\left[1 + \frac{1}{(y^*)^2}\right]^{1/2} + 2\left[1 + \frac{1}{(2-y^*)^2}\right]^{1/2}$$

$$G(y^*) = \sum_{n=0}^{7} C_n[1 + (y^*)^n]$$

$$K(x^*) = 1 - C_8\{1 + \tanh\,[C_9(x^* - x_0{}^*)]\}$$

where

$$x^* = x/H,\ y^* = y/\delta, \text{ and,}$$

$$\ell_p{}^* = \ell/\delta,\ 0 < y/\delta < 1$$

$$\ell_p{}^* = \ell(y = \delta)/\delta,\ y/\delta > 1$$

and κ, $x_0{}^*$ and C_0 through C_9 are empirical constants, the same as those specified for the three-dimensional model, namely

$$\kappa = 0.45 \quad C_1 = 1.15718 \quad C_4 = -10.65843 \quad C_7 = -10.36380$$

$$x_0{}^* = 46 \quad C_2 = 21.32706 \quad C_5 = 7.29654 \quad C_8 = 0.4$$

$$C_0 = -1.29982 \quad C_3 = -20.60664 \quad C_6 = 16.08880 \quad C_9 = 0.11$$

The function F was originally developed by Buleev [17]; G is a polynomial function designed to alter the asymptotic value of $\ell_p{}^*$ in the outer region of the flow for agreement with experimental results. K is a development length function which enables the asymptotic value of $\ell_p{}^*$ to increase monotonically as fully developed flow is approached. Figs. 2 and 3 indicate the agreement between the mixing length model and results obtained by operating on the data of Dean [18] and Comte-Bellot [19]. The present model also agrees well with the model of Acharya and Reynolds [20] for fully developed flow conditions: $\ell_p/\delta = (4/30)\,[1 - (1 - y/\delta)^3]$ and with the experimental data of Hussain and Reynolds [21]. In order to apply equation [12] in the viscous sublayer, van Driest's damping function was used.

$$\ell_{p,d}{}^* = \ell_p{}^*\,[1 - \exp\,(-y^+/A^+)] \tag{13}$$

Flow Results

Initial computations were performed for zero pressure gradient flow over a flat plate in order to select an appropriate value for A^+ in equation (13). These calculations and those for the duct were started from $x = 0$ without matching experimental inlet conditions and with ℓ_p applying from the inlet. On the basis of comparison with Klebanoff's results [22], A^+ was selected to be 29. This selection agrees with the recommendations of Hussain and Reynolds [21], who suggest that

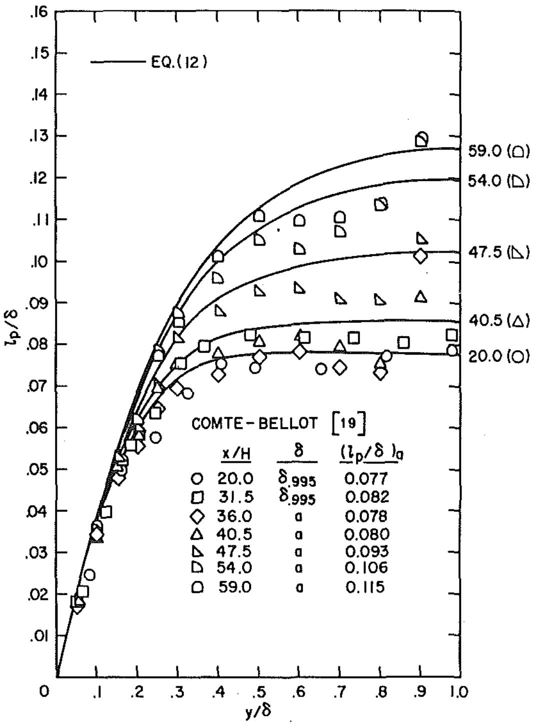

Fig. 3 Mixing length distribution in the entrance-region of a two-dimensional duct, $Re_b = 2.4 \times 10^5$

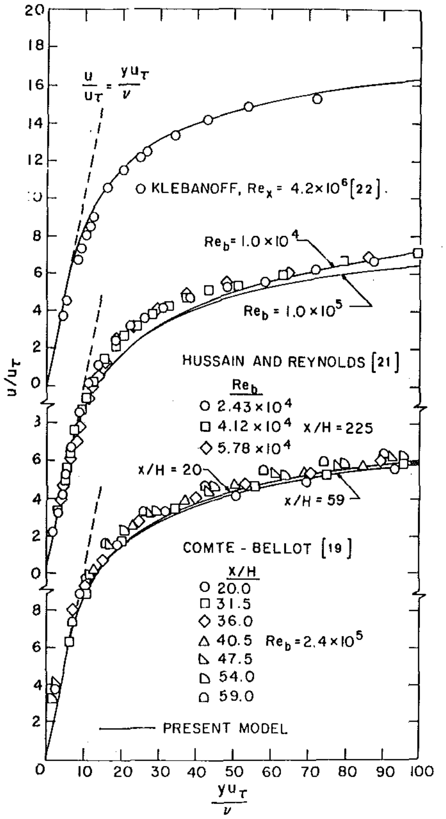

Fig. 4 Predicted and measured mean velocity profiles in the near wall region of some two-dimensional boundary layer flows

$\kappa = 0.45$ and $A^* = 29$ form a suitable combination for modeling fully developed flow in a two-dimensional duct. Fig. 4 shows that the near wall velocity distribution measured by Klebanoff agrees well with the distribution predicted by the proposed model. This figure also indicates that the prescribed mixing length variation models near-wall velocity profile behavior in two-dimensional duct flows reasonably well, both in the developing ($20 < x/H < 59$) and fully developed ($x/H = 225$) regions.

The predicted variation of axial center-line velocity with development length for two-dimensional duct flow is compared with experimentally measured profiles in Fig. 5. Additional comparisons between predicted and measured distributions of displacement thickness, momentum thickness and shape factor (δ^*/θ) are shown in Fig. 6. Predictions based on the shear layer interaction model proposed by Bradshaw, et al. [23], as presented by Dean [18], are also shown in order to demonstrate that the overall level of agreement between theory and experiment is comparable for both models. Dean's results are based on computations which start at $x/H = 26.5$ with an initial velocity profile matched to the experimental profile measured at this location. Computations referred to the present model were begun at $x/H = 0$ with uniform flow assumed at this station. Both models predict the local peaking of U, δ^*, and θ observed at $x/H = 40$ quite well. The present model also predicts the approach of each variable toward a constant (fully developed) value in a manner which agrees well with experimentally observed behavior. The model proposed by Bradshaw, et al., is not well-suited for this purpose, however, because of intrinsic numerical errors which lead to continued x-dependence of predicted quantities in the fully developed region [23]. These errors, in turn, lead to difficulties in determining fully developed values of the x-dependent variables, and are responsible, in part for the tail-up behavior observed in Figs. 5 and 6 when $x/H > 80$.

Fig. 7 compares mean velocity profiles predicted in the developing flow region with those measured by Dean [18]. In general, Dean's predictions and profiles predicted by the present model are in good agreement with the experimental results. It is evident, however, that the experimental profiles tend to develop more rapidly than distri-

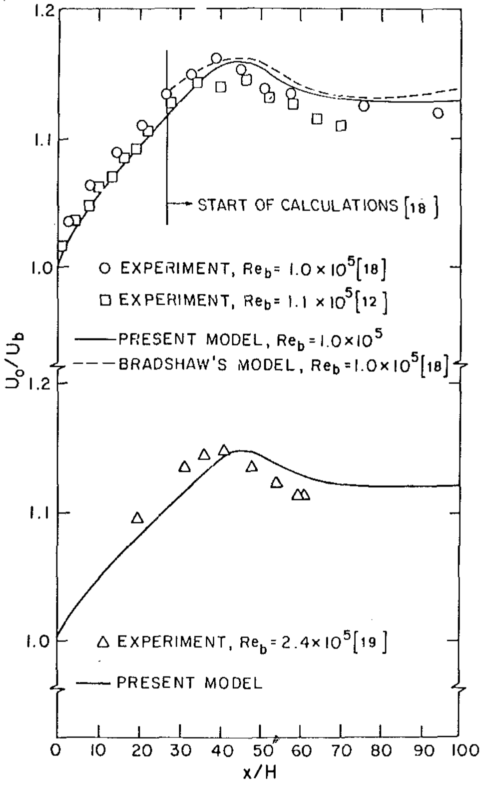

Fig. 5 Predicted and measured distributions of axial center-line velocity for developing flow in a two-dimensional duct

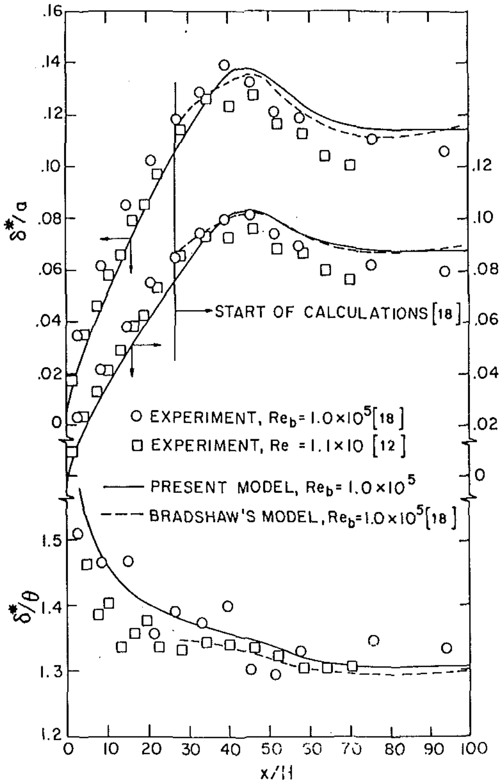

Fig. 6 Predicted and measured distributions of displacement thickness, momentum thickness and shape factor for developing flow in a two-dimensional duct

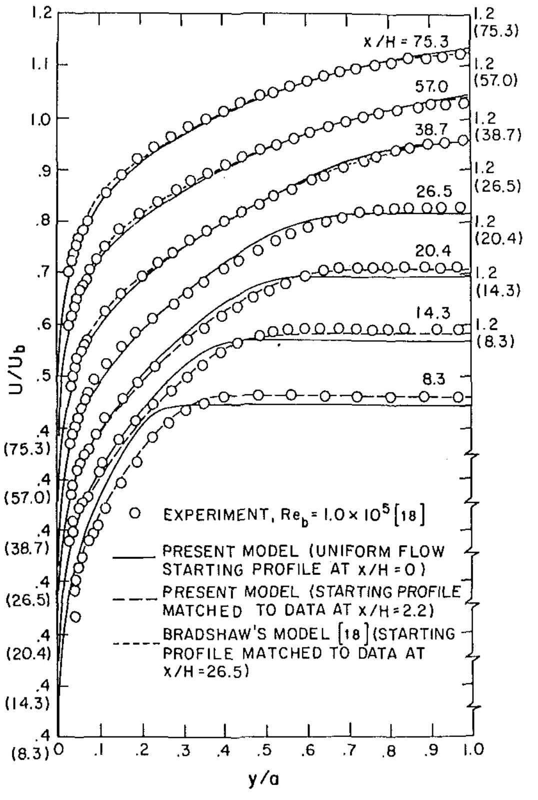

Fig. 7 Predicted and measured mean velocity profiles for developing flow in a two-dimensional duct, $Re_b = 1.0 \times 10^5$

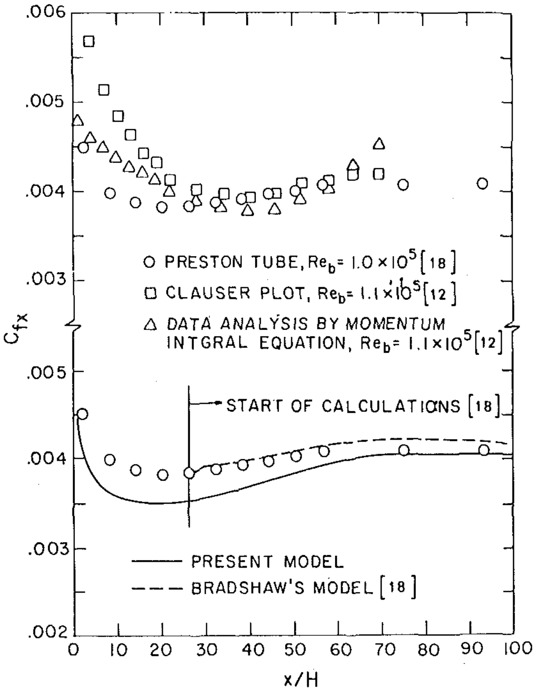

Fig. 8 Predicted and measured wall shear stress distributions for developing flow in a two-dimensional duct

butions predicted by the present model. Similar behavior can be seen in Figs. 5 and 6 where the experimental values tend to "lead" the predicted profiles. In order to determine the reason for these consistent differences, additional computations were performed by using a starting length. A value of x_s/H (= −3.8) was chosen to give the best agreement with Dean's results at $x/H = 2.2$ for δ and the u-velocity profile. Note that this has the effect of shifting the predicted distributions in Figs. 5 and 6 an increment $x/H = 3.8$ to the left, which leads to improved agreement between predicted and measured results.

Fig. 7 shows that velocity profiles computed from a matched velocity profile at $x/H = 2.2$ are in excellent agreement with their experimental counterparts at $x/H = 8.3$, 14.3, and 20.4. This behavior implies that the proposed mixing length model is not responsible for the differences observed in Fig. 7. A similar behavior was noted when the predictions were compared with the velocity profiles measured by Comte-Bellot at $Re_b = 2.4 \times 10^5$. These comparisons imply that the experimental data of Dean and Comte-Bellot are not representative of developing turbulent flow in a two-dimensional duct which starts from an essentially uniform flow at the inlet. Caution must be observed, therefore, when model predictions are compared with their experimental results.

In. Fig. 8, the streamwise variation of wall shear stress, as measured by Dean, is compared with values determined by Byrne, et al. [12] and predictions referred to the present model and Dean's predictions. The wall shear stress values referred to the data of Byrne, et al., were evaluated in two ways: (1) by means of a Clauser plot, and (2) by means of velocity profile integration via the momentum integral equation. Inasmuch as both methods are an indirect means of evaluating local wall shear stress, it is reasonable to presume that Dean's experimental results, which are based on a more direct method of measurement, are representative of actual behavior. This conclusion can be justified somewhat by noting that values of τ_w evaluated by means of a Clauser plot are apparently too high in the near entrance region ($x/H < 20$), whereas values of τ_w based on the momentum integral equation exhibit unacceptable tail-up behavior when $x/H > 60$. If Dean's results are adopted as a standard for comparison, then predictions referred to either the present model or the one proposed

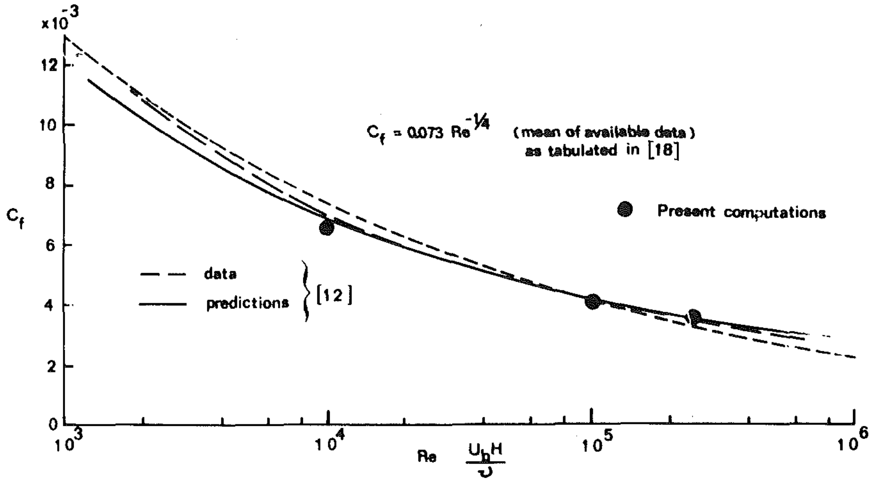

Fig. 9 Comparison of fully developed skin friction

by Bradshaw, et al. [23] are in good agreement with experimentally observed behavior. The apparently low values of τ_w predicted by the present model when $x/H < 50$ may not be directly comparable to Dean's experimental results, inasmuch as the predictions are based on assumed uniform flow at $x/H = 0$, whereas in accordance with earlier considerations, Dean's results are based on flow which has already developed to some extent at this location. Additional calculations with $\kappa = 0.45$ and $A^+ = 26$ yielded wall shear stress values which were in better overall agreement with the measured results, but computed velocity profiles in the near wall region did not agree well with the experimental profiles shown in Fig. 4.

Predicted fully-developed skin friction values are shown in Fig. 9 and compared to Dean's predictions and the mean of the presently available data as tabulated by Dean. Good agreement is seen to exist over a Reynolds number range from 10^4 to 2.4×10^5, which encompasses most of the experimental data.

Thermal Results

Temperature profiles were computed simultaneously with the velocity profiles for three cases: (1) constant wall temperature; (2) constant heat flux; (3) a constant heat flux with an unheated starting length. For these calculations, the turbulent Prandtl number was taken as 0.9. Fig. 10 compares the predicted Stanton number distributions with the data and integral method predictions of Byrne, et al. [12]. The predicted Stanton number had a minimum at $x/H = 24$, in comparison to Byrne's minimum value which occurred between $x/H = 20$ to 30, and a slight downstream increase for $x/H > 20$ which was comparable to Byrne's measured behavior. Fig. 11 shows the Reynold analogy factor. Since there is a fundamental relationship between the skin friction and the heat transfer through the analogy and since the integral prediction of the wall shear stress is high when compared to the data of Dean (Fig. 8), it is reasonable to assume that the Stanton number predictions will also be high. However, the prediction agrees well with the heat transfer data, which is much easier to obtain accurately than the wall shear stress. On the other hand, the numerical prediction is low for both wall shear stress and heat transfer. The shear stress discrepancy may be attributable to the difference between the experimental inlet profile and the assumed numerical profile, as noted in the previous section. A thermal computation was made with an unheated starting length to approximate Byrne's experimental conditions. Fig. 10 shows the improved agreement.

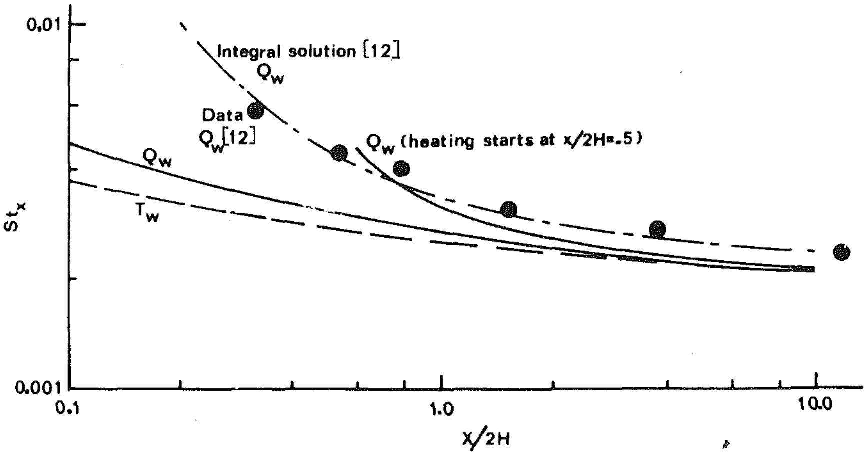

Fig. 10 Local heat transfer along the duct for constant heat flux (Q_W) or isothermal wall (T_W) conditions as compared to the results of Byrne, et al., for $Re_b = 1.0 \times 10^5$

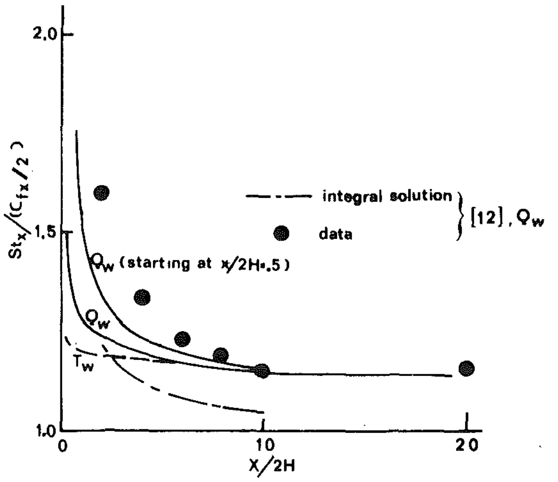

Fig. 11 Reynolds analogy factor for constant heat flux (Q_W) or isothermal wall (T_W) conditions as compared to the results of Byrne et al., for $Re_b = 1.0 \times 10^5$

Conclusions

Numerical computations based on a two-dimensional mixing length model are shown to be capable of predicting local flow behavior in the entrance region of a two-dimensional duct. There is a difference between measured and predicted results, but if a boundary layer starting length is used for the calculations, the agreement improves. The predicted heat transfer results are consistently low in the entrance region. This agreement is improved if an unheated starting length is matched to the experimental conditions.

Further improvements would depend upon the ability to match δ, δ^*, θ, C_f, μ_t and heat transfer conditions at the inlet to experimental data. However, the mixing length model will not accommodate such a detailed matching. Although more detailed matching is possible with the transport equation models, predictions based upon such models are costly and more difficult to perform.

Acknowledgment

This study was sponsored by the National Science Foundation under Grant GK-39956. A portion of the work was also performed while one of the authors (F. B. Gessner) was a Summer Faculty Fellow at NASA Ames.

References

1 Caretto, L. S., Curr, R. M., and Spalding, D. B., "Two Numerical Methods for Three Dimensional Boundary Layers," *Computer Methods in Applied Mechanics and Engineering,* Vol. 1, 1972, pp. 39–57.

2 Patankar, S. V., and Spalding, D. B., "A Calculational Procedure for Heat, Mass and Momentum Transfer on Three Dimensional Parabolic Flows," *International Journal of Heat and Mass Transfer,* Vol. 15, 1972, pp. 1787–1806.

3 Stephenson, P. L., "A Theoretical Study of Heat Transfer in Two Dimensional Turbulent Flows in a Circular Pipe and Between Parallel and Diverging Plates," *International Journal of Heat and Mass Transfer,* Vol. 19, 1976, pp. 413–423.

4 Pletcher, R. H., "On a Finite Difference Solution for The Constant Property Turbulent Boundary Layer," *AIAA Journal,* Vol. 7, 1969, pp. 305–311.

5 Pletcher, R. H., and Nelson, R. M., "An Explicit Scheme for The Calculation of Confined Turbulent Flows With Heat Transfer," *1974 Heat Transfer and Fluid Mechanics Institute,* Stanford University Press, 1974, pp. 154–170.

6 Jones, O. C., Jr., "An Improvement in The Calculation of Turbulent Friction in Rectangular Ducts," *Journal of Fluid Mechanics,* TRANS. ASME, Series I, Vol. 98, June 1976, pp. 173–181.

7 Po, J. K., "Developing Turbulent Flow in The Entrance Region of a Square Duct," MS thesis, Department of Mechanical Engineering, University of Washington, Feb. 1975.

8 Ahmed, S., "Turbulent Flow in Non-Circular Ducts," PhD thesis, Department of Mechanical Engineering, University of Waterloo, 1971; (see also *International Journal of Heat and Mass Transfer,* Vol. 14, 1971, pp. 365–375).

9 Brundrett, E., and Baines, W. D., "The Production and Diffusion of Vorticity in Duct Flow," *Journal of Fluid Mechanics,* Vol. 19, Part 3, 1964, pp. 375–394.

10 Sparrow, E. M., Lloyd, J. R., and Hixon, C. W., "Experiments on Turbulent Heat Transfer in an Asymmetrically Heated Rectangular Duct," JOURNAL OF HEAT TRANSFER, TRANS. ASME, Series C, Vol. 88, May 1966, pp. 170–175.

11 Sparrow, E. M., Novotny, J. L., McComas, S. T., and Eckert, E. R. G., "Heat Transfer for Turbulent Flow in Rectangular Ducts with Two Heated and Two Unheated Walls," *AIChE Journal,* Vol. 10, 1964, pp. 466–470.

12 Byrne, J., Hatton, A. P., and Marriott, P. G., "Turbulent Flow and Heat Transfer in The Entrance Region of a Parallel Wall Passage," *Proceedings of the Institution of Mechanical Engineers,* Vol. 184, 1969–70, pp. 697–712.

13 Roache, P. J., *Computational Fluid Dynamics,* Hermosa Publishers, Albuquerque, N. M., 1972.

14 Richtmyer, R. I., and Morton, K. W., *Difference Methods for Initial Value Problems,* Interscience Publishers, New York, 1967.

15 Gessner, F. B., and Emery, A. F., "A Reynolds Stress Model for Turbulent Corner Flows, Part I, Development of The Model," *Journal of Fluids Engineering,* TRANS. ASME, Series I, Vol. 98, June 1976, pp. 261–268.

16 Gessner, F. B., and Emery, A. F., "A Constitutive Model for Developing Turbulent Flow in a Rectangular Duct," (submitted for publication to the *Journal of Fluids Engineering*).

17 Buleev, N. I., "Theoretical Model of The Mechanism of Turbulent Exchange in Fluid Flows," AERE Translation 957, *Atomic Energy Research Establishment,* Harwell, England, 1963.

18 Dean, R. B., "An Investigation of Shear Layer Interaction in Ducts and Diffusers," PhD thesis, University of London, Feb. 1974.

19 Comte-Bellot, G., "Turbulent Flow Between Two Parallel Walls," PhD thesis, University of Grenoble, France, 1963; (also available as ARC 31 609).

20 Acharya, M., and Reynolds, W. C., "Measurements and Predictions of a Fully-Developed Turbulent Channel Flow With Imposed Controlled Oscillations," Technical Report No. TF-8, Thermosciences Division, Department of Mechanical Engineering, Stanford, May 1975.

21 Hussain, A. K. M. F., and Reynolds, W. C., "Measurements in Fully-Developed Turbulent Channel Flow," *Journal of Fluids Engineering,* TRANS. ASME, Series I, Vol. 97, 1975, pp. 568–580.

22 Klebanoff, P. S., "Characteristics of Turbulence in a Boundary Layer For Zero Pressure Gradient," NACA TN 3178, 1954.

23 Bradshaw, P., Dean, R. B., and McEligot, D. M., "Calculations of Interacting Turbulent Shear Layers: Duct Flow," *Journal of Fluids Engineering,* TRANS. ASME, Series I, Vol. 95, 1973, pp. 214–220.

K. N. Astill

Professor,
Department of Mechanical Engineering,
Medford, Mass.
Mem. ASME

An Analysis of Laminar Forced Convection Between Concentric Spheres

A numerical solution for predicting the behavior of laminar flow and heat transfer between concentric spheres is developed. Axial symmetry is assumed. The Navier-Stokes equations and energy equation are simplified to parabolic form and solved using finite-difference methods. Hydrodynamic and energy equations are uncoupled, which allows the hydrodynamic problem to be solved independently of the heat-transfer problem. Velocity and temperature are calculated in terms of the two spatial coordinates. Solutions depend on radius ratio of the concentric spheres, Reynolds number of the flow, Prandtl number, initial conditions of temperature and velocity, temperature distribution along the spherical surfaces, and azimuthal position of the start of the flow. The effect on flow and heat transfer of these variables, except surface temperature distribution, is evaluated. While the computer solution is not restricted to isothermal spheres, this is the only case treated. Velocity profiles, pressure distribution, flow losses, and heat-transfer coefficients are determined for a variety of situations. Local and average Nusselt numbers are computed, and a correlation is developed for mean Nusselt number on the inner surface as a function of Reynolds number, Prandtl number, and radius ratio. Flow separation is predicted by the analysis. Separation is a function of Reynolds number, radius ratio, and azimuthal location of the initial state. Separation was observed at the outer surface as well as from the inner surface under some conditions. In cases where separation occurred, the solution was valid only to the point of separation.

Introduction

Geometries incorporating concentric spheres frequently arise in systems requiring heat transfer. One example is the gimbals used in a gyroscopic guidance system. For the precise temperature control requirements, heat must be transferred from inner gimbals, primarily by free or forced convection, through air between the concentric spheres. A simple model for the forced-convection case is to introduce cooling air at one pole of the outer sphere, blow the air through the annular space between the spheres, and remove the air at the opposite pole. A sketch of this configuration is shown in Fig. 1. Heat is transferred from the inner sphere to the air and from the air to the outer sphere.

Cobble [1][1] treated the problem by assuming a tangential velocity distribution of the form $v_\theta = C(r \sin \theta)^{-1}$ and then calculating heat transfer from the energy equation. Bird, Stewart, and Lightfoot [2] solved for velocity profiles in creeping flow, neglecting inertial terms. Ward [3] demonstrated that the velocity profile cannot be predicted by assuming axial symmetry and a one-component flow. Unless the radial component of velocity is included, the solution leads to a contradiction. Heat-transfer coefficients between the inner surface and the air were measured for forced convection by Rundell, Ward, and Cox [4]. Correlations were obtained for two sets of spheres: one with an outer sphere having an inner diameter of 33.7 cm with radius ratios (RO) of 1.2 and 1.1, the second with an outer sphere having an inner diameter of 21.6 cm and radius ratios of 1.2 and 1.1. The correlation had the form

$$\mathrm{Nu} = C[\mathrm{Re}^{0.2}RO]^n \mathrm{Pr}^{1/3}\mathrm{Re}\, \pi(r_0{}^2 - r_i{}^2)$$

where the values of C and n were established as

$$C = 39.7 \text{ ft}^{-2} \quad n = -2.39 \text{ (small spheres)}$$

$$C = 106.2 \text{ ft}^{-2} \quad n = -3.69 \text{ (large spheres)}$$

This study apparently was for Reynolds numbers between 400 and 2000 for the large spheres. Flow visualization studies with air and

---

[1] Numbers in brackets designate References at end of paper.

Contributed by the Heat Transfer Division for publication in the JOURNAL OF HEAT TRANSFER. Manuscript received by the Heat Transfer Division April 12, 1976.

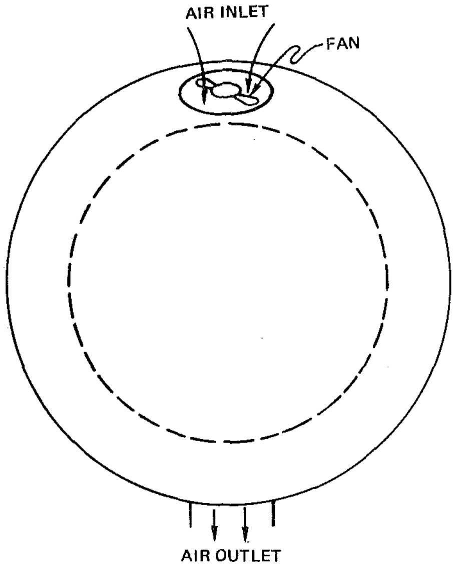

Fig. 1 Concentric spheres, flow model

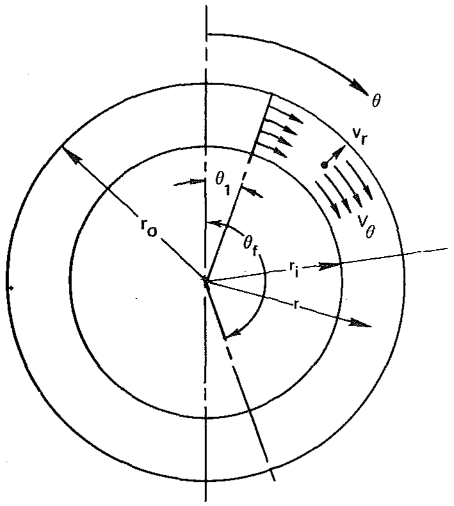

Fig. 2 Spherical coordinate system

water were included. Flow separated from the inner wall for all flows examined. Separation occurred at an angular location of $\theta = 45$ deg for both air and water.

Bozeman and Dalton [5] presented photographs of separation of flow between concentric spheres using water with fluorescein dye. Jetting of the fluid against the sphere at the inlet contributed to the separation and vortex formation. It was pointed out that local heat-transfer coefficients would be high in the region upstream of the separation point. Reynolds numbers ranged from 208 to 4020.

A program was initiated at the Charles Stark Draper Laboratory to study heat transfer between concentric spheres, both analytically and experimentally in forced and free convection. This paper presents a numerical analysis of laminar forced convection.

Formulation and Solution of Problem

Analytical Model. The model is based on the configuration of Fig. 1. Air enters at a pole and flows along meridians to the opposite pole, where it is exhausted; thus flow is axisymmetric. It is necessary to describe the temperature distribution on the spherical surfaces as a function of the angle θ (see Fig. 2) as well as the initial conditions of velocity, pressure, and temperature at θ_1. As shown in the sectional view in Fig. 2, flow is from the entrance conditions at θ_1 to the exit conditions at θ_f. It is not possible to treat the flow at $\theta = 0$ or $\theta = \pi$, as singularities arise. The flow is steady, incompressible, and laminar and is described by the Navier-Stokes equations, continuity equations, and the energy equation in spherical coordinates with axial symmetry.

To transform these equations into dimensionless form, it was first necessary to introduce a reference velocity, $\bar{V}$, defined as the mean velocity at the equator, $\theta = 90$ deg.

$$\bar{V} = \frac{m}{\rho\pi(r_0^2 - r_i^2)} \tag{1}$$

The following dimensionless variables were formed:

$$V = \frac{v_r}{\bar{V}};\ W = \frac{v_\theta}{\bar{V}};\ P = \frac{p - p_0}{\rho\bar{V}^2}$$

$$R = \frac{r}{r_i} \text{ and } T = \frac{t - t_o}{t_i - t_o} \tag{2}$$

The reference pressure p_0 will be examined later. As a result of these definitions, the radii of the inner and outer spheres are 1 and RO, respectively, while at $\theta = \theta_1$ the dimensionless temperatures of the inner and outer surfaces are 1 and 0, respectively.

These dimensionless variables were inserted into the Navier-Stokes continuity and energy equations written for steady incompressible flow and axial symmetry.

Nomenclature

C = a constant
c_p = specific heat at constant pressure
h = heat-transfer coefficient
k = thermal conductivity
L = loss factor
m = mass flow rate
n = constant exponent
NR = number of radial nodes
$NTHET$ = number of nodes in angular direction
Nu = Nusselt number, $\frac{h(r_0 - r_i)}{k}$
P = dimensionless pressure
p = pressure
p_0 = reference pressure
Pr = Prandtl number, $\frac{c_p\mu}{k}$
Re = Reynolds number, $\frac{\bar{V}(r_0 - r_i)}{\nu}$
R - dimensionless radius
RO = radius ratio, r_0/r_i
r = radius
T = dimensionless temperature
t = temperature
U = overall heat-transfer coefficient
V = dimensionless radial velocity
$\bar{V}$ = mean velocity at equator
v_r = dimensional radial velocity
v_θ = dimensional tangential velocity
W = dimensionless tangential velocity
δ = boundary-layer thickness
θ = angular coordinate
θ_1 = initial angular location
μ = viscosity
ν = kinematic viscosity
ρ = density

Subscripts

i = inner sphere; also used with j to designate grid location in difference equations
m = mean value
o = outer sphere
θ = local value at θ
1 = initial value

Using the traditional Prandtl boundary-layer assumptions [6], an order-of-magnitude analysis was made, dropping terms of order δ, where δ is a dimensionless boundary-layer thickness. The four governing equations were simplified to the following forms:

$$\frac{W^2}{R} = \frac{\partial P}{\partial R} \tag{3}$$

$$V\frac{\partial W}{\partial R} + \frac{W}{R}\frac{\partial W}{\partial \theta} = -\frac{1}{R}\frac{\partial P}{\partial \theta} + \frac{(RO-1)}{\text{Re}}\left[\frac{\partial^2 W}{\partial R^2} + \frac{2}{R}\frac{\partial W}{\partial R}\right] \tag{4}$$

$$\frac{\partial V}{\partial R} + 2\frac{V}{R} + \frac{1\,\partial W}{R\cdot\partial\theta} + \cot\theta\,\frac{W}{R} = 0 \tag{5}$$

$$V\frac{\partial T}{\partial R} + \frac{W}{R}\frac{\partial T}{\partial \theta} = \frac{RO-1}{\text{RePr}}\left[\frac{\partial^2 T}{\partial R^2} + \frac{2}{R}\frac{\partial T}{\partial R}\right] \tag{6}$$

These equations require the restriction that

$$\frac{RO-1}{\text{Re}} \approx O[\delta^2] \tag{7}$$

and $\text{Pr} \geq O$ [1].

The transformation of the equations by the order-of-magnitude analysis has reduced the system from elliptic form to a set of parabolic partial differential equations in the unknowns W, V, P, and T. Solution requires initial conditions at θ_1 for $W(R)$, $V(R)$, and $T(R)$ and boundary conditions at $R = 1$ and $R = RO$ for $W(\theta)$, $V(\theta)$, and $T(\theta)$. Notice that for a given set of W, the radial gradient of pressure is uniquely determined by equation (3).

Initial and Boundary Conditions. While any prescribed set of boundary or initial conditions does not seriously complicate the problem, the present study was confined to simple cases. Flat entrance profiles of velocity and temperature were assumed. Initial radial pressure distribution was calculated from equation (3). Values of pressure were obtained by setting $P(\theta_1, 1) = 0$. This guarantees a stable flow condition at the start, which may be difficult to obtain in a real situation. No-slip conditions governed the velocity boundary conditions at $R = 1$ and $R = RO$. Isothermal walls were assumed to establish the temperature conditions $T(\theta, 1) = 1$ and $T(\theta, RO) = 0$.

Numerical Solution of Governing Equations. Equations (3)–(6), along with appropriate initial and boundary conditions, comprise a complete set of parabolic partial differential equations in the unknowns $W(R, \theta)$, $V(R, \theta)$, $P(R, \theta)$, and $T(R, \theta)$. They are nonlinear but are tractable using finite-difference techniques. Finite differences must be selected in a form to make the resulting algebraic equations linear in the new values of the unknowns at $\theta + \Delta\theta$. The solution is produced by marching forward in the θ direction starting with the initial conditions at θ_1.

With values known at θ_j, the equations are solved for the new value at $\theta + \Delta\theta$, or θ_{j+1}. Variables with $j + 1$ subscripts are unknown in the finite-difference equations. A complete description of the difference forms is given elsewhere [10].

Concentrating first on the hydrodynamic problem, the finite-difference representations of equations (3), (4), and (5) can be arranged with the unknowns ($j + 1$ values) on the left-hand side.

$$P_{i-1,j+1} - P_{i,j+1} + \left(\frac{W_{i,j} + W_{i-1,j}}{2}\right)\frac{\Delta R}{R_i - \frac{\Delta R}{2}}(W_{i,j+1} + W_{i-1,j+1}) = P_{i,j} - P_{i-1,j} \tag{8}$$

$$\begin{aligned} P_{i,j+1} - W_{i-1,j+1}&\left[\frac{V_{i,j}}{2} + \left(\frac{RO-1}{\text{Re}}\right)\left(\frac{1}{\Delta R} - \frac{1}{R_i}\right)\right]\frac{R_i\Delta\theta}{R} \\ &+ W_{i,j+1}\left[\frac{W_{i,j}}{R_i}\frac{\Delta R}{\Delta\theta} + \frac{2}{\Delta R}\left(\frac{RO-1}{\text{Re}}\right)\right]\frac{R_1\Delta\theta}{\Delta R} \\ + W_{i+1,j+1}&\left[\frac{V_{i,j}}{2} - \left(\frac{RO-1}{\text{Re}}\right)\left(\frac{1}{\Delta R} + \frac{1}{R_i}\right)\right]\frac{R_i\Delta\theta}{\Delta R} = P_{i,j} + (W_{i,j})^2 \end{aligned} \tag{9}$$

$$\begin{aligned} V_{i,j+1} = &\left(\frac{R_i - \frac{3}{2}\Delta R}{R_i + \frac{1}{2}\Delta R}\right)V_{i-1,j+1} - (W_{i,j+1} + W_{i-1,j+1}) \\ &\times\left[\left(\frac{1 + \Delta\theta\cot\theta_{j+1}}{R_i + \frac{1}{2}\Delta R}\right)\right]\frac{\Delta R}{2\Delta\theta} + \left[W_{i,j} + W_{i-1,j}\left(\frac{1}{R_i + \frac{1}{2}R}\right)\left(\frac{\Delta R}{2\Delta\theta}\right)\right] \end{aligned}$$

The radial nodes are numbered beginning with 1 at $R = 1$ and ending at NR at $R = RO$.

Solution Procedure. Equations (8) and (9) form a set of equations in W and P. However, it is only possible to write equation (8) at $i = 2, 3, 4, \ldots, NR$ and equation (9) at $i = 2, 3, 4, \ldots, NR - 1$. Consequently there are only $2NR - 3$ equations in $2NR - 2$ unknowns ($W_{i,j+1}$ and $P_{i,j+1}$). Following the procedure first suggested by Bodia and Osterle [7] and extended by Coney and El-Shaarawi [8], *the additional equation can be formed from the integral form of the* continuity equation. For a given angular location θ, the volume flow can be written in dimensionless form as

$$\int_1^{RO} WRdR = \frac{1}{2\sin\theta_j}(RO^2 - 1) \tag{11}$$

Integration across the gap with Simpson's rule converts equation (11) to the algebraic expression

$$\begin{aligned} \frac{\Delta R}{3}[R_1W_1 + 4R_2W_2 + 2R_3W_3 + 4R_4W_4 + \ldots + 2R_{NR-2}W_{NR-2} \\ + 4R_{NR-1}W_{NR-1} + R_{NR}W_{NR}] = \frac{1}{2\sin\theta_j}(RO^2 - 1) \end{aligned} \tag{12}$$

This imposes the restriction that NR must be odd. There is some simplification because $W_1 = W_{NR} = 0$. There are now a total of $2NR - 2$ equations in $2NR - 2$ unknowns. The system formed from equations (8), (9), and (12) was solved using a Gauss-Jordan reduction procedure for $P_{i,j+1}$ and $W_{i,j+1}$. Having determined the values of $W_{i,j+1}$ it is possible to calculate the $V_{i,j+1}$ with equation (10) starting at the inner surface $V_{i-1,j+1} = 0$ and working toward the outer surface.

Boundary conditions are built into the equations, as indicated above. For the solution executed, $V_{i,j} = V_{NR,j} = W_{i,j} = W_{NR,j} = 0$. The initial conditions were based on a uniform velocity profile for v_θ, with $\overline{V} = 1$. For conservation of mass,

$$\begin{aligned} W_{i,1} &= \frac{1}{\sin\theta_1} \\ V_{i,1} &= 0 \end{aligned} \tag{13}$$

Initial pressures were found by calculating P_i with equation (3) written in finite-difference form. Calculations began at the inner surface, $i = 2$, setting $P_1 = 0$, and proceeding outward to $i = NR$.

Temperature Calculation. Having found the velocity and pressure values at $j + 1$, temperatures were calculated from equation (6) in finite-difference form. Equations can be written for radial mesh points $i = 2, 3, 4, \ldots, NR - 1$ providing $NR - 2$ equations for the $NR - 2$ temperatures at the next step in theta. Boundary conditions $T_{i,j} = 1$ and $T_{i,NR} = 0$ are incorporated directly into the equations. Initial values of $T_{2,1}, T_{3,1}, \ldots, T_{NR-1,1}$ must be supplied to the program. Calculations were made for uniform temperature profiles, either

$$T_{i,1} = 0 \quad \text{or} \quad T_{i,1} = 0.5$$

A routine was used for solving systems of linear equations with tridiagonal coefficient matrices as described elsewhere [9].

Heat-Transfer Parameters. The local heat-transfer coefficient from the inner surface $h_{i,\theta}$ is defined by the expression

$$dq_{i,\theta} = h_{i,\theta}(t_i - t_m)r_i^2\,d\theta\,2\pi\sin\theta \tag{14}$$

Expressing the heat flux $dq_{i,\theta}$ in terms of the wall temperature gradient at the inner surface, the heat-transfer coefficient can be determined. In dimensionless form, the Nusselt number at the inner surface is

$$\mathrm{Nu}_{i\theta} = \frac{-\left(\frac{\partial T}{\partial R}\right)_{R=1}(RO-1)}{1-T_m} \tag{15}$$

At the outer surface, the Nusselt number is

$$\mathrm{Nu}_{o,\theta} = -\frac{-\left(\frac{\partial T}{\partial R}\right)_{R=1}(RO-1)}{T_m} \tag{16}$$

To evaluate the Nusselt number, it is necessary to evaluate the temperature gradient and the mean temperature from the numerical results. The derivative was obtained by fitting a second-degree polynomial to the temperature at the wall and differentiating it. As a result, the derivatives were dependent on the wall temperature and the first two temperatures in the fluid.

The mean or mixing-cup temperature of the fluid was defined in the usual way, which in dimensionless form is

$$T_m = \frac{\int_1^{RO} TR\,dR}{\int_1^{RO} WR\,dR} \tag{17}$$

Integration was done numerically using Simpson's rule.

With local Nusselt numbers computed, it is useful to know the mean Nusselt number from the entrance, θ_1. This is the single Nusselt number that can be applied from the entrance to transfer the same heat as the integral of local values. Thus for the inner surface

$$\mathrm{Nu}_{i,m} = \frac{\int_{\theta_1}^{\theta} \mathrm{Nu}_{i,\theta} d\theta}{(\theta-\theta_1)} \tag{18}$$

A similar expression obtains at the outer surface. Integration was done numerically using Simpson's rule. This requires that mean values of the Nusselt number be computed, at best, at every other step in the calculation.

Fluid Flow Losses. As the flow progresses from the entrance toward the equator, the flow passage acts as a diffuser. After the equator, the area diminishes as the fluid approaches the other pole. Consequently the flow never reaches a developed state in the usual sense. There are a number of factors that affect pressure in the flow. Along the meridian, pressure changes because of (1) the diffusion effect, (2) wall frictional effects, and (3) the changing shape of the velocity profile. As there is curvature of the flow, the pressure is not uniform in the radial direction. As a result, it is not possible to express losses in terms of pressure drop or friction factors. Instead, the loss is expressed as the defect in total energy integrated across the gap. Putting the result in terms of the dimensionless variables, the loss from the initial condition to some value of θ is

$$L = 1 - \frac{\sin\theta \int_1^{RO} W\left(P + \frac{(W+V)^2}{2}\right) RdR}{\sin\theta_1 \left|\frac{W_1{}^2(RO^2-1)}{4} + \int_1^{\mathrm{RO}} \mathrm{P_1RdR}\right|} \tag{19}$$

Integration was done in the computation using Simpson's rule in both numerator and denominator.

Computer Solution. The finite-difference equations were solved by implicit techniques to reduce stability problems. It was determined that the solution was stable when $\Delta\theta \leq \Delta R$. The solution was unstable when this condition was not met.

Supplied to the program were radius ratio RO, starting and terminal theta θ_1 and θ_f, number of steps *NR* and *NTHET*, and Reynolds and Prandtl numbers. To compute for nonuniform inlet velocities or wall temperatures would require minor program modifications.

The program periodically printed velocity and temperature distributions as the calculation progressed. Results were given at specific values of θ for radial positions and corresponding values of W, V, P, and T. At the completion of the calculations, $\theta = \theta_f$, Nusselt numbers and loss factors were computed.

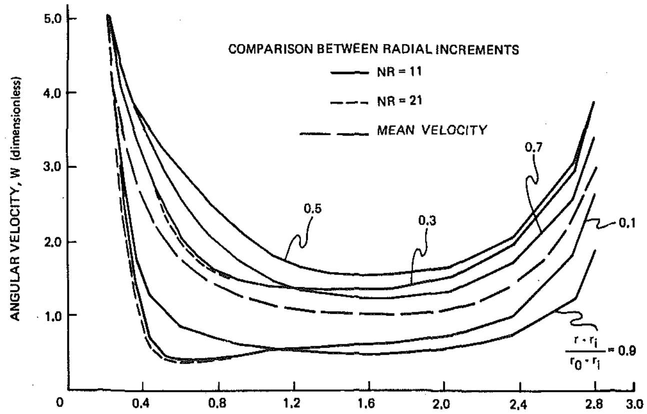

Fig. 3 Tangential velocity development, *RO* = 1.36

Discussion of Results

While the computer program is primarily for evaluation of designs, it is useful to make observations from specific sets of results. Several areas merit special attention, including the development of velocity and temperature profiles, flow separation, heat transfer, and limitations of the analysis.

Velocity Profiles. As the hydrodynamic equations are not coupled to the energy equation, it is convenient to discuss these results first.

To determine the effect the mesh size ΔR had on the solutions, runs were made with $NR = 21$ and $NR = 11$. These results are compared in Fig. 3 for a Reynolds number of 20 at a radius ratio of 1.36. Velocity is graphed at several radial positions as a function of angular position. There is a small difference between the results from $\theta = \theta_1$ to a value of $\theta \approx 0.9$. After that point the difference is not discernible. Calculations were made with $NR = 11$.

Fig. 3 also illustrates the effect of the change in cross section on the tangential velocity. The velocity decreases as the flow approaches the equator ($\theta = 1.57$), where the cross section normal to the flow is a maximum. At that point the mean velocity (shown as a dash line in the figure) reaches unity. From that point on the flow accelerates.

In addition to the built-in assumptions, such as the initial velocity and pressure distributions, it is possible to vary the results by changing radius ratio, Reynolds number, or starting point θ_1. Examples of the effect these variables have on velocity profiles are given elsewhere [10].

In Fig. 4 velocity profiles are plotted along the meridian for a radius ratio of 1.36 and a Reynolds number of 20. The spherical boundaries have been shown as parallel straight lines. Flow progresses from the initial state $\theta_1 = 0.2$ to $\theta_f = 2.8$ without separation. As the flow progresses the boundary layer thickens, and the profiles flatten as the equator is approached. The flow then accelerates as it goes through the other hemisphere. Note the appearance of an inflection in the profile near the inner wall in Fig. 4. Increasing the Reynolds number to 200 (Fig. 5) causes these inflections to grow into regions of reverse flow. When separation occurs (negative W) the computer results become meaningless, as the flow downstream is then affecting a previously calculated flow. This could only be examined by solving the equations in elliptic form.

The choice of the starting point of the calculation, θ_1, is important. In addition to altering profiles and pressure distribution, it is possible for flows that separate when started at $\theta_1 = 0.2$ to flow unseparated when started at larger angles.

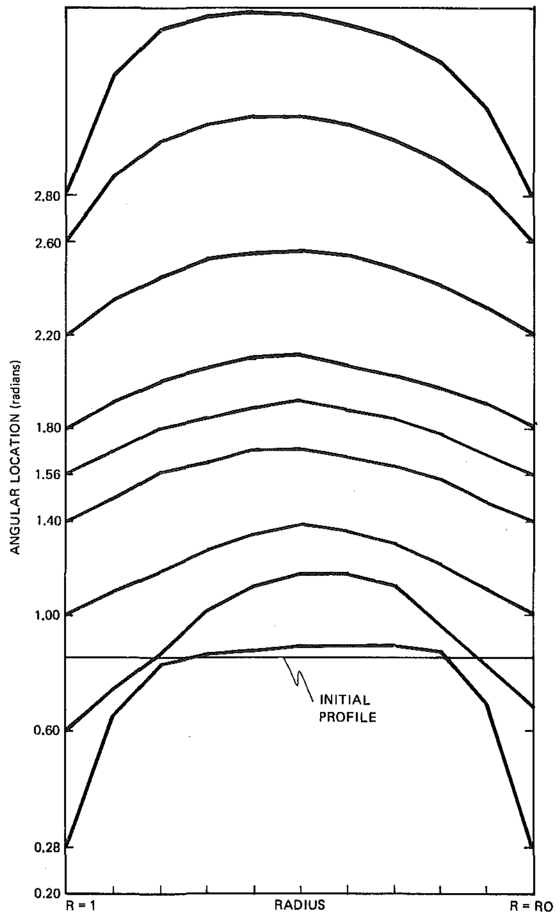

Fig. 4 Tangential velocity profiles along a meridian, $RO = 1.36$, $Re = 20$, and $\theta_1 = 0.2$

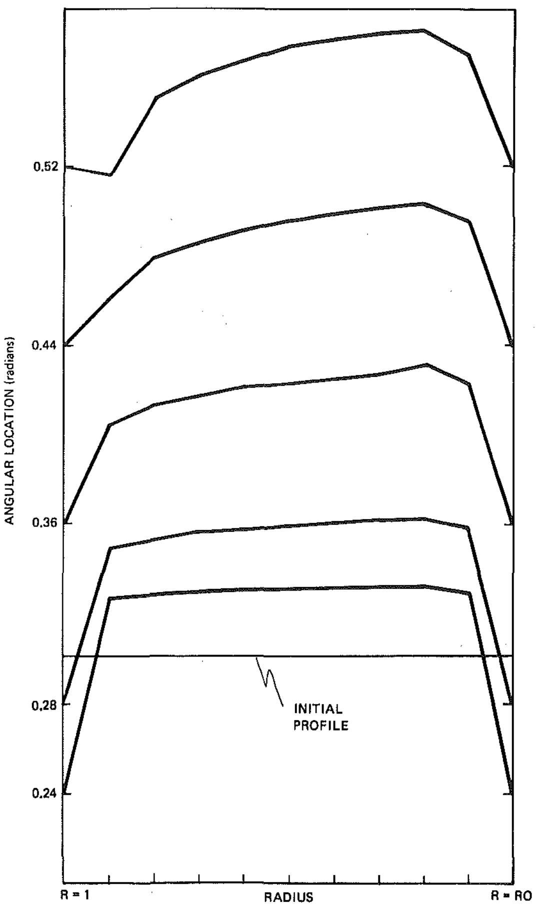

Fig. 5 Tangential velocity profiles along a meridian (showing flow separation at inner surface), $RO = 1.36$, $Re = 200$, and $\theta_1 = 0.2$

Radial Velocity. While the flow does not achieve a state that could be described as fully developed, it does reach a near-concentric flow pattern in that the radial component goes to zero. This is illustrated in Fig. 6, drawn from $RO = 1.36$ and Re = 20. In the early part of the flow there is a strong flow away from the inner sphere. This promotes the possibility of separation from the inner surface. The radial component has nearly disappeared at $\theta = 0.6$ radian and essentially is zero beyond that. This is typical of the cases studied.

In the case where the flow was started near the equator, the area changes are less severe, and the radial component behaves more nearly like a parallel-flow situation.

Pressure Distribution. Initial pressure distribution is calculated from equation (3) to provide a stable flow. No attempt was made to predict flow behavior for nonstable pressure distributions. As the flow progresses two factors affect the pressure. There is a tendency for the pressure to change because of the change in area, as well as a tendency for the pressure to fall because of wall shear.

The behavior of the pressure on the spheres along the flow path is shown in Fig. 7. Pressure on the outer sphere is always larger than that on the inner sphere. A comparison for the two cases illustrated at Re = 20 shows that the viscous effects dominate the flow in the narrow gap, causing the dimensionless pressure to go negative in the case shown. An increase in Reynolds number for the case $RO = 1.1$ causes the pressure rise from diffusion to overcome the viscous effects and the pressure to remain positive throughout the flow after going negative briefly on the inner sphere. These are representative of other cases computed.

If the pressure terms become negative and dominate the numerator of equation (19), the loss L can exceed unity. This means that the initial state is incorrect $[P(1, \theta_1) = 0]$. An additive constant of pressure would correct this. But the loss factor times the net energy loss would not be altered by this change. The net energy loss, which is the denominator of equation (19), is a function of radius ratio and θ only.

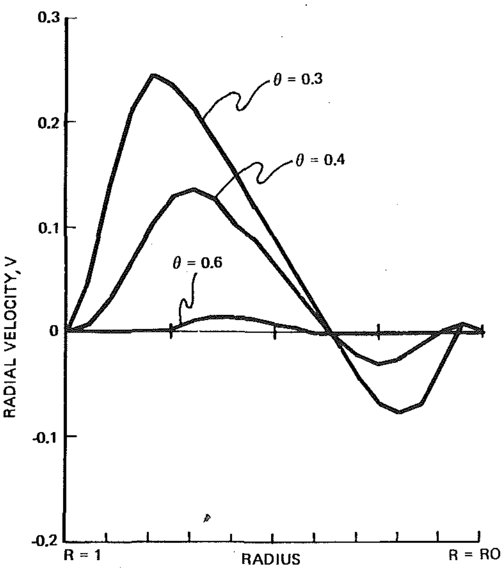

Fig. 6 Radial velocity, $RO = 1.36$, $Re = 20$, $\theta_1 = 0.2$

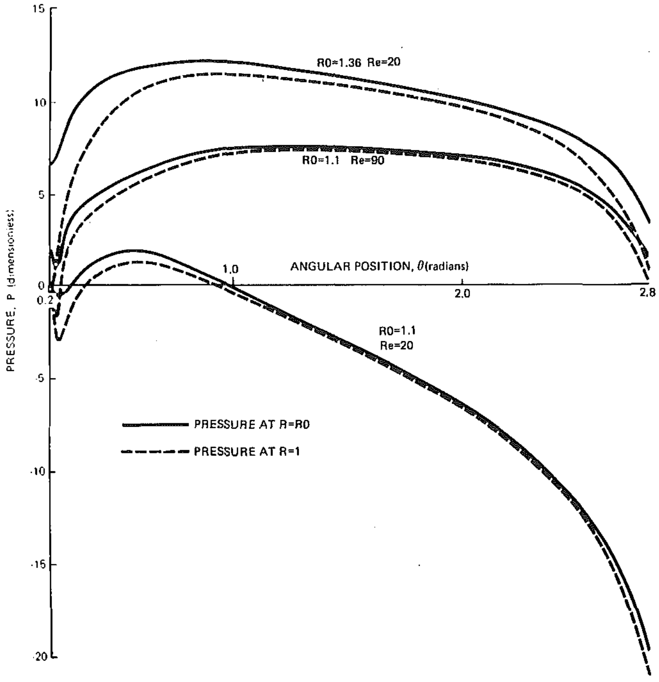

Fig. 7 Surface pressure along the spheres for several cases

The effect of Reynolds number on loss is shown in Fig. 8 for cases that did not separate at a radius of 1.1.

Separation. As noted earlier, the flow separates from the inner or outer wall for a particular geometry when the Reynolds number reaches a large enough value. A survey was made to map the separation as a function of Reynolds number and radius ratio. A test was made on *W* in the program to determine when it became negative. A negative in *W* for $NR = 11$ would obviously occur later in the calculation than it would for $NR = 21$. All results were compared on the basis of $NR = 11$; so in that respect they are consistent. Several computations were made at radius ratios of 1.1 and 1.36 to determine the angle at which separation occurred. These are shown in the graph of Fig. 9. Notice that the point of separation becomes independent of Reynolds number for large Reynolds numbers. This is consistent with the visual studies of Rundell, Ward, and Cox [4]. The radius ratio of 1.1 was surveyed to establish the minimum Reynolds numbers for which separation occurred. It was determined as 98. Below that value the flow did not separate.

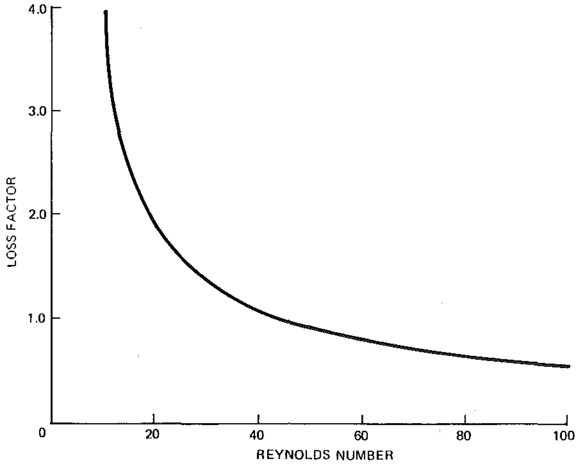

Fig. 8 Total loss factor as a function of Reynolds number for $RO = 1.1$

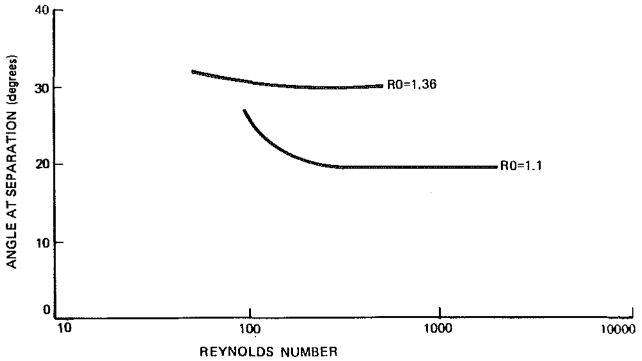

Fig. 9 Separation angle as a function of Reynolds number for two radius ratios

A series of computations was made at a Reynolds number of 200 for several radius ratios. The results are shown in Fig. 10. Below *RO* = 1.15 separation occurred at the outer surface. Above 1.15 it occurred at the inner surface. No separation appeared at a radius ratio of 1.15. The velocity along the meridian for this case was close to separation along the inner surface at $\theta = 0.92$ radians, but the flow began to accelerate near the wall at that point. That is not to say that a calculation with a smaller mesh would not have shown separation. One would expect separation from the inner surface due to centrifugal effects and would guess that larger radius ratios are more apt to have separated flows. It is not clear why there is a separation at the outer surface for smaller radius ratios. A computation at a radius ratio of 1.03 and a Reynolds number of 200 did not show flow separation.

Separation occurs during the diffusion process. Treating the flow area as a conical diffuser, it is evident that the diffusion angle is more severe for larger radius ratios. Furthermore, the diffusion angle decreases as the equator is approached.

Limitation of the Analysis. There are two limitations in the analysis. Flow separation imposes an upper limit on the Reynolds number. The lower limit is a result of the order-of-magnitude analysis, which requires

$$\frac{RO - 1}{\mathrm{Re}} < \delta^2$$

from equation (7). Assuming a maximum value of the boundary layer δ to be one-half the gap, $(RO - 1)/2$, minima can be found for Re from the expression $\mathrm{Re} = 4/(RO - 1)$. Minimum Reynolds numbers range from 11 at $RO = 1.36$ to 133 at $RO = 1.03$. With room air as a fluid, these correspond to mean velocities $\overline{V}$ of 0.02 m/s and 2.9 m/s, respectively. Smaller Reynolds numbers are valid in the early part of the flow.

Temperature Profiles. In addition to the variables that affect

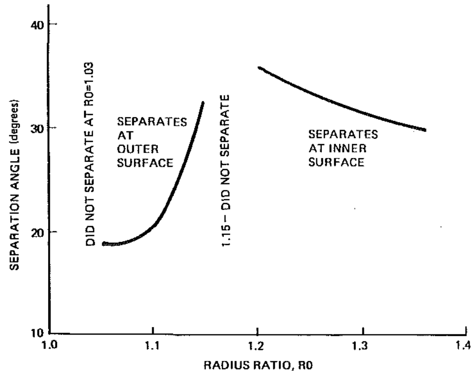

Fig. 10 Effect of radius ratio on separation at Re = 200

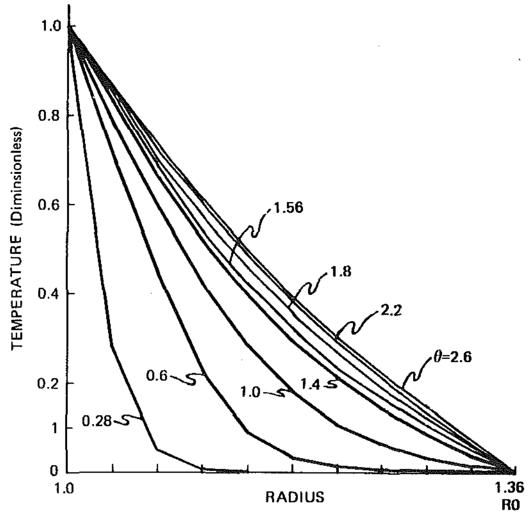

Fig. 11 Temperature profiles between concentric spheres, $RO = 1.36$, $Re = 20$, $\theta_1 = 0.2$, $Pr = 0.7$, $T_1 = 0.0$

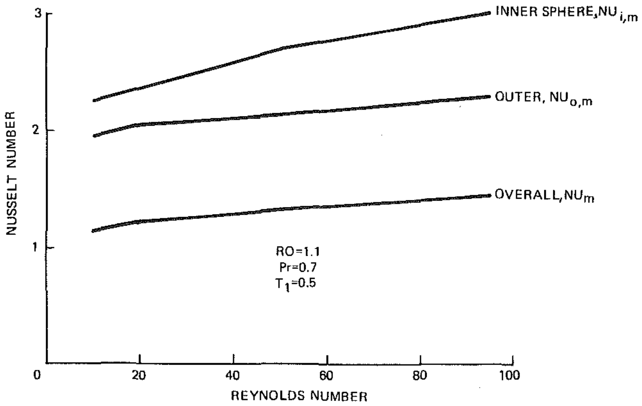

Fig. 13 Effect of Reynolds number of heat transfer

the velocity profiles, temperature is also dependent on the Prandtl number and the inlet temperature distribution. Profiles are shown for a uniform inlet temperature of $T_i = 0$ in Fig. 11. Profiles are shown developing along the meridian. Prandtl number is 0.7. Profiles for other Prandtl numbers and other initial states are given elsewhere [10].

In the case where the initial temperature was set at 0.5, energy was transferred from the inner surface to the outer surface. Very little energy was stored in the coolant, as indicated by the small change in mean temperature.

Heat Transfer. At each point in the calculation several Nusselt numbers were computed. These were local and mean values on the inner and outer surfaces, as described in equations (15), (16), and (18).

A comparison of mean Nusselt numbers on the inner surface is shown in Fig. 12. All results are for an initial coolant temperature of 0.5 and a Prandtl number of 0.7. It is apparent that the Nusselt number increases with an increase in Reynolds number and is larger for large gap than for small gap.

The effect of Reynolds number on the mean Nusselt number can be seen in the graph in Fig. 13. Inner, outer, and overall Nusselt numbers are plotted against Reynolds number for the spheres having a radius ratio of 1.1. These were calculated for an initial temperature of 0.5 and a fluid having a Prandtl number of 0.7. The overall Nusselt number is based on the overall heat-transfer coefficients U between the inner and outer spheres.

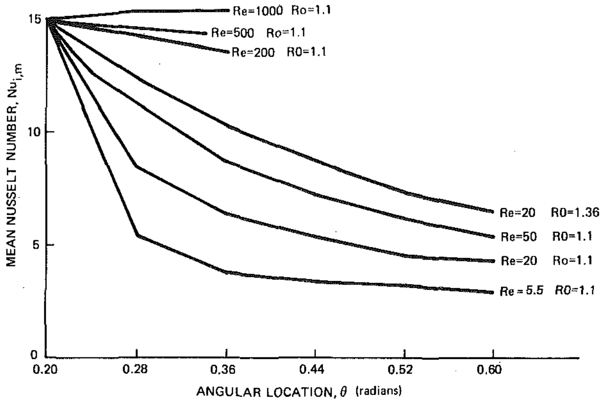

Fig. 12 Mean Nusselt number variation along the inner sphere, $Pr = 0.7$, $T_1 = 0.5$

$$\frac{1}{U} = \frac{1}{h_i} + \frac{1}{h_o(RO)^2} \tag{20}$$

For flow at low Reynolds numbers it is possible that free convection can become significant. Calculations were made by extrapolating experimental correlations for free convection between concentric spheres. For spheres of 25 cm diameter and radius ratio 1.36, with room temperature air in the gap, a temperature difference between spheres of about 4 C is required to produce a Nusselt number of 2. At the minimum Reynolds number for this case, approximately 11, the mean Nusselt number on the inner sphere was 2.9. The question of which mode of heat transfer (including gaseous conduction) dominates as the gap is reduced is currently being investigated by the author.

Initial Conditions. Assigned initial conditions of velocity, temperature, and starting angle affect the heat-transfer results and separation conditions. Normally the initial conditions will be chosen to model experimentally determined properties.

A set of calculations was made using initial conditions determined experimentally. With an initial angle of 0.35 radians the gap temperature was uniform, with $T_1 = 0$, and the tangential velocity profile was nearly triangular, being large near the inner surface. Comparing these results to $\theta_1 = 0.2$ and $T_1 = 0.5$, flow separation was detained due to the larger angle at the start. Using uniform profiles, Nusselt numbers on the inner surface were about 20 percent larger for $T_1 = 0$ than for $T_1 = 0.5$.

Triangular profiles of initial tangential velocity were used. In one case the maximum velocity was near the inner sphere, and it was near the outer sphere in a second case. In both cases separation was aggravated by the skewed profiles. Heat transfer was enhanced with peak velocity near the inner surface and impaired with the peak near the outer sphere. The change was about 13 percent compared to results with a uniform profile. Velocity profiles and local Nusselt numbers were different among these cases near the initial state, but they tended toward the same values in the upper hemisphere.

The program will handle any initial velocity profile of tangential velocity that is one-dimensional. The question of extending the analysis to cope with flow separation, while important, is difficult because equations must be solved in elliptic form.

Correlation. As noted earlier, Rundell, Ward, and Cox [4] presented a correlation of their experimental data in terms of Prandtl number, Reynolds number, and radius ratio having the form

$$\mathrm{Nu}_m = 106.2\,\mathrm{Re}^{0.262}\frac{\mathrm{Pr}^{1/3}\pi r_i^2}{RO^{3.69}}(RO^2 - 1) \tag{21}$$

for spheres having a diameter of about 25–30 cm. Based on the computed results of our analysis, the Nusselt number was expressed in terms of these variables as

$$\mathrm{Nu} = K\mathrm{Re}^{M}\mathrm{Pr}^{N}(RO - 1)^{P} \qquad (22)$$

Heat transfer is affected by initial conditions. For an initial gap temperature of $T_1 = 0.5$, the results were fit with the expression

$$\mathrm{Nu}_{i,m} = 2.41\ \mathrm{Re}^{0.15}(RO - 1)^{0.17}\mathrm{Pr}^{0.2} \qquad (23)$$

with a variance of 3 percent from the mean. For $T_1 = 0.5$ the results were correlated by the relation

$$\mathrm{Nu}_{i,m} = 2.28\ \mathrm{Re}^{0.23}(RO - 1)^{0.26}\mathrm{Pr}^{0.2} \qquad (24)$$

with a variance of 13 percent.

A comparison between Nusselt numbers computed with the correlations and equation (21) shows the results from the experiment [4] to be larger than those predicted by the analysis. This is not surprising, as the experiments were done with high Reynolds numbers, and all runs were separated, with vortices present in the flow. Furthermore, there is jetting of the fluid against the inner sphere at the entrance. All of these factors would tend to increase heat transfer in the experiment, while the analysis has assumed that the flow was laminar throughout.

Acknowledgment

This study was part of a program to investigate heat transfer between concentric spheres conducted at the Charles Stark Draper Laboratory while the author was a Summer Fellow. The author is indebted to the laboratory and to Mr. John Schmidt for making this research possible. Appreciation is expressed for the computing assistance provided by Mr. James Thys and for the technical advice and counsel of Mr. Richard Martorana and Dr. P. Kerney. Special thanks go to Jane Carmody for editing the paper.

Publication of this paper does not constitute approval by the U.S. Navy of the findings or conclusions contained herein. It is published for the exchange and stimulation of ideas.

References

1 Cobble, H. M., "Spherical Shell Heat Exchangers Dirichlet Problem," *Journal of Franklin Institute*, Sept. 1963, p. 197.

2 Bird, R. B., Stewart, W. E., and Lightfoot, E. N., *Transport Phenomena*, Wiley, New York, 1964, p. 117.

3 Ward, E. G., *Flow Through the Annulus Formed Between Concentric Spheres*, Master's thesis, University of Houston, Houston, Texas, Jan. 1966.

4 Rundell, H. A., Ward, E. G., and Cox, J. E., "Forced Convection in Concentric-Sphere Heat Exchangers," JOURNAL OF HEAT TRANSFER, TRANS. ASME, Series C, Vol. 90, No. 1, Feb. 1968, pp. 125–129.

5 Bozeman, J. D., and Dalton, C., "Flow in the Entrance Region of a Concentric-Sphere Heat Exchanger," JOURNAL OF HEAT TRANSFER, TRANS. ASME, Series C, Vol. 92, No. 1, Feb. 1970, pp. 184–185.

6 Schlichting, H., *Boundary Layer Theory*, 6th ed., McGraw-Hill, New York, 1968, pp. 117–121.

7 Bodia, J. R., and Osterle, J. F., "Finite Difference Analysis of Plane Poiseuille and Couette Flow Developments," *Appl. Sci. Res.* A 10, 1961, pp. 265–276.

8 Coney, J. E. R., and El-Shaarawi, M. A. I., "A Contribution to the Numerical Solution of Developing Laminar Flow in the Entrance Region of Concentric Annuli with Rotating Inner Walls," ASME Paper No. 74-FE-28.

9 Arden, B., and Astill, K. N., *Numerical Algorithms—Origins and Applications*, Addison-Wesley, Reading, Mass., 1970.

10 Astill, K. N., "An Analysis of Laminar Forced Convection between Concentric Spheres," Report No. R-835, Charles Stark Draper Laboratory, Cambridge, Mass., 1974.

N. M. Schnurr
Professor,
Department of Mechanical Engineering,
Vanderbilt University,
Nashville, Tenn.
Mem. ASME

V. S. Sastry
Assoc. Professor,
Department of Mechanical Engineering,
Tennessee State University,
Nashville, Tenn.
Mem. ASME

A. B. Shapiro
Graduate Student.
Department of Mechanical Engineering,
Vanderbilt University,
Nashville, Tenn.

A Numerical Analysis of Heat Transfer to Fluids Near the Thermodynamic Critical Point Including the Thermal Entrance Region

A two-dimensional numerical method has been developed to predict heat transfer to near critical fluids in turbulent flow through circular tubes. The analysis is applicable to the thermal entry region as well as fully developed flows. Agreement with experimental data for water at 31.0 MN/m^2 is quite good. A correlation in the form of the heat flux parameter of Goldmann was found to be satisfactory for water at that pressure. Results are presented in graphical form which apply to a wide range of heat fluxes, mass velocities, and tube diameters. Preliminary results in the entrance region show that film coefficients remain well above the corresponding fully developed values for a larger distance downstream than would be the case with a constant property fluid. This effect becomes more pronounced as the heat flux is increased.

Introduction

Heat transfer to fluids near the thermodynamic critical point in flow through circular tubes has been of interest for the past 20 years. The distinguishing feature of the process is the extremely sharp variations of thermodynamic and transport properties which occur near the pseudocritical temperature.[1] Although a supercritical fluid is clearly single-phase when in a state of thermodynamic equilibrium, it has been shown that relatively large relaxation times may be required for a thermally disturbed system to return to equilibrium so that nonequilibrium phenomena may occur near the critical point. In addition, there are extremely large density variations in this region causing free convection effects.

The great majority of work which has been reported has been experimental. Measurements of heat-transfer coefficients have been made for a variety of fluids (CO_2, H_2O, H_2, O_2, etc.). An excellent survey of the entire area of heat transfer to near-critical fluids by Hendricks, et al. [1][2] lists more than 40 references (prior to 1970) which present results of heated tube experiments. Some of these report sharp peaks in the heat-transfer coefficients while others find a degradation of the film coefficient resulting in a peak in the tube wall temperature. It is now evident that these results are not inconsistent since both increases and decreases in the film coefficient appear to occur for all fluids at certain combinations of heat fluxes, flow rates, and fluid bulk enthalpies.

In spite of the large number of experiments which have been run, the data available for design and even the understanding of the basic mechanism for heat transfer are inadequate. The large number of variables which affect the heat transfer and the difficult ranges of pressures and temperatures which must be produced make a truly comprehensive experimental program extremely difficult. It is therefore apparent that a reliable numerical solution would be a valuable tool for carrying out a systematic study of the effects of various parameters and for producing results which could be used in design and analysis.

Numerical solutions of the problem [2–6] have been carried out with limited success. The method used in these studies was a cross-stream

---

[1] The pseudocritical temperature is the temperature at which C_p is a maximum at a specified pressure.

Contributed by the Heat Transfer Division for publication in the JOURNAL OF HEAT TRANSFER. Manuscript received by the Heat Transfer Division February 17, 1976.

[2] Numbers in brackets designate References at end of paper.

numerical integration so that the effects of upstream conditions were not accounted for. Thus, the axial momentum term was not included. A recent numerical analysis by Kakarala and Thomas [7] used a surface-renewal based formulation to analyze the case of combined free and forced convection for turbulent flow in a vertical tube. Their method predicts the threshold limits on the conditions under which buoyancy terms are significant. They do not present results in the form of film coefficients, however.

A two-dimensional numerical analysis was recently presented by Sastry and Schnurr [8]. They used an adaptation of the Patankar-Spalding method [9] and found excellent agreement with experimental data [10] for water at pressures of 22.8 and 31.0 MN/m^2 for relatively low heat fluxes but agreement was less satisfactory for high heat flux cases and for the CO$_2$ data of [11]. This appeared to be partly caused by the inability of the numerical method to handle the thermal entry region. There is experimental evidence [11] which indicates that thermal entry effects may persist much farther downstream for near-critical fluids than for constant property fluids.

The purpose of the work reported here was to extend the analysis of reference [8] to include the thermal entry region and to use the resulting numerical method to predict the effect of all pertinent variables on the heat-transfer coefficient for the flow of near-critical fluids through tubes with constant wall heat fluxes.

The Numerical Method

The problem to be analyzed is heat transfer to a near-critical fluid flowing through a circular tube with a uniform wall heat flux. Axial conduction, viscous dissipation, and free convection effects are assumed negligible. The flow is assumed to be hydrodynamically fully developed and the enthalpy profile is uniform at the beginning of the heated section of tube.

The numerical method used in this work is an adaptation of the Patankar-Spalding method. Their method is an implicit finite difference marching procedure applicable to boundary layer[3] type flows. The governing differential equations in the von Mises coordinate system are

$$\frac{\partial u}{\partial x} = \frac{\partial}{\partial \psi}(\tau r) - \frac{1}{\rho u}\frac{dP}{dx} \tag{1}$$

$$\frac{\partial i}{\partial x} = -\frac{\partial}{\partial \psi}\{(J_i - u\tau)r\} \tag{2}$$

where

$$\tau = \mu_{\text{eff}}(\partial u/\partial r) \tag{3}$$

$$J_i = -(\mu_{\text{eff}}/\sigma_{\text{eff}})(\partial i/\partial r) \tag{4}$$

All symbols are defined in the Nomenclature. The effective viscosity, μ_{eff}, is the sum of laminar and turbulent contributions. The turbulent contribution may be computed using any of several empirical or semi-empirical formulations. The effective Prandtl number is calculated by assuming that the effective conductivity of the fluid is also composed of laminar and turbulent contributions. This concept leads to the relationship

$$\mu_{\text{eff}}/\sigma_{\text{eff}} = \mu/\sigma + (\mu_{\text{eff}} - \mu)/\sigma_T \tag{5}$$

The turbulent Prandtl number σ_T may be assumed constant or some formulation such as that suggested by Jenkins [12], or Eckelman and Hanratty [13] may be used.

The Patankar-Spalding method has several features which make it superior to most other numerical procedures. The use of the von Mises coordinate system eliminates the necessity for a separate continuity equation. It also allows developing flows to be analyzed without including a separate equation for conservation of momentum in the cross-stream direction. The most significant feature, however, is their treatment of the region near the wall. In this region the velocities are so small that axial convection terms are negligible. The flow is described by ordinary differential equations which can be directly integrated. This gives values and slopes of the dependent variables, velocity, and enthalpy at the edge of this "Couette flow" region. These values are boundary conditions for the finite difference solution which is used from the edge of the Couette flow region to the tube center line. This results in a significant reduction in the required number of cross-stream nodes.

Two major revisions were required to adapt this method to the case of heat transfer to near-critical fluids in circular tubes including thermal entrance effects. The first was the adaptation of the method to internal flows. Since the solution of the finite difference equations requires knowledge of the downstream pressure, an iterative scheme had to be developed in which a value of downstream pressure is assumed, downstream velocity and enthalpy profiles are computed, and the resulting radius of the flow region is calculated and compared to the tube radius. If the difference is larger than a specified tolerance, the assumed downstream pressure is adjusted and the process is repeated until satisfactory agreement is obtained.

The second major revision was the handling of the Couette flow region. If the thermal entry region is to be studied, it is necessary to use an extremely small spacing of node points near the wall. The Couette flow region will therefore lie entirely within the laminar

Nomenclature

C_p = specific heat at constant pressure
D = inside diameter of tube
g = acceleration of gravity
G = mass velocity
Gr = Grashof number = $((\rho_b - \rho_w)/\rho_w)(\rho_w/\mu_w)^2 D^3 g$
h = local heat transfer coefficient
i = specific enthalpy
$I_+ = (i - i_w)(\tau_w \rho_c)^{1/2}/q_w$
$J_i = (\mu_{\text{eff}}/\sigma_{\text{eff}})(\partial i/\partial r)$
K = thermal conductivity
K_{eff} = effective conductivity in turbulent flows
N = number of nodes in the radial direction
Nu = Nusselt number = hD/K_b
Nu$_R$ = reference Nusselt number defined by equation (16)
P = pressure
P_{cr} = critical pressure
P_r = reduced pressure = P/P_{cr}
$P_+ = \mu_c(dP/dx)(\tau_w{}^3\rho_c)^{-1/2}$
q_w = wall heat flux
r = local radius
Re$_b$ = Reynolds number = GD/μ_b
S = node spacing parameter
T = local temperature
u = local axial velocity
$u_+ = u/(\tau_w/\rho_c)^{1/2}$
x = axial distance
y = distance from the tube wall
$y_+ = y(\tau_w \rho_c)^{1/2}/\mu_c$
Δr = node spacing in the radial direction
ϵ = eddy diffusivity of momentum
ϵ_H = eddy diffusivity of heat
μ = fluid viscosity
μ_{eff} = effective viscosity for turbulent flow
$\mu_+ = \mu_{\text{eff}}/\mu_c$
ρ = fluid density
σ = Prandtl number = $\mu C_p/K$
σ_{eff} = effective Prandtl number
σ_T = turbulent Prandtl number = ϵ/ϵ_H
τ = local shear stress
$\phi = q_w D^{0.2}/G^{0.8}$
ψ = the stream function

Subscripts

b = bulk
c = edge of the Couette flow region
M = pseudocritical condition
0 = a reference condition
W = wall

---

[3] "Boundary Layer" has a somewhat broader connotation than usual. It includes all cases where derivatives of the dependent variables (velocity and enthalpy) in the streamwise direction are small compared to those in the cross-stream direction.

sublayer. If the temperature in that region is near the pseudocritical temperature of the fluid, variations in the viscosity and Prandtl number will be severe. It was therefore necessary to develop a special Couette flow solution consistent with these conditions.

The governing differential equations in the Couette flow region in dimensionless form are [9]

$$du_+/dy_+ = (1 + P_+ y_+)/\mu_+ \tag{6}$$

and

$$dI_+/dy_+ = \sigma/\mu \tag{7}$$

These equations are to be integrated from the wall to the opposite edge of the Couette flow region, which is selected at a point where y_+ is less than five to ensure that this region lies completely within the laminar sublayer.

Typical variations of properties for a fluid near the critical point[4] are shown in Fig. 1. Since the thickness of the Couette flow region is very small and the temperature change across that region is not excessive, the variation of viscosity may be assumed linear with distance. Therefore

$$\mu_+ = \mu_{+w} + (1 - \mu_{+w})(y_+/y_{+c}) \tag{8}$$

Integration of equation (6) in conjunction with equation (8) yields

$$u_{+c} = P_+ y_{+c}{}^2(1 - \mu_{+w} + \mu_{+w} \log \mu_{+w})/(1 - \mu_{+w})^2 - (y_{+c}/(1 - \mu_{+w})) \log \mu_{+w} \tag{9}$$

The Prandtl number variation is quite similar to the C_p variation and reaches a sharp peak at the transposed critical temperature. Integration of equation (7) is carried out for two separate cases. If the transposed critical temperature lies between the temperatures at the wall and that at the edge of the Couette flow region ($T_c < T_M < T_w$), the Prandtl number is expressed by two straight line segments

$$\sigma = \sigma_w + (\sigma_M - \sigma_w)(I_+/I_{+M}) \qquad 0 \le I_+ \le I_{+M} \tag{10}$$

and

$$\sigma = \sigma_M + (\sigma_c - \sigma_M)(I_+ - I_{+M})/(I_{+c} - I_{+M}) \qquad I_{+M} \le I_+ \le I_{+c} \tag{11}$$

The integration of equation (7) using (8), (10), and (11) yields

$$I_{+c} = I_{+M} - [(\log(\sigma_M/\sigma_w))/(\sigma_M - \sigma_w) + y_{+c}(\log \mu_{+w})/(1 - \mu_{+w})](\sigma_c - \sigma_M)/\log(\sigma_c/\sigma_M) \tag{12}$$

If T_M does not lie between T_w and T_c, the Prandtl number is given by

$$\sigma = \sigma_w + (\sigma_c - \sigma_w)(I_+/I_{+c}) \tag{13}$$

and integration of (7) using (8) and (13) gives

$$I_{+c} = (\sigma_c - \sigma_w) \log(1/\mu_{+w}) y_{+c}/((1 - \mu_{+w}) \log(\sigma_c/\sigma_w)) \tag{14}$$

Equations (6), (7), (9), and (12), or (14) are used simultaneously with the set of finite difference equations to determine downstream profiles of velocity and enthalpy. The wall shear stress and heat-transfer coefficient may then be calculated.

Since the foregoing analysis is based on an assumption of laminar flow throughout the Couette flow region, the radial distribution of node points must be chosen to ensure that the point nearest the wall is at a dimensionless distance of $y_+ < 5$. It should also be noted that variations of "effective" properties are most severe in the laminar sublayer since the laminar viscosity and Prandtl number are highly temperature dependent. In the turbulent core the eddy viscosity and conductivity dominate, and they are much less temperature sensitive. Finally, the rapid changes in enthalpy and velocity occur very near the wall in entrance region flows. All of these considerations dictate a highly nonuniform node spacing with the greatest concentration of node points near the wall. A variety of node-point distribution schemes were tried. The one which proved most successful was based on the equation

$$\Delta r_I = (2)^{-1/S} \Delta r_{I-1} \qquad 1 \le I \le N \tag{15}$$

where $I = 1$ corresponds to the node on the tube center line. Various combinations of N and S were tried and comparison of the results with those obtained using other combinations as well as with experimental results were used to determine the best values. The most satisfactory combination depended on the fluid, heat flux, pressure, and bulk enthalpy. Nevertheless, $N = 30$ and $S = 2$ was found to give good results for most cases.

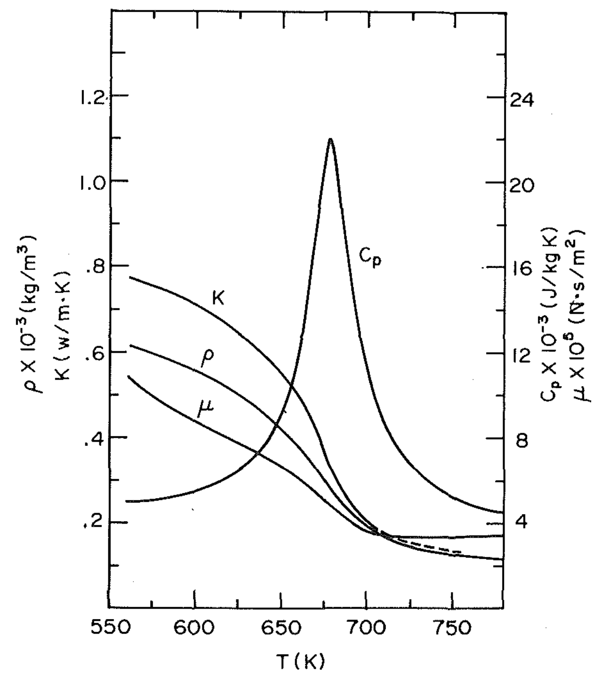

Fig. 1 Properties of water at a pressure of 31.0 MN/m^2

Selection of a suitable downstream step size also presented an interesting problem. The Patankar-Spalding method is basically a forward differencing procedure since derivatives of the dependent variables are evaluated at the downstream end of the axial step. The values of the transport properties are evaluated at the upstream station, however, so that the linearity of the finite difference equations will be preserved. Therefore, the method is not universally stable and if the downstream step size is not kept below a particular value, instability will result. This maximum allowable step size is a complex function of the transport properties and their derivatives with respect to velocity and enthalpy. It was found to be most expedient to determine the maximum allowable step size by a trial-and-error procedure. In regions where the wall temperature was well below the transposed critical temperature or the center-line temperature was well above it, step sizes as large as 1 diameter could be used. When the temperature in the laminar sublayer was near T_M, however, much shorter steps were necessary. The worst case occurs when T_M falls within the laminar sublayer but outside the Couette flow region. The peaks in C_p and σ are not accounted for in the finite difference portion of the solution as well as they are within the Couette flow region. This difficulty was minimized by using small enough node spacings and step lengths to ensure good accuracy. In such cases a step length in the range of 0.025–0.1 diameters was used. The most critical case occurred when such conditions occurred near the beginning of the entrance region. In these cases an initial step length as small as 0.001 diameters had to be used. Since the step length was adjustable, computation time was conserved by appropriate variation of the step

---

[4] Additional discussion of thermal properties of near critical fluids is given in the Appendix.

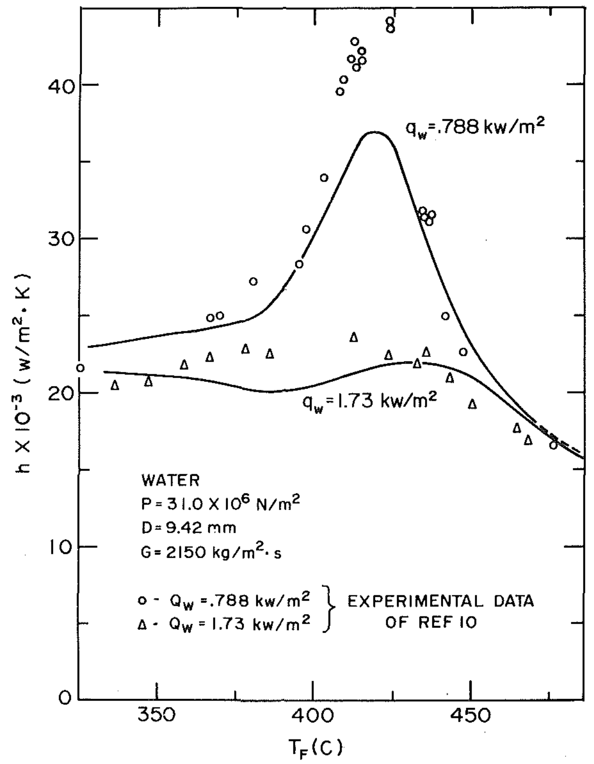

Fig. 2 Comparison of numerical results to the experimental data of [10]

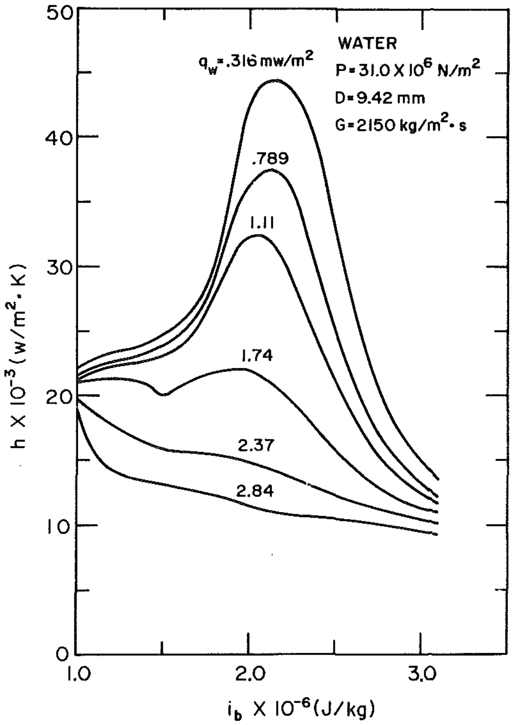

Fig. 3 The effect of heat flux on the film coefficient

length as the calculation proceeded downstream.

The accuracy of the numerical method was checked by comparison of results with those of other analytical studies and with experimental data from several sources. The first comparisons were for heat transfer to constant property fluids in turbulent flow through circular tubes with a uniform wall heat flux. Agreement with standard empirical correlations [14] for fully developed flows were excellent for Prandtl numbers in the range of 0.7–10 and for Reynolds numbers from 30,000 to 500,000. Several additional comparisons were made for heat transfer to near-critical fluids. These are discussed in the following section.

Results—Fully Developed Flow

The first case considered was water at a pressure of 31.0 MN/m² (P_r = 1.40). This case was selected because a significant amount of reliable experimental data are available at that pressure for two different values of wall heat flux. It also had the advantage of less severe property variations than would occur closer to the critical point. Therefore a larger downstream step size could be used and an extensive study of the effects of several variables could be made with a relatively modest amount of computer time.

A comparison of the numerical results with those of reference [10] is shown in Fig. 2. The abscissa in Fig. 2 is a film temperature defined as $(T_b + T_w)/2$. The maximum difference is about 15 percent. This agreement is significantly better than that obtained by the authors in the previous analytical study [8], particularly for the higher heat flux. This is apparently due to the more precise accounting of the property variations in the new Couette flow solution and the higher concentration of nodes in the wall-near region.

The effect of heat flux on the film coefficient was studied by producing additional results at values of heat flux ranging from 0.316 to 2.84 MW/m². These results are shown in Fig. 3. The film coefficients reach a peak at $i_b \approx i_M$ for low values of heat flux. At higher heat fluxes this peak disappears, and at very high heat fluxes, h drops rather sharply to values less than ¼ of the corresponding values for the low heat flux case. The combination of high q_w and low h results in very high tube wall temperatures.

The enhancement of h for the low heat flux cases is simply due to the very high fluid Prandtl numbers which occur at temperatures spanning the transposed critical. This peak in h would in fact be predicted by a constant property correlation of the type

$$\mathrm{Nu}_R = 0.023\,\mathrm{Re}_b^{0.8}\sigma_b^{0.4} \qquad (16)$$

At higher heat fluxes the radial variation of enthalpy (and temperature) is very large. The wall temperature is well above T_M when the bulk of the fluid is still at temperatures below T_M. The fluid near the wall has a low thermal conductivity causing a large thermal resistance in the laminar sublayer. The average velocity of the fluid is still relatively low, however, since the core of the fluid is at a temperature below T_M and the density is high. This results in the low values of h. As heating continues, the density decreases in the core with a corresponding increase in velocity and improvement in the heat transfer coefficient.[5]

The effects of heat flux, mass velocity, and tube diameter on the film coefficient were investigated for water at 31.0 MN/m² by calculating h versus i_b for various combinations of q_w, G, and D. A listing of all cases considered is given in Table 1. The calculated Nusselt numbers were normalized by dividing by reference Nusselt numbers calculated from equation (16) at the same bulk enthalpy. The variation of Nu/Nu$_R$ with i_b for all cases is shown in Fig. 4.

As the heat flux approaches zero, the property variations become negligible and the Nusselt number ratio would be expected to approach unity. Note that for the lowest heat flux considered here (Case 1, q_w = 0.317 MW/m²) the normalized Nusselt number is approximately equal to unity except for bulk enthalpies spanning the transposed critical where the ratio reaches a value of about 1.2. This occurs because the property variations in the radial direction are still significant at this heat flux. A correlation accounting for viscosity variation would be expected to give a more accurate prediction of the

---

[5] This explanation is essentially the same as that given by Shiralkar and Griffith.

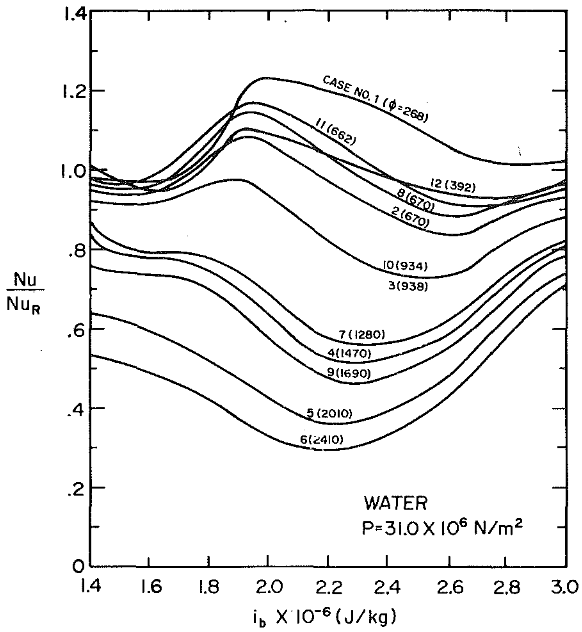

Fig. 4 Correlation of results for water at 31 MN/m^2

Nusselt number. The Nusselt numbers for Case 1 were also compared to a correlation recommended by Kays [14] having the form

$$\mathrm{Nu} = 0.0155\,\mathrm{Re}_b{}^{0.83}\sigma_b{}^{0.5}(\mu_b/\mu_w)^{0.36} \qquad (17)$$

Agreement was within 5 percent over the entire range of bulk enthalpies. Even though equation (17) is a more accurate correlation than equation (16), the latter is used as the normalizing Nusselt number since it can more easily be used in a design situation where T_w is unknown at the outset.

The ranges of independent variables covered in this series of runs were

$$3.2 \leq D \leq 18.8\ \mathrm{mm}$$

$$0.32 \leq q_w \leq 3.5\ \mathrm{MW/m^2}$$

$$1020 \leq G \leq 5120\ \mathrm{kg/m^2s}$$

The resulting Reynolds numbers covered a range of 3×10^4 to 2×10^6. Several methods of correlating the results were tried. The method which proved best was the use of the heat flux parameter $\phi = q_w D^{0.2}/G^{0.8}$ used by Goldmann [3]. Values of this parameter are given in Table 1 and on the corresponding curves in Fig. 4. The values of this parameter increase quite smoothly as the curves shift downward. This set of curves may be considered a correlation of results for water at a pressure of 31.0 MN/m^2 subject to the limitations on q_w, D, and G listed before and to the added restriction that free convection effects are not important. According to Shiralkar and Griffith [11], buoyancy effects will be negligible if $\mathrm{Gr/Re}^2 < 0.032$ for water. Hall [15] uses the criterion $\mathrm{Gr/Re}^{1.8} < 0.1$ which is a somewhat more stringent condition. Values of both of these parameters are given in Table 1 for each case.

A few additional runs were made for water at a pressure of 22.8 MN/m^2 ($P_r = 1.03$). The predicted results were found to agree with the experimental data of [10] within 10 percent. The step length used for this solution had to be limited to an extremely small value to maintain stability. The computer time was therefore quite large and it was not feasible to run a large number of cases at that pressure.

Results—The Thermal Entry Region

Experimental results [4] have shown that entrance effects continue farther downstream for near-critical fluids than would occur in the constant fluid property case. The numerical procedure was applied to the thermal entry region in an attempt to determine the importance of these effects. The marching procedure was allowed to proceed downstream solving only the momentum equation until the velocity profile was fully developed. The enthalpy profile was a specified uniform value during this "starting length." Then the solution to the energy equation was included and the thermal entry solution was begun. The first cases were run for the purpose of checking the accuracy of the thermal entry solution. Constant fluid property cases using Prandtl numbers of 0.7 and 10 were run for several values of Reynolds numbers. Results were found to agree with those of [16] within ±2 percent for $x/D \geq 1$. A case was then run for near-critical hydrogen for comparison to the experimental data of Hendricks, et al. [17]. These results are shown in Fig. 5. The reduced pressure is 1.28 for this case and the heat flux is quite large with the result that $T_b < T_M < T_w$ for the entire entrance region. The very good agreement indicates that this program can be used to predict thermal entry effects with some confidence.

Since thermal entry results are functions of bulk enthalpy as well as G, D, q_w, and fluid pressure, it did not appear feasible to attempt any type of correlation at this time. More comparisons with experimental data from a variety of sources would be required to further increase the confidence in the numerical method. Nevertheless, a series of runs was made for water at 31.0 MN/m^2 to predict the effects of inlet enthalpy and heat flux in the thermal entry region. A reference run was made using a very low inlet enthalpy to produce the fully developed Nu versus i_b curve. Thermal entrance runs were then made with higher inlet enthalpy values. The predicted Nusselt number for those cases asymptotically approached the fully developed results for large x/D values. It was then possible to isolate the thermal entrance effects in the form $\mathrm{Nu/Nu}_\infty$ versus x/D. Results are presented in this form for three different heat flux levels in Fig. 6. It does appear that entrance effects are more pronounced and persist much farther downstream for higher heat fluxes. It was also found that even for the low heat flux cases, the entrance effect is more pronounced when $T_b < T_M < T_w$.

Discussion

An area of great importance which has not yet been discussed is the

Table 1 Cases analyzed–water, 31.0 MN/m^2

Case No.	D (mm)	G (kg/m^2·s)	q_w Mw/m^2	Gr/Re^2	Gr/Re$^{1.8}$	$q_w D^{0.2}/G^{0.8}$ ws$^{0.8}$ m$^{-0.2}$ kg$^{-0.8}$
1	9.42	2150	0.316	0.0007	0.009	268
2	9.42	2150	0.789	0.0023	0.029	670
3	9.42	2150	1.11	0.0036	0.045	938
4	9.42	2150	1.74	0.0063	0.075	1470
5	9.42	2150	2.37	0.0088	0.102	2010
6	9.42	2150	2.84	0.0104	0.116	2410
7	9.42	1080	0.868	0.0224	0.236	1280
8	9.42	5120	1.58	0.0004	0.006	670
9	9.42	4310	3.47	0.0018	0.024	1690
10	18.8	1080	0.552	0.0288	0.358	934
11	18.8	4310	1.18	0.0010	0.017	662
12	3.17	1020	0.316	0.0019	0.017	392

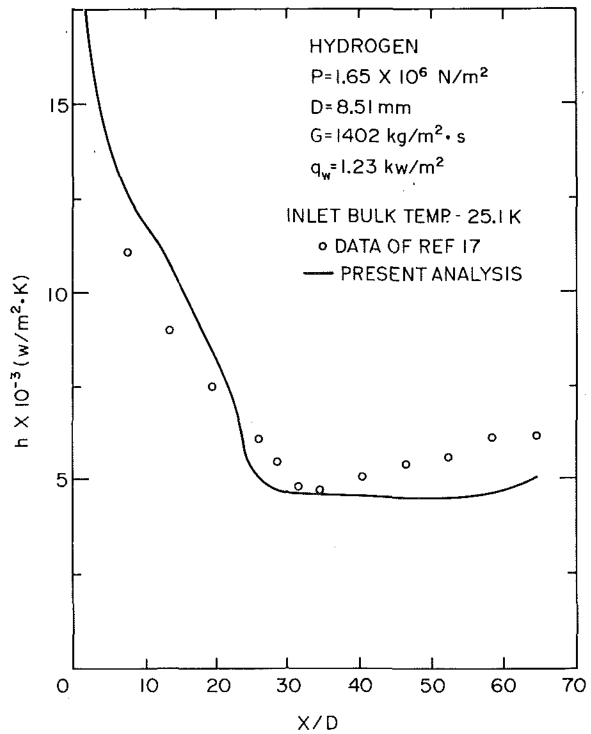

Fig. 5 Comparison of numerical results to the experimental data of [17]

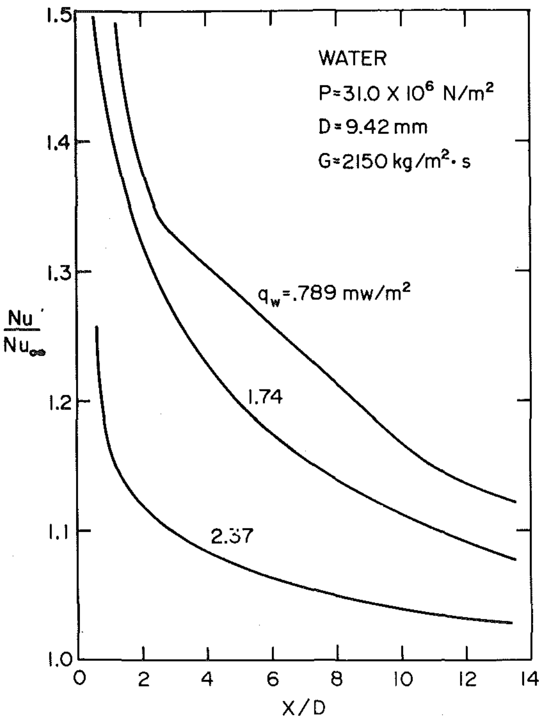

Fig. 6 The effects of inlet enthalpy on heat transfer in the thermal entry region

effective viscosity formulation. There are a variety of eddy viscosity formulations which have been proposed. Until recently almost all theories used in numerical calculations were based on the Prandtl mixing length theory [18] with an exponential decay near the wall as proposed by Van Driest [19]. Patankar and Spalding [9] suggest using local values of ρ, μ, and τ rather than wall values to improve accuracy in variable property flows. This results in an effective viscosity of the form

$$\mu_{\text{eff}} = \mu + \rho\kappa^2 y^2[1 - \exp[-y\sqrt{\tau\rho}/(\mu A_+)]^2|\partial u/\partial y| \qquad (18)$$

where $\kappa = 0.4$ and $A_+ = 26$. All results reported here used this formulation.

Various refinements have been suggested for use with near-critical fluids. Hess and Kunz [10] have proposed altering A_+ of equation (18) as a function of kinematic viscosity. Their formulation is empirical and is applicable only to hydrogen. It was used for the run shown in Fig. 5 and gave film coefficients slightly higher than those using equation (18). Additional runs would be required over a variety of conditions to determine whether the Hess and Kunz approach is indeed an improvement.

Hsu and Smith [21] have proposed an enhancement of the eddy viscosity caused by density gradients. The theoretical analysis on which their enhancement factor is based is open to some question.[6] Their formulation was tried for water at 31.0 MN/m^2 and gave excellent results for low heat flux cases but badly overpredicted the film coefficients at higher heat fluxes.

There is a variety of closure schemes based on the equation of the mean kinetic energy of turbulence of Prandtl [22]. These methods involve the simultaneous solution of the momentum and energy equations with one or more turbulent energy partial differential equations. These have not yet been tried, due primarily to the added complexity and increased computation time. The only justification which can be offered for the use of the simpler mixing-length based formulation is its apparent success in comparison with experimental data. Use of the turbulent-energy methods is planned in future studies.

The major difficulty remaining is the large computation time required. It ranged from 15 to 70 min of XDS Sigma-7 computer time for each case depending on the heat flux level. This would correspond to about 1–5 min on a CDC 6600 computer. A complete revision to develop a universally stable method is planned. It is hoped that the advantages gained from the larger step length will not be significantly offset by the increased computation time required to solve the system of nonlinear algebraic equations at each step.

Conclusion

A two-dimensional numerical method has been developed to predict heat transfer to near-critical fluids in turbulent flow through circular tubes. The analysis is applicable to the thermal entry region as well as fully developed flows. Agreement with experimental data for water at 31.0 MN/m^2 is quite good. A correlation in the form of the heat flux parameter of Goldmann was found to be satisfactory for water at that pressure. Results are presented in graphical form which apply to a wide range of heat fluxes, mass velocities, and tube diameters.

Preliminary results in the entrance region show that film coefficients remain well above the corresponding fully developed values for a larger distance downstream than would be the case with a constant property fluid. This effect becomes more pronounced as the heat flux is increased.

Acknowledgments

This work was supported by the National Science Foundation under grant No. ENG75-06238. The authors are indebted to John Schindler for his assistance in developing the computer code.

References

1 Hendricks, R. C., et al., "Survey of Heat Transfer to Near Critical Fluids," NASA TN D-5886, Nov. 1970.

2 Deissler, R. G., "Heat Transfer and Fluid Friction for Fully Developed Turbulent Flow of Air and Supercritical Water with Variable Fluid Properties," TRANS. ASME, Vol. 76, 1954, p. 73.

---

[6] See discussion at the end of [21].

3 Goldmann, K., "Heat Transfer to Supercritical Water and Other Fluids With Temperature Dependent Properties," *Chemical Engineering Progress Symposium*, Series II, Vol. 50, 1954, p. 105.

4 Shiralkar, B. S., and Griffith, P., "Determination in Heat Transfer to Fluids at Supercritical Pressure and High Heat Fluxes," JOURNAL OF HEAT TRANSFER, TRANS. ASME, Series C, Vol. 9, No. 1, Feb. 1969, pp. 27–36.

5 Hess, H. L., and Kunz, H. R., "A Study of Forced Convection Heat Transfer to Supercritical Hydrogen," JOURNAL OF HEAT TRANSFER, TRANS. ASME, Series C, Vol. 87, No. 1, Feb. 1965, pp. 41–48.

6 Hsu, Y. Y., and Smith, J. M., "The Effect of Density Variation on Heat Transfer in the Critical Region," JOURNAL OF HEAT TRANSFER, TRANS. ASME, Series C, Vol. 83, No. 2, May 1961, pp. 176–182.

7 Kakarala, C. R., and Thomas, L. C., "Turbulent Combined Forced and Free Convection Heat Transfer in Vertical Tube Flow of Supercritical Fluids," ASME Paper 75-WA/HT-59.

8 Sastry, V. S., and Schnurr, N. M., "An Analytical Investigation of Forced Convection Heat Transfer to Fluids Near the Thermodynamic Critical Point," JOURNAL OF HEAT TRANSFER, TRANS. ASME, Series C, Vol. 97, No. 2, 1975, pp. 226–230.

9 Patankar, S. V., and Spalding, D. B., *Heat and Mass Transfer in Boundary Layers*, 2nd ed., Intertext Books, London, 1970.

10 Swenson, H. S., et al., "Heat Transfer to Supercritical Water in Smooth-Bore Tubes," JOURNAL OF HEAT TRANSFER TRANS. ASME, Series C, Vol. 87, No. 4, Nov. 1965, pp. 477–484.

11 Shiralkar, B. S., and Griffith, P., "The Deterioration in Heat Transfer to Fluid at Supercritical Pressure and High Heat Fluxes," Report No. DSR 70332-55, Dept. of Mechanical Engineering, M.I.T., Cambridge, Mass.

12 Jenkins, R., *Heat Transfer*, Fluid Mech. Inst. Stanford University Press, Palo Alto, Calif. 1951, p. 147.

13 Eckelman, L. D., and Hanratty, T. J., "Interpretation of Measured Variations of the Eddy Conductivity," *International Journal of Heat and Mass Transfer*, Vol. 15, 1972, pp. 2231–2239.

14 Kays, W. M., *Convective Heat and Mass Transfer*, McGraw-Hill, New York.

15 *Advances in Heat Transfer*, Vol. 7, 1971, Academic Press, New York.

16 Sparrow, E. M., et al., *Applied Science Research*, Series A, Vol. 7, 1957, pp. 37–52.

17 Hendricks, R. C., et al., "Experimental Heat Transfer Results for Cryogenic Hydrogen Flowing in Tubes at Subcritical and Supercritical Pressures to 800 Pounds Per Square Inch Absolute," NASA TN D-3095, Mar. 1966.

18 Prandtl, L., "Bericht über Untersuchungen zur ausgebildeten Turbulenz," *ZAMM*, Vol. 5, 1925, p. 136.

19 Van Driest, E. R., "On Turbulent Flow Near a Wall," *Journal Aero Science*, Vol. 23, 1956, pp. 1007–1011.

20 Hess, H. L., and Kunz, H. R., "A Study of Forced Convection Heat Transfer to Supercritical Hydrogen," JOURNAL OF HEAT TRANSFER, TRANS. ASME, Series C, Vol. 87, No. 1, Feb. 1965, pp. 41–48.

21 Hsu, Yih-Yun, and Smith, J. M., "The Effect of Density Variation on Heat Transfer in the Critical Region," JOURNAL OF HEAT TRANSFER, TRANS. ASME, Series C, Vol. 83, No. 2, May 1961, pp. 176–182.

22 Prandtl, L., "Uber eine neues Formelsystem für die ausgebildete Turbulenz," *Nachrichten der Akad.* Wiss., Göttingen, Mathphys. pp. 6–19, Van den Loeck & Ruprecht, Göttingen (1945).

23 Sengers, and Michels, A., "The Thermal Conductivity of Carbon Dioxide in the Critical Region," *Second Symposium on Thermophysical Properties*, ASME, Jan. 24–26, 1962, New York, Academic Press, 1962, p. 434.

24 Roder, H. M., and Weber, L. A., *ASRDI Oxygen Technology Survey, Volume 1: Thermophysical Properties*, NASA SP-3071, 1972.

25 McCarty, R. D., and Weber, L. A., "Thermophysical Properties of Parahydrogen from the Freezing Liquid Line to 5000 R for Pressures to 10,000 PSIA," NBS TN 617, 1972.

26 McCarty, R. D., "Thermophysical Properties of Helium—4 From 2 to 1500 K with Pressures to 1000 ATM," NBS TN 631, Nov. 1972.

APPENDIX

The property data in Fig. 1 are for water at a reduced pressure of 1.40. The thermal conductivity and viscosity decrease monotonically with temperature while C_p and Prandtl number exhibit a peak at $T = T_M$. At a pressure much closer to critical, the thermal conductivity may also exhibit a peak at the critical temperature. Examination of data for CO_2 (23), O_2 (24), H_2 (25), and He (26) indicates that the peak in k is much less severe than that in C_p at the critical isobar so that the Prandtl number still exhibits a peak. As the pressure increases, the peak in k disappears quickly and variations in all properties are then similar to those shown in Fig. 1.

P. Saha[1]
Nuclear Energy Systems Division,
General Electric Company,
San Jose, Calif.
Assoc. Mem. ASME

M. Ishii
Reactor Analysis and Safety Division,
Argonne National Laboratory,
Argonne, Ill.
Assoc. Mem. ASME

N. Zuber
Reactor Safety Research,
U. S. Nuclear Regulatory Commission,
Washington, D. C.
Mem. ASME

An Experimental Investigation of the Thermally Induced Flow Oscillations in Two-Phase Systems

An experimental study on the onset of thermally induced two-phase flow oscillations has been carried out in a uniformly heated boiling channel using Freon-113 as the operating fluid. The effects of inlet subcooling, system pressure, inlet and exit restrictions, and inlet velocity have been studied. The experimental data have been compared with the equilibrium as well as the nonequilibrium theory including the effect of subcooled boiling. It has been found that the effect of thermal nonequilibrium should be included in a theoretical model for accurate prediction of the onset and the frequency of thermally induced flow oscillations. A simplified stability criterion has also been presented and compared with the experimental data.

Introduction

The phenomenon of thermally induced two-phase flow instability is of interest for design and operation of many industrial systems and equipment such as steam generators, thermosiphon reboilers, and other chemical process units. Of all the various types of two-phase flow instabilities, an account of which can be found in the paper by Bouré, Bergles, and Tong [1],[2] the low-frequency oscillations, or the so-called density wave oscillations, are the most common type encountered in practical systems. The time period of these oscillations is typically on the order of the time required for a kinematic (continuity) wave to travel through the system. Although this particular type of oscillatory instability has been studied extensively during the last 15 years, yet not all the aspects associated with this instability are fully understood. One of the reasons is the lack of systematic, well-controlled experimental data on the onset and the frequency of this type of oscillation at various system conditions, and with various operating fluids.

The main purpose of this paper is to present new experimental data on the oscillatory instabilities which were obtained in a uniformly heated boiling channel with Freon-113 as the operating fluid. The effects of various system parameters such as inlet subcooling, system pressure, inlet and exit restrictions, and inlet velocity are discussed. The data are then compared with the equilibrium theory of Ishii and Zuber [2, 3], as well as with the nonequilibrium theory of Saha and Zuber [4, 5]. Both the theories are valid for all fluids including Freon-113 and water at high pressure. According to the equilibrium model, no significant vapor generation starts until the liquid bulk temperature reaches the saturation value, and beyond that all the heat added to the system goes to generate vapor. In reality, however, due to a thermal boundary layer near the heated surface, significant vapor generation is possible even if the liquid bulk temperature is below saturation. This, in effect, increases the length of the region occupied by the two-phase mixture, but at the same time reduces the local rate of vapor generation because a part of the heat added is utilized to increase the bulk temperature of the liquid. In the nonequilibrium model, this important aspect of two-phase flow is included and it allows us to determine the significance of thermal nonequilibrium in predicting the onset of flow instabilities. Finally, a simplified stability criterion which can be used for preliminary estimation of the system stability boundary has been proposed.

Experimental Apparatus

The Boiling Loop. A schematic of the boiling loop that was used for this study is shown in Fig. 1. Freon-113 was chosen as the operating fluid because of its low critical pressure (34.1 bar), low boiling point (47.5°C at atmospheric pressure), and low latent heat of vaporization

---

[1] Present address: Brookhaven National Laboratory, Department of Applied Science, Upton, N. Y.

[2] Numbers in brackets designate References at end of paper.

Contributed by the Heat Transfer Division and presented at the Winter Annual Meeting, Houston, Texas, November 30–December 5, 1975, of THE AMERICAN SOCIETY OF MECHANICAL ENGINEERS. Revised manuscript received by the Heat Transfer Division August 17, 1976. Paper No. 75-WA/HT-6.

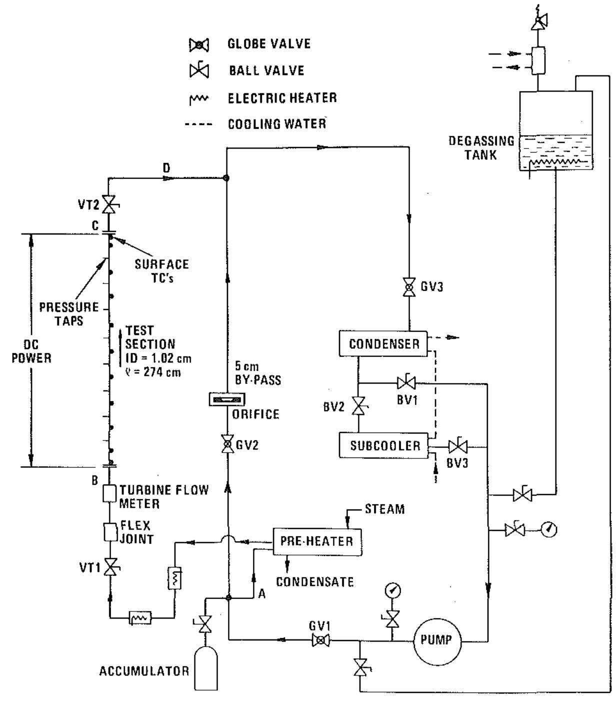

Fig. 1 Schematic of the boiling loop

(14.7 × 10^4 J/kg at atmospheric pressure). All of these features of Freon-113 led to a low capital and operating cost.

The test section is a 274.3 cm long, vertical round tube made of 304 stainless steel with outside diameter of 12.7 mm (0.5 in.) and inside diameter of 10 mm (0.402 in.). It is heated directly by a dc power supply. Because of the constant wall thickness of the tube, the heat flux is essentially uniform.

Except for the test section and a few secondary tubings, all the pipings are of standard hard drawn copper tubes of 50 mm (2 in.) and 38 mm (1½ in.) dia. A 50 mm dia bypass, fitted with a globe valve (GV2) and an orifice flowmeter, runs parallel to the test section. A preheating unit consisting of a heat exchanger heated by steam and two 1.5 kW variac-controlled electric immersion heaters regulates the liquid temperature at the inlet of the heated test section. There are two 12.7 mm (½ in.) Jamesbury ball valves (VT1 and VT2), one at the inlet and the other at the exit of the test section. The purpose of these two valves is to put desired amount of throttling at the inlet and the exit of the test section.

A degassing tank equipped with an immersion heater and a cooling coil is mounted at the top of the loop for several reasons. First, to provide sufficient NPSH for the pump; second, to accommodate volume expansion during heat addition; and third, to facilitate degassing of the test fluid after the initial charge. The pressure in the tank is kept slightly above the atmosphere. The operating range of the loop can be summarized as follows:

Pressure	up to 16.5 bar (240 psia)
Total flow rate	0–6.31 × 10^{-3} m^3/s (100 gpm)
Test section flow rate	0–0.32 × 10^{-3} m^3/s (5 gpm)
Inlet subcooling	0–110°C
Test section power	0–100 kW

The loop was not provided with a filter-dryer because there was no possibility of contaminating the Freon with water. However, it was provided with a porous filter for separating the fine solid particles, and the Freon in the loop was degassed periodically.

Loop Instrumentation. Simple instruments have been used to measure the flow rate, pressure, temperature, and power to the test section. An ITT Barton 12.7 mm (½ in.) stainless-steel turbine meter is used to measure the inlet flow through the test section. A turbine meter was chosen because of its fast response to a slight variation in flow. The output signal from the meter is fed into an ITT Barton flow indicator as well as into a Hewlett Packard two-channel strip chart recorder. The accuracy of the flow measurement is ±1 percent of the full-scale flow.

An Acco Helicoid test gauge of range 0–21.7 bar (300 psig) with an accuracy of ±0.25 percent is installed to measure the pressure at the inlet of the test section. This pressure is considered the system pressure. The pressure drops across the inlet section (between points A and B in Fig. 1) and the exit section (between points C and D in Fig. 1) of the test section assembly are measured with two ITT Barton differential pressure indicators, each having a differential pressure range of 0–1.7 bar (25 psi). A Statham differential strain-gage type pressure transducer is used to measure the pressure drop across the entire test section assembly (i.e., points A and D in Fig. 1) or any other desired length. The output from this transducer is fed into the same Hewlett-Packard strip chart recorder where the pressure drop across

Nomenclature

A_c = cross-sectional area of the channel, m^2
C_0 = void distribution parameter, $\langle \alpha j \rangle / (\langle \alpha \rangle \langle j \rangle)$
c_p = specific heat at constant pressure, J/kg—°C
D_h = hydraulic diameter, m
$D_h{}^*$ = nondimensional hydraulic diameter, D_h/ℓ
f = frequency of oscillation, cycle/s
f_f = single-phase liquid friction factor
f_m = two-phase mixture friction factor
i = specific enthalpy, J/kg
j = volumetric flux density, m/s
K = thermal conductivity, W/m—°C
k_i, k_e = inlet and exit orifice coefficient, $\Delta P/\rho v^2$
ℓ = length of the heated channel, m
$N_{\mathrm{pch,eq}}$ = equilibrium phase change number, $\Omega_{\mathrm{eq}}\ell/v_{fi}$
N_{sub} = subcooling number $(\Delta\rho/\rho_g)(\Delta i_{\mathrm{sub}}/\Delta i_{fg})$
P_s = system pressure, bar (1 bar = 10^5 N/m^2)
Pe = Peclet number $(\rho_f v_{fi} D_h c_{p,f})/K_f$
$\dot{Q}$ = net heat added to the channel, W
$\dot{q}_w{}''$ = wall heat flux, W/m^2
Re_{fs} = flow Reynolds number, $\rho_f v_{fi} D_h/\mu_f$
v = velocity, m/s
v_{fi} = velocity at the inlet of the channel, m/s
V_{gj} = vapor drift velocity, $v_g - j$, m/s
$x_{e,\mathrm{eq}}$ = exit equilibrium quality
z = axial coordinate, m
α = vapor void fraction
Γ_g = mass rate of vapor generation per unit volume, kg/m^3-s
λ = distance of the boiling boundary from the inlet, m
μ = dynamic viscosity, kg/m-s
ξ_h = heated perimeter, m
ρ = density, kg/m^3
$\Delta\rho$ = density difference between the phases, $\rho_f - \rho_g$, kg/m^3
Δi_{fg} = latent heat of vaporization, J/kg
Δi_{sub} = inlet subcooling $(i_{f,\mathrm{sat}} - i_i)$, J/kg
Δi_λ = subcooling at the point of net vapor generation $(i_{f,\mathrm{sat}} - i_\lambda)$, J/kg
ΔP = pressure drop, bar
Ω_{eq} = equilibrium frequency of phase change, $\Gamma_{g,\mathrm{eq}}\Delta\rho/(\rho_g\rho_f)$, rad/s

Subscripts

e = exit of the channel
eq = thermal equilibrium assumption
ex = external (supply) to the system
f = liquid phase
g = vapor phase
i = inlet of the channel
λ = point of net vapor generation

Special Notation

$\langle\,\rangle$ = area averaged

the chosen length can be recorded simultaneously with the test section inlet flow rate.

Copper-constantan immersion thermocouples are used to measure fluid temperature at the inlet and the exit of the heated test section. A number of copper-constantan thermocouples are attached to the outside surface of the test section. Sauereisen Insa-Lute cement was used to hold the thermocouple beads on the tube wall, and complete electrical insulation between a bead and the electrically heated test section was checked. A maximum allowable wall temperature of 400°C was set to protect the test section in the event of severe dryout. It should be noted, however, that the maximum Freon temperature during this study was only 155°C. Therefore, the problem of decomposition of Freon was not critical.

Power to the test section is measured with a voltmeter of range 0–100 V and an ammeter of range 0–1500 amps. A digital voltmeter is also used for a more accurate reading. From a number of steady-state single-phase tests, the maximum uncertainty in power measurement was found to be ±4 percent of the measured power.

Experimental Procedure and Results

The experiment was conducted in such a way that the data on the onset of flow instability could be easily plotted on the subcooling number versus the equilibrium phase change number plane introduced by Ishii and Zuber [2, 3]. For one set of data, i.e., one stability map, the system pressure, the positions of the inlet and the exit throttling valves (VT1 and VT2), and the inlet velocity through the test section (i.e., the flow Reynolds number) were kept constant. The positions of the throttling valves specify a particular system geometry. In theoretical analysis, all the equipment at the inlet of the test section (point A to B in Fig. 1) is lumped together and considered as an inlet orifice. Similarly, the exit valve VT2 is considered as an exit orifice. Due to the presence of complicated components like the immersion heater, flexible joint, turbine flowmeter, etc., it was impossible to calculate the values of inlet and exit orifice coefficients theoretically. These values were, therefore, determined experimentally. After the valves VT1 and VT2 were set at desired positions, the flow and the pressure drop excluding gravity were measured without heat addition to the test section. The values of the orifice coefficients, k_i and k_e, were then determined from

$$\Delta P_i = k_i \rho_f v_f^2 \tag{1}$$

and

$$\Delta P_e = k_e \rho_f v_f^2 \tag{2}$$

Once the system pressure, the inlet and the exit restrictions, and the inlet velocity were set, an inlet subcooling was established by adjusting the preheating system. The test section power was then increased in small steps until sustained flow oscillations were observed. Sufficient time was allowed between two successive power steps so that the true nature of the system (steady-state or oscillatory) could be understood. At the advent of two-phase mixture in the test section, the flow through the test section might change due to different pressure drop characteristics of two-phase flow. In that case, a slight adjustment of the bypass valve (GV2) was necessary to maintain the chosen flow through the test section. However, because of the high bypass to test section flow ratio (15–20), the boundary condition of constant pressure drop, which results from the steady-state flow rate, across the test section at the onset of flow instability was still maintained. This was the same as having a flat pump characteristic, i.e.,

$$\frac{\partial \Delta P_{ex}}{\partial v_{fi}} = 0 \tag{3}$$

A typical trace of the test section inlet flow with increasing power is shown in Fig. 2. It shows that the average fluctuation of the flow increases with increasing test section power. The power at the onset of flow oscillation is the power where the amplitude of flow fluctuation starts to increase rapidly (see Fig. 3). The heat loss to the surroundings is then subtracted from the test section power to obtain the actual power to the fluid at the onset of flow oscillation. The frequency of oscillation is determined from the flow trace.

To complete *one* set of experiments, data points (i.e., actual powers at the onset of flow oscillations) at various inlet subcoolings were taken. Seven such sets of experiments were conducted to study the effects of system pressure, inlet and exit restrictions, and the inlet velocity. A summary of these tests is presented in Table 1. The details can be found in [4].

General Observation

Unlike some other studies [6, 7], only one mode of sustained well-defined oscillations of significant amplitude could be detected in the present program. Attempts were made to increase the test section power well beyond the first mode of oscillation; but vigorous oscillation and, in some cases, excessively high wall temperature endangered the entire system and thus put a limit on the input power.

For any particular set, as the inlet subcooling was increased, the power corresponding to the onset of instability dropped until a certain subcooling, and started to increase thereafter. However, the time

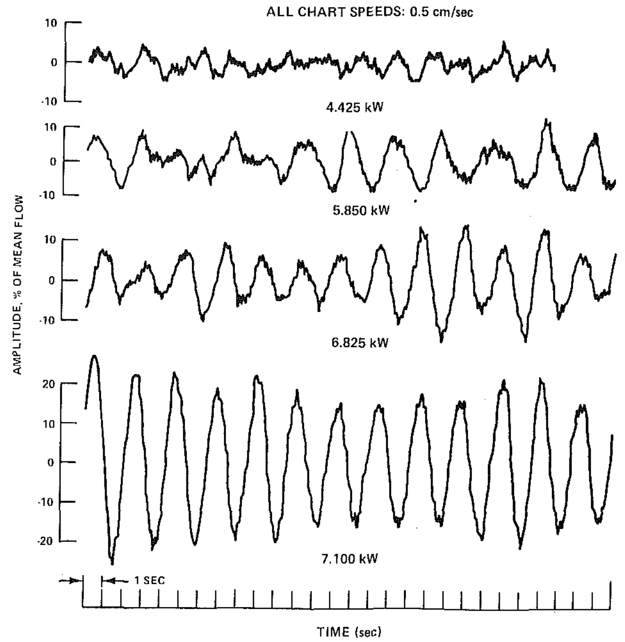

Fig. 2 A typical inlet flow trace with increasing power input (Δi_{sub} = 2.44 × 10^4 J/kg, set No. IV)

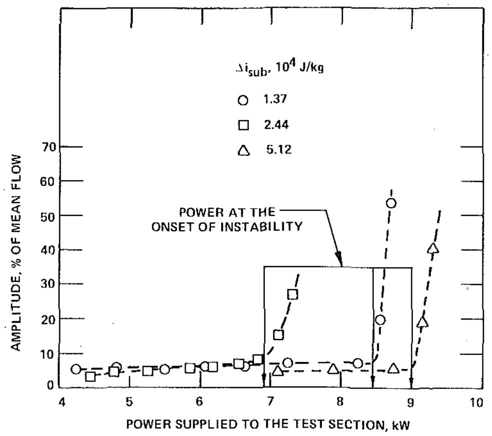

Fig. 3 Determination of the point of inception of flow instability (set No. IV)

Table 1 The Experimental Results

Set No.	Pressure (bar)	k_i	k_e	v_{fi} (m/s)	$\mathrm{Re}_{fs} \times 10^{-4}$	Δi_{sub} (10^4 J/kg)	$\dot{Q}$ (kW)	f (cycle/s)
I	12.1	2.85	2.03	0.98	5.9	1.14–5.42	4.3–9.0	0.833–0.333
II	13.8	2.85	2.03	0.94	5.9	1.81–6.44	4.3–10.3	0.448–0.324
III	10.3	2.85	2.03	1.02	5.9	0.72–4.35	4.6–7.6	0.912–0.344
IV	12.1	6.55	2.03	0.98	5.9	1.37–5.12	6.1–8.8	0.788–0.342
V	12.1	6.55	2.03	0.72	4.3	1.23–5.28	3.7–7.8	0.540–0.330
VI	12.1	6.55	2.03	1.49	8.9	1.44–5.21	9.3–15.2	0.868–0.412
VII	12.1	2.85	10.66	0.98	5.9	0.93–4.58	4.2–7.6	0.646–0.288

period of oscillation (inverse of the frequency of oscillation), which was indeed on the order of the transit time of the kinematic wave (i.e., on the order of ℓ/v_{fi}), increased monotonically with increasing inlet subcooling. These trends of input power and time period of oscillation are completely in agreement with the theories discussed later in this paper.

Significant time lag between the system (point A to D) pressure drop (*cause*) and the inlet flow (*effect*) was observed during the *unstable* operation. A typical trace is shown in Fig. 4, where the phase shift is in between 90 and 180 deg. From other traces, it was found that the inlet subcooling had no appreciable effect on the phase shift. However, it should be kept in mind that the pressure fluctuation during the stable operation and at the onset of instability was negligibly small.

Two thermocouples mounted near the exit end of the test section were monitored during the flow oscillations. No appreciable fluctuation of wall temperature could be observed at either of the two locations. This suggests that a flow oscillation does not necessarily trigger a large amplitude wall temperature oscillation in the two-phase region.

Comparison of Data With Theories

The major difference between the thermal equilibrium theory of Ishii and Zuber [2, 3] and the thermal nonequilibrium theory of Saha and Zuber [4, 5] is in the location of the boiling boundary (the boundary between the single-phase liquid region and the two-phase mixture region) and the rate of vapor generation in the mixture region. According to the equilibrium model, the distance of the boiling boundary from the inlet of the heated channel is given by

$$\lambda_{\mathrm{eq}} = \frac{\rho_f v_{fi} A_c \Delta i_{\mathrm{sub}}}{\dot{q}_w{}'' \xi_h} \tag{4}$$

and, the mass rate of vapor generation per unit volume is

$$\Gamma_{g,\mathrm{eq}} = \frac{\dot{q}_w{}'' \xi_h}{A_c \Delta i_{fg}} \tag{5}$$

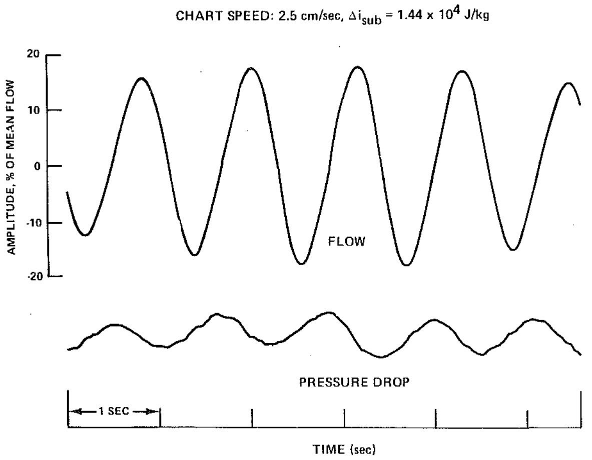

Fig. 4 Trace of inlet flow and system pressure drop (run No. OT 34, set No. VI)

According to the nonequilibrium model, the boiling boundary is the point where significant vapor generation starts and its distance from the inlet can be given by [8]

For

$$\Delta i_{\mathrm{sub}} \geq \Delta i_\lambda, \quad \lambda = \frac{\rho_f v_{fi} A_c (\Delta i_{\mathrm{sub}} - \Delta i_\lambda)}{\dot{q}_w{}'' \xi_h} \tag{6}$$

where

$$\Delta i_\lambda = 0.0022 \frac{\dot{q}_w{}'' D_h c_{p,f}}{K_f}, \quad \text{if Pe} \leq 70{,}000 \tag{7}$$

and

$$\Delta i_\lambda = 154 \frac{\dot{q}_w{}''}{\rho_f v_{fi}}, \quad \text{if Pe} \geq 70{,}000 \tag{8}$$

For

$$\Delta i_{\mathrm{sub}} \leq \Delta i_\lambda, \quad \lambda = 0 \tag{9}$$

The mass rate of vapor generation per unit volume, in the nonequilibrium theory, is taken as

$$\Gamma_g = \Gamma_{g,\mathrm{eq}} \left[1 - \exp\left\{ -\frac{z - \lambda}{\lambda_{\mathrm{eq}} - \lambda} \right\} \right] \tag{10}$$

Both the theories are, however, similar in their formulation, and assume a constant two-phase friction factor and a constant vapor drift velocity. They also neglect the effect of heat storage in the tube wall. The details of the theoretical analyses can be found in [2–5].

The data on the onset of instability for set I–III, i.e., data for various pressures, but the same inlet and exit restrictions and Reynolds number, are compared with the equilibrium and the nonequilibrium theories in Fig. 5. The simplified stability criterion of Ishii [2]:

$$N_{\mathrm{pch,eq}} - N_{\mathrm{sub}} = x_{e,\mathrm{eq}} \frac{\Delta\rho}{\rho_g} = \frac{2\left[k_i + \dfrac{f_m}{2D_h{}^*} + k_e\right]}{1 + \dfrac{1}{2}\left[\dfrac{f_m}{2D_h{}^*} + 2k_e\right]} \tag{11}$$

which is based on thermal equilibrium model and is applicable for high subcooling number ($N_{\mathrm{sub}} > \pi$) is also shown. The subcooling number, $(\Delta\rho/\rho_g)$ $(\Delta i_{\mathrm{sub}}/\Delta i_{fg})$, scales the inlet subcooling and is the dimensionless residence time of a fluid particle in the single-phase liquid region under the thermal equilibrium assumption. The inverse of the characteristic frequency of phase change under the thermal equilibrium assumption, Ω_{eq} $(\equiv \Gamma_{g,\mathrm{eq}}\Delta\rho/\rho_f\rho_g)$, is used as the scaling parameter for time. The equilibrium phase change number, $\Omega_{\mathrm{eq}}\ell/v_{fi}$, scales the rate of phase change due to heat addition and is similar to the Damkoeler group I in chemical kinetics.

In the theoretical analyses, the effect of pressure is absorbed by the nondimensional parameters, namely the subcooling number and the equilibrium phase change number. From Fig. 5 it appears that the data are indeed scattered around one single stability boundary. However, it should be noted that the exit quality corresponding to a particular value of equilibrium phase change number increases with increasing pressure. Both the theories and the data show same general trend. However, at low subcooling region, the nonequilibrium theory predicts results which are in close agreement with the experimental stability boundary. In this region where $\Delta i_{\mathrm{sub}} < \Delta i_\lambda$, there is no single-phase liquid region, i.e., there is no time delay in the single phase

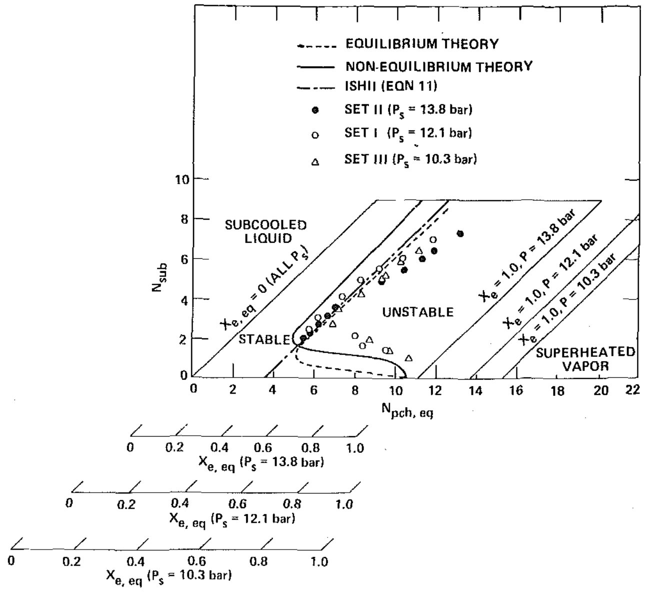

Fig. 5 The effect of system pressure, and comparison of data with various theories, with $k_i = 2.85$, $k_e = 2.03$, $Re_{fs} = 5.9 \times 10^4$, and $f_m = 2f_f$

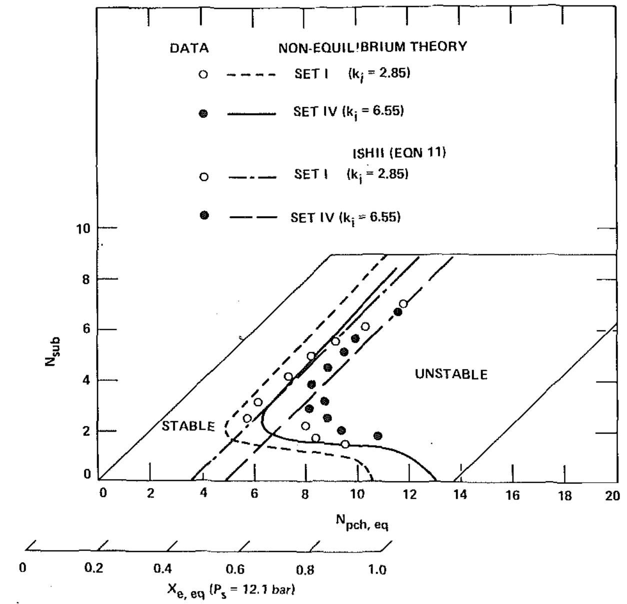

Fig. 7 The effect of inlet restrictions, with $k_e = 2.03$, $Re_{fs} = 5.9 \times 10^4$, and $f_m = 2f_f$

region and no fluctuation of boiling boundary. This results in a more stable system as predicted by the nonequilibrium theory. As the subcooling number is increased beyond a critical value, the single-phase liquid region appears and the system becomes less stable. It can be seen from Fig. 5 that in this region the nonequilibrium theory predicts a less stable system than the equilibrium theory and is conservative with respect to the data on the onset of instability. However, the importance of the nonequilibrium model becomes visible from Fig 6, where the data on the frequency of oscillation, f, are compared with the theoretical predictions.

The effects of inlet and exit restrictions are shown in Fig. 7 and Fig. 8, respectively. As the inlet throttling is increased, the data as well as the theories indicate a more stable system because a larger fraction of the system pressure drop is now in phase with the inlet velocity. The converse should be true for exit restriction. However, from the data shown in Fig. 8, it appears that the system becomes less stable with the increasing exit restriction only at low subcooling number.

The effect of inlet velocity is shown in Fig. 9. Although the data show a significant dependence on inlet velocity, the theories, at present, cannot predict such dependence. Further studies, possibly with variable two-phase friction factor and variable vapor drift velocity, are required to ascertain the observed effect of inlet velocity on the system stability.

One common feature can be observed from all seven sets of data presented here. As the subcooling number is increased beyond a critical value, the experimental stability boundary bends toward the right-hand side from a constant equilibrium exit quality line. This is in contrast with the theoretical predictions which remain almost parallel to a constant equilibrium exit quality line. In the theories, the value of the void distribution parameter, C_0 [9], defined as

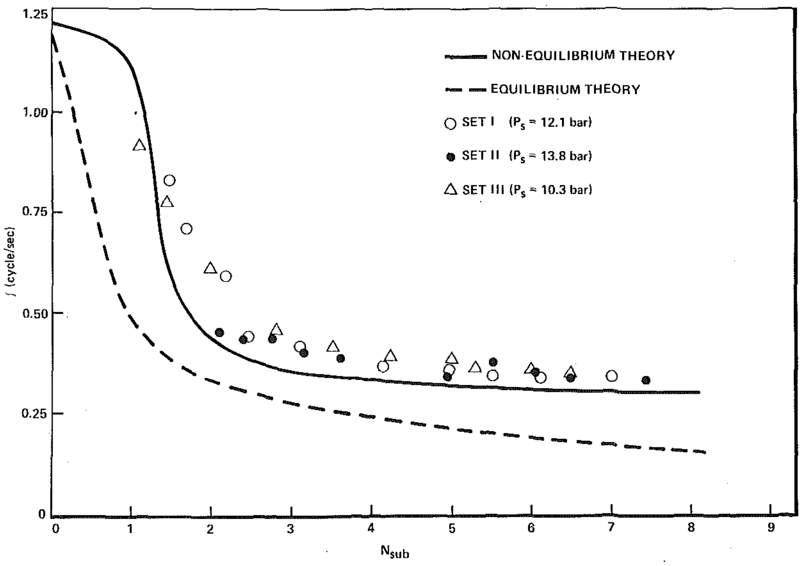

Fig. 6 Comparison of experimental data on the frequency of oscillation with various theoretical predictions

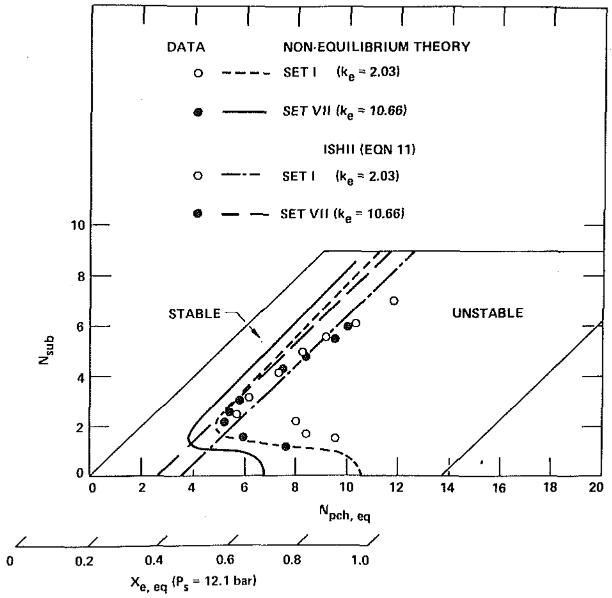

Fig. 8 The effect of exit restrictions, with $k_i = 2.85$, $\text{Re}_{fs} = 5.9 \times 10^4$, and $f_m = 2f_f$

$\langle \alpha j\rangle/(\langle\alpha\rangle\langle j\rangle)$, is taken as one and the vapor drift velocity for the bubbly churn turbulent flow is used irrespective of the flow regime. In actual system, however, the value of the distribution parameter is usually greater than one [8, 9], and in annular flow regime the relative velocity between the phases can be much higher than what is accounted for in the theories. These aspects of the actual system lead to a lower void fraction, i.e., a higher mixture density, which has a stabilizing effect. This provides a possible explanation for the discrepancy in the trends of the data and the theories at high subcooling number.

Simplified Stability Criterion

From the previous section, it is apparent that at high subcooling number, the simplified criterion of Ishii (equation (11)) can be used

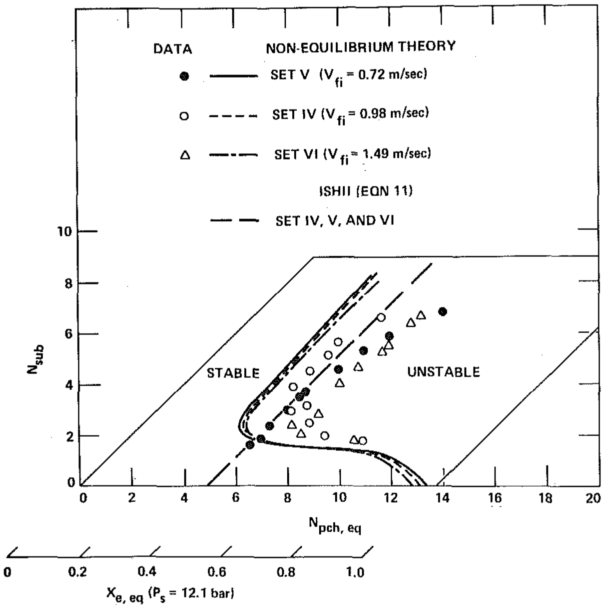

Fig. 9 The effect of inlet velocity, with $k_i = 6.55$, $k_e = 2.03$, and $f_m = 2f_f$

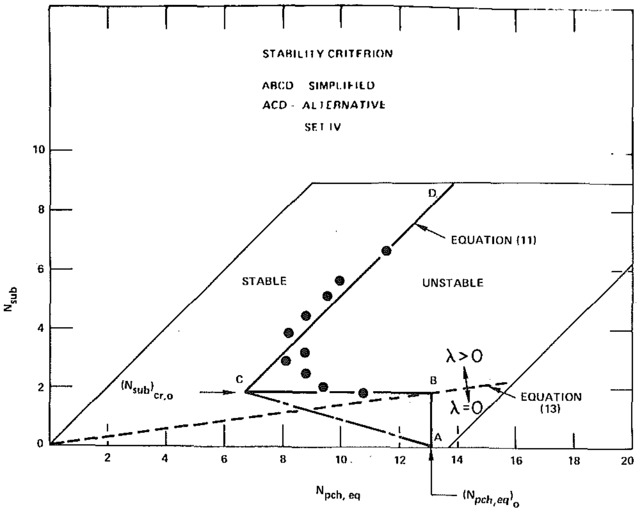

Fig. 10 Construction of the simplified stability criterion

for preliminary estimation of the stability boundary. However, a *simplified criterion applicable to the low subcooling number is still* required. It has been shown that the nonequilibrium theory predicts the data at low subcooling number much better than the equilibrium theory, and from equation (9), the vapor generation starts from the inlet of heated channel until the subcooling number exceeds a critical value of $(\Delta\rho/\rho_g)(\Delta i_\lambda/\Delta i_{fg})$. Applying the criteria for the point of net vapor generation (equations (7) and (8)), one can express this critical number by

$$(N_{\rm sub})_{\rm cr} = 0.0022\,{\rm Pe}\,\frac{A_c}{\xi_h \ell}\,N_{\rm pch,eq} \quad \text{if Pe} \le 70{,}000 \tag{12}$$

and

$$(N_{\rm sub})_{\rm cr} = 154\,\frac{A_c}{\xi_h \ell}\,N_{\rm pch,eq} \quad \text{if Pe} \ge 70{,}000 \tag{13}$$

It is found that once the stability criterion corresponding to the zero subcooling, i.e., $(N_{\rm pch,eq})_0$, is determined from the equilibrium or the nonequilibrium theory, a simple stability boundary can be constructed (see Fig. 10). It consists of three parts:

1 A constant equilibrium phase change number $(N_{\rm pch,eq})_0$ for $N_{\rm sub} < (N_{\rm sub})_{\rm cr,0}$, i.e., the part AB.

2 A constant subcooling number $(N_{\rm sub})_{\rm cr,0}$, i.e., the part BC.

3 A *constant equilibrium exit quality line, equation* (11), *for* $N_{\rm sub} > (N_{\rm sub})_{\rm cr,0}$, i.e., the part CD.

An alternative, and a more conservative, stability boundary for $N_{\rm sub} < (N_{\rm sub})_{\rm cr,0}$ could be the straight line AC, as shown in Fig. 10.

Summary and Conclusions

New experimental data on the onset of so-called density wave oscillations and their frequency of oscillations have been presented. Significant time lag between the system pressure drop and the inlet flow was observed during the unstable operation.

When compared with the thermal equilibrium and the thermal nonequilibrium theories, the data on the onset of instability at low subcooling number and the data on the frequency of oscillation show better agreement with the nonequilibrium theory. This success of the nonequilibrium theory is primarily due to a more realistic description of the boiling boundary. The discrepancy between the trend of the theories (equilibrium as well as nonequilibrium) and the data on the onset of instability at high subcooling number is believed to be due to a higher value of the void distribution parameter, C_0, and a higher relative velocity in the actual system. Further work is needed in this area.

The effects of system pressure and inlet and exit restrictions are well predicted by the theories. However, further studies are necessary to ascertain the observed effect of the inlet velocity.

A simplified stability criterion for low subcooling number has been proposed which can be used for a preliminary estimation of the system stability boundary along with the simplified criterion of Ishii (equation (11)) for high subcooling number.

Acknowledgments

The study was sponsored by the National Science Foundation under grant number GK-16023 and was carried out in the School of Mechanical Engineering, Georgia Institute of Technology, Atlanta, Georgia.

References

1 Bouré, J. A., Bergles, A. E., and Tong, L. S., "Review of Two-Phase Flow Instability," ASME Paper No. 71-HT-42.

2 Ishii, M., "Thermally Induced Flow Instabilities in Two-Phase Mixtures in Thermal Equilibrium," PhD thesis, School of Mechanical Engineering, Georgia Institute of Technology, Atlanta, Ga., June 1971.

3 Ishii, M., and Zuber, N., "Thermally Induced Flow Instabilities in Two-Phase Mixtures," Paper No. B5.11, 4th International Heat Transfer Conference, Paris, 1970.

4 Saha, P., "Thermally Induced Two-Phase Flow Instabilities Including the Effect of Thermal Non-Equilibrium Between the Phases," PhD thesis, School of Mechanical Engineering, Georgia Institute of Technology, Atlanta, Ga., June 1974.

5 Saha, P., and Zuber, N., "An Analytical Study of the Thermally Induced Two-Phase Flow Instabilities Including the Effect of Thermal Nonequilibrium," submitted for publication in the *International Journal of Heat and Mass Transfer.*

6 Yadigaroglu, G., and Bergles, A. E., "Fundamentals and Higher-Mode Density-Wave Oscillations in Two-Phase Flow," JOURNAL OF HEAT TRANSFER, TRANS. ASME, Series C, Vol. 94, 1972, pp. 189-195.

7 Harvie, J. D., "An Experimental Investigation of Flow Instability in Freon-12 and Comparison with Water Data," Paper No. E1, Multi-Phase Flow Systems: A Symposium at the University of Strathclyde, Glasgow, Scotland, Apr. 1974.

8 Saha, P., and Zuber, N., "Point of Net Vapor Generation and Vapor Void Fraction in Subcooled Boiling," *Heat Transfer 1974,* Proceedings of the 5th International Heat Transfer Conference, Vol. IV, 1974, pp. 175-179.

9 Zuber, N., and Findlay, J. A., "Average Volumetric Concentration in Two-Phase Flow Systems," JOURNAL OF HEAT TRANSFER, TRANS. ASME, Series C, Vol. 87, 1965, pp. 453-468.

R. L. Judd
Assoc. Professor.

K. S. Hwang
Research Assistant.

McMaster University,
Hamilton, Ontario, Canada

A Comprehensive Model for Nucleate Pool Boiling Heat Transfer Including Microlayer Evaporation

The results of an experimental investigation are presented in which dichloromethane (methylene chloride) boiling on a glass surface was studied using laser interferometry and high-speed photography. New data for active site density, frequency of bubble emission, and bubble departure radius were obtained in conjunction with measurements of the volume of microlayer evaporated from the film underlying the base of each bubble for various combinations of heat flux and subcooling. These results were used to support a model for predicting boiling heat flux incorporating microlayer evaporation, natural convection, and nucleate boiling mechanisms. Microlayer evaporation heat transfer is shown to represent a significant proportion of the total heat transfer for the range of heat flux and subcooling investigated.

Introduction

In recent years, considerable effort has been devoted to evaluation of the microlayer evaporation phenomenon in which energy is transferred from a nucleate boiling heat-transfer surface by evaporation of a thin layer of liquid at the base of each of the bubbles formed on the surface. Moore and Mesler [1][1] originally deduced the existence of the microlayer from observations of rapid fluctuations in the temperature of a surface on which bubbles were being generated; they postulated that the temperature fluctuations were indicative of rapid variations in surface heat flux in response to the evaporation of a thin film of liquid at the base of each bubble. This explanation of the temperature fluctuations was indirectly supported by the work of Rogers and Mesler [2] and Hendricks and Sharp [3], who determined experimentally that decreasing surface temperature was associated with the interval during which a bubble was present, whereas increasing surface temperature was associated with the interval during which the nucleation site was unoccupied. Further indirect evidence of the existence of the microlayer was provided by Cooper and Lloyd [4,5], who measured the variation of surface temperature with time at a number of locations beneath an arbitrarily initiated bubble, computed the spatial distribution of surface heat flux, and deduced the thickness of the microlayer that must have evaporated by an analysis of the enthalpy extracted from the heat-transfer surface over the lifetime of the bubble.

The first direct evidence of the existence of the microlayer was provided by Sharp [6], who used interferometry to observe the formation, evaporation, and dryout of a thin film of liquid underlying vapor bubbles generated on a boiling heat-transfer surface. Hospeti and Mesler [7] substantiated this observation by reporting on the deposition of material suspended in a boiling solution in the vicinity of the nucleation site, presumably as a result of evaporation and dryout of a liquid film. Jawurek [8] performed an interferometric study somewhat similar to that of Sharp in which interferometry and high-speed photography were combined to determine instantaneous microlayer thickness as a function of radius and time.

A number of investigators contributed to the evaluation of the microlayer evaporation phenomenon by demonstrating the necessity of including microlayer evaporation in the analysis of bubble growth. Cooper [9] was the first to present a theory for predicting the rate of growth of a bubble in saturated boiling conditions that incorporated the microlayer evaporation phenomenon; the predictions of the analysis agreed reasonably well with the results of experiments for various fluids under conditions for which the assumptions were approximately valid. In addition, the theory permitted determination of the conditions under which microlayer evaporation might be expected to have a significant effect on bubble growth. Van Ouwerkerk [10] reformulated the problem, eliminating some of the approxima-

---

[1] Numbers in brackets designate References at end of paper.

Contributed by the Heat Transfer Division for publication in the JOURNAL OF HEAT TRANSFER. Manuscript received by the Heat Transfer Division June 23, 1976.

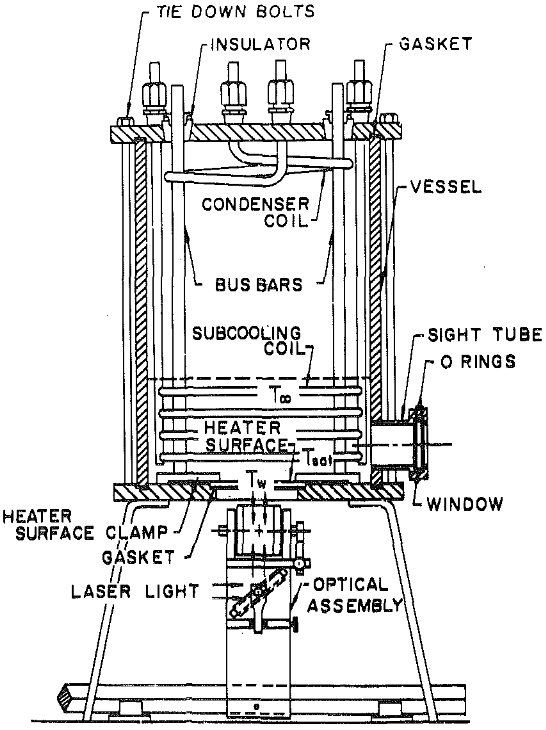

Fig. 1 Test assembly

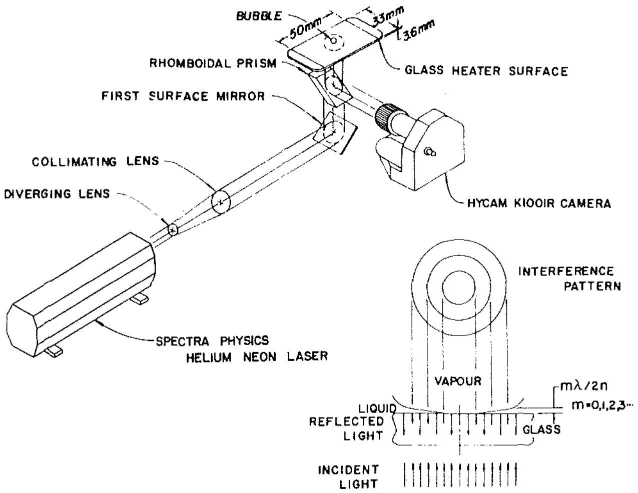

Fig. 2 Schematic representation of interferometer

tions contained in the previous analysis, and showed that Cooper's relationship for bubble growth rate was inexact except in extreme cases. Subsequently Cooper and Merry [11] presented a general expression for the rate of evaporation of a liquid layer on a solid body, free of the simplifying assumptions associated with the previous analyses, and applied this theory to the analysis of bubble growth rate. In comparing the results of the analyses above with experimental results, microlayer evaporation considerations were essential under certain conditions, thereby attesting to the existence of the microlayer evaporation phenomenon.

However, none of the references cited previously addresses the significance of microlayer evaporation heat transfer to the total boiling heat-transfer process, and therefore the contribution of Graham and Hendricks [12] is particularly noteworthy in this regard. The boiling heat-transfer model which these authors proposed and verified with the data available when the model was formulated combined time and surface-averaged values of a transient thermal conduction mechanism involving the thermal layer that formed at the nucleation sites between periods of bubble nucleation, a turbulent natural convection mechanism taking place in the regions uninvolved in bubble nucleation, and a microlayer evaporation mechanism occurring at the nucleation sites while bubbles were present. Experimental verification of the Graham and Hendricks model showed how combination of the three mechanisms mentioned above could adequately predict the surface-averaged boiling heat flux. The purpose of this paper is to further investigate the mechanisms of boiling heat transfer and to evaluate the significance of microlayer evaporation heat transfer to the total boiling heat-transfer process at various levels of heat flux and subcooling.

Experimental Investigation

In similarity to the investigation reported in Voutsinos' recently completed thesis [13], dichloromethane (methylene chloride) was boiled on a borosilicate glass heater surface coated with a half-wavelength thickness of stannic oxide which conducted electric current and generated heat, causing the liquid to boil. The glass heater surface, the test vessel, and the associated equipment are depicted in Fig. 1. A schematic representation of the laser interferometer and high-speed camera used to record the instantaneous variation of the liquid film underlying the bubbles forming on the transparent heater surface is presented in Fig. 2. The procedure used was identical to that described by Voutsinos and Judd [14]; boiling taking place at randomly located naturally occurring nucleation sites in the stannic oxide coating was observed in a region near the center of the glass heater surface. Each experiment comprised a number of tests at different levels of heat flux under saturated and subcooled boiling conditions. During each test, the pressure in the test vessel was maintained constant at approximately one-half atm in order to decrease the number of active nucleation sites and to increase the size of the vapor bubbles. Surface and liquid temperature measurements made with thermocouples attached to the underside of the glass heater surface and located approximately 25 mm above the glass heater surface were obtained after test conditions had been established and maintained

Nomenclature

A_T = heater surface area
A_{NC}/A_T = area fraction devoted to natural convection
C_l = liquid specific heat
f = frequency of bubble emission
g = gravitational constant
h_{fg} = latent heat
k_l = liquid thermal conductivity
K = constant
N/A_T = active site density
(q/A) = heat flux existing within area of influence
q_M/A_T = measured heat flux
q_{NB}/A_T = nucleate boiling component of predicted heat flux
q_{NC}/A_T = natural convection component of predicted heat flux
q_{ME}/A_T = microlayer evaporation component of predicted heat flux
q_P/A_T = predicted heat flux
r = radius
t = time
$(T_w - T_\infty)$ = temperature difference
$(T_w - T_{sat})$ = superheat
$(T_{sat} - T_\infty)$ = subcooling
V_{ME} = volume of microlayer evaporated
β = volumetric coefficient of expansion
$\delta_0(r)$ = initial microlayer thickness
$\delta(r, t)$ = instantaneous microlayer thickness
μ_l = liquid viscosity
ρ_l = liquid density
τ = departure time

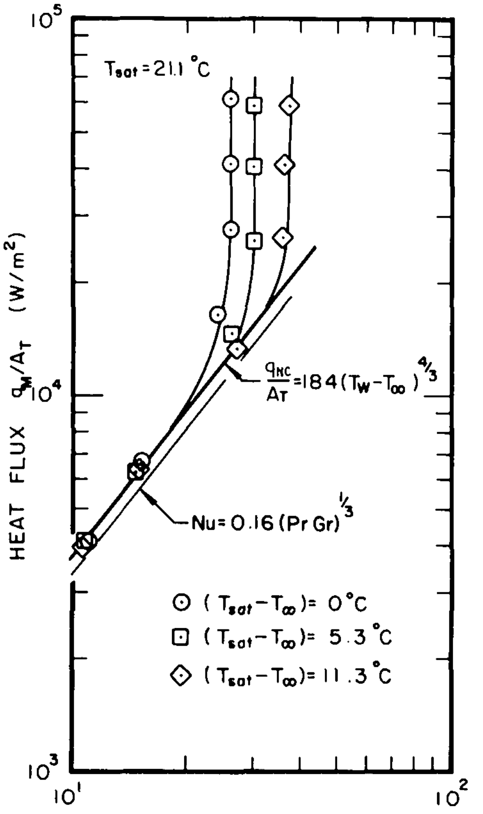

Fig. 3 Characteristic boiling curves

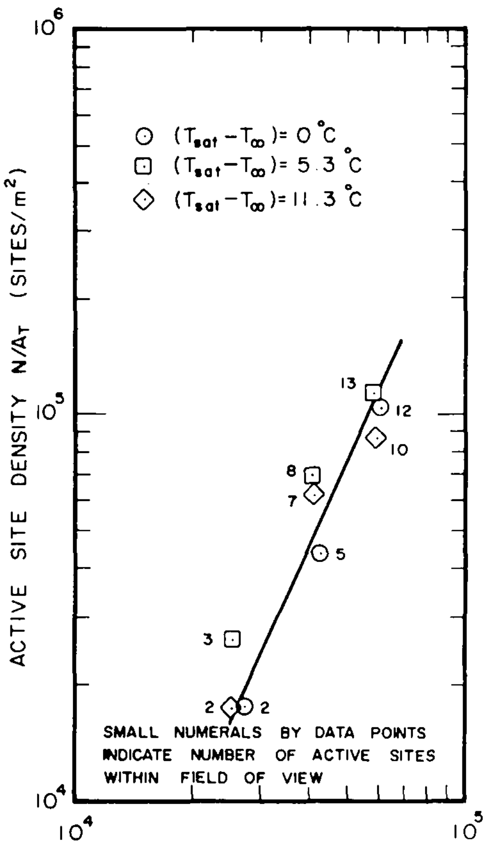

Fig. 4 Active site density results

constant for approximately 5 min, after which a length of Kodax 2X film was exposed at a normal 4000 frames/s framing rate.

Data Analysis

A complete set of temperature measurements and high-speed motion-picture film was obtained for dichloromethane boiling at a pressure of one-half atm ($T_{sat} = 21.1$°C) for three different levels of heat flux at each of three levels of subcooling. The thermometric data obtained are presented in Fig. 3, in which the measured heat flux q_M/A_T has been plotted as a function of the temperature difference $(T_w - T_\infty)$. Although this is not the customary manner in which to present boiling data, this procedure has the advantage of clearly delineating the subcooling effect, inasmuch as each curve which diverges from the straight line corresponding to $q_{NC}/A_T = 184\,(T_w - T_\infty)^{4/3}$ represents a different level of subcooling, as indicated. Despite the marked increase of temperature difference with increasing subcooling, the heater surface superheat remained essentially invariant within the range of test conditions investigated; the increase in $(T_w - T_\infty)$ was precisely accounted for by the increase in $(T_{sat} - T_\infty)$, implying that $(T_w - T_{sat})$ remained constant. However, this interrelationship between $(T_{sat} - T_\infty)$ and $(T_w - T_{sat})$ is only valid for relatively small values of subcooling, inasmuch as Judd and Merte [15] and Wiebe and Judd [16], among others, have shown that superheat generally decreases with increasing subcooling at constant heat flux once subcooling becomes sufficiently great. At low enough values of heat flux, superheat can even become negative, in which case nucleate boiling ceases entirely and the total heat load is carried by natural convection alone.

The films obtained were sufficiently detailed to permit simultaneous measurement of active site density, frequency of bubble emission, and bubble departure radius, as well as the time-dependent variation of the thickness of the microlayer and the area of the dry spot underlying the bubble. Fig. 4 depicts the variation of active site density N/A_T as a function of the measured heat flux q_M/A_T. Inasmuch as site activation is primarily governed by superheat, in accordance with the findings of Griffith and Wallis [17] and Shoukri and Judd [18], it is not surprising that active site density appears to be independent of subcooling in the present investigation, considering of the lack of dependence between superheat and subcooling discussed above. However, by studying Fig. 3 it can be deduced that superheat increases slightly with increasing heat flux, sufficient to account for the significant increase in active site density with increasing heat flux seen in Fig. 4.

Fig. 5 presents the variation in bubble emission frequency f, while Fig. 6 depicts the variation in bubble flux density $(N/A_T)f$ obtained by multiplying active site density and frequency of bubble emission as a function of measured heat flux q_M/A_T and subcooling $(T_{sat} - T_\infty)$. The same subcooling effect observed in Fig. 5 is observed in Fig. 6 as well. It is reasonable to assume that this effect will reverse as subcooling increases beyond the range of subcooling investigated in this investigation, since the formation of vapor bubbles will cease at sufficiently great levels of subcooling, as discussed above, in which case bubble flux density must tend toward zero. The bubble departure radius R_b, the maximum radius attained by the bubble before lifting off the surface, has been plotted against measured heat flux q_M/A_T in Fig. 7. At each level of subcooling $(T_{sat} - T_\infty)$ investigated, bubble departure radius decreases with increasing heat flux as the active nucleation sites per unit area become more numerous.

The average volume of microlayer evaporated $\overline{V}_{ME}$ is presented in Fig. 8 as a function of the measured heat flux q_M/A_T. The techniques outlined by Voutsinos and Judd [14] in which instantaneous microlayer profiles $\delta(r, t)$ were plotted for each bubble examined permitting the initial microlayer thickness profile $\delta_0(r)$ to be located, were used in this investigation as well. The volume of microlayer evaporated for

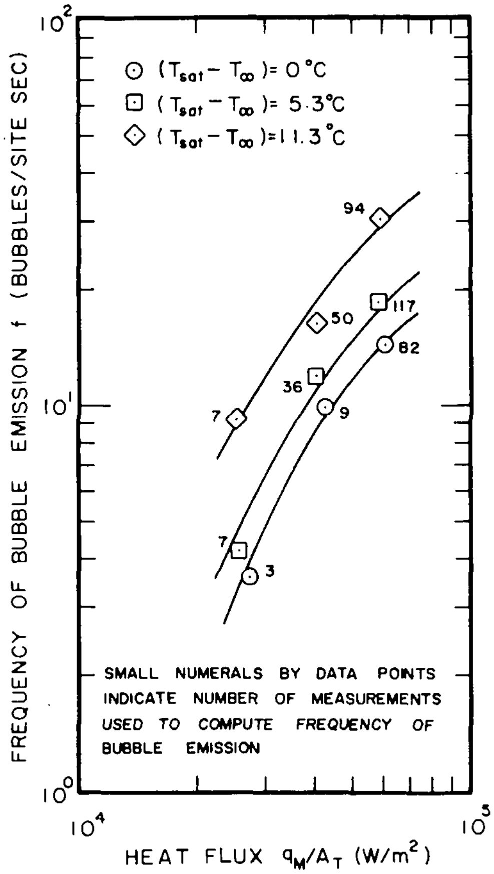

SMALL NUMERALS BY DATA POINTS INDICATE NUMBER OF MEASUREMENTS USED TO COMPUTE FREQUENCY OF BUBBLE EMISSION

Fig. 5 Bubble emission frequency results

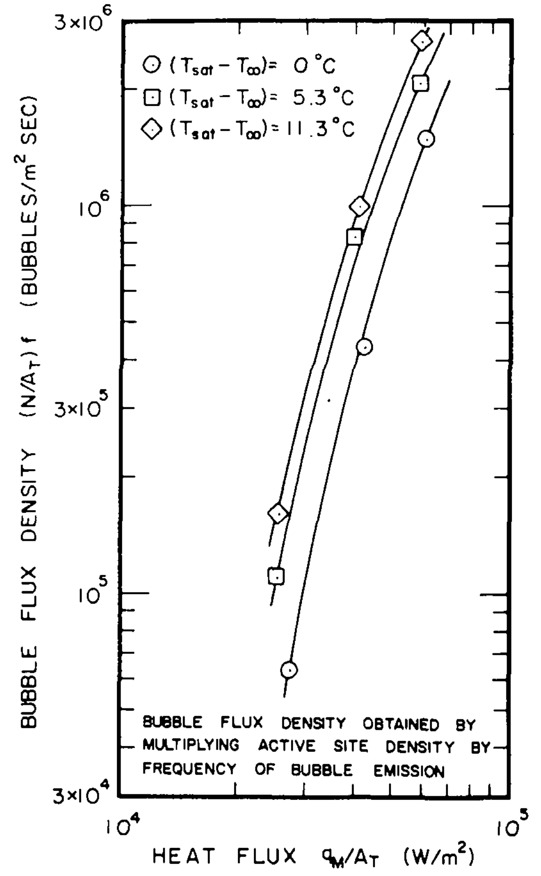

BUBBLE FLUX DENSITY OBTAINED BY MULTIPLYING ACTIVE SITE DENSITY BY FREQUENCY OF BUBBLE EMISSION

Fig. 6 Bubble flux density results

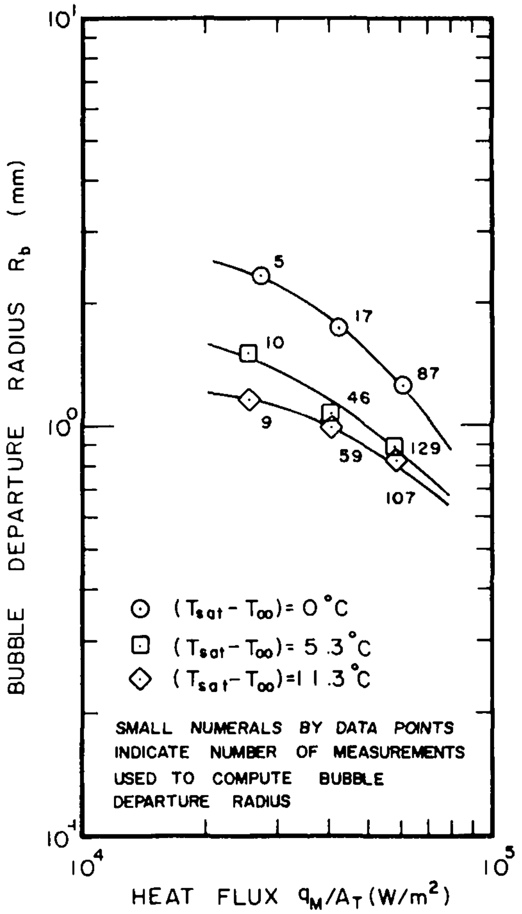

SMALL NUMERALS BY DATA POINTS INDICATE NUMBER OF MEASUREMENTS USED TO COMPUTE BUBBLE DEPARTURE RADIUS

Fig. 7 Bubble departure radius results

each bubble examined was determined by integration according to the relationship

$$V_{ME} = 2\pi \int_0^{R_b} [\delta_0(r) - \delta(r, \tau)] r\, dr \quad (\mathrm{m}^3) \qquad (1)$$

where $\delta(r, \tau)$ represents the instantaneous microlayer profile at the instant of departure $t = \tau$. The average volume of microlayer evaporated $\overline{V}_{ME}$ was obtained by averaging the results for a number of bubbles selected from each of the active sites on the boiling surface within the field of view of the high-speed camera. Because there was considerable variability among the bubbles examined insofar as the size of the bubble and the volume of the microlayer evaporated were concerned, sufficient independent estimates of the volume of the microlayer evaporated had to be included in the average to produce a value that was representative of the bubbles forming within the field of view of the high-speed camera; it is thought that the value obtained is representative of the entire surface as well.

The rate of heat transfer by microlayer evaporation q_{ME}/A_T obtained by multiplying the average energy transferred per bubble due to microlayer evaporation $\rho_l h_{fg} \overline{V}_{ME}$ by the bubble flux density $(N/A_T)f$

$$q_{ME}/A_T = \rho_l h_{fg} (N/A_T)\, f\, \overline{V}_{ME}$$
$$= 4.35 \times 10^8\, (N/A_T)\, f\, \overline{V}_{ME} \qquad (\mathrm{W/m^2}) \quad (2)$$

has been plotted in Fig. 9 as a function of the measured heat flux q_M/A_T. The single test result reported previously [14] can be seen to be in excellent agreement with the results of the present investigation. The results presented in Voutsinos' thesis [13], which are not thought to be as reliable as the results of the present investigation, are seen to be in good agreement as well. Furthermore, a very curious obser-

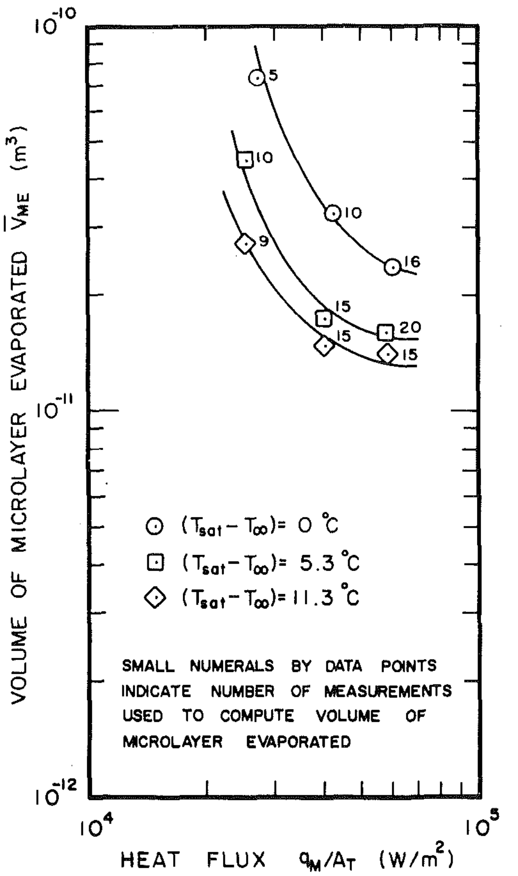

Fig. 8 Average volume of microlayer evaporated

vation is seen in connection with the correlation of the results, inasmuch as subcooling appears to have no influence on the rate of heat transfer by microlayer evaporation. The decrease in the average volume of microlayer evaporated resulting from increasing subcooling appears to have been exactly compensated by the increase in frequency of bubble emission, so that the average volume of microlayer evaporated per site per unit time obtained by multiplying the average volume of microlayer evaporated by the frequency of bubble emission appears to be independent of subcooling. Since active site density is independent of subcooling as well, the rate of heat transfer by microlayer evaporation computed by the equation above also appears to be independent of subcooling. As already pointed out in connection with the discussion of bubble flux density, the behavior observed must be considered to be restricted to the range of subcooling investigated; ultimately bubble flux density will decrease with increasing subcooling, and since the average volume of microlayer evaporated monotonically decreases with increasing subcooling, the rate of heat transfer by microlayer evaporation must decrease with increasing subcooling as well.

The reason for the observations reported above, particularly the apparent insensitivity of the rate of heat transfer by microlayer evaporation to changing levels of subcooling, is not obvious. It may be of some significance that in this particular investigation superheat was also independent of subcooling. However, it is most likely that the behavior observed was governed by the interaction of the various mechanisms of heat transfer adjusting to carry the total heat load in response to changes in heat flux and subcooling, in which case the observed effect of subcooling on the rate of heat transfer by microlayer evaporation has no particular significance. This point requires further study and may form the subject of a subsequent paper. A theoretical model incorporating three interrelated mechanisms of heat transfer (microlayer evaporation, natural convection, and nucleate boiling) similar to that proposed by Graham and Hendricks [12] will be developed in the next section in an attempt to demonstrate the self-consistency of the measurements presented above.

Boiling Heat-Transfer Model

Consider a predicted heat flux q_P/A_T to be comprised of three components: a microlayer evaporation component q_{ME}/A_T, a natural convection component q_{NC}/A_T, and a nucleate boiling component q_{NB}/A_T. The components are envisaged as acting independently within specific regions of influence, as depicted schematically in Fig. 10, which portrays a section of heat-transfer surface. By virtue of the action of vortex rings formed in the wake of departing bubbles, nucleate boiling is assumed responsible for the transport of energy from the heat-transfer surface to the surrounding liquid by displacement of a portion of the superheated layer contained within an area of influence surrounding the nucleation site that formed after the departure of the preceding bubble. Further, during the formation and growth of the bubbles a microlayer is assumed to have formed, thus permitting additional energy transfer from the heat-transfer surface by microlayer evaporation. Although these mechanisms occur within the same region of influence, the heat transfer associated with the displacement of the superheated layer occurs in the interval after the bubble has departed from the heat-transfer surface, whereas the heat transfer associated with microlayer evaporation occurs in the interval during which the bubble is growing at the nucleation site. In this way the two mechanisms complement each other. Natural convection is assumed to occur in those regions uninvolved in the formation and growth of bubbles.

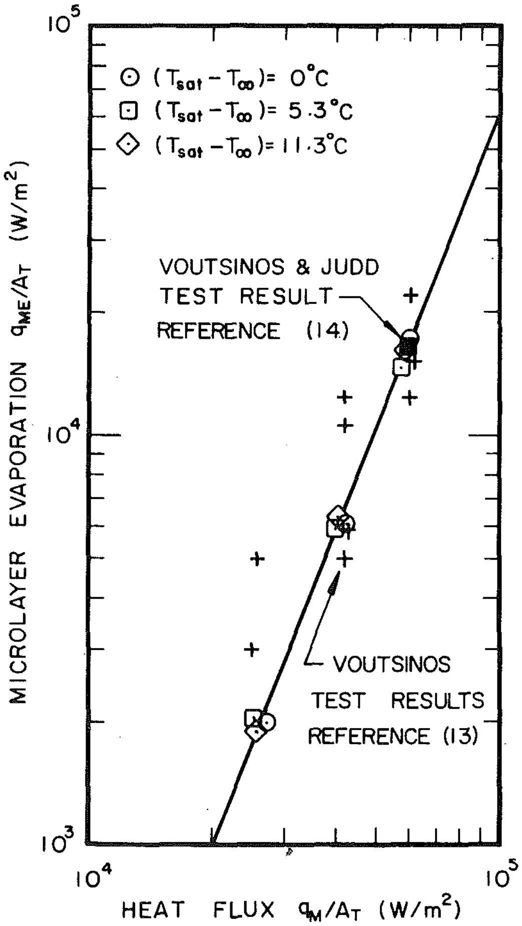

Fig. 9 Microlayer evaporation heat-transfer correlation

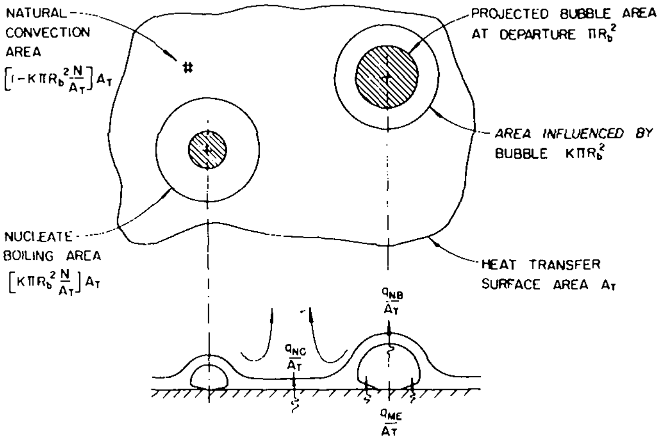

Fig. 10 Schematic representation of boiling heat-transfer model

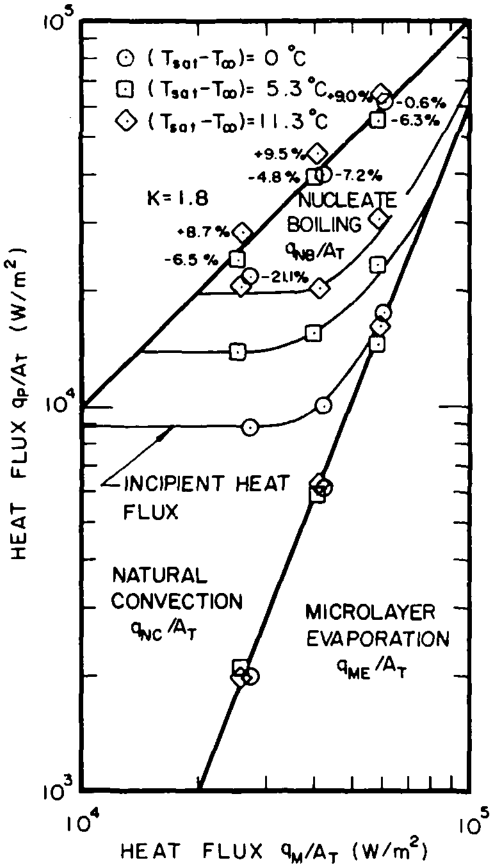

Fig. 11 Verification of boiling heat-transfer model

The microlayer evaporation component q_{ME}/A_T will be computed by equation (2), as represented in Fig. 9. The natural convection component q_{NC}/A_T will be predicted by a relationship in which heat transfer by natural convection (q_{NC}/A_{NC}) is multiplied by a ratio representing the portion of the surface not involved in nucleate boiling and microlayer evaporation $[1 - K\pi R_b{}^2(N/A_T)]$

$$q_{NC}/A_T = (q_{NC}/A_{NC})\,(A_{NC}/A_T)$$
$$= 0.18\,k_l \left[\left(\frac{g\beta\rho_l{}^2}{\mu_l{}^2}\right)\left(\frac{\mu_l C_l}{k_l}\right)\right]^{1/3} (T_w - T_\infty)^{4/3}\,(A_{NC}/A_T)$$
$$= 184\,(T_w - T_\infty)^{4/3}\,[1 - K\pi R_b{}^2(N/A_T)] \quad (\mathrm{W/m^2}) \quad (3)$$

Using a Mikic and Rohsenow [19] formulation in which the nucleate boiling heat transfer is obtained by multiplying the average heat flux resulting from the extraction of energy from the heat-transfer surface to form the superheated layer (q/A) by a ratio representing the portion of the surface involved in nucleate boiling and microlayer evaporation $[K\pi R_b{}^2(N/A_T)]$

$$q_{NB}/A_T = K\pi R_b{}^2(N/A_T)\,(q/A) = 2\sqrt{\pi}\,\sqrt{\rho_l C_l k_l}\,KR_b{}^2\sqrt{f}(N/A_T)$$
$$\times\,(T_w - T_\infty) = 1543\,KR_b{}^2\sqrt{f}(N/A_T)\,(T_w - T_\infty) \quad (\mathrm{W/m^2}) \quad (4)$$

In each of the equations above, K is a parameter greater than unity relating the area of influence around a nucleation site from which energy is transported by nucleate boiling to the projected bubble area at departure.

Summing equations (2), (3), and (4) yields the relationship

$$q_P/A_T = 4.35 \times 10^8\,(N/A_T)\,f\,\overline{V}_{ME}$$
$$+\,184(T_w - T_\infty)^{4/3}\,[1 - K\pi R_b{}^2(N/A_T)]$$
$$+\,1543\,KR_b{}^2\sqrt{f}(N/A_T)\,(T_w - T_\infty) \quad (\mathrm{W/m^2}) \quad (5)$$

in which K is the only unknown, since all of the other parameters have been obtained by experimental measurements.

Verification of equation (5) using the measurements reported in the previous section is presented in Fig. 11. Each component of the equation (microlayer evaporation, natural convection, and nucleate boiling) is identified separately. Note that at each level of subcooling $(T_{sat} - T_\infty)$ the sum of the three components representing the predicted heat flux q_P/A_T closely approaches the measured heat flux q_M/A_T, with a discrepancy of the order of ± 10 percent. Han and Griffith [20] deduced from experimental observations that a sphere departing from the bottom of a tank of water induced flow toward the vortex ring forming in the wake of the sphere within a circle twice the diameter of the sphere. Should this observation be applicable to bubbles departing from a heat-transfer surface, it is implied that the area of influence is four times the projected area of the bubble at departure. Substitution of $K = 4$ into equation (5) would have caused the predicted heat flux to exceed the measured heat flux by a considerable margin; $K = 1.8$ resulted in the best fit when all of the data were considered. It is not unreasonable to imagine that while a departing bubble might influence flow over a considerable area, only that portion of the thermal layer contained within the area of influence would be transported into the surrounding fluid, as the results of the present investigation seem to indicate.

Conclusions

The results of the present investigation comprise a comprehensive set of measurements which substantiates a model for predicting boiling heat flux incorporating microlayer evaporation, natural convection, and nucleate boiling mechanisms. Microlayer evaporation heat transfer is a prominent feature of this model, accounting for one-third of the total heat transfer at the greatest level of heat flux investigated, although it would seem to be independent of subcooling. The relative proportions of natural convection and nucleate boiling vary, but the sum of the three components closely approximates the total heat transfer for each combination of heat flux and subcooling.

Acknowledgment

The authors wish to acknowledge the efforts of Mr. Stephen Lane, who obtained the experimental results. The support of the National Research Council of Canada through grant A 4362 is also gratefully acknowledged.

References

1 Moore, F. D., and Mesler, R. B., "The Measurement of Rapid Surface Temperature Fluctuations during Nucleate Boiling of Water," *AIChE Journal*, Vol. 7, 1961, pp. 620–624.

2 Rogers, T. F., and Mesler, R. B., "An Experimental Study of Surface Cooling by Bubbles during Nucleate Boiling of Water," *AIChE Journal*, Vol. 10, 1964, pp. 656–660.

3 Hendricks, R. C., and Sharp, R. R., "Initiation of Cooling due to Bubble Growth on a Heating Surface," NASA TN D-2990, 1964.

4 Cooper, M. G., and Lloyd, A. J. P., "Transient Local Heat Flux in Nucleate Boiling," *Proceedings of the Third International Heat Transfer Conference*, Chicago, 1966.

5 Cooper, M. G., and Lloyd, A. J. P., "The Microlayer in Nucleate Pool Boiling," *International Journal of Heat and Mass Transfer*, Vol. 12, 1969, pp. 895–913.

6 Sharp, R. R., "The Nature of Liquid Film Evaporation during Nucleate Boiling," NASA TN D-1997, 1964.

7 Hospeti, N. B., and Mesler, R. B., "Deposits Formed Beneath Bubbles during Nucleate Boiling of Radioactive Calcium Sulfate Solutions," *AIChE Journal*, Vol. 11, 1965, pp. 662–665.

8 Jawurek, H. H., "Simultaneous Determination of Microlayer Geometry and Bubble Growth in Nucleate Boiling," *International Journal of Heat and Mass Transfer*, Vol. 12, 1969, pp. 843–848.

9 Cooper, M. G., "The Microlayer and Bubble Growth in Nucleate Pool Boiling," *International Journal of Heat and Mass Transfer*, Vol. 12, 1969, pp. 915–933.

10 Van Ouwerkerk, "The Rapid Growth of a Vapour Bubble at a Liquid–Solid Interface," *International Journal of Heat and Mass Transfer*, Vol. 14, 1971, pp. 1415–1430.

11 Cooper, M. G., and Merry, J. M. D., "A General Expression for the Rate of Evaporation of a Layer of Liquid on a Solid Body," *International Journal of Heat and Mass Transfer*, Vol. 16, 1973, pp. 1811–1815.

12 Graham, R. W., and Hendricks, R. C., "Assessment of Convection and Evaporation in Nucleate Boiling," NASA TN D-3943, 1967.

13 Voutsinos, C. M., "Laser Interferometric Investigation of Microlayer Evaporation for Various Levels of Subcooling and Heat Flux," MEng thesis, McMaster University, Hamilton, Ontario, Canada, April 1976.

14 Voutsinos, C. M., and Judd, R. L., "Laser Interferometric Investigation of the Microlayer Evaporation Phenomenon," JOURNAL OF HEAT TRANSFER, TRANS. ASME, Series C, Vol. 97, No. 1, Feb. 1975, pp. 88–92.

15 Judd, R. L., and Merte, H., Jr., "Evaluation of Nucleate Boiling Heat Flux Predictions at Varying Levels of Subcooling and Acceleration," *International Journal of Heat and Mass Transfer*, Vol. 15, 1972, pp. 1075–1096.

16 Wiebe, J. R., and Judd, R. L., "Superheat Layer Thickness Measurements in Saturated and Subcooled Nucleate Boiling," JOURNAL OF HEAT TRANSFER, TRANS. ASME, Series C, Vol. 93, No. 4, Nov. 1971, pp. 455–461.

17 Griffith, P., and Wallis, J. D., "The Role of Surface Conditions in Nucleate Boiling," *Chemical Engineering Progress Symposium Series*, Vol. 56, 1960, pp. 49–63.

18 Shoukri, M., and Judd, R. L., "Nucleation Site Activation in Saturated Boiling," JOURNAL OF HEAT TRANSFER, TRANS. ASME, Series, C, Vol. 97, No. 1, Feb. 1975, pp. 93–98.

19 Mikic, B. B., and Rohsenow, W. M., "A New Correlation of Pool-Boiling Data Including the Effect of Heating Surface Characteristics," JOURNAL OF HEAT TRANSFER, Series C, Vol. 91, No. 2, May 1969, pp. 245–250.

20 Han, C. Y., and Griffith, P., "The Mechanism of Heat Transfer Nucleate Pool Boiling," *International Journal of Heat and Mass Transfer*, Vol. 8, 1965, pp. 887–913.

R. P. Roy
Assist. Professor,
Nuclear Engineering Program,
University of Illinois,
Urbana, Ill.

G. Yadigaroglu
Assoc. Professor,
Department of Nuclear Engineering,
University of California,
Berkeley, Calif. Mem. ASME

An Investigation of Heat Transport In Oscillatory Turbulent Subcooled Flow

An experiment has been conducted to investigate transient radial heat transport effects created by oscillatory flow in uniformly heated tubes. Departures from one-dimensional, quasi-steady-state behavior have been quantified in the frequency range of density-wave oscillations. The data show a substantial radial dependence of both the amplitude and the phase of the liquid temperature perturbations even at frequencies as low as 0.1 Hz. The orderly axial enthalpy perturbation propagation breaks down at frequencies above 0.5 Hz. These effects must be taken into consideration in predicting the behavior of the point of net vapor generation in a boiling channel under oscillatory flow conditions.

Introduction

The motivation for the present work [1][1] was derived from the conclusions of a previous analytical and experimental investigation [2] of density-wave oscillations, a class of thermo-hydrodynamic instabilities encountered in boiling channels. The predictions of the threshold of stability by the analytical model proposed in [2] agreed qualitatively but not quantitatively with the experimental data. Lack of quantitative agreement was partly attributed to the radial heat conduction and diffusion effects in the single-phase region of the flow channel affecting the axial propagation of enthalpy perturbations, and to the effects of thermal nonequilibrium, i.e., subcooled boiling.

Recently, Saha incorporated the effects of subcooled boiling in the dynamic model of a boiling channel [3]. There is promising but somewhat limited evidence that this resulted in a better analytical prediction of experimental system stability limits with reference to density-wave oscillations. No systematic study of the influence of the radial heat transport effects on the propagation of enthalpy perturbation exists.

Density-wave oscillations in a boiling channel are due to multiple regenerative feedback between the flow rate, the vapor generation rate, and the pressure drop (flow-void feedback instabilities [4]). If the point of net vapor generation (NVG), i.e., the point beyond which the void fraction increases rapidly, is adopted as the boundary between the single-phase and the two-phase regions, its time-dependent (oscillating) position in the channel will be of paramount importance in determining stability with respect to density-wave oscillations [5]. This oscillation of the NVG point, as characterized by its phase and amplitude, is primarily dependent on the phase and amplitude of the temperature and velocity perturbations in the liquid region adjacent to the heated wall [6–8]. Thus, radial transport of heat and momentum in the single-phase region is of importance in the investigation of oscillations of the point of NVG.

In references [2–5] and in all other analytical treatments of density-wave oscillations, the single-phase region of the boiling channel has been treated in the axial space dimension only. The inherent assumption here is that the time-dependent radial momentum and heat transport effects, under oscillatory flow conditions, can be adequately described by a quasi-steady-state variation of the liquid temperature and velocity profiles and/or instantaneous mixing in the radial direction. The importance of radial heat diffusion effects has been recognized by Shotkin [9], who applied a "heat-source correction" to the calculated power-to-flow transfer function of a boiling loop. However, he ignored the effect of the velocity profile. Akcasu [10] proposed an averaged transfer function to take into account the spread in transit time (velocity distribution effect) without considering the heat diffusion effect. Silady [12] developed a unified method for the analysis of entrance-region transient heat transfer to incompressible fluids in hydrodynamically fully developed flow in annuli

---

[1] Numbers in brackets designate References at end of paper.

[2] *Previous assertion to the effect that the perturbations propagated at twice the flow velocity is incorrect and was based on the observation that the delay of the enthalpy propagation varies by 180° in one wavelength.*

Contributed by the Heat Transfer Division and presented at the Winter Annual Meeting, Houston, Texas, November 30–December 5, 1975, of THE AMERICAN SOCIETY OF MECHANIAL ENGINEERS. Revised manuscript received by the Heat Transfer Division January 20, 1976. Paper No. 75-WA/HT-2.

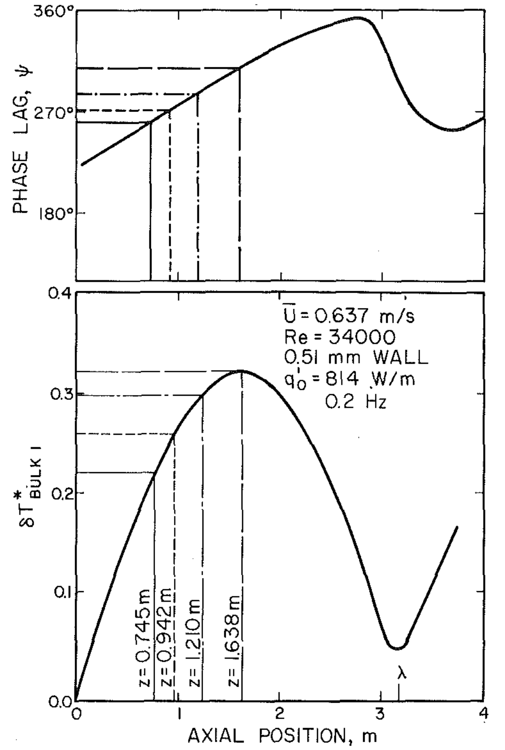

Fig. 1 One-dimensional-model prediction of the phase lag (with respect to flow perturbation) and amplitude of the bulk temperature perturbations at 0.2 Hz

and tubes. The possibility of the basic turbulent exchange mechanisms of the flow being altered by flow oscillations [13] was not considered in his work. Indeed, at the present time there is no information on this question.

A complete analytical consideration of the radial effects under oscillatory turbulent flow conditions is difficult if not impossible. Consequently, an experiment was set up to measure the radial distribution of the amplitude and phase of the local temperature perturbations in the single-phase region of heated tubes, in order to quantify departures from the one-dimensional quasi-steady-state analysis. Measurements of the radial distribution of velocity perturbations under isothermal flow conditions were also made and are reported elsewhere [11]. The investigation was carried out in the frequency range associated with density-wave oscillations. Measurements were made for frequencies between 0.1 and 1.2 Hz at various axial locations along the heated channel. Relatively large diameter round tubes (24.4 and 22.1 mm ID) were used to facilitate probing of the flow.

In other analytical and experimental studies undertaken in the area of heat transfer with oscillating flow, the quantity of interest has been the time average of the local or average heat transfer coefficient. The phenomenon of propagation of the temperature perturbations, which is of particular interest to two-phase flow stability studies, was of no interest in these investigations and therefore was not considered.

Analysis

One-Dimensional Approximation of the Dynamics of the Single-Phase Region. The thermohydrodynamics of the single-phase region of a diabatic, two-phase flow channel under oscillatory flow conditions has been investigated, taking into account the dynamics of the heater wall [1, 5]. A quasi-steady-state velocity profile and instantaneous thermal mixing in the radial direction were assumed. The flow-to-enthalpy transfer function, $H(z, s) \triangleq \delta h(z, s)/\delta w(s)$, for the single-phase region of the boiling channel was obtained by solving the linearized one-dimensional energy equation for the fluid, coupled to the radial conduction equation for the wall, through the use of a flow-dependent convection heat transfer coefficient at the tube inner wall.

For an internally cooled tubular channel with temporally constant and axially uniform wall heat generation rate, the transfer function is [5]

$$H(z, s) \triangleq \frac{\delta h(z, s)}{\delta \omega(s)} = \frac{L(s)}{K(s)}\left(e^{-K(s)z} - 1\right) \tag{1}$$

where

$$L(s) = \frac{q_0'}{w_0^2}\left[(1-a) + a\frac{C}{F(s)+C}\right]$$

$$K(s) = \frac{1}{\bar{U}_0}\left[s + \frac{1}{\tau_c}\frac{F(s)}{F(s)+C}\right]$$

$$F(s) = -\sqrt{\tau_k s}\cdot\frac{M'(\sqrt{\tau_k s})}{M(\sqrt{\tau_k s})}$$

$$M(x) = I_0(x) + \frac{I_1\left(\sqrt{\dfrac{s}{\alpha_w}}\,r_2\right)}{K_1\left(\sqrt{\dfrac{s}{\alpha_w}}\,r_2\right)}\cdot K_0(x)$$

$$C = \frac{h_c{}^\circ r_1}{k_w}$$

Fig. 1 shows, as an example, the phase lag and the nondimensionalized amplitude of the bulk temperature perturbation at a flow os-

Nomenclature

A = cross-sectional flow area
a = exponent of Reynolds number in Nusselt number correlation
c = specific heat
D = tube inner diameter
h = enthalpy of the liquid
h_c = forced-convection heat transfer coefficient
k = thermal conductivity
q' = linear heat input rate
r_1 = tube inner radius
r_2 = tube outer radius
s = Laplace variable
T = temperature
$\bar{U}$ = bulk axial velocity of the liquid
w = mass flow rate
z = axial coordinate
α = thermal diffusivity
λ = average wavelength, $\bar{U}_0\tau$
ρ = density
τ = period of oscillation
$\tau_c = \dfrac{\rho_f c_f A}{(2\pi r_1)h_c{}^\circ}$
$\tau_k = r_1{}^2/\alpha_w$
ψ = phase lag of local temperature perturbation w.r.t. the cross-sectional-average inlet velocity perturbation, see Fig. 3.
δT^* = nondimensional amplitude of temperature perturbation, $\dfrac{\delta T/(\Delta T_b)_{1m}}{\delta U_1/\bar{U}}$; $(\Delta T_b)_{1m}$ is the steady-state bulk temperature increase for z = 1 m
ω = circular frequency

Subscripts and Operators

0 = steady-state value
1 = fundamental-frequency component
b = bulk (mixed-mean)
f = liquid phase

cillation frequency of 0.2 Hz, as a function of axial position, z, along the tube. A standing wave pattern is clearly visible. The wavelength, λ, is equal to the product of the bulk flow velocity and the period of flow oscillation τ. The solution gives rise to a well-defined enthalpy perturbation waveform at all frequencies. Thus, the phases and amplitudes of local enthalpy perturbations are predicted to be strong functions of axial position at all frequencies. The enthalpy perturbations propagate axially at the flow velocity according to the one-dimensional model.[2]

$H(z, s)$ can be utilized to arrive at the flow-to-position-of-boiling-boundary transfer function [2], the boiling boundary being the plane where the bulk liquid reaches saturation. As mentioned in the Introduction and shown later, if one considers the NVG point instead of the boiling boundary, then the radial space dimension must be introduced in the flow-to-enthalpy transfer function in order to predict the enthalpy perturbations near the wall correctly.

The General Energy Equation. The general energy equation for the fluid in the single-phase region of the heated tube, with both axial and radial dependence, has been discussed in detail in [1]. It has been postulated that the basic turbulent exchange mechanism is affected by the oscillating nature of the flow [1, 13].

The energy equation, with the proper initial and boundary conditions imposed, cannot be solved rigorously at present. However, nondimensionalization of this equation gives rise to the following three dimensionless groups: (*a*) RePrS (as coefficient of the time-derivative term); (*b*) RePr (as coefficient of the convective term); (*c*) $(1 + \epsilon_H/\alpha)$ in the diffusion term. ϵ_H will, in general, be a function of r and ω, but it was assumed to be a constant (e.g., value for turbulent core) for the purpose of forming the dimensionless group. S is a Strouhal number, defined by $D\omega/\bar{U}$. These dimensionless groups will be used later to arrive at a proposed criterion for the validity of the one-dimensional model.

Experimental Work

The goal of the experimental work reported here was to study the enthalpy perturbation propagation phenomenon in the single-phase region by measuring the phase and amplitude of the local temperature perturbations as a function of radius, frequency, and axial position in a vertical heated tube.

Refrigerent-113 (R-113) was the experimental fluid. Advantages of R-113 included the low heating power requirements and compatibility with anemometry probes. However, one disadvantage of using R-113 is the relative ease with which incipience of boiling may occur on the heated wall. The pressure in the test section was kept at approximately 2.5×10^5 N/m^2 above saturation (saturation pressure corresponding to R-113 inlet temperature of 20°C is 3.63×10^4 N/m^2) to eliminate the possibility of incipience of boiling on the walls. Possible accentuation of radial effects, due to the lower thermal and eddy diffusivities of R-113 (compared to water, for example), was another reason for selection of R-113 as the experimental fluid.

The Experimental Loop. The loop consisted of the vertical test section, a helicoidal-tube cooler, a circulating pump, a flow-oscillating valve, a venturi for flow rate measurements, flow control valves, and a bladder-type pressurizer. The test section, made from thin-walled stainless-steel tubing, consisted of an unheated hydrodynamic entrance length and a resistivity-heated length. A single section of tubing was used for both these lengths to avoid any geometrical perturbations in the flow path. Two different test sections (25.4 mm OD; 0.51 and 1.67 mm wall thickness) were used to study the effect of wall heat capacity on the results.

An anemometry probe mounting section was located at the end of the heated length. Fig. 2 shows schematically the heated test section and the probe section. The probe extended beyond the current-carrying copper flange B into the heated section. A calibrated micrometer arrangement was used to traverse the probe radially. Measurements along various axial positions of the heated section were simulated by moving the current-carrying copper flange A toward flange B starting from the longest heated length. This was done to eliminate the need for insertion of the probe through the thin-walled test section. Thermal analysis of the ends of the heated length using a conduction code showed that, for the insulated test section, typically no more than 2 percent of the total heat generated in the wall was lost through the ends.

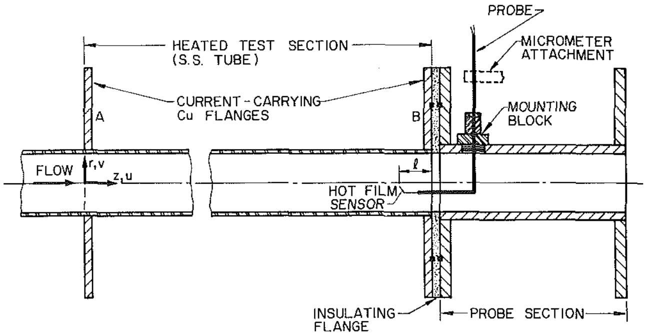

Fig. 2 Schematic diagram of the heated section and the probe section

A perforated plate upstream of the hydrodynamic entrance length was introduced to promote mixing and reduce the radial variation of phase and amplitude of the local velocity perturbation. The liquid flowed vertically downward in the test section.

The sinusoidal flow modulation was obtained by a closed-loop feedback control system controlling a valve located upstream of the test section. This servomechanism had an inner valve-position feedback loop and an outer flow feedback loop. A master sine oscillator provided the command signal to the servocontroller. Details of the flow oscillating system can be found in reference [1]. Second-harmonic distortion of the flow signal, as represented by the ratio of the amplitude of the second-harmonic component to the amplitude of the fundamental, was found to be always less than 4 percent. The amplitudes of the higher harmonics were not measured and could have occasionally been of some importance.

Temperature Measurements. A quartz-coated cylindrical hot-film sensor probe was used as a resistance thermometer, in conjunction with a temperature measurement module (Thermo Systems 1040). The sensor had a diameter of 0.025 mm and a sensing length of 0.51 mm. Steady-state temperature profiles were measured at each axial position to ascertain that the thermal boundary layer had reached the tube center line. The measured temperature profiles agreed reasonably well with fully developed computed profiles [14] corresponding to the experimental conditions. Copper-constantan thermocouples were used to monitor the test section external wall temperature at several axial positions as well as the liquid temperatures at the center line of test section inlet and outlet. The wall thermocouples were insulated from the test section wall by a very thin layer of mica.

Signal Analysis. An amplifier and bias circuit [1] were used to remove the mean value of the signal to be processed and then to amplify the residual fluctuating component. A Wave Form Eductor (Princeton Applied Research Corporation) provided phase-averaging of this amplified signal, thereby reducing the random turbulent component considerably and making frequency analysis of the signal easier. A Lock-In Amplifier (Ithaco 391) was used to measure the amplitude and the phase of the fundamental-frequency component of the signal.

Since the thermo-hydrodynamic system under study is nonlinear in nature and the transfer-function representation assumes linearity, the input flow perturbation amplitudes were limited to less than 8 per cent of the mean flow values to reduce nonlinear effects.

Data and Observations

Figs. 3–8 show the radial distribution of the phase lag, ψ, and the nondimensional amplitude, $\delta T_1{}^*$, of the fundamental-frequency component of the temperature perturbations with respect to the cross-sectionally averaged inlet velocity perturbation at frequencies

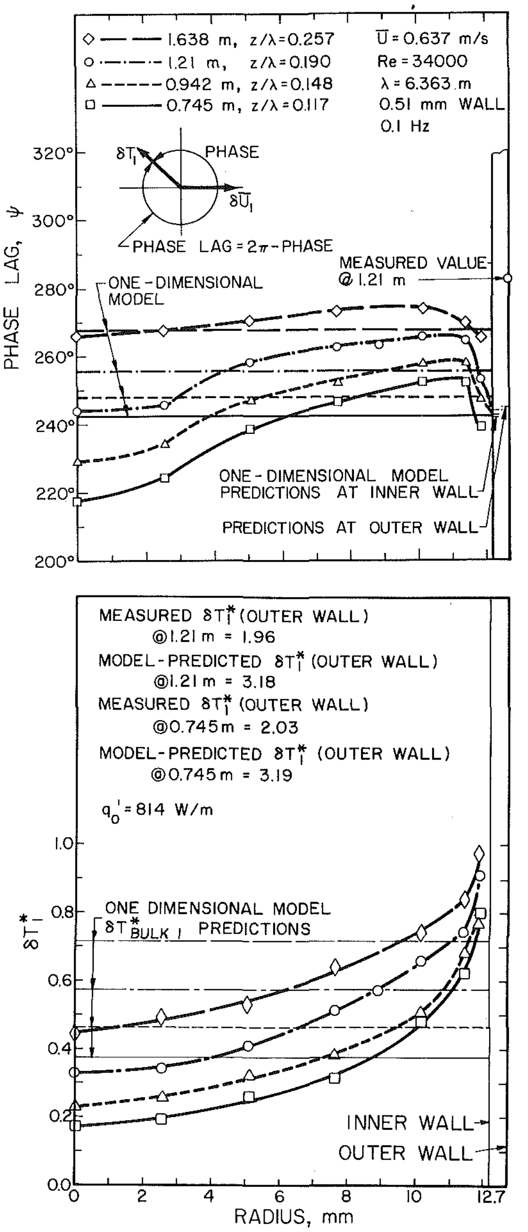

Fig. 3 Phase lag (with respect to cross-sectional average inlet-velocity perturbation) and amplitude of local temperature pertubation at 0.1 Hz

of 0.1, 0.2, 0.3, 0.5, 0.7, and 0.9 Hz, respectively. The average inlet velocity perturbations were obtained by integrating over the flow area the fundamental-frequency components of the velocity perturbations that were measured by a constant-temperature anemometry probe and by obtaining the fundamental-frequency component of the average signal. This signal differed from the flow perturbation signal measured by a venturi [11]. The plots contain data at four axial locations, z = 1.638, 1.210, 0.942, and 0.745 m, for the 0.51-mm-wall test section. Data at 1.2 Hz as well as data for the 1.67-mm-wall test section can be found in reference [1]. The phase values are estimated to be accurate to within ±3° at the lower frequencies (0.1 and 0.2 Hz) and within ± 5° at the higher frequencies (0.7 Hz and higher). All amplitude measurements are believed to be correct within 15 per cent. Phase measurements became exceedingly difficult or impossible at the locations where the amplitudes of the temperature perturbations were very small. This explains the lack of data at certain radial positions in the tube (e.g., Fig. 6, at ≈7.9 mm). All data were found to be symmetrical with respect to the tube center line. The figures also show the one-dimensional model predictions of phase lags and amplitudes for comparison.

Some of the test section outer-wall temperature perturbations, as measured by thermocouples, are also shown in Figs. 3–8. The thin mica layer between the thermocouple junction and the test section wall obviously introduces an additional phase lag on these measurements. The wall temperature perturbation amplitudes were found to be substantial when compared to the liquid temperature perturbations.

The Frequency-Dependent Radial Effect. It is clear from studying Figs. 3–8 that the radial effect (both in amplitude and in phase) becomes increasingly important as the frequency of flow oscilltion increases. If we compare the maximum phase lag spread, $\Delta\psi$ (i.e., the maximum deviation in phase lag values along the radius) at

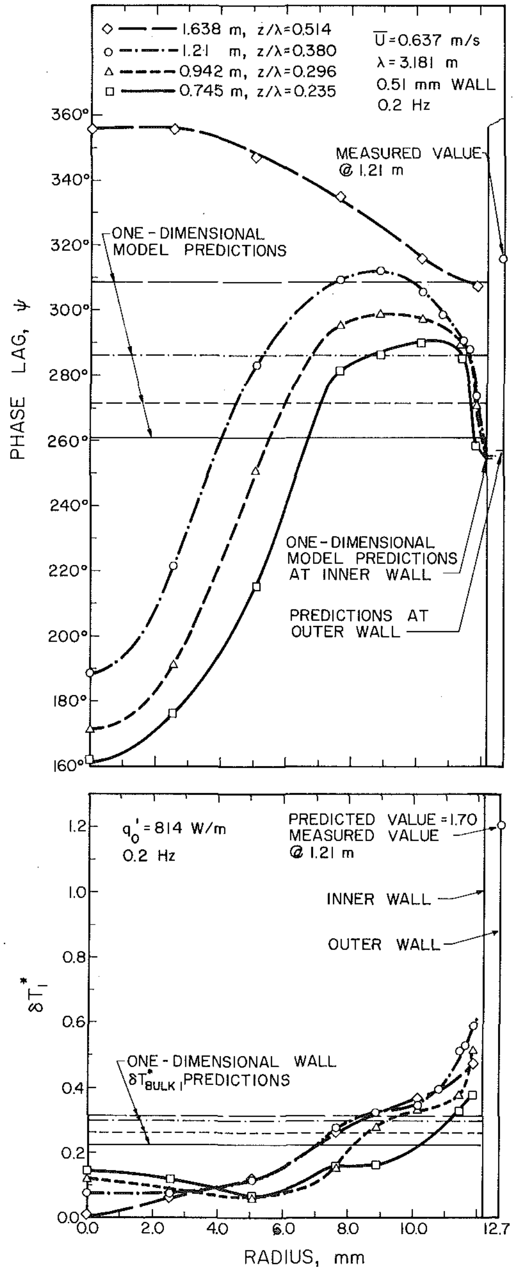

Fig. 4 Phase lag (with respect to cross-sectional average inlet-velocity perturbation) and amplitude of local temperature perturbation at 0.2 Hz

any particular axial position, we see that this spread increases monotonically with the oscillation frequency. As a typical example, Table 1 shows the $\Delta\psi$ values at two axial positions in the 0.51-mm-wall test section.

It is also seen from the data that the amplitude of temperature perturbations measured in the vicinity of the test section wall is appreciably larger than the values predicted by the one-dimensional model. The measured phase lags near the wall, especially at the higher frequencies (0.5 Hz and above) are also considerably different from the model predictions of the *bulk* temperature perturbations but approximately agree with the *wall* temperature perturbation predictions at low frequencies.

Table 1 Maximum phase lag spread along radius at two axial positions ($\Delta\psi$)

Frequency (Hz)	$\Delta\psi$ @ z = 1.21 m	$\Delta\psi$ @ z = 1.638 m	Figure No.
0.1	25°	10°	3
0.2	124°	48°	4
0.3	148°	207°	5
0.5	178°	202°	6
0.7	259°	250°	7
0.9	281°	276°	8
1.2	348°	Not measured	reference [1]

It should be noted that at the higher frequencies (Figs. 5–8) large phase jumps (of the order of 180°) always occurred at the radial locations where the amplitude tended to very small values. Referring to Fig. 1, we can see that this characteristic is in agreement with the one-dimensional model behavior.

The Frequency-Dependent Axial Propagation Effect. It was pointed out earlier in the paper that, according to the one-dimensional model, the enthalpy perturbations should exhibit an axial standing-wave behavior at all frequencies.

Figs. 3 and 4 (0.1 and 0.2 Hz) show that the variation of phase lag

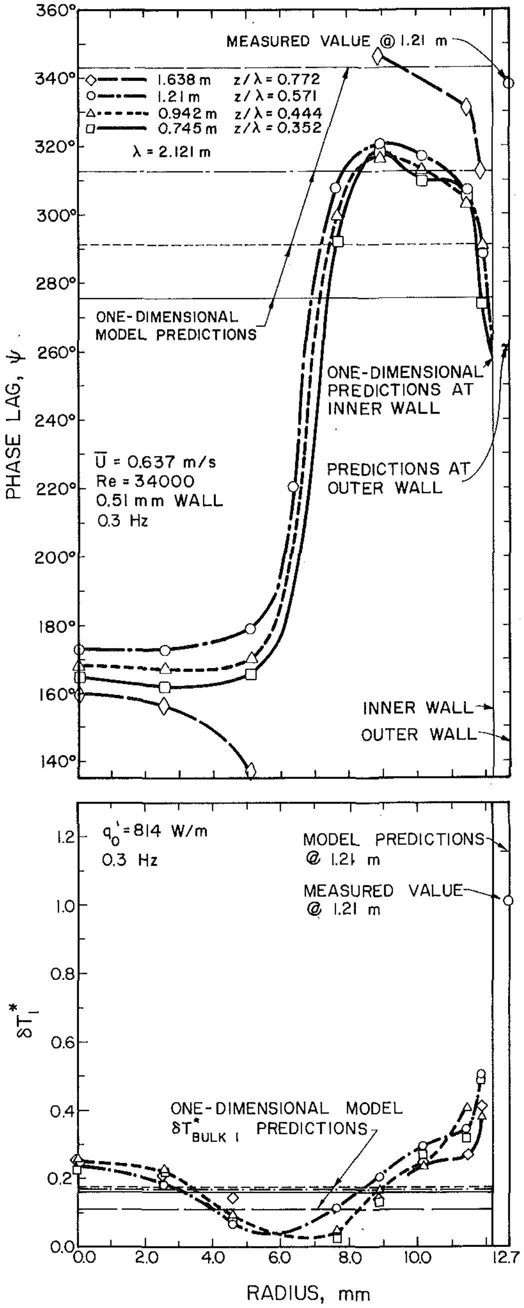

Fig. 5 Phase lag (with respect to cross-sectional average inlet-velocity perturbation) and amplitude of local temperature perturbations at 0.3 Hz

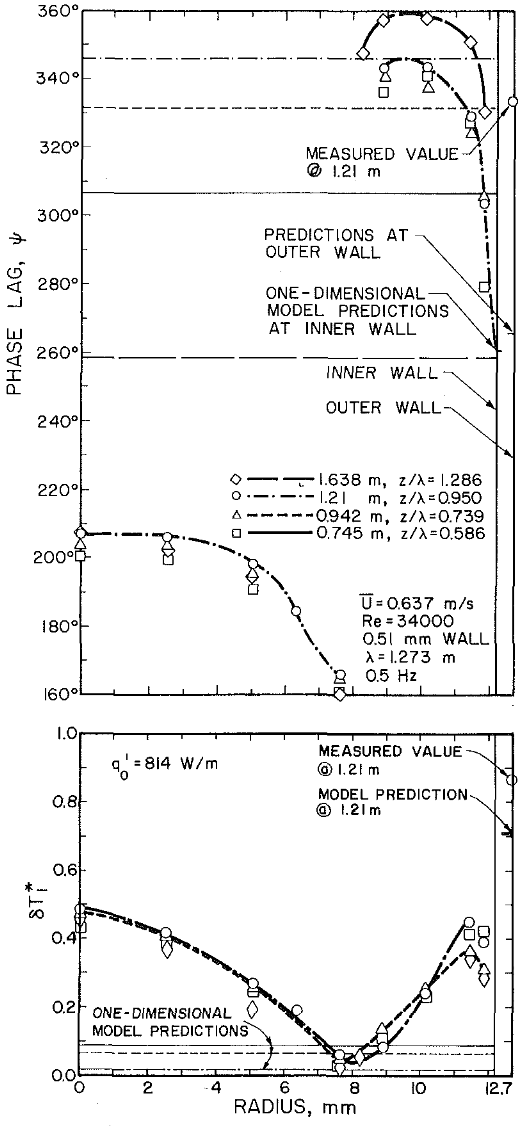

Fig. 6 Phase lag (with respect to cross-sectional average inlet-velocity perturbation) and amplitude of local temperature perturbation at 0.5 Hz

of the local temperature perturbations as a function of axial position in the test section (at least up to the longest heater length of 1.638 m) is, both qualitatively and approximately quantitatively, in agreement with the predictions of the one-dimensional model. The same trend is noticed in the amplitude data. It should be noted that the amplitudes are known only to within 15 per cent, thus making observations of trends of amplitudes more difficult as compared to phase lags. It can be concluded that an axially propagating enthalpy perturbation exists at these low frequencies as predicted by the one-dimensional model.

In Fig. 5, however, corresponding to 0.3 Hz, the axial dependence of the data is considerably weaker in comparison to the one-dimensional model predictions. In addition, we note that the data at 1.638 m and in the turbulent-core region, for the first time start showing evidence of nonconformance with the axial trend predicted by the model. Fig. 6 indicates that at 0.5 Hz the axial dependence of the phase lag is barely discernible. It can be concluded that the concept of axial enthalpy propagation has broken down already at this frequency since the perturbations are almost in phase all along the tube. Figs. 7 and 8 and data at 1.2 Hz [1] further confirm this conclusion.

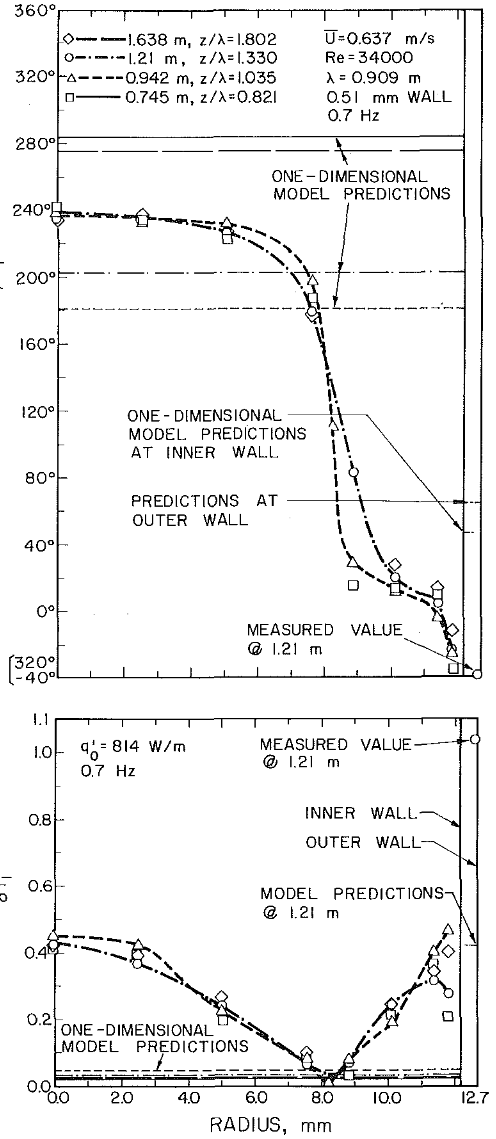

Fig. 7 Phase lag (with respect to cross-sectional average inlet-velocity perturbation) and amplitude of local temperature perturbation at 0.7 Hz

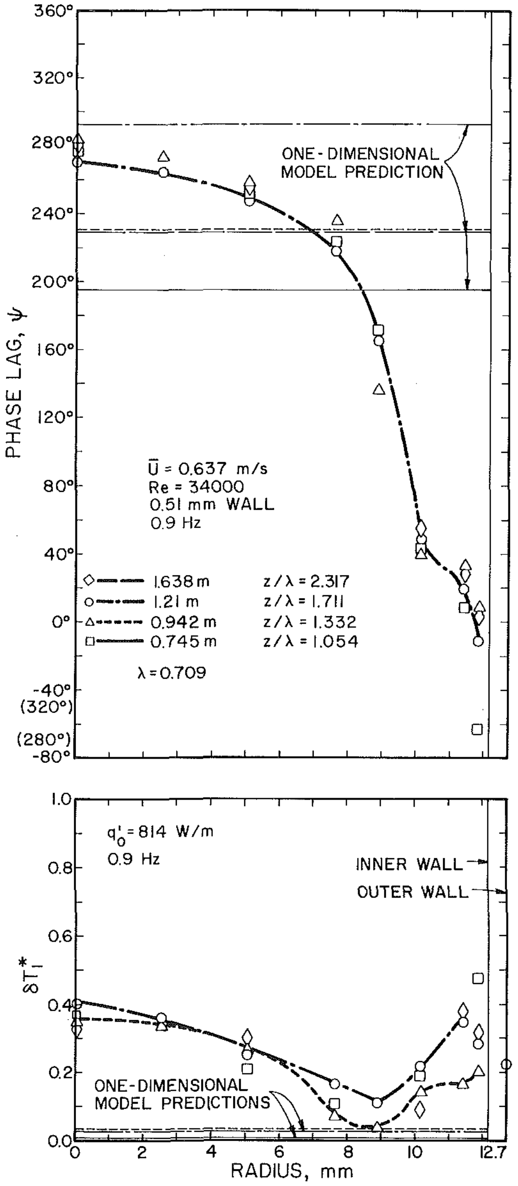

Fig. 8 Phase lag (with respect to cross-sectional average inlet-velocity perturbation) and amplitude of local temperature perturbation at 0.9 Hz

The Wall Heat Capacity Effect. The one-dimensional model, which includes the formulation of transient conduction of heat in the tube wall, can be employed to predict the effect of varying tube wall thickness.

In order to show the effect of wall thickness alone, all other parameters influencing the data had to be closely matched. Since the flow velocity and consequently the wavelength, λ, were adjusted to keep the Reynolds number approximately constant for both test sections, it became necessary, in order to make comparisons at the same values of z/λ, to obtain the values for the 0.51-mm-wall tube by interpolation of data obtained at intermediate values of z/λ. Thus, for example, the values of Fig. 9 were obtained by interpolating between the z = 0.942 and 1.210 m data.

Fig. 9 shows the results for 0.1 Hz. The agreement between data and the model is seen to be reasonably good. Similar agreement was found [1] for 0.2 Hz. This suggests that the dynamics of the heated wall are well-represented by the model at these frequencies. However, at 0.3 Hz and above, the model was unable to predict the experimental [1] trends consistently.

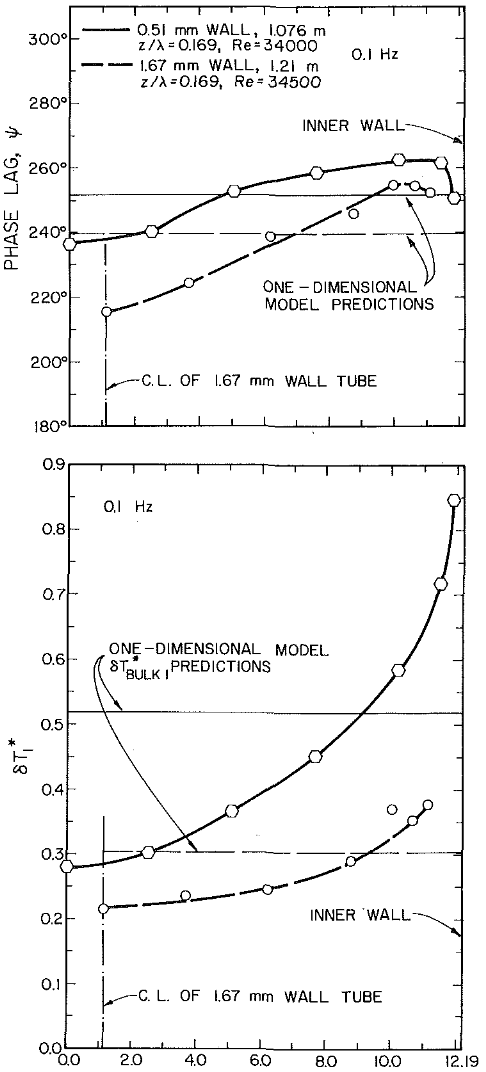

Fig. 9 The wall capacity effect at 0.1 Hz

Discussion

Possible explanations of the physical phenomena causing the data trends discussed herein will now be presented.

Radial Transient Heat Diffusion Effects. If we estimate the phase and the amplitude of the temperature perturbation as a function of radial location in the tube by following the transient radial diffusion of the heat generated at the wall through the laminar sublayer, the buffer layer, and the turbulent core and ignoring any axial transport effects (analysis similar to [9]), we find that the phase lag increases monotonically while the amplitude monotonically decreases as we move inward. Inspection of Figs. 5–8 shows that both the phase lag and the amplitude behavior are consistent with the foregoing estimate in the region beginning from the wall and extending well into the turbulent core up to a point of minimum amplitude. The point of minimum δT_l^* is seen to approach the wall as the frequency increases. The amplitude of the temperature perturbation grows again as we proceed inward from the minimum point. It can be postulated by observing the 180° phase difference between the perturbations at points bracketing this region that temperature perturbations of opposite phases cancel each other at the minimum point.

The Thermal Entrance Length Effect. Fig. 10 shows schematically the heated test section and a specific plane of measurement of the liquid temperature perturbations. Small oscillations are superimposed on the flow, which is assumed to be hydrodynamically fully developed at the heated section entrance. *EDCBA* denotes, schematically, the developing thermal boundary layer, which might be altered from the steady-state case because of the oscillations.

Consider the fluid elements at *E, D, C, B,* and *A*, at time $t = t_0$, from a Lagrangian viewpoint. At $t > t_0$ the elements begin exchanging heat with their environment as they proceed downstream. The elements arrive at the plane of measurement having traversed different path lengths within the effective heat-exchange region. Considering the fact that the axial movement of fluid particles is responsible in general for the axial enthalpy-propagation phenomenon, we conclude that the fluid elements will have different phases on arrival at the plane of measurement. However, another effect that must also be considered is the radial movement of the fluid elements, as they are moving downstream, caused by eddy motion (the turbulent exchange mechanism).

Thus, the phase of the temperature perturbation at the plane of measurement at any radial position is affected by both the development of the thermal boundary layer and the time-dependent radial diffusion of heat from the heated wall. Near the wall, we would expect the temperature perturbation data to be dominated by the phase and amplitude of the wall temperature perturbation and the phase lag should increase as we move away from the wall. On the other hand, if the plane of measurement is not "far" removed from the thermal entrance region, its effects should be observable and should lead to variation of phase lag similar to the one shown in Fig. 1 as we move away from the center of the tube (i.e., as the distance traveled by the fluid elements increases with radial position). Inspecting the phase lag data at 0.1, 0.2, and 0.3 Hz (Figs. 3–5) for the three shortest heated lengths, we indeed find such expected behavior patterns. The two separate radial regions of dominance are indicated by differences in signs of the radial gradient of the phase lag values. No thermal entrance length effect is visible at higher frequencies and for the longest heated length at 0.2 and 0.3 Hz. Thus, thermal entrance length effect was visible only for "short" heated lengths at frequencies below 0.3 Hz.

The relative axial position of the plane of measurement, z, with respect to the wavelength λ (as denoted by the ratio z/λ) is of significance in determining the "shortness" of the heated length. The axial location z, the frequency of the oscillation, and the flow velocity enter in this ratio. It seems that if $z/\lambda < 0.5$, the heated length can be considered to be "short."

Effect of Oscillations on the Retention of Past History by the Fluid Elements. We have seen that as the frequency of oscillation increases, conformance to the axial enthalpy wave-propagation phenomenon is gradually lost. The phase lag and the amplitude of the temperature perturbation, at any location, apparently become increasingly dependent on very recent history, thereby losing their axial dependence. The radial position and the wall effects now become the important parameters to be considered.

It is suggested here that probably the "orderly" axial propagation phenomenon, observed at the lower frequencies, is broken up by the additional turbulent exchange mechanism generated by the "rapid" oscillations.

Proposed Criterion for the Validity of the One-Dimensional Model. The dimensionless groups appearing in the energy equation governing the propagation of enthalpy perturbations were mentioned

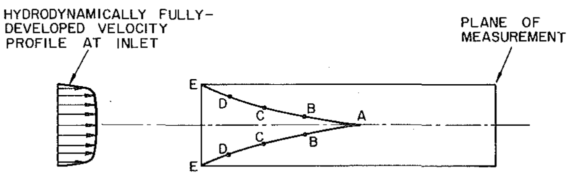

Fig. 10 The thermal entrance length effect

earlier. The ratio $\mathrm{Re}S\mathrm{Pr}/(1+\epsilon_H/\alpha)$ is equal to $\omega D^2/(\alpha+\epsilon H)$, which is a measure of the nondimensionalized time constant for radial turbulent heat diffusion. Furthermore, the ratio $\mathrm{RePr}/\mathrm{Re}S\mathrm{Pr} = 1/S$ is a measure of the time period of the flow oscillations nondimensionalized by a characteristic axial transport time $D/\overline{U}$. It is proposed here that if

$$\frac{\omega D^2}{\alpha+\epsilon_H(\omega)} < \frac{1}{S}$$

then the one-dimensional approximation will be valid. If we use the steady-state turbulent-core eddy diffusivity value for $\epsilon_H(\omega)$, the foregoing criterion suggests that under the present experimental conditions the one-dimensional model becomes invalid above 0.2 Hz, in agreement with the experimental observations. The criterion proposed herein does not, however, take into account the influence of the thermal entrance length and any effects of the space and possibly frequency dependence of the eddy diffusivity. A criterion for the domain of influence of the entrance effects was discussed in a previous section.

Concluding Remarks

1 The two-dimensional transient measurements confirm the validity of the one-dimensional analytical model at very low frequencies only (below 0.2 Hz). Under the conditions of the present experiment, a substantial radial spread of temperature perturbation phase lags exists even at 0.1 Hz. Significant departures from the one-dimensional model predictions appear at frequencies as low as 0.3 Hz. Criteria for the validity of the one-dimensional model are proposed.

2 The temperature perturbations in the liquid layers immediately adjacent to the wall follow the wall temperature perturbations. At the lowest frequencies, the measured liquid temperature perturbations near the wall are seen to be close to the *wall* temperature perturbations calculated using the one-dimensional model.

3 Under the present experimental conditions, the enthalpy perturbation propagation phenomenon breaks down at frequencies above 0.5 Hz. It is suggested that the perturbations become increasingly dependent on very recent history of the fluid, on local wall effects, and on transient radial heat diffusion from the wall with increases in frequency, thereby losing axial dependence. The additional heat transport mechanism generated by the oscillation may be a major cause of such behavior.

4 The effect of thermal entrance length on the temperature perturbations decreased as the frequency of flow oscillation increased.

5 The effect of tube wall heat capacity is substantial. The one-dimensional analytical model could predict this effect reasonably well at the lower frequencies.

6 These results have important implications for stability studies of density-wave oscillations in diabatic two-phase flow systems. It has been shown [5,6] that the movements of the point of net vapor generation have considerable importance in channel stability. Since the transient location of the NVG point will be dictated by the phase and amplitude of the liquid temperature and velocity perturbations near the wall, it appears that one-dimensional models of the single-phase region may often be inadequate in predicting the time-dependent location of this point. When the NVG point is used to delineate the interface between the single and the two-phase regions, a two-dimensional model of the single-phase region of the channel becomes necessary. It is important also to keep in mind that the presence of voidage near the channel wall, upstream of the NVG point, will further alter the turbulent exchange in this region.

Acknowledgment

Acknowledgment is made to the Donors of the Petroleum Research Fund, administered by the American Chemical Society, for partial support of this research. The research work was carried out at the Department of Nuclear Engineering, University of California, Berkeley.

References

1 Roy, R. P., "An Investigation of Momentum and Heat Transport in Turbulent Oscillatory Subcooled Flow and Its Importance in the Analysis of Density-Wave Oscillations," PhD Thesis, University of California, Berkeley, 1975.

2 Yadigaroglu, G., and Bergles, A. E., "An Experimental and Theoretical Study of Density-Wave Oscillations in Two-Phase Flow," MIT Report DSR-74629-3, Dec. 1969.

3 Saha, P., "Thermally Induced Two-Phase Flow Instabilities Including the Effect of Thermal Non-Equilibrium Between the Phases," PhD thesis, Georgia Institute of Technology, 1974.

4 Neal, L. G., Zivi, S. M., and Wright, R. W., "The Mechanism of Hydrodynamic Instabilities in Boiling Systems," *Proceedings of the Symposium on Two-Phase Flow Dynamics,* EURATOM, The Technological University of Eindhoven, 1967.

5 Yadigaroglu, G., and Bergles, A. E., "Fundamental and Higher-Mode Density-Wave Oscillations in Two-Phase Flow," JOURNAL OF HEAT TRANSFER, TRANS. ASME, Series C, Vol. 94, 1972, pp. 189–195.

6 Saha, P., and Zuber, N., "Point of Net Vapor Generation and Vapor Void Fractions in Subcooled Boiling," *Heat Transfer 1974,* Fifth International Heat Transfer Conference, Tokyo, Vol. IV, 1974, pp. 175–179.

7 Staub, F. W., "The Void Fraction in Subcooled Boiling—Prediction of the Initial Point of Net Vapor Generation," JOURNAL OF HEAT TRANSFER, TRANS. ASME, Series C, Vol. 90, 1968, pp. 151–157.

8 Levy, S., "Forced Convection Subcooled Boiling—Prediction of Vapor Volumetric Fraction," *International Journal of Heat and Mass Transfer,* Vol. 10, 1967, pp. 951–965.

9 Shotkin, L. M., "Flow of Boiling Water in Heated Pipes," *Nuclear Science and Engineering,* Vol. 26, 1966, pp. 293–304.

10 Akcasu, A. Z., "Theoretical Feedback Analysis in Boiling Water reactors," ANL-6221, 1960.

11 Roy, R. P., and Yadigaroglu, G., "An Investigation of Time-Dependent Velocity Profiles in Oscillatory Turbulent Isothermal Liquid Flow," submitted for Publication to JOURNAL OF HEAT TRANSFER, TRANS. ASME.

12 Silady, F. A., "A Unified Method for the Analysis of Heat Transfer to Fluids in Tubes and Annuli," PhD thesis, University of Illinois, 1974.

13 Bogdanoff, D. W., "A Study of the Mechanisms of Heat Transfer in Oscillating Flow," Technical Report No. 483-f, Department of Mechanical and Aerospace Sciences, Princeton University, 1967.

14 Patankar, S. V., and Spalding, D. B., *Heat and Mass Transfer in Boundary Layers,* Second ed., Intext Education Publishers, 1970.

D. A. Nelson
Assist. Professor,
Department of Mechanical Engineering,
The Pennsylvania State University,
University Park, Pa.

Radiation Heat Transfer Through Multiband Molecular Gases

Exact characterization of radiation heat transfer through multiband molecular gases is obtained in some limits of considerable importance. An approximate procedure based upon these results is also suggested.

Introduction

Radiation heat transfer through molecular gases has long been recognized as an important mode of energy transfer in combustion devices and in planetary atmospheres. There is as well a growing realization of its importance in quantitative fire research problems. For practical calculations of very specific problems, it has been common to rely upon a knowledge of isothermal emissivities and atmospheric transmission functions in graphical or tabular form [1, 2].[1] These serve their intended purpose well but contribute inadequately to generalized or fundamental questions. These are best studied in simple geometries but can involve accounting for complex spectral absorption characteristics in terms of the total band absorption [3, 4]. Many contributions involving pure radiative transfer as well as interactions with conduction and convection have been made following this line of analysis, with particular emphasis upon the behavior of molecular gases [5–20]. Usually, it has been found necessary to place physical restrictions upon the problem, thus limiting the range of applicability. Constant properties are nearly universally assumed but this is not considered a serious simplification [17]. The most basic problems are inherently nonlinear even for pure radiative transfer because in general there are multiple absorption-emission bands, each depending upon the temperature in a different way. Thus, simplifications include single band, multiple bands with identical band properties, and linearized radiation. The first is reasonable only for diatomic molecules with weak overtone bands but these do not occupy a position of great importance in radiating systems; the second is of theoretical but not practical interest because band absorption properties of a given molecular gas may vary widely [4]; the third has proven to be the most valuable and has led to the solution of many important problems due to the great simplification it affords.

In this paper the problem of radiative equilibrium of a constant property, multiband, planar, molecular gas is considered. None of the three simplifications mentioned is employed. It is found that they are not needed for problems of pure radiative transfer in some important limits. The exact analytical results suggest an approximate procedure that could yield useful engineering estimates of multiband radiative transfer effects in problems of interest.

Fundamentals

For a planar medium bounded by black, isothermal walls and interacting with thermal radiation in N nonoverlapping narrow bands, the radiative flux and its divergence may be written

$$Q = 1 + \sum_{i=1}^{N} B_i \left[2K_3[\tau_{h_i}\eta] + 2\tau_{h_i} \int_0^1 \phi_i(\eta') K_2[\tau_{h_i}|\eta - \eta'|] \operatorname{sgn}(\eta - \eta')\, d\eta' \right] \quad (1)$$

$$\frac{dQ}{d\eta} = 2 \sum_{i=1}^{N} B_i \tau_{h_i} \left\{ 2\phi_i(\eta) - K_2[\tau_{h_i}\eta] - \tau_{h_i} \int_0^1 \phi_i(\eta') K_1[\tau_{h_i}|\eta - \eta'|]\, d\eta' \right\} \quad (2)$$

where

$$Q = q^r/\sigma(T_1{}^4 - T_2{}^4)$$
$$B_i = [E_{\nu i}(T_1) - E_{\nu i}(T_2)]D_i/\sigma(T_1{}^4 - T_2{}^4)$$
$$\phi_i(\eta) = [E_{\nu i}(\eta) - E_{\nu i}(T_2)]/[E_{\nu i}(T_1) - E_{\nu i}(T_2)]$$
$$\eta = y/h$$

and physical properties have been taken independent of temperature. Through use of integration by parts these equations may also be written

$$Q = 1 + 2 \sum_{i=1}^{N} B_i \left\{ [1 - \phi_i(0)]K_3[\tau_{h_i}\eta] + \phi_i(1)K_3[\tau_{h_i}(1 - \eta)] - \int_0^1 \frac{d\phi_i(\eta')}{d\eta'} K_3[\tau_{h_i}|\eta - \eta'|]\, d\eta' \right] \quad (3)$$

$$\frac{dQ}{d\eta} = 2 \sum_{i=1}^{N} B_i \tau_{h_i} \left\{ [\phi_i(0) - 1]K_2[\tau_{h_i}\eta] + \phi_i(1)K_2[\tau_{h_i}(1 - \eta)] + \int_0^1 \frac{d\phi_i(\eta')}{d\eta'} K_2[\tau_{h_i}|\eta - \eta'|] \operatorname{sgn}(\eta - \eta')\, d\eta' \right\} \quad (4)$$

---

[1] Numbers in brackets designate References at end of paper.

Contributed by the Heat Transfer Division for publication in the JOURNAL OF HEAT TRANSFER. Manuscript received by the Heat Transfer Division April 29, 1976.

The foregoing equations are often more convenient than equations (1) and (2) for analytical purposes. The K_n functions have been discussed in [21].

Other formulations for multiband media have allowed for a temperature-dependent absorption coefficient at the expense of assuming equal characteristic values for every band [22]. Most molecular gases, however, show a pronounced variation of optical parameters from band to band [4]. Consequently, it seems more appropriate to retain this characteristic and to rely on scaling methods to account for temperature dependence in practical applications [23, 24]. For the problem of radiative equilibrium considered here, $dQ/d\eta = 0$ and equation (4) reduces to

$$\sum_{i=1}^{N} B_i \tau_{h_i} \left\{ [\phi_i(0) - 1] K_2[\tau_{h_i}\eta] + \phi_i(1) K_2[\tau_{h_i}(1-\eta)] \right. \\ \left. + \int_0^1 \frac{d\phi_i(\eta')}{d\eta'} K_2[\tau_{h_i}|\eta - \eta'|] \operatorname{sgn}(\eta - \eta')\, d\eta' \right\} = 0 \quad (5)$$

Since the quantity in braces is not in general independent of the index, i, and all of the ϕ_i depend upon the local temperature T in a different way, it is clear that solving (5) for the temperature distribution $T(\eta)$ is a formidable task. The difficulty has been overcome or reduced in the past in any one of several ways. The reduction to a single band is not of special interest here. Linearization has proven very popular and informative. In this case all the ϕ_i are identical and new transfer functions can be defined which superficially eliminate the summation. The optically thin limit accomplishes something similar in that $K_2(x)$ becomes equal to one for all bands and a new dependent function can be defined which again eliminates the summation for computing purposes. A similar summation elimination can be accomplished by assuming all band optical depths, τ_{h_i}, to be the same. Then, without assuming the D_i to be the same, a new dependent variable can be defined and the problem is rather similar to that of the single band. Most, if not all, of these methods have been used previously with occasional minor modifications. There is a clear unifying result of each of these methods in that the summation has at least been symbolically eliminated in every case.

A Criterion for Symbolic Summation Elimination

If one gives careful consideration to equation (5) it might first be noticed that the transfer function $K_2(x)$ appears in every term. Since previous work has indicated that useful results are likely to be obtained if the summation can somehow be eliminated from equation (5), it appears useful to consider the conditions necessary for this to be accomplished.

All of the methods previously mentioned accomplished this purpose, but every one imposed some condition that it is desirable to avoid. It appears that the least restrictive criterion is to assume that $K_2[\tau_{h_i}x]$ is factorable in the form $K_2[\tau_{h_i}x] = g(\tau_{h_i})f(x)$; then equation (5) can be written

$$\sum_{i=1}^{N} B_i \tau_{h_i} g(\tau_{h_i}) \left\{ [\phi_i(0) - 1] f(\eta) + \phi_i(1)\, f(1-\eta) \right. \\ \left. + \int_0^1 \frac{d\phi_i(\eta')}{d\eta'} f[|\eta - \eta'|] \operatorname{sgn}(\eta - \eta')\, d\eta' \right\} = 0 \quad (6)$$

This equation provides the necessary ingredients for a relatively general treatment of multiband radiative transfer. To begin one defines the dimensionless variable,

$$\psi = \frac{\sum_{i=1}^{N} B_i \tau_{h_i} g(\tau_{h_i}) \phi_i}{\sum_{i=1}^{N} B_i \tau_{h_i} g(\tau_{h_i})}$$

Equation (6) then becomes

$$[\psi(0) - 1] f(\eta) + \psi(1) f(1-\eta) \\ + \int_0^1 \frac{d\psi(\eta')}{d\eta'} f[|\eta - \eta'|] \operatorname{sgn}(\eta - \eta')\, d\eta' = 0 \quad (7)$$

The remarkable characteristic of this equation is that ψ is a universal function of η. In terms of ψ, equation (1) for the radiative flux is now

$$Q = 1 + 2 \sum_{i=1}^{N} B_i \left\{ K_3[\tau_{h_i}] + \tau_{h_i} g(\tau_{h_i}) \int_0^1 \psi(\eta') f[1 - \eta']\, d\eta' \right\} \quad (8)$$

in which η has been set equal to one since Q is a constant for radiative equilibrium. It is significant that equation (7) is a linear form, whereas equations (5) and (6) are not.

Applications

There are some cases of special interest in which $K_2(x)$ can be factored as indicated in the previous section. These include the optically thin limit, the square-root limit, and the logarithmic limit for molecular gases. Particular results are considered in what follows.

Optically Thin Limit. This is the simplest condition for which K_2 factors and is independent of spectral absorption models. Since $K_2(x) \to 1$ as $x \to 0$, one finds that $f = g = 1$. The solution of equation (7) is readily found to be $\psi = \frac{1}{2}$. The temperature is a constant and is found by solving the transcendental equation

$$2 \sum_{i=1}^{N} [E_{\nu i}(T) - E_{\nu i}(T_2)]\, S_i = \sum_{i=1}^{N} [E_{\nu i}(T_1) - E_{\nu i}(T_2)]\, S_i \quad (9)$$

where S_i is the integrated band intensity and

$$E_{\nu i}(T) = \frac{2\pi \hbar c^2 \nu_i{}^3}{\exp(\hbar c \nu_i / kT) - 1} \quad (10)$$

The flux follows from equation (8) by using the limit $K_3(x) \to -x$ as $x \to 0$. The integral term yields $\tau_{h_i}/2$, which is half the total dimensionless emission from an individual band directed toward the cold wall. Equation (8) thus gives

$$Q = 1 - \sum_{i=1}^{N} B_i \tau_{h_i} \quad (11)$$

valid for $\tau_{h_i} \ll 1$.

It is worth noting that equation (11) expresses a superposition principle in that exactly the same result is obtained by ignoring the coupling between bands and solving for the net absorption of each band as though it existed in its own state of radiative equilibrium independently of the others. Indeed, the validity of a superposition

Nomenclature

$B_i = [E_{\nu i}(T_1) - E_{\nu i}(T_2)] D_i / \sigma(T_1{}^4 - T_2{}^4)$
C = a constant
C' = a constant
c = speed of light
D_i = width parameter for ith band
$E_{\nu i}$ = Planck function at wavenumber ν_i
h = slab thickness
$\hbar$ = Planck constant
K_n = radiative transfer functions
k = Boltzmann constant
Q = total radiative flux, $q^r/\sigma(T_1{}^4 - T_2{}^4)$
Q^r = negative of net radiative flux absorbed by the gas, dimensionless
$Q_e{}^r$ = gas radiative emission to the cold boundary, dimensionless
q^r = radiative flux
S_i = integrated intensity of ith band
T_n = boundary temperatures, $n = 1, 2$
y = spatial coordinate
β_i = fine structure parameter for ith band
γ = Euler-Mascheroni constant, 0.5772 . . .
$\eta = y/h$
θ = dimensionless temperature, $\theta = (T - T_2)/(T_1 - T_2)$
ν = spectral wave number
ρ_a = absorbing medium density
σ = Stefan-Boltzmann constant
τ_{h_i} = optical depth of the ith band, $\tau_{h_i} = \rho_a S_i h / D_i$
$\phi_i = [E_{\nu i}(T) - E_{\nu i}(T_2)]/[E_{\nu i}(T_1) - E_{\nu i}(T_2)]$
ψ = defined just prior to equation (7)

principle for determining the radiative flux is guaranteed by the form of equation (7) because ψ is a function of η alone and is the same irrespective of the number of individual bands.

Square-Root Limit. The square-root limit is determined by every significant band satisfying the two conditions $\tau_{h_i}/\beta_i \gg 1$ and $\beta_i \tau_{h_i} \ll 1$. Under these conditions $K_2(\tau_{h_i}x) = (2/3)(\beta_i/\tau_{h_i}x)^{1/2}$ so that $g = (2/3)(\beta_i/\tau_{h_i})^{1/2}$ and $f(x) = x^{-1/2}$. It is a regrettable fact that radiative *equilibrium solutions for single-band media are not readily available* in this limit. Nevertheless, from equation (8) with $K_3[\tau_{h_i}] = -(4/3)(\beta_i \tau_{h_i})^{1/2}$ the flux is expected to be given by

$$Q = 1 - C \sum_{i=1}^{N} B_i(\beta_i \tau_{h_i})^{1/2} \tag{12}$$

where C is a constant. It is interesting to observe that if $\beta_i = 1$ the foregoing result applies to bands with a Lorentz profile provided that $\tau_{h_i} \gg 1$. In this case the constant C can be determined from the calculations of Crosbie and Viskanta [22] to be approximately 0.894 for Lorentz bands.

Logarithmic Limit. It is reasonably well established that for many molecular gases at large optical depth there is a fairly extensive logarithmic region. The evidence is largely experimental in nature although Edwards and Menard [25] have shown that such a limit is expected for nonrigid rotators. For this case $K_2[x] \rightarrow 1/2x$ [21] so that one finds $g = 1/2\tau_{h_i}$ and $f(x) = 1/x$. Furthermore, it is known that at large τ_{h_i} a condition of thermal continuity at the boundaries of a medium in radiative equilibrium is approached [22, 26]. Thus, one may use the conditions $\psi(0) \rightarrow 1$ and $\psi(1) \rightarrow 0$. Equation (7) then reduces to the form obtained originally by Mighdoll and Cess [9] for linearized radiative transfer. Consequently, their solution applies equally well here with the result

$$\psi(\eta) = \frac{1}{2} + \frac{1}{\pi} \sin^{-1}(1 - 2\eta) \tag{13a}$$

where

$$\psi(\eta) = \frac{\sum_{i=1}^{N} [E_{\nu i}(T) - E_{\nu i}(T_2)]D_i}{\sum_{i=1}^{N} [E_{\nu i}(T_1) - E_{\nu i}(T_2)]D_i} \tag{13b}$$

These may be solved for $T(\eta)$ through use of equation (10). However, since one can choose $T_1 \geq T \geq T_2$, it is easiest to invert equation (13a) to obtain

$$\eta = \frac{1}{2}\left\{1 + \sin\left[\pi\left(\frac{1}{2} - \psi(T)\right)\right]\right\} \tag{14}$$

which gives η explicitly for each choice of temperature T.

Use of equation (13a) in equations (8) shows that the integral term has the value ln 2. The dimensionless emission from the gas absorbed at the cold boundary is thus $2 \ln 2 = 1.386$ [27] for each band. This value is independent of the actual value of τ_{h_i} and is the same for all band absorption equations with a logarithmic asymptote. The flux given by equation (8) in the logarithmic limit is obtained by making use of the fact that $2K_3[x] \sim -\ln x - C$ where C is a constant depending upon the band absorption equation being used [21]. It may *incorporate the band structure effects of* β_i *as well. Equation (8) in* the logarithmic limit therefore becomes

$$Q = 1 + \sum_{i=1}^{N} B_i Q^r(\tau_{h_i}) \tag{15a}$$

where

$$Q^r(\tau_{h_i}) = -\ln \tau_{h_i} - C + \ln 4 \tag{15b}$$

For an overlapped-line, exponential band profile, $C = \gamma + ½$, and equation (15b) has been shown to have acceptable error for $\tau_{h_i} > 10$; for larger τ_{h_i} the error asymptotically approaches zero fairly rapidly [27]. It is of significance that the last two terms of (15b) are negligible only at extremely large values of τ_{h_i} due to the slow rate at which $\ln \tau_{h_i}$ increases.

An Approximation for Arbitrary Optical Depths

All of the preceding results have required that each band fall within the same absorption regime, yet it is certainly conceivable that important conditions may arise in which band parameters are distributed in such a way that significant effects are due to bands falling in adjacent or transitional regions. In that case the transmission function $K_2(x)$ either factors in a different way for each band or cannot be factored at all and a simple result like equation (7) is not rigorously possible.

Nevertheless, an equation of the form of (15a) holds a strong appeal as an approximation for arbitrarily distributed band parameters, since its application requires only a single band solution for the dimensionless flux Q^r as a function of optical depth and line structure parameters. Such a solution appears to be available only for the overlapped line limit [22]. There are a number of reasons why such an approximation might prove valuable. Among them is the fact that the linear, square-root, and logarithmic limits will be correctly evaluated. Furthermore, reference to equation (1) shows that $Q^r(\tau_{h_i})$ may be defined by the terms in braces. Of these, the first represents absorption of surface radiation and this can be evaluated without reference to the solution of the energy equation. The second, integral term represents gas emission and it is only this term that the proposed approximation would seek to estimate. The relative importance of the second term is greatest in the optically thin limit when the error in Q^r would be of the same magnitude as the error in the estimate of emission. The error behavior as a function of optical depth is best illustrated by an application to follow.

The approximate procedure also is supported by the observation that in most cases of interest significant emission is due to only a few bands and the error will be dominated by the strongest of them. One might also observe that the uncertainties in the band absorption equations themselves [4, 21] might well dominate all error considerations.

Application to the Overlapped-Line Limit. At high pressure and/or temperature the band fine structure becomes diffused and the overlapped-line limit is applicable. Since exact numerical solutions for a single band are available they may be used to construct an approximate treatment and to provide guidance for an extension to less restrictive conditions. Crosbie and Viskanta [22] have tabulated $Q^r(\tau_h)$ over the range $0.01 \leq \tau_h \leq 100$ for an exponential as well as other band shapes. For smaller and larger values of τ_{h_i} one has $Q^r \sim -\tau_{h_i}$ and $Q^r \sim -\ln \tau_{h_i} - \gamma - 1/2 + \ln 4$ [27], respectively. For extensive comparitive calculations, tabulations are inefficient and an analytical approximation of Q^r is especially desirable. Since Q^r can be written

$$Q^r(\tau_h) = 2K_3[\tau_h] + Q_e{}^r(\tau_h) \tag{16}$$

only an expression for $Q_e{}^r$ is needed. The radiative emission is asymptotic to τ_h and ln 4 at optically thin and logarithmic limits. An equation that satisfies these limits can be obtained by a modification of a result obtained in reference [21]. The modified equation is

$$Q_e{}^r \approx \ln 4\,[1 - (2/3)\,\{E_3(\tau_h/\ln 4) + [1 - \exp(-\tau_h/\ln 4)]/(\tau_h/\ln 4)\}] \tag{17}$$

and this is compared with the exact values in Table 1. Table 2 compares values of Q^r, which indicates to some degree the extent of the effect of errors in $Q_e{}^r$ on Q^r. These errors are well within the limits of uncertainty of any band absorption correlation.

Equation (17) is a modified form of the equation for emission from a medium with linear emissive power distribution. Equivalent equations for other logarithmic type absorption equations are also available in [21] and can be similarly modified, although there is no certainty that errors will be exactly like those in Tables 1 and 2.

The rather favorable comparison of approximate and exact values of $Q_e{}^r$ and Q^r suggests the extension to bands of arbitrary line structure parameter.

Application to Edwards' Wide Band Model. The simplest extension to bands with line structure can be made using the band absorption equations of Edwards and Menard [25]. This is not only the

Table 1 Exact and approximate predictions of exponential band emission from a slab in radiative equilibrium

τ_h	Q_e^r Reference [22]	Q_e^r Equation (17)	ϵ_e Percent error
0.2	0.1682	0.1689	0.425
0.5	0.3538	0.3580	1.187
1.0	0.5658	0.5790	2.325
2.0	0.8094	0.8406	3.860
5.0	1.0795	1.1330	4.953
10.0	1.2081	1.2582	4.147
20.0	1.2856	1.3222	2.844
50.0	1.3403	1.3607	1.517
100.0	1.3613	1.3735	0.897

Table 2 Exact and approximate predictions of exponential band flux attenuation through a slab in radiative equilibrium

τ_h	$-Q^r$ Reference [22]	$-Q^r$ Equations (16), (17)	ϵ_r % error	$\lvert\epsilon_r/\epsilon_e\rvert$
0.2	0.1703	0.1695	−0.421	0.99
0.5	0.3685	0.3643	−1.140	0.96
1.0	0.6211	0.6080	−2.118	0.91
2.0	0.9798	0.9485	−3.190	0.83
5.0	1.6074	1.5539	−3.330	0.67
10.0	2.1717	2.1216	−2.307	0.56
20.0	2.7873	2.7507	−1.312	0.46
50.0	3.6489	3.6285	−0.558	0.37
100.0	4.3211	4.3089	−0.283	0.32

simplest model available but is also the only one for which extensive compilations of correlation constants have been made [4]. Following the discussion of Nelson [21] expressions for $K_3(\tau_h)$ and $Q_e{}^r$ are readily found. Employing the modification of $Q_e{}^r$ suggested earlier these are

$$2K_3(\tau_h) = \begin{cases} -2\tau_h + [(\beta^3+2)/6\beta]\tau_h{}^2; & \tau_h \le \beta \\ -8(\beta\tau_h)^{1/2}/3 + (\beta\tau_h)^2/6 + \beta; & \beta \le \tau_h \le \beta^{-1} \\ -\ln(\beta\tau_h) - 5/2 + \beta; & \tau_h \ge \beta^{-1} \end{cases} \tag{18}$$

$$Q_e{}^r = \begin{cases} \ln 4\,[\tau_h{}^* - [(\beta^3+2)/9\beta]\tau_h{}^{*2}]; & \tau_h{}^* \le \beta \\ \ln 4\,[8(\beta\tau_h{}^*)^{1/2} - (\beta\tau_h{}^*)^2 - \beta^2/\tau_h{}^*]/9; & \beta \le \tau_h{}^* \le \beta^{-1} \\ \ln 4\,[1 - [2/\beta\tau_h{}^* + \beta^2/\tau_h{}^*]/9]; & \tau_h{}^* \ge \beta^{-1} \end{cases} \tag{19}$$

where $\tau_h{}^* = \tau_h/\ln 4$ and $\beta \le 1$. If the actual calculated β exceeds one, the value used must be one. Equations (15a), (16), (18), and (19) provide the basis of an approximate procedure for all optical depths and line structure parameters.

Comparison With the Isothermal-Gas Zone Method. The most common approximation in lieu of exact numerical solution is to assume the gas to be isothermal at a temperature determined by the condition of no net energy transfer from the gas. With this assumption the last term of equation (3) vanishes. If the resulting equation is evaluated at $\eta = 0$ and $\eta = 1$ and these are subtracted, the result must be zero and the gas temperature is determined by

$$\sum_{i=1}^{N} 2E_{\nu i}(T)\,D_iK_3[\tau_{h_i}] = \sum_{i=1}^{N} [E_{\nu i}(T_1) + E_{\nu i}(T_2)]D_iK_3[\tau_{h_i}] \tag{20}$$

Use of the foregoing result in equation (3) with $\eta = 0$ gives the result

$$Q = 1 + \sum_{i=1}^{N} B_iK_3[\tau_{h_i}] \tag{21}$$

Both equations (20) and (21) are correct in the optically thin limit. In the square-root and logarithmic limits the isothermal approximation will introduce some error since the emission term is incorrectly predicted to be $-K_3[\tau_{h_i}]$. In the square-root limit $Q_e{}^r(\tau_{h_i}) = 4C'\sqrt{\beta_i\tau_{h_i}}/3$, where C' is a constant different from one for the nonisothermal gas and equal to one for the isothermal gas. Thus the isothermal approximation mispredicts the emission by the factor $1/C'$ while the percent error in Q^r is $(C'-1)/(2-C')$ in the square-root limit. The error problem becomes particularly acute in the logarithmic limit where $Q_e{}^r(\tau_{h_i}) = \ln 4$ is exact but the isothermal approximation predicts $(\ln \tau_{h_i} + \gamma + 1/2)/2$ so that the error for each band will be somewhat different. The band percent error in Q^r is $(F(\tau_{h_i}) - 1)/(2 - F(\tau_{h_i}))$, where $F(\tau_{h_i}) = (\ln 16)/(\ln \tau_{h_i} + \gamma + 1/2)$. If every $\tau_{h_i} \to \infty$ the isothermal approximation underpredicts the magnitude of Q^r by a factor of two. This is the maximum error expected but it is quite substantial. It thus appears that the present approximation procedure should be superior to the isothermal-gas method because in practice there is always a nonisothermal region near a wall. If the wall is cooler than the gas the emission to it is reduced, especially so at larger optical depth [16–18].

Results and Discussion

There are a number of radiatively active gases of importance in engineering applications. However, it is generally conceded that water vapor and carbon dioxide are of most importance in the majority of cases. Water vapor is rather more difficult to characterize because of its more complex structure. Carbon dioxide, although complex, is more tractable. Among the results obtained, those at large optical depth in the logarithmic limit are the most interesting. There is something to be gained from a specific example. For this purpose a hot wall temperature of 1,000 K and a cold wall temperature of 300 K are taken to bound a pure carbon-dioxide gas at reasonably high pressure. For convenience, properties are evaluated at the boundary mean temperature of 650 K. In Fig. 1 several different thermal distributions are plotted for CO_2. θ represents the dimensionless temperature distribution obtained from equation (14), ψ is from equation (13), and the ϕ_i's represent the dimensionless emissive power distribution for each band corresponding to the actual temperature distribution. A dominant band would have a ϕ distribution close to that of ψ. In the present case this is true for the 4.3 μm band. The difference between ϕ_i and ψ is an indication of the local imbalance of absorption and emission for a given band. Values of ϕ_i less than ψ indicate absorption dominating emission while the opposite holds if ϕ_i exceeds ψ. It is clear that some bands contribute positive and others negative components to the local flux divergence and this lends physical support of the mathematical analysis. Many prior multiband calculations have been obtained in the limit of linearized radiation. For this reason calculations for a cold wall temperature of 950 K were also performed. This gives a ratio $(T_1 - T_2)/T_1$ of 0.05, a value that is expected to show

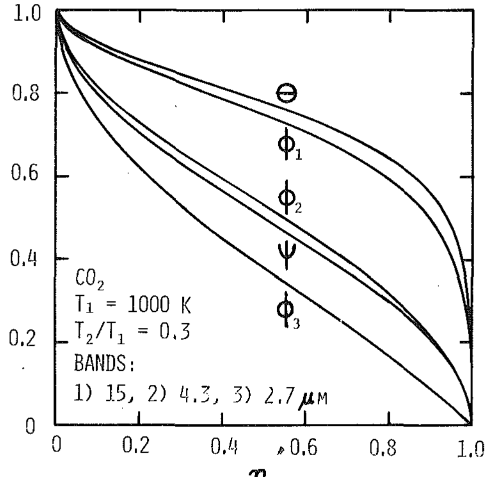

Fig. 1 Thermal profiles for an optically thick slab of carbon-dioxide gas

some degree of nonlinear effects although these are not expected to be overly significant. Qualitatively the results are similar to those of Fig. 1, but as would be expected all of the distributions cluster rather closely about that of ψ. Nevertheless, the deviation from linearized behavior is detectable under these conditions. Similar observations follow from the work of Novotny and coworkers [7, 11, 12] for substantially different maximum temperature.

Although results of calculations for the energy flux based upon the proposed approximate procedure would be of interest, there are at this time no exact calculations for multiband radiation with which a meaningful comparison could be made. Nevertheless, it is clear that this approximation would be superior to others currently employed.

Conclusions

The analysis has been based upon the assumption of radiative equilibrium but has a wider applicability. In particular, several prior studies of pure radiative transfer, which have been restricted to linearized radiation or single band models, can be immediately reinterpreted in terms of the multiband dependent variable if conditions allow the factorable $K_2(x)$ function. Much of the work of Cess and coworkers [14] on radiating media with uniform heat generation can be extended beyond his linearization restriction by an almost trivial reformulation. In a similar fashion the single-band perturbation analysis of Lin and Chan [26] also holds for multiband media. This work was analytically restricted to large optical depth, but it was found that the results were also valid in the optically thin limit and gave good results at intermediate optical depth. This suggests that the $K_2(x)$ function is almost factorable at all optical depth for the exponential band model and further supports the premise of the approximate procedure suggested. It is an interesting observation that the various gray-band models that have been used from time to time do not yield to a simple multiband formula for the radiative flux because the $K_2(x)$ function cannot be factored except in the optically thin limit. This problem is not overcome through use of a differential formulation. Thus, multiband radiative transfer is an example of a problem that can actually be made more complicated by the common, multiple, narrow, gray-band assumption.

The results obtained may have a wider applicability than is immediately apparent. Nelson [28] has shown that coupled thermal conduction and nongray radiative transfer is reasonably approximated by simple superposition. It was also observed that this appeared to be true for nonlinear as well as linearized radiation. If the two effects can be separated the number of absorption-emission bands should be irrelevant and superposition is expected to give reasonable estimates for combined conduction-radiation through multiband, planar media.

References

1 Hottel, H. C., and Sarofim, A. F., *Radiative Transfer*, McGraw-Hill, New York, 1967.

2 Goody, R. M., *Atmospheric Radiation*, Oxford University Press, London, 1964.

3 Tien, C. L., "Thermal Radiation Properties of Gases," *Advances in Heat Transfer*, Vol. 5, Academic Press, New York, 1968.

4 Edwards, D. K., and Balakrishnan, A., "Thermal Radiation by Combustion Gases," *International Journal of Heat and Mass Transfer*, Vol. 16, 1973, p. 25.

5 Cess, R. D., Mighdoll, P., and Tiwari, S. N., "Infrared Radiative Heat Transfer in Nongray Gases," *International Journal of Heat and Mass Transfer*, Vol. 10, 1967, p. 1521.

6 Wang, L. S., "An Integral Equation of Radiative Equilibrium in Infrared Radiating Gases," *Journal Quant. Spectrosc. Radiat. Transfer*, Vol. 8, 1968, p. 851.

7 Novotny, J. L., and Kelleher, M. D., "Conduction in Nongray Radiating Gases," *International Journal of Heat and Mass Transfer*, Vol. 11, 1968, p. 365.

8 Cess, R. D., and Tiwari, S. N., "The Interaction of Thermal Conduction and Infrared Gaseous Radiation," *Applied Scientific Research*, Vol. 20, 1969, p. 25.

9 Mighdoll, P., and Cess, R. D., "Infrared Radiative Equilibrium Under Large Path Length Conditions," *AIAA Journal*, Vol. 6, 1968, p. 1778.

10 Schimmel, W. P., Novotny, J. L., and Kast, S., "Effect of Surface Emittance and Approximate Kernels in Radiation-Conduction Interaction," *Wärme-und Stoffübertragung*, Vol. 3, 1970, p. 1.

11 Schimmel, W. P., Novotny, J. L., and Olsofka, F. A., "Interferometric Study of Radiation-Conduction Interaction," *Proceedings, Fourth International Heat Transfer Conference*, Elsevier Publishing Co., Amsterdam, 1970.

12 Novotny, J. L., and Olsofka, F. A., "Influence of a Nonabsorbing Gas in Radiation-Conduction Interaction," *Prog. in Aero. and Astro.*, Vol. 24, MIT Press, 1971, p. 410.

13 Edwards, D. K., Glassen, L. K., Hauser, W. C., and Tuchscher, J. S., "Radiation Heat Transfer in Nonisothermal Nongray Gases," JOURNAL OF HEAT TRANSFER, TRANS. ASME, Series C, Vol. 89, 1967, p. 219.

14 Cess, R. D., and Tiwari, S. N., "Infrared Radiative Energy Trnasfer in Gases," *Advances in Heat Transfer*, Vol. 8, Academic Press, New York, 1972.

15 Greif, R., and McEligot, D. M., "Thermally Developing Laminar Flows With Radiative Interaction Using the Total Band Absorptance Model," *Applied Scientific Research*, Vol. 25, 1971, p. 234.

16 Edwards, D. K., and Balakrishnan, A., "Nongray Radiative Transfer in a Turbulent Gas Layer," *International Journal of Heat and Mass Transfer*, Vol. 16, 1973, p. 1003.

17 Edwards, D. K., and Balakrishnan, A., "Self-Absorption of Radiation in Turbulent Molecular Gases," *Comb. and Flame*, Vol. 20, 1973, p. 401.

18 Balakrishnan, A., and Edwards, D. K., "Established Laminar and Turbulent Channel Flow of a Radiating Molecular Gas," *Proceedings, Fifth International Heat Transfer Conference*, Vol. 1, Japan Society of Mechanical Engineers—The Society of Chemical Engineers, Japan, 1974, p. 93.

19 Bratis, J. C., and Novotny, J. L., "Radiation-Convection Interaction in the Boundary Layer Regime of an Enclosure," *International Journal of Heat and Mass Transfer*, Vol. 17, 1974, p. 23.

20 Nelson, D. A., and Edwards, D. K., "Spectrally Dependent Radiative Transfer in a Heat Conducting Medium," *Wärme-und Stoffübertragung*, Vol. 8, 1975, p. 11.

21 Nelson, D. A., "A Study of Band Absorption Equations for Infrared Radiative Transfer in Gases," *J. Quant. Spectrosc. Radiat. Transfer*, Vol. 14, 1974, p. 69.

22 Crosbie, A. L., and Viskanta, R., "Effects of Band or Line Shape on the Radiative Transfer in a Nongray Planar Medium," *J. Quant. Spectrosc. Radiat. Transfer*, Vol. 10, 1970, p. 487.

23 Chan, S. H., and Tien, C. L., "Total Band Absorptance of Nonisothermal Infrared Radiating Gases," *Journal Quant. Spectrosc. Radiat. Transfer*, Vol. 9, 1970, p. 487.

24 Edwards, D. K., and Morizumi, S. J., "Scaling of Vibration-Rotation Band Parameters for Nonhomogeneous Gas Radiation," *Journal Quant. Spectrosc. Radiat. Transfer*, Vol. 10, 1970, p. 175.

25 Edwards, D. K., and Menard, W. A., "Comparison of Models for Correlation of Total Band Absorption," *Applied Optics*, Vol. 3, 1964, p. 621.

26 Lin, C. C., and Chan, S. H., "An Analytical Solution for a Planar Nongray Medium in Radiative Equilibrium," JOURNAL OF HEAT TRANSFER, TRANS. ASME, Series C, Vol. 97, 1975, p. 29.

27 Nelson, D. A., "Radiation Heat Transfer Through Molecular Gases at Large Optical Depth," JOURNAL OF HEAT TRANSFER, TRANS. ASME, Series C, Vol. 98, 1976, p. 310.

28 Nelson, D. A., "On the Uncoupled Superposition Approximation for Combined Conduction-Radiation Through Infrared Radiating Gases," *International Journal of Heat and Mass Transfer*, Vol. 18, 1975, p. 711.

N. M. Schnurr
Professor.
Mem. ASME

A. B. Shapiro
Graduate Student.

M. A. Townsend
Professor.
Mem. ASME

Department of Mechanical Engineering,
Vanderbilt University,
Nashville, Tenn.

Optimization of Radiating Fin Arrays With Respect to Weight

A nonlinear optimization approach is used to determine the minimum weight design for radiating fin arrays used in space applications. Straight and circular fins of rectangular and triangular profile are considered for emissivities in the range of 0.8 to 1.0. The heat transfer analysis includes fin to fin and fin to base radiative interactions. The results, presented in graphical form, give the optimum geometries for the profiles considered in terms of dimensionless parameters. Thus, for specified values of heat transfer rate, base cylinder surface temperature and thermal properties of the fin material, these curves may be used to design minimum weight fin arrays. Two numerical examples are given.

Introduction

The rejection of heat in space is accomplished by the use of radiating surfaces. The problem considered here is the heat transfer from a long cylinder of specified radius r_i, emissivity ϵ, and surface temperature T_b. If the required rate of heat transfer per unit length of cylinder is greater than $2\pi r_i \sigma \epsilon T_b{}^4$, the effective surface area must be increased by the addition of fins.

The two types of fin arrays which appear to be most suitable use either circular or straight fins (see Fig. 1). In either case there are several possible fin profiles which could be selected. A rectangular profile is probably the least expensive, but a triangular profile may be preferable from the standpoint of heat transfer per unit weight. It is unlikely that a nontrapezoidal profile would be selected due to manufacturing difficulties.

Analyses have been reported by Sparrow, et al. [1][1] for circular fins of rectangular profile with $\epsilon = 1$ and by Karlekar and Chao [2] for straight fins of trapezoidal profile. The results given in reference [2] could be used to obtain a minimum mass design. Fin to base interactions were neglected in their analysis, however, and the results may not be directly applied to cases where the heat transfer rate is specified and the geometry of the fin array is to be determined.

More recent analyses [3, 4] have treated both types of fin arrays. The radiating surfaces are assumed gray and the fin profiles are trapezoidal. Fin-to-fin and fin-to-base radiative interactions are included. Utilizing dimensionless design and operating parameters, results are presented in [3, 4] which can be used to predict the heat transfer from a fin array for specified values of base surface temperature, emissivity and thermal conductivity of the fin material, and geometrical parameters. These results can be used to obtain a minimum weight design, but this entails a trial-and-error procedure and a large amount of cross-plotting. The purpose of the work reported here is to perform the optimization with respect to weight for straight

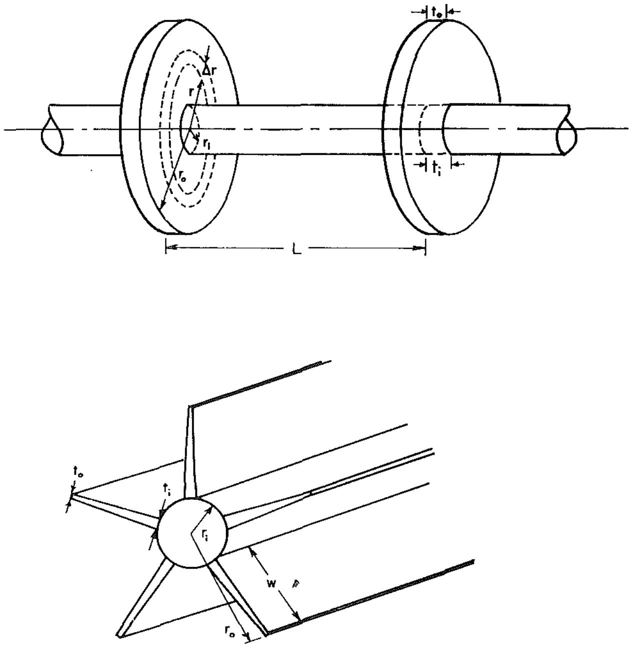

Fig. 1 Circular and straight fin arrays

---

[1] Numbers in brackets designate References at end of paper.

Contributed by the Heat Transfer Division for publication in the JOURNAL OF HEAT TRANSFER. Manuscript received by the Heat Transfer Division May 10, 1976.

and circular fin arrays of rectangular and triangular profiles and to present results which can easily be used to obtain the minimum weight designs.

Optimization of Fin Arrays

The numerical method consists of two major algorithms. The first is the numerical solution of the temperature distribution and resulting heat transfer for the specified type of fin array (circular or straight). The second algorithm performs the optimization of the fin array with respect to weight. Each of these algorithms will be discussed in some detail.

Heat Transfer Algorithm for Circular Fin Arrays. The analysis is based on the following assumptions.

1 Steady-state operation is assumed.
2 The temperature distribution in the fin is one-dimensional.
3 The tube surface is isothermal.
4 All surfaces are radiatively gray and diffuse and have the same emissivity.
5 There is no incident radiation from external sources.
6 Thermal conductivity is a constant.
7 The fin thickness at the base is small compared to the spacing between the center planes of adjacent fins.

The determination of the temperature distribution in the fin and the heat flux from the array requires the simultaneous solution of the differential equation for heat conduction in the fin and the equations of radiant heat transfer in a nonisothermal gray enclosure formed by two adjacent fins, the segment of tube surface between them, and space. The conduction equation is

$$\frac{d^2T}{dr^2} + \frac{1}{t}\left(\frac{dt}{dr} + \frac{t}{r}\right)\frac{dt}{dr} = \frac{2q_r}{kt} \qquad (1)$$

The boundary conditions are

$$T = T_b \qquad \text{at } r = r_i$$

and

$$dT/dr = -\sigma\epsilon T^4/k \qquad \text{at } r = r_0$$

Equation (1) may be nondimensionalized using

$$X = r/r_0, \qquad Y = t/t_i, \qquad N_t = t_0/t_i$$

and

$$N_c = 2\sigma\epsilon T_b{}^3 r_i{}^2/k_0 t_i$$

The result is

$$\frac{d^2\theta}{dX^2} + \frac{1}{Y}\left(\frac{dY}{dX} + \frac{Y}{X}\right)\frac{d\theta}{dX} = \frac{N_R{}^2 N_C (q_r/\sigma T_b{}^4)}{\epsilon Y} \qquad (2)$$

For a trapezoidal profile

$$Y = 1 + (XN_R - 1)(N_t - 1)/(N_R - 1) \qquad (3)$$

and

$$\frac{dY}{dX} = (N_t - 1)\,N_R/(N_R - 1) \qquad (4)$$

The boundary conditions are

$$\theta = 1 \qquad \text{at } X = 1/N_R \qquad (5)$$

and

$$\frac{d\theta}{dX} = \frac{\sigma\epsilon T_b{}^3 r_0}{k}\,\theta^4 \qquad \text{at } X = 1 \qquad (6)$$

The relationship between q_r and T must be obtained by solving the problem of radiation with a nonisothermal gray enclosure. Since a numerical solution is used, it is convenient to introduce the finite-difference approximation, and assume that each annular strip of fin surface (shown in Fig. 1) having width Δr and circumference $2\pi(r + \Delta r/2)$ has a uniform temperature T_j, where $1 \leq j \leq N$ and N is the number of strips. The applicable radiation equations [5] are

$$\sum_{j=1}^{N+1} \chi_{ij} B_j = \Omega_i \qquad (7)$$

where

$$\chi_{ij} = \frac{\delta_{ij} - (1 - \epsilon_i) F_{A_i - A_j}}{\epsilon_i} \qquad (8)$$

$$\Omega_j = \sigma T_j{}^4 \qquad (9)$$

and

$$\delta_{ij} = \begin{matrix} 0 & i \neq j \\ 1 & i = j \end{matrix}$$

Note that the isothermal tube surface is also included, giving rise to $(N + 1)$ equations. The local surface heat flux may be computed from

$$q_{r_i} = \sum_{j=1}^{N+1} \Lambda_{ij} \Omega_j$$

or in dimensionless form

$$\frac{q_{r_i}}{\sigma T_b{}^4} = \sum_{j=1}^{N+1} \Lambda_{ij} \theta_j{}^4 \qquad (10)$$

where

$$\Lambda_{ij} = [\epsilon_i/(1 - \epsilon_i)](\delta_{ij} - \psi_{ij}) \qquad (11)$$

and

$$[\psi] = [\chi]^{-1}$$

The simultaneous solution of equations (3)–(11) constitutes the solution of the problem.

The numerical method used to obtain the temperature distribution and heat flux in the fin array proceeds as follows. The parameters N_R, N_L, and N_t specify the geometry. In addition, ϵ and N_C are specified. A subroutine is then called which calculates all angle factors using the

Nomenclature

A_p = total profile area of a straight fin array, $N_F w(t_i + t_0)/2$
A_R = reference area, $\sigma T_b{}^3 r_i{}^3/k$
F = combined design criterion
k = thermal conductivity
L = center to center spacing between circular fins
p = penalty function parameter
q_r = local radiant heat flux
Q = heat transfer rate per unit length of fin array
r = radial location
r_i = tube radius
r_0 = outside radius of circular fin
t = local fin thickness
t_i = thickness of fin at the root
t_0 = thickness of fin at the tip
T = local fin temperature
T_b = base temperature
V_R = total fin volume per unit length of array for circular fins of rectangular profile, equation (4)
V_T = total fin volume per unit length of array for circular fins of triangular profile, equation (3)
$\overline{V}$ = dimensionless volume per unit length of fin array
w = width of straight fin
ϵ = emissivity
σ = Stefan-Boltzmann constant
N_C = conduction number, $2\sigma\epsilon T_b{}^3 r_i{}^2/(kt_i)$
N_F = number of straight fins
$N_L = L/r_i$
$N_R = r_0/r_i$
$N_t = t_0/t_i$
$N_w = w/r_i$
$Q^* = Q/(2\pi r_i \epsilon\sigma T_b{}^4)$

contour integral method discussed in reference [5]. Then the $[\chi]$ matrix is calculated using equation (8) and is inverted to form the $[\psi]$ matrix. Note that if emissivity is assumed constant, the inversion is done only once since the terms are not temperature dependent. The $[\Lambda]$ matrix may then be calculated from equation (11).

An initial assumption of the temperature distribution is now made and an iterative solution proceeds as follows.

1 The local radiant heat flux (based on the assumed temperature distribution) is calculated from equations (9) and (10).

2 The total heat transfer from the fin is computed by summing the local fluxes multiplied by their respective areas, and adding the radiative loss at the end of the fin.

3 The radiative heat transfer is equated to conduction at the base to determine $d\theta/dX$ at the fin base (first node point).

4 The Runge-Kutta-Nyström method [6] is then used along with the local radiant heat fluxes obtained in step 3 to calculate a new temperature distribution.

5 If the distribution is not identical to the assumed distribution within a set tolerance, steps 1–4 are repeated until convergence is obtained.

6 Results including the dimensionless total heat flux[2] from the fin array, Q^*, are then computed.

The final result of this numerical analysis may be expressed functionally as

$$Q^* = f_1(N_R, N_L, N_t, N_C, \epsilon) \tag{12}$$

Given any combination of the independent dimensionless parameters in equation [12], the heat transfer algorithm may be used to compute Q^*.

The total fin volume per unit length of array for circular fins of triangular profile is

$$V_T = \pi t_i[\tfrac{1}{3}(r_0^2 + r_0 r_i - 2r_i^2)]/L \tag{13}$$

For fins with a rectangular profile, the volume is

$$V_R = \pi t_i(r_0^2 - r_i^2)/L \tag{14}$$

Note that these parameters have units of (length)^2. A dimensionless volume per unit length may then be found by dividing these values by the reference area

$$A_R = \sigma T_b^3 r_i^3/k$$

The resulting expressions are

$$\overline{V} = \tfrac{2}{3}\pi\epsilon(N_R^2 + N_R - 2)/(N_C N_L) \tag{15}$$

and

$$\overline{V} = 2\pi\epsilon(N_R^2 - 1)/(N_L N_C) \tag{16}$$

for triangular and rectangular profiles, respectively.

Heat Transfer Algorithm for Straight Fin Arrays. The procedure used for straight fin arrays is quite similar to that used for the circular fin arrays: The heat transfer algorithm [4] (similar to that used for circular fins except for changes related to geometry) is used to calculate

$$Q^* = f_2(N_F, N_w, N_t, N_C, \epsilon) \tag{17}$$

The variables N_F and N_w replace the N_R and N_L values used in the circular fin analysis. Note, however, that N_F takes on only integer values. The dimensionless volume in this case is obtained by dividing the profile area (volume per unit length of array) by the reference area A_R. The profile area is

$$A_P = N_F w(t_i + t_0)/2 \tag{18}$$

Then

$$\overline{V} = N_F N_w \epsilon(1 + N_t)/N_C \tag{19}$$

$\overline{V}$ is minimized with respect to the independent variables N_w and N_F.

Optimization Technique. In a practical design situation, values of k, ϵ, r_i, T_b, and Q would be specified. The value of N_t $(= t_0/t_i)$ is selected as either zero or unity (triangular or rectangular profile) and Q^* is calculated. To be determined would be the remaining geometrical parameters, viz

circular fins, r_0, L, t_i
straight fins, r_0, t_i

compatible with the specified parameters such that the total array weight is minimized. Finding the minimum weight design is, for all intents and purposes, equivalent to minimizing volume. Accordingly, the problem is now to

minimize array volume $\overline{V}$
subject to a specified value of Q^*

for each of the fin types and profiles. The following table identifies the respective equations from the preceding analyses.

Fin type	(Equation number) Objective, $\overline{V}$	Constraint Q^*
Circular fin		
rectangular profile	(16)	(12)
triangular profile	(15)	(12)
Straight fin		
rectangular profile	(19)	(17)
triangular profile	(19)	(17)

For each type of fin array the entire nonlinear heat transfer problem as presented in the foregoing must be solved to determine these quantities, for each hypothesized design. The problem is now formulated as a nonlinear optimization problem, for which there are a number of standard algorithms which may be used to optimize a nonlinear function of several variables subject to various types of constraints.

After a fairly large amount of "experimentation" with different algorithms, a combined approach using the Fletcher-Reeves conjugate gradient method followed by a Hooke-Jeeves direct search was employed. To use these algorithms in their standard forms [7] entails formulation of a combined design criterion, or penalty function, as follows

$$\text{minimize } F = \overline{V} + p(Q^*_{\text{DESIGN}} - Q^*_{\text{CALCULATED}})^2 \tag{20}$$

where the second term penalizes deviations from the desired Q^*. For each value of a sequence of increasing p, F is minimized until the deviations are arbitrarily small, indicating an optimal (minimal) value of $\overline{V}$ in terms of the design variables for a specified Q^*. This approach is equivalent to the original problem and is a standard technique [8].

It is not uncommon—as was the case here—to find some algorithms which perform better than others on given types of problems, for reasons which very often are not clear. These problems appear due to the strongly nonlinear nature of the basic model.[3] To illustrate the nature of the problem and the necessity of the tandem algorithm approach, consider the shape of the design objective function for the circular fin of triangular profile, as shown in Fig. 2.

The objective function is characterized by being relatively flat with respect to N_L, but shows distinct minima for N_R and N_C, when each variable is considered independently for representative values of the other variables. The second derivative $\partial^2\overline{V}/\partial N_L^2$ is very small in the vicinity of $(N_{R_{\text{opt}}}, N_{C_{\text{opt}}})$. Thus, N_L could be varied by a relatively large

---

[2] *Q^* is the ratio of radiation from the fin array (including the tube) to the radiation which would be emitted by an unfinned tube having the same temperature and emissivity.*

[3] This also results in long computation times of approximately 12 s per function evaluation on a XDS Sigma-7 computer for circular fin cases.

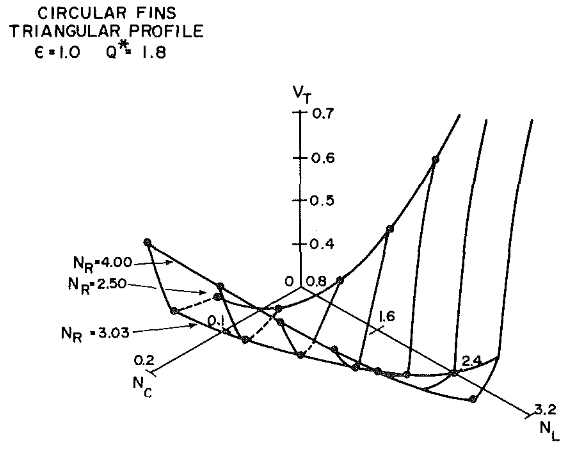

Fig. 2 Design region

amount without any appreciable variation in $\overline{V}$ minimum. Typical values in this region for ΔN_L and $\Delta \overline{V}$ were 0.08 and 0.001, respectively. Thus in the vicinity of the optimum, the design space (Fig. 2) is seen to be an elongated narrow valley. The slope of the sides of the valley become steeper as a result of the distortion introduced by the penalty function. From a design point distant from the valley, the Fletcher-Reeves (gradient-type) algorithm moved rapidly to a region containing an optimum, then bogged down, resulting in a number of pseudo-optima. (The Hooke-Jeeves direct search would also "work" from such starting points, but *very slowly*.) Once in the valley the initially more rapid Fletcher-Reeves algorithm generated directions nearly orthogonal to the best direction to go to get to the minimum of $\overline{V}$ (due to indistinctness of the partial derivatives) and would cease to make progress. At this point, the solution technique was switched to the more robust (but slow) Hooke-Jeeves algorithm which then converged to a minimum. This interrelationship of the algorithms and heat transfer solutions are shown in the flow chart, Fig. 3.

To summarize, the direct search algorithm performed very slowly from distant starting points. Accordingly a number of "optima" were calculated using Fletcher-Reeves and a single value of the penalty parameter p. These were used as starting points for the Hooke-Jeeves direct search. The Hooke-Jeeves algorithm was then implemented with a progressively increasing weighting factor in the penalty function. This technique proved very successful in generating the remaining points for the design curves presented in Figs. 4–7. In most cases final convergence was obtained in under 5 min of computer time. For each of the four cases considered here convergence to an optimum always occurred, and essentially the same optimum was achieved from various starting point, implying global optima in all cases.

In the case of the circular fins, all variables (N_L, N_R, N_C) are manipulated simultaneously in the optimization algorithm. For straight fins because N_F takes an integer value only a value of N_f is selected and optimization is then carried out with respect to N_w and N_C. This is repeated for different values of N_F to determine the optimum design.

Results

Results for circular fins of different profiles are presented in Figs. 4–6, which give optimum values of N_L, N_R, N_C as functions of Q^* for emissivities between 0.8 and 1.0. Fig. 7 and Table 1 give results for straight fins in terms of N_C and N_F.

The results presented here may easily be used to obtain the minimum weight design of an array of straight or circular fins of triangular or rectangular profile having emissivities between 0.8 and 1.0. It is assumed that ϵ, k, r_i, T_b, and Q are given. Q^* may then be calculated. Sample calculations using a range of T_b and Q which might occur in practical applications show the straight fins to be superior from the standpoint of heat transfer per unit weight. These studies also reiterate the fact that triangular profiles are superior to rectangular profiles for both designs.

Circular Fin Arrays. The results plotted in Figs. 4–6 are optimal at each value of Q^*, since in general the value of Q^* is determined by the application. Other values of N_L, N_R, and N_C will give heavier arrays. It is interesting but probably not significant that in Fig. 5 a maximum spacing between fins is indicated at $Q^* \approx 3.0$ for triangular profiles and 2.0 for rectangular profiles. Similarly $N_{C_{\text{opt}}}$ shows minima

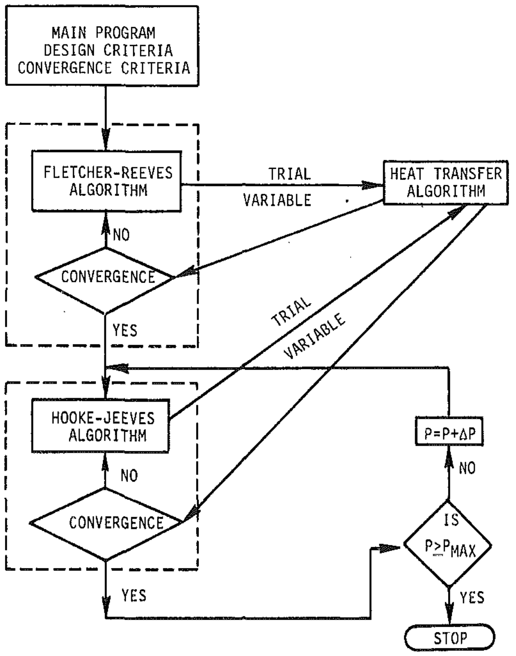

Fig. 3 Flow chart

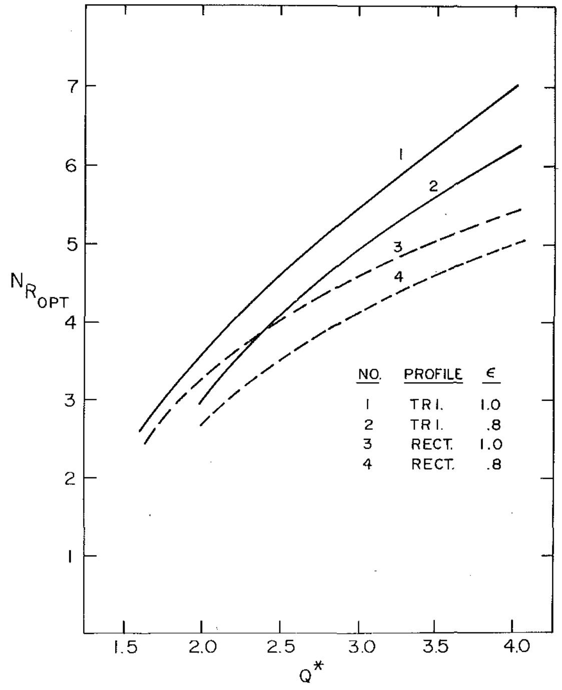

Fig. 4 $N_{R_{\text{opt}}}$ versus Q^* for a circular fin array of minimum weight

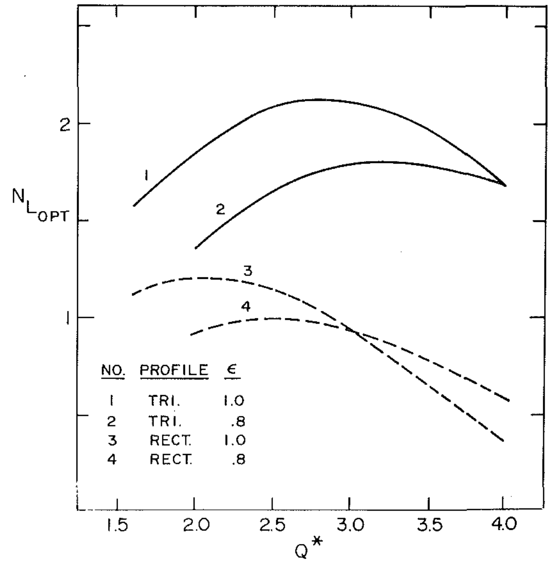

Fig. 5 $N_{L_{\mathrm{opt}}}$ **versus** Q^* **for a circular fin array of minimum weight**

at high Q^*, in Fig. 6. Example calculations are given in the Appendix. The triangular profile is lighter than fins of rectangular profile for the same independent variables.

Straight Fins. Four fins were found to be optimum for both the triangular and rectangular profiles with $\epsilon = 1$. Five fins were found to be slightly better for the $\epsilon = 0.8$ cases. This is in agreement with the result of reference [2]. The difference in weight between the best designs using 4 and 5 fins was only about 5 percent so that results are presented for both cases. The variation of $N_{W_{\mathrm{opt}}}$ with Q^* was found to be linear and may be represented by

$$N_{W_{\mathrm{opt}}} = C(Q^* - 1) \qquad (21)$$

where C is given for each of the six cases considered in Table 1. The variation of $N_{C_{\mathrm{opt}}}$ with Q^* is given in Fig. 7. If straight fins are selected, Table 1 is used to find the optimum number of fins and the coefficient to be used in equation (21) for the calculation of $N_{W_{\mathrm{opt}}}$. For ϵ between 0.8 and 1.0, 4 fins may be selected and linear interpolation may be used to obtain C. Fig. 7 is used to determine $N_{C_{\mathrm{opt}}}$. The fin thickness and width are then computed from the definitions of N_w and N_C. As with circular fins, triangular profiles are superior (lighter) for a given heat transfer. Example calculations are in the Appendix.

Table 1 Results for straight fin arrays

CASE	PROFILE	ϵ	N_F	C	OPTIMUM
1	triangular	1.0	4	2.20	YES
2	triangular	0.8	4	2.03	NO
3	rectangular	1.0	4	2.04	YES
4	triangular	0.8	5	1.90	YES
5	rectangular	0.8	4	1.89	NO
6	rectangular	0.8	5	1.76	YES

Conclusions

The results presented here may be used to obtain the minimum weight design of an array of straight or circular fins of triangular or rectangular profile having emissivities between 0.8 and 1.0. It is assumed there is no incident radiation from any external source. The procedure for obtaining the optimum design is illustrated by the example problems. The heat transfer algorithms used in this work were shown [3, 4] to give excellent agreement with the analyses of references [1, 2]. These results are directly applicable when the required heat transfer rate, tube surface temperature, and material thermal properties are known and the array geometry is to be determined.

Sample calculations using a range of values of T_b and Q which might occur in practical applications show the straight fins to be superior from the standpoint of heat transfer per unit weight. These studies also show the triangular profiles to be superior to rectangular profiles.

Computations times on an XDS Sigma-7 computer were in general quite long especially in the case of the circular fins due to the difficulty of the problem. Using an algorithm combining Fletcher-Reeves and Hooke-Jeeves methods. Convergence to an optimum always occurred (in 5–10 min) and the same optima were achieved from various starting points, implying global optima.

Acknowledgment

The authors wish to acknowledge the contribution of John Yen in the early stages of this work.

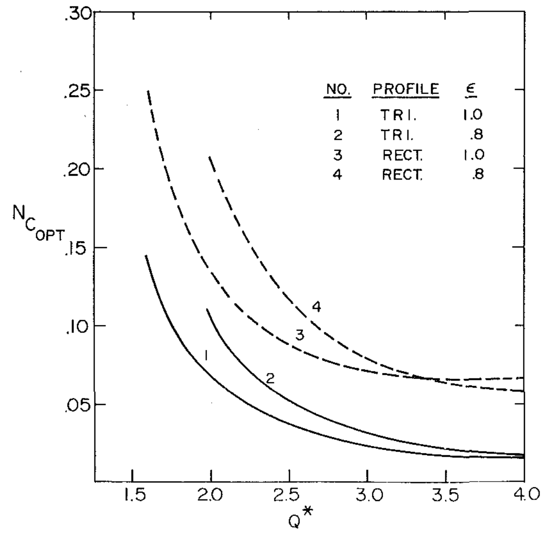

Fig. 6 $N_{C_{\mathrm{opt}}}$ **versus** Q^* **for a circular fin array of minimum weight**

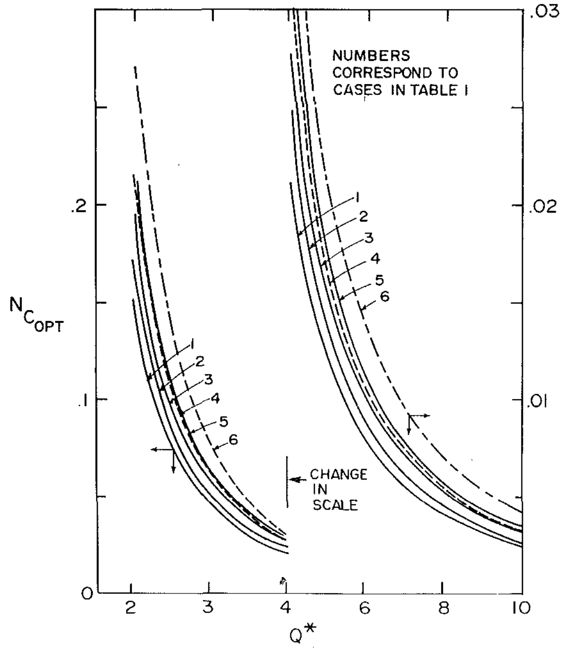

Fig. 7 $N_{C_{\mathrm{opt}}}$ **versus** Q^* **for a straight fin array of minimum weight**

References

1 Sparrow, E. M., Miller, G. B., and Jonsson, V. K., "Radiative Effectiveness of Annular Finned Space Radiators Including Mutual Irradiation Between Radiator Elements," *J. Aero. Sci.*, Vol. 29, 1962, pp. 1291–1299.

2 Karlekar, B. V., and Chao, B. T., "Mass Minimization of Radiating Trapezoidal Fins With Negligible Base Cylinder Interaction," *International Journal of Heat and Mass Transfer*, Vol. 6, 1963, pp. 33–48.

3 Schnurr, N. M., and Cothran, C. A., "Radiation From an Array of Gray Circular Fins of Trapezoidal Profile," *AIAA Journal*, Vol. 12, No. 11, Dec. 1974, pp. 1476–1480.

4 Schnurr, N. M., "Radiation From an Array of Longitudinal Fins of Triangular Profile," *AIAA Journal*, Vol. 13, No. 5, May 1975, pp. 691–693.

5 Sparrow, E. M., and Cess, R. C., *Radiation Heat Transfer*, Brooks/Cole, Belmont, Calif., 1966, pp. 89–90.

6 Kreyszig, E., *Advanced Engineering Mathematics*, Wiley, New York, 1962, pp. 161–162.

7 Kuester, J. L., and Mise, J. H., *Optimization Techniques With Fortran*, McGraw Hill, New York, 1973.

8 Himmelblau, D. M., *Applied Nonlinear Programming*, McGraw Hill, New York, 1972.

APPENDIX

Example Problem-Circular Fin Array. Consider a tube having an outside diameter of 3 cm transporting a condensing fluid at a temperature of 150°C. Heat is to be rejected at a rate of 500 W/m of length. Circular aluminum (k = 208W/m K) fins of triangular profile are to be used. A surface coating gives $\epsilon = 0.9$. Determine the optimum fin array design.

$$Q^* = Q/(2\pi r_i \epsilon \sigma T_b{}^4) = 3.25$$

From Figs. 4–6, interpolating between curves 1 and 2 $N_{R_{\text{opt}}} = 5.6$, $N_{L_{\text{opt}}} = 1.9$, and $N_{C_{\text{opt}}} = 0.023$. Then $r_0 = N_R r_i = 4.88$ cm, $L = N_L r_i = 2.85$ cm, and $t_i = 2\sigma\epsilon T_b{}^3 r_i{}^2/(kN_C) = 0.0363$ cm. The total fin volume per unit length of array (equation (13)) is 0.355 cm^3. For a rectangular profile, using the same procedure, the fin volume per unit length of array is 1.35 cm^3.

Example Problem-Straight Fin Array. The example considered here is identical to that used previously for the circular fin array except an array of straight fins of triangular profile is to be used.

Again, $Q^* = 3.25$

We select 4 fins. This number is optimal for $\epsilon = 1.0$ and gives a mass within 5 percent of the minimum (obtained with a 5 fin array) at $\epsilon = 0.8$. Interpolating between cases 1 and 2, $C = 2.12$.

From equation (21), $N_{W_{\text{opt}}} = 4.77$.
From Fig. 7, $N_{C_{\text{opt}}} = 0.04$.
Then $w = N_w r_i = 7.16$ cm
$t_i = 2\sigma\epsilon T_b{}^3 r_i{}^2/(kN_C) = 0.0209$ cm

The total fin volume per unit length of array (equation 18) is 0.299 cm^3. Note that this is smaller than that for the circular fin array by a factor of 1.19. For a rectangular profile, the fin volume per unit length of array is 0.452 cm^3.

G. J. Kowalski
J. W. Mitchell

University of Wisconsin,
Madison, Wisc.

Heat Transfer From Spheres in the Naturally Turbulent, Outdoor Environment

Heat transfer coefficients from spheres were measured in a naturally turbulent, outdoor environment and compared to measurements made in wind tunnels at various turbulent intensities. The experiments were performed using spheres of three different diameters placed at different heights relative to the ground surface. The time-average values of Nusselt number and Reynolds number were obtained over 5-min time periods. Over the Reynolds number range 2000–35,000, the value of the Nusselt number obtained outdoors was up to 2.2 times the values determined in low turbulent intensity wind tunnels. The data, averaged for each sphere at each height, showed an average enhancement of the Nusselt number that decreased with height from 1.8 to 1.1. The heat transfer enhancement was found to be essentially independent of Reynolds number and correlated with the ratio of height above the surface to the sphere diameter. Standard micrometeorological theory was used to estimate the turbulence intensity as a function of height above the ground. The enhancement in heat transfer was found to be mainly correlated with turbulence intensity. The results for all but the lowest placed spheres are in substantial agreement with results using artificially induced turbulence.

Introduction

The recent interest in mechanistic ecology has encouraged the development of models for the thermal response of animals in the outdoor environment. The convective heat flow to or from an animal is determined by both the microclimate and the shape and orientation of the animal. The convection coefficient is usually predicted using the results of wind tunnel tests on either physical models of the animal or simple geometric models such as spheres, cylinders, or circular disks. An inherent deficiency in this approach is that the wind tunnel flow does not reproduce the character of the turbulence found in the outdoor environment. The natural wind has larger turbulent intensities and scale than the usual wind tunnel air stream.

The effect of atmospheric turbulence is to increase the heat transfer coefficient over that from wind tunnel correlations for low turbulence intensity. In an experimental investigation using circular disks to model plant leaves, Pearman, et al. [1][1] found 50 percent higher heat transfer coefficients outdoors than in low turbulent intensity wind tunnels. Jackson [2], in a study on deer antlers, found a 30 percent increase in the heat transfer rate from cylinders outdoors over standard correlations. While plant leaves may be satisfactorily represented by disks, animals are more closely modeled by spheres and cylinders. In this paper, an experimental investigation of heat transfer from spheres located at different heights in the atmospheric boundary layer near the earth's surface will be described. These results will be useful to engineers, biologists, zoologists, etc., studying heat and mass transfer from shapes outdoors.

Heat transfer results for spheres in wind tunnels both with and without artificially induced turbulence have been obtained by a number of authors. The early work of Williams, as reported by McAdams [3], is commonly referenced in many textbooks as the standard correlation for spheres. The correlation of Knudsen and Katz [4], also widely reported, yields about 40 percent lower heat transfer coefficients over the Reynolds number range of 10^3–10^5. Recent studies by Yuge [5] and Raithby and Eckert [6] yield results in good agreement with the correlation of Knudsen and Katz. This indicates that the correlation presented in McAdams does not represent low turbulent intensity conditions.

Experimental evaluations of the overall heat transfer coefficient for spheres in wind tunnels with artificially induced turbulence have been made by Maisel and Sherwood [7], Yuge [5], Lavender and Pei [8], Galloway and Sage [9, 10], and Raithby and Eckert [6]. These results have been analyzed by Galloway and Sage [9] to provide a correlation of the heat transfer with the turbulent parameters. The results from these studies show that heat transfer enhancement over

---

[1] Numbers in brackets designate References at end of paper.

Contributed by the Heat Transfer Division and presented at the Winter Annual Meeting, Houston, Texas, November 30–December 5, 1975, of THE AMERICAN SOCIETY OF MECHANICAL ENGINEERS. Manuscript received by the Heat Transfer Division. Paper No. 75-WA/HT-57.

the low turbulence intensity value is dependent on turbulence intensity, and increases with increasing Reynolds number. The work of Yuge indicates little enhancement below a Reynolds number of about 4×10^4. All of these results indicate that the scale of turbulence has a small or insignificant effect. The results of these studies will be discussed in more detail in comparison with the experiments presented here.

In order to compare the heat transfer from spheres located in the atmospheric boundary layer with that obtained in wind tunnel testing, the turbulence parameters must be known. The velocity profile, turbulence intensity, and eddy size will be evaluated using known micrometeorological relations [11, 12] which are presented later.

The adiabatic velocity profile for the atmospheric boundary layer is given by

$$u/v_* = (1/K)\ln(z/z_0 + 1) \tag{1}$$

This relation is developed for adiabatic conditions, but is valid within about 2 m of the surface under daytime heating conditions [11, 12]. For the test site at Fort Collins, Colorado, the roughness height z_0 was determined from the measured velocity profiles to be 1 cm. The nondimensional measured velocity profile is shown in Fig. 1. The data were taken over a three week period and demonstrate that equation (1) is valid for these tests.

The theoretical development of equation (1) is based on the mixing length theory of Prandtl applied to the atmospheric boundary layer. The average mixing length, which will be used to estimate the turbulent scale of the flow, is given by [12]

$$\ell = K(z + z_0) \tag{2}$$

The average fluctuating velocity component in the flow direction, u', is related to the average mixing length by

$$u' = \ell\,\partial u/\partial z \tag{3}$$

By combining the logarithmic velocity profile, equation (1), and the mixing length, equation (2), the fluctuating component from equation (3) can be equated to the shear velocity:

$$u' = v_* \tag{4}$$

The turbulent intensity for the atmospheric boundary layer can be obtained by combining equations (1) and (4) to yield

$$T_u = K/\ln(z/z_0 + 1) \tag{5}$$

The calculated turbulent intensity and scale for the atmospheric boundary layer are shown in Fig. 1 for the test site. The mixing length increases linearly with distance above the surface to 80 cm at 200 cm. The turbulence intensity decreases with increasing height from about 20–30 percent near the surface to about 8 percent at 200 cm.

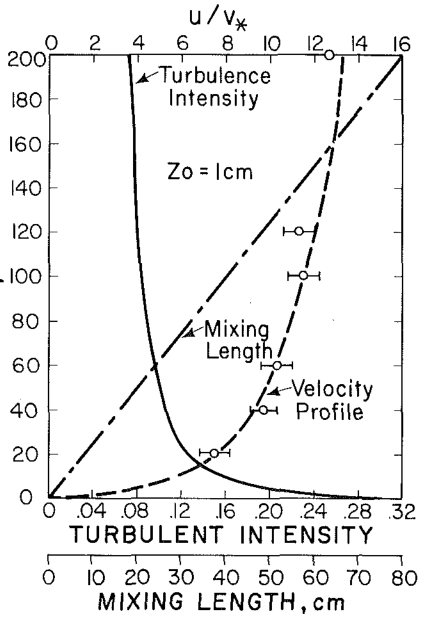

Fig. 1 Turbulence intensity, mixing length, and velocity profile within the atmospheric boundary layer

Experimental Method

Field Tests. The site at which the heat transfer tests were conducted was a short grass prairie located near Fort Collins, Colorado. There were no major obstructions for approximately 0.8 km (0.5 mi) up-wind of the test area. The wind varied from 1 to 8.5 m/s during the tests. The tests were conducted using pairs of heated and unheated spheres with diameters of 3.81, 5.08, and 7.62 cm (1.5, 2, and 3 in.). The unheated sphere was used as a reference for the heated sphere to cancel out solar and long wave radiation inputs.

The large 7.62 cm dia spheres were copper spherical shells with a shell thickness of 0.159 cm and instrumented with electrical resistance heaters. The temperature variation between four thermocouples soldered to the inside surface was found to be less than 0.4°C, verifying that the sphere was isothermal. These thermocouples were connected in parallel to allow an accurate measurement of the average sphere temperature during heat transfer tests. The two smaller heated spheres were solid copper and the corresponding unheated spheres were solid aluminum. Thermocouples were located within 0.635 cm of the surface to measure surface temperature. These solid spheres were assumed to be isothermal since the maximum Biot number for the field tests was 0.003.

The electrical leads from the heaters and thermocouples for each sphere passed through a stem constructed of stainless steel tubing. The stem was attached to the sphere by means of a teflon insert to

Nomenclature

A = surface area of the sphere
A_p = projected area of sphere
D = diameter
h = convection coefficient
K = Karman constant (0.4)
k = air thermal conductivity
ℓ = mixing length
(mc) = thermal capacitance
Nu_T = Nusselt number for high turbulence intensity, hD/k
Nu = Nusselt number for low turbulence intensity
P = electrical power dissipation
$\dot{q}_{ir}$ = net longwave radiation interchange between the sphere and the sky, ground, and air
$\dot{q}_{sol}$ = incident solar radiation
$\dot{q}_{stem}$ = conducted heat flow along
Re = Reynolds number, uD/ν
S = Strouhal number, fD/u
T = temperature
Tu = turbulent intensity, $\sqrt{\overline{u'^2}}/u$
u = time-averaged velocity
u' = fluctuating velocity component in flow direction
v_* = shear velocity = $\sqrt{\tau_\omega/\rho}$
z = height
z_0 = soil surface roughness height
α = solar absorptivity
τ = time

Subscripts

a = air
h = heated sphere
s = sphere
u = unheated sphere

reduce stem conduction. The ratio of the surface area of the teflon insert to the sphere surface area was less than 0.03, with the ratio of the stem diameter to sphere diameter less than 0.13. Spheres were tested with the stem vertical.

The energy balance for the unheated surface equates the difference between the solar and net infrared radiation inputs and the stem conduction and convection outputs to the change in thermal energy stored.

$$\alpha_u A_{p,u}\dot{q}_{\text{sol}} + \dot{q}_{ir} - \dot{q}_{\text{stem},u} - h_u A_u (T_u - T_a) = (mc)_u \frac{dT_u}{d\tau} \qquad (6)$$

The energy balance on the heated sphere includes the electrical power input P

$$\alpha_h A_{p,h}\dot{q}_{\text{sol}} + \dot{q}_{ir} + P - \dot{a}_{\text{stem},h} - h_h A_h (T_h - T_a) = (mc)_h \frac{dT_h}{d\tau} \qquad (7)$$

Equation (6) shows that the temperature of an unheated sphere will not necessarily be equal to ambient air temperature due to solar and long wavelength radiation inputs. Equations (6) and (7) can be combined to simplify the calculations and cancel these environmental inputs.

The temperature difference between the two spheres was directly recorded. It is convenient to express the difference in energy storage using the measured temperature difference as

$$(mc)_h \frac{dT_h}{d\tau} - (mc)_u \frac{dT_u}{d\tau} = (mc)_h \frac{d(T_h - T_u)}{d\tau} \qquad (8)$$

where the (mc) product is taken as the thermal capacitance of the heated sphere. The capacitance of the heated spheres was not equal to that of the unheated spheres. However, the change in the temperature of an unheated sphere was less than 0.1°C for any test, while that for a heated sphere was as large as 5°C. Thus, the unheated spheres remained essentially at constant temperature relative to the heated sphere during testing, and equation (8) is a valid approximation.

The difference in the net longwave radiation term for the two pairs of copper and aluminum spheres was found to be less 0.3 percent of the convection losses and was neglected. Measurements and supporting calculations showed that the maximum temperature difference due to differences in solar radiation properties of the two polished smaller spheres was less than 0.8°C, with an average difference of 0.25°C. This is about 3 percent of the overall temperature difference, and negligible. The largest spheres were both of copper with no discernable difference in thermal properties.

The difference between the stem conduction terms for the heated and unheated spheres was found to be less than 2.5 percent of the power input and storage terms and was neglected. The convection coefficient was determined by combining equations (6)–(8)

$$h = \left[P - (mc)_h \frac{d(T_h - T_u)}{d\tau}\right] \Big/ [A(T_h - T_u)] \qquad (9)$$

For nominal conditions the expected error in the convection coefficient computed from equation (9) is ±8 percent based on the given information and with instrument errors in P and $(T_h - T_u)$ of 3 and 2 percent, respectively.

During the field tests, a pair of polished spheres was placed at heights of 10, 40, and 200 cm above the ground. A cup anemometer was located at the sphere test height and adjacent to the support stand to provide a measurement of the air velocity over each sphere. Air temperature was measured using shielded thermocouples.

The power input to the heated sphere was set to produce an initial temperature difference of 15°C between the two spheres. This difference insured accurate temperature measurements, and did not create free convection effects during relatively calm conditions. The power and anemometer readings were averaged over 5-min intervals, and the sphere temperature difference was continuously measured using a Rustrak recorder.

The nature of the wind is that the wind speed is not constant over time periods on the order of 5 min. The heated sphere temperature is thus also not constant and two convection coefficients can be calculated from the data using equation (9). An instantaneous convection coefficient can be calculated from the heat flow divided by the instantaneous temperature difference, and this can be averaged over the test period. A mean convection coefficient can be calculated using the total heat flow and the average temperature difference. The difference between these two convection coefficients was 2 percent. In the present study, mean convection coefficients based on 5-min test periods are used.

Wind Tunnel Tests. The convection coefficients for the spheres were also measured in a wind tunnel to verify the field measurement techniques and also to provide a base for comparisons between the standard relations and those for the outdoor environment. A 15.25-cm (6-in.) dia free discharge wind tunnel with a turbulent intensity less than 2 percent was used. Air speed was measured with a hot wire anemometer.

A sphere was mounted in the discharge plane of the wind tunnel, and heated 20°C above the air temperature. Corrections were made for radiation and stem conduction. Blockage effects due to the relatively large frontal area of the spheres compared to the wind tunnel area were found to be important, and the velocity was corrected using one-dimensional flow relations for this tunnel [13]. This correction to the velocity was 33.3 percent for the 7.62-cm spheres and 6.6 percent for the 3.81-cm spheres. The error in the heat transfer coefficient was estimated to be 5 percent.

Results and Discussion

The measured convection coefficients for the wind tunnel tests are summarized in Fig. 2. The least-squares regression for the wind tunnel tests was found to be

$$\text{Nu} = 0.43\text{Re}^{0.54} \qquad (10)$$

for the test Reynolds number range of 2000–35,000. The Nusselt-Reynolds number correlation of McAdams [3] over the Reynolds number range 17–7 × 10^4 is

$$\text{Nu} = 0.37\text{Re}^{0.6} \qquad (11)$$

Knudsen and Katz [4] give for the Reynolds number range 1–7 × 10^4 the following relation

$$\text{Nu} = 2.0 + 0.6\text{Pr}^{1/3}\text{Re}^{0.5} \qquad (12)$$

The data of Yuge [5] for Reynolds number greater than 1.8 × 10^3 is correlated by

$$\text{Nu} = 2 + 0.3\text{Re}^{0.5664} \qquad (13)$$

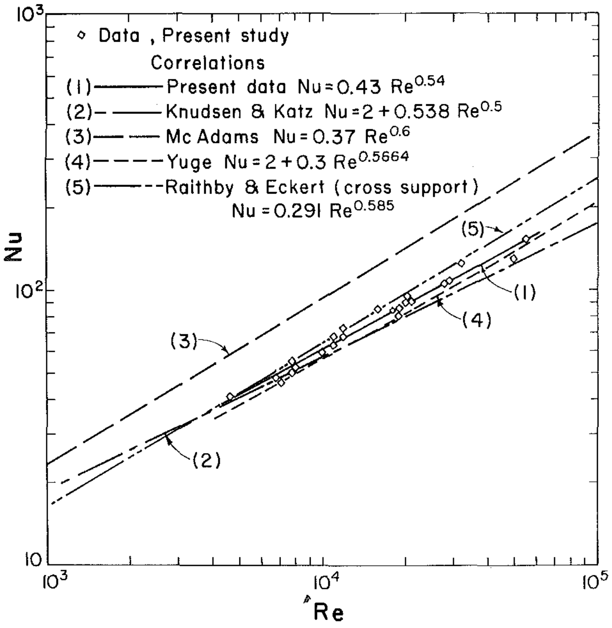

Fig. 2 Comparison of wind tunnel results to results cited by McAdams [11] and Knudsen and Katz [12]

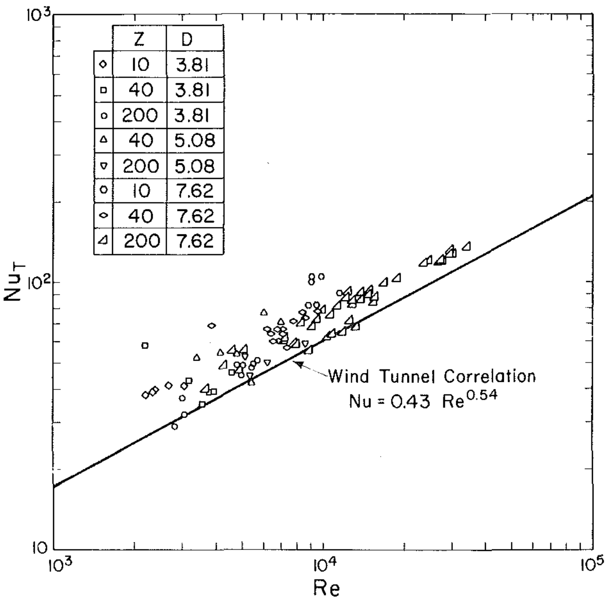

Fig. 3 Nusselt-Reynolds number for field data

The correlation of Raithby and Eckert [6] for a sphere supported by a cross support is

$$\mathrm{Nu} = 0.291\mathrm{Re}^{0.585} \tag{14}$$

Equations (11)–(14) are also shown in Fig. 2 in comparison to the present wind tunnel data. The present results are in good agreement with the more recent correlations over the Reynolds number range of the tests. Equation (10) was used as a base for determining enhancement in order to account for any biases introduced by the experimental technique.

The heat transfer results from the field tests are shown in Fig. 3 in comparison with the wind tunnel tests. The outdoor heat transfer coefficient is consistently higher than the wind tunnel value at a given Reynolds number. There is considerable variation in the data, with up to a two-to-one difference between tests of the same sphere at the same height. This variation is probably due to the different wind velocity-time pattern over different test periods; the wind speed fluctuates by up to a factor of three-to-one over a 5-min period. The cup anemometer measures a different velocity (approximately the root mean square) than that sensed by the heated sphere (approximately the average of the square root of the velocity). Thus, the same time-average velocity may not always yield the same total heat flow.

The field data are assumed to be related to wind tunnel data by a constant enhancement defined as the ratio of the field to wind tunnel Nusselt number. This assumes enhancement is independent of Reynolds number, which differs from other studies. For our data, there is no statistically significant effect of Reynolds number on enhancement. The overall average enhancement for the field data is 1.23. The enhancement for each sphere at a given height ranges from 1.0 to 2.2 with standard deviations of ±0.2. As discussed later, the enhancement for the field data is a function both of sphere diameter and height above the ground surface, and an average enhancement is not too meaningful.

The average enhancement over all velocities was determined for each sphere at each height. As shown in Fig. 1, eddy size and turbulent intensity are functions of height only, and thus this average will not obscure the interactions between the turbulent parameters and the size of the spheres. The average enhancement is plotted as a function of height in Fig. 4. The standard deviation of the data about the average for each group is approximately ±10 percent. The data show that the enhancement decreases with height, while at any given height the enhancement is greater for a larger sphere.

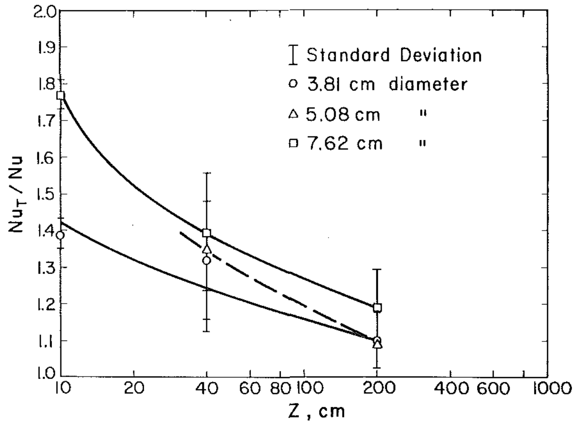

Fig. 4 Average increase in heat transfer for spheres versus height

The enhancement factors are replotted as a function of the ratio of height to sphere diameter in Fig. 5. The correlation with z/D as presented in Fig. 5 shows a more consistent trend of decreasing enhancement with increased relative height than does the relation represented in Fig. 4.

The present results may be compared to the results of other investigators who employed artificially induced turbulence in wind tunnels. The comparison is made with the empirical relation determined by Galloway and Sage [9]. This relation includes the work of 20 studies, and for the low Reynolds number range of the present test is given by reference [9], equation (14):

$$(\mathrm{Nu} - 2)/(\mathrm{Re}^{1/2}\mathrm{Pr}^{1/3}) = 0.5747 + [0.1674\, T_u(T_u - 0.05628) + 0.001449]\mathrm{Re}^{1/2}\mathrm{Pr}^{1/6} \tag{15}$$

The standard deviation of data used to generate the correlation is 0.0786, or about 10 percent of the value from equation (15). Fig. 3 of Galloway and Sage also demonstrates the variations that exist even for tests performed in controlled environments with artificial turbulence.

Equation (15) was evaluated for the turbulent intensities corresponding to heights of 10, 40, and 200 cm and the relations are plotted in Fig. 6. There is seen to be a consistent enhancement of heat transfer with both increasing Reynolds number and turbulent intensity. While the data from any one investigation may differ from that of Fig. 6, equation (15) does represent a consensus of the results.

The data of the present study are compared to the correlation in

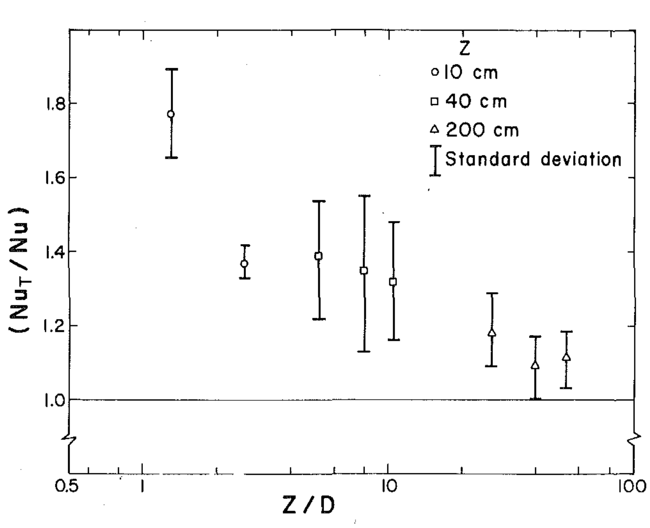

Fig. 5 Heat transfer enhancement as a function of the ratio of sphere height to sphere diameter

Fig. 6. For the 200- and 40-cm heights, the value of Nusselt number for all three spheres was averaged to facilitate the comparison. For the 10-cm height, the heat transfer for each sphere alone was used. It is seen that within the spread of the present data and the accuracy of the correlation, the tests at 200 and 40 cm, and the 3.81-cm sphere at 10 cm agree with the results obtained using artificially induced turbulence.

The results for the 7.62-cm sphere at 10 cm are considerably higher than those of other investigators. A possible reason for this difference is the interaction between the sphere and the ground. A maximum blockage effect can be estimated assuming that the sphere is in a square duct with sides equal to twice the height of the sphere from the ground. This would increase the velocity around the sphere 13 percent at most, and produce a 7 percent increase in Nusselt number. This would not account for the observed 26 percent difference in enhancement between the two spheres at 10 cm. It is also possible that the presence of the ground would act to confine the wake at the rear, but the magnitude of this effect is not known. Also, the sphere is in the atmospheric boundary layer, which is a shear flow, and there would be a deflection of the wind downward. However, the deflection would have to be on the order of several meters to produce the observed increase, which is unreasonable.

It is also possible that the length scale of turbulence influences this particular test. The ratio of mixing length to sphere diameter (ℓ/D) is 0.46 for this condition. However, other studies have determined that the scale effect is small. The results of Raithby and Eckert [6] show a small (4 percent) change in enhancement as ℓ/D changes from 0.08 to 1.0. The correlation of Yuge [5] would indicate a 15 percent difference between the two tests at 10-cm height. The conclusions of Maisel and Sherwood [7], Lavender and Pei [8], and Galloway and Sage [10] are that scale has a negligible effect, and these studies include tests conducted at values of ℓ/D up to 0.5. It appears that near the ground, different mechanisms may influence the transfer of heat from the sphere.

The results in Fig. 6 show a slight increase in enhancement with Reynolds number. This is a result of using the experimental relation, equation (10), as a base for computing Nusselt number at any height for Fig. 6. If the "standard" relation, equation (12), had been used, the present results would not have shown a variation with Reynolds number. They would still, though, be in agreement with the results of other investigators. The comparison between the artificially induced turbulence tests and the outdoor tests show that wind tunnel tests may be used to estimate convection in natural environment at large relative heights. However, near the ground, the two situations may not be similar.

The results shown in Fig. 5 have significant implications regarding the computation of convective heat and mass flow from animals and plants in the outdoor environment. Ground dwelling animals and low growing plants have a value of z/D on the order of 0.5–1. Thus, enhancement is high. Plant leaves and seed pods and flying or climbing animals have very large z/D with consequently little enhancement.

Summary

The average convection coefficients from spheres in a naturally turbulent outdoor environment were measured and compared to the standard low turbulent intensity correlations obtained in wind tunnels. The enhancement in heat transfer was found to be a function of turbulent intensity for all tests with height-to-diameter ratios greater than 2.5. For low values of the ratio, the increase in heat transfer is higher than what would be attributed to turbulent intensity alone. The results presented may be used to estimate heat transfer from surfaces in the outdoor environment.

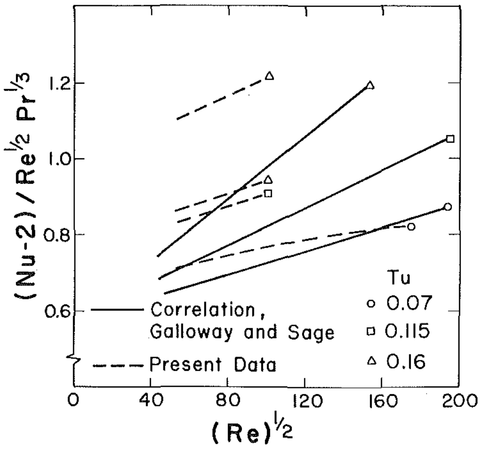

Fig. 6 Comparison of the present results with the correlation of Galloway and Sage [9]

Acknowledgments

The assistance of W. P. Porter, G. Liljedahl, and R. Philbin is appreciated. This work was supported by NSF Grant No. GB-31043A.

References

1 Pearman, G. I., Weaver, H. L., and Tanner, C. B., "Boundary Layer Transport Coefficients Under Field Conditions," *Ag. Meteor*, Vol. 10, No. 1–2, 1972, pp. 83–92.

2 Jackson, G. F., "Heat Transfer From Velvet Stage Antlers of White Tailed Deer," PhD thesis, University of Wisconsin, 1975.

3 McAdams, W. H., *Heat Transmission*, McGraw-Hill, New York, 1954, p. 266.

4 Knudsen, J. G., and Katz, D. L., *Fluid Dynamics and Heat Transfer*, McGraw-Hill, New York, 1958, p. 512.

5 Yuge, T., "Experiments on Heat Transfer of Spheres," Report Institute High Speed Mechanics, Vol. 11, No. 108, 1959–1960.

6 Raithby, G. D., and Eckert, E. R., "The Effect of Turbulence Parameters and Support Position on the Heat Transfer From Spheres," *International Journal. of Heat and Mass Transfer*, Vol. 11, 1968, pp. 1233–1252.

7 Maisel, D., and Sherwood, T., "Effect of Air Turbulence on the Rate of Evaporation of Water," *Chem. Engr. Prog.*, Vol. 46, 1950, pp. 172–175.

8 Lavender, W. J., and Pei, D. T., "The Effect of Fluid Turbulence on the Rate of Heat Transfer From Spheres," *International Journal of Heat and Mass Transfer*, Vol. 10, 1967, pp. 529–539.

9 Galloway, T. R., and Sage, B. H., "Thermal and Material Transport From Spheres," *International Journal of Heat and Mass Transfer*, Vol. 10, 1967, pp. 1195–1210.

10 Galloway, T. R., and Sage, B. H., "Local and Macroscopic Thermal Transport From a Sphere in a Turbulent Air Stream," *AIChE Journal*, Vol. 18, 1972, pp. 287–293.

11 Mitchell, J. W., Beckman, W. A., Bailey, R. T., and Porter, W. P., "Microclimatic Modeling of the Desert," *Heat and Mass Transfer in Biosphere*, DeVries, D. A., and Afgan, N. H., Scripta, Washington, D.C., 1975, pp. 275–286.

12 Sutton, O. G., *Micrometeorology*, McGraw-Hill, New York, 1953, pp. 77–83.

13 Mitchell, J. W., "Base Heat Transfer in Two Dimensional Subsonic Fully Separated Flows," JOURNAL OF HEAT TRANSFER, TRANS. ASME, Series C, Vol. 93, 1971, pp. 342–347.

A. R. P. van Heiningen
Graduate Student.

A. S. Mujumdar
Asst. Professor.
Assoc. Mem. ASME

W. J. M. Douglas
Professor.

Department of Chemical Engineering,
McGill University,
Pulp and Paper Research Institute of Canada,
Montreal, Canada

Numerical Prediction of the Flow Field and Impingement Heat Transfer Caused by a Laminar Slot Jet

The effects of uniform suction and nozzle exit velocity profile on the flow and heat-transfer characteristics of a semiconfined laminar impinging slot jet were investigated numerically. The full Navier-Stokes and energy equations were solved using a hybrid or upwind finite-difference representation of the equations cast into their vorticity-stream-function form. The importance of the nozzle exit profile is shown by comparison of the computed heat-transfer distribution with the available experimental data in the laminar range. Application of suction at the impingement surface is shown to enhance the local heat-transfer rates by a constant amount. The nondimensional heat-transfer coefficient and skin friction at the plate are computed as functions of the nozzle Reynolds number, the suction rate, and the nozzle velocity profile. The effect of temperature-dependent physical properties is included in the analysis.

Introduction

Single and multiple impinging jets are encountered commonly in industrial practice because of their excellent heat- and mass-transfer characteristics. Notable among their numerous applications are turbine blade cooling, cooling of high-energy-density electronic components, heat treatment of nonferrous metal sheets, tempering of glass, and drying of textiles and paper [1, 2].[1]

Application of suction is known to have a favorable influence on the transfer rates. Clearly, a combination of an impinging flow and suction applied at the target would further enhance the transfer rates. This is particularly attractive in the case of industrial drying of permeable webs (e.g., newsprint and textiles), since the percolation flow removes the vapor as it is formed, and thus high heat-transfer rates are obtainable without impairment of product quality. This combination of impingement and throughflow has been used in the recently developed Papridryer for newsprint [3, 4], which provided the primary motivation for this work.

The objective of this work is to present the results of a numerical investigation of the flow and heat transfer characteristics of a two-dimensional semiconfined laminar jet impinging on a plane permeable wall. The computational procedure developed by Gosman, et al. [5] was used to solve the full Navier-Stokes and energy equations in two dimensions. Laminar impinging jets may be encountered in practice especially when the jet dimensions and the nozzle-to-target distance are small and the fluid is at a high temperature (e.g., drying). The application of suction, the effect of nozzle velocity profile, and the presence of a confining wall parallel to the impingement wall are features that have not been considered in earlier investigations.

Literature Review

Laminar impinging jets have received little attention in the literature. Some theoretical work has been done by Ehrich [6], who solved the potential flow for a jet with a flat velocity profile at the nozzle exit that was impinging on a flat impermeable surface. The potential flow solution of [6] was used by Miyazaki and Silberman [7] to obtain the free-stream boundary condition for the boundary-layer equations that describe the flow close to the plate. The solutions for the skin friction and heat-transfer distribution at the plate were obtained for different nozzle-to-plate spacings. However, for higher spacings the solutions are not valid because the jet entrainment before impingement must be taken into account.

A more exact criterion for neglecting the diffusion terms is given by Sparrow and Lee [8], who used essentially the same approach as

---

[1] Numbers in brackets designate References at end of paper.

Contributed by the Heat Transfer Division and presented at the Winter Annual Meeting, Houston, Texas, November 30 December 5, 1975 of THE AMERICAN SOCIETY OF MECHANICAL ENGINEERS. Revised manuscript received by the Heat Transfer Division September 1, 1976. Paper No. 75-WA/HT-99.

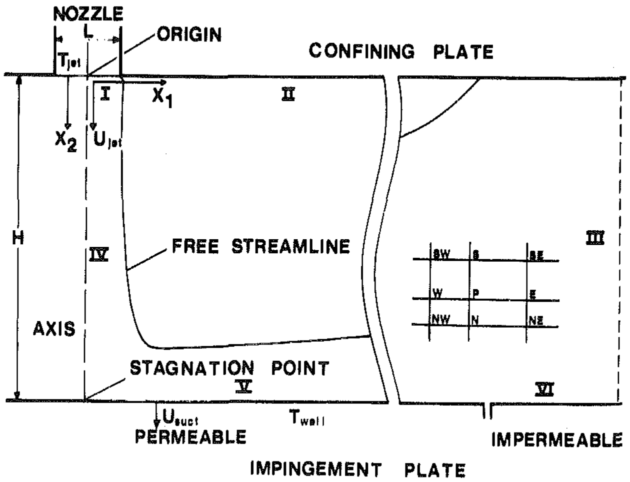

Fig. 1 Impinging jet system

the previous authors for a jet with a flat and a parabolic velocity profile at the nozzle exit.

Wolfshtein [9] predicted the flow and temperature fields of turbulent and laminar free slot jets impinging on an impermeable flat plate using the method of Gosman, et al. [5]. However, the results are of limited value because the velocity profile for a fully developed two-dimensional turbulent jet was used as the upstream boundary condition for the laminar case.

Two experimental studies involving laminar impinging slot jets have been reported. Gardon and Akfirat [10] measured the local heat transfer under an unconfined slot jet impinging on an impermeable flat plate for Reynolds numbers ranging from 450 to 22,000. In their study it appears that the velocity profile at the nozzle exit was neither flat nor fully developed. More recently, Sparrow and Wong [11] measured impingement transfer coefficients due to initially laminar fully developed slot jets impinging unconfined on an impermeable flat plate. They used the naphthalene sublimation technique and converted their mass-transfer results to the corresponding heat-transfer values by using the heat–mass-transfer analogy.

Mathematical Description of the Problem. The impinging jet system is shown in Fig. 1. Following Gosman et al. [5], the equations of motion in their vorticity–stream-function form and the energy equation can be represented by a general differential equation, which after nondimensionalization is

$$a_\phi\left\{\frac{\partial}{\partial X_1^*}\left(\phi^*\frac{\partial\psi^*}{\partial X_2^*}\right)-\frac{\partial}{\partial X_2^*}\left(\phi^*\frac{\partial\psi^*}{\partial X_1^*}\right)\right\}-\frac{\partial}{\partial X_1^*}\left\{b_\phi\frac{\partial}{\partial X_1^*}(c_\phi\phi^*)\right\}-\frac{\partial}{\partial X_2^*}\left\{b_\phi\frac{\partial(c_\phi\phi^*)}{\partial X_2^*}\right\}+d_\phi=0 \qquad (1)$$

Table 1 Coefficients in equation (1)

ϕ^*	a_ϕ	b_ϕ	c_ϕ	d_ϕ
ω^*	1	$\frac{L}{H}\frac{1}{\text{Re}}$	μ^*	$-S_\rho^*-\frac{L}{H}\frac{1}{\text{Re}}S_\mu^*$
ψ^*	0	$1/\rho^*$	1	$-\omega^*$
T^*	1	$\frac{L}{H}\frac{1}{\text{Re Pr}}$	1	0

in two-dimensional cartesian coordinates. The general nondimensional dependent variable ϕ^*, with corresponding coefficients a_ϕ, b_ϕ, c_ϕ, and d_ϕ, is listed in Table 1, where ϕ^* stands for the vorticity ω^* and stream function ψ^*, which are defined as

$$\omega^*=\frac{\partial U_2^*}{\partial X_1^*}-\frac{\partial U_1^*}{\partial X_2^*} \qquad (2)$$

and

$$\rho^*U_1^*=\frac{\partial\psi^*}{\partial X_2^*} \quad \text{and} \quad \rho^*U_2^*=-\frac{\partial\psi^*}{\partial X_1^*} \qquad (3)$$

and the nondimensional temperature T^*, where

$$T^*=(T-T_{\text{wall}})/(T_{\text{jet}}-T_{\text{wall}}) \qquad (4)$$

S_ρ^* and S_μ^* are nonzero when the physical properties are changing, and they are defined as

$$S_\rho^*=\frac{\partial}{\partial X_1^*}\left(\frac{U_1^{*2}+U_2^{*2}}{2}\right)\frac{\partial\rho^*}{\partial X_2^*}-\frac{\partial}{\partial X_2^*}\left(\frac{U_1^{*2}+U_2^{*2}}{2}\right)\frac{\partial\rho^*}{\partial X_1^*} \qquad (5)$$

$$S_\mu^*=2\frac{\partial^2}{\partial X_1^{*2}}\left(\mu^*\frac{\partial U_1^*}{\partial X_2^*}\right)-2\frac{\partial^2}{\partial X_2^{*2}}\left(\mu^*\frac{\partial U_2^*}{\partial X_1^*}\right)+2\frac{\partial^2}{\partial X_1^*\partial X_2^*}\left\{\mu\left(\frac{\partial U_2^*}{\partial X_2^*}-\frac{\partial U_1^*}{\partial X_1^*}\right)\right\} \qquad (6)$$

The assumptions pertaining to these equations are the following: laminar flow, neglect of viscous dissipation and temperature change due to compression, and no buoyancy effects.

The following boundary conditions were specified:

Boundary I: Nozzle exit. For a fully developed velocity profile

$$\psi^*=-\frac{3}{2}X_1^*\left\{1-\frac{4}{3}\left(\frac{L}{H}\right)^{-2}X_1^{*2}\right\},$$

and

$$\omega^*=-12\left(\frac{L}{H}\right)^{-2}X_1^*, \qquad T^*=1 \qquad (7)$$

For a flat velocity profile

$$\psi^*=-X_1^*, \qquad \omega^*=0, \qquad T^*=1 \qquad (8)$$

Boundary II: Upper (nozzle) plate. Impermeability of the confining

Nomenclature

c_p = specific heat at constant pressure
D_{AB} = diffusivity
H = nozzle-to-plate distance
k = thermal conductivity
k_L = mass-transfer coefficient
L = nozzle width
T = temperature (subscripted)
U = velocity (subscripted)
U_{suct} = suction velocity
X = coordinate (subscripted)
X_{1s}^* = permeable plate length
c_f = skin friction coefficient, $2\tau_{\text{wall}}/(\rho_{\text{jet}}U_{\text{jet}}^2)$

Nu = Nusselt number, $\alpha L/k_{\text{jet}}$
Pr = Prandtl number, $\mu_{\text{jet}}c_p/k_{\text{jet}}$
Re = Reynolds number, $\rho_{\text{jet}}U_{\text{jet}}L/\mu_{\text{jet}}$
Sc = Schmidt number, $\mu/\rho D_{AB}$
Sh = Sherwood number, $k_L L/D_{AB}$
St = Stanton number, $\alpha/(\rho_{\text{jet}}c_pU_{\text{jet}})$
α = heat-transfer coefficient
μ = absolute viscosity (subscripted)
ω = vorticity, equation (2)
ψ = stream function, equation (3)
ρ = density (subscripted)
τ = shear stress
ϕ = general variable

Subscripts

0 = condition at stagnation point
1 = parallel to impingement plate
2 = perpendicular to impingement plate
jet = condition at nozzle
nw = condition at grid node adjacent to a wall
wall = condition at impingement plate
ϕ = belonging to variable ϕ

Superscript

* = nondimensionalized variable, equation (1)

plate and the no-slip condition [5] yield

$$\psi^* = -\frac{1}{2}\frac{L}{H}, \qquad T^* = 1 \tag{9}$$

and

$$\omega_{\text{wall}}^* = -3\frac{(\psi_{nw}^* - \psi_{\text{wall}}^*)}{\rho^*(\Delta X_2^*)^2} - \frac{1}{2}\omega_{nw}^* \tag{10}$$

Boundary III: Outflow boundary.

$$\frac{\partial \psi^*}{\partial X_1^*} = \frac{\partial \omega^*}{\partial X_1^*} = \frac{\partial T^*}{\partial X_1^*} = 0 \tag{11}$$

Boundary IV: Axis of symmetry.

$$\psi^* = \omega^* = \frac{\partial T^*}{\partial X_1^*} = 0 \tag{12}$$

Boundary V: Permeable impingement plate.

$$\psi^* = -\frac{U_{\text{suct}}}{U_{\text{jet}}} X_1^*, \qquad T^* = 0 \tag{13}$$

and equation (10).

Boundary VI: Same as boundary V except for the stream function

$$\psi^* = -\frac{U_{\text{suct}}}{U_{\text{jet}}} X_{1s}^* \tag{14}$$

Numerical Procedure. The approximation of the general differential equation by a general finite-difference equation is described by Gosman, et al. [5]. The only change to the Gosman procedure was the replacement of the upwind difference approximation of the convective terms by a hybrid difference approximation. In the "hybrid formulation" central differences are used when the magnitude of the convective term is larger than the corresponding diffusion term. If this is not the case, the "upwind formulation" is used, and the corresponding diffusion term is neglected. The alternate formulations are discussed fully by Runchal [12]. The hybrid formulation is more accurate than the upwind formulation, while the convergence properties are essentially the same for both.

A nonuniform grid was used throughout the present computations. The gridlines parallel and adjacent to the impingement plate are very closely spaced, and the spacing between the gridlines is monotonically increasing in the X_1 direction. This leads to greatly elongated grid cells in the lower right corner of the flowfield, causing divergence of the numerical procedure for small values of L/H and large values of Re. No definite cure has been found for this divergence problem as yet.

Results and Discussion

Effect of Reynolds Number and Jet Velocity Profile. In the beginning of this work it was felt that boundary III should be sufficiently far out to enclose all of the elongated recirculation "bubble" (Fig. 1), thus ensuring only outflow at this boundary. However, this either required too many gridlines or destabilized the numerical procedure, probably because of the presence of gridcells of very large $\Delta X_1^*/\Delta X_2^*$ ratio. On the other hand, for solutions with inflow at boundary III, the effect of equation (11), which is exact only for fully developed flow, will propagate into the computational area.

Fortunately it was established that although different boundary conditions at boundary III strongly affected the results in the recirculation "bubble" their influence was hardly felt in the regions of interest, which are the impingement and wall jet region.

The boundary conditions tested other than equation (11) had the effect of blocking the inflow by a frictionless wall or allowing entrainment of irrotational fluid along streamlines of slope equal to the streamline slope immediately inside boundary III. Also, variation of the location of boundary III hardly affected the flow and temperature characteristics near the impingement plate.

The results of the computations for three Reynolds numbers and two velocity profiles at the nozzle exit, parabolic and flat, are displayed in Figs. 2(*a*) and 2(*b*) in the form of the free streamline. The physical properties are taken to be constant. Only for the case of Re = 100 was the total recirculation area covered by the computational grid, which extended up to $X_1^* = 4.1$. For Re = 950 the solution showed inflow at boundary III, with boundary III located at $X_1^* = 19.1$.

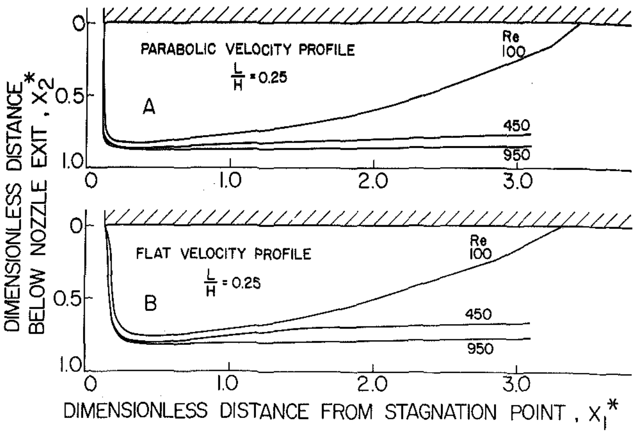

Fig. 2 Free streamline contours for various Re (100, 450, 950) and parabolic and flat velocity profiles

An interesting result is that the jet contracts slightly below the nozzle for a parabolic profile, while for a flat profile the jet expands continuously. It can also be noticed that the free streamline is significantly closer to the impingement plate for the parabolic velocity profile owing to its higher momentum and the described spreading behavior. Consequently the velocity and temperature gradients at the impingement plate are steeper for a jet with a parabolic velocity profile than for a flat velocity profile at the nozzle exit. The nondimensional representations of these gradients are given in Figs. 3 and 4.

The use of the proportionality to $\text{Re}^{1/2}$ for laminar flows almost leads to a collapse of the results for different Re to a single curve. This effect is more pronounced for the heat transfer than for the skin friction. The curves for Re = 100 deviate the most from a general curve because of significant relative retardation of the jet on its way from the nozzle to the plate.

The maximum heat transfer is found at the stagnation point. The slight increase some distance from the stagnation point for Re = 450 and 950 in Fig. 3 is the result of the inherent inaccuracy of the finite-difference approximation. For a flat velocity profile the maxi-

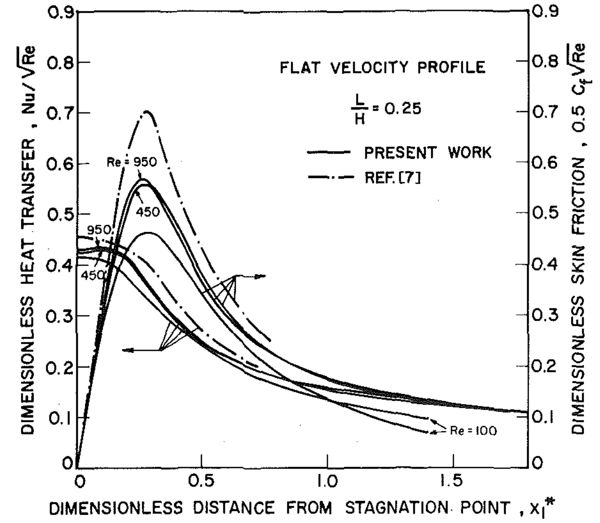

Fig. 3 Nondimensional velocity and temperature gradients with a flat velocity profile

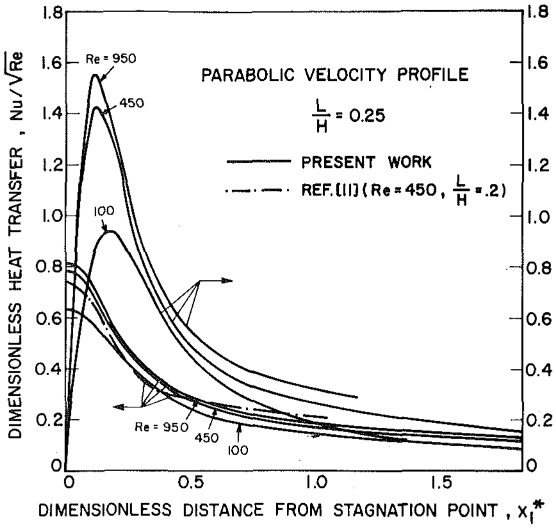

Fig. 4 Nondimensional velocity and temperature gradients with a parabolic velocity profile

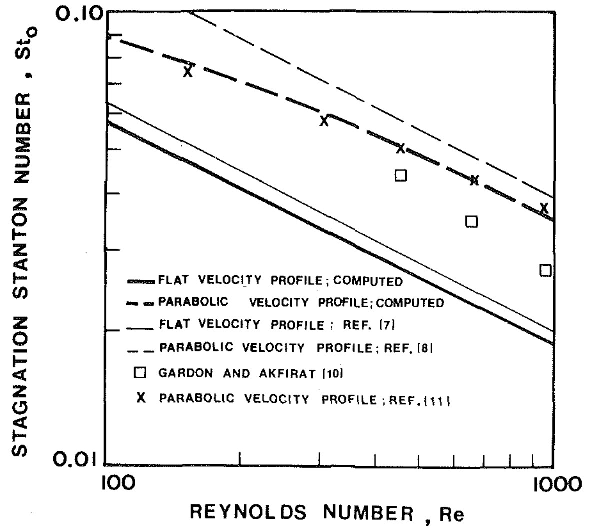

Fig. 5 Stagnation Stanton numbers as function of Reynolds number

mum skin friction is located about one nozzle width from the stagnation point. The theoretical results of Miyazaki and Silberman [7] represented in Fig. 3 are consistently higher than our predictions because of the assumption of potential flow for the flow outside the boundary layer. Another significant difference is that their analysis leads to results that are independent of Re.

The laminar flow assumption is valid for the cases studied, as can be derived from previous experimental results [10, 11]. Gardon and Akfirat [10] used a fast-response heat-flux sensor with which it is possible to identify laminar and turbulent flow regions, and their heat-transfer results show that the flow is laminar for Re = 450 and 950 at $L/H = 0.25$ up to a value of X_1^* of 10 and 1.0, respectively. From the shape of the data of Sparrow and Wong [11] one can conclude that a jet with a parabolic velocity profile at the nozzle will be laminar on impact when $H/L < 10$ or 16 for Re = 950 and 450, respectively.

For a jet with a parabolic velocity profile it can be seen in Fig. 4 that the maximum skin friction is located ½L from the stagnation point. It is particularly striking that the stagnation heat transfer for a parabolic velocity profile is 1.5 to 2 times the value for a flat velocity profile. The qualitative explanation of this result is the contraction and the higher momentum of the parabolic jet. For the maximum skin friction this ratio is about 2.7 for Re = 950.

Included in Fig. 4 are results derived from the experimental mass-transfer data of Sparrow and Wong [11] for an unconfined slot jet with a parabolic velocity profile at the nozzle exit impinging on a naphthalene plate. The mass-transfer data were converted using the heat–mass-transfer analogy relation

$$\mathrm{Nu} = \left(\frac{\mathrm{Pr}}{\mathrm{Sc}}\right)^{0.4} \mathrm{Sh} \qquad (15)$$

There is good agreement between their results and ours, taking into account the difference in L/H and the absence of an upper plate in their case. A reason for the relative higher experimental values some distance from the stagnation point in their case could be the finite length of the naphthalene plate.

The stagnation Stanton numbers as a function of the Reynolds number, with the jet velocity profile as parameter, are displayed in Fig. 5. The two heavy lines are the numerical results for the jets with parabolic and flat velocity profiles. For the flat velocity profile the St_0 values are proportional to $Re^{-0.49}$, and for the parabolic velocity the best fit over the Reynolds number range of 100 to 1000 is $St_0 \propto Re^{-0.4}$. The two thin lines are the theoretical results of references [7] and [8] for the two velocity profiles. The results for a parabolic velocity profile are progressively higher than our results at decreasing Re because of the increasing importance of the neglected diffusion terms at lower Re. The heat-transfer equivalent of Sparrow and Wong's experimental results [11] corresponds very closely to our computed results, indicating that the presence of a confining plate has only a minor effect on conditions at the stagnation point.

The data of Gardon and Akfirat [10] are in between the numerical results for flat and parabolic velocity profiles, because the velocity profile generated in their nozzle is in fact intermediate between these two limiting cases. Therefore, Gardon and Akfirat's correlation for the stagnation heat transfer includes the effect of velocity profile at the nozzle exit as an unspecified, dependent variable. This was tested by using the velocity profile that would have been generated in their nozzle for Re = 450 as input to the numerical procedure. Agreement between the experimental data and our computed results is excellent except at the stagnation point, as can be seen in Fig. 6. It is inevitable that experimental results directly at the stagnation point must be slightly below the true value as a result of the averaging effect due to the finite size of the sensor.

Effect of Suction. The plate was taken to be permeable up to $X_1 = 6H$, because significant extension of the permeable plate length did not appreciably change the results in the impingement and wall jet region.

The effect of suction on the Stanton number distribution along the impingement plate is displayed in Fig. 7. The upwind formulation is

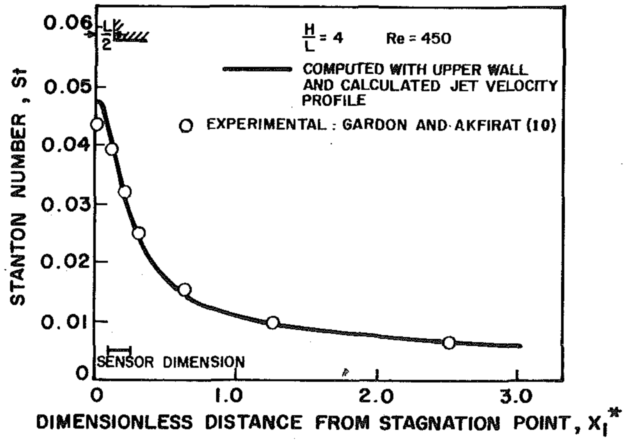

Fig. 6 Lateral heat transfer distribution; comparison with reference [10]

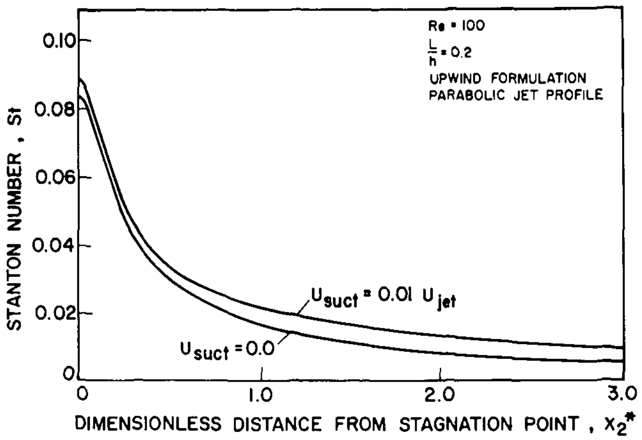

Fig. 7 **Influence of suction on the Stanton number distribution**

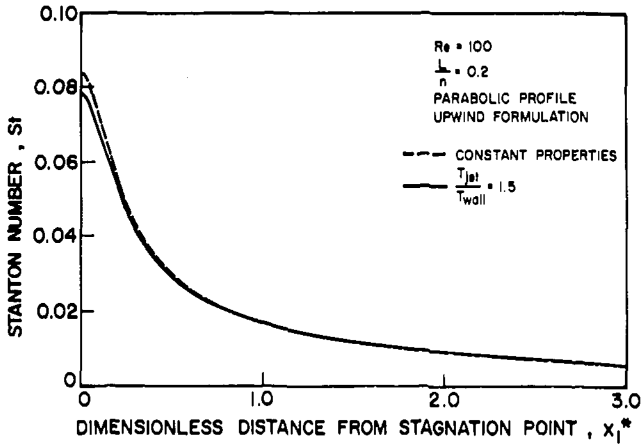

Fig. 8 **Influence of variable properties on the Stanton number distribution**

used here, in contrast with the previous computations. It is seen that the relative effect of suction is smallest in the stagnation region, as the absolute increase in heat transfer does not vary greatly over the length of the plate. The increase in the Stanton number for $L/H = 0.2$, Re = 100, and $U_{suct}/U_{jet} = 0.01$ is around 0.047 ± 15 percent. In these computations boundary III was located at $X_1 = 19.1H$.

Effect of Variable Properties. The influence of variable properties on the Stanton number distribution is shown in Fig. 8. The jet temperature was taken as 450 K and the temperature of the plate as 300 K.

The viscosity of air was calculated using the Van Driest interpolation formula

$$\frac{\mu}{\mu_r} = \left(\frac{T}{T_r}\right)^{3/2}\left(\frac{T_r + 110}{T + 110}\right) \qquad (16)$$

where μ_r is the viscosity at the reference temperature T_r (= 450 K).

The thermal conductivity was calculated from the viscosity using the fact that the Prandtl number and the specific heat of air are constant. S_μ [equation (6)] was assumed to be negligible.

It was found that the nondimensional temperature gradient at the wall was different for variable and constant properties. However, the analysis of the present study establishes that the heat-transfer coefficient in the form of the Stanton number, based on the properties at the nozzle, is hardly affected by the change to variable properties over the temperature range studied, as can be seen in Fig. 8. This is in agreement with the theoretical solutions of the influence of variable properties on two-dimensional stagnation flow and laminar boundary-layer flow over a flat plate without a pressure gradient.

References

1 Keeble, T. S., "Impingement Cooling," Aero. Res. Council, Department of Defense, Australia, ARL/ME 308, Aug. 1969.

2 Hardisty, H., "Industrial Drying Using Impinging Air Jets," Rep. No. 226 and 227, University of Bath, School of Engineering, 1973.

3 Burgess, B. W., Chapman, S. M., and Seto, W., "The Papridryer Process, Part I, The Basic Concepts and Laboratory Results," *Pulp Paper Mag. Can.*, Vol. 73, No. 11, Nov. 1972, pp. 314–322.

4 Burgess, B. W., et al., "The Papridryer Process, Part II, Mill Trials," *Pulp Paper Mag. Can.*, Vol. 73, No. 11, Nov. 1972, pp. 323–331.

5 Gosman, A. D., et al., *Heat and Mass Transfer in Recirculating Flows*, Academic Press, New York, 1969.

6 Ehrich, F. F., "Some Hydrodynamic Aspects of Valves," ASME Paper No. 55-A-114.

7 Miyazaki, H., and Silberman, E., "Flow and Heat Transfer on a Flat Plate Normal to a Two-Dimensional Laminar Jet Issuing from a Nozzle of Finite Height," *International Journal of Heat and Mass Transfer*, Vol. 15, Nov. 1972, pp. 2097–2107.

8 Sparrow, E. M., and Lee, L., "Analysis of Flow Field and Impingement Heat/Mass Transfer Due to a Nonuniform Slot Jet," JOURNAL OF HEAT TRANSFER, TRANS. ASME, Series C, Vol. 97, No. 2, May 1975, pp. 191–197.

9 Wolfshtein, M., "Convection Processes in Turbulent Impinging Jets," PhD dissertation, London University, 1968.

10 Gardon, R., and Akfirat, J. C., "Heat Transfer Characteristics of Impinging Two-Dimensional Air Jets," JOURNAL OF HEAT TRANSFER, TRANS. ASME, Series C, Vol. 88, No. 1, Feb. 1966, pp. 101–108.

11 Sparrow, E. M., and Wong, T. C., "Impingement Transfer Due to Initially Laminar Slot Jets," *International Journal of Heat and Mass Transfer*, Vol. 18, May 1975, pp. 597–605.

12 Runchal, A. K., "Convergence and Accuracy of Three Finite Difference Schemes for a Two-Dimensional Conduction and Convection Problem," *International Journal of Numerical Methods in Engineering*, Vol. 4, 1972, pp. 541–550.

T. R. Bott
Chemical Engineering Department,
Birmingham University,
Birmingham, England

D. V. Law
Chevron Oil (U.K.) Ltd.,
Croydon, England

Heat Transfer Between a Moving Surface and a Flowing Medium

Certain processes involve heat transfer across a moving surface and application of the well-known "penetration theory" to scraped-surface heat transfer, suggests that this theory might be applied to this situation. At high water flows and high surface speeds experimental results agree well with the theory, but at lower values the experimental heat-transfer rates are much higher than those predicted from the theory, and at high surface speeds and lower water velocities the experimental value of the heat transfer coefficient is lower than predicted. The differences are attributed to additional turbulence and secondary-flow (back-mixing) effects, which would be extremely difficult to allow for in the theory.

1 Introduction

In certain operations heat is transferred across a moving surface that is in contact with a heating or cooling medium. An example is a direct-contact water cooler on the surface of steel strip mill rolls, which has certain advantages over the traditional spray cooling [1].[1] Similar and other applications such as the direct cooling of conveyer belts can be imagined.

Heat transfer to and from viscous liquids has presented problems to many industrial process engineers, due to the well-known effects of the slow moving laminar layer at the heat transfer surface, and attempts have been made to overcome the high heat transfer resistance of this layer. Thin-film agitators have been designed in which the laminar layer is agitated or disturbed by the action of some blade system; and scraped-surface heat exchangers have also been designed in which the blades actually scrape the heat transfer surface. Scraped surface equipment can be of two types: that in which the unit runs full with liquid, and the falling-film design in which the liquid moves as a thin film along the vessel wall. The agitation and scraping remove material from the wall and mix it with the bulk liquid, at the same time allowing fresh material to contact the wall. Heat is then carried physically, if the liquid is being heated, from the wall into the bulk liquid. Much of the published work with scraped-surface heat transfer has been empirical in nature although some theory has been attempted. A comprehensive review [2] was published some years ago.

If a box-shaped cooler is placed onto a moving surface such that the cooling medium (e.g., water) flow is contained within the channel by the moving surface itself, medium agitation is achieved not only by the turbulence of flow but also by the effects of the moving surface (see Fig. 1). The basic concept has been used in the cooling of steel strip mill rollers [1]. The technique can be regarded as an adaptation of the more well-known operation of scraped-surface heat transfer, although clearly the surface effects within the fluid could be different.

2 Penetration Theory Applied to Scraped-Surface Heat Transfer and Its Application to Heat Transfer Across a Moving Surface

Little success has been achieved in a theoretical study of scraped-surface heat transfer based on conduction through a film [3–5], but more progress has been made using the "penetration theory."

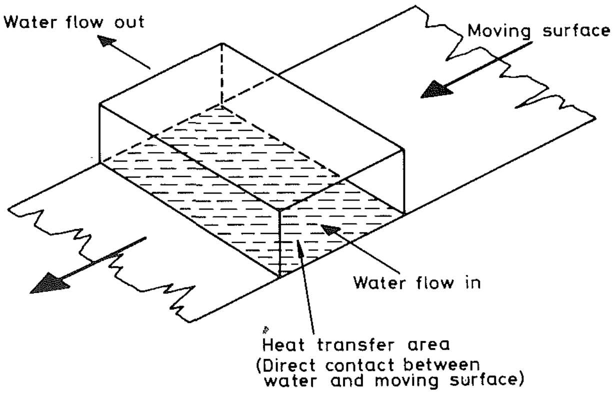

Fig. 1 The heat transfer situation

---

[1] Numbers in brackets designate References at end of paper.

Contributed by the Heat Transfer Division for publication in the JOURNAL OF HEAT TRANSFER. Manuscript received by the Heat Transfer Division.

Harriott [6] suggested that the rate of heat transfer would depend more on the rate of transient conduction into a frequently renewed layer than on the rate of steady conduction through the entire film as proposed by Kern and Karakas [5]. The layer at the surface is almost completely removed by the shearing action and a fresh layer comes back to the surface at the bulk temperature. Heat transfer occurs by conduction until the thin layer is removed. The small variation in the velocities within the thin heat transfer layer may be neglected, since the depth of conductive heat penetration is small. If it is also assumed that entrance and longitudinal flow effects are rendered unimportant by the intensity of cross-sectional mixing, the heat transfer mechanism is identical to molecular conduction into a semi-infinite solid, where the contact time is the time between successive blade passes. The analysis gives

$$h = \frac{2}{\sqrt{\pi}}\sqrt{\frac{C_p \rho k}{t}} \tag{1}$$

Experimental data published by Houlton [7] agreed well with the theory [8]. In the correlation of some experimental results for "thin film" scraped-surface exchangers, the equation had to be modified by the inclusion of a factor dependent upon the Prandtl number of the process fluid [9, 10].

Because of the apparent similarities observed between the scraped and moving surfaces (in the former the blades act upon the fluid through their own movement, in the latter the blades act upon the fluid through the movement of the surface), it is not unreasonable to expect similarities in the theoretical description of the two processes of heat transfer. The basic concept of a heat transfer mechanism identical to molecular conduction into a semi-infinite solid could be assumed to apply in each situation.

3 Experimental Apparatus and Calculations

In order to test the application of the theory and to give some operating experience, an experimental apparatus was devised which simulated the moving-surface problem. Heat was transferred from an electrically heated aluminum block in contact with a moving stainless steel belt to a direct-contact water cooler on the opposite side of the belt (see Fig. 2). The dimensions of the cooler were 2.5 cm wide × 1.25 cm deep × 18.5 cm long (across the belt). The stainless steel belt was 20.3 cm wide. Water flow rate was measured by a "Rotameter," periodically checked by direct weighing, and the water temperatures by accurate mercury in glass thermometers. The cooler ran "full," i.e., the rectangular flow channel made up of three sides of the "box" together with the moving surface was completely filled with water generally moving at right angles to the belt direction. Spring loaded contact thermocouples were used to measure the surface temperatures of the stainless steel belt in conjunction with a recorder, so that the temperature driving force between the surface in contact with the water and the bulk water temperature could be estimated. Proving tests demonstrated that the measured temperatures were reliable.

Considerable difficulty in achieving a water-tight seal at the moving surface was experienced. After trial and error tests using a number of different materials, satisfactory results were obtained using expanded polyethylene coated with P.T.F.E.

Good thermal contact between the heating block and the moving belt was obtained by the use of several layers of aluminum foil placed on the heater surface. The initial problem had been one of obtaining good contact without excessive friction and surface scratching.

In the calculations the following concepts and simplifications were used:

1 The heat transferred was based on the water flow rate and the temperature change in the water as it passed through the cooler. It was not possible to use the electrical energy input to the heater as a measure of the heat transferred due to the rather large physical size of the thermally insulated heater block and the difficulty of measuring (or estimating) the heat losses from the block. The lowest temperature rise in the water was 4.2°C (18.2–22.4°C) and the highest rise 30.2°C (19.2–59.4°C).

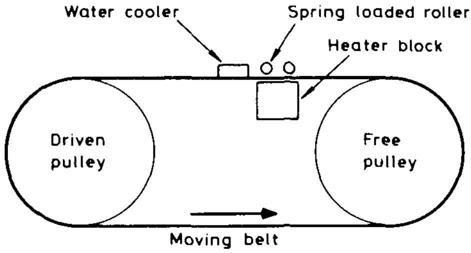

Fig. 2 Schematic diagram of apparatus

2 The moving surface temperature (T_w°C) was calculated by averaging the six point surface temperatures (three in front of the "leading edge" of the cooler and three behind the "trailing edge"). Variations in the measured surface temperatures were not excessive and depended, as might be expected, on the experimental conditions. The maximum difference between any two measurements was of the order of 10°C, but in many instances the differences were only of the order of 1° or 2°C. Belt surface temperature was generally in the range 30–90°C, the actual temperature level for any particular run depending upon the experimental conditions.

3 The mean water temperature was obtained by averaging the inlet and outlet temperatures.

4 The temperature distribution is basically a crossflow situation, and because of the relatively small temperature changes, it was considered satisfactory to calculate the surface heat transfer coefficient using a temperature driving force equal to the difference between the mean moving surface temperature and the mean water temperature. The temperature driving force was within the range 8–38°C, depending upon experimental conditions, but in the majority of experiments it was between 20 and 30°C.

5 Any effects of back mixing have been ignored [11].

The accuracy of the measurements and reproducibility was good, but due to these necessary simplifications it is estimated that the calculated convective heat transfer coefficient accuracy is only of the order of ±5 percent.

4 Results and Discussion

As would be anticipated, the experimentally determined value of the moving-surface heat transfer coefficient increases with water flow rate and moving-surface speed.

The range of Reynolds number for the flow in the cooler was 250–2500. The flow rate was kept deliberately low since it was felt that an interest in the technique would depend upon the use of the minimum amount of water (as in the cooling of steel strip mill rolls). The turbulence generated by the moving surface alone is enough to ensure a high heat transfer coefficient [1]; even at low water velocities the values are very much greater than those with no surface movement. The enhancement of heat transfer rate is not attributed to possible boiling effects since the moving belt temperature was deliberately kept well below 100°C. (Previous studies [1] had suggested an improvement in heat transfer due to "boiling effects" at the surface.)

The broken curve superimposed on Fig. 3 is a plot of the estimated moving-surface heat transfer coefficient with belt speed using the

Nomenclature

C_p = specific heat at constant pressure
h = heat transfer coefficient
k = thermal conductivity
t = contact time
ρ = density

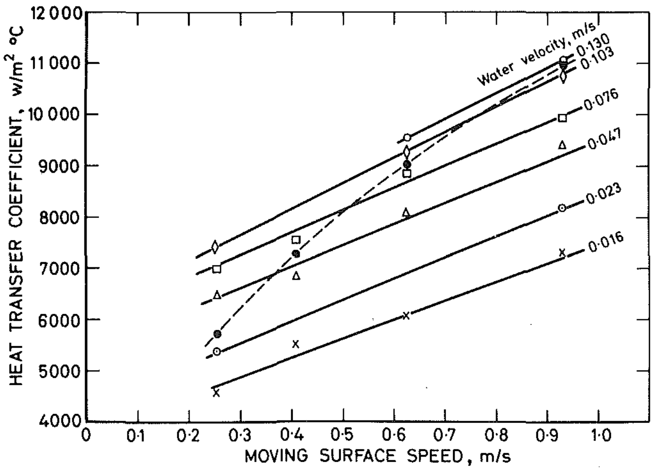

Fig. 3 **Variation of heat transfer coefficient with moving-surface speed**

penetration theory prediction given by equation (1). The values of the contact time were calculated from a knowledge of the moving surface speed and the width of the flow channel (2.54 cm), i.e., the time taken for a point on the belt surface to move from one side of the channel to the other.

The basis for the theory is an assumption that heat flow can be described as unsteady heat conduction, provided that the lifetime of the layers in contact with the surface is small, due to the prevailing hydrodynamic conditions. Deviations from this ideal concept would be expected to produce results significantly different from those predicted by the theory. A number of different conditions can be visualized, which would be contrary to the basic assumption, when it is appreciated that the level of turbulence within the flow channel, due to the combined action of the flow and moving surface, is high. (Largely unsuccessful attempts at flow visualization and back-mixing measurements, within a "Perspex" model, demonstrated, however, how effective fluid mixing was within the channel, particularly at right angles to the water flow under all run conditions.)

1 Eddy penetration into the laminar layer and consequent reduction in the effective contact time between the layer and the surface would clearly result in an improved rate of heat transfer.

2 Possible secondary-flow or back-mixing effects associated with the complex force pattern acting on the water may decrease the rate of heat transfer due to the effect on temperature driving force. (Recirculation is possible parallel to the direction of the moving surface and parallel to the direction of the water flow.)

The theory predicts that as the contact time decreases (moving surface speed increases) the rate of heat transfer increases. The experimental results show this trend. At the higher surface speeds for the highest water flow rate studied, the theoretical predictions and the experimental results are very similar. Under these conditions the results suggest that the estimated contact time is so short that the effect is equivalent to the extent of the penetration of the laminar film found in practice (if indeed it can be considered that such a film forms at all, bearing in mind the fluid condition prevailing in the cooler), and the secondary-flow effects would be excluded. As the surface speed and water flow rates are reduced, there is likely to be a greater influence due to these secondary effects. The extent to which the heat transfer coefficient is affected will depend upon the relative importance of the conditions. The experimental results do show deviations from the theoretical predictions, at lower water velocities; even at relatively high moving-surface speeds, the heat transfer coefficients are low and for the range of water velocity at low moving-surface speeds they are high.

A theoretical model that would allow for all the variations in flow conditions would be extremely difficult to devise, since the flow pattern is so complex.

It is anticipated that provided the moving surface speeds, water velocities, and channel flow cross-sectional area are employed in industrial applications with the same approximate water and surface temperature ranges, the resulting heat transfer coefficients would be of the same order as those obtained in the experiments. For larger channel flow cross section, the same results should be obtained provided the channel is divided into a number of small channels similar to the single channel of the experiments. It would be difficult to predict the effects of changing the variables outside the range employed in the experiments, except at the higher surface speeds and Reynolds numbers where the "penetration theory" appears satisfactory.

5 Conclusions

The "penetration model" theory predicts the heat transfer coefficient at a moving surface under the conditions of the experiments only for high surface speed and high water velocity, but it cannot be regarded as generally applicable to all flow and surface movement conditions. At high surface speeds and lower water velocities the experimental value of the heat transfer coefficient is lower than the predicted values, whereas at lower surface speeds and lower water velocity the experimental value of the heat transfer coefficients is higher than the predicted value. The discrepencies are considered to be due to turbulence and secondary-flow effects not accounted for in the model.

The heat transfer coefficients measured in the experiments should be obtained in industrial equipment operating under similar conditions

Acknowledgments

The authors would like to express their appreciation of the facilities provided by the Chemical Engineering Department, Birmingham University, to enable this work to be carried out. Thanks are also due to the Science Research Council for the provision of a research studentship in connection with these studies.

References

1 Bott, T. R., and Ward, J., "Proceedings of a Symposium on Chemical Engineering in the Iron and Steel Industry," *I. Chem. E.*, 1968, p. 115.

2 Penney, W. R., and Bell, K. J., *Ind. Eng. Chem.*, Vol. 59, No. 4, 1967, p. 47.

3 Kirschbaum, E., and Dieter, K., *Chem. Ing. Tek.*, Vol. 30, 1958, p. 715.

4 Lustenader, E. L., et al., JOURNAL OF HEAT TRANSFER, TRANS. ASME, Series C, Vol. 81, 1959, p. 297.

5 Kern, D. Q., and Karakas, H. J., *Chem. Eng. Prog. Symp.*, Series 29, 1959, p. 141.

6 Harriott, P., *Chem. Engng. Prog. Symp.*, Series 29, 1959, p. 137.

7 Houlton, H. G., *Ind. Engng. Chem.*, Vol. 36, No. 6, 1944, p. 522.

8 Latinen, G. A., *Chem. Engng. Sci.*, Vol. 9, 1959, p. 263.

9 Azoory, S., and Bott, T. R., *Cand. Chem. Engng.*, . 48, 1970, p. 373.

10 Bott, T. R., and Nair, B., *Chem. Engr.* No. 231 CE, 1969, p. 361.

11 Bott, T. R., Azoory, S., and Porter, K. E., *Trans. Inst. Chem. Engrs.*, Vol. 46, 1968, p. 733.

R. Viskanta
Professor.
Mem. ASME

R. O. Johnson[1]
Graduate Assistant.

R. W. Bergstrom Jr.[2]
Postdoctoral Fellow.

Heat Transfer Laboratory,
School of Mechanical Engineering,
Purdue University,
West Lafayette, Ind.

Modeling of Temperature and Pollutant Concentration Distributions in Urban Atmospheres

An unsteady two-dimensional transport model is constructed to study the short-term effects of urbanization and air pollution on the thermal structure and dispersion in an urban atmosphere. The model includes horizontal and vertical advection as well as turbulent diffusion and radiative transfer in the planetary boundary layer (PBL). The gaseous and particulate pollutants as well as the natural constituents in the atmosphere absorb, emit, and anisotropically scatter radiation. The variation of the physical properties of the soil, the radiation characteristics of the earth's surface, and the urban heat and pollutant emissions along the city are modeled. A number of numerical simulations for summer conditions modeling a typical Midwestern city are performed and the effects of various parameters arising in the problem have been investigated. The diurnal variation of the temperature structure and pollutant concentrations are discussed. It was found that the temperature changes caused by radiatively participating pollutants are generally smaller than the effects induced by urbanization. A maximum urban heat island of approximately 3°C was predicted and found to be in good agreement with observations.

Introduction

The climate of cities has been influenced on a local scale by the urbanization, industrialization, and air pollutants injected into the atmosphere [1].[3] It is recognized, for example, that air pollutants affect sunshine, visibility, temperature, precipitation, and fog frequency. This modification of the urban environment has observable adverse effects on human, animal, and plant life [2]. As the urban areas grow, the effects begin to be measurable on a regional scale [3] and many atmospheric scientists even consider air pollution to be a potential cause of irreversible changes in the global climate. These concerns have been voiced in the Study of Critical Environmental Problems [4], in the Study of Man's Impact on Climate [5], and numerous other publications.

The mechanisms by which the gaseous and particulate pollutants alter the temperature of the earth and the atmosphere are quite simple. The key to climate is the balance of radiation. The earth and atmosphere maintain their thermal energy balances by absorbing shortwave solar radiation and by reradiating energy back to space at longer wavelengths (as thermal radiation). The presence of air pollutants alters the radiative transfer in the atmosphere by changing the spectral absorption and scattering characteristics of the atmosphere itself. Solar radiation is absorbed by gaseous pollutants and absorbed and scattered by particulate pollutants. This can tend to raise the temperature of the atmosphere and cool the surface. However, increased absorption and emission of thermal radiation by pollutant gases tends to increase net radiative flux reaching the surface and raise its temperature.

At present, the lack of understanding of detailed physical processes in the atmosphere and the limitations in available data have made it impossible to arrive at definitive conclusions concerning the effects of pollutants on the global and local climate. Calculations of a globally averaged radiative energy budget [6, 7] have been inconclusive since it has been shown that the net influence of the aerosol could be warming or cooling depending upon its radiative properties and the surface reflectance. Also, there is considerable uncertainty in the globally averaged aerosol properties and surface reflectance. Except

---

[1] Presently member of Division of Engineering Design, Tennessee Valley Authority, Knoxville, Tenn.

[2] Presently National Research Council Research Associate at NASA Ames Research Center, Moffett Field, Calif.

[3] Numbers in brackets designate References at end of paper.

Contributed by the Heat Transfer Division for publication in the JOURNAL OF HEAT TRANSFER. Manuscript received by the Heat Transfer Division December 12, 1975.

for those of Mitchell [8], the predictions have also failed to account for the interaction of atmospheric radiation and sensible and latent heating on the terrestrial energy budget. On a local scale, the best documented and unquestioned climatic effect is the urban influence on temperature in the atmosphere. The urban heat island phenomenon is clearly a result of the modification of surface and atmospheric parameters by urbanization, which in turn lead to an altered energy balance. The causes of the urban heat island are well recognized [1]. However, quantitative studies of individual effects such as physical and radiative property differences between urban and rural areas, flow changes induced by the roughness elements, anthropogenic heat sources, and radiatively participating pollutants have not yet been sufficiently studied and are not completely understood.

Observational programs and mathematical modeling are needed to gain understanding of the physical processes in the urban environment. Unfortunately, the very nature of the urban area and the fact that extensive measurements are needed over a long period of time make such observations difficult and costly. Therefore, mathematical models can be employed to advantage to help understand and extend the observational data by numerically simulating the transport processes in the atmosphere. To the extent that the mathematical model simulates the real atmosphere, it can then become valuable, for example, in micrometeorological weather prediction, forecasting pollution episodes, urban planning, interpretation of field data, calculation of pollutant dispersion, identification of pollutants using remote sensing methods, and many others. In addition to the foregoing, numerical simulations can also be a valuable guide to observational programs such as the Regional Air Pollution Study (RAPS) sponsored by the United States Environmental Protection Agency for the St. Louis metropolitan area. The main advantage of numerical simulation lies in its ability to predict what will happen for any given set of changes in the urban parameters or in the boundary and/or initial conditions.

The specific purpose of this paper is to study the short-term effects of urbanization on the transport processes in an atmosphere over an urban area. To this end, an unsteady two-dimensional transport model is constructed which accounts for the interaction between the pollutants and the dynamics to predict the temperature structure and pollutant concentrations in the atmosphere. The emphasis in the paper is on the potential effects of urbanization and air pollution on the thermal structure of the urban planetary boundary layer. As an example, results of numerical simulations modeling of a typical city in midwestern United States are discussed. The paper extends models and supplements the results of related studies which have been reported in the literature [9–14].

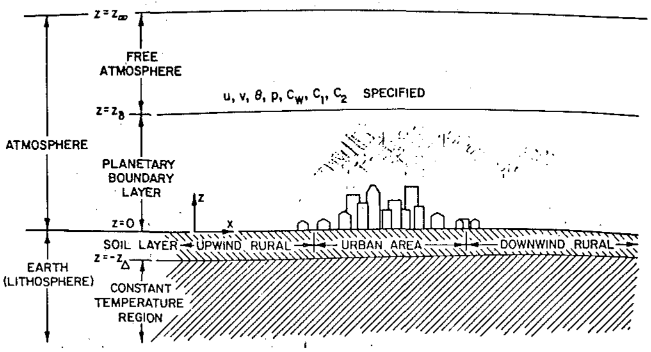

Fig. 1 Schematic representation of the urban environment and of influences analyzed by the urban boundary layer model

Analysis

Physical Model and Assumptions. This analysis is a generalization of an unsteady one-dimensional transport model in an urban planetary boundary layer (PBL) described elsewhere [13, 14]. The physical model of the atmosphere is illustrated in Fig. 1. The earth-atmosphere system is assumed to be composed of four layers: (1) the "free" ("natural") atmosphere which is not affected greatly by surface processes and where the meteorological variables are considered to be time independent; (2) the "polluted" atmosphere (the planetary boundary layer) where the meteorological variables such as the horizontal, vertical, and lateral wind velocities, temperature, water vapor and pollutant concentrations are functions of height, time, and distance along the urban area; (3) the soil layer, where the energy transport is one-dimensional (with depth only), but the soil properties and the radiation characteristics are considered to vary in the horizontal direction; and (4) the lithosphere where the temperature is assumed to be constant during the simulation period. The atmosphere is assumed to be cloud free with no variation in the topography of the urban area being accounted for.

In the polluted urban planetary boundary layer the transport of momentum, energy, and species is by vertical and horizontal advection as well as vertical and horizontal turbulent diffusion. In addition, energy is also transported by solar (shortwave) and thermal (longwave) radiation. The interaction of both natural atmospheric constituents and gaseous as well as particulate pollutants with solar and thermal radiation is accounted for. The coupling between the plan-

Nomenclature

C_n = concentration of species n
$\dot{C}_n$ = volumetric mass source rate of species n
c_p = specific heat at constant pressure
D_n = binary mass diffusion coefficient for species n
e_t = thermal emittance of soil
$\mathcal{F}$ = radiant flux in the z-direction
F = unidirectional flux
f = Coriolis parameter
h_{fg} = latent heat of evaporation
$K_{j,i}{}^M$ = turbulent diffusivity of momentum parallel to j plane in the i-direction
$K_i{}^\theta$ = turbulent diffusivity of heat in the i-direction
$K_i{}^{C_n}$ = turbulent diffusivity of species n in the i-direction
k = thermal conductivity or ratio of specific heats
L = extent of the urban area
M = Halstead's moisture parameter
m_p = anthropogenic (manmade) pollutant emission surface flux
p = pressure
p_0 = surface pressure
$\dot{q}$ = volumetric heat generation rate
Q = anthropogenic (manmade) heat emission surface source
R = gas constant
T = thermodynamic temperature
t = time
u = horizontal east velocity component
u_g = geostrophic east velocity component
v = horizontal north velocity component
v_g = geostrophic north velocity component
w = vertical velocity component
x = horizontal east coordinate
y = horizontal north coordinate
z = vertical coordinate
z_0 = roughness length
z_δ = planetary boundary layer height, see Fig. 1
z_∞ = top of atmosphere, see Fig. 1
z_Δ = depth of soil layer, see Fig. 1
α = thermal diffusivity
θ = potential temperature, $\theta = T(p/p_0)^{R/c_p}$
λ = wavelength
μ = dynamic viscosity
ρ = density or reflectance
σ = Stefan-Boltzmann constant

Subscripts

n = nth species
s = refers to solar part of spectrum or soil
t = refers to thermal part of spectrum
w = refers to water vapor
p = refers to pollutant (1-aerosol, 2-gas)

Superscripts

$+$ = positive z-direction
$-$ = negative z-direction

etary boundary and soil layers is affected by both energy and species balances at the atmosphere-soil interface. The horizontal variation of the urban parameters such as anthropogenic heat and pollutant sources, surface solar albedo (reflectance) and thermal emittance, surface roughness, thermal diffusivity, conductivity of the soil, and moisture parameters are arbitrarily prescribed functions of position along the urban area. It is well recognized [2] that urban heat and pollutant emissions, for example, vary during the diurnal cycle; however, a more realistic modeling of these sources during the diurnal cycle must await more complete observational data.

It should be emphasized that the flow field, temperature, and radiative transfer in an urban area is three-dimensional and would require a very fine grid structure for complete simulation over an urban area and does not appear to be warranted. In addition, a truly detailed and accurate treatment of the present problem is extremely difficult not only because of the lack of necessary data but also because it is beyond the capability of most present-day computers. Since the primary objective of this research is to simulate the thermal structure and pollutant dispersion, some details of the complicated urban flow field have been ignored. The two-dimensional model, however, should provide a more realistic description than the one-dimensional one [13, 14] and the temperature and pollutant concentration distributions should not be extremely sensitive to the fine details of the flow field.

Model Equations. The numerical model is based on the conservation equations of mass, momentum, energy, and species. The equations used to describe the planetary boundary layer are well known in the literature [15] and can be written as follows for a polluted atmosphere:

Mass:

$$\frac{\partial(\rho u)}{\partial x} + \frac{\partial(\rho w)}{\partial z} = 0 \tag{1}$$

Momentum (x-direction):

$$\rho\left(\frac{\partial u}{\partial t} + u\frac{\partial u}{\partial x} + w\frac{\partial u}{\partial z}\right) = \rho f(v - v_g) + \frac{\partial}{\partial x}\left[(\mu + K_{x,x}{}^{M})\frac{\partial u}{\partial x}\right] + \frac{\partial}{\partial z}\left[(\mu + K_{x,z}{}^{M})\frac{\partial u}{\partial z}\right] \tag{2}$$

Momentum (y-direction):

$$\rho\left(\frac{\partial v}{\partial t} + u\frac{\partial v}{\partial x} + w\frac{\partial v}{\partial x}\right) = -\rho f(u - u_g) + \frac{\partial}{\partial x}\left[(\mu + \rho K_{y,x}{}^{M})\frac{\partial v}{\partial x}\right] + \frac{\partial}{\partial z}\left[(\mu + \rho K_{y,z}{}^{M})\frac{\partial v}{\partial z}\right] \tag{3}$$

Momentum (z-direction):

$$0 = +\frac{\partial p}{\partial z} + \rho g \tag{4}$$

Energy:

$$\rho c_p\left(\frac{\partial\theta}{\partial t} + u\frac{\partial\theta}{\partial x} + w\frac{\partial\theta}{\partial z}\right) = \frac{\partial}{\partial x}\left[(k + \rho c_p K_x{}^{\theta})\frac{\partial\theta}{\partial x}\right] + \frac{\partial}{\partial z}\left[(k + \rho c_p K_z{}^{\theta})\frac{\partial\theta}{\partial z}\right] - \left[\frac{\partial\mathcal{F}}{\partial z} - \dot{q}\right]\left(\frac{p_0}{p}\right)^{(k-1)/k} \tag{5}$$

Species:

$$\frac{\partial C_n}{\partial t} + u\frac{\partial C_n}{\partial x} + w\frac{\partial C_n}{\partial z} = \frac{\partial}{\partial x}\left[(D_n + K_x{}^{C_n})\frac{\partial C_n}{\partial x}\right] + \frac{\partial}{\partial z}\left[(D_n + K_z{}^{C_n})\frac{\partial C_n}{\partial z}\right] + \dot{C}_n \tag{6}$$

The energy equation in the soil layer is:

$$\frac{\partial T_s}{\partial t} = \alpha_s\frac{\partial^2 T_s}{\partial z^2} \tag{7}$$

At the top of the PBL, the meteorological variables are specified and held constant during the simulation; that is,

$$\phi(t, \chi, z) = \text{constant} \quad \text{at} \quad z = z_\delta \tag{8}$$

where ϕ represents the horizontal east velocity u, the horizontal north velocity v, the potential temperature θ, and the species concentration C_n. This assumes that the larger scale flow (i.e., synoptic scale weather pattern) remains constant during the simulation period. At the bottom of the soil layer the temperature remains constant:

$$T_s(t, x, z) = \text{constant} \quad \text{at} \quad z = -z_\Delta \tag{9}$$

At the earth's surface the velocities vanish:

$$u(t, x, z) = v(t, x, z) = w(t, x, z) = 0 \quad \text{at} \quad z = 0 \tag{10}$$

Along the interface, the surface temperature is predicted from an energy balance

$$[1 - r_s(x)]F_s{}^{-}(t, x, 0) + e_t(x)F_t{}^{-}(t, x, 0) - e_t(x)\sigma T^4(t, x, 0) + (k + \rho C_p K_z{}^{\theta})\left.\frac{\partial\theta}{\partial z}\right|_{0^+} + h_{fg}(D_w + K_z{}^{C_w})\left.\frac{\partial C_w}{\partial z}\right|_{0^+} - k_s\left.\frac{\partial T_s}{\partial z}\right|_{0^-} + Q = 0 \tag{11}$$

In this equation, the first two terms account for absorption of solar and thermal radiation, the third term represents thermal emission, the fourth and fifth terms account for sensible and latent heat transfer by molecular and turbulent diffusion, the sixth term represents heat conduction into the ground, and the final term is the anthropogenic heat source.

The water vapor concentration at the surface is prescribed by Halstead's moisture parameter [16] using the expression

$$C_w(t, x, 0) = MC_{w,\text{sat}}[T(t, x, 0)] + (1 - M)C_w(t, x, z_1) \tag{12}$$

where z_1 is the first grid point above the surface and $C_{w,\text{sat}}$ is the water vapor concentration at saturated conditions. The values of the parameter M range from 1 for water $[C_w(t, x, 0) = C_{w,\text{sat}}]$ to 0 for dry soil $[C_w(t, x, z) - C_w(t, x, 0) = 0]$. The moisture parameter M, the fraction of area which is saturated with water, depends on soil type, root distribution, water table depth, and other variables [17]. In addition, the soil in urban areas is partly covered by buildings, pavement, etc., and this fraction cannot be readily estimated. In addition, in writing equation (12) anthropogenic water vapor sources have been neglected. More detailed models for predicting temperature distribution in the soil and the evaporation from the earth's surface are available [18]. Unfortunately, hydraulic and thermal properties of soil such as moisture potential, effective permeability (hydraulic conductivity), and moisture content as well as thermal diffusivities are not known for the soil types and textures encountered in urban areas [19].

The surface boundary condition for the pollutant concentration is written for a surface source by specifying the surface mass flux, m_p, i.e.,

$$m_p = -(D_p + K_z{}^{C_p})\frac{\partial C_p}{\partial z} \quad \text{at} \quad z = 0 \tag{13}$$

It should be noted that in an urban area the pollutants are not all introduced into the atmosphere from the surface, and this formulation then has certain physical limitations. Again, as with the moisture parameter M, there is little quantitative data on sources of individual pollutants at the surface.

At the upwind rural boundary, the meteorological variables are predicted from the one-dimensional model of Bergstrom and Viskanta [13, 14]. This assumes that the flow into the urban area is fully developed and parallel and possesses no vertical velocity. Downwind of the city (i.e., in the rural area) it is assumed that all the meteorological and air pollution variables change slowly, or

$$\frac{\partial\phi}{\partial x} = 0 \quad \text{at} \quad x = L \tag{14}$$

This condition implies that the downwind rural area is far away from the city center and that nearly fully developed conditions have been developed. At the initial time the variables are specified everywhere and are assumed to be independent of the horizontal coordinate x.

Radiation Transfer Model. The radiation transfer model used has been discussed in detail elsewhere [20] and therefore only a summary is included here. The urban atmosphere is again considered to be cloudless, plane-parallel, and consist of two layers: (1) the free atmosphere and (2) the urban PBL where most pollutants are concentrated. From below, the boundary layer is bounded by an opaque earth's surface which not only emits but also reflects radiation. The emission characteristics and albedo (reflectance) of the earth's surface in the model are arbitrary but prescribed functions of wavelength. The radiative transfer between the free atmosphere and the polluted PBL are coupled. The gaseous and particulate atmospheric constituents are considered to absorb, scatter, and emit radiation. Since multidimensional radiative transfer is quite complex, it is assumed that the transport of radiation can be approximated by a quasi-two-dimensional field based on the vertical temperature and water vapor and pollutant distributions at several predetermined horizontal positions. The radiative fluxes in the atmosphere can then be evaluated at these prescribed horizontal locations with suitable interpolation and used to determine the radiative fluxes between these locations.

The radiative fluxes and flux divergences were evaluated by dividing the entire electromagnetic spectrum into a solar ($0.3 \leq \lambda \leq 4$ μm) and a thermal ($4 \leq \lambda < 100$ μm) part. The computational details can be found in an earlier publication [20]. Suffice it to note that total emissivity data for water vapor and carbon dioxide were used and scattering was neglected in predicting radiative transfer in the thermal (longwave) part of the spectrum. It was assumed that the influence of gaseous pollutants could be confined to the 8–12 μm spectral region due to the relative opacity of the H_2O and CO_2 bands. Ethylene and sulfur dioxide were considered to be representative pollutants. The spectral absorption and scattering characteristics of the aerosol in a polluted atmosphere were determined from the model developed by Bergstrom [21]. The infrared properties of the aerosol were neglected for simplicity, but it should be noted that their effect would be the same as increasing the relative strength of the gaseous pollutant infrared absorption. Similarly, the solar absorption properties of the gases were neglected.

Turbulent Diffusivities. Specification of turbulent diffusivities for an urban atmosphere in connection with numerical modeling of the PBL is a very difficult task and has been a subject of a recent review [22]. The semi-empirical equations developed by Pandolfo, et al. [16] were first employed. The decay of turbulence in the upper part of PBL was accounted for following Blackadaar [23]. Late at night, when the atmosphere became quite stable, unrealistically deep inversions resulted. The Richardson numbers were found to exceed the critical value. For these cases the diffusivities predicted by Pandolfo's eddy diffusivity-Richardson number correlations were not applicable. In order to overcome this difficulty, the cubic polynomial developed by O'Brien [24] and used by Bornstein [10] was employed for diffusivity prediction in the transition layer.

Pandolfo's diffusivity model was employed in the entire PBL except under stable conditions. Stable conditions were assumed to exist when the average Richardson number in the lowest 25 m of the atmosphere was greater than zero. When this condition was reached, Pandolfo's model was used only near the surface while the polynomial was employed in the transition layer. Otherwise, Pandolfo's model was used throughout the entire PBL. If the Richardson number exceeded 3/8, it was automatically reset to this value so that unreasonable diffusivity values would not be predicted under very stable conditions.

Method of Solution

The alternating-direction-implicit (ADI) method [25] was employed to solve the transport equations. The finite difference approximations for the spatial derivatives and the numerical algorithm are discussed in detail by Johnson [26].

In order to improve the resolution near the surface, a logarithmic-uniform grid spacing was chosen in the vertical direction. The logarithmic spacing extended to about 1 km from the earth's surface while from there to the assumed top of the PBL (~2 km) the spacing was uniform. This was accomplished by the transformation, $\zeta = A\ell n[(z + B)/B]$, where A and B were arbitrary constants. Equidistant spacing was chosen for the horizontal direction. The results reported in the paper have been obtained using 22 nodes in the vertical direction and 17 in the horizontal.

Three-distinct time steps (one for the 2-D momentum equations, one for the other 2-D transport equations, and one for the 1-D transport equations) were varied and convergence studied. Also, to obtain some appreciation for the sensitivity of the model, numerical experiments were performed using different horizontal grid spacings and different vertical distribution of coordinates. The downwind error propagation has also been investigated. The detailed findings of these computations are given by Johnson [26].

Results and Discussion

Numerical Experiments. The numerical model has been tested and a number of numerical experiments have been performed. Because of the length and scope of the paper, it is possible to include only some selected results that have been obtained. More extensive results including those for Gaussian distribution of urban heat and pollutant emissions along the city are given elsewhere [26]. The experiments were designed to simulate the thermal structure and pollutant dispersion in the atmosphere and study the effects of various parameters. This was accomplished in the simulation by variation of (1) geostrophic wind speed, (2) characteristics of atmosphere-soil interface, (3) urban heat and pollutant emission parameters, (4) pollutant gas, and (5) distribution of urban parameters along the area. The interfacial parameters used are specified in Table 1. The horizontal distribution for the surface characteristics was established by selecting the values of parameters at the rural and urban center locations and, for the lack of any better data or information, a Gaussian distribution curve was fitted between the rural and urban center locations. A rectangular distribution was used for the urban heat and pollutant emissions along the surface. Out of a total 17 grid points in the horizontal x-direction, points 1 and 2 were in the upwind rural area and points 15, 16, and 17 were in the downwind rural area. The values for parameters Q, m_1, and m_2 given in Table 1 represent mean values over the city. The simulations were started at noon (12:00) solar time and continued for a 24-hr period.

The initial temperature profiles used were taken from Lettau and Davidson [27] for August 24, 1954, and were imposed over the entire city (no x-variation). The initial horizontal and lateral velocity fields were either the same or decreased by a factor of two or four of those given by Lettau and Davidson for the O'Neill Great Plains Turbulence Study. The pollutant concentration profiles were initialized to a constant background value of 50 $\mu g/m^3$. The top of the PBL was arbitrarily chosen to be at the height of 2000 m. The lower soil layer below the surface ($z = -z_\Delta = 50$ cm) was held constant at a temperature of 295.5 K. The horizontal grid Δx was chosen to be 1500 m, thus modeling an urban area 24 km along the x-direction. The latitude was taken as 38.5 deg and summer conditions (solar declination 21 deg) were assumed. A summer day was chosen because most of the serious pollution episodes occur then and because solar radiation is the greatest.

Table 1 Numerical values of interface parameters for simulations [26]

Parameter	Upwind rural	Urban center
Solar albedo, r_s	0.18	0.12
Thermal emittance, e_t	0.90	0.95
Soil thermal conductivity, k_s(W/mK)	0.1	0.5
Soil thermal diffusivity, α_s (10^7 m^2/s)	1	2.5
Surface roughness, z_0(m)	0.2	1.0
Halstead's moisture parameter, M	0.1	0.05
Lower soil boundary temperature, T_Δ(K)	295.5	295.5
Urban heat source, Q(W/m^2)	2	20
Aerosol pollutant source, m_1 (μg/m^2-s)	0	2.5
Pollutant gas source, m_2 (μg/m^2-s)	0	2.5

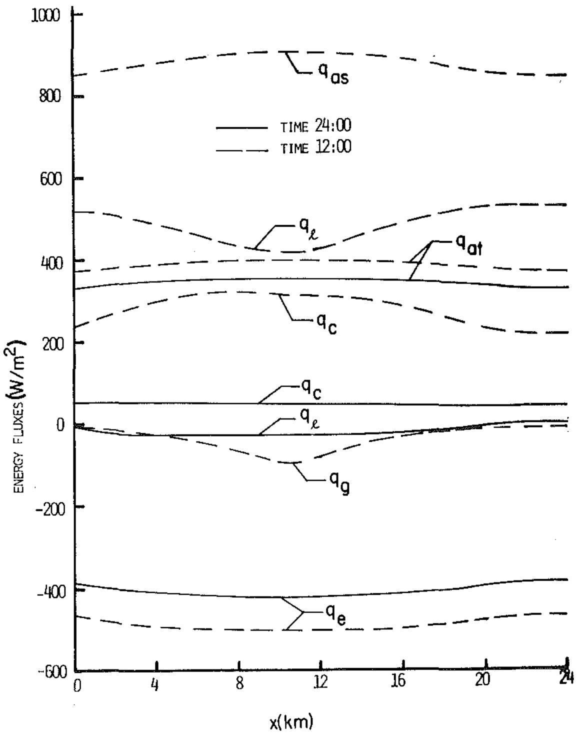

Fig. 2 Variation of the energy balance flux components (q_{as} = absorbed solar, q_{at} = absorbed thermal, q_e = emission, q_c = convection, q_ℓ = latent, q_g = soil conduction, Q = urban heat source) at the surface at 24:00 of the first day and 12:00 of the second day; rectangular distribution, radiatively nonparticipating, u_g = 6 m/s and v_g = 4 m/s

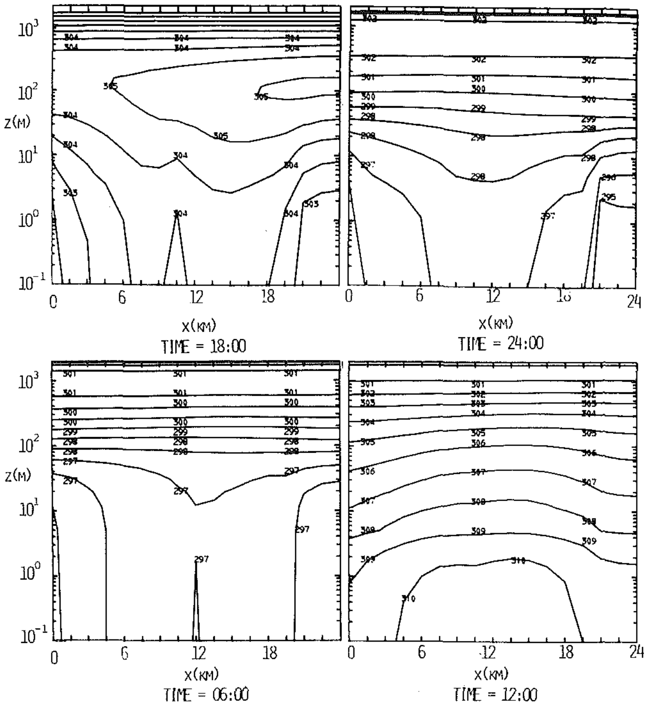

Fig. 3 Isopleths of potential temperature (in K); rectangular distribution, radiatively nonparticipating, u_g = 6 m/s, v_g = 4 m/s

Components of the Energy Balance at the Surface. The surface temperature is a very important parameter as far as "forcing" of the model is concerned. For this reason the variation of the energy budget components along the urban area are presented in Fig. 2 at midnight (24:00) of the first day and noon (12:00) of the second day. Inspection of the figure shows that the emitted (q_e) and the absorbed thermal (q_{at}) fluxes are the dominant components. The convective (q_c), the latent (q_ℓ), the soil conduction (q_g) (between 0.95 W/m^2 in the upwind rural area and 11.8 W/m^2 at the city center), and the anthropogenic urban heat (Q) (20 W/m^2, not shown in the figure) fluxes are significantly smaller. However, at noon the absorbed solar flux (q_{as}) is the largest term in the energy balance and the urban heat source (Q) is the smallest. The reason q_{as} is maximum at the urban center is because the solar albedo, r_s, is minimum there, see Table 1. At the urban center, x = 10.5 km, the soil heat conduction term (q_g) amounts to only about 10 percent of the absorbed solar flux. The convective (q_g) and the latent (q_ℓ) fluxes are the two components which are quite sensitive to wind speed and show the greatest variation along the urban area. The reason the convective heat flux increases to a maximum at the city center is that the turbulent eddy diffusivity increases as a result of roughness changes along the city while the latent flux reaches a minimum at the center due to decreased evaporation (reduction in the moisture parameter M in the city) which is controlled by M and not the surface roughness height z_0.

Temperature Distribution. The isopleths of the two-dimensional potential temperature fields at 6-hr intervals for a simulation with radiatively nonparticipating pollutants are presented in Fig. 3. At 18:00 the atmosphere is nearly adiabatic, especially in the upwind rural area, with a thermal plume having a temperature of about 305 K (note that the last digit denoting the temperature of the isotherms at 18:00, 24:00, and 06:00 hours has been truncated by the contour plotting program) forming at a height of about 100 m downwind of the city center (x = 10.5 km). However, the presence of the plume is not felt downwind since the upwind and downwind surface temperatures are nearly identical. A surface temperature inversion develops at night (parts at 24:00 and 06:00) and is seen to be deeper over the rural area than the city. This is indicative of the nocturnal heat island which decreases the stability of the atmosphere. The magnitude of this heat island is larger at night than during the day. This type of behavior is well documented [1, 28]. Just after sunrise (06:00) the surface inversion erodes rapidly due to the absorption of solar radiation at the earth's surface. The surface inversion breaks up after sunrise because of the increased turbulence resulting from warmer surface temperatures. By 09:00 all traces of the inversion have then disappeared. Clarke and McElroy [29] did not observe a surface inversion over Columbus, Ohio, or St. Louis, Missouri. The disagreement between predictions and observations indicates that the value of the anthropogenic heat source Q used in the simulations may have been too small or more likely that the turbulence model employed is inadequate under stable meteorological conditions.

The greatest temperature difference between a simulation without radiatively participating pollutants and a simulation with participating ones occurs at the surface; therefore, a comparison of the surface temperatures is presented in Fig. 4. In the simulation with radiatively interacting pollutants ethylene (C_2H_4) was considered to be the representative gaseous pollutant. The choice of ethylene was made because of the availability of radiative property data and the fact that it has strong infrared absorption. Certainly the infrared spectra of a polluted urban atmosphere is much more complicated, but ethylene can be considered to be an approximation to an atmosphere with a large amount of hydrocarbon pollution. Sulfur dioxide (SO_2), which is a considerably weaker absorber of radiation, has also been considered as a typical pollutant [26]. During the day the particulate and gaseous pollutants appear to have compensating effects on the surface temperature. The aerosols decrease the solar flux while the gaseous pollutants increase the thermal flux incident at the surface. Results presented in Fig. 4 show that for the urban parameters and the particular conditions considered, the surface temperatures for a simulation with radiatively interacting pollutants are always higher than for the simulation without radiatively noninteracting pollutants. The largest difference between the two surface temperatures occurs just before sunrise (05:00) and the smallest takes place about noon (12:00).

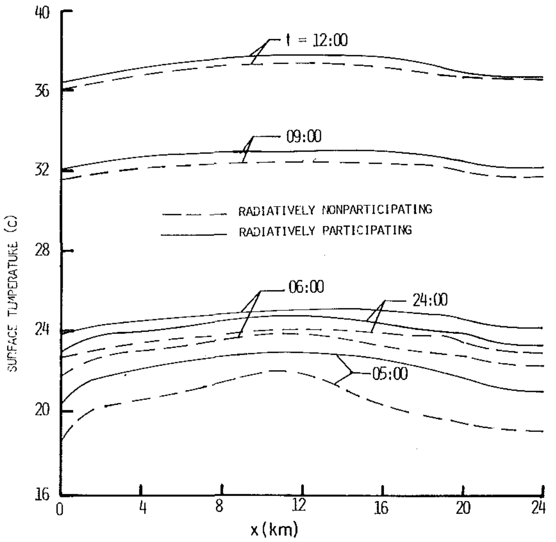

Fig. 4 Comparison of surface temperatures along the city between a simulation with and without radiatively participating pollutants; u_g = 6 m/s, v_g = 4 m/s, ethylene (C_2H_4) pollutant gas

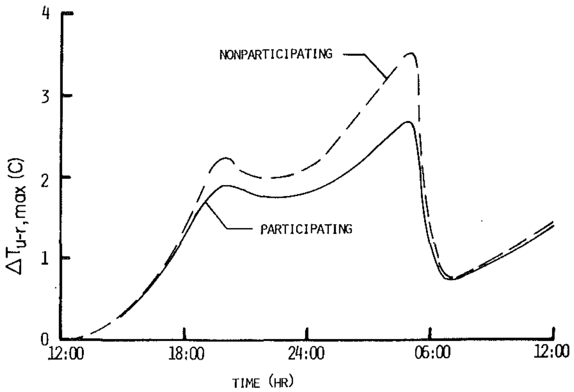

Fig. 5 Comparison of maximum urban minus upwind rural surface differences; u_g = 6 m/s, v_g = 4 m/s, ethylene (C_2H_4) pollutant gas

Also, the highest surface temperature occurs at the center of the city or a small distance (about 1.5–6 km) downwind of the center. This is caused by the heating of air as it flows over the warm city.

The diurnal variation of the surface temperatures at the upwind rural and the central urban locations for both the radiatively nonparticipating and participating simulations are given in Table 2. The results show that the largest surface temperature difference between the two simulations occurs just before sunrise (between 04:00 and 06:00) and is about 1°C higher for the radiatively participating simulation. By noon the next day the difference has decreased to 0.4°C. The fact that the surface temperatures are warmer in the morning hours for the radiatively participating simulation is significant. Higher surface temperatures result in decreased stability of the atmosphere at times in the morning when the dispersion of pollutants is most critical. The results also show that the presence of radiatively participating pollutants in the atmosphere dampens the amplitude of the diurnal surface temperature variations.

The urban heat island is a well known and accepted fact [1, 28]. The heat island intensity (maximum difference between upwind rural and highest urban surface temperature, $\Delta T_{u-r,\max}$) predictions are shown in Fig. 5; also see Table 2. For the assumed rectangular distribution of urban heat sources the maximum surface temperature difference occurred downwind of the center. The results presented in the figure show that there is a double peak in $\Delta T_{u-r,\max}$. The first smaller peak is noted in the evening about 20:00. It arises because of more rapid cooling at the upwind rural area than in the city. The second peak occurs before sunrise and increases to a value of about 3.5°C for the simulation with nonparticipating pollutants. The latter peak is primarily due to the differences in the physical properties of the soil and the radiation characteristics of the surface in the urban and rural areas as well as the stability of the atmosphere, which affects the eddy diffusivities and through them the surface temperatures. For the population of the urban area and wind speeds of the simulation, this value is in good agreement with the observations and empirical correlation of Oke [21]. For a simulation with lower wind speeds $u_g \simeq$ 3 m/s and $v_g \simeq$ 2 m/s, which are not reported here, the maximum heat island intensity reached about 8°C. The results are in good agreement with nighttime and daytime observed temperature excesses between the urban and rural locations [28, 30]. What is particularly encouraging is that urban-rural temperature differences of about 3°C have been observed by Clarke and McElroy [29] for the city of St. Louis, Missouri, near sunrise during several observational periods in August 1973. The meteorological conditions for the observed value of 3°C were similar to those for the simulation runs.

Table 2 Comparison of surface temperatures (in K) at the upwind rural (x = 0) and urban central (x = 10.5 km) locations for the radiatively nonparticipating and participating simulations

	Radiatively nonparticipating		Radiatively participating	
Time (hr)	Upwind rural	City center	Upwind rural	City center
12:00	308.89	308.89	308.89	308.89
14:00	309.72	310.02	309.98	310.23
16:00	308.18	308.51	308.47	308.75
18:00	302.83	303.80	303.20	304.17
20:00	296.93	299.05	298.05	299.83
22:00	296.03	297.99	297.01	298.73
24:00	294.96	297.07	296.10	297.89
02:00	293.64	296.25	295.17	297.19
04:00	292.20	295.47	294.00	296.53
06:00	295.90	297.27	297.07	298.25
08:00	302.35	303.05	302.95	303.67
10:00	306.74	307.72	307.20	308.23
12:00	309.23	310.47	309.59	310.87

The maximum urban-rural surface temperature differences are a result of complex interaction of the flow of air over a rough urban area, the manmade heat and pollutant sources, and the radiative participation by the aerosol and gaseous pollutants. Individual influences cannot be readily attributed. The primary reason for the smaller $\Delta T_{u-r,\max}$ for the simulations with the radiatively participating pollutants is the change in the upwind rural conditions. In the radiatively interacting simulation the presence of background pollutants increased the downward thermal flux incident on the surface and as a result the rural surface temperatures were somewhat higher for this experiment; see Table 2. Background pollutants were introduced in the upwind rural area because the atmosphere is not completely free of pollutants a few kilometers upwind and downwind of the city. The concentration used in the simulations may have been too high and a lower value may have yielded more realistic urban-rural temperature differences.

Pollutant Concentration Distribution. The pollutant concentration isopleths (in μg/m^3) over the city for the simulation with radiatively nonparticipating pollutants with a rectangular distribution of pollutant emissions along the city at 6-hr intervals are presented in Fig. 6. Since the aerosol emission flux (m_1) was assumed to be identical to that of the pollutant gas, the aerosol concentrations are identical to those of the gaseous pollutant. The pollutant emission fluxes m_1 and m_2 were chosen to produce reasonable concentrations in the atmosphere. At any given time the average pollutant concentration in the PBL did not exceed 70 μg/m^3. The results show the buildup of pollutant concentrations during the night. After sunrise (06:00), the atmosphere becomes unstable, and the pollutants are

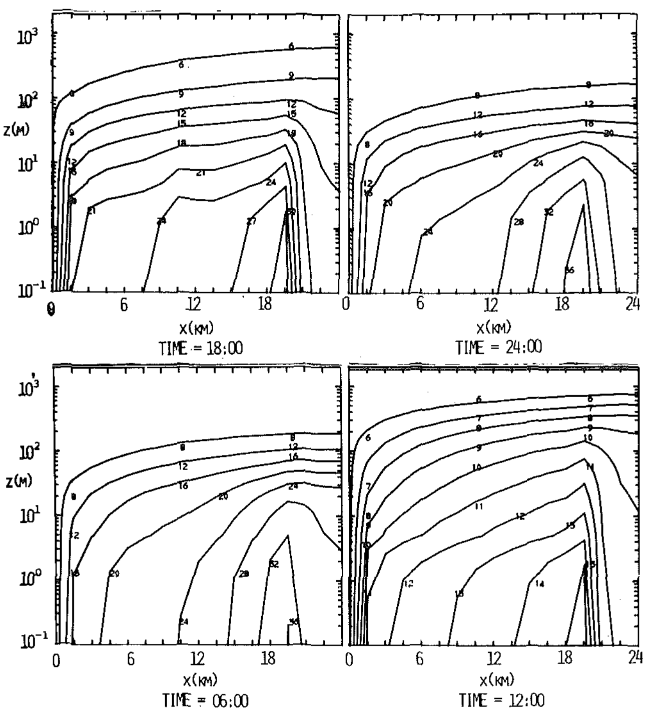

Fig. 6 Pollutant concentration isopleths (multiply numbers in the figures by 10 to obtain concentrations in $\mu g/m^3$); radiatively nonparticipating pollutants, $u_g = 6$ m/s, $v_g = 4$ m/s

dispersed rather effectively by vertical diffusion and horizontal advection. The worst times for dispersion are in the late evening and early morning, while the middle of the day is generally the best [2]. The isopleths show the formation of a pollutant plume downwind of the city center. The highest pollutant concentrations are at the surface and are confined to heights less than 10 m. Modeling of all pollutant emissions as surface sources is somewhat unrealistic. The surface concentrations are very sensitive to the turbulent diffusivities at the first few grid points above the ground. The diurnal trends in the surface pollutant concentrations can be explained on the basis of the diurnal variation of turbulent diffusivity at the first vertical grid point. The pollutant concentration isopleths for a simulation with radiatively participating pollutants are similar to those of Fig. 6 and are therefore not presented for the sake of brevity but can be found elsewhere [26].

The pollutant concentrations near the ground reach a maximum just before sunrise (05:00) and then decrease sharply as the earth's surface is heated by absorption of solar radiation and the stable layer is eroded. The results obtained show that for the particular values of urban parameters and meteorological conditions considered in the simulations, the radiatively participating pollutants in the atmosphere raise the urban surface temperature, decrease stability, and lower pollutant concentrations. The maximum reduction is before sunrise (05:00) and amounts to over 25 percent while at noon (12:00) the reduction is only 2 percent. The results obtained show that the radiative participation by pollutants may have the potential of affecting their own dispersion, especially peak concentrations before and after sunrise. The meteorological conditions considered in the numerical simulations were not critical for pollutant dispersion. Under more adverse dispersion conditions such as may arise for lower wind speeds and/or stable elevated layers, the coupling between the radiatively participating pollutants and their own dispersion may be stronger.

Conclusions

An unsteady two-dimensional transport model which accounts for the interaction between pollutants and the dynamics has been developed. The model is capable of simulating temperature structure and pollutant dispersion in an urban atmosphere. The numerical simulations performed with the model predicted an urban heat island, which is in agreement with observations for St. Louis, Missouri. For the urban parameters and meteorological conditions considered in the simulations, the radiatively participating pollutants are relatively unimportant in forming the urban heat island when compared to other factors. During the night, the radiatively interacting gaseous pollutant increased the surface temperature in the city. The higher temperature decreased stability of the atmosphere near the ground and reduced pollutant concentration when compared with noninteracting pollutants. The net effect of gaseous and particulate pollutants during daytime on temperatures and pollutant concentrations near the ground is relatively small. There is a tendency within the earth-atmosphere system for compensation, but radiative transfer is important in the energetics of the PBL.

The feedback mechanism between pollution, thermal structure, stability, and dispersion has the potential of being significant in modifying temperature and pollutant dispersion in the atmosphere near the surface under more stable conditions and higher pollutant mass loadings. However, the magnitudes of the changes are dependent on the coupling between the radiative properties of air pollution and buoyancy-induced turbulence, neither of which is really well understood. Thus, the magnitude of the change is uncertain.

The numerical model has been partially verified by observations; however, it needs continuous modification as more understanding is gained. The model can be a valuable tool, for example, in urban planning. It can be used to examine the potential environmental impact resulting from proposed urban changes and to provide answers to other questions which cannot be answered by observations.

Acknowledgments

This work was supported by the Division of Meteorology, U. S. Environmental Protection Agency, under Grant Nos. R801102 and R803514. Computer facilities were made available by Purdue University and the National Center of Atmospheric Research, which is supported by the National Science Foundation. The interest and support of Dr. J. T. Peterson, the Grant Project Officer, is acknowledged with sincere thanks. The authors also wish to acknowledge Mr. A. Venkatram for his contributions to this effort.

References

1 Peterson, J. T., "The Climate of Cities: A Survey of Recent Literature," U. S. Public Health Service, National Air Pollution Control Administration Publication No. AP-59, Washington, 1969.

2 Stern, A. C., Wholers, H. C., Boubel, R. W., and Lowry, W. P., *Fundamentals of Air Pollution,* Academic, Press, New York, 1972.

3 Landsberg, H. E., "Actual and Potential Effects of Pollutants on Climate," International Conference on Environment and Assessment (ICESA), Paper No. 32-1, Las Vegas, Nev., Sept. 14–19, 1975.

4 SCEP, *Man's Impact on the Global Environment: Assessments and Recommendations for Action,* MIT Press, Cambridge, Mass., 1970.

5 SMIC, *Inadvertant Climate Modification, Report of the Study of Man's Impact on Climate (SMIC),* MIT Press, Cambridge, Mass., 1971.

6 Rasool, S. I., and Schneider, S. H., "Atmospheric Carbon Dioxide and Aerosols: Effects of Large Increases on Global Climate," *Science,* Vol. 173, 1971, pp. 138–141.

7 Ensor, D. S., Porch, W. M., Pilat, J. J., and Charlson, R. J., "Influence of the Atmospheric Aerosol on Albedo," *Journal of Applied Meteorology,* Vol. 10, 1971, pp. 1303–1306.

8 Mitchell, J. M., "The Effect of Atmospheric Aerosols on Climate With Special Reference to Temperature Near the Earth's Surface," *Journal of Applied Meteorology,* Vol. 10, 1971, pp. 703–714.

9 Atwater, M. A., "Thermal Changes Induced by Urbanization," *Conference on Urban Environment and Second Conference on Biometeorology,* American Meteorological Society, Boston, 1972, pp. 153–158.

10 Bornstein, R. D., "Two-Dimensional, Nonsteady Numerical Simulation of Nighttime Planetary Boundary Layer Over a Rough Warm City," *Conference on Urban Environment and Second Conference on Biometeorology,* American Meteorological Society, Boston, 1972, pp. 89–94.

11 Wagner, N. K., and Yu, T.-W., "Heat Island Formation: A Numerical Experiment," *Conference on Urban Environment and Second Conference on Biometeorology,* American Meteorological Society, Boston, 1972, pp. 83–88.

12 Atwater, M. A., "Thermal Changes Induced by Pollutants for Different Climatic Regions," *Symposium on Atmospheric Diffusion and Air Pollution,* American Meteorological Society, Boston, 1974, pp. 147–150.

13 Berstrom, R. W., Jr., and Viskanta, R., "Modeling of Thermal Structure

and Dispersion in Polluted Urban Atmospheres," ASME Paper No. 73-HT-8.

14 Bergstrom, R. W., Jr., and Viskanta, R., "Modeling of the Effects of Gaseous and Particulate Pollutants in the Urban Atmosphere. Part I: Thermal Structure," *Journal of Applied Meteorology,* Vol. 12, No. 6, Sept. 1973, pp. 901–912.

15 Plate, E. J., *Aerodynamic Characteristics of Atmospheric Boundary Layers,* U. S. Atomic Energy Commission, Division of Technical Information, Oak Ridge, Tenn., 1971.

16 Pandolfo, J. P., Atwater, M. A., and Anderson, G. E., "Prediction by Numerical Models of Transport and Diffusion in an Urban Boundary Layer," The Center for the Environment and Man, Inc., Final Report CEM Contract No. 4082, Hartford, Conn. 1971.

17 Halstead, M. H., Richman, R. L., Covery, M., and Merryman, J. D., "Preliminary Design of a Computer for Micrometeorology," *Journal of Meteorology,* Vol. 14, No. 4, Aug. 1957, pp. 308–325.

18 Sasamori, T., "A Numerical Study of Atmospheric and Soil Boundary Layers," *Journal of the Atmospheric Sciences,* Vol. 27, No. 10, Oct. 1970, pp. 1122–1137.

19 Eagelson, P. S., *Dynamic Hydrology,* McGraw-Hill, New York, 1970.

20 Bergstrom, R. W., Jr., and Viskanta, R., "Prediction of the Solar Radiant Heat Flux and Heating Rates in a Polluted Atmosphere," *Tellus,* Vol. 25, No. 5, 1973, pp. 486–498.

21 Bergstrom, R. W., Jr., "Predictions of the Spectral Absorption and Extinction Coefficients of an Urban Air Pollution Model," *Atmospheric Environment,* Vol. 6, No. 4, Apr. 1972, pp. 247–258.

22 Oke, T. K., *A Review of Urban Meteorology: 1963–1972,* Department of Geography, The University of British Columbia, Vancouver, 1973.

23 Blackadaar, A. K., "The Vertical Distribution of Wind and Turbulent Exchange in a Neutral Atmosphere," *Journal of Geophysical Research,* Vol. 67, 1962, pp. 3095–3102.

24 O'Brien, J. J., "A Note on the Vertical Structure of the Eddy Exchange Coefficient in the Planetary Boundary Layer," *Journal of the Atmospheric Sciences,* Vol. 27, No. 11, Nov. 1970, pp. 1213–1215.

25 Roache, P. J., *Computational Fluid Dynamics,* Hermosa Publishers, Albuquerque, N. M., 1972.

26 Johnson, R. O., "The Development of an Unsteady Two-Dimensional Transport Model in a Polluted Urban Atmosphere," MS thesis, Purdue University, West Lafayette, Ind., 1975.

27 Lettau, H. H., and Davidson, B., eds., *Exploring the Atmosphere's First Mile,* Vol. 1 and 2, Pergamon Press, New York, 1957.

28 Oke, T. K., "City Size and Urban Heat Island," *Atmospheric Environment,* Vol. 7, No. 8, Aug. 1973, pp. 769–779.

29 Clarke, J. F., and McElroy, J. L., "Effects of Ambient Meteorology and Urban Meteorological Features on the Vertical Temperature Over Cities," Air Pollution Control Association Annual Meeting Paper No. 74–73, Denver, Colo.

30 DeMarrais, G. A., "Nocturnal Heat Island Intensities and Relevance to Forecasts of Mixing Heights," *Monthly Weather Review,* Vol. 104, No. 3, Mar. 1975, pp. 235–245.

journal of
heat
transfer

technical notes

This section consists of contributions of 1500 words or equivalent. In computing equivalence, a typical one-column figure or table is equal to 250 words. A one-line equation is equal to 30 words. The use of a built-up fraction or an integral sign or summation sign in a sentence will require additional space equal to 10 words. Technical notes will be reviewed and approved by the specific division's reviewing committee prior to publication. After approval such contributions will be published as soon as possible, normally in the next issue of the journal.

An Analysis of Free Convective Heat Transfer With Density Inversion of Water Between Two Horizontal Concentric Cylinders

N. Seki,[1] S. Fukusako,[2] and M. Nakaoka[3]

Nomenclature

$C_p{}^*$ = dimensionless specific heat of fluid, C_p/C_{pi}
d = cylinder diameter
Gr = Grashof number, $gr^3/\nu_i{}^2$
L = gap width, $(d_0 - d_i)/2$
$\mathrm{Nu}_{\mathrm{loc}}$ = local Nusselt number, $qL/(\Delta T\lambda)$
Nu = average Nusselt number, $Q_tL/(\pi d_i\lambda_i\Delta T)$
Pr = Prandtl number, $\mu C_p/\lambda$
q = local heat flux
Q_t = total heat transfer rate per unit length
r = radial-direction coordinate
R = dimensionless radial-direction coordinate, r/r_i
T = temperature
ΔT = temperature difference, $T_0 - T_i (= T_0)$
V = dimensionless velocity, $v\{r_i/(\nu_i\sqrt{\mathrm{Gr}})\}$
β = coefficient of thermal expansion (absolute value)
Θ = dimensionless temperature, $(T - T_i)/(T_0 - T_i)$
μ^* = dimensionless viscosity, μ/μ_i
ν^* = dimensionless kinematic viscosity, ν/ν_i
ρ^* = dimensionless density, ρ/ρ_i
ϕ = angle
Ψ = dimensionless stream function, $\psi/(\nu_i\sqrt{\mathrm{Gr}})$
Ω = dimensionless vorticity, $\omega\{r_i{}^2/(\nu_i\sqrt{\mathrm{Gr}})\}$
λ^* = dimensionless thermal conductivity, λ/λ_i

Subscripts

i = inner cylinder
0 = outer cylinder
r = r-direction
ϕ = ϕ-direction

Introduction

Free convective heat transfer between horizontal concentric cylinders has been extensively investigated both experimentally and analytically [1–3].[4] It must be noted, however, that little attention has been devoted to the related problem of free convective heat transfer involving density inversion. An experimental study of free convective heat transfer with density inversion of water for the title system was recently carried out by the authors [4]. Observation of the flow patterns and determination of the heat transfer were performed under the condition that the temperature of inner cylinder was maintained at 0°C, while the temperature of outer cylinder was varied from 1 to 15°C. It was concluded that the flow patterns of water in the annular gap were significantly altered by density inversion and that the average Nusselt number was a peculiar function of the temperature difference between inner and outer cylinder surface temperatures.

The purpose of this technical note is to report the results of an analytical study of the free convective heat transfer of water in the presence of density inversion for the system described in [4] and to compare them with the previous experimental results.

Analysis

The basic geometrical configuration considered is that of a cylindrical fluid enclosed between two horizontal concentric cylinders. It is assumed that the temperature of each cylinder is uniform, the inner cylinder being colder and at 0°C. One uses cylindrical coordinates, the angular coordinate ϕ being measured clockwise from the uppermost point of the cylinders. It is also assumed that the flow is symmetric with respect to the vertical plane through the axis of the cylinders. Accordingly, attention is confined to the range $0 \leq \phi \leq \pi$.

The governing equations consist of the conservation laws of mass, momentum, and energy for the plane, cylindrical laminar flow. The analytical studies by Watson [5] and Seki, et al. [6] on free convective heat transfer under the influence of density inversion in a rectangular vessel suggested that the effect of physical property variation such as viscosity or thermal conductivity on flow field and convection heat

---

[1] Professor, Department of Mechanical Engineering, Hokkaido University, Sapporo, Japan.

[2] Assist. Professor, Department of Mechanical Engineering, Hokkaido University, Sapporo, Japan.

[3] Graduate Student, Department of Mechanical Engineering, Hokkaido University, Sapporo, Japan.

Contributed by the Heat Transfer Division of THE AMERICAN SOCIETY OF MECHANICAL ENGINEERS. Manuscript received by the Heat Transfer Division March 23, 1976.

[4] Numbers in brackets designate References at end of technical note.

Table 1 The functions *a, b, c,* and *d* of equation (4)

Ξ	a	b	c	d
Ω	1	μ^*	$1/\sqrt{Gr}$	$-\{[R(\partial\rho^*/\partial R)\sin\phi + (\partial\rho^*/\partial\phi)\cos\phi] + RES^+\}$
Ψ	0	$1/\rho^*$	1	$-R\Omega$
Θ	$Pr_i C_p^*$	λ^*	$1/\sqrt{Gr}$	0

$^+$ RES denotes terms associated with higher order derivatives of ρ and μ with respect to R or ϕ.

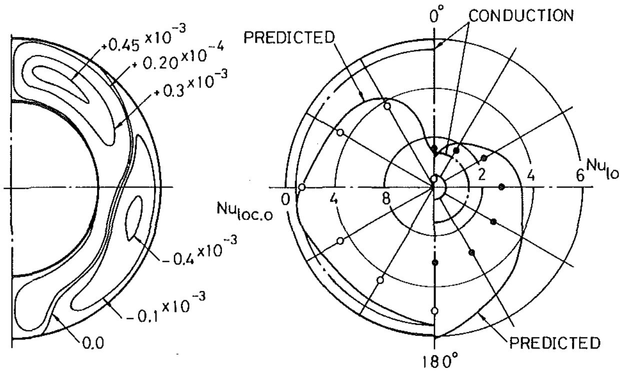

Fig. 1 Streamline pattern and local Nusselt number, d_0 = 121.5 mm, d_i = 69.6 mm, and T_0 = 6°C

transfer could not be neglected. All fluid properties, therefore, are considered to be dependent on temperature, each approximated as a function of temperature by a polynomial of the 4th or the 5th degree. For example, the density-temperature relationship is approximated by the following form [8].

$$\rho^* = 1/(1 + a'T + b'T^2 + c'T^3 + d'T^4)$$

where

$$a' = -0.678964520 \times 10^{-4}(1/°\text{C}),$$
$$b' = 0.907294338 \times 10^{-5}(1/°\text{C})^2,$$
$$c' = -0.964568125 \times 10^{-7}(1/°\text{C})^3$$
$$\text{and} \quad d' = 0.873702983 \times 10^{-9}(1/°\text{C})^4$$

As usual, the vorticity component ω is introduced according to:

$$\omega = (1/r)\partial(rv_\phi)/\partial r - (1/r)\partial v_r/\partial\phi \tag{2}$$

where v_r and v_ϕ can be eliminated via the stream function ψ:

$$v_r = (\rho_i/\rho)(1/r)\partial\psi/\partial\phi, \quad v_\phi = -(\rho_i/\rho)\partial\psi/\partial r \tag{3}$$

Then, a common representation of the governing equations in terms of the dimensionless quantities introduced in the Nomenclature can be devised. After various rearrangement and utilizing equations (2) and (3) we obtain

$$a\left[\frac{\partial}{\partial R}\left(\Xi\frac{\partial\Psi}{\partial\phi}\right) - \frac{\partial}{\partial\phi}\left(\Xi\frac{\partial\Psi}{\partial R}\right)\right] - c\frac{\partial}{\partial R}\left(bR\frac{\partial\Xi}{\partial R}\right) - c\frac{\partial}{\partial\phi}\left(b\frac{1}{R}\frac{\partial\Xi}{\partial\phi}\right) + d = 0 \tag{4}$$

where Ξ is a general dependent variable representing either Ω, Ψ, or Θ. The functions a–d are listed in Table 1. The derivation of the finite-difference form of equation (4) is described in great detail in [7]. One divides the flow field into a number of rectangular grids with spacing k and ℓ, respectively in the r- and ϕ-directions. Let the numbers of the grids in the r- and ϕ-directions be M and N. Then, $k = (R_0 - R_i)/M$ and $\ell = \pi/N$. In the present analysis the mesh size of $M = 25$, $N = 36$ was employed. The boundary conditions are based on the vanishing of velocity and the uniformity of temperature on the solid surfaces and the assumption that flow is symmetric with respect to the vertical plane through the axis of the cylinders. The iterative procedure used to solve equation (4) is repeated until the following condition is satisfied:

$$\max\{|\Xi_{i,j}^{(m)} - \Xi_{k,\ell}^{(m-1)}|/|\Xi_{i,j}^{(m-1)}|\} \leq 5 \times 10^{-4}(i = 1, 2, \ldots, M, j = 1, 2, \ldots, N) \tag{5}$$

where the superscripts (m) and $(m - 1)$ indicate the values at the (m)th and $(m - 1)$th iterations, respectively, and max{ } denotes the maximum of the entity in { }.

Results and Discussions

A typical pattern of calculated streamline and a corresponding local Nusselt number on inner and outer cylinder for T_0 = 6°C are shown in Fig. 1 along with the experimental data reported earlier in [4]. The similarity of the streamline patterns shown in Fig. 1 with those of Fig. 4 of [4] is evident. They indicate the existence of two counter eddies of almost equal size, which are believed to be due to the effect of density inversion of water at 4°C. It can also be seen that there are discrepancies between the analytical heat transfer results and the experimental data, especially over the surface of inner cylinder. It should be noted that the local heat flux for the outer cylinder is evaluated from electric input to each main heater which consists of twelve independently controllable heaters with individual guard heaters, while the local heat flux for the inner cylinder is obtained from measured temperature gradient adjacent to the surface.

Further comparison with experiments is afforded by the average Nusselt number. The calculated average Nusselt number for d_0/d_i = 3.44 is shown in Fig. 2 along with the experimental results of [4]. It is seen that both the analytically and experimentally determined Nusselt numbers do not increase monotonously with increasing ΔT

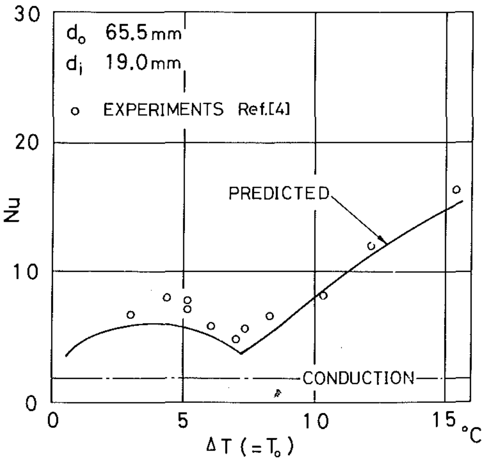

Fig. 2 Average Nusselt number, d_0/d_i = 3.44

as is the case when density inversion is absent. The appearance of such a sharp minimum of the calculated average Nusselt number seems to have a relation with the coexistence of two counter standing eddies of approximately the same size and the same strength, followed by the abrupt change of the streamlines and the isotherms through critical ΔT. Generally speaking, qualitative trends of the present prediction are in good agreement with the experimental data, even though the analytical results are underpredicted by about 10 percent. The disagreement may be due to the inadequacy of boundary conditions used in the analytical model. However, it is reasonable to conclude that the complex flow patterns and the heat transfer characteristics obtained earlier by the authors and reported in [4] can indeed be predicted by analysis with good success.

References

1 Powe, R. E., Carley, C. T., and Bishop, E. H., "Free Convective Flow Patterns in Cylindrical Annuli," JOURNAL OF HEAT TRANSFER, TRANS. ASME, Series C, Vol. 91, 1969, pp. 310–314.

2 Itoh, M., Fujita, T., Nishiwaki, N., and Hirata, M., "A New Method Correlating Heat-Transfer Coefficients for Natural Convection in Horizontal Cylindrical Annuli," *International Journal of Heat and Mass Transfer,* Vol. 13, 1970, pp. 1364–1368.

3 Mack, L. R., and Bishop, E. H., "Natural Convection Between Horizontal Concentric Cylinder for Low Rayleigh Numbers," *Quarterly Journal of Mechanics and Applied Mathematics,* Vol. 11, Part 2, 1968, pp. 223–241.

4 Seki, N., Fukusako, S., and Nakaoka, M., "Experimental Study on Natural Convection Heat Transfer With Density Inversion of Water Between Two Horizontal Concentric Cylinders," JOURNAL OF HEAT TRANSFER, TRANS. ASME, Series C, Vol. 97, 1975, pp. 556–561.

5 Watson, A., "Effect of the Inversion Temperature on the Convection of Water in an Enclosed Rectangular Cavity," *Quarterly Journal of Mechanics and Applied Mathematics,* Vol. 15, 1972, pp. 423–446.

6 Seki, N., Fukusako, S., and Sugawara, M., "Natural Convection Heat Transfer With Density Inversion of Water by Vertical Opposite Walls in a Closed Rectangular Vessel," *Preprint of JSME-Meeting of Heat Engineering,* Paper No. 740-17. 1974, pp. 87–90.

7 Gosman, A. D., Pun, W. M., Runchal, A. K., Spalding, D. B., and Wolfshtein, M., *Heat and Mass Transfer in Recirculating Flows,* Academic Press, London and New York, 1969.

8 Fujii, T., and Fujii, M., "On Grashof Number in Natural Convection of Water With Density Inversion," *Preprint of 11th Japan Heat Transfer Symposium,* C 101, pp. 369–372.

Experimental Study of Free Convective Heat Transfer From Inclined Cylinders

P. H. Oosthuizen[1]

Nomenclature

A = constant in horizontal cylinder equation
B = constant in vertical cylinder equation
D = cylinder diameter
G_D = Grashof number based on D
G_ℓ = Grashof number based on ℓ
h = heat transfer coefficient
k = conductivity of model material
ℓ = heated length of cylinder
$\ell^* = \ell/(D \tan \phi)$
N_D = Nusselt number based on D
N_{DH} = value of N_D given by horizontal cylinder equation
N_{DV} = value of N_D given by vertical cylinder equation
N_ℓ = Nusselt number based on ℓ
n = index in equation (7)
Pr = Prandtl number
ϕ = angle of cylinder to horizontal

Table 1

Model Number	Diameter, D mm	Heated Length, ℓ mm	$\frac{\ell}{D}$
1	25.4	203.2	8.00
2	19.1	203.2	10.67
3	19.1	152.4	8.00
4	19.1	304.8	16.00

Introduction

The present study is concerned with the experimental determination of mean heat transfer rates by free convection from circular cylinders, inclined at an angle ϕ to the horizontal, to air, the situation considered being shown diagrammatically in Fig. 1. In this situation there are, of course, in general, components of the buoyancy force both normal to, and parallel to, the axis of the cylinder. For this reason, the flow over the cylinder will, in general, be three-dimensional.

A number of studies of free convection from horizontal cylinders, i.e., where $\phi = 0$ deg, and from vertical cylinders, i.e., where $\phi = 90$ deg, are available, the flow over the cylinder in these two limiting situations being, of course, two-dimensional. Correlation equations for the heat transfer rate in these two situations are well-established, e.g., see reference [1].[2] Little attention appears, however, to have been given to the case where the cylinder is inclined at an arbitrary angle to the horizontal, the numerical study described in reference [2] appearing to be the most relevant to the present study.

Experimental Procedure

Four cylindrical models were used in the present study, their main dimensions being listed in Table 1. All of these cylinders were made of solid aluminum with nylon insulating pieces of the same diameter as the model attached to each end as indicated in Fig. 1, these bringing the overall length of all the assembled models to approximately 0.42 m. A series of five small-diameter holes were drilled longitudinally to various depths into each model. Thermocouples were inserted into these holes, allowing the model temperature to be measured at various axial locations. The depth of the holes was such that the thermocouples were approximately equally spaced along the length of the model. The models could be mounted, in turn, in a pivoted frame which allowed them to be set at various angles to the horizontal. This frame was placed in a large chamber vented to the atmosphere.

Heat transfer rates from the models were determined by measuring the rates at which they cooled after being uniformly heated. Each model, in turn, was mounted in the frame and was then set at the desired angle. The model was then heated to a temperature of about 110°C. After allowing a period for equilibrium conditions to be reached, the temperatures at the various thermocouple positions were sequentially recorded at 1-s intervals during the period in which the mean model temperature dropped from approximately 100–90°C. The time that this cooling took depended, of course, on the size of the model being tested, typically being of the order of 300 s. Consideration of the orders of magnitude of the terms in the governing equations, therefore, indicates that the time-dependent terms in these equations are negligible compared to the other terms and the measured heat transfer rates will, consequently, effectively be equal to those applicable to steady-state heat transfer under the same conditions.

---

[1] Professor, Department of Mechanical Engineering, Queen's University, Kingston, Ontario, Canada.

Contributed by the Heat Transfer Division of THE AMERICAN SOCIETY OF MECHANICAL ENGINEERS. Manuscript received by the Heat Transfer Division June 9, 1976.

[2] Numbers in brackets designate References at end of technical note.

as is the case when density inversion is absent. The appearance of such a sharp minimum of the calculated average Nusselt number seems to have a relation with the coexistence of two counter standing eddies of approximately the same size and the same strength, followed by the abrupt change of the streamlines and the isotherms through critical ΔT. Generally speaking, qualitative trends of the present prediction are in good agreement with the experimental data, even though the analytical results are underpredicted by about 10 percent. The disagreement may be due to the inadequacy of boundary conditions used in the analytical model. However, it is reasonable to conclude that the complex flow patterns and the heat transfer characteristics obtained earlier by the authors and reported in [4] can indeed be predicted by analysis with good success.

References

1 Powe, R. E., Carley, C. T., and Bishop, E. H., "Free Convective Flow Patterns in Cylindrical Annuli," JOURNAL OF HEAT TRANSFER, TRANS. ASME, Series C, Vol. 91, 1969, pp. 310–314.

2 Itoh, M., Fujita, T., Nishiwaki, N., and Hirata, M., "A New Method Correlating Heat-Transfer Coefficients for Natural Convection in Horizontal Cylindrical Annuli," *International Journal of Heat and Mass Transfer*, Vol. 13, 1970, pp. 1364–1368.

3 Mack, L. R., and Bishop, E. H., "Natural Convection Between Horizontal Concentric Cylinder for Low Rayleigh Numbers," *Quarterly Journal of Mechanics and Applied Mathematics*, Vol. 11, Part 2, 1968, pp. 223–241.

4 Seki, N., Fukusako, S., and Nakaoka, M., "Experimental Study on Natural Convection Heat Transfer With Density Inversion of Water Between Two Horizontal Concentric Cylinders," JOURNAL OF HEAT TRANSFER, TRANS. ASME, Series C, Vol. 97, 1975, pp. 556–561.

5 Watson, A., "Effect of the Inversion Temperature on the Convection of Water in an Enclosed Rectangular Cavity," *Quarterly Journal of Mechanics and Applied Mathematics*, Vol. 15, 1972, pp. 423–446.

6 Seki, N., Fukusako, S., and Sugawara, M., "Natural Convection Heat Transfer With Density Inversion of Water by Vertical Opposite Walls in a Closed Rectangular Vessel," *Preprint of JSME-Meeting of Heat Engineering*, Paper No. 740-17. 1974, pp. 87–90.

7 Gosman, A. D., Pun, W. M., Runchal, A. K., Spalding, D. B., and Wolfshtein, M., *Heat and Mass Transfer in Recirculating Flows*, Academic Press, London and New York, 1969.

8 Fujii, T., and Fujii, M., "On Grashof Number in Natural Convection of Water With Density Inversion," *Preprint of 11th Japan Heat Transfer Symposium*, C 101, pp. 369–372.

Experimental Study of Free Convective Heat Transfer From Inclined Cylinders

P. H. Oosthuizen[1]

Nomenclature

A = constant in horizontal cylinder equation
B = constant in vertical cylinder equation
D = cylinder diameter
G_D = Grashof number based on D
G_ℓ = Grashof number based on ℓ
h = heat transfer coefficient
k = conductivity of model material
ℓ = heated length of cylinder
$\ell^* = \ell/(D \tan \phi)$
N_D = Nusselt number based on D
N_{DH} = value of N_D given by horizontal cylinder equation
N_{DV} = value of N_D given by vertical cylinder equation
N_ℓ = Nusselt number based on ℓ
n = index in equation (7)
Pr = Prandtl number
ϕ = angle of cylinder to horizontal

Table 1

Model Number	Diameter, D mm	Heated Length, ℓ mm	$\frac{\ell}{D}$
1	25.4	203.2	8.00
2	19.1	203.2	10.67
3	19.1	152.4	8.00
4	19.1	304.8	16.00

Introduction

The present study is concerned with the experimental determination of mean heat transfer rates by free convection from circular cylinders, inclined at an angle ϕ to the horizontal, to air, the situation considered being shown diagrammatically in Fig. 1. In this situation there are, of course, in general, components of the buoyancy force both normal to, and parallel to, the axis of the cylinder. For this reason, the flow over the cylinder will, in general, be three-dimensional.

A number of studies of free convection from horizontal cylinders, i.e., where $\phi = 0$ deg, and from vertical cylinders, i.e., where $\phi = 90$ deg, are available, the flow over the cylinder in these two limiting situations being, of course, two-dimensional. Correlation equations for the heat transfer rate in these two situations are well-established, e.g., see reference [1].[2] Little attention appears, however, to have been given to the case where the cylinder is inclined at an arbitrary angle to the horizontal, the numerical study described in reference [2] appearing to be the most relevant to the present study.

Experimental Procedure

Four cylindrical models were used in the present study, their main dimensions being listed in Table 1. All of these cylinders were made of solid aluminum with nylon insulating pieces of the same diameter as the model attached to each end as indicated in Fig. 1, these bringing the overall length of all the assembled models to approximately 0.42 m. A series of five small-diameter holes were drilled longitudinally to various depths into each model. Thermocouples were inserted into these holes, allowing the model temperature to be measured at various axial locations. The depth of the holes was such that the thermocouples were approximately equally spaced along the length of the model. The models could be mounted, in turn, in a pivoted frame which allowed them to be set at various angles to the horizontal. This frame was placed in a large chamber vented to the atmosphere.

Heat transfer rates from the models were determined by measuring the rates at which they cooled after being uniformly heated. Each model, in turn, was mounted in the frame and was then set at the desired angle. The model was then heated to a temperature of about 110°C. After allowing a period for equilibrium conditions to be reached, the temperatures at the various thermocouple positions were sequentially recorded at 1-s intervals during the period in which the mean model temperature dropped from approximately 100–90°C. The time that this cooling took depended, of course, on the size of the model being tested, typically being of the order of 300 s. Consideration of the orders of magnitude of the terms in the governing equations, therefore, indicates that the time-dependent terms in these equations are negligible compared to the other terms and the measured heat transfer rates will, consequently, effectively be equal to those applicable to steady-state heat transfer under the same conditions.

---

[1] Professor, Department of Mechanical Engineering, Queen's University, Kingston, Ontario, Canada.

Contributed by the Heat Transfer Division of THE AMERICAN SOCIETY OF MECHANICAL ENGINEERS. Manuscript received by the Heat Transfer Division June 9, 1976.

[2] Numbers in brackets designate References at end of technical note.

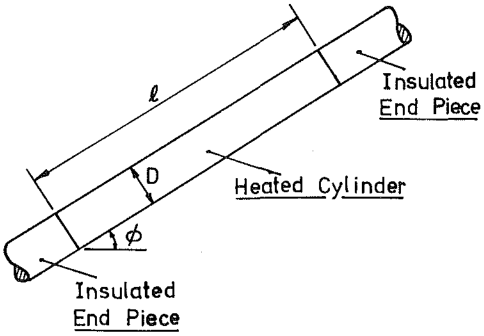

Fig. 1 Situation being considered

Although the temperature remained effectively uniform across all sections of the model due to the small Biot numbers involved in the process (hD/k was less than 0.001 in all cases), small variations existed in the axial direction along the models when they were tested in the near vertical positions, the overall temperature variation at a given instant of time being of the order of 2°C at most. Sufficient temperature readings were, however, taken to allow the mean model temperature at a given time to be determined. Experience with similar models used in the study of heat transfer from vertical cylinders has indicated that the number of thermocouples used was adequate to define the mean model temperature. The mean heat transfer rate was then determined in the usual way from the measured variation of mean temperature with time, it being assumed that the heat transfer coefficient was constant over the relatively narrow temperature range over which measurements were made and that the heat transfer between the model and the nylon end pieces was negligible. A correction for radiant heat transfer was applied, this amounting to about 5 percent of the total heat transfer. Conduction heat transfer between the model and the insulating end pieces, of course, takes place during the cooling process. Attempts have been made to deduce the effect of this on the results, but this is rendered difficult by the unsteady nature of the problem and the unknown initial conditions in the end pieces. However, all attempted analyses have indicated that the effect will be small and will probably cause an error of less than 1 percent in the predicted value of h.

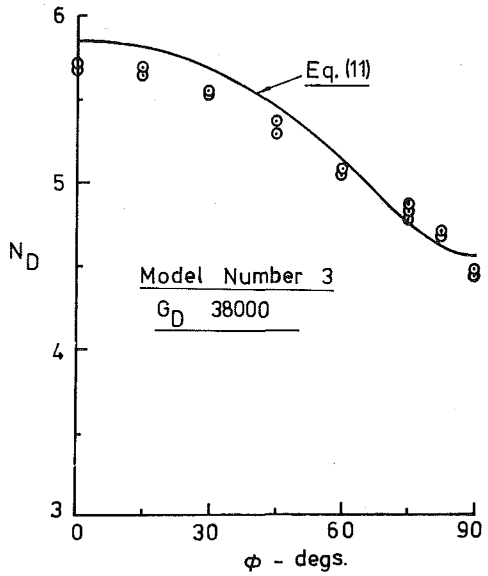

Fig. 2 Typical variation of heat transfer rate with angle of inclination

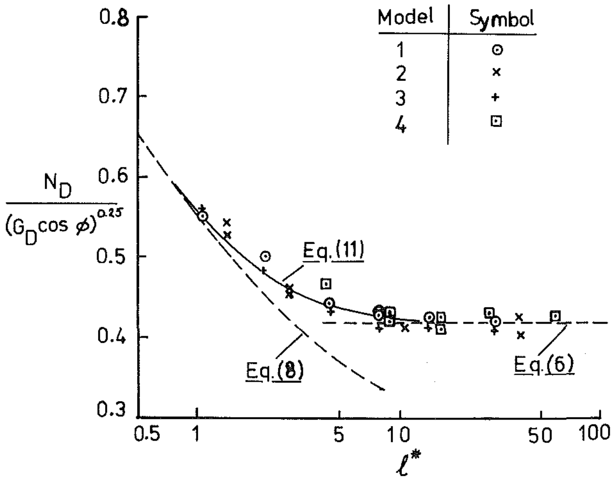

Fig. 3 Correlated results for all models

Tests were carried out, in the manner described previously, with each of the four models at angles ϕ of 0, 15, 30, 45, 60, 75, 82.5, and 90 deg to the horizontal.

Results and Discussion

The results will, of course, be presented in terms of Nusselt and Grashof numbers. The fluid properties in these numbers were evaluated at the average of the mean model temperature during the test (approximately 95°C) and the ambient temperature. A typical variation of Nusselt number with angle is shown in Fig. 2.

Now, for the range of Grashof numbers covered by the present tests, (G_D was approximately 90,000 for model 1 and 40,000 for the other models), previous studies have indicated that for $\phi = 0$ deg, the heat transfer rate is given by an equation of the form

$$N_D/G_D{}^{0.25} = A(\mathrm{Pr}) \tag{1}$$

Since the Prandtl number remained essentially constant in the present tests, A is constant, the average value obtained from the tests with all models being 0.42. This value is within the scatter of data obtained in previous experimental studies.

Further, for the range of Grashof numbers covered by the tests, (G_ℓ lies approximately in the range 2×10^7–2×10^8) previous studies have indicated that for $\phi = 90$ deg, the heat transfer rate is given by an equation of the form

$$N_D/G_\ell{}^{0.25} = B(\mathrm{Pr}) \tag{2}$$

The present tests give B as 0.55 which is also within the scatter of available data for this Grashof number range.

For an arbitrary angle of inclination ϕ, [2] indicates that, provided the boundary layer equations apply, which will be the case for the Grashof number range covered by the present tests, then for a given Prandtl number

$$\begin{aligned} N_D/(G_D \cos \phi)^{0.25} &= \text{function } (\ell/D \tan \phi) \\ &= \text{function } (\ell^*) \end{aligned} \tag{3}$$

This result is obtained by rewriting the boundary layer equations in terms of suitable dimensionless variables.

The results for all of the models are plotted in terms of the variable given in this equation in Fig. 3, from which it will be seen that relatively good correlation is obtained, the results for all models agreeing to within approximately 10 percent when plotted in this way. For large values of ℓ^*, the component of buoyancy force parallel to the axis of the cylinder will have a negligible effect on the flow, which is then effectively two-dimensional, and, therefore, in view of equation (1), the following will apply.

$$N_D/(G_D \cos \phi)^{0.25} = 0.42 \tag{4}$$

Similarly, for small values of ℓ^* the component of buoyancy force normal to the axis will have a negligible effect on the flow which is then, again, effectively two-dimensional and in this case, therefore, in view of equation (2), the following will apply

$$N_\ell/(G_\ell \sin \phi)^{0.25} = 0.55 \tag{5}$$

This can be rearranged to give

$$N_D/(G_D \cos \phi)^{0.25} = 0.55/\ell^{*0.25} \tag{6}$$

The variations given by equations (4) and (6) are shown in Fig. 3. It will be seen that for ℓ^* greater than about 10, equation (4) applies while for ℓ^* less than about 1, equation (6) applies. Thus, it is only between ℓ^* of about 1 and 10 that three-dimensional effects are important. In this intermediate three-dimensional region, the heat transfer rate is higher than that given by either of the two-dimensional flow equations, i.e., equations (4) and (6).

In the intermediate range it will be assumed that the variation of N_D can be approximately represented by an equation of the form

$$N_D{}^n = N_{DH}{}^n + N_{DV}{}^n \tag{7}$$

where N_{DH} and N_{DV} are given by equations (4) and (6), respectively. Using these two equations, equation (7) can be rearranged to give

$$N_D/(G_D \cos \phi)^{0.25} = 0.42[1 + (1.31/\ell^{*0.25})^n]^{1/n} \tag{8}$$

It will be seen from Fig. 3 that an equation of this form does correlate the results relatively well when n is set equal to 8. With this value of n, equation (8) becomes

$$N_D/(G_D \cos \phi)^{0.25} = 0.42[1 + (1.31/\ell^{*0.25})^8]^{0.125} \tag{9}$$

This equation will, of course, only apply in the Grashof number range in which equations (1) and (2) apply, i.e., Grashof numbers approximately between 10^4 and 10^9.

Conclusions

The results indicate that free convective heat transfer rates from inclined cylinders, for the Grashof number range considered, can be correlated in terms of the variables given in equation (3). The results indicate that for ℓ^* greater than about 10, the flow over the cylinder is essentially the same as that over a horizontal cylinder while for ℓ^* less than about 1, the flow is essentially the same as that over a vertical cylinder, the appropriate buoyancy force component being used in both cases and, in both cases, the flow being essentially two-dimensional. In the intermediate region between ℓ^* of 1 and 10, in which the flow will be three-dimensional, the heat transfer rate is reasonably well correlated using the empirical equation given in equation (9).

Acknowledgments

This work was supported by the National Research Council of Canada.

References

1 Kreith, F., *Principles of Heat Transfer*, third ed., Intext, New York, 1973, pp. 392–393.

2 Oosthuizen, P. H., "Numerical Study of Some Three-Dimensional Laminar Free Convective Flows," ASME Paper No. 76-HT-34.

Flow and Heat Transfer Over a Flat Plate With Uniformly Distributed, Vectored Surface Mass Transfer

T. S. Chen[1] and E. M. Sparrow[2]

Introduction

The study of forced convection over a heated surface with mass injection and suction at the surface finds many important applications in engineering, such as film cooling of rocket engines and boundary layer control of aerodynamic bodies. Almost all of the analytical work to date deals with mass transfer that is normal to the surface. In practice, however, the surface mass transfer may include a streamwise velocity component u_w as well as a normal component v_w. This constitutes "vectored" surface mass transfer. In an extensive analytical study, Inger and Swean [1][3] investigated the effect of vectored mass transfer on laminar flow and heat transfer over a flat plate under conditions where similarity solutions exist, i.e., $v_w \sim x^{-1/2}$ and u_w = constant. From the practical point of view, however, vectored blowing or suction with uniform v_w may be more easily realized than with $v_w \sim x^{-1/2}$. The present study was undertaken to provide flow and heat transfer results corresponding to vectored surface mass transfer where both v_w and u_w are uniform along the surface.

Analysis

Consider a flat plate aligned parallel to a uniform free stream having velocity u_∞ and temperature T_∞. The plate is maintained at a uniform temperature T_w, and there is a surface mass transfer characterized by velocity components u_w and v_w, both of which are spatially uniform. The governing equations for mass, momentum, and energy conservation are the steady, two-dimensional, laminar boundary layer equations for a constant-property fluid. Similarity solutions are precluded because v_w is a constant.

As the first step in the analysis, one introduces the new dimensionless coordinates

$$\xi = (v_w/u_\infty)(2u_\infty x/\nu)^{1/2}, \qquad \eta = y(u_\infty/2\nu x)^{1/2} \tag{1}$$

along with a reduced stream function $f(\xi, \eta)$ and a dimensionless temperature $\theta(\xi, \eta)$

$$f(\xi, \eta) = \psi(x, y)/(2\nu u_\infty x)^{1/2}, \qquad \theta(\xi, \eta) = (T - T_\infty)/(T_w - T_\infty) \tag{2}$$

In terms of f and θ, the x-momentum and energy equations along with their boundary conditions assume the form

$$f''' + ff'' = \xi(f'\partial f'/\partial\xi - f''\partial f/\partial\xi) \tag{3}$$

$$f'(\xi, 0) = u_w/u_\infty, \qquad f(\xi, 0) + \xi\partial f(\xi, 0)/\partial\xi = -\xi, \qquad f'(\xi, \infty) = 1 \tag{4}$$

$$\frac{1}{\mathrm{Pr}}\theta'' + f\theta' = \xi(f'\partial\theta/\partial\xi - \theta'\partial f/\partial\xi) \tag{5}$$

$$\theta(\xi, 0) = 1, \qquad \theta(\xi, \infty) = 0 \tag{6}$$

In the foregoing equations, the primes stand for partial differentiation with respect to η.

To cope with the fact that equations (3)–(6) do not admit a similarity solution, the local nonsimilarity method was employed. The procedures for generating and solving local nonsimilarity equations at various levels of truncation are well-documented elsewhere (see, for example, [2–3]) and, to conserve space, will not be repeated here. For the present problem, solutions were obtained at the third level

---

[1] Department of Mechanical and Aerospace Engineering, University of Missouri-Rolla, Rolla, Mo.

[2] Department of Mechanical Engineering, University of Minnesota, Minneapolis, Minn.

[3] Numbers in brackets designate References at end of technical note.

Contributed by the Heat Transfer Division of THE AMERICAN SOCIETY OF MECHANICAL ENGINEERS. Manuscript received by the Heat Transfer Division May 13, 1976.

$$N_D/(G_D \cos \phi)^{0.25} = 0.42 \qquad (4)$$

Similarly, for small values of ℓ^* the component of buoyancy force normal to the axis will have a negligible effect on the flow which is then, again, effectively two-dimensional and in this case, therefore, in view of equation (2), the following will apply

$$N_\ell/(G_\ell \sin \phi)^{0.25} = 0.55 \qquad (5)$$

This can be rearranged to give

$$N_D/(G_D \cos \phi)^{0.25} = 0.55/\ell^{*0.25} \qquad (6)$$

The variations given by equations (4) and (6) are shown in Fig. 3. It will be seen that for ℓ^* greater than about 10, equation (4) applies while for ℓ^* less than about 1, equation (6) applies. Thus, it is only between ℓ^* of about 1 and 10 that three-dimensional effects are important. In this intermediate three-dimensional region, the heat transfer rate is higher than that given by either of the two-dimensional flow equations, i.e., equations (4) and (6).

In the intermediate range it will be assumed that the variation of N_D can be approximately represented by an equation of the form

$$N_D{}^n = N_{DH}{}^n + N_{DV}{}^n \qquad (7)$$

where N_{DH} and N_{DV} are given by equations (4) and (6), respectively. Using these two equations, equation (7) can be rearranged to give

$$N_D/(G_D \cos \phi)^{0.25} = 0.42[1 + (1.31/\ell^{*0.25})^n]^{1/n} \qquad (8)$$

It will be seen from Fig. 3 that an equation of this form does correlate the results relatively well when n is set equal to 8. With this value of n, equation (8) becomes

$$N_D/(G_D \cos \phi)^{0.25} = 0.42[1 + (1.31/\ell^{*0.25})^8]^{0.125} \qquad (9)$$

This equation will, of course, only apply in the Grashof number range in which equations (1) and (2) apply, i.e., Grashof numbers approximately between 10^4 and 10^9.

Conclusions

The results indicate that free convective heat transfer rates from inclined cylinders, for the Grashof number range considered, can be correlated in terms of the variables given in equation (3). The results indicate that for ℓ^* greater than about 10, the flow over the cylinder is essentially the same as that over a horizontal cylinder while for ℓ^* less than about 1, the flow is essentially the same as that over a vertical cylinder, the appropriate buoyancy force component being used in both cases and, in both cases, the flow being essentially two-dimensional. In the intermediate region between ℓ^* of 1 and 10, in which the flow will be three-dimensional, the heat transfer rate is reasonably well correlated using the empirical equation given in equation (9).

Acknowledgments

This work was supported by the National Research Council of Canada.

References

1 Kreith, F., *Principles of Heat Transfer*, third ed., Intext, New York, 1973, pp. 392–393.

2 Oosthuizen, P. H., "Numerical Study of Some Three-Dimensional Laminar Free Convective Flows," ASME Paper No. 76-HT-34.

Flow and Heat Transfer Over a Flat Plate With Uniformly Distributed, Vectored Surface Mass Transfer

T. S. Chen[1] and E. M. Sparrow[2]

Introduction

The study of forced convection over a heated surface with mass injection and suction at the surface finds many important applications in engineering, such as film cooling of rocket engines and boundary layer control of aerodynamic bodies. Almost all of the analytical work to date deals with mass transfer that is normal to the surface. In practice, however, the surface mass transfer may include a streamwise velocity component u_w as well as a normal component v_w. This constitutes "vectored" surface mass transfer. In an extensive analytical study, Inger and Swean [1][3] investigated the effect of vectored mass transfer on laminar flow and heat transfer over a flat plate under conditions where similarity solutions exist, i.e., $v_w \sim x^{-1/2}$ and $u_w =$ constant. From the practical point of view, however, vectored blowing or suction with uniform v_w may be more easily realized than with $v_w \sim x^{-1/2}$. The present study was undertaken to provide flow and heat transfer results corresponding to vectored surface mass transfer where both v_w and u_w are uniform along the surface.

Analysis

Consider a flat plate aligned parallel to a uniform free stream having velocity u_∞ and temperature T_∞. The plate is maintained at a uniform temperature T_w, and there is a surface mass transfer characterized by velocity components u_w and v_w, both of which are spatially uniform. The governing equations for mass, momentum, and energy conservation are the steady, two-dimensional, laminar boundary layer equations for a constant-property fluid. Similarity solutions are precluded because v_w is a constant.

As the first step in the analysis, one introduces the new dimensionless coordinates

$$\xi = (v_w/u_\infty)(2u_\infty x/\nu)^{1/2}, \qquad \eta = y(u_\infty/2\nu x)^{1/2} \qquad (1)$$

along with a reduced stream function $f(\xi, \eta)$ and a dimensionless temperature $\theta(\xi, \eta)$

$$f(\xi, \eta) = \psi(x, y)/(2\nu u_\infty x)^{1/2}, \qquad \theta(\xi, \eta) = (T - T_\infty)/(T_w - T_\infty) \qquad (2)$$

In terms of f and θ, the x-momentum and energy equations along with their boundary conditions assume the form

$$f''' + ff'' = \xi(f'\partial f'/\partial\xi - f''\partial f/\partial\xi) \qquad (3)$$

$$f'(\xi, 0) = u_w/u_\infty, \qquad f(\xi, 0) + \xi\partial f(\xi, 0)/\partial\xi = -\xi, \qquad f'(\xi, \infty) = 1 \qquad (4)$$

$$\frac{1}{\mathrm{Pr}}\theta'' + f\theta' = \xi(f'\partial\theta/\partial\xi - \theta'\partial f/\partial\xi) \qquad (5)$$

$$\theta(\xi, 0) = 1, \qquad \theta(\xi, \infty) = 0 \qquad (6)$$

In the foregoing equations, the primes stand for partial differentiation with respect to η.

To cope with the fact that equations (3)–(6) do not admit a similarity solution, the local nonsimilarity method was employed. The procedures for generating and solving local nonsimilarity equations at various levels of truncation are well-documented elsewhere (see, for example, [2–3]) and, to conserve space, will not be repeated here. For the present problem, solutions were obtained at the third level

---

[1] Department of Mechanical and Aerospace Engineering, University of Missouri-Rolla, Rolla, Mo.

[2] Department of Mechanical Engineering, University of Minnesota, Minneapolis, Minn.

[3] Numbers in brackets designate References at end of technical note.

Contributed by the Heat Transfer Division of THE AMERICAN SOCIETY OF MECHANICAL ENGINEERS. Manuscript received by the Heat Transfer Division May 13, 1976.

of truncation. If, in addition to f, auxiliary dependent variables $g = \partial f/\partial\xi$ and $h = \partial^2 f/\partial\xi^2$ are used, the governing equations for the velocity problem are

$$f''' + ff'' = \xi(f'g' - f''g)$$

$$g''' + fg'' - f'g' + 2f''g - \xi(g'g' - g''g) = \xi(f'h' - f''h)$$

$$h''' + fh'' - 2f'h' + 3f''h + 4gg'' - 2g'g' = 0 \tag{7}$$

$$f'(\xi, 0) = u_w/u_\infty, \qquad f(\xi, 0) = -\xi/2, \qquad f'(\xi, \infty) = 1$$

$$g'(\xi, 0) = 0, \qquad g(\xi, 0) = -1/2, \qquad g'(\xi, \infty) = 0$$

$$h'(\xi, 0) = 0, \qquad h(\xi, 0) = 0, \qquad h'(\xi, \infty) = 0 \tag{8}$$

For the temperature problem, with $\phi = \partial\theta/\partial\xi$ and $\chi = \partial^2\theta/\partial\xi^2$, one can derive

$$\frac{1}{\mathrm{Pr}}\theta'' + f\theta' = \xi(f'\phi - \theta'g)$$

$$\frac{1}{\mathrm{Pr}}\phi'' + f\phi' - f'\phi + 2g\theta' - \xi(g'\phi - \phi'g) = \xi(f'\chi - \theta'h)$$

$$\frac{1}{\mathrm{Pr}}\chi'' + f\chi' - 2f'\chi + 4g\phi' - 2g'\phi + 3h\theta' = 0 \tag{9}$$

$$\theta(\xi, 0) = 1, \qquad \theta(\xi, \infty) = 0, \qquad \phi(\xi, 0) = 0, \qquad \phi(\xi, \infty) = 0$$

$$\chi(\xi, 0) = 0, \qquad \chi(\xi, \infty) = 0 \tag{10}$$

The physical quantities of interest are the local friction factor C_f and local Nusselt number Nu_x defined by

$$C_f = \tau_w/(\rho u_\infty{}^2/2), \qquad \mathrm{Nu}_x = q_w x/k(T_w - T_\infty) \tag{11}$$

These can readily be related to the solution variables via the expressions

$$C_f\mathrm{Re}_x{}^{1/2} = \sqrt{2}\,f''(\xi, 0), \qquad \mathrm{Nu}_x\mathrm{Re}_x{}^{-1/2} = -\theta'(\xi, 0)/\sqrt{2} \tag{12}$$

where $\mathrm{Re}_x = u_\infty x/\nu$.

Results and Discussion

Numerical results for the wall shear and surface heat transfer were obtained for a wide range of values of the ξ parameter from -1.0 to 1.0 and values of the tangential surface velocity u_w/u_∞ covering both downstream vectoring ($u_w > 0$) and upstream vectoring ($u_w < 0$). The wall shear results $C_f\mathrm{Re}_x{}^{1/2}/\sqrt{2}$ for downstream vectoring are illustrated in Fig. 1 for $u_w/u_\infty = 0, 0.25, 0.50$, and 0.75. The corresponding surface heat transfer results $\sqrt{2}\mathrm{Nu}_x\mathrm{Re}_x{}^{-1/2}$ for gases having a Prandtl number of 0.7 are shown in Fig. 2. Also included in these figures for comparison purposes are the results from the similarity case (i.e., $v_w \sim x^{-1/2}$) for $u_w/u_\infty = 0$ and 0.50.

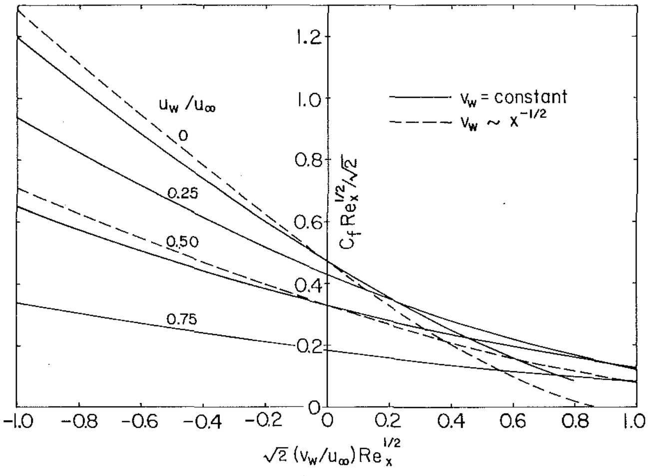

Fig. 1 Wall shear results for downstream vectoring

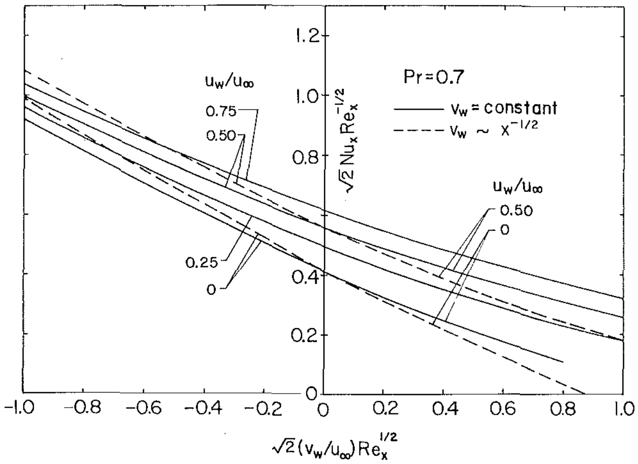

Fig. 2 Surface heat transfer results for downstream vectoring

Fig. 1 shows that for a given value of $u_w/u_\infty > 0$, the wall shear decreases monotonically with ξ as the suction intensity decreases from -1.0 to 0 and as the injection intensity increases from 0 to 1.0. This behavior is the same as that for the case in which the mass transfer is normal to the surface. The ordering of the curves with u_w/u_∞ is governed by two factors: (1) The decreasing variation of u across the boundary layer which accompanies an increase in u_w/u_∞, (2) the extraction or introduction of x-momentum at the wall. The first of these factors gives rise to a lower shear stress with increasing u_w/u_∞. For suction, the spread among the curves is accentuated by the extraction of x-momentum at the surface. On the other hand, the introduction of x-momentum which accompanies injection tends to increase the wall shear, and this accounts for the crossing of the curves for positive ξ values.

The heat transfer results for downstream vectoring, Fig. 2, show that for a given u_w/u_∞ value, the local surface heat transfer rate, like that of the wall shear, decreases monotonically as the suction intensity decreases and as the injection intensity increases. However, in contrast to Fig. 1, the ordering of the curves is reversed and there are no crossings in the ξ range corresponding to injection. The higher rates of the surface heat transfer associated with larger values of u_w/u_∞ are due to the presence of a nonzero streamwise velocity at the wall.

A comparison of the present results with those of the similarity case (i.e., $v_w \sim x^{-1/2}$) for two values of $u_w/u_\infty = 0$ and 0.5 in Figs. 1 and 2 shows that the similarity case predicts smaller values of the wall shear and surface heat transfer for injection. The opposite trend is in evidence for suction. It can also be seen that the blow-off condition (i.e., $f''(\xi, 0) = 0$) occurs at a larger ξ value for the uniform injection than for the similarity injection and, furthermore, that blow-off occurs at larger injection intensities as u_w/u_∞ increases. Thus, as compared to normal injection, downstream vectoring not only increases the rate of surface heat transfer, but also delays blow-off and the related flow separation.

The dashed curves of Figs. 1 and 2 not only portray the results for similarity mass transfer, but also represent the local similarity solution corresponding to uniform u_w and v_w. It is seen that the local similarity model does not yield accurate results for intermediate and large values of the injection parameter ξ.

The wall shear and surface heat transfer results for upstream vectoring ($u_w < 0$) with $u_w/u_\infty = -0.25$ and -0.50 are illustrated in Fig. 3 in which the $\sqrt{2}\mathrm{Nu}_x\mathrm{Re}_x{}^{-1/2}$ results are referred to the upper abscissa. As already noted and discussed in [1], dual solutions exist for the similarity case ($v_w \sim x^{-1/2}$) below a certain ξ value for each u_w/u_∞. The high shear solutions are characterized by ordinary attached-flow boundary layer velocity profiles, whereas the low shear solutions display wake-like velocity profiles [1]. The physical significance of

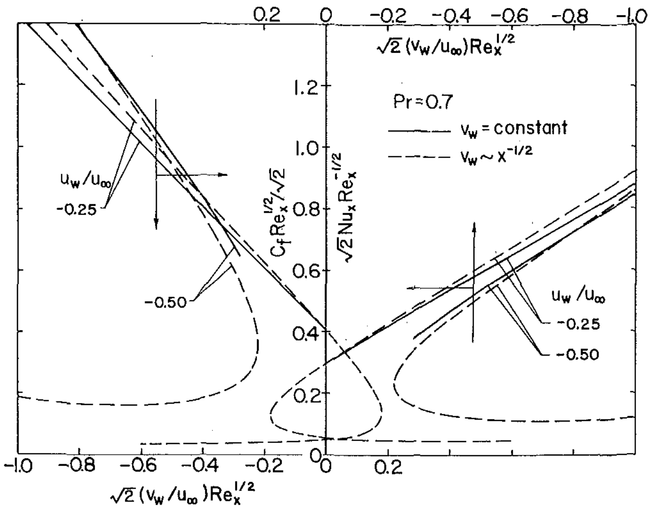

Fig. 3 Wall shear and surface heat transfer results for upstream vectoring

the low shear solutions is not clear. For the case of uniform u_w and v_w, only high shear solutions could be obtained in spite of a concerted effort to find low shear solutions. Dual solutions for upstream vectoring may be a phenomenon that is particular to similarity mass transfer.

Acknowledgment

The work of T. S. Chen was partially supported by a grant from the National Science Foundation (NSF ENG 75-15033).

References

1 Inger, G. R., and Swean, T. F., "Vectored Injection Into Laminary Boundary Layers With Heat Transfer," *AIAA Journal,* Vol. 13, 1975, pp. 616–622.

2 Sparrow, E. M., Quack, H., and Boerner, C. J., "Local Nonsimilarity Boundary-Layer Solutions," *AIAA Journal,* Vol. 8, 1970, pp. 1936–1942.

3 Sparrow, E. M., and Yu, H. S., "Local Non-Similarity Thermal Boundary-Layer Solutions," JOURNAL OF HEAT TRANSFER, TRANS. ASME, Series C, Vol. 93, 1971, pp. 328–334.

A Simple Parameterization for the Water Vapor Emissivity[1]

R. D. Cess[2] and M. S. Lian[2]

Conventionally the emissivity of water vapor, or any other gas whose absorption spectrum consists of rotational lines, is expressed as a function of three parameters, $\epsilon = \epsilon(P_wL, P_e, T)$, where ϵ is the gas emissivity, P_w the water vapor partial pressure, L the appropriate physical dimension, P_e the effective broadening pressure, and T the gas temperature. For application to radiative transfer calculations, it is useful to have an analytical representation of the gas emissivity, and approximate formulations have been presented, for example, by Hottel and Sarofim [1],[3] Hadvig [2], and Taylor and Foster [3]. The purpose of the present note is to present an extremely simple parameterization of the water vapor emissivity. For this purpose we employ the emissivity chart of Hottel (Hottel and Sarofim [1], McAdams [4]), restricting our use of his emissivity chart to the parameter ranges which correspond to actual experimental measurements. As discussed by Tien [5] and Penner [6], it would appear that Hottel's emissivity results are valid providing one excludes the extrapolated portions of the emissivity chart.

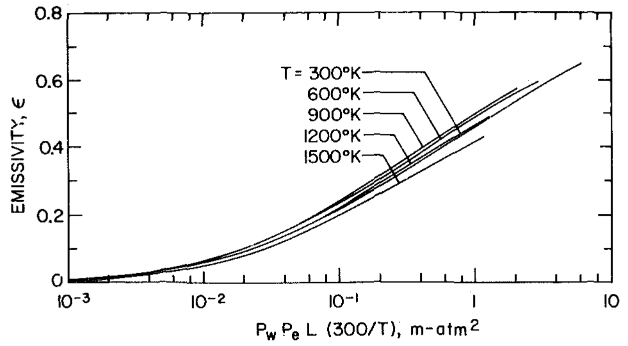

Fig. 1 Hottel's emissivity results for water vapor plotted as a a function of the strong-line correlation parameter

In most radiation problems of practical concern, the radiative transfer process corresponds to the limit of strong rotational lines (e.g., Penner and Varanasi [7], Rodgers [8], and Cess [9]). In this limit P_wL and P_e do not appear as separate parameters; instead they reduce to one parameter formed by their product, such that $\epsilon = \epsilon(P_wP_eL, T)$. In addition, it appears that the dependence upon temperature may be reduced through a temperature scaling of the pressure path length P_wL. Goody [10], for example, indicates that for temperatures characteristic of the terrestrial atmosphere, the water vapor emissivity is a relatively weak function of temperature when the emissivity is expressed in terms of absorber amount, ρ_wL, rather than P_wL, where ρ_w is the partial density of water vapor. This conclusion is consistent with the emissivity calculations of Manabe and Wetherald [11], and Rodgers [8], which again refer to temperatures of atmospheric interest. Employing the perfect gas law, and choosing 300 K as a convenient reference temperature, the preceding suggests that the parameter

$$X = P_wP_eL(300/T) \tag{1}$$

may prove useful as an emissivity correlation parameter.

Fig. 1 illustrates Hottel's water vapor emissivity results [1, 4] plotted as a function of the foregoing parameter and, as for the atmospheric applications, the emissivity is only weakly dependent upon temperature. Although it would be useful to provide a physical explanation for this relative temperature insensitivity, there are numerous, and evidently competing, mechanisms which contribute to the temperature dependence of the emissivity. For present purposes we simply regard this weak temperature effect as a useful empirical result.

Fig. 1 employs Hottel's emissivity chart for H_2O-air mixtures with P_e = 1 atm and $P_w/P_e \rightarrow 0$. Thus, P_e refers to line broadening by air. The application of the emissivity results to broadening pressures other than 1 atm is automatically taken into account through use of the strong-line parameter P_wP_eL. However, if the broadening gas is not air, then P_e must be modified to account for the difference in line broadening. If we consider H_2O-air mixtures when P_w/P_e is not small, for example, then $P_e = P_a + bP_e$, where P_a is the partial pressure of

---

[1] This work was supported by the National Science Foundation through Grants ENG72-04175 and ENG75-02986.

[2] Laboratory for Planetary Atmospheres Research, State University of New York, Stony Brook, N. Y.

Contributed by the Heat Transfer Division of THE AMERICAN SOCIETY OF MECHANICAL ENGINEERS. Manuscript received by the heat Transfer Division March 18, 1976.

[3] Numbers in brackets designate References at end of technical note.

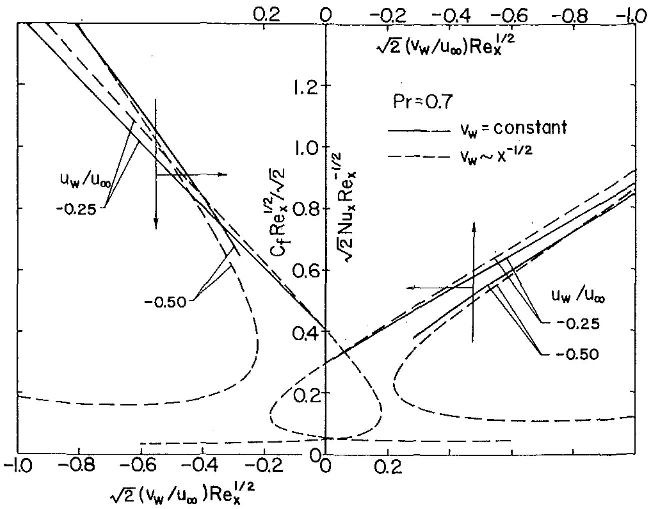

Fig. 3 Wall shear and surface heat transfer results for upstream vectoring

the low shear solutions is not clear. For the case of uniform u_w and v_w, only high shear solutions could be obtained in spite of a concerted effort to find low shear solutions. Dual solutions for upstream vectoring may be a phenomenon that is particular to similarity mass transfer.

Acknowledgment

The work of T. S. Chen was partially supported by a grant from the National Science Foundation (NSF ENG 75-15033).

References

1 Inger, G. R., and Swean, T. F., "Vectored Injection Into Laminary Boundary Layers With Heat Transfer," *AIAA Journal,* Vol. 13, 1975, pp. 616–622.

2 Sparrow, E. M., Quack, H., and Boerner, C. J., "Local Nonsimilarity Boundary-Layer Solutions," *AIAA Journal,* Vol. 8, 1970, pp. 1936–1942.

3 Sparrow, E. M., and Yu, H. S., "Local Non-Similarity Thermal Boundary-Layer Solutions," JOURNAL OF HEAT TRANSFER, TRANS. ASME, Series C, Vol. 93, 1971, pp. 328–334.

A Simple Parameterization for the Water Vapor Emissivity[1]

R. D. Cess[2] and M. S. Lian[2]

Conventionally the emissivity of water vapor, or any other gas whose absorption spectrum consists of rotational lines, is expressed as a function of three parameters, $\epsilon = \epsilon(P_wL, P_e, T)$, where ϵ is the gas emissivity, P_w the water vapor partial pressure, L the appropriate physical dimension, P_e the effective broadening pressure, and T the gas temperature. For application to radiative transfer calculations, it is useful to have an analytical representation of the gas emissivity, and approximate formulations have been presented, for example, by Hottel and Sarofim [1],[3] Hadvig [2], and Taylor and Foster [3]. The purpose of the present note is to present an extremely simple parameterization of the water vapor emissivity. For this purpose we employ the emissivity chart of Hottel (Hottel and Sarofim [1], McAdams [4]), restricting our use of his emissivity chart to the parameter ranges which correspond to actual experimental measurements. As discussed by Tien [5] and Penner [6], it would appear that Hottel's emissivity results are valid providing one excludes the extrapolated portions of the emissivity chart.

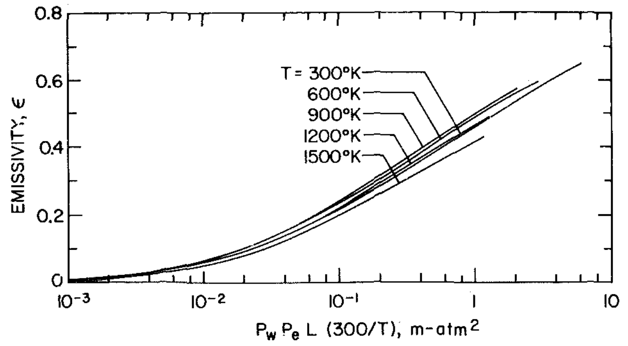

Fig. 1 Hottel's emissivity results for water vapor plotted as a a function of the strong-line correlation parameter

In most radiation problems of practical concern, the radiative transfer process corresponds to the limit of strong rotational lines (e.g., Penner and Varanasi [7], Rodgers [8], and Cess [9]). In this limit P_wL and P_e do not appear as separate parameters; instead they reduce to one parameter formed by their product, such that $\epsilon = \epsilon(P_wP_eL, T)$. In addition, it appears that the dependence upon temperature may be reduced through a temperature scaling of the pressure path length P_wL. Goody [10], for example, indicates that for temperatures characteristic of the terrestrial atmosphere, the water vapor emissivity is a relatively weak function of temperature when the emissivity is expressed in terms of absorber amount, ρ_wL, rather than P_wL, where ρ_w is the partial density of water vapor. This conclusion is consistent with the emissivity calculations of Manabe and Wetherald [11], and Rodgers [8], which again refer to temperatures of atmospheric interest. Employing the perfect gas law, and choosing 300 K as a convenient reference temperature, the preceding suggests that the parameter

$$X = P_wP_eL(300/T) \qquad (1)$$

may prove useful as an emissivity correlation parameter.

Fig. 1 illustrates Hottel's water vapor emissivity results [1, 4] plotted as a function of the foregoing parameter and, as for the atmospheric applications, the emissivity is only weakly dependent upon temperature. Although it would be useful to provide a physical explanation for this relative temperature insensitivity, there are numerous, and evidently competing, mechanisms which contribute to the temperature dependence of the emissivity. For present purposes we simply regard this weak temperature effect as a useful empirical result.

Fig. 1 employs Hottel's emissivity chart for H_2O-air mixtures with P_e = 1 atm and $P_w/P_e \rightarrow 0$. Thus, P_e refers to line broadening by air. The application of the emissivity results to broadening pressures other than 1 atm is automatically taken into account through use of the strong-line parameter P_wP_eL. However, if the broadening gas is not air, then P_e must be modified to account for the difference in line broadening. If we consider H_2O-air mixtures when P_w/P_e is not small, for example, then $P_e = P_a + bP_e$, where P_a is the partial pressure of

---

[1] This work was supported by the National Science Foundation through Grants ENG72-04175 and ENG75-02986.

[2] Laboratory for Planetary Atmospheres Research, State University of New York, Stony Brook, N. Y.

Contributed by the Heat Transfer Division of THE AMERICAN SOCIETY OF MECHANICAL ENGINEERS. Manuscript received by the heat Transfer Division March 18, 1976.

[3] Numbers in brackets designate References at end of technical note.

Table 1 Values of a_0 and a_1 as a function of temperature

T (°K)	a_0	a_1 ($m^{-\frac{1}{2}}atm^{-1}$)
300	0.683	1.17
600	0.674	1.32
900	0.700	1.27
1200	0.673	1.21
1500	0.624	1.15

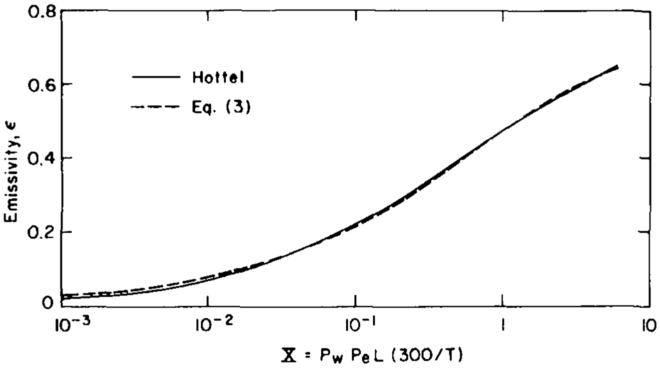

Fig. 2 Comparison of equation (3) with Hottel's emissivity results for T = 300 K

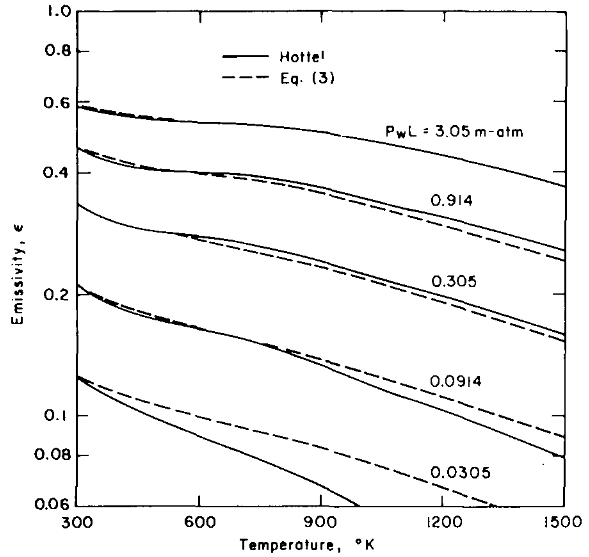

Fig. 3 Comparison of equation (3) with Hottel's emissivity chart for P_e = 1 atm and $P_w/P_e \to 0$

air, while b is the self-broadening coefficient for which Edwards and Balakrishnan [12] recommend

$$b = 5.0(300/T)^{1/2} + 0.5 \tag{2}$$

It is further possible to express $\epsilon(X)$ in a simple analytical form. As illustrated by Cess [9], a useful analytical approximation is

$$\epsilon = a_0[1 - \exp(-a_1\sqrt{X})] \tag{3}$$

This expression may be partially justified on theoretical grounds, since it has the asymptotic form

$$\epsilon = a_0 a_1\sqrt{X}; \quad a_1\sqrt{X} \ll 1 \tag{4}$$

which is the well-known square-root dependence for the limit of nonoverlapping strong lines (e.g., Penner and Varanasi [7]). Thus, equation (4) applies for nonoverlapping strong lines while equation (3) empirically accounts for line overlap.

The form of equation (3) is identical to that which would be obtained by application of the statistical model to account for line overlap (Goody [10]), suggesting that there may be further theoretical justification in the form of equation (3). But it must be realized that the statistical model applies only to narrow spectral intervals, whereas equation (3) refers to the entire infrared spectrum. The resemblance of equation (3) to an application of the statistical model is most likely coincidental, and we regard equation (3) as strictly an empirical means of accounting for line overlap.

We have employed a least-squares fit of equation (3) to the emissivity curves of Fig. 1 in order to evaluate a_0 and a_1 as a function of temperature. These results are listed in Table 1 and, as would be expected, the values are only weakly dependent upon temperature. The values of a_0 and a_1 for 300 K differ slightly from those of Cess [9], as a consequence of the different method of curve fitting which has presently been employed. A comparison of equation (3) with Hottel's results is shown in Fig. 2 for 300 K.

In Fig. 3 we illustrate a direct comparison of equation (3) with an abbreviated version of Hottel's chart. For $\epsilon > 0.1$ the maximum difference between equation (3) and Hottel's values is less than 8 percent. Deviations for $\epsilon < 0.1$ are most likely due to a departure from the strong-line limit, and it would appear that $\epsilon \gtrsim 0.1$ constitutes the range of applicability of equation (3), a limit which is not severe with respect to radiation problems of practical concern. Moreover, for broadening pressures substantially less than one atmosphere, such as arise in atmospheric problems, equation (3) will apply for much smaller emissivities, since line saturation increases with decreasing broadening pressure. The simplicity of equation (3) is such that it should prove useful in radiative transfer formulations; illustrative applications involving atmospheric water vapor are given by Cess [7, 13, 14].

Equation (3) is somewhat analogous to Hottel and Sarofim's suggestion [1] of visualizing a real gas as a weighted sum of gray gases, with equation (3) corresponding to one clear gas (providing $a_0 < 1$) and one gray gas. The difference between Hottel and Sarofim's formulation and equation (3) lies in the argument of the exponential; Hottel and Sarofim take this to be proportional to P_wL. Since the emissivity of a gray gas is $\epsilon = 1 - \exp(-\kappa P_w L)$, with κ the gray gas absorption coefficient, the equivalent "gray gas" depicted by equation (3) behaves differently from a conventional gray gas, with the result that the equivalent gray absorption coefficient is not a gas property, but depends upon the path length L. Hottel and Sarofim also point out that their formulation really requires a composite of gray gases, resulting in the emissivity being expressed as a sum of exponentials. Within the range of applicability of equation (3), however, only a single exponential is required as a consequence of our use of equation (1) as an emissivity correlation parameter.

References

1 Hottel, H. C., and Sarofim, A. F., *Radiative Transfer*, McGraw-Hill, New York, 1967, pp. 225–258.

2 Hadvig, S. A. P., see p. 234 of Hottel and Sarofim [1].

3. Taylor, P. B., and Foster, P. J., "The Total Emissivities of Luminous and Non-Luminous Flames," *International Journal of Heat and Mass Transfer*, Vol. 17, 1974, pp. 1591–1606.

4 McAdams, W. H., *Heat Tramsmission*, McGraw-Hill, New York, 1954, pp. 82–112.

5 Tien, C. L., *Advances in Heat Transfer*, J. P. Hartnett and T. F. Irvine, eds., Vol. 5, Academic Press, New York, 1968.

6 Penner, S. S., *Handbook of Heat Transfer*, W. M. Rohsenow and J. P. Hartnett, eds., Section 15-D, McGraw-Hill, New York, 1973.

7 Penner, S. S., and Varanasi, P., "Approximate Band Absorption and Total Emissivity Calculations for H_2O," *Journal Quant. Spectrosc. Radiat. Transfer*, Vol. 5, 1965, p. 391.

8 Rodgers, C. D., "The Use of Emissivity in Atmospheric Radiation Calculations," *Q. J. Roy. Meteor. Soc.*, Vol. 93, 1967, pp. 43–54.

9 Cess, R. D., "Radiative Transfer Due to Atmospheric Water Vapor: Global Considerations of the Earth's Energy Balance," *Journal Quant. Spectrosc. Radiat. Transfer*, Vol. 14, 1974, pp. 861–871.

10 Goody, R. M., *Atmospheric Radiation*, Oxford University Press, London, 1964, p. 198.

11 Manabe, S., and Wetherald, R. T., "Thermal Equilibrium of the Atmosphere With a Given Distribution of Relative Humidity," *Journal Atmos. Sci.*, Vol. 24, 1967, pp. 241–259.

12 Edwards, D. K., and Balakrishnan, A., "Thermal Radiation by Combustion Gases," *International Journal of Heat and Mass Transfer*, Vol. 16, 1973, pp. 25–40.

13 Cess, R. D., "Global Climate Change: An Investigation of Atmospheric Feedback Mechanisms," *Tellus*, Vol. 27, 1975, pp. 193–198.

14 Cess, R. D., "Climate Change: An Appraisal of Atmospheric Feedback Mechanisms Employing Zonal Climatology," *Journal Atmos. Sci.* (in press).

Temperature Regulation of a Plastic-Insulated Wire in Radiant Heating

Y. Jaluria[1]

Introduction

A frequently encountered process in the manufacture of plastic-insulated wires and cables, and in several subsequent heat treatment operations, is that of radiation heating. This may happen during the curing of the plastic, the application of the insulation, the surface treatment for environment protection or for shielding, and during molding processes for obtaining a desired cable configuration [1–4].[2] Radiant heating is employed mainly because of the high rates of heat transfer and the generally noncontaminative medium, which might be of concern in convective heating. In most cases, it is essential to regulate the temperature of the plastic insulation. Usually this is either in the form of a restriction on the temperature of the insulation, in order to avoid damage to the plastic, or a specified time for which the temperature must be maintained at a given level to complete the thermal treatment. The present study considers the thermal transients in these cases and the parameters on which the temperature regulation of the plastic-insulated wire depends. The methods for restricting and controlling the temperature of the plastic are outlined and the thermal transient behavior of the insulation under these different conditions determined. The study employs numerical methods to present quantitative results on this frequent problem, on which very little information exists at present.

Analysis

A detailed study of the transient heat transfer in insulated wires has recently been carried out by Jaluria [5]. However, this work was mainly concerned with the general features of heat transfer in the configuration under study and brought out several important aspects in its thermal response under various boundary conditions. The present study employs the analysis developed and the numerical method outlined in reference [5] to consider the question of temperature regulation of the plastic insulation in radiant heating.

Employing the usual nondimensionalization for transient heat transfer, references [5–7], the one-dimensional radial heat transfer problem for the cylindrical configuration represented by long insulated wires is governed by

$$\frac{\partial^2 t'}{\partial r'^2} + \frac{1}{r'}\frac{\partial t'}{\partial r'} = \frac{\partial t'}{\partial \tau'} \tag{1}$$

Here the nondimensional temperature t', radial distance r', and time τ' are given in terms of the respective physical quantities t, r, and τ as:

$$t' = \frac{t}{t_i}, \qquad r' = \frac{r}{R}, \qquad \tau' = \frac{\alpha\tau}{R^2} \tag{2}$$

where t_i is the initial temperature of the insulated wire, R its outside radius, and α the thermal diffusivity of the plastic.

Since the system under study consists of a highly conducting inner cylinder sheathed in a plastic insulating material of low thermal conductivity, the temperature variation exists mainly in the insulation, the conducting core being essentially isothermal. With this assumption, the boundary condition at the interface between the conductor and the insulation is [5]:

$$G \cdot \frac{1-P}{2} \cdot \frac{\partial t'}{\partial \tau'} = \frac{\partial t'}{\partial r'}, \qquad \text{at } r' = 1 - P \tag{3}$$

where G is the thermal capacity ratio, which is defined as the ratio of the thermal capacity of the conductor material, $(\rho C)_c$, to that of the plastic insulation material, $(\rho C)_p$. Therefore, $G = (\rho C)_c/(\rho C)_p$, where ρ is the density and C the specific heat of the materials. P is the insulation thickness ratio, which is the ratio of the thickness of the insulation to the outer radius R.

The boundary condition at the outer surface of the wire, for radiant heating, is:

$$\frac{\partial t'}{\partial r'} = \frac{QR}{kt_i} = Q_s, \qquad \text{at } r' = 1 \tag{4}$$

where Q is the heat flux absorbed at the surface, k the thermal conductivity of the plastic and Q_s a dimensionless heat flux parameter that thus arises. A more general boundary condition at the surface is one which incorporates convective heat transfer in addition to the radiant flux Q. This is given by:

$$\frac{\partial t'}{\partial r'} = Q_s + \mathrm{Bi}(t_F' - t_S'), \qquad \text{at } r' = 1 \tag{5}$$

where Bi is the Biot number ($= hR/k$, h being the convective heat transfer coefficient), t_S' is the surface temperature, and t_F' the nondimensional fluid, or ambient, temperature.

The governing equation (1) is solved numerically with the appropriate boundary conditions, employing the method outlined in [5]. For all the results presented in the following, the thermal capacity ratio G of the conductor material to that of the plastic is taken as 2.0 and the insulation thickness ratio P as 0.5. These were chosen as they represent typical values generally employed in practice and as the dependence of the transient thermal response on G and P has been considered in detail earlier [5]. The basic features concerning the temperature regulation of the plastic insulation are discussed on the basis of the numerical results obtained, as presented in the following.

Numerical Results. The transient response of the outside and inner surface, or core, temperatures of the plastic insulation is shown in Fig. 1, for varying values of the nondimensional heat flux Q_s. Following an initial starting transient, in which the rate of temperature rise is very different for the outer and inner surfaces, the temperature variation across the insulation approaches a value constant with time and the rate of temperature rise becomes the same throughout the insulation. This linear temperature rise, following the initial transient, arises from the exponential decay of nonlinear terms, as pointed out in reference [5]. It is observed that, for a constant heat flux input at the surface of the insulated wire, the temperature continues to increase indefinitely. In actual practice, of course, the radiation and convective loss from the wire increases as the temperature rises, thereby allowing the insulation to attain a constant temperature.

---

[1] Asst. Professor, Department of Mechanical Engineering, Indian Institute of Technology, Kanpur, India.

[2] Numbers in brackets designate References at end of technical note.

Contributed by the Heat Transfer Division of THE AMERICAN SOCIETY OF MECHANICAL ENGINEERS. Manuscript received by the Heat Transfer Division May 10, 1976.

8 Rodgers, C. D., "The Use of Emissivity in Atmospheric Radiation Calculations," *Q. J. Roy. Meteor. Soc.*, Vol. 93, 1967, pp. 43-54.

9 Cess, R. D., "Radiative Transfer Due to Atmospheric Water Vapor: Global Considerations of the Earth's Energy Balance," *Journal Quant. Spectrosc. Radiat. Transfer*, Vol. 14, 1974, pp. 861-871.

10 Goody, R. M., *Atmospheric Radiation*, Oxford University Press, London, 1964, p. 198.

11 Manabe, S., and Wetherald, R. T., "Thermal Equilibrium of the Atmosphere With a Given Distribution of Relative Humidity," *Journal Atmos. Sci.*, Vol. 24, 1967, pp. 241-259.

12 Edwards, D. K., and Balakrishnan, A., "Thermal Radiation by Combustion Gases," *International Journal of Heat and Mass Transfer*, Vol. 16, 1973, pp. 25-40.

13 Cess, R. D., "Global Climate Change: An Investigation of Atmospheric Feedback Mechanisms," *Tellus*, Vol. 27, 1975, pp. 193-198.

14 Cess, R. D., "Climate Change: An Appraisal of Atmospheric Feedback Mechanisms Employing Zonal Climatology," *Journal Atmos. Sci.* (in press).

Temperature Regulation of a Plastic-Insulated Wire in Radiant Heating

Y. Jaluria[1]

Introduction

A frequently encountered process in the manufacture of plastic-insulated wires and cables, and in several subsequent heat treatment operations, is that of radiation heating. This may happen during the curing of the plastic, the application of the insulation, the surface treatment for environment protection or for shielding, and during molding processes for obtaining a desired cable configuration [1-4].[2] Radiant heating is employed mainly because of the high rates of heat transfer and the generally noncontaminative medium, which might be of concern in convective heating. In most cases, it is essential to regulate the temperature of the plastic insulation. Usually this is either in the form of a restriction on the temperature of the insulation, in order to avoid damage to the plastic, or a specified time for which the temperature must be maintained at a given level to complete the thermal treatment. The present study considers the thermal transients in these cases and the parameters on which the temperature regulation of the plastic-insulated wire depends. The methods for restricting and controlling the temperature of the plastic are outlined and the thermal transient behavior of the insulation under these different conditions determined. The study employs numerical methods to present quantitative results on this frequent problem, on which very little information exists at present.

Analysis

A detailed study of the transient heat transfer in insulated wires has recently been carried out by Jaluria [5]. However, this work was mainly concerned with the general features of heat transfer in the configuration under study and brought out several important aspects in its thermal response under various boundary conditions. The present study employs the analysis developed and the numerical method outlined in reference [5] to consider the question of temperature regulation of the plastic insulation in radiant heating.

Employing the usual nondimensionalization for transient heat transfer, references [5-7], the one-dimensional radial heat transfer problem for the cylindrical configuration represented by long insulated wires is governed by

$$\frac{\partial^2 t'}{\partial r'^2} + \frac{1}{r'}\frac{\partial t'}{\partial r'} = \frac{\partial t'}{\partial \tau'} \tag{1}$$

Here the nondimensional temperature t', radial distance r', and time τ' are given in terms of the respective physical quantities t, r, and τ as:

$$t' = \frac{t}{t_i}, \qquad r' = \frac{r}{R}, \qquad \tau' = \frac{\alpha\tau}{R^2} \tag{2}$$

where t_i is the initial temperature of the insulated wire, R its outside radius, and α the thermal diffusivity of the plastic.

Since the system under study consists of a highly conducting inner cylinder sheathed in a plastic insulating material of low thermal conductivity, the temperature variation exists mainly in the insulation, the conducting core being essentially isothermal. With this assumption, the boundary condition at the interface between the conductor and the insulation is [5]:

$$G \cdot \frac{1-P}{2} \cdot \frac{\partial t'}{\partial \tau'} = \frac{\partial t'}{\partial r'}, \qquad \text{at } r' = 1 - P \tag{3}$$

where G is the thermal capacity ratio, which is defined as the ratio of the thermal capacity of the conductor material, $(\rho C)_c$, to that of the plastic insulation material, $(\rho C)_p$. Therefore, $G = (\rho C)_c/(\rho C)_p$, where ρ is the density and C the specific heat of the materials. P is the insulation thickness ratio, which is the ratio of the thickness of the insulation to the outer radius R.

The boundary condition at the outer surface of the wire, for radiant heating, is:

$$\frac{\partial t'}{\partial r'} = \frac{QR}{kt_i} = Q_s, \qquad \text{at } r' = 1 \tag{4}$$

where Q is the heat flux absorbed at the surface, k the thermal conductivity of the plastic and Q_s a dimensionless heat flux parameter that thus arises. A more general boundary condition at the surface is one which incorporates convective heat transfer in addition to the radiant flux Q. This is given by:

$$\frac{\partial t'}{\partial r'} = Q_s + \mathrm{Bi}(t_F' - t_S'), \qquad \text{at } r' = 1 \tag{5}$$

where Bi is the Biot number ($= hR/k$, h being the convective heat transfer coefficient), t_S' is the surface temperature, and t_F' the nondimensional fluid, or ambient, temperature.

The governing equation (1) is solved numerically with the appropriate boundary conditions, employing the method outlined in [5]. For all the results presented in the following, the thermal capacity ratio G of the conductor material to that of the plastic is taken as 2.0 and the insulation thickness ratio P as 0.5. These were chosen as they represent typical values generally employed in practice and as the dependence of the transient thermal response on G and P has been considered in detail earlier [5]. The basic features concerning the temperature regulation of the plastic insulation are discussed on the basis of the numerical results obtained, as presented in the following.

Numerical Results. The transient response of the outside and inner surface, or core, temperatures of the plastic insulation is shown in Fig. 1, for varying values of the nondimensional heat flux Q_s. Following an initial starting transient, in which the rate of temperature rise is very different for the outer and inner surfaces, the temperature variation across the insulation approaches a value constant with time and the rate of temperature rise becomes the same throughout the insulation. This linear temperature rise, following the initial transient, arises from the exponential decay of nonlinear terms, as pointed out in reference [5]. It is observed that, for a constant heat flux input at the surface of the insulated wire, the temperature continues to increase indefinitely. In actual practice, of course, the radiation and convective loss from the wire increases as the temperature rises, thereby allowing the insulation to attain a constant temperature.

---

[1] Asst. Professor, Department of Mechanical Engineering, Indian Institute of Technology, Kanpur, India.

[2] Numbers in brackets designate References at end of technical note.

Contributed by the Heat Transfer Division of THE AMERICAN SOCIETY OF MECHANICAL ENGINEERS. Manuscript received by the Heat Transfer Division May 10, 1976.

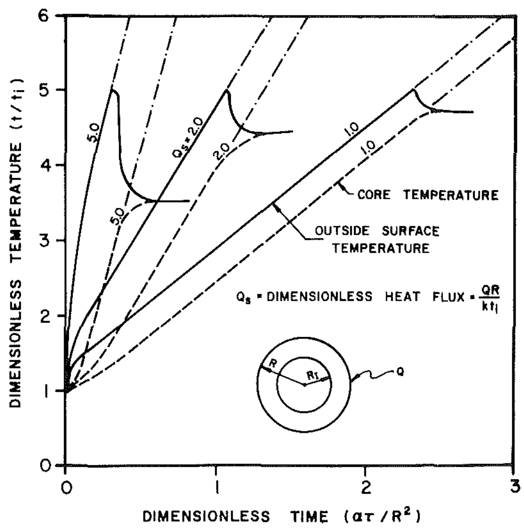

Fig. 1 The transient response of the outer and inner surface, or core, temperatures of the insulation for heating at various heat flux levels Q_s, followed by no heat transfer at the surface, beyond the point where the surface temperature attains a value five times the initial temperature

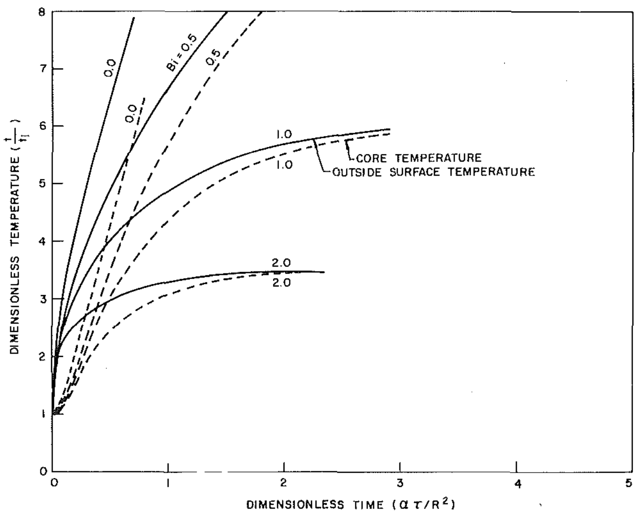

Fig. 3 The transient response of the insulated wire under combined radiation and convection, at heat flux Q_s = 5.0 with varying Biot number Bi and with $t_F = t_i$

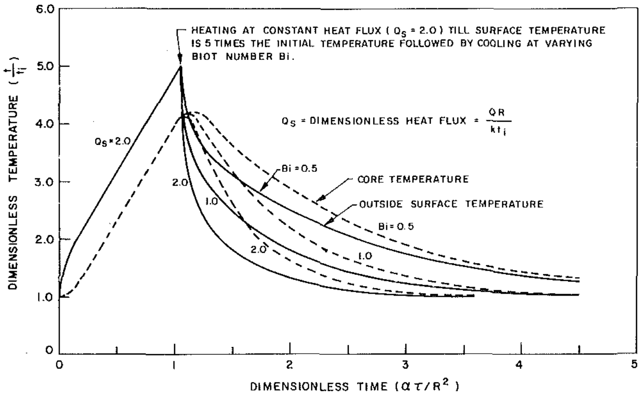

Fig. 2 Heating of the insulated wire at a constant heat flux, Q_s = 2.0, followed by convective cooling at various values of the Biot number Bi, for $t_F = t_i$

However, the melt temperature of most plastics is far below this temperature, in industrial applications of interest, and the wire temperature must be restricted by some method to a value below the melt temperature to avoid damaging it.

Fig. 1 shows the circumstance when the insulated wire is subjected to a constant heat flux till the outside surface temperature attains a given value. This represents the restriction on the temperature and is taken at a typical value of 5.0 in the given curves. The radiation is cut off as soon as this value is attained. The temperature variation that exists across the insulation at this point is a function of the heat flux Q_s, and also of the parameters P and G, as discussed earlier. Fig. 1 indicates the transient response of the insulation if there exists no external heat transfer beyond the point of heat flux cut off. The temperature variation across the insulation decreases sharply to give a uniform temperature in the insulation. The uniform temperature thus attained is also a function of Q_s, being smaller for a larger heat flux. This is an obvious consequence of the greater temperature variation across the insulation for a larger Q_s. Though Fig. 1 represents a hypothetical situation, it does point out the effect of a steep reduction in the heat flux, particularly the fact that the insulation becomes isothermal in a very short time.

Considering now a more practical situation, in which the heat flux cut off is followed by convective cooling, the results obtained at varying values of the Biot number Bi, with initial heating at Q_s = 2.0, are shown in Fig. 2. As seen from equation (5), Bi determines the rate of convective loss from the plastic, for t_S' greater than t_F', being greater for a larger value of Bi. Fig. 1 is the circumstance when Bi = 0. For the curves in Fig. 2, the fluid temperature t_F is taken at the initial temperature of the insulation, which may be the room temperature. In all the curves shown, the outer surface temperature initially drops sharply, the drop being faster for larger Biot number Bi. The inner surface temperature continues to increase for some time and then gradually decreases. The final approach to the fluid temperature, as expected, is a gradual process for both the temperatures. The observed dependence of the temperature response on Bi indicates that a lower value of Bi tends to keep the temperature variation across the insulation lower and the temperature drop from the maximum value attained more gradual. The fluid temperature t_F may also be varied to control the final temperature of the plastic and the rate of cooling.

The regulation of the temperature of the plastic can, therefore, be effectively achieved by the addition of convective heat transfer to the constant radiant heat flux, as given by equation (5). Fig. 3 shows the results for Q_s = 5.0 at varying values of Bi, when $t_F = t_i$. In this circumstance, the plastic approaches a constant temperature, determined by the parameters in the problem. Though wasteful in energy, this method provides as excellent control over the temperature of the plastic insulation. By a proper choice of t_F and Bi, the temperature variation across the insulation, the final temperature and the rate of temperature rise can be controlled. The main advantage of this process is the high rate of heat transfer to the insulation in the initial stages. This is increased even more if t_F is greater than t_i. As the insulation heats up and t_S becomes greater than t_F, a control on the temperature is automatically exercised by an increase in the convective loss. This would also allow the maintaining of a fairly isothermal plastic at a given temperature for a specified period, in order to allow the completion of a thermal treatment process. This is particularly important in molding processes, as in coiling of wires and cables [4].

Fig. 4 shows the theoretical heat flux profile required for heating the insulation to a given temperature and then maintaining it at that temperature, assuming no heat loss from the wire. Clearly, the required variation of the heat flux with time is not easy to obtain in practice. Since it is desirable to obtain a fast heat up initially, a cou-

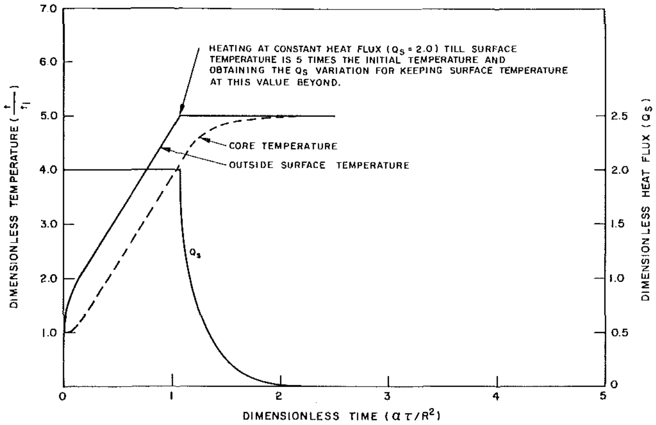

Fig. 4 The variation of the heat flux Q_s, with time, required to heat the insulation surface to a given temperature and then maintain it at that value.

pling of radiant heating with convective heat transfer would allow a better and easier control of the process.

As mentioned earlier, the present study is motivated by actual problems in industry. A few may be mentioned here. During the radiant heating of plastic-insulated cables for surface treatment for environmental protection and for bonding with other such cables and with metallic shields, etc., the temperature must be maintained at a given value over a period of time. At the same time, the temperature must not rise beyond the melt temperature of the plastic. In this case, the addition of convection, or the proper regulation of the radiant flux, allows the necessary control of the insulation temperature. Similarly, during drying of paper-insulated wires, the temperature has to be raised above the boiling point of water, without burning the paper. Again, addition of air cooling and regulation of radiant flux has helped in solving this problem. A similar configuration arises in the coiling of telephone cords [4] in which the temperature of the plastic must be maintained at a given level for sometime to achieve coiling and a restriction on maximum temperature also exists. Convective cooling has been added in the process to achieve the required control. Radiation flux has also been varied. Many components and connecting wires, which are represented by the configuration under study, are also often exposed to radiant heating during manufacture. In these cases too, the present study indicates the methods of temperature regulation.

Conclusions

An analytical study of the regulation of the transient temperature of a plastic-insulated wire, subjected to radiation heating, has been carried out. The two aspects considered in detail are the restriction on surface temperature and the maintenance of the temperature at a given value for a specified time. The problem is treated as an initial heating process under radiant heating with a cut off at a given temperature, followed by a different heat transfer circumstance to regulate the temperature of the insulation.

It is found that the insulation becomes isothermal, following the cut off, very rapidly, if no heat transfer occurs at the surface. If the cut off is followed by convective cooling, the temperature uniformity in the insulation is found to be greater at a lower value of the surface heat transfer coefficient h. The regulation of the temperature which requires raising it to a given value and maintaining it at this level can be theoretically achieved by a particular variation of radiant flux with time. However, the variation is very hard to achieve in practice and the best method is found to be through a proper coupling of radiant flux with convective cooling. The necessary regulation can then be achieved by varying the surface convective coefficient and the fluid temperature.

References

1 Barnes, C. C., *Power Cables*, Second ed., Chapman and Mall Ltd., London, particularly, Chapter 13, "Power Cable Manufacture" and Chapter 22, "Plastic-Insulated Power Cables," 1966.

2 Clark, F. M., *Insulating Materials for Design and Engineering Practice*, Wiley, New York, Chapter 14(I), "Insulated Wires and Conductors" and Chapter 3, "Insulation Technology," 1962.

3 Kertscher, E., "Recent Developments in High Speed Insulation of Quality Telephone Wires," 22nd Inter. Wire and Cable Symposium, 1973; see also, *Proceedings 19th International Wire and Cable Symposium,* 1970.

4 Hardesty, E. C., and Myers, D. L., "Coiling Spring Cords," *The Western Electric Engineer*, Ap. 1962, p. 11.

5 Jaluria, Y., "A Study of Transient Heat Transfer in Long Insulated Wires," JOURNAL OF HEAT TRANSFER, TRANS. ASME, Series C, Vol. 98, 1976, p. 127.

6 Carslaw, H. S., and Jaeger, J. C., *Conduction of Heat in Solids,* Second ed., Oxford, 1959.

7 Gebhart, B., *Heat Transfer,* Second ed., McGraw-Hill, New York, 1971.

Approximate Solution for Convective Fins With Variable Thermal Conductivity

A. Muzzio[1]

Nomenclature

h = convective heat transfer coefficient
k = thermal conductivity
L = length of fin
N = dimensionless fin parameter = $[2hL^2/k_a w]^{1/2}$
T = temperature
w = thickness of fin
x = distance from insulated end
X = dimensionless distance = x/L
ϵ = thermal conductivity parameter = $(k_b - k_a)/k_a$
η = fin efficiency
θ = dimensionless temperature = $(T - T_a)/(T_b - T_a)$
σ = slope of the dimensionless thermal conductivity-temperature curve

Subscripts

a = ambient
b = base of fin

Introduction

The performance of fins (convecting, radiating, of both) has been shown by several workers to be significantly affected by variable thermal properties, particularly when large temperature differences exist.

While most methods of solution of these nonlinear problems involve numerical procedures, recently Aziz and Enamul Huq [4][2] have presented a closed form solution for a straight convecting fin with temperature dependent thermal conductivity obtained by the regular perturbation method.

---

[1] Asst. Professor, Faculty of Engineering, University of Pavia, Pavia, Italy.

[2] Numbers in brackets designate References at end of technical note.

Contributed by the Heat Transfer Division of THE AMERICAN SOCIETY OF MECHANICAL ENGINEERS. Manuscript received by the Heat Transfer Division April 12, 1976.

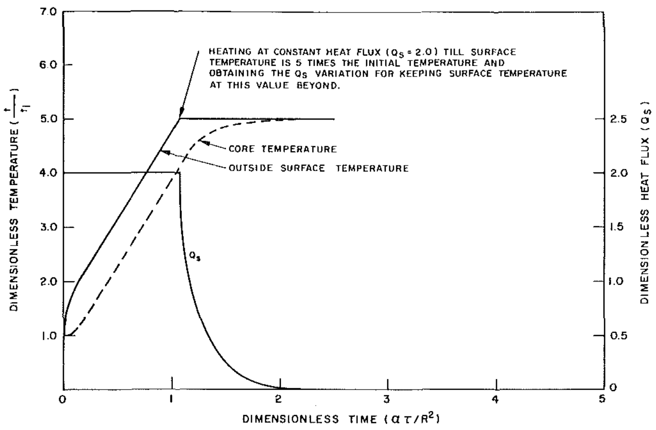

Fig. 4 The variation of the heat flux Q_s, with time, required to heat the insulation surface to a given temperature and then maintain it at that value.

pling of radiant heating with convective heat transfer would allow a better and easier control of the process.

As mentioned earlier, the present study is motivated by actual problems in industry. A few may be mentioned here. During the radiant heating of plastic-insulated cables for surface treatment for environmental protection and for bonding with other such cables and with metallic shields, etc., the temperature must be maintained at a given value over a period of time. At the same time, the temperature must not rise beyond the melt temperature of the plastic. In this case, the addition of convection, or the proper regulation of the radiant flux, allows the necessary control of the insulation temperature. Similarly, during drying of paper-insulated wires, the temperature has to be raised above the boiling point of water, without burning the paper. Again, addition of air cooling and regulation of radiant flux has helped in solving this problem. A similar configuration arises in the coiling of telephone cords [4] in which the temperature of the plastic must be maintained at a given level for sometime to achieve coiling and a restriction on maximum temperature also exists. Convective cooling has been added in the process to achieve the required control. Radiation flux has also been varied. Many components and connecting wires, which are represented by the configuration under study, are also often exposed to radiant heating during manufacture. In these cases too, the present study indicates the methods of temperature regulation.

Conclusions

An analytical study of the regulation of the transient temperature of a plastic-insulated wire, subjected to radiation heating, has been carried out. The two aspects considered in detail are the restriction on surface temperature and the maintenance of the temperature at a given value for a specified time. The problem is treated as an initial heating process under radiant heating with a cut off at a given temperature, followed by a different heat transfer circumstance to regulate the temperature of the insulation.

It is found that the insulation becomes isothermal, following the cut off, very rapidly, if no heat transfer occurs at the surface. If the cut off is followed by convective cooling, the temperature uniformity in the insulation is found to be greater at a lower value of the surface heat transfer coefficient h. The regulation of the temperature which requires raising it to a given value and maintaining it at this level can be theoretically achieved by a particular variation of radiant flux with time. However, the variation is very hard to achieve in practice and the best method is found to be through a proper coupling of radiant flux with convective cooling. The necessary regulation can then be achieved by varying the surface convective coefficient and the fluid temperature.

References

1 Barnes, C. C., *Power Cables*, Second ed., Chapman and Mall Ltd., London, particularly, Chapter 13, "Power Cable Manufacture" and Chapter 22, "Plastic-Insulated Power Cables," 1966.

2 Clark, F. M., *Insulating Materials for Design and Engineering Practice*, Wiley, New York, Chapter 14(I), "Insulated Wires and Conductors" and Chapter 3, "Insulation Technology," 1962.

3 Kertscher, E., "Recent Developments in High Speed Insulation of Quality Telephone Wires," 22nd Inter. Wire and Cable Symposium, 1973; see also, *Proceedings 19th International Wire and Cable Symposium*, 1970.

4 Hardesty, E. C., and Myers, D. L., "Coiling Spring Cords," *The Western Electric Engineer*, Ap. 1962, p. 11.

5 Jaluria, Y., "A Study of Transient Heat Transfer in Long Insulated Wires," JOURNAL OF HEAT TRANSFER, TRANS. ASME, Series C, Vol. 98, 1976, p. 127.

6 Carslaw, H. S., and Jaeger, J. C., *Conduction of Heat in Solids*, Second ed., Oxford, 1959.

7 Gebhart, B., *Heat Transfer*, Second ed., McGraw-Hill, New York, 1971.

Approximate Solution for Convective Fins With Variable Thermal Conductivity

A. Muzzio[1]

Nomenclature

h = convective heat transfer coefficient
k = thermal conductivity
L = length of fin
N = dimensionless fin parameter = $[2hL^2/k_a w]^{1/2}$
T = temperature
w = thickness of fin
x = distance from insulated end
X = dimensionless distance = x/L
ϵ = thermal conductivity parameter = $(k_b - k_a)/k_a$
η = fin efficiency
θ = dimensionless temperature = $(T - T_a)/(T_b - T_a)$
σ = slope of the dimensionless thermal conductivity-temperature curve

Subscripts

a = ambient
b = base of fin

Introduction

The performance of fins (convecting, radiating, of both) has been shown by several workers to be significantly affected by variable thermal properties, particularly when large temperature differences exist.

While most methods of solution of these nonlinear problems involve numerical procedures, recently Aziz and Enamul Huq [4][2] have presented a closed form solution for a straight convecting fin with temperature dependent thermal conductivity obtained by the regular perturbation method.

---

[1] Asst. Professor, Faculty of Engineering, University of Pavia, Pavia, Italy.

[2] Numbers in brackets designate References at end of technical note.

Contributed by the Heat Transfer Division of THE AMERICAN SOCIETY OF MECHANICAL ENGINEERS. Manuscript received by the Heat Transfer Division April 12, 1976.

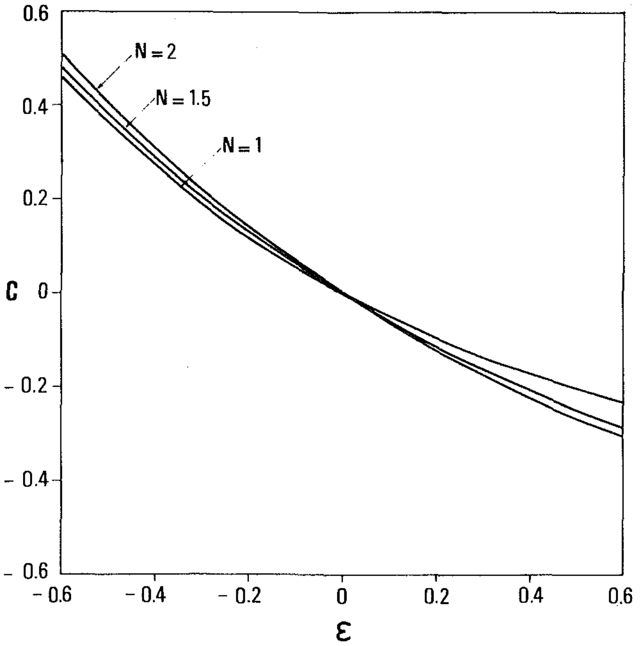

Fig. 1 Values of the coefficient C

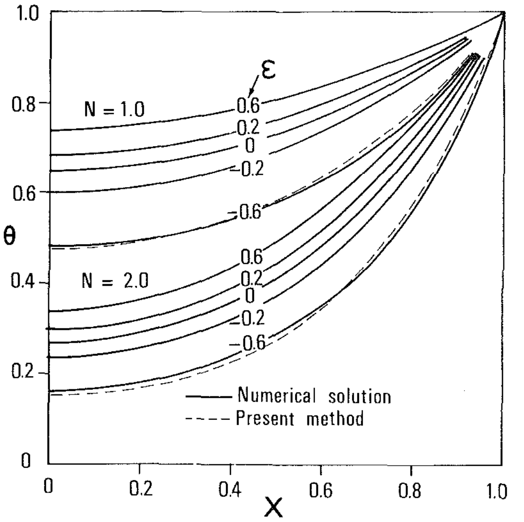

Fig. 2 Temperature distribution in convecting fins with variable thermal conductivity

This note treats an alternative approach based on the Galerkin method for obtaining approximate analytical solutions.

The results are compared with both the numerical and the perturbation solution.

Analysis

The analysis is referred to a straight rectangular convecting fin insulated at the tip under steady-state conditions. Both the convective heat transfer coefficient h and ambient fluid temperature T_a are assumed uniform. These conditions may not necessarily hold in all cases.

The thermal conductivity k of the fin's material is assumed to be a linear function of temperature according to:

$$k = k_a(1 + \sigma(T - T_a)) \tag{1}$$

where k_a is the thermal conductivity at temperature T_a. With reference to the sketch inserted in Fig. 3 in the one-dimensional approximation the energy balance equation gives:

$$P(\theta) = (1 + \epsilon\theta)\frac{d^2\theta}{dX^2} + \epsilon\left(\frac{d\theta}{dX}\right)^2 - N^2\theta = 0 \tag{2}$$

where

$$\theta = \frac{T - T_a}{T_b - T_a}, \quad X = \frac{x}{L}, \quad N^2 = \frac{2hL^2}{k_a w}, \quad \epsilon = \sigma(T_b - T_a) \tag{3}$$

Equation (2) is to be solved with boundary conditions:

$$\text{at } X = 0 \quad \frac{d\theta}{dX} = 0 \tag{4}$$

$$\text{at } X = 1 \quad \theta = 1 \tag{5}$$

An approximate solution is sought in the form:

$$\theta = \phi_0(X) + C\phi_1(X) = \frac{\cosh NX}{\cosh N} + C\left(\frac{\cosh 2NX}{\cosh 2N} - \frac{\cosh NX}{\cosh N}\right) \tag{6}$$

which identically satisfies the boundary conditions (4) and (5).

According to the Galerkin process the coefficient C is defined by the condition:

$$\int_0^1 P(\theta)\phi_1(X)dX = 0 \tag{7}$$

After substitution of equation (6) into equation (7) and integration one has:

$$\alpha C^2 + \beta C + \gamma = 0 \tag{8}$$

where:

$$\begin{aligned}\alpha = \epsilon\Bigg[& -\frac{2}{3}\tanh^3 2N - \frac{27}{40}\tanh 2N + \frac{1}{3}\tanh^3 N + \frac{3}{5}\tanh N \\ & + \frac{177}{40}\tanh 2N \tanh^2 N - 4\tanh N \tanh^2 2N + \frac{96}{15}\tanh 2N \\ & \tanh^2 N \frac{1 - \tanh^2 N}{1 + \tanh^2 N} + \frac{3}{8}N(1 - \tanh^2 N)^2 \frac{\tanh 2N}{\tanh N}\Bigg]\end{aligned} \tag{9}$$

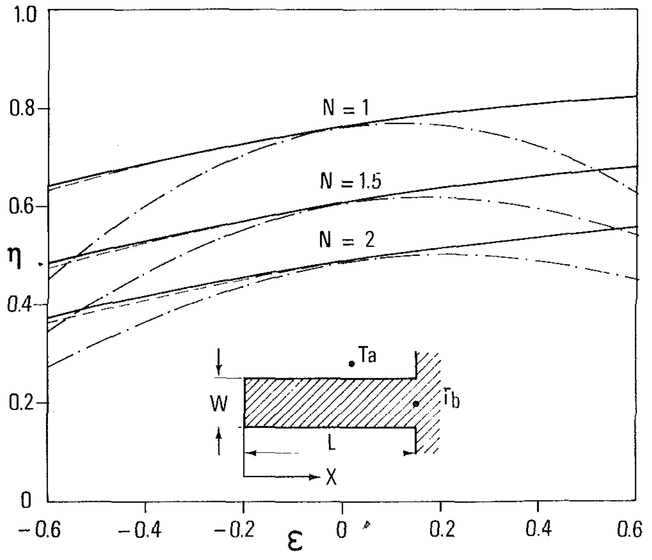

Fig. 3 Efficiency of convecting fins: — numerical solution; - - - present method; – • – perturbation solution [4]

$$\beta = \epsilon \left[\frac{14}{5} \tanh N - \frac{2}{3} \tanh^3 N - \frac{31}{40} \tanh 2N - \frac{59}{40} \tanh 2N \tanh^2 N \right.$$
$$- \frac{32}{15} \tanh 2N \tanh^2 N \frac{1 - \tanh^2 N}{1 + \tanh^2 N}$$
$$\left. - \frac{5}{8} N \frac{\tanh 2N}{\tanh N} (1 - \tanh^2 N)^2 \right]$$
$$- \frac{3}{2} \left[N(\tanh^2 2N - 1) - \tanh 2N \left(\frac{1}{3} \tanh^2 N - \frac{1}{2} \right) \right] \quad (10)$$

$$\gamma = \epsilon \left[\frac{1}{3} \tanh^3 N - \frac{1}{2} \tanh N + \frac{1}{4} N \frac{\tanh 2N}{\tanh N} (1 - \tanh^2 N)^2 \right] \quad (11)$$

The appropriate root of equation (8) is such that $\epsilon C \leq 0$; the other root has to be discarded since it gives rise to physically meaningless temperature distributions.

In Fig. 1 the values of the coefficient C are shown plotted versus ϵ with N as a parameter.

A comparison is made in Fig. 2 of the temperatures distributions $\theta(X)$, obtained by the present method for different values of N and ϵ, and the numerical solutions of the problem. It is observed that the accuracy of the approximate solution decreases as $|\epsilon|$ increases particularly for negative values of this parameter. However, the comparison is remarkably good since, for $\epsilon = -0.6$ and $N = 2$, the largest error does not exceed 9.7 percent.

In order to have a better accuracy with the larger $|\epsilon|$ values the trial function (6) would require modification to allow greater flexibility in approximating the true solution. The efficiency of the fin η defined as the ratio of the actual heat transfer rate to the heat transfer rate of an isothermal fin at temperature T_b is obtained from equation (6) as:

$$\eta = \int_0^1 \theta(X) dX = \frac{\tanh N}{N} \left[1 - C \frac{\tanh^2 N}{1 + \tanh^2 N} \right] \quad (12)$$

The values of η computed from equation (12) are shown in Fig. 3 versus ϵ ranging from -0.6 to 0.6 for three values of N, namely $N = 1.0, 1.5, 2.0$.

For purposes of comparison the corresponding curves obtained by numerical integration together with the perturbation solution [4] are plotted on the same figure.

The present solution matches almost exactly the numerical solution, the maximum value of the error being 3.6 percent, while the perturbation solution is significantly in error for ϵ exceeding ± 0.2.

From the analysis of the results it appears that the present solution can predict quite accurately the performance of fins with variable thermal conductivity.

References

1 Mikhlin, S. G., *The Numerical Performance of Variational Methods*, Wolters-Noordhoff Publishing, 1971.

2 Hung, H. M., and Appl, F. C., "Heat Transfer of Thin Fins With Temperature Dependent Thermal Properties and Internal Heat Generation," JOURNAL OF HEAT TRANSFER, TRANS. ASME, Series C, Vol 89, May 1967, p.p. 155–162.

3 Kosarev, D. A., and Nevrovskii, V. A., "Calculating Heat Transfer Through Finned Surfaces With Variable Coefficient of Thermal Conductivity of the Material," *Thermal Engineering*, No. 2, 1972, pp. 140–141.

4 Aziz, A., and Enamul Huq, S. M., "Perturbation Solution for Convecting Fin With Variable Thermal Conductivity," JOURNAL OF HEAT TRANSFER, TRANS. ASME, Series C, Vol. 97, May 1975, pp. 300–301.

Condensation on a Rotating Disk With Constant Axial Suction

S. P. Chary[1] and P. K. Sarma*[2]

An excellent review of the problem of convective heat transfer in rotating systems has been given by Frank Kreith [1].[3] The problems of condensation of vapors on cooled rotating disks and cones have been solved by Sparrow, et al. [2–4]. The effects of uniform suction on the steady flow due to a rotating disk has been studied by Stuart [5]. Jain and Bankoff [6], Yang [7], and Murthy, et al. [8] solved the problem of laminar film condensation on vertical surfaces with suction applied at the permeable wall. The results indicate profound influence of suction parameter on the compactness of the condenser.

This note is an extension of the pioneering work of Sparrow and Gregg [2, 3] on the phenomena of condensation on a rotating disk. The physical configuration and the coordinate system are essentially the same as those outlined in [2, 3]. However, the dependant variable describing the velocity in Z-direction is redefined. In problems pertaining to rotating disks, it is a standard practice to assume the velocity in Z-direction to be totally independent of the radial coordinate r. As such, constant β can be added to, or subtracted from, $H(\eta)$ to account for blowing or suction, respectively, at the permeable wall, still retaining the facility and ease of applying similarity transformations and the boundary conditions as suggested by Sparrow, et al. [2, 3]. Thus,

$$V_z = \sqrt{\nu\omega}\, [H(\eta) - \beta] \quad (1)$$

where

$$\beta = \frac{V_0}{\sqrt{\nu\omega}} \quad \text{and} \quad \eta = Z \left(\frac{\omega}{\nu} \right)^{1/2}$$

V_0 being the suction velocity at the permeable wall and η being the dimensionless coordinate normal to the disk surface.

$$V_r = r\omega F(\eta) \quad (2)$$

$$V_\phi = r\omega G(\eta) \quad (3)$$

Substituting equations (1)–(3) in the respective equations of conservation of mass, momentum, and energy, and further simplifying the resulting set of ordinary differential equations yields:

$$H''' = H'' (H - \beta) - \frac{1}{2} (H')^2 + 2G^2 \quad (4)$$

$$G'' = (H - \beta)G' - H'G \quad (5)$$

$$\theta'' = \Pr(H - \beta)\theta' \quad (6)$$

Thus, equations (4)–(6), together with the following boundary conditions, will constitute a full set of equations that gives complete solution to the velocity and temperature distributions in the condensate layer.

At the permeable wall at $\eta = 0$

---

[1] Department of Mechanical Engineering, Delhi College of Engineering, Delhi, India.

[2] Department of Mechanical Engineering, Andhra University, Waltair, India; presently Visiting Professor, Department of Mechanical Engineering, Military Technical College, Bagdad, Iraq.

[3] Numbers in brackets designate References at end of technical note.

Contributed by the Heat Transfer Division of THE AMERICAN SOCIETY OF MECHANICAL ENGINEERS. Manuscript received by the Heat Transfer Division March 8, 1976.

$$\beta = \epsilon\left[\frac{14}{5}\tanh N - \frac{2}{3}\tanh^3 N - \frac{31}{40}\tanh 2N - \frac{59}{40}\tanh 2N\tanh^2 N - \frac{32}{15}\tanh 2N\tanh^2 N\,\frac{1-\tanh^2 N}{1+\tanh^2 N} - \frac{5}{8}N\,\frac{\tanh 2N}{\tanh N}(1-\tanh^2 N)^2\right] - \frac{3}{2}\left[N(\tanh^2 2N - 1) - \tanh 2N\left(\frac{1}{3}\tanh^2 N - \frac{1}{2}\right)\right] \quad (10)$$

$$\gamma = \epsilon\left[\frac{1}{3}\tanh^3 N - \frac{1}{2}\tanh N + \frac{1}{4}N\,\frac{\tanh 2N}{\tanh N}(1-\tanh^2 N)^2\right] \quad (11)$$

The appropriate root of equation (8) is such that $\epsilon C \leq 0$; the other root has to be discarded since it gives rise to physically meaningless temperature distributions.

In Fig. 1 the values of the coefficient C are shown plotted versus ϵ with N as a parameter.

A comparison is made in Fig. 2 of the temperatures distributions $\theta(X)$, obtained by the present method for different values of N and ϵ, and the numerical solutions of the problem. It is observed that the accuracy of the approximate solution decreases as $|\epsilon|$ increases particularly for negative values of this parameter. However, the comparison is remarkably good since, for $\epsilon = -0.6$ and $N = 2$, the largest error does not exceed 9.7 percent.

In order to have a better accuracy with the larger $|\epsilon|$ values the trial function (6) would require modification to allow greater flexibility in approximating the true solution. The efficiency of the fin η defined as the ratio of the actual heat transfer rate to the heat transfer rate of an isothermal fin at temperature T_b is obtained from equation (6) as:

$$\eta = \int_0^1 \theta(X)dX = \frac{\tanh N}{N}\left[1 - C\,\frac{\tanh^2 N}{1+\tanh^2 N}\right] \quad (12)$$

The values of η computed from equation (12) are shown in Fig. 3 versus ϵ ranging from -0.6 to 0.6 for three values of N, namely N = 1.0, 1.5, 2.0.

For purposes of comparison the corresponding curves obtained by numerical integration together with the perturbation solution [4] are plotted on the same figure.

The present solution matches almost exactly the numerical solution, the maximum value of the error being 3.6 percent, while the perturbation solution is significantly in error for ϵ exceeding ± 0.2.

From the analysis of the results it appears that the present solution can predict quite accurately the performance of fins with variable thermal conductivity.

References

1 Mikhlin, S. G., *The Numerical Performance of Variational Methods*, Wolters-Noordhoff Publishing, 1971.

2 Hung, H. M., and Appl, F. C., "Heat Transfer of Thin Fins With Temperature Dependent Thermal Properties and Internal Heat Generation," JOURNAL OF HEAT TRANSFER, TRANS. ASME, Series C, Vol 89, May 1967, p.p. 155–162.

3 Kosarev, D. A., and Nevrovskii, V. A., "Calculating Heat Transfer Through Finned Surfaces With Variable Coefficient of Thermal Conductivity of the Material," *Thermal Engineering*, No. 2, 1972, pp. 140–141.

4 Aziz, A., and Enamul Huq, S. M., "Perturbation Solution for Convecting Fin With Variable Thermal Conductivity," JOURNAL OF HEAT TRANSFER, TRANS. ASME, Series C, Vol. 97, May 1975, pp. 300–301.

Condensation on a Rotating Disk With Constant Axial Suction

S. P. Chary[1] and P. K. Sarma*[2]

An excellent review of the problem of convective heat transfer in rotating systems has been given by Frank Kreith [1].[3] The problems of condensation of vapors on cooled rotating disks and cones have been solved by Sparrow, et al. [2–4]. The effects of uniform suction on the steady flow due to a rotating disk has been studied by Stuart [5]. Jain and Bankoff [6], Yang [7], and Murthy, et al. [8] solved the problem of laminar film condensation on vertical surfaces with suction applied at the permeable wall. The results indicate profound influence of suction parameter on the compactness of the condenser.

This note is an extension of the pioneering work of Sparrow and Gregg [2, 3] on the phenomena of condensation on a rotating disk. The physical configuration and the coordinate system are essentially the same as those outlined in [2, 3]. However, the dependant variable describing the velocity in Z-direction is redefined. In problems pertaining to rotating disks, it is a standard practice to assume the velocity in Z-direction to be totally independent of the radial coordinate r. As such, constant β can be added to, or subtracted from, $H(\eta)$ to account for blowing or suction, respectively, at the permeable wall, still retaining the facility and ease of applying similarity transformations and the boundary conditions as suggested by Sparrow, et al. [2, 3]. Thus,

$$V_z = \sqrt{\nu\omega}\,[H(\eta) - \beta] \quad (1)$$

where

$$\beta = \frac{V_0}{\sqrt{\nu\omega}} \quad \text{and} \quad \eta = Z\left(\frac{\omega}{\nu}\right)^{1/2}$$

V_0 being the suction velocity at the permeable wall and η being the dimensionless coordinate normal to the disk surface.

$$V_r = r\omega F(\eta) \quad (2)$$

$$V_\phi = r\omega G(\eta) \quad (3)$$

Substituting equations (1)–(3) in the respective equations of conservation of mass, momentum, and energy, and further simplifying the resulting set of ordinary differential equations yields:

$$H''' = H''(H - \beta) - \frac{1}{2}(H')^2 + 2G^2 \quad (4)$$

$$G'' = (H - \beta)G' - H'G \quad (5)$$

$$\theta'' = \Pr(H - \beta)\theta' \quad (6)$$

Thus, equations (4)–(6), together with the following boundary conditions, will constitute a full set of equations that gives complete solution to the velocity and temperature distributions in the condensate layer.

At the permeable wall at $\eta = 0$

---

[1] Department of Mechanical Engineering, Delhi College of Engineering, Delhi, India.

[2] Department of Mechanical Engineering, Andhra University, Waltair, India; presently Visiting Professor, Department of Mechanical Engineering, Military Technical College, Bagdad, Iraq.

[3] Numbers in brackets designate References at end of technical note.

Contributed by the Heat Transfer Division of THE AMERICAN SOCIETY OF MECHANICAL ENGINEERS. Manuscript received by the Heat Transfer Division March 8, 1976.

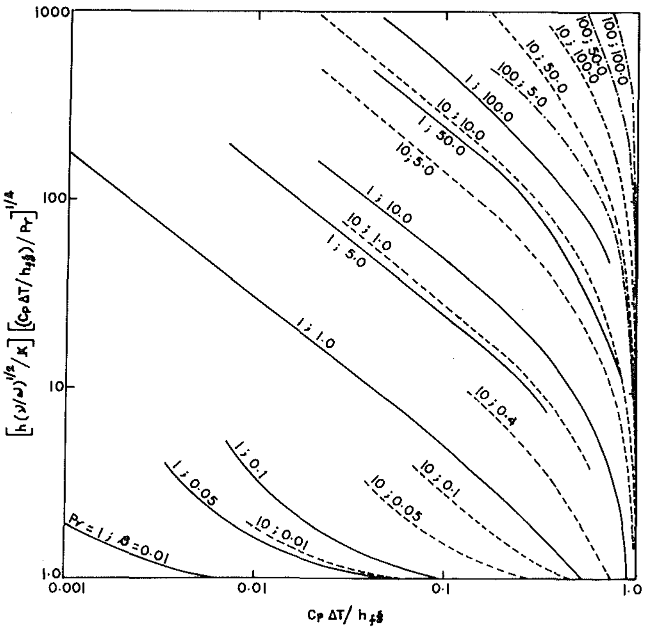

Fig. 1

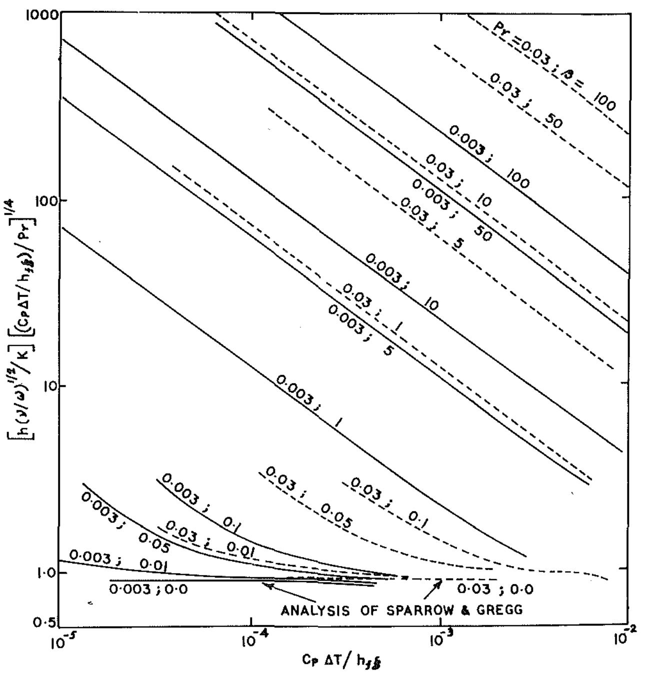

Fig. 2.

$$H = H' = F = 0 \quad G = 1,$$

$$V_z = -V_0 \text{ (suction velocity)}$$

$$\theta = (T - T_w)/(T_s - T_w) = 0 \tag{7}$$

Further, assuming zero shear condition at the interface, i.e., at $\eta = \eta_\delta$

$$H'' = G' = 0, \quad \theta = 1 \tag{8}$$

When β is made zero the problem reduces to the case solved by Sparrow and Gregg [2, 3]. Then the overall energy balance can further be added to interpret the condensate film thickness in terms of $C_p\Delta T/h_{fg}$, the heat capacity parameter.

Thus, we have

$$(\mathrm{Pr}/(C_p\Delta T/h_{fg})) \quad [H(\eta_\delta) - \beta] = \theta'(\eta_\delta) \tag{9}$$

Heat Transfer Coefficient

From a practical point of view, it is the heat transfer coefficient that is important and it can be calculated as follows:

$$\frac{h}{K}\left(\frac{\nu}{\omega}\right)^{1/2} = \left.\frac{\partial\theta}{\partial\eta}\right|_{\eta=0} \tag{10}$$

Equations (4)–(6) are solved simultaneously on IBM 360 for different values of η_δ employing Runge-Kutta numerical procedure with the necessary iterative techniques satisfying boundary conditions (7) and (8). The heat transfer coefficients are shown plotted in Figs. 1 and 2 and the ranges investigated are $0.003 \leqslant \mathrm{Pr} \leqslant 100$ for $0.01 \leqslant \beta \leqslant 100$. From the plots it is obvious that as the suction parameter β increases, heat transfer rates increase for a given value of the heat capacity parameter $C_p\Delta T/h_{fg}$. It is obvious that at low values of $(C_p\Delta T/h_{fg})$ the increase in condensation heat transfer is considerable. For example: when $\beta = 50$, $\mathrm{Pr} = 10$, $C_p\Delta T/h_{fg} = 0.4$, and $(h_\beta/h_{\beta} = 0) = 339$, which is undoubtedly a substantial gain in the heat transfer rates within a practicable range of $C_p\Delta T/h_{fg}$.

Limiting Solutions

The limiting solution for very thin films of the condensate can be obtained making use of the equations (26)–(28) of reference [2] with $H(\eta_\delta)$ being replaced by $[H(\eta_\delta) - \beta]$

Hence, we have

$$H(\eta_\delta) - \beta = -\left[\frac{2}{3}\eta_\delta{}^3 + \beta\right] \tag{11}$$

$$\theta'(\eta_\delta) = -1/\eta_\delta \tag{12}$$

Thus, equations (9), (11), and (12) yield

$$\frac{\mathrm{Pr}}{C_p\Delta T/h_{fg}}\left(\beta + \frac{2}{3}\eta_\delta{}^3\right) = \frac{1}{\eta_\delta} \tag{13}$$

The heat transfer coefficient can be obtained from equation (10) as

$$\frac{h\left(\frac{\nu}{\omega}\right)^{1/2}}{K} = \frac{1}{\eta_\delta} \tag{14}$$

Thus, for given values of β, η_δ we can, respectively, obtain $(\mathrm{Pr}/C_p\Delta T/h_{fg})$ and the nondimensional heat transfer coefficient from equations (13) and (14). It is observed that the limiting solutions are in agreement with the computer results for small values of η_δ.

In conclusion this note presents the problem of phase transformation of vapors into liquid state in the presence of constant axial suction at the permeable condensing surface and the significant conclusion is that the heat transfer coefficient can be increased to any desired level by properly choosing the value of β, the suction parameter.

References

1 Kreith Frank, "Convective Heat Transfer in Rotating Systems," *Advances in Heat Transfer,* Vol. 5, Thomas F. Irvine and James P. Hartnett, eds., 1968.

2 Sparrow, E. M., and Gregg J. L., "A Theory of Rotating Condensation," JOURNAL OF HEAT TRANSFER, TRANS. ASME, Series C, Vol. 81, 1959, pp. 113–120.

3 Sparrow, E. M., and Gregg, J. L., "The Effect of Vapor Drag on Rotating Condensation," JOURNAL OF HEAT TRANSFER TRANS. ASME, Series C, Vol. 82, 1960, No. 1 pp. 71–72.

4 Sparrow, E. M., and Hartnett, J. P., "Condensation on a Rotating Cone," JOURNAL OF HEAT TRANSFER, TRANS. ASME Series C Vol. 83, 1961, No. 1 pp. 101–102.

5 Stuart, J. T., "On the Effects of Uniform Suction on the Steady Flow Due

to a Rotating Disc" *Quarterly Journal of Mechanics and Applied Mathematics*, Vol. 7, 1954, pp. 446–467.

6 Jain, K. C., and Bankoff, S. G., "Laminar Film Condensation on a Porous Vertical Wall With Uniform Suction Velocity" JOURNAL OF HEAT TRANSFER TRANS. ASME, Series C, Vol. 86, 1964, pp. 481–489.

7 Yang J. W., "Effect of Uniform Suction on Laminar Film Condensation on a Porous Vertical Wall," JOURNAL OF HEAT TRANSFER, TRANS. ASME, Series C, Vol. 92, 1970, pp. 252–256.

8 Murthy, K. N., Sarma, C. K., and Sarma, P. K. "Analysis of Laminar Film Condensation on Vertical Plates With Variable Suction" Paper presented at Fifth International Heat and Mass Transfer Conference held in Tokyo, Sept. 3–7, 1974.

journal of heat transfer
discussion

Perturbation Solution for Convecting Fin With Variable Thermal Conductivity[1]

R. J. Krane.[2] The authors have provided us with an interesting example demonstrating the utility of perturbation techniques in solving heat transfer problems. It appears, however, that they have incorrectly retained terms of $0(\epsilon^2)$ in equations (13), (14), and (15) since there are contributions to these terms from the second-order solution which they do not include. This can easily be shown by displaying equation (13) in the following form:

$$\frac{qL}{k_a w(T_b - T_a)} = (1+\epsilon)\left.\frac{d\theta}{dX}\right|_{X=1}$$

$$= (1+\epsilon)\left(\left.\frac{d\theta_0}{dX}\right|_{X=1} + \epsilon\left.\frac{d\theta_1}{dX}\right|_{X=1} + \epsilon^2\left.\frac{d\theta_2}{dX}\right|_{X=1} + \cdots\right)$$

Expanding and retaining terms up to $0(\epsilon^2)$ gives

$$\frac{qL}{k_a w(T_b - T_a)} = \left.\frac{d\theta_0}{dX}\right|_{X=1} + \epsilon\left(\left.\frac{d\theta_0}{dX}\right|_{X=1} + \left.\frac{d\theta_1}{dX}\right|_{X=1}\right) + \epsilon^2\left(\left.\frac{d\theta_1}{dX}\right|_{X=1} + \underline{\left.\frac{d\theta_2}{dX}\right|_{X=1}}\right) + \cdots$$

where the missing terms of $0(\epsilon^2)$ in equation (13) of the technical note arise from the underlined term above. This error is then propagated into equations (14) and (15) and Fig. 2.

Thus, for a solution correct to $0(\epsilon)$, equations (13), (14), and (15) should read

$$\frac{qL}{k_a w(T_b - T_a)} = N \tanh N(1 + \tfrac{1}{3}\epsilon \tanh^2 N) \qquad (13)$$

$$\eta = (\tanh N/N)(1 + \tfrac{1}{3}\epsilon \tanh^2 N) \qquad (14)$$

and

$$6N(1 + \epsilon \tanh^2 N) = \sinh 2N + \tfrac{2}{3}\epsilon \tanh N \sinh^2 N \qquad (15)$$

The solution of the correct form of equation (15) is shown here plotted along with the authors' solution from Fig. 2 of the technical note. The original solution is shown to have an error of approximately 6 percent at $\epsilon = \pm 0.5$.

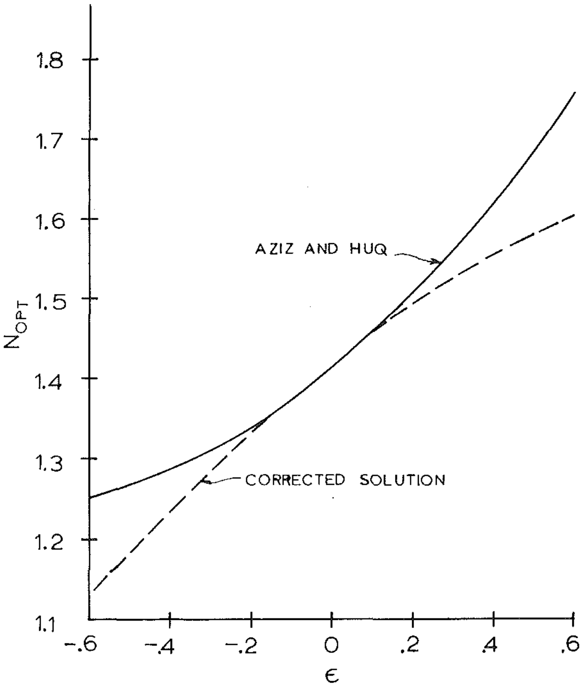

Fig. 1

Authors' Closure

It is true that part of the contribution from second-order term was *inadvertently retained in deriving equations* (13), (14), and (15). The forms of these equations correct to $0(\epsilon)$ are the ones given by Prof. R. J. Krane. However, it has since been found that with the inclusion of second-order term, the perturbation solution virtually coincides with the numerical solution in the ranges of ϵ and N considered previously.[1] The second-order problem is

$$\frac{d^2\theta_2}{dX^2} - N^2\theta_2 = -\theta_0\frac{d^2\theta_1}{dX^2} - \theta_1\frac{d^2\theta_0}{dX^2} - 2\frac{d\theta_0}{dX}\frac{d\theta_1}{dX} \qquad (16)$$

$$X = 0,\quad \frac{d\theta_2}{dX} = 0;\quad X = 1,\quad \theta_2 = 0 \qquad (17)$$

---

[1] By A. Aziz and S. M. Enamual Huq, published in the May 1975 issue of the JOURNAL OF HEAT TRANSFER, TRANS. ASME, Series C, Vol. 97, pp. 300–301.

[2] Asst. Professor, Department of Mechanical Engineering and Mechanics, West Virginia University, Morgantown, W. V.

and the solution is[3]

$$\theta_2 = \frac{1}{6}\operatorname{sech}^3 N\left[\left(\frac{4}{3}\operatorname{sech}^2 N\cosh^2 2N - \frac{9}{8}\operatorname{sech} N\cosh 3N - \frac{1}{2}N\tanh N\right)\cosh NX - \frac{4}{3}\operatorname{sech} N\cosh 2N\cosh 2NX + \frac{9}{8}\cosh 3NX + \frac{1}{2}NX\sinh NX\right] \quad (18)$$

Based on the three-term solution, q is given by

$$\frac{qL}{k_a w(T_b - T_a)} = N\tanh N + \frac{1}{3}\epsilon N\tanh^3 N + \epsilon^2\left\{\frac{1}{3}N\tanh^3 N - N\tanh N + \frac{1}{6}\operatorname{sech}^3 N\left[\left(\frac{4}{3}\operatorname{sech}^2 N\cosh^2 2N - \frac{9}{8}\operatorname{sech} N\cosh 3N - \frac{1}{2}N\tanh N\right)N\sinh N - \frac{8}{3}N\operatorname{sech} N\cosh 2N\sinh 2N + \frac{27}{8}N\sinh 3N + \frac{1}{2}N(\sinh N + N\cosh N)\right]\right\} \quad (19)$$

The fin efficiency η is obtained by simply dividing equation (19) by N^2. Equation giving N_{opt} follows from equation (19) but is not given here because it was found that the inclusion of second-order term does not appreciably alter the curve showing the relationship between N_{opt} and ϵ obtained from the two-term solution. The authors, therefore, recommend the use of equation (19) for heat transfer rate and fin efficiency but for N_{opt}, the corrected solution provided by Krane may be used.

---

[3] Aziz, A., and Benzies, J. Y., "Application of Perturbation Techniques to Heat Transfer Problems With Variable Thermal Properties," *International Journal of Heat and Mass Transfer*, Vol. 19, 1976, pp. 271–276.

ERRATUM

Erratum: A. S. El-Ariny, J. A. Sabbagh, and M. A. Obeid, "Laminar Film Condensation Heat Transfer in the Presence of Electric and Magnetic Fields," published in the Nov. 1975 issue of the JOURNAL OF HEAT TRANSFER, pp. 628–629.

The definition of R_E appearing on the third line below equation (3) should read

$$R_E = E/BU_\infty$$